SCHOLARLY PUBLICATIONS

A CURRENT AWARENESS BULLETIN
OF RESEARCH OUTPUT

@DTU

(20th Edition)

AUGUST 2014

BY: CENTRAL LIBRARY

DELHI TECHNOLOGICAL UNIVERSITY
(FORMERLY *DELHI COLLEGE OF ENGINEERING)*
GOVT. OF N.C.T. OF DELHI
SHAHBAD DAULATPUR, MAIN BAWANA ROAD
DELHI 110042

PREFACE

This is the Twentieth Issue of Current Awareness Bulletin started by Delhi Technological University, Central Library. The aim of the bulletin is to compile, preserve and disseminate information published by the faculty, students and alumni for mutual benefits. The bulletin also aims to propagate the intellectual contribution of Delhi Technological University (DTU) as a whole to the academia.

The bulletin contains information resources available in the internet in the form of articles, reports, presentations published in international journals, websites, etc. by the faculty and students of DTU. The publications of faculty and student which are not covered in this bulletin may be because of the reason that the full text either was not accessible or could not be searched by the search engine used by the library for this purpose.

The learned faculty and students are requested to provide their uncovered publications to the library either through email or in CD, etc to make the bulletin more comprehensive.

This issue contains the information published during August 2014. The arrangement of the contents is alphabetical. The full text of the article which is either subscribed by the university or available in the web is provided in this bulletin.

Central Library

CONTENTS

1. A GENETIC ALGORITHM FOR FINITE STATE AUTOMATA, ***Aviral Takkar,*** Computer Engineering Department. DTU

2. A local theory of effect of beam pre-modulation on gain and efficiency in a surface wave pumped free electron laser, ***Suresh C. Sharma***, Department of Applied Physics, DTU, Jyotsna Sharma, Anuradha Bhasin and V. K. Jain

3. A New Classification and Applicability of Software Reliability Models Kuldeep Singh Kaswan, Sunita Choudhary, ***Kapil Sharma,*** Computer Science & Engineering, DTU

4. A study on particle creation in modified f(R, T) theory of gravity, ***Vijay Singh*** and ***C. P. Singh***, Department of Applied Mathematics, DTU

5. AN IMPROVED METHOD FOR SOIL DNA EXTRACTION TO STUDY THE MICROBIAL ASSORTMENT WITHIN RHIZOSPHERIC REGION, Faria Fatima, Neelam Pathak and ***Smita Rastogi Verma***, Department of Biotechnology, DTU

6. Average Absolute Frequency Deviation Value Based Active Islanding Detection Technique, R. S. Bhatia, and D. K. Jain, ***Pankaj Gupta***, electrical engineering, DTU

7. Composite Wound Dressing for Drug Release, ***Roli Purwar***, ***Poonam Rajput***, and ***Chandra Mohan Srivastava***, Applied Chemistry and Polymer Technology, DTU

8. Detecting Computer Viruses, ***Manju Khari***, Chetna Bajaj

9. Effect of dust charge fluctuations on upper hybrid wave instabilities in magnetized dusty plasma, Jyotsna Sharma, Ajay Gahlot, V. K. Jain and ***Suresh C. Sharma,*** Applied Physics, DTU

10. Effluent Treatment for Sago Industry Using Zeolite and Activated Carbon, ***S. Anbukumar1, Narad Muni Prasad1, M. Ashok Kumar***, Civil Engineering, DTU

11. Energy transfer and NIR emission in rare earth tri-doped barium lanthanum fluoro tellurite glasses, J. Suresh Kumar, K. Pavani, G. Venkataiah, M. P. F. Graça, M. J. Soares and ***M. Jayasimhadri***, Applied Physics, DTU

12. Fault prediction considering threshold effects of objectoriented metrics, ***Ruchika Malhotra,*** Software Engineering, ***and Ankita Jain Bansal***, Computer Engineering, DTU

13. Feature Level Fusion of Multimodal Images Using Haar Lifting Wavelet Transform, Jayant Bharadwaj and ***Sudipta Majumdar***, Electronics & Communication Engineering

14. In silico analysis and modeling of putative T cell epitopes for vaccine design of Toscana virus, Amisha Jain, Pranav Tripathi, Ritu Chaudhary, Ajeet Singh and ***Aniket Shrotriya,*** Department of Biotechnology, DTU

15. In situ grafted nanostructured ZnO/carboxymethyl cellulose nanocomposites for efficient delivery of curcumin to cancer, Laxmi Upadhyaya, Vishnu Agarwal, A.C. Pandey, Shiv P. Verma, Parimal Das, R. P. Tewari and ***Jay Singh***, Applied Chemistry, DTU

16. Luminescence characterization of Eu3þ doped Zinc Alumino Bismuth Borate Glasses for Visible Red Emission Applications, K.Swapna1, Sk.Mahamuda, T. Sasikala, P. Packiyaraj, L. Rama Moorthy and G. Vijaya Prakash and, ***A. Srinivasa Rao,*** Applied Physics, DTU

17. Method for Improving Thermal Performances of Vapour Compression Refrigeration Systems Using Energy and Exergy Analysis for Reducing Global Warming and Ozone Depletioning Using Ecofriendly Refrigerants, ***R.S. Mishra,*** Mechanical Engineering Department, DTU

18. Microstructure and mechanical properties of thermoelectric nanostructured n-type silicon-germanium alloys synthesized employing spark plasma sintering, Bhasker Gahtori, S. K. Tripathy, Kriti Tyagi, A. K. Srivastava, and Ajay Dhar, ***Sivaiah Bathula*** and ***M. Jayasimhadri***, Applied Physics, DTU

19. Motor Vehicle Exhaust Emissions in Delhi, Manish Jain, ***Shashank Mohan*** and ***Amit Pal***, Mechanical Engineering, DTU

20. Mutational Consequences of Aberrant Ion Channels in Neurological Disorders, ***Dhiraj Kumar, *Rashmi K. Ambasta*** and Pravir Kumar, Department of Biotechnology, DTU

21. NFC Based Secure Mobile Healthcare System, ***Divyashikha Sethial, *Daya Gupta, *Tanuj Mittal, *Ujjwal Arora,*** Computer Engineering, DTU and Huzur Saran

22. Non-Blind Audio Watermarking Scheme Based on Empirical Mode Decomposition, ***Jeebananda Panda***, Karan Raj Gera, and ***Asok Bhattacharyya***, Deptt of Electronics and Communication Engineering, DTU

23. Performance Analysis of a Shunt Compensator Controlled Using Modified Synchronous Reference Theory, ***Alka Singh,*** Department of Electrical Engineering, DTU

24. Plastic Waste in India- Management and Utilisation, ***Aakriti Makker, *Arushi Gupta*** and ***Lovleen Gupta***, Department of Environmental Engineering, DTU

25. REALIZATION OF MULTIPLEOPERAND ADDER-SUBTRACTOR BASED ON VEDIC MATHEMATICS, ***NEETA PANDEY, *RAJESHWARI PANDEY, *SAMIKSHA AGARWAL, *PRINCE KUMAR***, Department of Electronics and Communication Engineering, DTU

26. SINGLE CDBA BASED CURRENT MODE FIRST ORDER MULTIFUNCTION FILTER, RISHI PAL, RAMESH CHANDRA TIWARI, ***RAJESHWARI PANDEY*** and ***NEETA PANDEY,*** Dept.of Electronics and Communication Engineering, DTU

27. STRENGTH & DENSITY OF AN AUTOCLAVED AERATED CONCRETE USING VARIOUS AIR ENTRAINING AGENTS, ***Shashank Gupta*** and ***Shiva Garg,*** Civil Engineering, DTU

28. Tb3+ doped Zinc Alumino Bismuth Borate Glasses for Green Emitting Luminescent Devices, K. Swapna, Sk. Mahamuda, ***A. Srinivasa Rao***, ***M. Jayasimhadri***, Suman Shakya and G. Vijaya Prakash, Applied Physics, DTU

29. Time-Domain Solution for Transmitted Field through Low-loss Dielectric Obstacles in a Microcellular and Indoor Scenario for UWB Signals, P. Tewari, ***S. Soni***, and ***B. Bansal***, Electronics and Communication Engineering, DTU

30. Women Engineers: A Comparative Study between India and Australia, Er. Susan Lee Fenton and ***Dr. Seema Singh,*** Economics, DTU

***Faculty**	**@Research Scholar**	**$PG Scholar**
#Alumni	**£Undergraduate Student**	**~ Ex Faculty**
! Teaching-cum-Research Fellow	**<Ex Research Scholar**	**>Ex PG Scholar**

Plasma Science and Applications (ICPSA 2013)
International Journal of Modern Physics: Conference Series
Vol. 32 (2014) 1460351 (7 pages)
© The Author
DOI: 10.1142/S2010194514603512

World Scientific
www.worldscientific.com

A local theory of effect of beam pre-modulation on gain and efficiency in a surface wave pumped free electron laser

Jyotsna Sharma

Physics Group, School of Environmental Sciences, Jawaharlal Nehru University, New Delhi-110067, India
bjyotsna28@yahoo.com

Suresh C. Sharma

Department of Applied Physics, Delhi Technological University, Shahbad Daulatpur, Delhi-110042, India
suresh321sharma@gmail.com

Anuradha Bhasin

Department of Electronics and Communications, NIEC, Delhi, India
anudr123@gmail.com

V. K. Jain

Physics Group, School of Environmental Sciences, Jawaharlal Nehru University, New Delhi-110067, India
vkj0400@mail.jnu.ac.in

Published 13 August 2014

A pre-modulated relativistic electron beam (REB) counter propagating to the surface wave in the vacuum region Compton backscatters the surface wave into a high frequency radiation. The surface wave extends into the vacuum region and can be employed as a wiggler for the generation of sub-millimeter waves. The growth rate and gain were evaluated for a typical FEL (Free Electron Laser) parameters and It is found that the growth rate and gain of the surface wave pumped free electron laser increases with the modulation index. Moreover, the growth rate of the FEL (Free electron Laser) instability scales as one-third power of the beam density in the Compton regime.

Keywords: Relativistic electron beam; Compton backscatters; Growth rate.

1. Introduction

The free electron laser (FEL) is an attractive and high power microwave device in which a relativistic electron beam propagating through a periodic magnetic field is used to amplify or generate coherent radiation of emission[1-4].

This is an Open Access article published by World Scientific Publishing Company. It is distributed under the terms of the Creative Commons Attribution 3.0 (CC-BY) License. Further distribution of this work is permitted, provided the original work is properly cited.

Int. J. Mod. Phys. Conf. Ser. 2014.32. Downloaded from www.worldscientific.com
by 14.139.251.100 on 08/18/14. For personal use only.

Recently, there has been a great deal of interest in studying the free electron laser (FEL) and Cerenkov free electron laser (CFEL)[3,5-15] using pre-bunched electron beams. Sharma and Bhasin[9] have studied the gain and efficiency enhancement in a Cerenkov free electron laser using pre-bunched electron beam in a dielectric loaded waveguide. They have found that the growth rate, efficiency and gain of the (Cerenkov Free Electron Laser) CFEL increase with the modulation index. They have the largest value when the modulation index approaching unity and the velocity of pre-bunched beam is comparable to the phase velocity of the radiation wave. Sharma and Tripathi[11] have also examined the effect of beam pre-bunching on gain and efficiency in a free electron laser.

In this paper, we have studied the generation of sub-millimeter waves by employing pre-modulated relativistic electron beams using surface plasma wave over a plasma–vacuum interface as a wiggler. The surface waves acquire large wave number k_{z0} around pump wave frequency $\omega_0 = \omega_p/\sqrt{2}$, hence can produce sub-millimeter waves using not too high energy electron beams.

Int. J. Mod. Phys. Conf. Ser. 2014.32. Downloaded from www.worldscientific.com
by 14.139.251.100 on 08/18/14. For personal use only.

2. Theoretical Model

Consider a plasma–vacuum interface at $x=0$ with plasma occupying the half space ($x<0$). The plasma is unmagnetized with effective permittivity given by

$$\varepsilon = 1 - \frac{\omega_p^2}{\omega^2}. \tag{1}$$

It can be characterized by lattice dielectric constant ε_L and a.c. conductivity σ i.e,

$$\varepsilon = \varepsilon_L - \frac{4\pi i\sigma}{\omega_0}$$

where the value of ε_L is 1 for plasma, and $\sigma = \frac{n_0 e^2}{m_e \omega_0}$, n_0 is the plasma density, e and m_e are the charge and mass of the electrons, respectively. Hence, on solving Eq. (1) the effective permittivity of plasma is given as

$$\varepsilon = 1 - \frac{\omega_p^2}{\omega_0^2}, \tag{2}$$

where ω_0 is the frequency of surface plasma wave, ω_p is the plasma frequency and is given as $\omega_p^2 = 4\pi n_0 e^2/m_e$. Consider a surface wave propagating along the interface with electric field vector given as

$$\overrightarrow{E} = \overrightarrow{a_0}\, e^{-i(\omega_0 t - k_{z0} z)} \tag{3}$$

Where $\overrightarrow{a_0}$ shows the amplitude of the surface wave. Applying the continuity of E_z and εE_z at $x = 0$, one obtains the dispersion relation for SPW $\varepsilon = \frac{k_{II}}{k_I}$, which gives

$$k_{z0}^2 = \frac{\omega_0^2}{c^2}\left(\frac{\varepsilon}{1+\varepsilon}\right). \tag{4}$$

The surface wave remains localized near the plasma –vacuum interface and is spatially damped away from the interface when $1+\varepsilon < 0, i.e., \omega_0 < \omega_p/\sqrt{2}$ and from eq. (4) we get

$$k_{z0}^2 = \frac{\omega_0^2(1-\omega_p^2/\omega_0^2)}{c^2\ 2(1-\omega_p^2/2\omega_0^2)}. \tag{5}$$

As ω_0/ω_p increases, the phase velocity of SPW decreases. It means the surface waves are strongly localized near the surface.

3. Parametric Instability Analysis

Let a relativistic pre-bunched electron beam of density n_{0b}, velocity $v_{0b}\hat{z}$, relativistic gamma factor $\gamma = \gamma_0(1+\Delta\sin\omega_{01}\tau)$, where Δ=($V_1/V_b$) is the modulation index and its value ranges from 0 to1. The phase of the pre-bunched electron beam is given by $\psi = \omega_{01}\tau = \omega_{01}(t - z/v_{b0})$. The equation of motion is

$$m_e \frac{d}{dt}(\gamma\overrightarrow{v_0}) = -e(\overrightarrow{E} + \frac{1}{c}\overrightarrow{v_0}\times\overrightarrow{B}) \tag{6}$$

we obtain

$$v_{z0} = \frac{eE_{z0}}{im_e\gamma_0^3(\omega_0 - k_{z0}v_b)}, \tag{7}$$

and

$$v_{x0} = \frac{eE_{z0}}{m_e\omega_0\gamma_0}\left(\frac{k_{z0}}{k_{0I}} + \frac{k_{0I}v_b}{(\omega_0 - k_{z0}v_b)}\right), \tag{8}$$

Int. J. Mod. Phys. Conf. Ser. 2014.32. Downloaded from www.worldscientific.com by 14.139.251.100 on 08/18/14. For personal use only.

where m_e, e, c, k_{z0}, ω_0 are the mass of the electrons, electronic charge, speed of light in vacuum, SPW (Surface plasma wave) wave number and frequency, respectively. We perturb this equilibrium by an azimuthally symmetric TM (Transverse mode) mode

$$\overrightarrow{E_1} = \hat{\mathrm{x}}\,\overrightarrow{a_1} e^{-i(\omega_1 t - k_{z1} z)} \tag{9}$$

where, $\overrightarrow{a_1}$ is the amplitude of the perturbed wave.

The linearized equation of motion yields the perturbed velocity $\overrightarrow{v_1}$

$$\overrightarrow{v_1} = \frac{e\overrightarrow{E_1}}{im_e\omega_1\gamma_0}.$$

Here, $\overrightarrow{F_p} = -\frac{m}{2}(\vec{v}*.\nabla)\vec{v} - \frac{e}{2c}(\vec{v}\times\vec{B}*)$, is the Pondromotive force.

By solving the equation of motion and continuity, we obtain the perturbed velocity and density given as

$$v_2 = -\frac{ek_z\phi_p}{m_e\gamma^3(\omega - k_z v_b)}, \tag{10}$$

$$n_{2b} = -\frac{n_{0b}k_z^2 e\phi_p}{m_e\gamma^3(\omega - k_z v_b)^2}, \tag{11}$$

where

$$\phi_p = -\frac{m_e\gamma v_{x1}v_{x0}^*}{2e},$$

$k_z(=k_{z0}+k_{z1})$ and $\omega(=\omega_0+\omega_1)$ are the wave number and frequency of the space charge wave, respectively. The perturbed current density can be written as

$$\overrightarrow{J_1} = -\frac{1}{2}n_{2b}ev_{x0}\hat{\mathrm{x}}. \tag{12}$$

Using the value of n_{2b} from Eq. (11), Eq. (12) can be rewritten as

$$\overrightarrow{J_1}(\omega_1, k_1) = -\frac{\omega_{pb}^2 k_z^2 v_{x0}^2 E_{1x}\hat{\mathrm{x}}}{i16\pi\gamma^3(\omega - k_z v_b)^2\omega_1}, \tag{13}$$

Int. J. Mod. Phys. Conf. Ser. 2014.32. Downloaded from www.worldscientific.com
by 14.139.251.100 on 08/18/14. For personal use only.

Int. J. Mod. Phys. Conf. Ser. 2014.32. Downloaded from www.worldscientific.com
by 14.139.251.100 on 08/18/14. For personal use only.

where

$$\omega_{pb}^2 = \frac{4\pi n_{0b} e^2}{m}.$$

Applying Maxwell equations $\nabla \times \vec{E} = (-1/c)(\partial \vec{B}/\partial t)$ and $\nabla \times \vec{H} = \frac{4\pi}{c}\vec{J}_1 + \frac{1}{c}\frac{\partial \vec{E}_1}{\partial t}$ along with equation (13), we get the wave equation

$$(\omega_1^2 - k_{z1}^2 c^2)(\omega - k_z v_b)^2 = \frac{k_z^2 v_{x0}^2 \omega_{pb}^2}{4\gamma^3}. \tag{14}$$

Here $\omega_1 \sim k_{z1}c$ corresponds to the radiation mode and $\omega \sim k_z v_b$ corresponds to the beam mode. We are looking for solutions when $k_{z1}c \sim k_z v_b$, i.e., when the pre-bunched beam is in Cerenkov resonance with the radiation mode. In this case, the two factors on the left hand side of Eq. (14) are simultaneously zero in the limit as $n_{0b} \to 0$ (i.e., in the absence of beam).When $n_{0b} \neq 0$, we expand ω_1 as $\omega_1 = k_{z1}c + \delta = k_z v_b + \delta$, where δ is the modification in ω_1 due to finite RHS of Eq. (14).

It gives the growth rate, i.e., the imaginary part of δ

$$\Gamma = \mathrm{Im}\,\delta = \left[\frac{\omega_{pb}^2 k_z^2 v_{x0}^2}{8\omega_1 \gamma^3}\right]^{1/3} \frac{\sqrt{3}}{2}. \tag{15}$$

Gain: If l_1 is the length of the interaction region, then the gain (in dB) G is given by

$$G = 10\log(\frac{A}{A_0}) = 10\frac{\Gamma l_1}{c}, \tag{16}$$

where A and A_0 are the amplitudes of the wave at the distances $z = 0$ and $z = z$ The growth rate of the surface plasma wave FEL (Free Electron Laser) device increases with the modulation index and consequently the gain of the surface plasma wave pumped FEL (Free Electron Laser) also increase with the modulation index.

4. Numerical Results

In the numerical calculations we have used typical parameters of SPW pumped free electron laser. In Fig. 1, we have plotted the variation of the growth Γ (rad. /sec) as a function of modulation index Δ for the following typical parameters: electron beam energy E_b=0.08 MeV, beam radius r_0=2 cm, radiation frequency ω_1=1.87×10^{12} rad./s, modulation frequency ω_{10}=1.8×10^{12} rad./s. In Fig. 2, we have plotted the variation of the growth rate Γ (rad./sec) as a function of the phase of pre-modulated electron beam for the same parameters as Fig. 1 and for modulation index Δ = 0.80 i.e., the beam is 80% modulated.

Int. J. Mod. Phys. Conf. Ser. 2014.32. Downloaded from www.worldscientific.com
by 14.139.251.100 on 08/18/14. For personal use only.

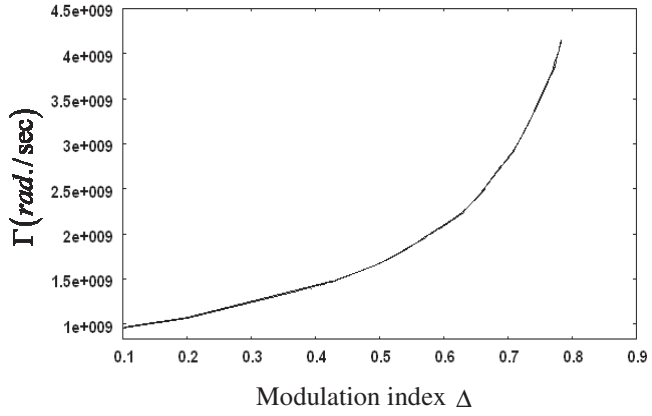


Fig. 1 Growth rate Γ (rad. /sec) as a function of modulation index Δ.

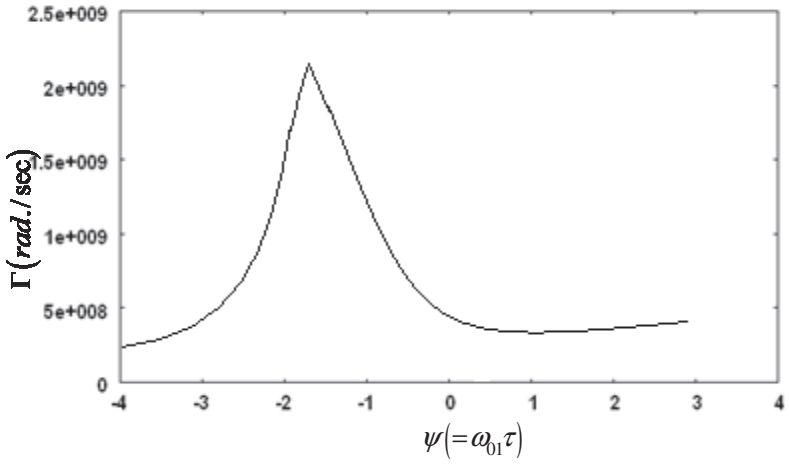


Fig. 2 Growth rate Γ (rad./sec) as a function of phase angle $\psi\left(=\omega_{01}\tau\right)$ of the pre- modulated electron beam.

The growth rate of surface plasma wave pumped FEL (Free Electron Laser) instability is maximum when the phase of the pre-bunched beam is $-\pi/2$, and the growth rate becomes minimum when the phase of the pre-bunched beam is $+\pi/2$,i.e., when the beam electrons are in the accelerating zone.

In conclusion, we may say that the pre-modulated beam on surface plasma wave pumped FEL (Free Electron Laser) instability offers considerable enhancement in growth rate and gain. The growth rate and gain increase with the increase in the modulation index and reaches maximum as $\Delta \sim 1$ in addition to when the frequency and wave number of the pre-bunched beam are comparable to that of the radiation wave.

Int. J. Mod. Phys. Conf. Ser. 2014.32. Downloaded from www.worldscientific.com
by 14.139.251.100 on 08/18/14. For personal use only.

References

1. T. C. Marshall *Free Electron Laser (*Macmillan, New York 2 1985).
2. C. Brau, *Free Electron Laser* (Academic, San Diego) 11 (1990).
3. C. Joshi, T. Katosouleas, J.M. Dawson, Y.T. Yan and J.M. Slater, *IEEE J. Quantum Electron.*, **QE-23**,1571 (1987).
4. U.A. Balakirev, V.I. Miroshnichenko, and Ya.B. Iainberg, *J. Plasma Phys.* **12**, 563 (1986).
5. R. A. Kehs, Y. Carmel, V. L. Granatstein and W.W. Destler, *Phys. Rev .Lett.* **60**, 279 (1988).
6. J. Krall And Y.Y. Lau, *Appl. Phys. Lett.* **52**, 431 (1988).
7. T. C. Marshall *Free Electron Laser.,(*New York : Macmillan, 191 1985).
8. Kazuyoshi Saito, Ken Takayama, Toshiyuki Ozaki, *Nucl. Instr. and Methods in Phys. Res.* **A375**, 237 (1996).
9. S. C. Sharma and Anuradha Bhasin *Phys. Plasmas* **14**, 73102 (2007).
10. Anamika Sharma and V.K. Tripathi, *Phys. Fluids* **B2**, 2787 (1990).
11. S. C. Sharma and V.K. Tripathi, *IEEE Trans. on Plasma Science* **23**, 792 (1995).
12. Yukio Shibata, Kimihiro Ishi, and Shuichi Ono, *Phys. Rev. Lett.***78**, 2740 (1997).
13. T. M. Tran, B.G. Danly and J.S. Wurtele, *IEEE J. Quantum Electron* **QE-23**, 1578 (1987).
14. V. K. Tripathi and C.S. Liu, *Phys. Lett.* **132**, 47 (1988).

ISSN: 2321-7782 (Online)
Volume 2, Issue 7, July 2014
International Journal of Advance Research in Computer Science and Management Studies
Research Article / Survey Paper / Case Study
Available online at: www.ijarcsms.com

A New Classification and Applicability of Software Reliability Models

Kuldeep Singh Kaswan[1]
Research Scholar, Department of Computer Science
Banasthali Vidyapith, Banasthali
Rajasthan – India

Sunita Choudhary[2]
Department of Computer Science
Banasthali Vidyapith, Banasthali
Rajasthan – India

Kapil Sharma[3]
Department of Computer Science & Engineering
Delhi Technological University
Delhi – India

Abstract: ***Today everyone demands for error free software, as we have already seen that even a single software error can results in a terrific loss and damage for life. It is the significance of software reliability in software development that today there are a number of reliability models available in software engineering. These models are classified into different categories and their classifications, are based on different parameters such as failure history, data requirements, number of failure counting, probabilistic assumptions, software structure, nature of debugging strategy, software development life cycle (SDLC) etc. These classifications have an important role in software reliability modeling. In this paper, we have discussed the existing classifications of software reliability models and further purposed a new classification scheme based on applicability of software reliability models according to the software development life cycle including the maintenance phase, which plays a critical role in software development now a days in the competitive world.***

Keywords: Software Reliability models, empirical models, Black box, White box, SRGM, SDLC, NHPP.

I. INTRODUCTION

Software engineering is an engineering discipline that is concerned with all aspects of software production. According to IEEE definition Software Engineering: is the application of a systematic, disciplined, quantifiable approach to the development, operation, and maintenance of software; that is, the application of engineering to software.

Software reliability, an important attribute of software quality, can be defined as the probability of failure-free software operation for a specified period of time in a specified environment [1], [2], [3]. During different phases of software development life cycle software failures are introduced by the system analysts, designers, programmers and managers. To detect and remove these errors, the software system is tested. The quality of software system in terms of reliability is measured by the removal of these errors.

This paper is organized as follows: section II includes need of classification, existing classifications and potential gap between these classifications. In section III a new classification as per Software Development Life Cycle is introduced. Applicability of these software reliability models as per SDLC is given in section IV. Finally, the paper concludes with section V.

© 2014, IJARCSMS All Rights Reserved

II. Related Work

Software reliability models have been used for a long time and have an interesting history. Till today different models have been proposed, discussed, modified and generalized while some models have also suffered from a lot of critiques. In this section we have reviewed the existing software reliability classification, its need and potential gap between the existing classifications.

Need of classification scheme

1. Software reliability models classification is useful in comparison of different reliability models
2. Different sets of models make it easy to obtain new models which are more realistic than the existing ones by identifying the unrealistic assumptions made for these existing models.
3. Help managers/management to select a group of software reliability models based on their requirement. This classification empowers managers to reject more than 80% of software reliability models as per the requirement and choose the particular model out of 20% remaining models.

Existing Software Reliability Models classification

Based on SDLC, Ramamoorthy and Bastani (1982) classified the software reliability models based on the software development life cycle on which these models are applicable. A model can be classified as development phase models, validation phase, operational maintenance phase models and correctness measure models [4].

According Musa (1984) the software reliability models based on the number of failure counting are divided into two categories as finite failure and infinite failure models [5]. Exponential, Weibull and Pareto software reliability models are finite failure category models while Geometric, Inverse Linear, Inverse Polynomial and power are family of infinite failure category models.

Ramamoorthy and Bastani (1986) classified the software reliability models according to the nature of debugging strategy. Another classification based on fault counting or non-fault counting models is also introduced by Bastani and Ramamoorthy.

According to Mellor (1987) the software reliability models have been classified according to software structure into different classes.

Based on probabilistic assumptions M. Xie divides the models into dynamics aspects and without dynamics aspects models. Dynamics describes the dynamics aspects of failure occurrence process. Markovian Models, NHPP and models based on Bayesian analysis are examples of dynamics aspects of failure occurrence, while the input domain models, fault seeding models and software metrics models are without dynamics aspects. [6]

Razeef and Nazir (2012) considered the four classes of the software reliability models as design phase models, Unit Testing phase models, Integration testing phase models, Acceptance testing and Operational Phase models [4]. A reliability model can be applied on more than one phase of software development life cycle.

Based on failure history, Shanmugam (2012) divide the software reliability models into four groups as time between failure models, Fault count models, Fault seeding models and Input domain based models. [7] Based on data requirements, Shanmugam also classified the models in two main groups as Empirical models and Analytic models. Miranda Models, Hallstead Models and Schneider Models are the example of empirical models. Analytical models further can be divided into two groups as Static models and Dynamic models.

Potential Gap in existing reliability models classification

1. As software reliability world is growing very fast so we need time to time updation in the existing reliability models.
2. Maintenance phase models not included in the existing software reliability classifications.

© 2014, IJARCSMS All Rights Reserved

III. Purposed Classification as per Software Development Life Cycle

In this section we have purposed a new classification of software reliability models as per the software development life cycle [26] with the maintenance phase, as shown in Figure -1.

a) Early prediction Models

Early software reliability prediction is the prediction before testing in the absence of failure of failure data. Early reliability prediction attracts both software developers as well as managers as it provides an opportunity for the early identification of software quality, optimal development strategies and cost overrun [8].

b) Architecture Based Models

In this approach software is examined based on the design requirements and classified into different architectural styles. Overall system reliability can be measured by examined each individual architectural style. [9]

c) Mixed White-Box Models

It is the combination of early prediction models and architecture based models.

d) Mixed Black-Box Models

These models are the combination of software reliability growth models and input domain based models.

e) Software Reliability Growth Models

This model is applicable during the testing phase of software development and quantifies the software reliability in terms of estimated number of software error remaining in software or estimated time intervals between software failures. Software reliability growth is defined as the phenomenon that the number of software errors remaining in the system decreases with the progress of testing. For software growth modeling and analysis, the calendar time or CPU time is often used as the unit of software error detection period. [8]

f) Input Domain Based Models

An input-domain based model considers the software input space from which test cases are chosen and the studied quantity is the probability that a randomly chosen input datum according to the operational profile, will lead to a failure. [9]

© 2014, IJARCSMS All Rights Reserved

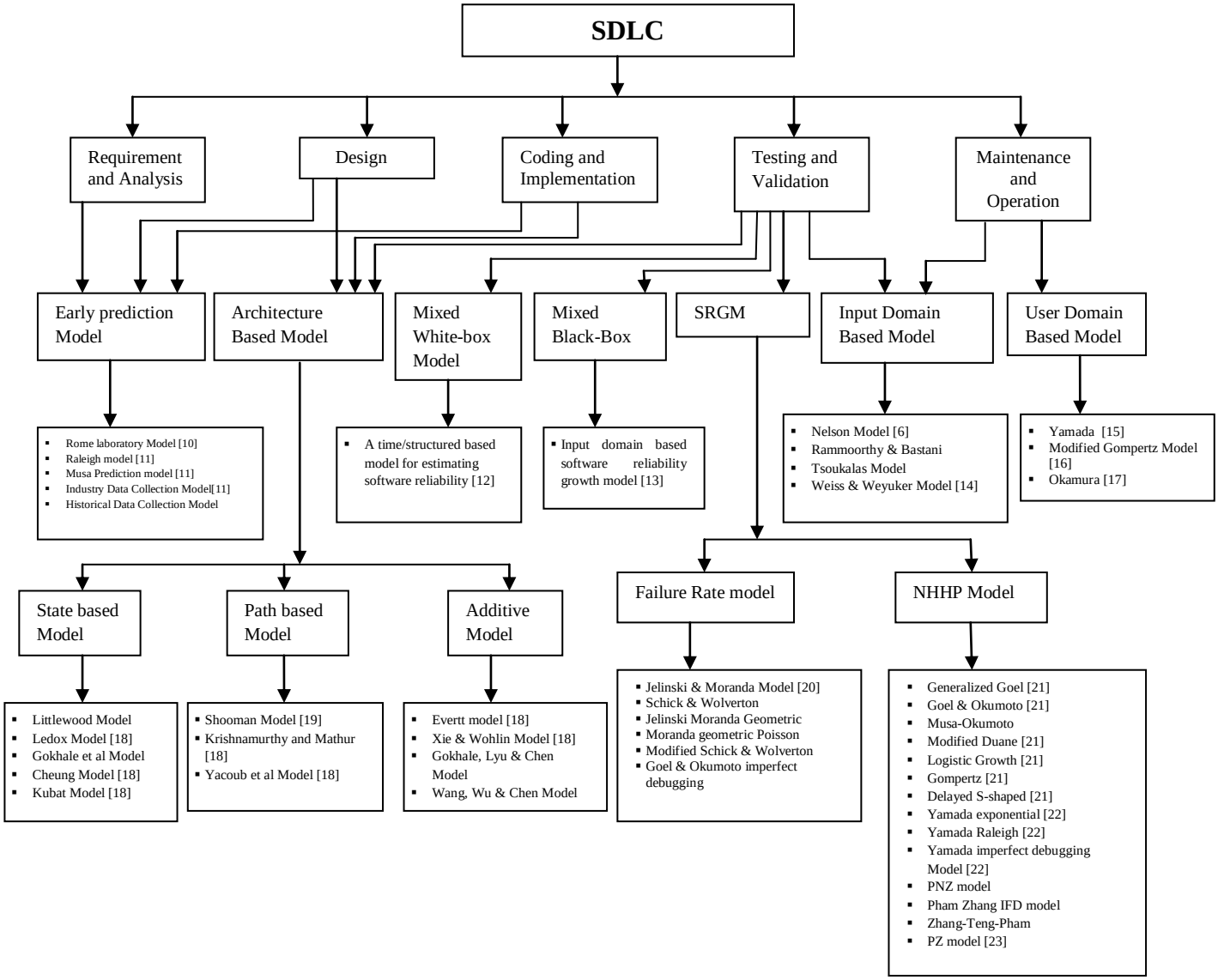


Fig.1 Software reliability models selection based on Software Development Life Cycle

g) User Domain Based Models

The software reliability in maintenance phase exhibits many types of systematic or irregular behaviors. These may include cyclic behavior as well as long-term evolutionary trends. The cyclic behavior may involve multiple periodicities and may be asymmetric in nature. [4]

IV. Applicability of Software Reliability Modeling as per Software Development Life Cycle

Requirement and Analysis Phase Models

These models applicability was proved by Rome Laboratory RL-TR-92-52. For this data was collected from a variety of sources, including the Software Engineering Laboratory.

In this experiment, 33 data sources represent 59 different projects, which include 9 factors: Application, Development Organization, Software anomaly management, Software traceability, Software quality, Software language, Software complexity, Software modularity and Software standards review, which are used to predict the fault density of the software application [24].

Design Phase Models

Wen-Li Wang [19] estimates architecture-based software reliability by designing a model, in this model we assess the reliability of each component, the operational profile, and the architecture of software, to validate the correctness of this model a simulator of an ATM bank system is utilized.

© 2014, IJARCSMS All Rights Reserved

Coding and Implementation Phase Models

Both requirement and analysis phase models, and design phase models can be applicable on this phase.

Testing and Validation Phase Models

The input domain method was used for a preliminary estimation of the reliability of software used in a space application. The reliability estimation was limited to a subset of the system software modules due to the effort required by the application.

In particular we evaluated only those modules that are more critical for the instrument functionality, and examined only the usual operational condition, without considering software for diagnostic & failure containment. In practice, the reliability estimation was limited to 2.4 KLOC out of the 4.9 KLOC of the whole system [25].

Maintenance Phase models

Chen-Tsai-Chen [12] proves the applicability of proposed maintenance phase model through a numerical for which real tracking database records of a shop floor control system utilized in an electronic factory.

Yamada [15] assesses the software product reliability in the maintenance phase by developing a new method based on the empirical knowledge.

Okumura [17] also propose a new method based on accelerated life testing for software product reliability assessment in maintenance phase.

V. CONCLUSION

In this paper we discuss about the need of software reliability models classification, existing classifications, its drawbacks and need of a new classification scheme. Then we proposed a new classification of reliability models and discussed the applicability of these models on different phases of software development life cycle with maintenance phase.

References

1. Kapur, P.K. and Garg, R.B., "Cost reliability optimum release policies for a software system with testing effort, " Operations Research, Vol. 27, No. 2, pp. 109-116, 1990.
2. Musa J.D., Software Reliability Engineering: More Reliable Software, Faster Development and Testing, McGraw-Hill, 1999.
3. Musa, J.D., Iannino, A. and Komodo, K., Software Reliability: Measurement, Prediction and Application, McGraw-Hill, 1987.
4. C. V. Ramamoorthy and Farokh B. Bastani, "Software Reliability-Status and Perspectives", in IEEE Transactions on software engineering, Vol. SE-8, No. 4, July 1982.
5. J. D. Musa and K. Okumoto, "A Logarithmic Poisson Execution Time Model for Software Reliability Measurement", 0270-5257/84/0000/0230501.00© 1984 IEEE.
6. M. Xie, "software reliability modeling", World Scientific Pub. 1991
7. Latha Shanmugam, Dr. Lilly Florence, "In Overview of Software Reliability Models", International Journal of Advanced Research in Computer Science and Software Engineering, Vol. 2, Issue 10, Oct. 2012
8. Ajeet Kumar Pandey, Neeraj Kumar Goyal, "early Software reliability prediction: A fuzzy logic approach", ISBN 978-81-322-1175 4(print)
9. Wen-Li Wang. Dai Pan. Mei-Hwa Chen, "Architecture-Based Software Reliability Modeling", Computer Science Department. Suny Albany
10. Yung-Chung Chen, Shih-Ying Tsai and Peter Chen, "Reliability Models for Application Software in Maintenance phase", IEMS Vol. 7, No. 1, pp. 51-56, 2008.
11. C. Smidts, R. W. Stoddard, and M. Stutzke, "Software reliability models: An approach to early reliability prediction," IEEE Trans. Reliability, Vol. 47, No. 3, pp. 268–278, 1998.
12. S. S. Gokhale and K. S. Trivedi, "A time/structure based software reliability model", Analysis of Softw. Engineering, Vol. 8, pp. 85–121, 1999.
13. S. S. Gokhale, P. N. Marinos, and K. S. Trivedi, "Important milestones in software reliability modeling", Proc. of Softw. Engineering and Knowledge Engineering (SEKE '96), Lake Tahoe, NV, pp. 345–352, 1996
14. S. N. Weiss and E. J. Weyuker, "An extended domain-based model of software reliability", IEEE Trans. Software Engineering, Vol. SE-14, pp. 1512–1524, 1988.
15. Yamada, S., Tanio Y., and Osaki, S., "A software reliability evaluation method during operation phase", Trans IEICE, J72-D-I, 797-803, 1989.
16. Vladimir Zeljkovie, Nela Radovanovie and Dragomir Ilie, "Software Reliabilty: Models and Parameters Estimation", Science Technical Review, Vol. 61, No 2, pp. 57-60, 2011.

© 2014, IJARCSMS All Rights Reserved

17. Okamura, H., Tadashi, D., and Shunji, O., "A reliability assessment method for software products in operational phase-Proposal of an accelerated life testing model", Electronics and Communications in Japan, Part 3, 84(8), 25-33, 2001.
18. K. Popstajanova and K. Trivedi, "Architecture based approach to reliability assessment of software systems," Performance Evaluation, Vol. 45, No. 2, June 2001
19. W. Wang, Y. Wu, and M. H. Chen, "An architecture-based software reliability model", in Proc. of Pacific Rim Dependability Symposium, Hong Kong, December 1999.
20. Z. Jelinski and P. B. Moranda, "Software Evaluation", W. Freiberger, Ed. New York: Academic Press, 1972.
21. C. Y. Huang, M. R. Lyu, and S. Y. Kuo, "A unified scheme of some non-homogenous Poisson process models for software reliability estimation", IEEE Trans. Softw. Engineering, Vol. 29, No. 3, pp. 261–269, March 2003.
22. H. Pham, "Software reliability and cost models: perspectives, comparison and practice", European J. of Operational Research, Vol. 149, pp. 475–489, 2003
23. H. Pham and X. Zhang, "An NHPP software reliability models and its comparison", International J. of Reliability, Quality and Safety Engineering, Vol. 14, No. 3, pp. 269–282, 1997.
24. McCall, W. Randell, J. Dunham, L.Lauterbach, "Software Reliability, Measurement, and Testing Software Reliability and Test Integration RL-TR-92-52", Produced for Rome Laboratory, Rome, NY, 1992
25. Alberto Pasquini, Elio De Agostino and Giuseppe Di Marco, "An Input-Domain Based Method to Estimate Software Reliability", IEEE Transactions on Reliability, Vol. 45, No. 1, 1996.
26. Kapil Sharma, Rakesh Garg, C. K. Nagpal, and R. K. Garg, "Selection of Optimal Software Reliability Growth Models Using a Distance Based Approach", IEEE Transactions on Reliability, Vol. 59, No. 2, June 2010

AUTHOR(S) PROFILE



Kuldeep Singh Kaswan was born in Haryana, India in 1982. He is pursuing a Doctors Degree in Computer Science under the faculty of Computer Science at Banasthali Vidyapith, Rajasthan. He has obtained his Master Degree in Computer Science and Engineering from Choudhary Devi Lal University, Sirsa (Haryana) and Bachelor Degree from Kurukshetra University, Kurukshetra (Haryana). His area of interests includes software engineering and reliability.



Sunita Choudhary was born in Rajasthan, India in 1978. She received Doctors Degree in Computer Science under the Faculty of Computer Science at the Banasthali University (Rajasthan), India. She has obtained his Bachelor of Science in Computer Science and Master of Computer Application Degrees from Banasthali University in 1999, and 2001 respectively. Presently, she is working as an associate professor in Department of Computer Science at Banasthali University, Rajasthan, India. Her research interests include Algorithms and Distributed Computing.



Kapil Sharma was born in Haryana, India in 1977. He received Doctors Degree in Computer Science and Engineering under the Faculty of Engineering and Technology at the M. D. University, Rohtak (Haryana), India. He has obtained his Bachelor of Engineering and Master of Technology Degrees in Computer Science & Engineering and Information Technology from M. D. University, Rohtak, and IASE, Rajasthan, India in 2000, and 2005 respectively. Presently, he is working as an associate professor in Department of Computer Science at Delhi Technological University, Delhi, India. His research interests include software engineering, and reliability.

© 2014, IJARCSMS All Rights Reserved

A study on particle creation in modified $f(R,T)$ theory of gravity

Vijay Singh[1], **C. P. Singh**[2]

[1,2]Department of Applied Mathematics,
Delhi Technological University
(Formerly Delhi College of Engineering)
Bawana Road, Delhi-110 042, India.

arXiv:1408.0633v1 [gr-qc] 4 Aug 2014

Abstract The theoretical and observational consequences of thermodynamics of open systems, which allow particle creation are investigated in modified $f(R,T)$ (R is the Ricci scalar and T is the trace of energy-momentum tensor) theory of gravity within the framework of a flat Friedmann-Robertson-Walker line element. A suitable form of $f(R,T) = R + 2f(T)$ and "gamma-law" equation of state $p = (\gamma - 1)\rho$ are assumed to explore the role of particle creation in the early and late time evolution of the universe. A power-law expansion model is proposed for $0 \leq \gamma \leq 2$ by considering the natural phenomenological particle creation rate $\psi = 3\beta nH$, where β is a pure number of the order of unity. A Big Rip singularity is observed for $\gamma < 0$, which describes the phantom cosmology. We observe that the accelerated expansion of the universe is driven by the particle creation without any exotic "quintessence" component or a cosmological constant. It is also found by density parameter that the model becomes of negative curvature due to particle creation and the entropy increases with the evolution of the universe. Some kinematics tests such as lookback time, luminosity distance, proper distance, angular diameter versus redshift are discussed in detail to observe the role of particle creation in early and late time evolution of the universe.

Keywords: Modified gravity theory, Particle creation.

PACS number(s): 98.80-k, 98.80-cq, 04.20-q.

[1]gtrcosmo@gmail.com
[2]cpsphd@rediffmail.com

1 Introduction

Many theoretical and observational studies of the universe, such as Type Ia supernovae [1-3], cosmic microwave background (CMB) anisotropy [4], large scale structures (LSS) [5] etc., have been shown that a pure Friedmann-Lamaitre-Robertson-Walker (FLRW) cosmology with matter and radiation could not explain all the large scale properties of our universe. The observations suggest that our universe is spatially flat and consists of about 70 percent dark energy with negative pressure, nearly 25 percent of dark matter, which populates the galaxy halos and 5 percent of baryonic matter. The late time cosmic acceleration is usually assumed to be driven by a cosmic fluid/field generically known as dark energy (DE) [6-8], which can be observed only by its gravitational effects [9-11]. Since the time of this discovery in 1998, a large number of probable candidates of DE have been proposed to explain late time acceleration of the universe. The two most accepted DE models are that of a cosmological constant [12] (assumed possibly to be the quantum vacuum energy) and a slowly rolling scalar field (quintessence models) [13-17]. All of these DE cosmological models are based on the Big Bang cosmology. In the context of early universe, the standard Big Bang model presents theoretical and observational difficulties, such as the singularity problem [18], flatness and horizon problem, reheating during the inflationary epoch [19], confliction between the age of the universe and the age of the oldest stars in globular clusters (age problem) [20], the entropy problem [21,22] etc.

The flatness and horizon problems together with the entropy problem have been resolved (up to a certain extent) by the inflationary model proposed by Guth [23] and Linde [24]. The age confliction [25] is not an isolated complication, it comes with another serious one trouble that is structure formation through gravitational amplification of small primeval density perturbation. These issues open the door of investigations of different alternative theories of gravity for studying not only unpredicted late time cosmic acceleration but early universe as well [26-29]. Many pioneer concepts have been introduced by theorists to alleviate the problems of early and late universes. Among the ways to resolve the problems of early universe, Dirac's large number hypothesis inspired a class of new cosmology named particle creation [30-32]. The steady state model introduced by Bondi and Gold [33] on the foundation of perfect cosmological principle (PCP) also asserts the continuous generation of matter in the universe. Hoyle [34] and Narlikar [35] independently proposed a creation field theory and studied the matter creation during the evolution of the universe. Tryon [36] and Fomin [37)] in their individual work proposed a theoretical concept of the creation of the universe as a vacuum fluctuation. Brout et al. [38-41] putted a strong foundation of simultaneous creation of matter and curvature from a quantum fluctuation of the Minkowskian space-time vacuum.

Later on, Gunzig et al. [42] and Prigogine et al. [43] established the theoretical scenario of matter creation in the framework of cosmology. The authors applied the thermodynamics of an open system to cosmology allowing particle creation and entropy production. They showed that the second law of thermodynamics might be modified to accommodate the flow of energy from gravitational field to the matter field, resulting in the creation of particles and consequently entropy. The work might suggest that at the expense of the gravitational field, particle creation takes place as an irreversible process constrained by the usual requirements of the non-equilibrium thermodynamics, however, the reverse process (matter destruction)

thermodynamically forbidden. Calváo et al. [44] extended this new concept of matter creation under adiabatic conditions. The further results were generalized by Lima and Germano [45] through a contravariant formulation allowing specific entropy variation as usually expected for non-equilibrium process in fluids. Lima and Alcaniz [46] and Alcaniz and Lima [47] investigated observational consequences of FRW models driven by adiabatic matter creation through some kinematics tests. After the discovery of accelerating universe the particle creation theory was reconsidered to explain it and got unexpected results. The negative pressure due to particle creation, might play the role of exotic matter component. Zimdahl et al. [48] tested the particle creation with SNe Ia data to get the result of accelerating universe. Qiang et al. [49] studied a model with adiabatic particle creation which is also consistent with SNe Ia data. Singh and Beesham [50, 51], and Singh [52, 53] studied early universe in FRW cosmology with particle creation through some kinematical tests. This theoretical formulation of continuous creation of matter in the universe may reinterpret several predictions of the standard Big Bang cosmology.

On the other hand, many modifications of general relativity (GR) have been proposed to reconcile the problems plagued in cosmology [54]. Among such modifications the simplest one is replacing the Ricci scalar curvature R with the general function of R called $f(R)$ theories of gravity, describe transition from decelerated to accelerated expansion of the universe [55]. Bertolami et al. [56] have generalized $f(R)$ theories by introducing an explicit coupling between arbitrary function of the Ricci scalar R and the matter Lagrangian density. Harko [57] has extended this new concept to the arbitrary coupling between matter and geometry. Harko et al. [58] have considered another extension of GR, where the gravitational Lagrangian is given by an arbitrary function of the Ricci scalar R and of the trace T of the stress-energy tensor, so called $f(R,T)$ theory of gravity. The justification of choosing T as an argument for the Lagrangian is from exotic imperfect fluids or quantum effects. The authors have argued that due to the coupling between matter and geometry the theory depends on a source term, representing the variation of the matter-stress-energy tensor with respect to the metric. Consequently, the cosmic acceleration in $f(R,T)$ gravity results not only from geometrical effect but also from the matter contribution. These interesting features of $f(R,T)$ gravity motivate many authors to study it for resolving several issues of current interest in cosmology and astrophysics.

Jamil et al. [59] have reconstructed cosmological models in the framework of $f(R,T)$ gravity, showing dust fluid ΛCDM, phantom-non-phantom era and phantom cosmology, which are good agreement with BAO observational data for low-redshift $z < 2$. Houndjo [60] has reconstructed $F(R,T) = f_1(R) + f_2(T)$ using auxiliary scalar field with two known examples of scale factors corresponding to an accelerating universe. Houndjo and Piatella [61] have numerically reconstructed $f(R,T)$ theory with dark matter and holographic DE, describing the same expansion history in GR. Houndjo et al. [62] have investigated $f(R,T)$ gravity models which reproduce four types of future finite-time singularities. Sharif and Zubair [63] have discussed a non-equilibrium thermodynamics in $f(R,T)$ gravity by taking two forms of the energy-momentum tensor of dark components which endorses second law of thermodynamics holds both in phantom and non-phantom phases. Jamil et al. [64] have proved, in general, the first law of black hole thermodynamics is violated in $f(R,T)$ gravity. Alvarenga et al. [65] have paid special attention on $f(R,T) = R + 2f(T)$ assuming special function $f(T)$ showing

energy conditions can be satisfied for suitable input parameters. Sharif et al. [66] and Sharif and Zubair [67] have derived energy conditions in the context of $f(R,T)$ gravity, which can reduce to the well-known conditions in $f(R)$ and GR. Chakraborty [68] has shown that a part of an arbitrary function $f(R,T)$ can be determined taking into account of the conservation of stress-energy tensor. Alvarenga et al. [69] have studied the evolution of scalar cosmological perturbations in the background of metric formalism in $f(R,T)$ theory. Pasqua et al. [70] have considered modified holographic Ricci DE (MHRDE) model in $f(R,T)$ modified gravity, which explained a quintessence-like behavior of the model. Shabani and Farhaudi [71] have studied the cosmological solutions of $f(R,T)$ gravity through phase space analysis. Sharif and Zubair [72] have considered $f(R,T)$ theory as an effective description for the holographic and new agegraphic DE and reconstructed the corresponding models, which explain phantom or quintessence regimes of the universe. Recently, Singh and Singh [73] have reconstructed the particular form $f(R,T) = R+2f(T)$ by assuming de-Sitter and power-law expansion of scale factors and showed the reconstructed forms of $f(R,T)$ could explain DE models successfully. However, all these mentioned works have been carried out in FRW spacetime. Some authors have also explored $f(R,T)$ theory in anisotropic background [74-77] and higher dimension [78]. Thus, the newly proposed $f(R,T)$ gravity motivates us to study the particle creation phenomena in the early and late time evolution of the universe.

In this paper, we investigate the theoretical and observational significance of particle creation in modified $f(R,T)$ gravity theory in the framework of a flat Friedmann-Robertson-Walker model. Exact solutions of the field equations are obtained by assuming the suitable form of $f(R,T) = R + 2f(T)$, equation of state, and particle creation rate. We obtain the non-singular power-law solution for the scale factor. A Big Rip singularity is also observed which describes the phantom cosmology. We study some kinematical tests to explain the physical significance of particle creation during early and late time evolution of the universe.

The paper is organized as follows. The thermodynamics of particle creation is presented in the Sec. 2. A brief review of modified $f(R,T)$ gravity theory and its field equations are given in Sec. 3. In Sec. 4, the model and field equations are presented with particle creation. The exact solutions of the field equations with suitable assumptions are obtained in Sec. 5. Sec. 6 and its subsections are devoted to study some kinematics tests of the model. Finally, the outcomes are summarized in Sec. 7.

2 Thermodynamics of particle creation

If we regard the whole universe as a closed thermodynamical system in which number of the particles in a given volume is constant, then the laws of thermodynamics have the form

$$d(\rho_m V) = dQ - p_m dV, \tag{1}$$

and

$$TdS = d(\rho_m V) + p_m dV, \tag{2}$$

where ρ_m, V, p_m, T and S are the energy density, volume, thermodynamical pressure, temperature, and entropy, respectively. Here, dQ is the heat received by the system during time dt. It is observed from (1) and (2) that the entropy production is given by

$$TdS = dQ. \tag{3}$$

Eq. (3) shows that the entropy remains stationary, i.e., $dS = 0$ for a closed adiabatic system for which $dQ = 0$. However, if we treat the universe as an open thermodynamic system allowing irreversible matter creation from the energy of the gravitational field, we can account for entropy production right from the beginning, and the second law of thermodynamics is also incorporated into the evolutionary equations in a more meaningful way. Thus, the creation of matter acts as a source of internal energy. In such situation the number of particles N in a given volume V is not to be a constant but is time dependent. Therefore, Eq. (1) modifies as

$$d(\rho_m V) = dQ - p_m dV + (h/n)\ d(nV), \tag{4}$$

where $N = nV$, n is the particle number density, and $h = (\rho_m + p_m)$ is the enthalpy per unit volume of the system. In case of adiabatic system where $dQ = 0$, Eq. (4) for an open system reduces to

$$d(\rho_m V) + p_m dV = (h/n)\ d(nV). \tag{5}$$

We see that in such a system the thermal energy is received due to the change of the number of particles. In cosmology, this change may be considered as a transformation of energy from gravitational field to the matter.

In the context of an open system, Eq.(5) can be rewritten as

$$d(\rho_m V) = -(p_m + p_c)dV, \tag{6}$$

where

$$p_c = -(h/n)(dN/dV). \tag{7}$$

Equation (6) suggests that the creation of matter in an open thermodynamic system corresponds to a supplementary pressure p_c, which must be considered as a part of the cosmological pressure entering into the Einstein field equations (decaying of matter leads to a positive decay pressure) and is equivalent to adding the term p_c given by (7) to the thermodynamic pressure p_m. It is to be noted that p_c is negative or zero depending on the presence or absence of particle creation.

Since the increment in entropy for an adiabatic system is only caused by creation of matter, the entropy is an extensive property of the system. In present scenario, S is proportional to the number of particles included in the system. Therefore, the entropy change dS for open systems from (2) and (5) becomes

$$TdS = (h/n)\ d(nV) - \mu\ d(nV) = (TS/N)dN \Rightarrow \frac{dS}{S} = \frac{dN}{N}, \tag{8}$$

where μ is the chemical potential given by $\mu = (h - Ts)/n$, $s = S/V$. Since the second law of thermodynamics is a fundamental law in physics, the presence or absence of particle creation can not affect it. This law basically requires $dS \geq 0$, consequently, Eq. (8) gives

$$dN \geq 0. \tag{9}$$

The above inequality implies that the space-time can produce matter, whereas the reverse process is thermodynamically not admissible.

The basic idea of this entire formulation is to modify the usual energy momentum conservation law in an open thermodynamical system, which leads to the explicit use of a balance equation for the number density of the particles created, in addition to Einstein's field equations.

The particle flux vector is given by

$$N^{\alpha} = nu^{\alpha}, \tag{10}$$

and N^{α} is assumed to satisfy the balance equation [44, 79]

$$N^{\alpha}_{;\alpha} = \psi, \tag{11}$$

where the function ψ denotes a source term of particle creation which is positive or negative depending on whether there is production or annihilation of particles. In standard cosmology ψ is usually assumed to be zero.

3 A brief review of Modified $f(R,T)$ gravity theory

The $f(R,T)$ theory is a modified theory of gravity, in which the Einstein-Hilbert Lagrangian is modified by replacing Ricci scalar curvature R by an arbitrary function of R and trace T of energy-momentum tensor, i.e., $f(R,T)$. So the gravitational action for $f(R,T)$ modified theory of gravity [58] in the units $G = 1 = c$ takes the following form.

$$S = \frac{1}{8\pi}\int d^4x\sqrt{-g}\left[\frac{f(R,T)}{2} + \mathcal{L}_m\right], \tag{12}$$

where g is the determinant of the metric tensor $g_{\mu\nu}$ and $\mathcal{L}_m$ corresponds to matter Lagrangian. The energy-momentum tensor $T_{\mu\nu}$, defined by fluid Lagrangian density is given by

$$T_{\mu\nu} = -\frac{2}{\sqrt{-g}}\frac{\delta(\sqrt{-g}\,\mathcal{L}_m)}{\delta g^{\mu\nu}}, \tag{13}$$

and its trace, $T = g^{\mu\nu}T_{\mu\nu}$. By assuming that the matter Lagrangian density $\mathcal{L}_m$ depends only on the metric tensor components $g_{\mu\nu}$, not on its derivatives, we obtain

$$T_{\mu\nu} = g_{\mu\nu}\mathcal{L}_m - 2\frac{\partial\mathcal{L}_m}{\partial g^{\mu\nu}}. \tag{14}$$

The equations of motion by varying the action (12) with respect to metric tensor become

$$f_R(R,T)R_{\mu\nu} - \frac{1}{2}f(R,T)g_{\mu\nu} + (g_{\mu\nu}\Box - \nabla_\mu\nabla_\nu)f_R(R,T) = 8\pi T_{\mu\nu} - f_T(R,T)T_{\mu\nu} - f_T(R,T)\ominus_{\mu\nu}, \tag{15}$$

where f_R and f_T denote the derivatives of $f(R,T)$ with respect to R and T, respectively. Here, ∇_μ is covariant derivative and $\Box \equiv \nabla_\mu\nabla^\mu$ is the d'Alembert operator and $\ominus_{\mu\nu}$ is defined by

$$\ominus_{\mu\nu} \equiv g^{\alpha\beta}\frac{\delta T_{\alpha\beta}}{\delta g^{\mu\nu}}. \tag{16}$$

Using (14) into (16), we get

$$\ominus_{\mu\nu} = -2T_{\mu\nu} + g_{\mu\nu}\mathcal{L}_m - 2g^{\alpha\beta}\frac{\partial^2\mathcal{L}_m}{\partial g^{\mu\nu}\partial g^{\alpha\beta}}. \tag{17}$$

Since the field equations of $f(R,T)$ gravity depend on $\ominus_{\mu\nu}$, i.e., on the physical nature of the matter, several models corresponding to different form of $f(R,T)$ would generate depending on the nature of the matter source. We however do not consider the general case, but restrict ourselves to the following form

$$f(R,T) = R + 2f(T), \tag{18}$$

where $f(T)$ is an arbitrary function of the trace of energy-momentum tensor of matter. Using (18), one can re-write the gravitational field equations defined in (15) as

$$R_{\mu\nu} - \frac{1}{2}Rg_{\mu\nu} = 8\pi T_{\mu\nu} - 2(T_{\mu\nu} + \ominus_{\mu\nu})f'(T) + f(T)g_{\mu\nu}. \tag{19}$$

Here, a prime stands for derivative of $f(T)$ with respect to T.

The main issue now arises on the matter contents of the universe through the energy momentum tensor and consequently on the matter Lagrangian $\mathcal{L}_m$ and the trace of the energy momentum tensor. We assume the universe is filled with a perfect fluid which is incorporated in the next section.

4 Model and field equations

We consider a homogenous and isotropic universe with spatially flat geometry described by flat Friedmann-Robertson-Walker (FRW) metric

$$ds^2 = dt^2 - a^2(t)(dx^2 + dy^2 + dz^2), \tag{20}$$

where $a(t)$ is the scale factor, which is a function of cosmic time t only.

In the formalism of particle creation, the second law of thermodynamics leads naturally to a modification of the energy momentum tensor with an additional creation pressure depends on the rate of creation of particles. In the presence of particle creation, the energy momentum tensor of perfect fluid is given by

$$T_{\mu\nu} = (\rho_m + p_m + p_c)u_\mu u_\nu - (p_m + p_c)g_{\mu\nu}, \tag{21}$$

where u_μ is the four velocity of the fluid such that $u_\mu u^\nu = 1$, and in comoving coordinates $u^\mu = \delta^\mu_0$.

The trace of energy momentum tensor (21), gives

$$T = \rho_m - 3(p_m + p_c). \tag{22}$$

We treat the scalar invariant $\mathcal{L}_m$ as the effective pressure of the perfect fluid matter and pressure originated by creation of particles. Therefore, the matter Lagrangian may be assumed as $\mathcal{L}_m = -(p_m + p_c)$, therefore, Eq. (17) becomes

$$\ominus_{\mu\nu} = -2T_{\mu\nu} - (p_m + p_c)g_{\mu\nu}. \tag{23}$$

In view of (23), the field equations (19) can be rewritten as

$$R_{\mu\nu} - \frac{1}{2}g_{\mu\nu}R = 8\pi T_{\mu\nu} + 2\left[T_{\mu\nu} + g_{\mu\nu}(p_m + p_c)\right] f'(T) + g_{\mu\nu}f(T). \tag{24}$$

The field equations (24) for a fluid endowed with matter creation (21) in the background of metric (20), yield

$$3H^2 = 8\pi\rho_m + 2(\rho_m + p_m + p_c)f'(T) + f(T), \tag{25}$$

$$2\dot{H} + 3H^2 = -8\pi(p_m + p_c) - f(T), \tag{26}$$

where $H(t) = \dot{a}/a$ is the Hubble parameter. A dot denotes derivative with respect to cosmic time t.

For adiabatic matter creation, the pressure p_c in Eq. (7) takes the following form [44]

$$p_c = -\frac{(\rho_m + p_m)}{3nH}\,\psi. \tag{27}$$

For a complete formulation of the problem, we consider one more relation between the particle number n and $V = a^3$, describing the dynamics of n as a result of matter creation (decay) processes. This relation is given by Eq. (11), which for the metric (20) takes the form

$$\dot{n} + 3nH = \psi, \tag{28}$$

5 Solution of field equations

The field equations (25)-(28) have seven unknowns, namely, a, ρ_m, p_m, p_c, n, $f(T)$ and $\psi(t)$. We have only three equations plus the constraint (27). Therefore, one needs three more relations in order to construct a definite cosmological scenario.

In first choice, we consider a particular function given by [58]

$$f(T) = \lambda T, \quad (\lambda \quad \text{is a constant}). \tag{29}$$

With this assumption, the field equations (25) and (26) yield

$$3H^2 = (8\pi + 3\lambda)\rho_m - \lambda(p_m + p_c), \tag{30}$$

$$2\dot{H} + 3H^2 = -(8\pi + 3\lambda)(p_m + p_c) + \lambda\rho_m. \tag{31}$$

In order to obtain the exact solution of the field equations, we assume two more additional relations: the equation of state and the matter creation rate. In the cosmological domain, the former is usually given by the gamma-law

$$p_m = (\gamma - 1)\rho_m, \tag{32}$$

where γ is a constant lies in the interval [0, 2] and known as the EoS parameter of the perfect fluid.

Using (32) into (30) and (31), and simplifying, we get a single evolution equation for H:

$$2\dot{H} + (8\pi + 2\lambda)(\gamma\rho_m + p_c) = 0. \tag{33}$$

We confine our attention to the simple phenomenological expression for the matter creation rate [21]

$$\psi(t) = 3\beta nH, \tag{34}$$

where the parameter β lies in the interval $(0, 1)$ and is assumed to be a constant.

Using (32) and (34) into (27), we have

$$p_c = -\beta\gamma\rho_m, \tag{35}$$

Putting (32) and (35) into (30), we obtain

$$\rho_m = \frac{3H^2}{8\pi + 4\lambda - \gamma\lambda(1-\beta)}. \tag{36}$$

Substituting (35) and (36) into (33) gives

$$\dot{H} + \frac{3}{2}\frac{\gamma(8\pi + 2\lambda)(1-\beta)}{[8\pi + 4\lambda - \gamma\lambda(1-\beta)]}\, H^2 = 0. \tag{37}$$

The solution of (37) for $\gamma \neq 0$ and for all values of λ and β is given by

$$H(t) = \left(C + \frac{3}{2}\frac{\gamma(8\pi + 2\lambda)(1-\beta)}{[8\pi + 4\lambda - (1-\beta)\gamma\lambda]}\, t\right)^{-1}, \tag{38}$$

where C is an integration constant. For $\gamma = 0$, the well known de-Sitter scale factor $a(t) = a_0\, e^{H_0 t}$ is obtained.

From Eq. (38) we find the following expression for the scale factor

$$a(t) = D\left(C + \frac{3}{2}A\gamma\, t\right)^{\frac{2}{3A\gamma}}, \tag{39}$$

where D is a new integration constant and $A = (8\pi + 2\lambda)(1-\beta)/8\pi + 4\lambda - \gamma\lambda(1-\beta)$.

The above scale factor may be rewritten as

$$a(t) = a_0\left(1 + \frac{3}{2}A\gamma H_0(t - t_0)\right)^{\frac{2}{3A\gamma}}, \tag{40}$$

where $H = H_0 > 0$ at $t = t_0$. The subscript '0' refers to the present values of parameters. Since $0 \leq \gamma \leq 2$, we must have $A > 0$ for expansion of the universe. Also, $A > 0$ implies $\lambda > 0$ as $0 \leq \beta < 1$.

If $\gamma < 0$ then we have a Big Rip singularity at a finite value of cosmic time $t_{br} = t - t_0 = -2/3H_0A\gamma$. Thus, we have a phantom cosmology for $\gamma < 0$. If one choose $t_0 = 2H_0^{-1}/3A\gamma$ then (40) takes the familiar form of power-law expansion of the universe, i.e.,

$$a(t) = a_0\left(\frac{3}{2}A\gamma H_0\, t\right)^{\frac{2}{3A\gamma}}. \tag{41}$$

If $\lambda = 0 = \beta$, (39) and (41) reduce to the well-known expressions of power-law expansion of scale factor for a flat FRW model in GR.

By use of (40) one may express the energy density of matter, particle creation pressure and the particle number density as functions of the scale factor a. These parameters respectively have the following forms

$$\rho_m = \rho_0 \left(\frac{a_0}{a}\right)^{3A\gamma}, \tag{42}$$

$$p_c = -\beta\gamma\rho_0 \left(\frac{a_0}{a}\right)^{3A\gamma}, \tag{43}$$

$$n = n_0 \left(\frac{a_0}{a}\right)^{3(1-\beta)}, \tag{44}$$

where $\rho_0 = 3H_0^2/[8\pi + 4\lambda - \gamma\lambda(1-\beta)]$ is the present value of energy density. Here, n_0 is the present value of particle number density for any values of β. The above results show that the transition from one phase to other phase, in the course of expansion, happens exactly as in the standard cosmological model.

The number of particles N in a given volume V is given by

$$N = N_0 \left(\frac{a}{a_0}\right)^{3\beta}, \tag{45}$$

which shows that N increases with time. If $\beta = 0$, N would remain constant throughout the evolution of the universe and we would recover the standard FRW model of the universe in $f(R,T)$ theory. Again, from (8) $S = S_0(N/N_0)$, the entropy in terms of scale factor is

$$S = S_0 \left(\frac{a}{a_0}\right)^{3\beta}. \tag{46}$$

The deceleration parameter defined as $q = -a\ddot{a}/\dot{a}^2$, gives

$$q = -1 + \frac{3\gamma A}{2} = \left[\frac{3\gamma}{2}\frac{(8\pi + 2\lambda)(1-\beta)}{[8\pi + 4\lambda - (1-\beta)\gamma\lambda]} - 1\right]. \tag{47}$$

which shows that q is independent of cosmic time t. Therefore, q may be positive or negative for a given set of values of β and λ. We know that the model accelerates for $q < 0$, therefore, the value of A must be $0 < A < 2/3\gamma$ for an accelerated universe.

As expected, the above solutions reduce to the standard FRW model of GR for $\beta = 0$ and $\lambda = 0$ and for all values of γ. In what follows, we study the role of $f(R,T)$ gravity and particle creation in early and late time evolution of the universe.

Case I: $\gamma = \frac{2}{3}$

Fig. 1(a) plots the scale factor as a function of time for $\gamma = 2/3$ and some selected values of λ and β. We observe that if $\beta = 0$, $q < 0$ for all $\lambda > 0$, therefore, we find that the universe accelerates in $f(R,T)$ gravity without particle creation. Similarly, if $\lambda = 0$, i.e., in

the absence of $f(T)$, $q = -\beta < 0$ for any values of $\beta > 0$. Thus, the acceleration occurs due to particle creation. The rate of expansion increases more rapidly for non-zero values of β and λ. It is to be noted that if $\lambda = 0 = \beta$ then the the marginal inflationary phase of GR is recovered, i.e., $a \sim t$ and $q = 0$.

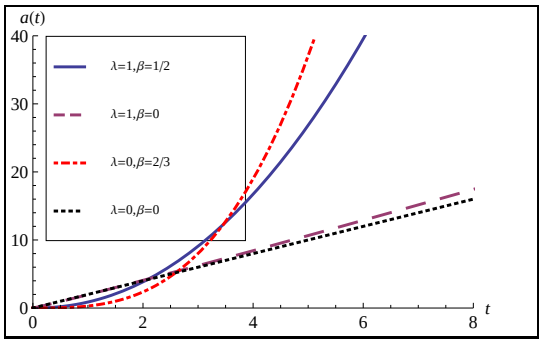


Fig. 1(a). Scale factor as a function of time for $\gamma = \frac{2}{3}$ and some selected values of λ and β.

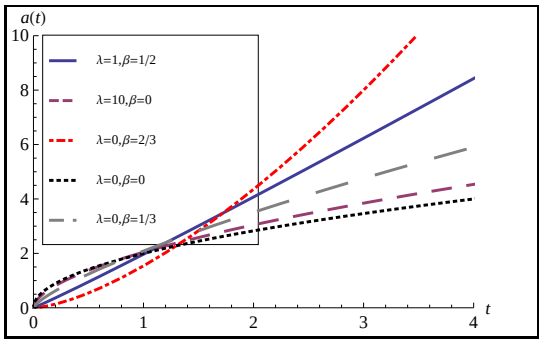


Fig.1(b). Scale factor as a function of time for $\gamma = \frac{4}{3}$ and some selected values of λ and β.

Case II: $\gamma = \frac{4}{3}$

In this case, if $\beta = 0$ and $\lambda > 0$, we have $q > 0$. This shows that the universe decelerates in the absence of particle creation. If $\lambda = 0$ then $q \geq 0$ for $0 < \beta \leq 1/2$, and $q < 0$ for $1/2 < \beta < 1$. Therefore, the universe decelerates or accelerates depending on the rate of particle creation. However, if $\lambda \neq 0$ and $\beta \neq 0$, the deceleration or acceleration of the universe depend on the following constrains, respectively:

$$0 < \beta \leq \frac{1}{4},\ \lambda > 0 \ \ or \ \ \frac{1}{4} < \beta < \frac{1}{2},\ 0 < \lambda < \frac{6\pi - 12\pi\beta}{-1 + 4\beta}, \tag{48}$$

$$\frac{1}{4} < \beta \leq \frac{1}{2},\ \lambda > \frac{6\pi - 12\pi\beta}{-1 + 4\beta} \ \ or \ \ \frac{1}{2} < \beta < 1,\ \lambda > 0. \tag{49}$$

The behavior of scale factor versus time is shown in Fig. 1(b) for some selected values of λ and β. The figure shows that the universe accelerates fast due to higher particle creation rate. For $\lambda = 0 = \beta$, $a \sim t^{1/2}$ and $q = 1$, which is the radiation phase in GR.

Case III: $\gamma = 1$

In this case, the universe expands with decelerated rate as $q > 0$ for $\beta = 0$ and $\lambda > 0$. Fig. 1(c) plots graph between scale factor versus time for some selected values of λ and β. For $\lambda = 0$, we have $q > 0$ for $0 < \beta < 1/3$, and $q < 0$ for $1/3 < \beta < 1$. The critical case ($\beta = 1/3$, $q = 0$), describes a coasting cosmology. For $\lambda \neq 0$ and $\beta \neq 0$, the model decelerates or accelerates under the following constraints:

$$0 < \beta < \frac{1}{3},\ 0 < \lambda < \frac{\pi - 3\pi\beta}{\beta}, \tag{50}$$

$$0 < \beta \leq \frac{1}{3},\ \lambda > \frac{\pi - 3\pi\beta}{\beta}\ \ or\ \ \frac{1}{3} < \beta < 1,\ \lambda > 0, \tag{51}$$

respectively. As expected, for $\lambda = 0 = \beta$, we have $a \sim t^{2/3}$ and $q = 1/2$, i.e., the model reduces to standard matter-dominated era of GR.

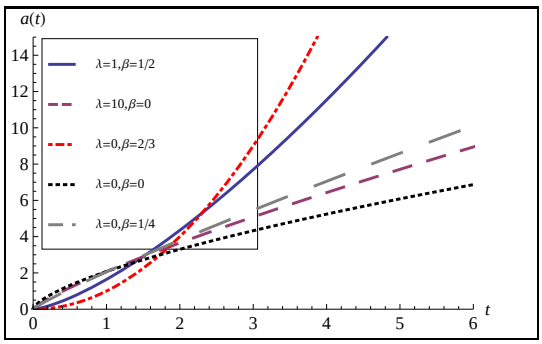


Fig. 1(c). Scale factor as a function of time for $\gamma = 1$ and some selected values of λ and β.

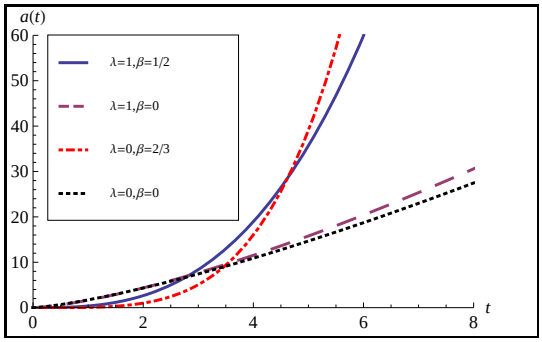


Fig. 1(d). Scale factor as a function of time for $\gamma = \frac{1}{2}$ and some selected values of λ and β.

Case IV: $\gamma = \frac{1}{2}$

In this case, if $\lambda = 0 = \beta$, $a \sim t^{4/3}$ and $q = -1/4$, which corresponds to the present accelerated phase of the universe of the standard FRW universe in GR. Since the universe accelerates even in absence of both $f(T)$ and particle creation, therefore, the contribution of $f(R,T)$ gravity or particle creation just enhance the rate of acceleration of the universe. Fig. 1(d) plots the dynamics of scale factor versus t, which is similar to case I.

6 Kinematic tests

Now, we derive some kinematical relations of the model as proposed in the preceding sections.

6.1 The density parameter

The density parameter, defined as $\Omega_m = \rho_m/\rho_c$, where $\rho_c = 3H^2/8\pi$, is given by

$$\Omega_m = \frac{8\pi}{8\pi + 4\lambda - (1-\beta)\gamma\lambda}. \tag{52}$$

Therefore, it is clear that $\Omega_m < 1$ for all values of $0 \leq \gamma \leq 2$, $0 < \beta < 1$ and $\lambda > 0$. Hence the universe is negatively curved. In absence of both λ and β, we have $\Omega_m = 1$ for all γ, i.e., the flat model of GR is recovered.

6.2 Lookback time-redshift

The lookback time $\Delta t = t_0 - t(z)$, is the difference between the age of the universe at the present time $z = 0$ and the age of the universe when a particular right ray at redshift z was emitted.

For a given redshift z, the scale factor $a(t_z)$ is related to a_0 by

$$a(t_z) = a_0(1+z)^{-1}. \tag{53}$$

From (41) and (53), the cosmic time in terms of redshift is given by

$$t(z) = \frac{2H_0^{-1}}{3\gamma A}(1+z)^{-\frac{3\gamma A}{2}}, \tag{54}$$

where H_0 is expressed in the usual practical observational units of $km\ s^{-1}\ Mpc^{-1}$ and its value is believing to be somewhere between 50-80 $km\ s^{-1}\ Mpc^{-1}$. However, H_0 is dimensionally similar to the reciprocal of time. The reciprocal of Hubble constant is called the Hubble time $t_H : t_H = H_0^{-1}$, where t_H is expressed in s and H_0 in s^{-1}. If H_0 is expressed in $km\ s^{-1}\ Mpc^{-1}$ and t_H in $gigayears$ ($1\ gr = 1\ milion\ years = 10^9\ years$) then $t_H = 977.8/H_0$.

Therefore, from (54) we have

$$t_0 - t(z) = \frac{2H_0^{-1}}{3\gamma A}\left[1 - (1+z)^{-\frac{3\gamma A}{2}}\right]. \tag{55}$$

Fig. 2 plots lookback time versus redshift for $\gamma = 1$ and some selected values of λ and β. All models coincide for lower redshift since they follow the same behavior. The graph shows that the lookback time increases for higher values of β. Thus, the universes with larger matter creation rate are older.

For small values of redshift, (55) becomes

$$H_0\,(t_0 - t(z)) = z - \left(1 + \frac{3\gamma A}{2}\right) z^2 + \cdots. \tag{56}$$

Taking lim $z \to \infty$ in (55), the present age of the universe is

$$t_0 = \frac{2H_0^{-1}}{3\gamma A} = \frac{H_0^{-1}}{1+q}. \tag{57}$$

Thus, the age of the universe depends on both parameters β and λ.

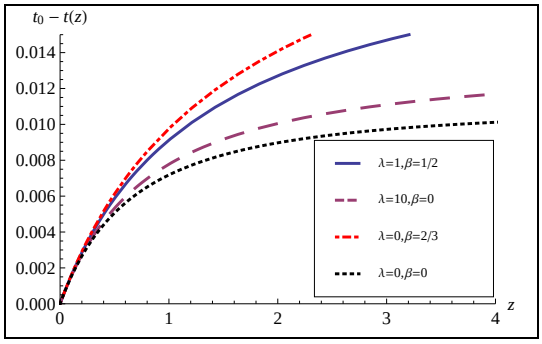


Fig. 2. Lookback time versus redshift for $\gamma = 1$, $H_0 = 60$ and some selected values of λ and β.

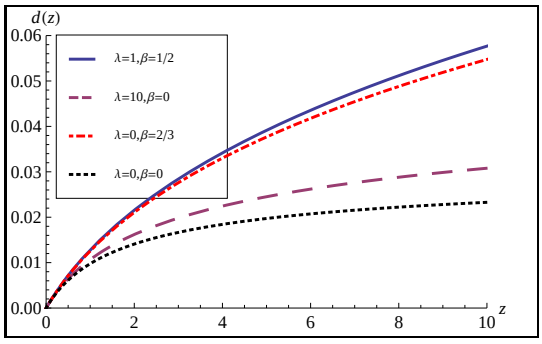


Fig. 3. Proper distance versus redshift for $\gamma = 1$, $H_0 = 60$ and some selected values of λ and β.

6.3 Proper distance-redshift

The proper distance between the source and observer is defined as $d(z) = a_0 r(z)$, where $r(z)$ is the radial distance of the object at light emission in term of redshift given by

$$r(z) = \int_t^{t_0} \frac{dt}{a(t)} = \frac{H_0^{-1}}{a_0\left(\frac{3\gamma A}{2} - 1\right)}\left[1 - (1+z)^{-\left(\frac{3\gamma A}{2}-1\right)}\right]. \tag{58}$$

Consequently, the proper distance becomes

$$d(z) = \frac{H_0^{-1}}{\left(\frac{3\gamma A}{2} - 1\right)}\left[1 - (1+z)^{-\left(\frac{3\gamma A}{2}-1\right)}\right]. \tag{59}$$

The proper distance as a function of redshift for some selected values of β and λ are displayed in Fig. 3. We observe that the $f(T)$ contribution in $f(R,T)$ and particle creation gives rise to proper distance.

Equation (59) can be rewritten as

$$H_0 d(z) = z - \frac{3\gamma A}{4} z^2 + \cdots . \tag{60}$$

From (59), it is observed that the distance dz is maximum at $z \to \infty$. Hence,

$$H_0 d(z \to \infty) = \frac{1}{\frac{3\gamma A}{2} - 1} = \frac{1}{q}. \tag{61}$$

6.4 Luminosity distance-redshift

The best-known way to trace the evolution of the universe observationally is to look into the redshift-luminosity distance relation. The luminosity distance d_l is defined by the relation $d_l^2 = \frac{l}{4\pi L}$, where l is the luminosity of the object and L is the measured flux from the object. In standard FRW cosmology it is defined in terms of redshift as

$$d_l = a_0(1+z)r(z) = (1+z)d(z). \tag{62}$$

From (59) and (62), we get

$$d_l H_0 = \frac{1}{\left(\frac{3\gamma A}{2} - 1\right)}\left[(1+z) - (1+z)^{-\left(\frac{3\gamma A}{2}-2\right)}\right]. \tag{63}$$

The graph between Luminosity distance and redshift for some selected values of β and λ is plotted in Fig. 4. One may observe that the luminosity distance corresponding to any specific value of redshift rises due to $f(R,T)$ gravity and particle creation.

Expanding (63) for small z, we find

$$H_0 d_l = z - \frac{1}{2}\left(\frac{3\gamma A}{2} - 2\right) z^2 + \cdots . \tag{64}$$

As expected, we find the same behavior for different models at $z \ll 1$ and the possible difference in behaviors for different models come at large redshift ($z \gg 1$). In Fig. 4 we observe that all curves start off with the linear Hubble law ($z = d_l H_0$) for small z, but then, only the curve for $q = 1$, i.e., $\beta = 0 = \lambda$ stays linear all the way. We also note that for the small redshift the luminosity distance is larger for lower values of q.

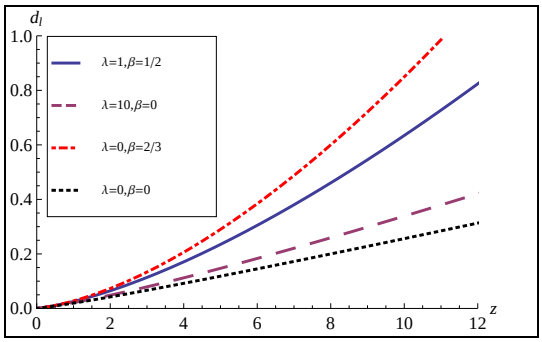


Fig. 4. Luminosity distance versus redshift for $\gamma = 1$, $H_0 = 60$ and some selected values of λ and β.

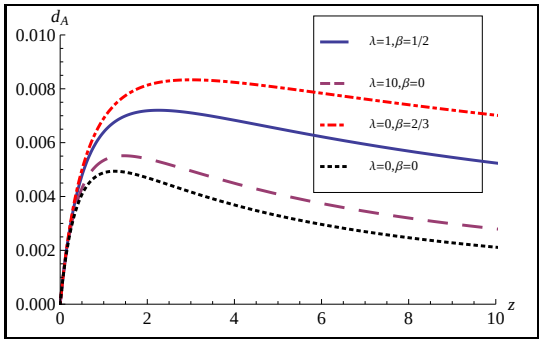


Fig. 5. Angular diameter distance versus redshift for $\gamma = 1$, $H_0 = 60$ and some selected values of λ and β.

6.5 Angular diameter distance-redshift

The angular diameter distance d_A is the ratio of physical transverse size of an object to its angular size (in radians). In terms of z, it is given by

$$d_A = \frac{d(z)}{1+z} = \frac{d_l}{(1+z)^2}. \tag{65}$$

Using (59), we have

$$H_0 d_A = \frac{1}{\left(\frac{3\gamma A}{2} - 1\right)} \left[(1+z)^{-1} - (1+z)^{-\frac{3\gamma A}{2}}\right]. \tag{66}$$

In Fig. 5 we plot the angular diameter distance versus redshift for some selected values of β and λ. The graph shows that the $f(R,T)$ and particle creation enhance the angular distance. The angular diameter distance initially increases with increasing z and eventually begins to decrease.

On expanding (66), we get

$$H_0 d_A = z + \left[1 - \frac{\left(\frac{3\gamma A}{2} + 1\right)\left(\frac{3\gamma A}{2} + 2\right)}{2\left(\frac{3\gamma A}{2} - 1\right)}\right] z^2 + \cdots. \tag{67}$$

7 Conclusion

In this paper, we have studied a flat FRW cosmological model described by an open thermodynamic system including particle creation at the expense of gravitational field in $f(R,T)$

theory of gravity. We have obtained exact solutions for the scale factor and various physical quantities by assuming a suitable form of $f(R,T) = R + 2f(T)$ and "gamma-law" equation of state. The model exhibits non-singular power-law expansion of the universe for $0 \leq \gamma \leq 2$. The model shows Big Rip singularity for $\gamma < 0$. The dynamics of the scale factor and other physical quantities have been examined through some graphical representations in various phases of evolution of the universe with some selected values of λ and β.

It has been observed that the scale factor always increases with decelerated and accelerated rate depending upon the contribution of particle creation and the parameter λ. It has been noticed that the universe expands with slow rate in early time but fast during late time. The energy density and effective pressure always decrease with time and both tend to zero in late time for $0 \leq \gamma \leq 2$. The number of particles increase with time in all phases. The number of particles in the absence of particle production remain constant throughout the evolution of the universe, which is quit obvious. The deceleration parameter has been found as a constant, which exhibits both decelerated and accelerated universe under some constraints on different parameters. The density parameter shows that the model becomes open in the presence of particle creation in $f(R,T)$ theory.

We have also discussed some observational consequences of the model through some kinematics tests such as lookback time, proper distance, luminosity distance and angular diameter distance with respect to redshift. The results for the cosmological tests are found to be compatible with the present observations. These tests are found to be depending on λ and β. The universe with particle creation is always older than the usual FRW model in absence of particle creation. The model of Lima et al. [21] may be recovered for $\lambda = 0$.

In summary, we have studied a cosmological model with particle creation in $f(R,T)$ gravity theory to understand the current acceleration expansion of the universe. We have found that the negative pressure due to the matter creation may play the role of dark energy and derive the accelerating expansion of the universe in $f(R,T)$ theory. We may expect that the process of particle creation is also an ingredient which accounts this unexpected observational results. The changes introduced by the particle creation process, which is quantified by the parameter β, provide reasonable observational results. The new fact justifying the present work is that we have considered the thermodynamics approach for which particle creation is at the expense of the gravitational field. A general expression relating the energy densities and particle number density as function of scale factor have been established. One may find that the particle creation changes the predictions of standard cosmology, thereby alleviating the problem of reconciling observations with the inflationary scenario. In future work, we plan to constraint cosmological model with matter creation using complimentary astronomical observations.

Acknowledgement VS expresses his sincere thank to University Grants Commission (UGC), India, for providing Senior Research Fellowship (SRF).

References

1. A.G. Riess et al., Astrophys. J. **116**, 1009 (1998)

2. S. Perlmutter et al., Astrophys. J. **517**, 565 (1999)

3. R.G. Vishwakarma, Mon. Not. Roy. Astron. Soc. **331**, 776 (2002)

4. C.B. Netterfield et al., Astrophys. J. **571**, 604 (2002)

5. D.N. Spergel et al., Astro J. Suppl. **148**, 175 (2003) [astro-ph/0302209]

6. V. Sahni, Lec. Notes Phys. **653**, 141 (2004) [astro-ph/0403324]

7. J. Frieman et al., Ann. Rev. Astron. Astrophys. **46**, 385 (2008) [astro-ph/0803.0982]

8. R.R. Caldwell, M. Kamionkowski, Ann. Rev. Nucl. Part. Sci. **59**, 397 (2008) [astro-ph/0903.0866]

9. L.M. Krauss, M. Turner, Gen. Rel. Grav. **27**, 1137 (1995)

10. M.S. Turner, M. White, Phys. Rev. D **56**, R4439 (1997)

11. T. Chiba, N. Sugiyama, T. Nakamura, Mon. Not. Roy. Astron. Soc. **289**, L5 (1997)

12. T. Padmanabhan, Phys. Rept. **380**, 235 (2003) [hep-th/0212290]

13. J. Martin, Mod. Phys. Lett. A **23**, 1252 (2008) [astro-ph/0803.4076]

14. U. Alam et al., Mon. Not. Roy. Astron. Soc. **354**, 275 (2004)

15. T. Chiba et al., Phys. Rev. D **62**, 023511 (2000)

16. T. Padmanabhan, T.R. Chaudhury, Phys. Rev. D **66**, 081301 (2002)

17. M.C. Bento et al., Phys. Rev. D **66**, 043507 (2002)

18. L.R.W. Abramo, J.A.S. Lima, Class. Quant. Grav. **13**, 2953 (1996)

19. W. Zimdhal, P. Pavón, Mon. Not. Roy. Astron. Soc. **266**, 872 (1994)

20. J.A.S. Lima, L.R.W. Abramo, Phys. Lett. A **257**, 123 (1999)

21. J.A.S. Lima, A.S. Germano, L.R.W. Abramo, Phys. Rev. D **53**, 4287 (1996)

22. I. Brevik, G. Stokkan, Astrophys. Space. Sci. **239**, 89 (1996)

23. A.H. Guth, Phys. Rev. D **23**, 347 (1981)

24. A.D. Linde, Phys. Lett. **108B**, 389 (1981)

25. W.L. Freedman, A. Olinto, J. Friemaan and D. Schramm, *Proceedings of the 18th texas Symposium on Relativistic Astrophys.* World Scietific (1998)

26. C. Brans, R.H. Dicke, Phys. Rev. D **124**, 925 (1961)

27. P.G. Bergmann, Int. J. Theor. Phys. **1**, 25 (1968)

28. K.Nortvedt, Astrophys. J. **161**, 1059 (1970)

29. R.V. Wagoner, Phys. Rev. D **1**, 3209 (1970)

30. P.A.M. Dirac, Nature **139**, 323 (1937)

31. V. Canuto, P.J. Adoms, S.H. Hsieh, E. Tsiang, Nature **261**, 438 (1976)

32. V. Canuto, P.J. Adoms, S.H. Hsieh, E. Tsiang, Phys. Rev. D **16**, 1643 (1977)

33. H. Bondi, T. Gold, Mon. Not. Roy. Astron. Soc. **108**, 252 (1948)

34. F. Hoyle, Mon. Not. Roy. Astron. Soc. **109**, 365 (1949)
35. J.V. Narlikar, *Nonstandard cosmologies*, in Vth Brazialian school of cosmology and Gravitation, ed. M. Novello (World Scientific, Singapore) 152 (1987)
36. E.P. Tryon, Nature **246**, 396 (1973)
37. P.I. Fomin, Dokl. Akad. Nank SSSR A **9**, 831 (1975)
38. R. Brout, F. Englert, E. Gunzig, Ann. Phys. (NY) **115**, 78 (1978)
39. R. Brout, F. Englert, E. Gunzig, Gen. Rel. Grav. **1**, 1 (1979)
40. R. Brout, F. Englert, F. Frére, J.M. Gunzig, P. Nardone, P. Spindel, C. Tuffin, E. Gunzig, Nucl. Phys. B **170**, 228 (1980)
41. R. Brout, F. Englert, P. Spindel, Phys. Rev. Lett. **43**, 417 (1979)
42. E. Gunzig, J. Gehenian, I. Prigogine, Nature **330**, 621 (1983)
43. I. Prigogine, J. Gohenian, E. Gunzig, P. Nardone, Proc. Natl. Acad. Sci. USA **85**, 7428 (1988)
44. M.O. Calvão, J.A.S. Lima, I. Waga, Phys. Lett. A **162**, 223 (1992)
45. J.A.S. Lima, A.S. Germano, Phys. Lett. A **170**, 373 (1992)
46. J.A.S. Lima, J.S. Alcaniz, Astron. Astrophys. **348**, 1 (1999)
47. J.S. Alcaniz, J.A.S. Lima, Astron. Astrophys. **349**, 72 (1999)
48. W. Zimdahl et al., Phys. Rev. D **64**, 063501 (2001)
49. Y. Qiang, T. Jiezhang, Y. Ze-Long, Astrophys. Space Sci. **311**, 407 (2007) [arXiv,astro-ph/0503123]
50. C.P. Singh, A. Beesham, Astrophys. Space Sci. **336**, 469 (2011)
51. C.P. Singh, A. Beesham, Int. J. Theor. Phys. **51**, 3951 (2012)
52. C.P. Singh, Astrophys. Space Sci. **338**, 411 (2012)
53. C.P. Singh, Mod. Phys. Lett. A **27**, 1250070 (2012)
54. T. Clifton, P.G. Ferreira, A. Padilla, C. Skordis, Phys. Rep. **513**, 1 (2012) [arXiv,astro-ph/1106.2476]
55. S. Nojiri, S.D. Odintsov, Phys. Rev. D **74**, 086005 (2006)
56. O. Bertolami, C.G. Bochmer, T. Harko, F.S.N. Lobo, Phys. Rev. D **75**, 104016 (2007)
57. T. Harko, Phys. Lett. B **669**, 376 (2008)
58. T. Harko, F.S.N. Lobo, S. Nojiri, S.D. Odintsov, Phys. Rev. D **84**, 024020 (2011) [arXiv,gr-qc/1104.2669]
59. M. Jamil, D. Momeni, M. Raza, R. Myrzakulov, Eur. Phys. J. C **72**, 1999 (2012)
60. M.J.S. Houndjo, Int. J. Mod. Phys. D **21**, 1250003 (2012) [arXiv,astro-ph/1107.3887]
61. M.J.S. Houndjo, O.F. Piattella, Int. J. Mod. Phys. D **2**, 1250024 (2012) [arXiv,gr-qc/1111.4275]
62. M.J.S. Houndjo, C.E.M. Batista, J.P. Campos, O.F. Piattella, Canadian. J. Phys. **91**, 548 (2013) [arXiv,gr-qc/1203.6084]
63. M. Sharif, M. Zubair, J. Cosmo. Astropart. Phys. **21**, 28 (2012) [arXiv,gr-qc/1204.0848]

64. M. Jamil, D. Momeni, R. Myrzakulov, Chin. Phys. Lett. **29**, 109801 (2012)

65. F.G. Alvarenga, M.J. Houndjo, A.V. Monwanou, J.B. Chabi Oron, J. Mod. Phys. **4**, 130 (2013) [arXiv,gr-qc/1205.4678]

66. M. Sharif, S. Rani, R. Myrzakulov, Eur. Phys. J. Plus **128**, 123 (2013) [arXiv,gr-qc/1210.2714]

67. M. Sharif, M. Zubair, J. Phys. Soc. Jpn. **82**, 014002 (2013) [arXiv,gr-qc/1210.3878]

68. S. Chakraborty, Gen. Rel. Grav. **45**, 2039 (2013) [arXiv,gen-ph/1212.3050]

69. F.G. Alvarenga, A. de la Cruz-Dombriz, M.J.S. Houndjo, M. E. Rodrigues, D. Sáez-Gómez, Phys. Rev. D **87**, 103526 (2013) [arXiv,gr-qc/1302.1866]

70. A. Pasqua, S. Chattopadhyay, I. Khomenkoc, Canadian J. Phys. **91**, 632 (2013)

71. H. Shabani, M. Farhoudi, Phys. Rev. D **88**, 044048 (2013)

72. M. Sharif, M. Zubair, J. Phys. Soc. Jpn. **82**, 064001 (2013) [arXiv,gr-qc/1310.1067]

73. C.P. Singh, V. Singh, Gen. Rel. Grav. **46**, 1696 (2014)

74. K.S. Adhav, Astrphys. Space. Sci. **339**, 365 (2013)

75. S.D. Katore, A.Y. Shaikh, Prespacetime J. **3**, 1087 (2012)

76. M. Sharif, M. Zubair, J. Phys. Soc. Jpn. **81**, 114005 (2012) [arXiv,gr-qc/1301.2251]

77. V.U.M. Rao, D. Neelima, Astrphys. Space. Sci. **345**, 427 (2013)

78. N. Ahmed, A. Pradhan, Int. J. Theor. Phys. **53**, 289 (2014)

79. I. Prigogine, J. Gohenian, E. Gunzig, P. Nardone, Gen. Rel. Grav. **21**, 767 (1989)

AN IMPROVED METHOD FOR SOIL DNA EXTRACTION TO STUDY THE MICROBIAL ASSORTMENT WITHIN RHIZOSPHERIC REGION

Faria Fatima[1], Neelam Pathak[1] and Smita Rastogi Verma[2]*

[1]Department of Biosciences, Integral University, Lucknow-226026, India

[2]Department of Biotechnology, Delhi Technological University, Delhi-110042

*Corresponding author email: smita_rastogi@rediffmail.com

ABSTRACT

The need for identification of soil microbial community mainly depends on direct extraction of DNA from soil, a multifaceted environment that is a major pool for microbial genetic diversity. The soil DNA extraction procedures usually suffer from two major problems, *viz.*, inappropriate rupturing of cells and contamination with humic substances. In the present study, five protocols for single type of rhizospheric soil were investigated and their comparison indicated that the inclusion of 120 mM phosphate buffered saline (PBS) for washing and mannitol in the lysis buffer allowed the processing of soil sample in minimal time with no specific equipment requirement. Furthermore, DNA purity and yield was also improved, which allowed the exploitation of genetic potential of soil microbes within soil sample thereby facilitating the amplification of metagenomic DNA. The effectiveness of methods was analyzed using random amplification of polymorphic DNA. The banding patterns revealed that both the abundance and the composition of indigenous microbial community depend on the DNA recovery method.

***Keywords**:* Ribosomal DNA Analysis, Random Amplification of Polymorphic DNA, Soil DNA Extraction Protocols, Soil Microbial Community.

INTRODUCTION

The biodiversity of microbes within soil is significant for the maintenance of healthy soil because these microbes are involved in many vital functions like crucial cycles of C, N, P, formation of soil, toxin removal and so on. Previously, studies on the development of microbial communities required the isolation of these microbes from soil sample by culture dependent techniques followed by a series test for phenotypic evaluation and their identification. However, the microbial diversity studies conducted in soil have been biased essentially due to the unculturability of many microbes. Specific media, which are used to culture microbes, are selective in nature and only subpopulations of microbes from environment sample that will grow mainly depend on the particular conditions. It is reported that only 1 % of microbes can be cultured in the laboratory using traditional culture techniques (Marchesi *et al.,* 1998).

To study the microbial community, microbiologists have adopted culture-independent techniques. These techniques employ molecular biology based methods, in which soil extracted nucleic acid is subjected to PCR amplification (Roh *et al.,* 2006). These methods provide a unique insight into richness, composition and structure of microbial community i.e., species richness and species evenness. The results thus rely not only on DNA extraction procedures but also on the factors affecting PCR amplification. Moreover, these culture-independent methods should address the problems like incomplete rupturing of cells and presence of soil organic substances namely, fulvic and humic acid, the presence of which inhibit the activity of DNA polymerase and interfere with the hybridization protocols (Luo *et al.,* 2003). Fractions like humic acids are usually the complex mixtures of related compounds (DNA) demonstrating a broad range spectrum of solubility and charge characteristics. Various physical and chemical treatments have been evaluated for cell rupture, which include shaking the sample in lysis buffers containing high concentration of sand, detergents or glass beads, inclusion of lysozyme (Frostegard, 1999). Furthermore, purification of silica and other bio gel columns have been reported to minimize the humic acid contamination. These procedures, however, make DNA isolation process expensive involving a large number

of steps, which makes these procedures lengthy, time taking and tedious. Therefore, an improved method is required for soil DNA extraction that allows efficient rupturing of microbial cells and simultaneously decreases the contamination of organic materials (humic acid) with ease in a cost-effective manner.

The analysis of microbial diversity in the soil DNA extracts is then based on ARDRA-amplified ribosomal DNA restriction analysis (Weidner *et al.,* 1996), DGGE-denaturing gradient gel electrophoresis and 'T'-RFLP–Transfer restriction fragment length polymorphism (Goldstein *et al.,* 1987). However, random amplification of polymorphic DNA (RAPD) technique is preferred, as the above described techniques may not amplify fragments from all community members with equal effectiveness (Pepper and Pillai, 1994). Such approach thus offers significant advantage over just 1 % of the microbial community accessible with standard, culture-based techniques. An additional advantage is that only small amount of soil sample is required for analyzing microbial diversity in a short span of time.

In the present study, four DNA extraction methods and a commercial *Soil Master*^{TM} DNA extraction kit were used to extract DNA directly from soil and the effectiveness of these methods was estimated by RAPD analysis.

MATERIAL AND METHODS

DNA extraction methods

Five DNA extraction methods were evaluated in this study with respect to the quality and purity of extracted DNA using single type of rhizospheric soil. Three modified mannitol-based methods (Fatima *et al.*, 2011), polyethylene glycol (PEG/NaCl) method (Yeates *et al.,* 1998) and a soil DNA extraction kit were compared for obtaining a high recovery and DNA with good yield and purity. Isolated soil samples isolated and immediately placed on dry ice, mixed and then stored at -20° C prior to DNA extraction.

(A) DNA extraction using polyethylene glycol (PEG)/NaCl method

One gram of soil sample was mixed with 10 ml of DNA extraction buffer [120 mM Na_2HPO_4 (pH 7.4), 5 % SDS (w/v) and 0.02 g PVPP] in centrifuge tubes and incubated

for 1 h at 65° C with occasional stirring. The supernatant was collected after centrifugation at 8,000 rpm for 10 min at 4° C and mixed with half volume PEG and 1 volume of NaCl and incubated at 4° C for overnight. Further, 1 volume of chloroform: isoamyl alcohol (24:1) was added and centrifuged at 12,000 rpm for 10 min at 4° C. The supernatant obtained was precipitated by addition of $1/10^{th}$ volume of 3 M sodium acetate (pH 5.2) and 2 volumes ethanol. Finally, the pellet was recovered by centrifugation at 12,000 rpm at 4° C and dissolved in 25 µl TE buffer [Tris-HCl 10 mM (pH 7.8); EDTA 1 mM (pH 8)].

(B) DNA extraction using soil DNA extraction kit (*Soil Master*™ DNA extraction kit)

DNA was extracted from soil sample (1 gm) according to the specifications of the supplier (EPICENTRE, Madison, WI, USA). The method involved direct cell lysis with pre-warmed 5 ml solution A at 65° C and vortexing for 10 min. This mixture was incubated for 15 min at 65° C. The supernatant were collected after centrifugation at 8,000 rpm at 4° C for 10 min and mixed with equal volume of solution B that led to precipitation. The steps were repeated two times when the color of supernatant changed to yellow. Finally the pellet was recovered by centrifugation at 12,000 rpm for 10 min at 4° C and dissolved in 25 µl TE buffer.

(C) Modified mannitol-based methods

One gram of soil sample was ground using liquid nitrogen. This was followed by addition of 5 ml of 120 mM phosphate buffer saline (pH 7.4) and shaking at 150 rpm for 10 min at 4° C. The soil suspension was centrifuged at 7,000 rpm for 10 min. The pellet was rewashed with PBS buffer and suspended in 10 ml of DNA extraction buffer containing 1 M Tris-HCl (pH 8.0), 5 M NaCl, 0.5 M EDTA (pH 8.0), 10 % CTAB, 10 % SDS and 0.2 M mannitol. The suspension was incubated for 1 h at 65° C with occasional stirring of 150 rpm and subjected to three different treatments as indicated:

(i) DNA extraction by Mannitol - Phosphate buffer saline - Polyethylene glycol/ Sodium chloride (Mannitol-PBS-PEG/NaCl) method

The soil suspension described above was centrifuged at 8,000 rpm for 10 min at 4° C and the supernatant obtained was mixed with half volume of polyethylene glycol-8000 (50 %) (PEG) and 1 volume of NaCl and allowed to incubate at 4° C for overnight. The pellet was recovered by centrifugation at 12,000 rpm, 4° C for 10 min and dissolved in 3 ml of TE buffer. The DNA sample was then purified by phenol: chloroform extraction. Finally DNA was precipitated by addition of $1/10^{th}$ volume of 3 M sodium acetate (pH 5.2) and 2 volumes of ethanol. The pellet was recovered by centrifugation at 12,000 rpm for 10 min at 4° C and dissolved in 25 µl TE buffer [Tris-HCl 10 mM (pH 7.8); EDTA 1 mM (pH 8)].

(ii) DNA extraction by Mannitol - Phosphate buffer saline - Phenol/ Chloroform/ Isoamyl alcohol (Mannitol-PBS-PCI) method

After centrifuging the soil suspension as previously described, the supernatant thus obtained was extracted with an equal volume of PCI by centrifugation at 12,000 rpm for 10 min at at 4° C. Aqueous fraction was mixed with $1/10^{th}$ volume of 3 M sodium acetate (pH 5.2) and 2 volume 70 % chilled ethanol at 4º C. Finally the pellet was recovered by centrifugation at 12,000 rpm for 10 min at 65º C and dissolved in 25 µl TE buffer [Tris-HCl 10 mM (pH 7.8); EDTA 1 mM (pH 8)].

(iii) DNA extraction by Mannitol -Phosphate buffer saline - Cetrimide (Mannitol-PBS-CTAB) method

After centrifugation of soil suspension, 50 µl of 5 M NaCl and 50 µl of 10 % CTAB (Cetrimide prepared in 0.7 M NaCl) were added to the supernatant and incubated at 4° C for 15 min. This was followed by addition of equal volume of PCI and centrifugation at 12,000 rpm, 4° C for overnight. Aqueous layer was allowed to precipitate overnight at 4° C with $1/10^{th}$ volume of 3 M sodium acetate (pH 5.2) and 2 volumes ethanol. Finally the pellet was recovered by centrifugation at 12,000 rpm for 10 min at 65º C and dissolved in 25 µl TE buffer [Tris-HCl 10 mM (pH 7.8); EDTA 1 mM (pH 8)].

DNA yield and purity

The DNA concentration of the soil sample was measured by examining the absorbance of the sample at 260 nm and amount of DNA was calculated (1.0 A_{260} unit =50 µg/ml of

DNA) (Yeates *et al.,* 1998). The purity of the extracted DNA was determined by taking absorbance at 230, 260 and 280 nm. A pure sample of DNA has the A_{260}/A_{280} ratio as 1.8, and the A_{260}/A_{230} ratio as 2.0, whereas DNA preparation that is contaminated with protein will have an A_{260}/A_{280} ratio lower than 1.8 (Sambrook *et al.,* 1989).

PCR amplification of isolated soil DNA using 16S rRNA primers for bacterial identification

Soil DNA was amplified by PCR using a PCR BIORAD Thermal Cycler (United Kingdom). Each 25 µl PCR mixture contained 1 µl (1:10 dilution) community DNA (10 ng-20 ng), 2.5 µl PCR buffer (1 X), 1 µl of each deoxyribonucleoside triphosphate (dNTP) (100 mM), 1 µl of forward and reverse primers (0.5 µM) and 0.5 µl *Taq* polymerase (3 U) (Fermentas). The 16S rRNA regions were amplified by using 16S rRNA primers, viz., (FP1) 5'-TGGGGAGCAAACAGGATTAG-3' and (RP1) 5'-TAAGGTTCTTCGCTTGCTT-3'. The amplification cycle consisted of an initial denaturation step of 30 min at 94° C, followed by 35 cycles of 1 min at 94° C (denaturation), 1 min at 55° C (annealing) and 2 min at 72° C (extension), with a final extension step for 5 min at 72° C. For visualizing PCR products, 5 µl of the amplified product was electrophoresed on 1 % agarose gel in 1 X TAE buffer, stained with ethidium bromide (EtBr 0.5 µg/ml) and analyzed by gel documentation system (BIORAD). Lambda DNA *Hin*d-*III/Eco*RI double digest was used as a molecular size marker.

PCR amplification of soil DNA extract using 18S rRNA primers for fungal identification

Soil DNA was submitted for PCR amplification by using PCR BIORAD Thermal Cycler (United Kingdom). A region from 18S rRNA gene was amplified using internal transcribed spacer (ITS) primers, viz., ITS 5: (5'-GGAAGTAAAAGTCGTAACAAGG-3') and ITS 4 (5'-TCCTCCGCTTATTGATATGC-3'). Each 25 µl reaction mixture contained 2 µl soil DNA (10 ng-20 ng), 2.5 µl PCR buffer (1 X), 0.5 µl deoxyribonucleoside triphosphate (dNTP mix) (100 mM), 0 .5 µl of forward and reverse primers (0.2 µM), 2 µl of $MgCl_2$ (25 mM) and 0.5 µl *Taq* polymerase (3 U)

(Fermentas). The amplification cycle consisted of an initial denaturation step of 5 min at 94° C, followed by 35 cycles of 1 min at 94° C (denaturation), 1 min at 59° C (annealing) and 2 min at 72° C (extension), with a final extension step for 10 min at 72° C.

Random amplification of polymorphic DNA (RAPD)

To test the efficiency of soil DNA extraction methods, RAPD was performed on community DNA. Four decameric RAPD primers, namely, OPA 3, OPA 13, OPA 15, OPA 20 (Operon Technologies) were investigated (Table 1). Random primers are short DNA fragments of arbitrary nucleotide sequence that can differentiate between genetically distinct individuals. The RAPD analysis was carried out through PCR amplification of total DNA. Amplification reactions were performed in a total volume of 25 µl containing 2.5 µl PCR-buffer (10 X), 2.5 µl dNTP mix (2 mM), 1 µl decameric primers (20 pmole), 2 µl template (soil) DNA (100 ng) and 0.5 µl *Taq* DNA polymerase (3 U). The final volume was made up to 25 µl using sterile distilled water. The amplification reaction was performed for 45 cycles, each cycle comprising of 3 min at 94º C (denaturation), 1 min at 32º C (annealing) and 2 min at 72º C (extension), with a final extension at 72° C for 10 min.

Table 1: Random primers used for RAPD analysis and their annealing temperature

Random primer	Primer sequences	Annealing temperature
OPA 3	5'-AGTCAGCCAC	32° C
OPA 13	5'-CAGCACCCAC	32° C
OPA 15	5'-TTCCGAACCC	32° C
OPA 20	5'-GTTGCGATCC	32° C

Analysis of PCR products

For visualizing PCR products, 5 µl of the amplified product was electrophoresed on 1 % agarose gel in 1 X TAE buffer, stained with ethidium bromide (0.5 µg/ml) and analyzed

by Gel Documentation system (BIORAD). Lambda DNA *Hin*d-*III/Eco*RI double digest was used as a molecular size marker.

RESULTS AND DISCUSSION

For soil microbial analysis, it is essential to design protocols which yield high quality soil DNA of appropriate yield and purity for PCR amplifications. Besides, the selected methods for soil DNA extraction should be cost-effective and time-saving. Effectiveness of soil DNA extraction procedures may be influenced by various parameters such as incomplete cell lysis, DNA sorption to soil surfaces, extraction of humic contaminants and DNA degradation. Thus, extraction of high molecular weight DNA, proper lysis of microbes and inhibitor-free DNA are the major requirements for any protocol used for metagenomic study (Gu *et al.,* 2005).

For cell lysis to be effective, mechanical treatment should be followed rather than chemical ones (More *et al.,* 1994). According to Frostegard (1999), proper grinding of sample ruptures and outcome in release of cellular DNA from the inner compartment.

Soil DNA extraction procedures should therefore be free from PCR inhibitors or their concentration must be low enough so that they do not interfere with the enzymatic reactions. Usually organic matter is the major source of inhibitors that may be co-extracted with the microbial DNA present with in the soil. Majorly, humic acids creates considerable problem like interference in activity of DNA polymerase used for PCR reactions (Courtois *et al.,* 2001). As, humic acid contains same charge and size characteristics like DNA, it exhibits absorbance at both 230 and at 260 nm and hence interferes in quantization of DNA. This characteristic can be used to find out the level of contamination of humic acid in an isolated DNA sample.

The present study involved comparison of five methods for isolation of soil DNA. Three methods having mannitol in their extraction buffer yielded an amount of DNA that was significantly higher than that obtained with the *Soil Master*^{TM} DNA extraction kit and PEG/NaCl method (Table 2). Moreover, the purity of DNA isolated by modified mannitol-based methods was significantly higher as compared to other methods (Table 2). The addition of mannitol in the extraction buffer has already been reported to enhance the efficiency of soil DNA extraction (Fatima *et al.,* 2011). Further modification of these

methods by inclusion of 120 mM phosphate buffered saline in the initial steps led to reduction in the level of organic contaminants such as humic acid at initial stages. (Table 2) *Soil Master*™ DNA extraction kit and PEG / NaCl method with liquid nitrogen method consistently extracted DNA with higher $A_{260/230}$ and $A_{260/280}$ ratios, thereby indicating that the DNA was contaminated with humic acid-like compounds and proteins, respectively. $A_{260/230}$ ratio of more than 2.0 was obtained with all the three mannitol-based methods, which was indicative of the fact that humic acid material very effectively reduced by these methods as compared to other two methods.

Table 2: Comparison of amount, purity of DNA and humic acid contamination extracted from various isolation protocols

DNA Extraction Protocol	**Amount of DNA (µg /ml)**	**$A_{260/230}$**	**$A_{260/280}$**
DNA extraction using PEG/NaCl Method (Yeates *et al.*, 1998)	0.73	1.12	1.26
DNA extraction using commercial soil DNA extraction kit (*Soil Master*™ DNA extraction kit; EPICENTRE, Madison, WI, USA)	0.79	1.21	1.32
DNA extraction by Mannitol-PBS-PEG/NaCl method	2.20	1.84	1.81
DNA extraction by Mannitol-PBS-PCI method	2.36	1.93	1.84
DNA extraction by Mannitol-PBS-CTAB method	2.67	2.07	1.85

The three modified mannitol-based methods led to the recovery of high molecular weight soil DNA (Figure 1). The recovery of high molecular weight DNA fraction is desirable for PCR assays used for microbial diversity analysis because the degraded DNA uphold the formation of chimera products. Moreover, these three modified mannitol-based methods were found to be more-suited for PCR amplification. Nuclear rRNA genes have been useful in the molecular study of bacterial and fungal diversity (Bruns and Horton, 2001).

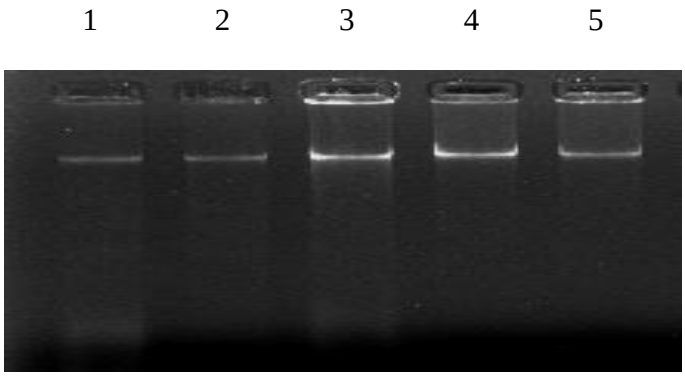


Figure 1: Visualization of soil DNA extracted by various methods. [lane 1: PEG / NaCl method without liquid nitrogen; lane 2: *Soil Master*^{TM} DNA extraction kit; lane 3: Mannitol-PBS-CTAB method; lane 4: Mannitol-PBS-PCI method; and lane 5: Mannitol-PBS-PEG/NaCl method]

High quality PCR amplicons with higher yields were observed in case of these three methods using 16S rRNA-specific and ITS-specific primers (ITS1/ITS4) for bacterial and fungal analysis, respectively. In each case, amplified products corresponded to expected sizes according to primers used. A single amplification product of ~1.2 Kbp for bacteria (Figure 2) and ~720 bp for fungi (Figure 3) were obtained. In case of other two methods, namely, PEG/NaCl with liquid nitrogen method and *Soil Master*^{TM} DNA extraction kit, an acceptable level of DNA was amplified for bacterial community (Figure 2; Lanes 1 and 4) but these two methods were not suitable for PCR amplification for fungal study (Figure 3; Lanes 2 and 5). Usually, an enzyme DNA polymerase used in amplification processes requires contamination-free sites for proper functioning. Furthermore, better PCR amplification of soil DNA isolated by the three modified mannitol-based methods demonstrated better DNA yield and quality as compared to other two methods. The study suggested that all three mannitol-based methods (PCI, PEG/NaCl and CTAB) gave very good yield of DNA which was suitable for the amplification study in comparison with other two methods which might be due to DNA-adhering substances like humic/fulvic acid having same charge characteristics as that of DNA that were co-precipitated in the mannitol-devoid methods. Humic acid impurities may affect DNA hybridization

efficiency too. In the methods investigated, where mannitol with liquid nitrogen was used, showed high-quality chemical lysis when compared with other methods. It also proves that an addition of PBS bufffer and mannitol may play an important role in proper chemical lysis of the cells as compared to other chemicals like CTAB, SDS, and EDTA etc.

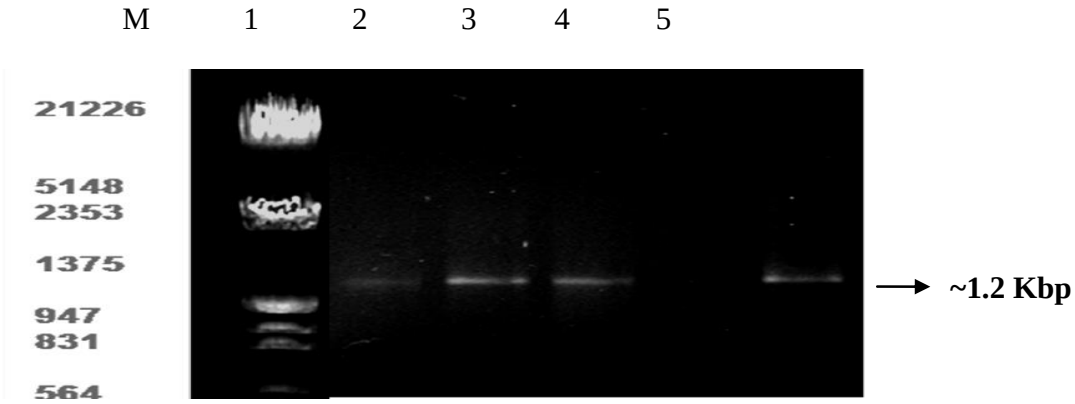


Figure 2: Visualization of PCR amplification products of soil DNA isolated by five different methods using 16S rRNA by different methods [lane M: λ DNA *Eco*RI/*Hin*d III double digest marker; lane 1: Mannitol-PBS-PCI method; lane 2: *Soil Master*^{TM} DNA extraction kit; lane 3: Mannitol-PBS-CTAB method; lane 4: PEG / NaCl method without liquid nitrogen; and lane 5: Mannitol-PBS-PEG/NaCl method]

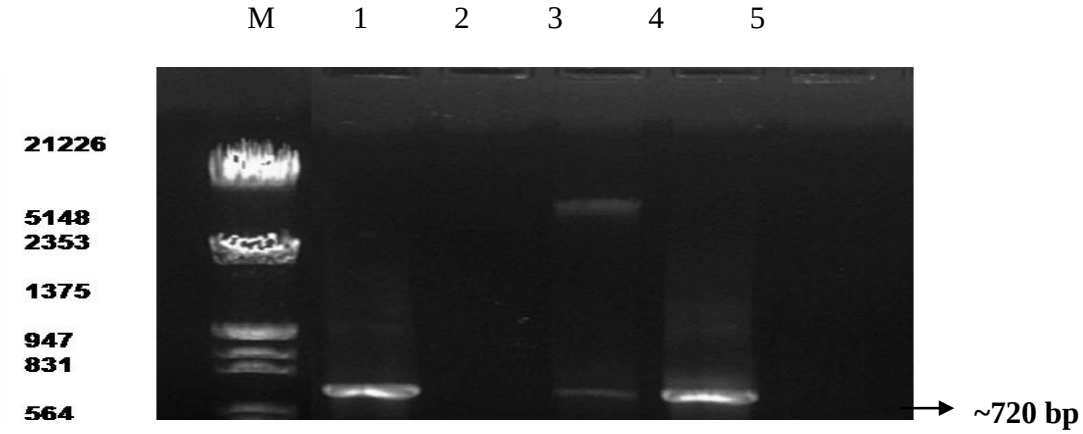


Figure 3: Visualization of PCR amplification products of soil DNA isolated by five different methods using 18S rRNA by different methods [lane M: λ DNA *Eco*RI/*Hin*d III double digest

marker; lane 1: Mannitol-PBS-CTAB method; lane 2: PEG / NaCl method without liquid nitrogen; lane 3: Mannitol-PBS-PEG/NaCl method; lane 4: Mannitol-PBS-PCI method; and lane 5*: Soil Master*™ DNA extraction kit]

Thus, these methods proves as a low-cost and practical alternative to accessing metagenomic content by addition of phosphate buffer (PBS) and mannitol within the soil sample.

Varying patterns of RAPD bands were found when soil community DNA samples were amplified using random primers. This indicated that the reported soil DNA extraction methods were quite feasible and reproducible for microbial diversity analysis (Figure 4 and Figure 5). It was observed that the soil DNA isolated by protocols having mannitol were amplified easier than the methods using PEG/NaCl and Soil DNA extraction kit.

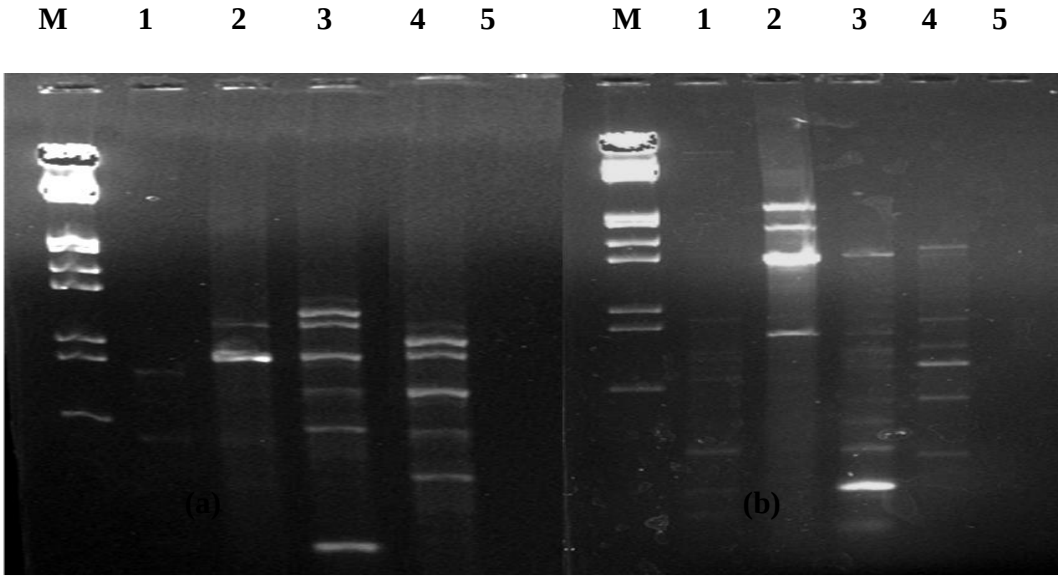


Figure 4: RAPD analysis of soil DNA samples isolated by five methods using random decameric primers. (a) OPA 3 (b) OPA 13 [lane M: λ DNA *Eco*RI/*Hin*d III double digest marker; lane 1: *Soil Master*™ DNA extraction kit; lane 2: Mannitol-PBS-CTAB method; lane 3: Mannitol-PBS-PEG/NaCl method; lane 4: Mannitol-PBS-PCI method; and lane 5: PEG / NaCl method without liquid nitrogen]

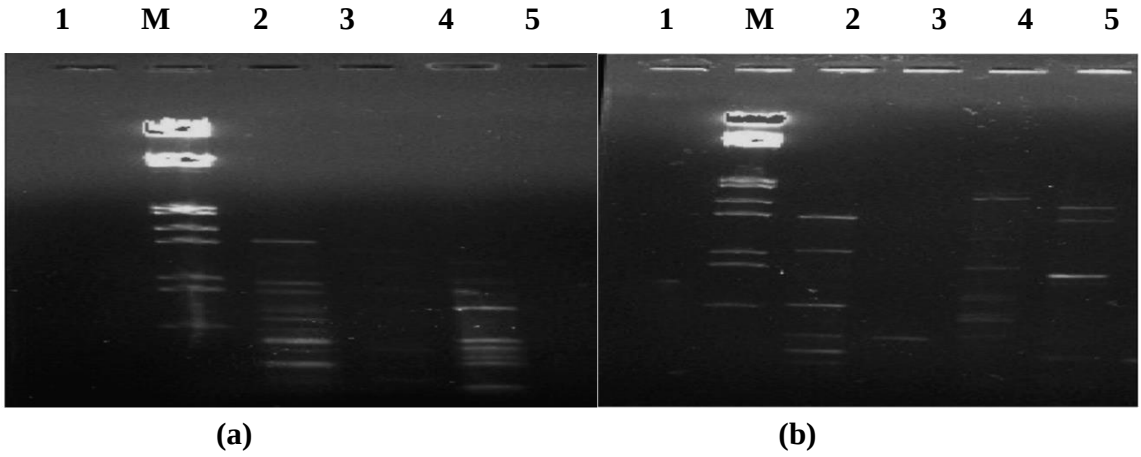


Figure 5: RAPD analysis of soil DNA samples isolated by five methods using random decameric primers. (a) OPA 15 (b) OPA 20 [lane M: λ DNA *Eco*RI/*Hin*d III double digest marker; lane 1: PEG / NaCl method without liquid nitrogen; lane 2: Mannitol-PBS-CTAB method; lane 3: *Soil Master*™ DNA extraction kit; lane 4: Mannitol-PBS-PCI method; and lane 5: Mannitol-PBS-PEG/NaCl method]

Thus, the procedure presented here proves to be an inexpensive procedure, which not only prevents the loss of DNA but also reduces the risk of contamination by laboratory DNA source. The protocols involved the usage of mannitol within the lysis buffer to isolate DNA from bacterial as well as from fungal mycelia. The methods used in the present study exhibited sufficient quality and integrity to amplify the genetic regions, which provided a complete information and understanding of microbial biota. An inclusion of mannitol and sodium chloride promoted cell disruption and extracted humic acid and other organic contaminants the presence of which would have otherwise inhibited PCR reaction. Hereby, it is demonstrated that a molecular approach using culture independent study can be used to complement more traditional methods used for the survey of microbial communities and provides an expanding toolbox, which helps the soil ecologists and taxonomists to explore microbial communities, which are still unidentified. The modified protocols can also contribute to *in situ* study of bacterial as well as fungal ecological processes.

CONCLUSION

In the present study, efficient soil DNA extraction procedures have been reported, which are simple, efficient and do not require elaborate instrumentation and yield good quality DNA suitable for the study of bacterial and fungal genes. It has been demonstrated that an additional step of using phosphate buffer saline with inclusion of mannitol was useful to achieve these objectives. The PCR amplification procedures involve several enzymatic reactions where the enzyme DNA polymerase requires sites, which should be contamination-free. It is suggested that the initial washing with PBS buffer led to removal of unwanted impurities such as humic acid present in the soil. Mannitol, having high salt nature, led the recovery of high molecular weight DNA. It probably interacted with cell wall resulting in cell disruption and extraction of humic acid near the beginning of the isolation procedure. Thus, these modified mannitol-based protocols help not only in improving the yield and quality of extracted soil DNA but also in exploitation of large-scale preparations which provide greater possibility of detecting genes present in low abundance within the soil environment. When combined with the methods developed for normalization of total metagenomic DNA, these modified protocols may offer an easy method for monitoring the population dynamics of the total microbial population in soils over time.

CONFLICT OF INTEREST

The authors declare that there is no conflict of interests.

ACKNOWLEDGEMENTS

The financial support in the form of research grant from UP State Biodiversity Board, India is highly acknowledged. The grant of UGC-Maulana Azad National Fellowship is gratefully acknowledged.

REFERENCES

1. Bruns, T., & Horton, T. (2001). The molecular revolution in ectomycorrhizal ecology: peeking into black box. Mol. Ecol,10,1855-1872.
2. Courtois, S., Frostegard, A.S., Goransson P. (2001). Quantification of bacterial subgroups in soil: comparison of DNA extracted directly from soil or from cells previously released by density gradient centrifugation. Environ. Microbiol., 7:431–439.
3. Fatima, F., Chaudhary, I., Ali, J., Rastogi, S., & Pathak, N. (2011). Microbial DNA extraction from soil by different methods and its PCR amplification. Biochem. Cell. Arch. Vol. 11, No. 1. ISSN 0972-5075.
4. Frostegard, A., Courtois, S., Ramisse, V., Clerc, S., Bernillon, D., Gall, F., Jeannin, P., Nesme, X., & Simont, P. (1999). Quantification of bias related to the extraction of DNA directly from soils. Appl. Environ. Microbiol., 65, 5409-5420.
5. Goldstein, AH., Liu, ST. (1987). Molecular cloning and regulation of a mineral phosphate solubilizing gene from *Erwinia herbicola.* Bio/Technology. 5, 72–4.
6. Gu, H.J., Li, Y., Zhao, W. (2005). Comparison of methods of DNA extraction from paddy soil. J. Jiangsu Univ, 15, 300–305.
7. Luo, H., Qi, H., Xue, K., Zhang, H. (2003). A preliminary application of PCR-DGGE to study microbial diversity in soil. Acta Ecologica Sini. 23:1570–1575. (in Chinese)
8. Marchesi, R., Weightman, J., Martin, T. A., Fry, J. C., Hiom, S. J., & Wade. W. (1998). Design and evaluation of useful bacterium specific PCR primer that amplify genes coding for bacterial 16S rRNA. Appl. Environ. Microbiol, 64, 795-799.
9. More, M., Herrick, J., Silva, B., Madisen. L. (1994). Quantitative cell lysis of indigenous microorganisms and rapid extraction of microbial DNA from sediment. Appl. Environ. Microbiol, 60, 1572-1580.

10. Roh, C., Villatte, F., Kim., B, & Schmid, R. (2006). Comparative study of methods for extraction and purification of environmental DNA from soil and sludge samples. Appl. Biochem. Biotechnol. 134, 97–112.

11. Sambrook, J., Fritsch, E F., and Maniatis, T. (1987). Molecular cloning – a laboratory manual. Cold Spring Harbor, USA, Cold Spring Harbor Laboratory Press.

12. Weidner, S., Arnold, W., Pühler, A. (1996). Diversity of uncultured microorganisms associated with the seagrass Halophila stipulacea estimated by restriction fragment length polymorphism analysis of PCR-amplified 16S rRNA genes, Appl. Environ. Microbiol., 62 , 766–771.

13. Yeates, C., Gillings, M.R.., Davison, A.D., Altavilla, N., Veal, D.A. (1998). Methods for microbial DNA extraction from soil for PCR amplification. Biol. Proc..1:40–47.

This article has been accepted for inclusion in a future issue of this journal. Content is final as presented, with the exception of pagination.

Average Absolute Frequency Deviation Value Based Active Islanding Detection Technique

Pankaj Gupta, R. S. Bhatia, and D. K. Jain

***Abstract*—An average absolute frequency deviation value based active islanding detection technique is proposed in this paper. The inverter's classical q-axis current controller is modeled with a continuous periodic reference current of a small value. During the loss of mains, the island's frequency deviates with respect to the variation in the reference current; this is detected by making the use of an average absolute frequency deviation value. In case of a stable island formation, there is a small periodic frequency deviation owing to the small value of the periodic reference current, and the frequency deviation is so small that it falls inside the nondetection zone (NDZ) of the frequency relay. The main advantage of the proposed algorithm is that it detects the stable island formation but without forcing the island to lose its stable operation. In case of nonislanding switching events, which may transiently impose a significant deviation in the frequency, the possibility of false detection is eliminated by reconfirming the occurrence of islanding once it is suspected. The reference current is kept to a small value to limit the degradation of the power quality and the power factor. Computer simulation is done with MATLAB.**

***Index Terms*—Average absolute frequency deviation value ($AFDV_{avg}$), distributed generation (DG), islanding detection technique (IDT).**

I. Introduction

UNINTENTIONAL islanding (UI) of a distributed generation (DG) may arise many safety and protection issue in the islanded portion of an electric power system (EPS) [1]–[3]. UI may result in an uncontrolled frequency and voltage, which may damage or reduce the life of the appliances and equipments present in the island. The safety of the utility line workers is at risk as they may get an electric shock due to the presence of an active DG in the island. Instantaneous reclosing of the DG to EPS is another major concern as it may result in the out of phase reclosing of the circuit breakers. The heavy mechanical torque and the high transient inrush current may even damage the islanded DG [4], [5]. UI may have various adverse consequences on the EPS and it is extremely essential to stop the operation of a DG during a UI. An islanding detection technique (IDT) must detect the islanding within the 2 s of the formation of an island and the DG operation must be ceased [1].

There are various IDT, which can be broadly classified into the remote techniques and the local techniques [4]. The remote techniques are based on the communication between the grid and the DG [5], [6]. These techniques are reliable but are very expensive and complex to implement. However, the local techniques are less expensive as they are based on the measurement of parameters at the local DG terminal and are generally preferred. These techniques are further classified into the passive [7]–[14] and the active techniques [15]–[22]. The passive islanding detection techniques fail to detect the islanding under the perfectly matched load condition of a DG. And when the power mismatch is small, it results in delay detection. Thus, they are not reliable due to their large inherent nondetection zone (NDZ) [13]. An active IDT applies a small perturbation to the selected system parameter at the DG terminal and observes the resulting reaction. Most of them force the island to lose its stable operation, which is one of the disadvantages of an active IDT [11]. Active techniques are comparatively fast and have a small NDZ but may affect the power quality of the system.

However, a good IDT is expected to detect the islanding even during the occurrence of a stable island, but without forcing the DG to lose its stable operation, as they may require keeping on energizing the islanded micro-grid [16]. The decision making algorithm of an IDT is important as it has to clearly detect the islanding state and to correctly rule out a nonislanding switching event which may transiently impose a significant deviation in the decision making parameter. However, in most of the previous literature the behavior of an active IDT during the nonislanding switching events such as switching of various types of load, adjacent inverter and capacitor bank had not been discussed [15]–[22]. However, performance of S-transform and wavelet based islanding detection under noisy scenarios is done in [26]. There are various active techniques for grid tied voltage source converter (VSC) [16]–[20], [27], [28], which injects current for islanding detection.

In the proposed method, the inverter's classical q-axis current controller is modeled with a continuous periodic reference current of a small value. During the stable islanding the utility loses control over the island's frequency and the island's frequency deviates with respect to the variation in

Manuscript received November 17, 2013; revised May 20, 2014; accepted June 29, 2014. Paper no. TSG-00858-2013.

P. Gupta is with the Department of Electronics and Communication Engineering, Indira Gandhi Delhi Technical University for Women, Delhi 110006, India (e-mail: joinpankaj@yahoo.co.in).

R. S. Bhatia is with the Department of Electrical Engineering, National Institute of Technology, Kurukshetra 136119, India (e-mail: rsibhatia@yahoo.co.in).

D. K. Jain is with the Department of Electrical Engineering, Deenbandhu Chhoturam University of Science and Technology, Murthal 131039, India (e-mail: jaindk66@gmail.com).

Color versions of one or more of the figures in this paper are available online at http://ieeexplore.ieee.org.

Digital Object Identifier 10.1109/TSG.2014.2337751

1949-3053 © 2014 IEEE. Personal use is permitted, but republication/redistribution requires IEEE permission.
See http://www.ieee.org/publications_standards/publications/rights/index.html for more information.

This article has been accepted for inclusion in a future issue of this journal. Content is final as presented, with the exception of pagination.

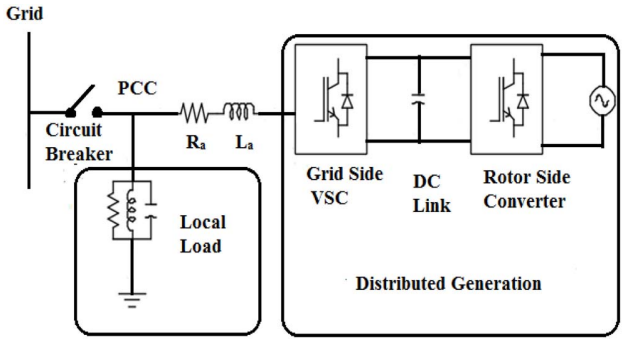


Fig. 1. Inverter based grid connected distributed generation.

the reference current. An average absolute frequency deviation value ($AFDV_{avg}$) based algorithm is proposed for the decision making. The method prefers an absolute value, so that the average frequency deviation over a cycle during an islanding state is always a positive detectable value. The averaging of frequency deviation over 5–6 cycles reduces the possibility of false detection.

The frequency deviations during the nonislanding switching events last only for first few cycles and are easily ruled out by the proposed method. A reconfirmation of an islanding state is done on the suspicion of islanding to clearly distinguish between an islanding and a nonislanding event which makes the method more reliable. The validity of the proposed method is tested under weak grid condition for various types of nonislanding switching such as load, an adjacent inverter, and a capacitor bank switching. The method is also able to detect the islanding during the stable operation of an islanded DG without destabilizing it. The technique can be utilized for a stable micro-grid operation and also for an intentional islanding purpose.

The paper is organized in seven sections. Section II describes the inverter interfaced grid connected distributed generation and q-axis current controller of the grid side inverter. Section III discusses the effect of a small periodic q-axis reference current over the point of common coupling (PCC) frequency and modeling of q-axis current controller. Section IV describes the $AFDV_{avg}$ based algorithm for the proposed islanding detection technique and suggests threshold limits for proposed technique. Section V presents the simulation results and evaluates the performance of the proposed technique. Section VI concludes this paper.

II. Inverter Based Grid Connected Distributed Generation

A typical single line diagram of an inverter interfaced grid connected distributed generation with a local load is presented in Fig. 1. The various circuit parameters are tabulated in Table I. The synchronization of inverter and the source (grid) is done with the help of a three-phase phase locked loop (PLL) [23], which simplifies the controller design by adjusting the angular speed of *dq* frame of reference to fundamental grid frequency (ω_0) so that the transformed quantities may be assumed to time invariant in steady state.

The block diagram of a three phase PLL is shown in Fig. 2. The angle δ for *abc* to *dq* and *dq* to *abc* transformation is the

TABLE I
Circuit Parameters

v_p Line-Line	575 V
i_{va} Line-Line	6.816 kA
P_{vsc}	4.8 MW
V_{dc}	1200 V
f_0 (*grid*)	60 Hz
R_a	5.95 mΩ
L_a	11.75 μH
f(*resonance*)	60Hz
R	68.88 mΩ
L	0.182 mH
C	38529 μF
Q_f	1
f(*PWM*)	1620 Hz
k_p	0.3Ω
k_i	6 Ω

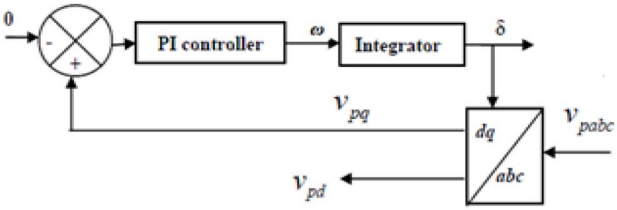


Fig. 2. Block diagram of a three phase PLL.

output of the PLL which is related to *dq* frame angular speed ω as in

$$\omega = \frac{d\delta}{dt}. \tag{1}$$

The inverter's output active and reactive powers at PCC are controlled on the basis of orthogonal components of the inverter currents i.e., *dq* frame of reference [23] and a proportional plus integral (PI) controller regulates the q-component of PCC voltage (v_{pq}) to zero. The simplified expression for instantaneous active and the reactive power at PCC can be expressed as (2) and (3). Thus

$$p_p = \frac{3}{2} v_{pd} i_{vd} \tag{2}$$

$$q_p = \frac{3}{2} v_{pd} i_{vq} \tag{3}$$

where i_{vd} and i_{vq} are the d-q components of the inverter currents, v_{pd} and v_{pq} are the d-q components of the PCC voltage.

For a balanced system with a stiff source, the zero sequence component of the current can be assumed to zero [18]. Applying Kirchhoff's voltage law to the circuit shown in Fig. 1, we can write the voltage equation in *dq* frame of reference as

$$v_{vd} - v_{pd} = i_{vd} R_a + L_a \frac{d}{dt} i_{vd} + \omega_0 L_a i_{vq} \tag{4}$$

$$v_{vq} - v_{pq} = i_{vq} R_a + L_a \frac{d}{dt} i_{vq} - \omega_0 L_a i_{vd} \tag{5}$$

where v_{vd} and v_{vq} are the d-q components of the inverter voltage and ω_0 is the fundamental grid frequency. Since v_{pq} is

This article has been accepted for inclusion in a future issue of this journal. Content is final as presented, with the exception of pagination.

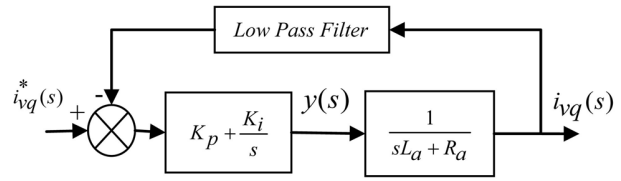


Fig. 3. Block diagram of inverter's q-axis current controller.

regulated to zero, (5) can also be expressed as

$$\frac{d}{dt}i_{vq} = -\frac{R_a}{L_a}i_{vq} + \frac{1}{L_a}\left[v_{vq} - \omega_0 L_a i_{vd}\right] \tag{6}$$

Let,

$$\left[v_{vq} - \omega_0 L_a i_{vd}\right] = y \tag{7}$$

where

$$y = \left(k_p + \frac{k_i}{s}\right)\left(i^*_{vq} - i_{vq}\right). \tag{8}$$

Taking the Laplace transformation of (6)

$$i_{vq}(s) = \frac{1}{[sL_a + R_a]}y(s). \tag{9}$$

Thus, from (9) and (3) we can say that independent control of i_{vq} and thereby q_p is possible. The q-axis current controller block diagram for grid side inverter can be represented as in Fig. 3. The harmonics generated due to switching (grid connected to island mode) are attenuated by a low pass filter.

III. Q-Axis Current Controller Modeling

The effect of q-axis current controller reference current (i^*_{vq}) on inverter's frequency is analyzed in this section. In a classical q-axis current controller the reference current is kept equal to zero so that the inverter can operate at unity power factor. The inverter current in *dq* frame of reference at steady state [16], can be written as

$$\begin{bmatrix} i_{vd} \\ i_{vq} \end{bmatrix} = \begin{bmatrix} i^*_{vd} \\ i^*_{vq} \end{bmatrix}. \tag{10}$$

By taking the inverse of Park's transformation, the (10) in *abc* coordinate system can be expressed as

$$\begin{bmatrix} i_{va} \\ i_{vb} \\ i_{vc} \end{bmatrix} = \begin{bmatrix} i^*_{vd}\cos(\omega_0 t) - i^*_{vq}\sin(\omega_0 t) \\ i^*_{vd}\cos(\omega_0 t - 2\pi/3) - i^*_{vq}\sin(\omega_0 t - 2\pi/3) \\ i^*_{vd}\cos(\omega_0 t + 2\pi/3) - i^*_{vq}\sin(\omega_0 t + 2\pi/3) \end{bmatrix}. \tag{11}$$

Let the inverter's q-axis current controller is modeled with a small periodic current i^*_{vq} as

$$i^*_{vq} = I_q \cos\omega_q t \tag{12}$$

where I_q is 1% of rated DG current and f_q be the frequency other than 60 Hz. The amplitude of reference current is kept to a small value so that the power factor of inverter can be maintained near to unity.

A balanced local load as shown in Fig. 1 is made to consume the rated DG capacity at unity power factor at a frequency of 60 Hz. Since the system under study is now a perfectly matched balanced load system, we can further analyze the system on per phase basis. Thus, from (12) the inverter current for phase "a" can be expressed as

$$i_{va} = i^*_{vd}\cos(\omega_0 t) - I_q\cos(\omega_q t)\sin(\omega_0 t) \tag{13}$$

or

$$i_{va} = i^*_{vd}\cos(\omega_0 t) - \frac{1}{2}I_q[\sin(\omega_1 t) + \sin(\omega_2 t)] \tag{14}$$

where

$$\omega_1 = 2\pi(f_0 - f_q) \tag{15}$$

$$\omega_2 = 2\pi(f_0 + f_q). \tag{16}$$

The f_0 and fq are the fundamental frequency and q-axis reference current frequency, respectively.

The current components at frequency ω_1 and ω_2, becomes effective during the islanding as they are forced to flow through the load [16], [18]. The individual current components of (14) are multiplied to the respective impedances at the corresponding frequencies and the PCC voltage of phase "a" is obtained by superimposing the voltages at corresponding frequencies

$$v_{pa} = v_p(\omega_0) + v_p(\omega_1) + v_p(\omega_2) \tag{17}$$

where

$$v_p(\omega_0) = Ri^*_{vd}\cos\omega_0 t \tag{18}$$

$$v_p(\omega_1) = -\frac{I_q}{2\left\{\left(1/R\right)^2 + \left(\omega_1 C - 1/\omega_1 L\right)^2\right\}^{\frac{1}{2}}}\sin(\omega_1 t + \varphi_1) \tag{19}$$

$$v_p(\omega_2) = -\frac{I_q}{2\left\{\left(1/R\right)^2 + \left(\omega_2 C - 1/\omega_2 L\right)^2\right\}^{\frac{1}{2}}}\sin(\omega_2 t + \varphi_2) \tag{20}$$

$$\varphi_1 = -\tan^{-1}\left[\frac{R\left(\omega_1^2 LC - 1\right)}{\omega_1 L}\right] \tag{21}$$

$$\varphi_2 = -\tan^{-1}\left[\frac{R\left(\omega_2^2 LC - 1\right)}{\omega_2 L}\right]. \tag{22}$$

From (17) we may say that the frequency of voltage at PCC is deviated if the q-axis reference current is a periodic signal with a frequency other than the fundamental frequency. Figs. 4 and 5 show the pre and post islanding frequency deviation curve, with q-axis reference current as zero and with reference current as a continuous periodic current, respectively. A periodic frequency deviation may be obtained as in Fig. 5, under the islanding state which can be utilized as an indication of islanding. Fig. 5 depicts the pre and post islanding frequency trends when inverter's q-axis current controller is modeled with a reference current having a frequency of 20 and 30 Hz. The result in Fig. 5 agrees to the conclusion drawn in this section. It has also been observed from the results in Fig. 5 that the lower is the injection current frequency; the higher is the frequency deviation amplitude during the islanding state.

This article has been accepted for inclusion in a future issue of this journal. Content is final as presented, with the exception of pagination.

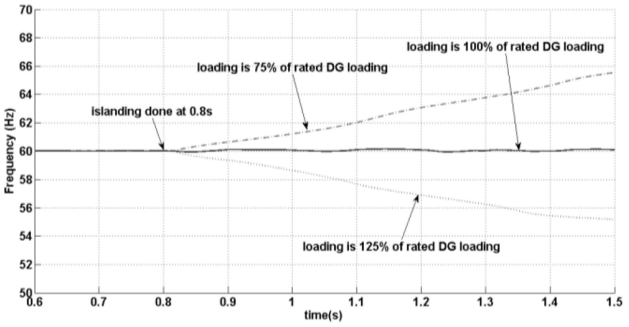


Fig. 4. Frequency trend at PCC during pre and post islanding.

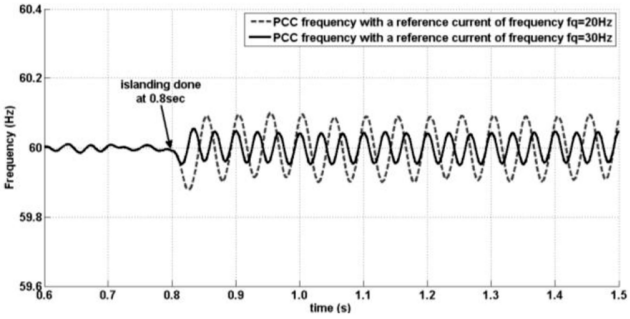


Fig. 5. Pre and post islanding frequency deviation for f_q = 20 Hz and 30 Hz with a constant amplitude of 1% to the rated current.

IV. Proposed Islanding Detection Technique

It has already been shown in Fig. 4 that for an active power mismatch condition of a DG the system frequency deviates during the occurrence of a UI. But for a perfectly matched load condition of the DG the system frequency remains inside the NDZ during the occurrence of a UI. Thus, for a perfectly matched load condition of a DG, the frequency deviation is achieved by modeling the classical q-axis current controller of grid side inverter with a small periodic current.

The measurement of the frequency deviation is done by an average absolute frequency deviation value (AFDV_{avg}) as given by

$$\text{AFDV}_{\text{avg}} = \frac{1}{N}\sum_{n=1}^{N} |F_D(n)| \tag{23}$$

$$N = \frac{M_w}{T_s} \tag{24}$$

where F_D is the instantaneous frequency deviation, M_w is the measurement window size in sec and T_s is the sampling time. A measurement window of 50 ms can be proposed so as to cover atleast three cycles of a 60 Hz signal. The proposed MATLAB simulation model is a discrete model having a sampling time of 50 μs. Thus, the total number of samples (N) in a measurement window of 50 ms will be 1000.

For an active power mismatch condition, the absolute frequency deviation curve can be approximated by a straight line as depicted in Fig. 6 having a slope m. Thus, the AFDV_{avg} for this condition can be calculated by

$$\text{AFDV}_{\text{avg}} = \frac{\frac{1}{2}M_w \times mM_w}{M_w}. \tag{25}$$

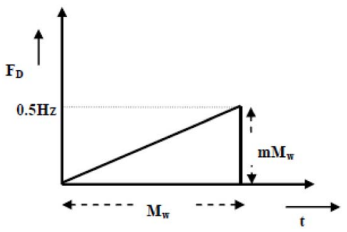


Fig. 6. AFDV_{avg} approximations for an active power mismatch condition.

TABLE II
AFDV_{avg} Threshold Limits For Quality Factor (Q_f) = 1

S. No.	f_q In Hz	F_m In Hz	AFDV_{avg} In Hz	Threshold Limits (0.95xAFDV_{avg}) In Hz
1.	30	0.036	0.026	Threshold1=0.0247
2.	20	0.082	0.057	Threshold2=0.0541

The frequency must deviate more than $\pm$0.5 Hz from its normal value for the confirmation of an islanding state. Thus, the AFDV_{avg} for the confirmation of an islanding state must exceed $\pm$0.25 Hz over a specified Mw. For a perfectly matched load condition of a DG the obtained frequency deviation is a periodic signal. The obtained absolute frequency deviation curve is similar to a full wave rectified sinusoidal waveform and hence the average value can be approximated as $2 \times \text{F}_m/\pi$ Hz over a cycle, where f_m is the obtained peak frequency deviation. For safety, the average value of frequency deviation may be approximated to 95% of the average value, as $0.95 \times 2 \times \text{F}_m/\pi$ Hz.

IEEE Standard 1547.1 proposes to use loads with quality factor $Q_f = 1$ for testing islanding [25]. Hence for the proposed AFDV_{avg} method, the threshold limits are obtained for the loads having a quality factor Q_f = 1 in Table II. The algorithm for the proposed technique is shown in Fig. 7.

During the occurrence of islanding under a general power mismatch condition the AFDV_{avg} crosses the predefined threshold limit of 0.25 Hz and confirms the islanding state. Otherwise the algorithm checks for the possibility of islanding under zero or low active power mismatch condition. If the AFDV_{avg} is greater than predefined threshold1 of 0.0247 Hz corresponding to a reference current frequency of 30 Hz, it suspects an islanding state. To eliminate the possibility of false tripping and for reconfirmation of an islanding state, the reference current frequency is now changed to 20 Hz. For a true islanding state, the AFDV_{avg} value will be greater than threshold2 of 0.057 Hz. Since this method reconfirms the occurrence of islanding once it is suspected, it avoids the possibility of nuisance tripping. The maximum time taken by this method for islanding detection is 0.1 s which is well within 2 s of IEEE standard 1547 criteria [1].

V. Results and Discussion

IEEE Standard 929 [2] suggests the use of load with quality factor $Q_f \leq 2.5$ for testing islanding, while UL1741 suggest $Q_f = 1.8$ [11] and recently IEEE 1547.1 suggested $Q_f = 1$.

This article has been accepted for inclusion in a future issue of this journal. Content is final as presented, with the exception of pagination.

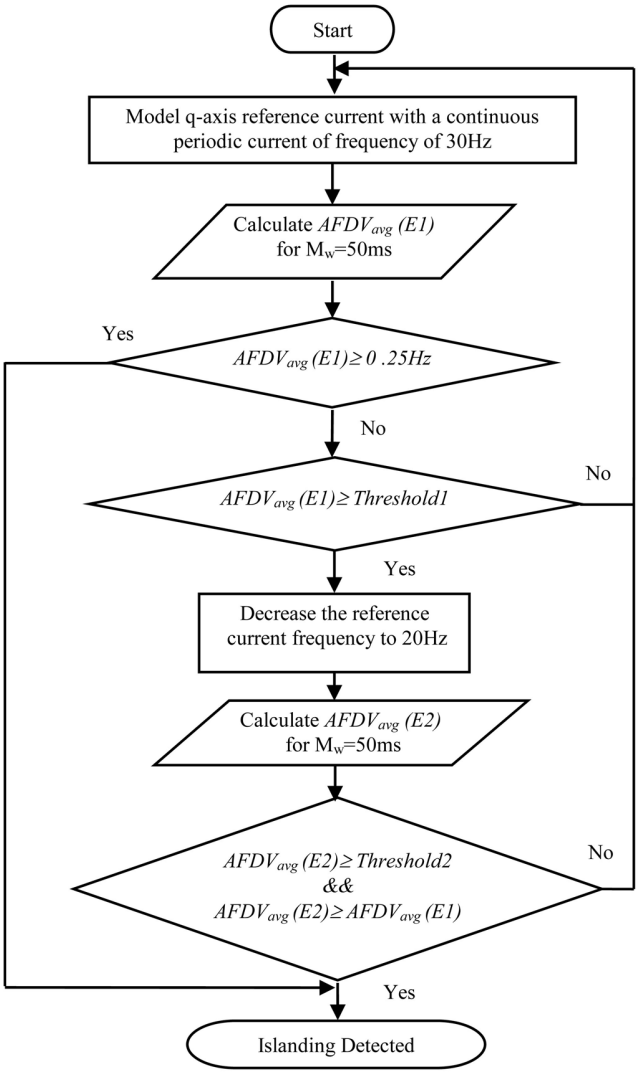


Fig. 7. Algorithm of the proposed technique.

TABLE III
MAX FREQUENCY DEVIATION (f_m) AND $AFDV_{avg}$ THRESHOLD LIMITS FOR VARIOUS QUALITY FACTOR (Q_f)

Quality Factor (Q_f)	f_q=10Hz		f_q=20Hz		f_q=30Hz	
	f_m(Hz)	$AFDV_{avg}$ (Hz)	f_m(Hz)	$AFDV_{avg}$ (Hz)	f_m(Hz)	$AFDV_{avg}$ (Hz)
1	0.115	0.073	0.089	0.057	0.041	0.026
1.5	0.088	0.056	0.084	0.054	0.038	0.024
1.8	0.084	0.054	0.082	0.052	0.036	0.023
2	0.081	0.051	0.079	0.050	0.034	0.021
2.5	0.078	0.049	0.072	0.046	0.031	0.020
3	0.075	0.048	0.067	0.043	0.030	0.019
3.5	0.072	0.046	0.063	0.040	0.030	0.019
4	0.070	0.045	0.062	0.039	0.029	0.018
4.5	0.067	0.043	0.059	0.038	0.029	0.018

The approximated $AVDV_{avg}$ threshold limits for various quality factors are given in Table III. The Q_f is varied by changing the values of L and C, while keeping R fixed to 68.88 mΩ. Table IV shows the obtained $AFDV_{avg}$ for various DG rating and quality factor (keeping fq = 20 Hz). It may be noted from Table IV, that for the same value of quality factor, the

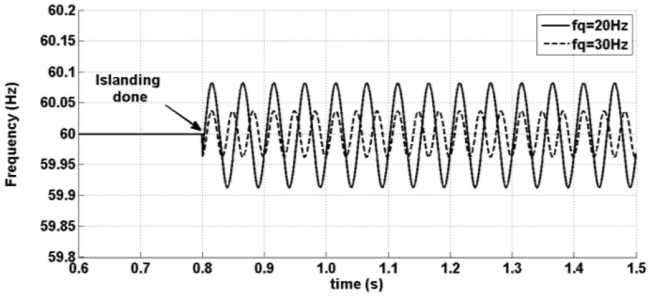


Fig. 8. PCC frequency trend for f_q = 30 and 20 Hz during the perfectly matched load condition of a DG.

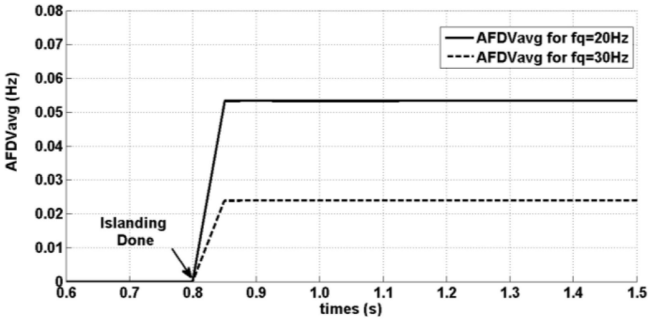


Fig. 9. $AFDV_{avg}$ trend for f_q = 20 and 30 Hz during the perfectly matched load condition of a DG.

$AFDV_{avg}$ does not changes. If the load is matched to the rated DG capacity, then $AFDV_{avg}$ does not depends upon the DG rating, however, a change in quality factor of the load affects the $AFDV_{avg}$.

Simulation results carried out in this section are under the perfectly matched load condition of a DG and islanding is done at 0.8 s. Figs. 8 and 9 show the pre and post islanding PCC frequency and $AFDV_{avg}$ trend for f_q = 30 and 20 Hz, respectively. The $AFDV_{avg}$ obtained in Fig. 9 during islanding under the perfectly matched load condition of DG agrees to the threshold values that were approximated in Table II. Thus, the proposed decision making algorithm discussed in Section IV can be successfully implemented for islanding detection under perfectly matched load condition. The technique is tested and evaluated for various cases in the next section.

A. Perfectly Matched Load Condition of DG

The proposed islanding detection technique is tested on the DG of Fig. 1 under perfectly matched load condition and islanding operation is done at 0.8 s. The obtained frequency and $AFDV_{avg}$ trend is plotted in Figs. 10 and 11, respectively. The frequency starts deviating at 0.8 s but with small amplitude and the $AFDV_{avg}$(E1) crosses the predefined threshold of 0.0247 Hz at 0.85 s as shown in Fig. 11 and suspects islanding at 0.85 s. A control signal as shown in Fig. 12 is triggered to decrease the reference current frequency to 20 Hz. The reference current trend plotted in Fig. 12 shows that at 0.85 s the frequency of reference current is switched to 20 Hz, which raises the frequency deviation as in Fig. 10. At 0.9 s the $AFDV_{avg}$(E2) crosses the predefined threshold2 (0.054 Hz)

This article has been accepted for inclusion in a future issue of this journal. Content is final as presented, with the exception of pagination.

TABLE IV
EFFECT OF CHANGE IN DG RATING AND QUALITY FACTOR ON $AFDV_{avg}$

DG Rating (MW)	Q_f	Itd* (A)	Iq (A)	R (mΩ)	L (mH)	C (μF)	Amplitude $\upsilon_p(\omega_0)$ (V)	Amplitude $\upsilon_p(\omega_1)$ (V)	Amplitude $\upsilon_p(\omega_2)$ (V)	Φ_1	Φ_2	f_m (Hz)	AFDVavg (Hz)
1	**1**	1420	14.2	330.62	0.877	8027	469.5	1.9	1.5	39.9	-30.3	0.0891	0.0567
1	**2**	1420	14.2	330.62	0.438	16054	469.5	1.3	0.9	59.1	-49.5	0.0792	0.0504
1	**3**	1420	14.2	330.62	0.292	24081	469.5	0.9	0.6	68.3	-60.3	0.0673	0.0428
1	**4**	1420	14.2	330.62	0.219	32108	469.5	0.7	0.5	73.4	-66.9	0.0617	0.0392
2	**1**	2840	28.4	165.31	0.438	16054	469.5	1.9	1.5	39.9	-30.3	0.0891	0.0567
2	**2**	2840	28.4	165.31	0.219	32108	469.5	1.3	0.9	59.1	-49.5	0.0792	0.0504
2	**3**	2840	28.4	165.31	0.146	48162	469.5	0.9	0.6	68.3	-60.3	0.0673	0.0428
2	**4**	2840	28.4	165.31	0.109	64216	469.5	0.7	0.5	73.4	-66.9	0.0617	0.0392
2.4	**1**	3408	34.08	137.76	0.365	19264	469.5	1.9	1.5	39.9	-30.3	0.0891	0.0567
2.4	**2**	3408	34.08	137.76	0.182	38529	469.5	1.3	0.9	59.1	-49.5	0.0792	0.0504
2.4	**3**	3408	34.08	137.76	0.121	57794	469.5	0.9	0.6	68.3	-60.3	0.0673	0.0428
2.4	**4**	3408	34.08	137.76	0.091	77059	469.5	0.7	0.5	73.4	-66.9	0.0617	0.0392
3.6	**1**	5112	51.12	91.84	0.243	28897	469.5	1.9	1.5	39.9	-30.3	0.0891	0.0567
3.6	**2**	5112	51.12	91.84	0.121	57794	469.5	1.3	0.9	59.1	-49.5	0.0792	0.0504
3.6	**3**	5112	51.12	91.84	0.081	86691	469.5	0.9	0.6	68.3	-60.3	0.0673	0.0428
3.6	**4**	5112	51.12	91.84	0.060	115588	469.5	0.7	0.5	73.4	-66.9	0.0617	0.0392
4.8	**1**	6816	68.16	68.88	0.182	38529	469.5	1.9	1.5	39.9	-30.3	0.0891	0.0567
4.8	**2**	6816	68.16	68.88	0.091	77059	469.5	1.3	0.9	59.1	-49.5	0.0792	0.0504
4.8	**3**	6816	68.16	68.88	0.060	115588	469.5	0.9	0.6	68.3	-60.3	0.0673	0.0428
4.8	**4**	6816	68.16	68.88	0.045	154118	469.5	0.7	0.5	73.4	-66.9	0.0617	0.0392

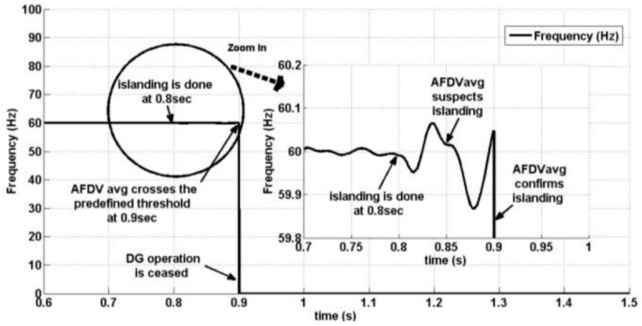


Fig. 10. PCC frequency trend during islanding under the perfectly matched load condition of a DG.

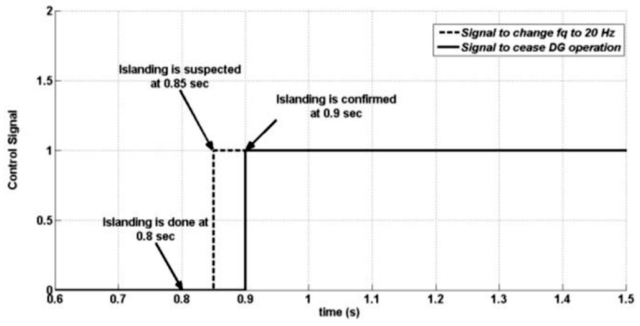


Fig. 12. Control signal.

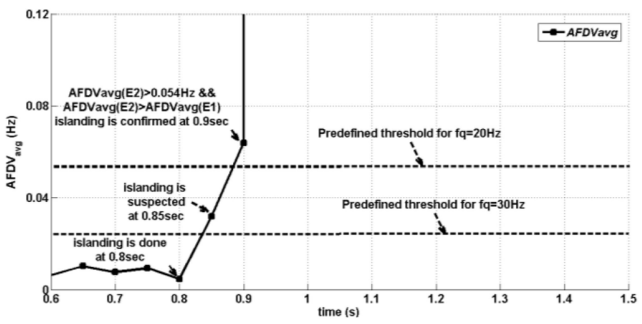


Fig. 11. $AFDV_{avg}$ trend during islanding under the perfectly matched load condition of a DG.

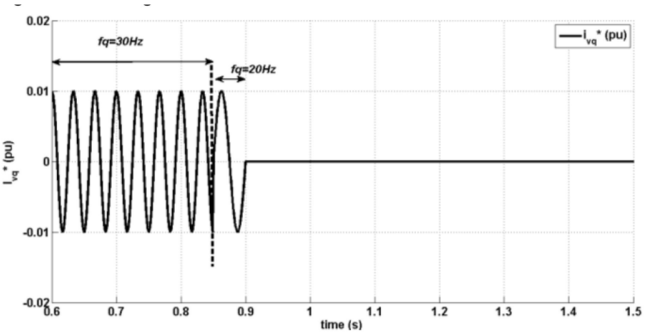


Fig. 13. i_{vq}^* (pu) trend during islanding under the perfectly matched load condition of a DG.

and satisfies $AFDV_{avg}(E2) > AFDV_{avg}(E1)$, thus confirming the islanding state. A control signal as shown in Fig. 13 is triggered at 0.9 s to cease the DG operation. The frequency falls to zero at 0.9 s as shown in Fig. 10, since the DG operation is now ceased.

B. Islanding Detection Under Various Power Mismatch Condition

The proposed method is a generalized method and is able to detect the islanding successfully under various power

This article has been accepted for inclusion in a future issue of this journal. Content is final as presented, with the exception of pagination.

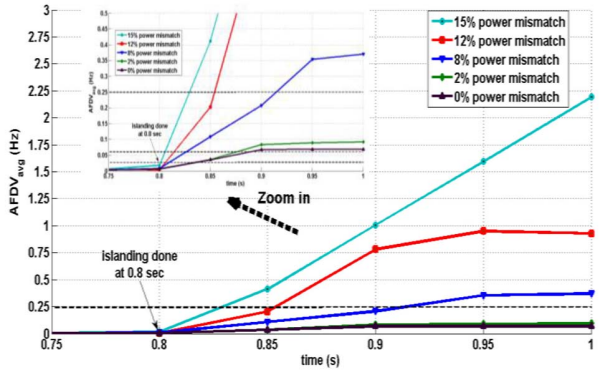


Fig. 14. $AFDV_{avg}$ trend during islanding under the various active power mismatch condition of a DG.

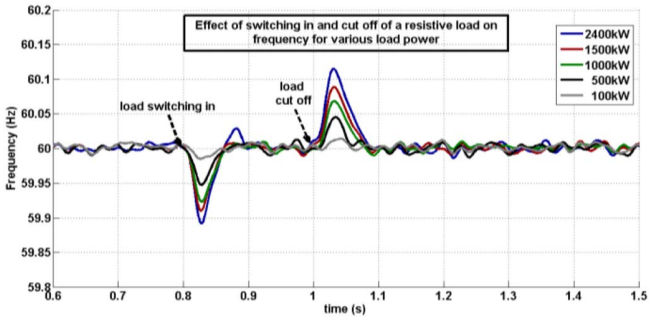


Fig. 15. PCC frequency during switching in and cut off of a resistive load.

mismatch conditions also. $AFDV_{avg}$ trends during islanding under various active power mismatch conditions have been plotted in Fig. 14. For an active power mismatch of greater than 12% the proposed technique is able to detect the islanding in 50 ms (3 cycles only). However, for an islanding under an active power mismatch of less than 12%, the proposed technique detects the islanding in 100 ms (6 cycles).

C. Nonislanding Events

The accuracy of any IDT depends on the factor how it is able to differentiate between an islanding event and a nonislanding event. A load is connected at PCC of the circuit shown in Fig. 1 in addition to the local load. The inverter's rated active load power is matched with local load in all the cases. The effect of switching in and cut off of a resistive load on the PCC frequency and the $AFDV_{avg}$ is shown in Figs. 15 and 16, respectively. A resistive load of 500 kW and above is switched in at 0.8 s. At 0.85 s the $AFDV_{avg}$(E1) crosses the predefined threshold1 and suspects the islanding. But at 0.9 s the $AFDV_{avg}$(E2) rule out the islanding state as the obtained $AFDV_{avg}$(E2) does not fulfills the set criteria. The time taken for decision making is 100 ms (6 cycles).

Similar results were obtained for a sudden cut off of a resistive load at 1 s. The results in Fig. 16 shows that the effect of switching in and cut of a resistive load on PCC frequency lasts not more than 3–5 cycles and thus the proposed

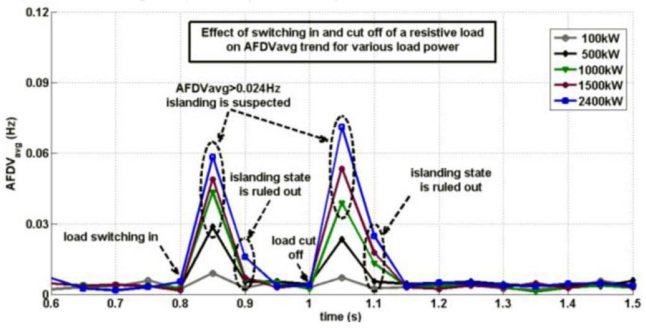


Fig. 16. $AFDV_{avg}$ during switching in and cut off of a resistive load.

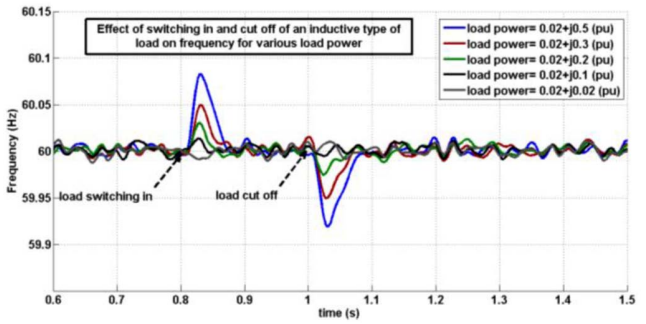


Fig. 17. PCC frequency during switching in and cut off of an inductive type of load.

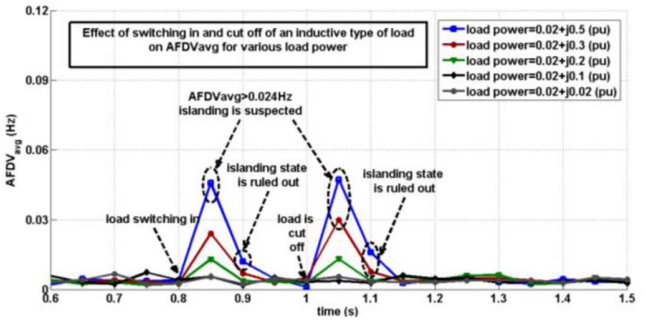


Fig. 18. $AFDV_{avg}$ during switching in and cut off of an inductive type of load.

algorithm in Fig. 7 is able to correctly rule out nonislanding state in 100 ms. Since a reconfirmation of islanding is done after a suspicion of an islanding state, the possibility of false detection is eliminated in both of the cases.

The frequency and the $AFDV_{avg}$ trend during the switching in and the cutoff of an inductive load have been obtained in Figs. 17 and 18. The switching in and cut off of an inductive load is done at 0.8 and at 1 s respectively. The islanding is suspected at 0.85 and 1.05 s, respectively. However, $AFDV_{avg}$ trend rule out the suspicion about islanding at 0.9 and 1.1 s, respectively, in a decision time of 100 ms (6 cycles).

For a capacitor bank switching in and cutoff, the frequency trends and the $AFDV_{avg}$ trends are plotted in Figs. 19 and 20, respectively. It can be observed from all the three cases that the proposed algorithm is successful in deciding it as a nonislanding event.

This article has been accepted for inclusion in a future issue of this journal. Content is final as presented, with the exception of pagination.

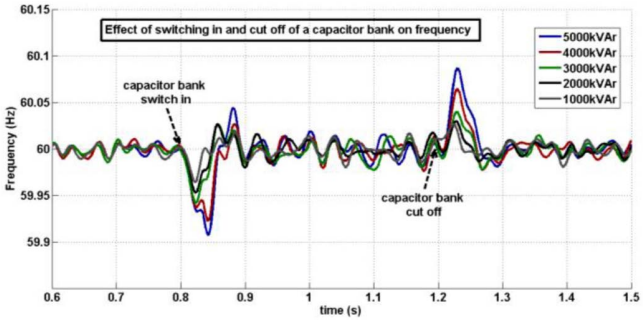


Fig. 19. PCC frequency during switching in and cut off of a capacitive load.

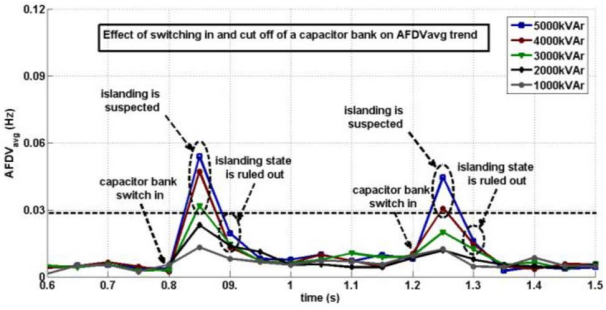


Fig. 20. $AFDV_{avg}$ during switching in and cut off of a capacitive load.

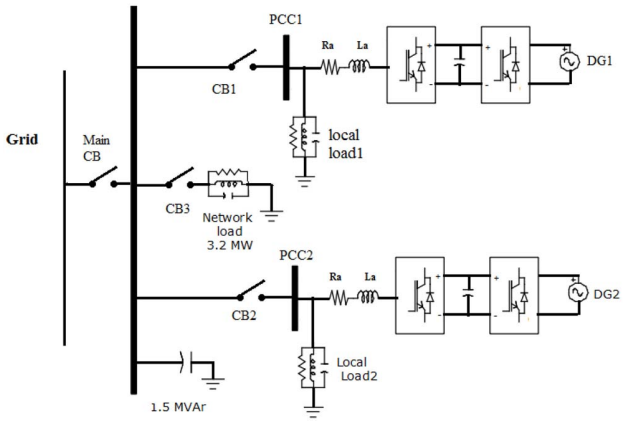


Fig. 21. Single line diagram of a grid connected two DG sets.

D. Effect of Islanding and Reclosing of Adjacent DG

Single line diagram of a grid connected two DG sets is shown in Fig. 21. Both the DG sets are identical and are of the same capacity. The details of the circuit parameters are tabulated in Table I. Both the DG sets are made to operate in synchronization with the grid. At 0.7 s the circuit breaker CB2 is opened and islanding of DG2 is done. At 0.9 s CB2 is closed again and reconnection of DG2 is done. The effect of disconnection and reconnection of DG2 on PCC1 frequency is plotted in Fig. 22. Islanding and reconnection of DG2 deviates the frequency at PCC1 although DG1 was in grid connected mode.

$AFDV_{avg}$ trend for PCC1 frequency during islanding and reconnection of DG2 is plotted in Fig. 23. Islanding of DG1 is suspected by $AFDV_{avg}$ at 0.75 and 0.95 s subsequent to

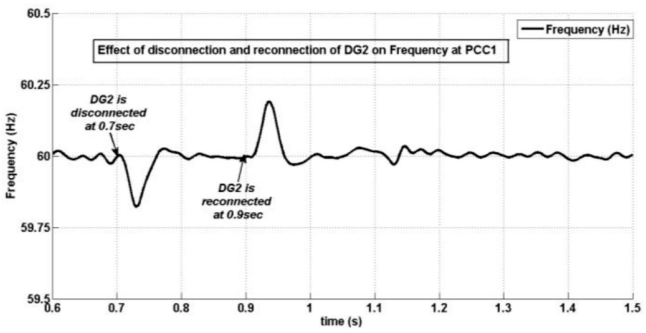


Fig. 22. PCC1 frequency trend during islanding and reconnection of DG2.

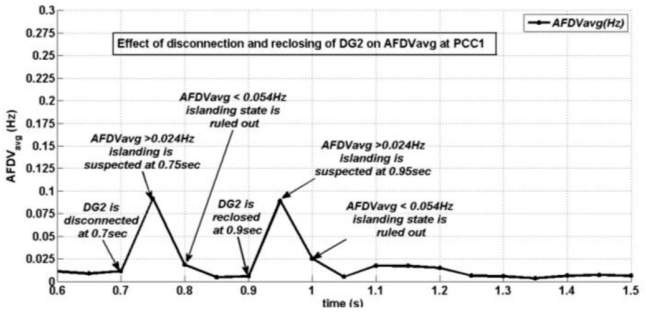


Fig. 23. $AFDV_{avg}$ trend for PCC1 frequency deviation during islanding and reconnection of DG2.

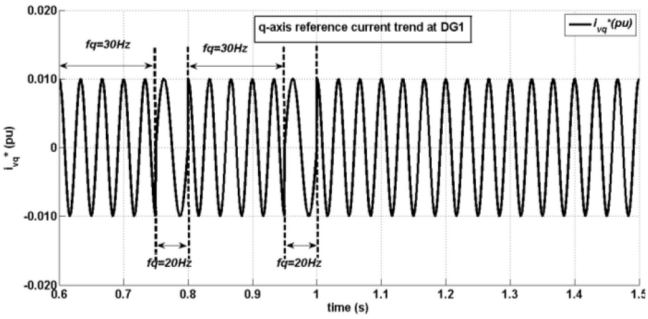


Fig. 24. i^*_{vq}(pu) trend during islanding and reclosing of DG2.

islanding and reconnection of DG2, respectively. But at 0.8 and 1 s the $AFDV_{avg}$ goes below the threshold2 and the islanding state is ruled out in both the cases. i^*_{vq} (pu) trend during islanding and reconnection of DG2 is plotted in Fig. 24.

E. Effect on Power Quality

This section focuses on the effect of the inverter's q-axis current controller reference current on the total harmonic distortion (THD) and the system's power factor. The THD trend and power factor trend is plotted in Figs. 25 and 26, respectively. Fig. 25 shows that changing the reference current frequency while keeping its amplitude to 1% of the rated DG current increases the THD but the obtained THD remains inside the tolerance limit of 5% and any frequency between 10 and 40 Hz can be recommended. However, a lower value of reference current frequency causes higher power factor degradation as shown in Fig. 26.

This article has been accepted for inclusion in a future issue of this journal. Content is final as presented, with the exception of pagination.

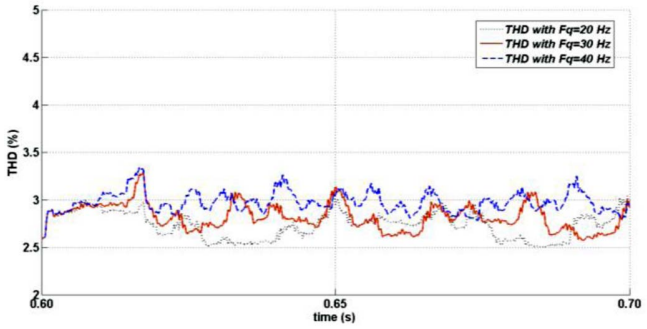


Fig. 25. PCC voltage THD trend for various reference current frequencies.

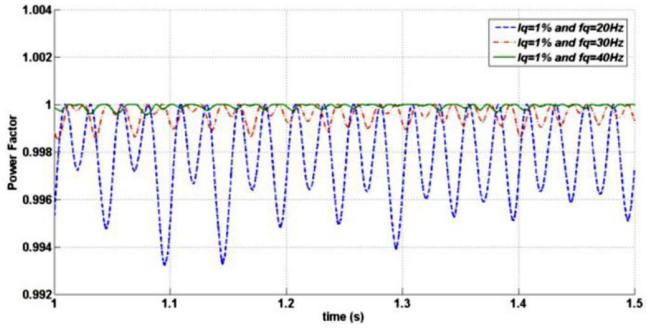


Fig. 26. System power factor trend for various reference current frequencies.

A periodic current of small amplitude of 1% to DG rated current with a frequency of 30 Hz can be recommended and hence chosen by the proposed technique, as it does not degrades the THD more than the permissible limit of 5% and the power factor is also maintained within the limits as shown in Figs. 25 and 26, respectively.

VI. Conclusion

The technique successfully detects islanding even during the worst case of islanding i.e., the perfectly matched load condition of a DG. For an active power mismatch of less than 12% the technique detects islanding in 100 ms (6 cycles), whereas for a value above 12% it takes only 50 ms (3 cycles). The proposed active $AFDV_{avg}$ technique has the ability to check the suitability of an islanded DG for a micro grid application or an islanded mode operation. It detects an islanding state without forcing the DG to lose its stable operation, which is the main advantage of this method. The method clearly distinguishes between a true islanding state and nonislanding switching events which makes it more accurate and reliable. Investigations which are suggested to identify the limitations of proposed technique and to enhance its effectiveness are as follows.

1) The technique is to be evaluated for a case of multiple inverters and needful modification may be developed before its implementation.
2) The behavior of the proposed technique is to be evaluated during various types of faults.

References

[1] *Standard for Interconnecting Distributed Resources with Electric Power Systems*, IEEE Std. 1547, 2003.
[2] *IEEE Recommended Practice for Utility Interface of Photovoltaic (PV) Systems*, IEEE Std. 929-2000, 2000.
[3] M. E. Ropp, M. Begovic, and A. Rohatgi, "Determining the relative effectiveness of islanding prevention techniques using phase criteria and non-detection zones," *IEEE Trans. Energy Convers.*, vol. 15, no. 3, pp. 290–296, Sep. 2000.
[4] R. S. Kunte and W. Gao, "Comparison and review of islanding detection techniques for distributed energy resources," in *Proc. 40th North Amer. Power Symp.*, Calgary, AB, USA, Sep. 2008.
[5] R. A. Walling, "Application of direct transfer trip for prevention of DG islanding," in *Proc. IEEE Power Energy Soc. Gen. Meeting*, San Diego, CA, USA, Jul. 2011.
[6] W. Xu *et al.*, "A power line signaling based technique for anti-islanding protection of distributed generators—Part I: Scheme and analysis," *IEEE Trans. Power Del.*, vol. 22, no. 3, pp. 1758–1766, Jul. 2007.
[7] W. Freitas, W. Xu, C. M. Affonso, and Z. Huang, "Comparative analysis between ROCOF and vector surge relays for distributed generation applications," *IEEE Trans. Power Del.*, vol. 20, no. 2, pp. 1315–1324, Apr. 2005.
[8] M. A. Redfern, O. Usta, and G. fielding, "Protection against loss of utility grid supply for a dispersed storage and generation unit," *IEEE Trans. Power Del.*, vol. 8, no. 3, pp. 948–954, Jul. 1993.
[9] S. Jang and K. Kim, "An islanding detection method for distributed generations using voltage unbalance and total harmonic distortion in currents," *IEEE Trans. Power Del.*, vol. 19, no. 2, pp. 745–752, Apr. 2004.
[10] S.-H. Lee and J.-W. Park, "New islanding detection method for inverter—Based distributed generation considering its switching frequency," *IEEE Trans. Ind. Appl.*, vol. 46, no. 5, pp. 2089–2098, Sep. 2010.
[11] H. H. Zeineldin, "A Q–F droop curve for facilitating islanding detection of inverter based distributed generation," *IEEE Trans. Power Electron.*, vol. 24, no. 3, pp. 665–673, Mar. 2009.
[12] H. Vahedi, R. Noroozian, A. Jalilvand, and G. B. Gharehpetian, "A new method for islanding detection of inverter—Based distributed generation using DC-link voltage control," *IEEE Trans. Power Del.*, vol. 26, no. 2, pp. 1176–1186, Apr. 2011.
[13] Z. Ye, A. Kolwalker, Y. Zhang, P. Du, and R. Walling, "Evaluation of anti-islanding schemes based on non-detection zone concept," *IEEE Trans. Power Electron.*, vol. 19, no. 5, pp. 1171–1176, Sep. 2004.
[14] A. Samui and S. R. Samantaray, "Wavelet singular entropy-based islanding detection in distributed generation," *IEEE Trans. Power Del.*, vol. 28, no. 1, pp. 411–418, Jan. 2013.
[15] L. A. C. Lopes and H. Sun, "Performance assessment of active frequency drifting islanding detection methods," *IEEE Trans. Energy Convers.*, vol. 21, no. 1, pp. 171–180, Mar. 2006.
[16] G. Hernandez-Gonzalez and R. Iravani, "Current injection for active islanding detection of electronically-interfaced distributed resources," *IEEE Trans. Power Del.*, vol. 21, no. 3, pp. 1698–1705, Jul. 2006.
[17] H. Karimi, A. Yazdani, and R. Iravani, "Negative-sequence current injection for fast islanding detection of a distributed resource unit," *IEEE Trans. Power Electron.*, vol. 23, no. 1, pp. 298–307, Jan. 2008.
[18] H. Y. Lee, B. M. Han, and H. J. Cha, "Novel islanding detection method for distributed generation," in *Proc. IEEE Energy Convers. Congr. Expo.*, pp. 3378–3384, Sep. 2009.
[19] A. Yafaoui, B. Wu, and S. Kouro, "Improved active frequency drift anti-islanding detection method for grid connected photovoltaic systems," *IEEE Trans. Power Electron.*, vol. 27, no. 5, pp. 2367–2375, May 2012.
[20] W. Cai, B. Liu, S. Duan, and C. Zou, "An islanding detection method based on dual-frequency harmonic current injection under grid impedance unbalanced condition," *IEEE Trans. Ind. Informat.*, vol. 9, no. 2, pp. 1178–1187, May 2013.
[21] V. Menon and M. H. Nehrir, "A hybrid islanding detection technique using voltage unbalance and frequency set point," *IEEE Trans. Power Syst.*, vol. 22, no. 1, pp. 442–448, Feb. 2007.
[22] Y. Zhou, H. Li, and L. Liu, "Integrated autonomous voltage regulation and islanding detection for high penetration PV applications," *IEEE Trans. Power Electron.*, vol. 28, no. 6, pp. 2826–2841, Jun. 2013.
[23] S. K. Chung, "A phase tracking system for three phase utility interface inverters," *IEEE Trans. Power Electron.*, vol. 15, no. 3, pp. 431–438, May 2000.

This article has been accepted for inclusion in a future issue of this journal. Content is final as presented, with the exception of pagination.

[24] C. Schauder and H. Mehta, "Vector analysis and control of advanced static VAR compensators," *IEE Proc. C, Gener., Transmiss. Distrib.*, vol. 140, no. 4, pp. 299–306, Jul. 1993.
[25] *IEEE Standard Conformance Test Procedures for Equipment Interconnecting Distributed Resources with Electric Power Systems*, IEEE Std. 1547.1, Jul. 2005.
[26] P. K. Ray, N. Kishor, and S. R. Mohanty, "Islanding and power quality disturbance detection in grid-connected hybrid power system using wavelet and S-transform," *IEEE Trans. Smart Grid*, vol. 3, no. 3, pp. 1082–1094, Sep. 2012.
[27] M. A. Zamani, A. Yazdani, and T. S. Sidhu, "A communication-assisted protection strategy for inverter-based medium-voltage microgrids," *IEEE Trans. Smart Grid*, vol. 3, no. 4, pp. 2088–2099, Dec. 2012.
[28] J. Zhang *et al.*, "An improved islanding detection method for a grid-connected inverter with intermittent bilateral reactive power variation," *IEEE Trans. Power Electron.*, vol. 28, no. 1, pp. 268–278, Jan. 2013.



Pankaj Gupta received the B.E. degree in electrical engineering from Bhilai Institute of Technology, Durg, India, in 2000, and the M.E. degree in electrical engineering from the Delhi College of Engineering, Delhi University, Delhi, India, in 2003. He is currently pursuing the Ph.D. degree at the National Institute of Technology, Kurukshetra, India.

He is an Assistant Professor with the Department of Electronics and Communication Engineering, Indira Gandhi Delhi Technical University for Women, Delhi, from 2005. His current research interests include power system protection, renewable energy systems, and islanding detection techniques.



R. S. Bhatia received the B.Tech. degree in electrical engineering from Guru Nanak Engineering College, Ludhiana, India, in 1987, M.Tech. and Ph.D. degrees in electrical engineering from Regional Engineering College, Kurukshetra, Haryana, India, in 1993 and 2008, respectively.

He is currently a Professor with the Department of Electrical Engineering, National Institute of Technology, Kurukshetra, India. His current research interests include power electronics, electric power quality, electrical circuits, and renewable energy systems.



D. K. Jain received the B.Sc. (Engineering), M.Tech., and Ph.D. degrees in electrical engineering from Regional Engineering College, Kurukshetra, Haryana, India, in 1987, 1993, and 2001, respectively.

He is currently a Professor with the Deparment of Electrical Engineering, Deenbandhu Chhoturam University of Science and Technology, Murthal, India. His current research interests include power system protection, electric power quality, electric drives, and renewable energy systems.

Fibers and Polymers 2014, Vol.15, No.7, 1422-1428 DOI 10.1007/s12221-014-1422-2

Composite Wound Dressing for Drug Release

Roli Purwar*, Poonam Rajput, and Chandra Mohan Srivastava

Department of Applied Chemistry and Polymer Technology, Delhi Technological University, Shahbad Daulatpur, Delhi 110042, India

(Received November 7, 2013; Revised January 31, 2014; Accepted February 12, 2014)

Abstract: Present study is focused on the preparation of two layers composite wound dressing for drug release. The outer layer is made of hydrogel which contains of drug and the core layer is made of fabric. The two layers structure of composite dressing is formed by grafting of polyacrylamide-co-acrylic acid hydrogel on cotton fabric using ammonium per sulphate (APS) as chemical initiator and polyethylene glycol (PEG) as crosslinker. The major factors affecting graft copolymerization of hydrogel on cotton fabric are optimized by varying concentration of monomers & initiator, reaction temperature and addition time of crosslinker. Maximum grafting of hydrogel is obtained at 5 % (w/v) APS and 15 % acrylamide/acrylic acid (1:1 w/w ratio) concentration. The FTIR spectra of composite dressing shows characteristics peak of acrylic acid and acrylamide. The composite wound dressing material is loaded with model drug bovine serum albumin (BSA) and drug release behaviour is studied at different pH. The dressing shows drug release in different pH with maximum release of drug in acidic medium.

Keywords: Hydrogel, Graft copolymerization, Drug release, Wound dressing

Introduction

Recently medicated dressings have gained its importance in wound healing process. These medicated dressings contain drug/antibiotic which releases locally at wound site. The use of dressings to deliver drugs/antibiotics to wound sites can provide tissue compatibility, low occurrence of bacterial resistance and reduced interference with wound healing [1].

Hydrogels are three dimensional crosslinked networks of water soluble polymer which have most of the desirable characteristics of an ideal dressing [2]. Hydrogels promote moist healing and cool the surface of the wound. Non adherent nature of hydrogel dressing reduces the dressing change pain. The physical properties of hydrogels have sparked interest in their use in drug delivery applications. Highly porous structure and aqueous swelling of hydrogels can easily be tuned by controlling the density of cross-links in the gel matrix. Porous structure also permits loading of drugs into the gel matrix and subsequent drug release at a rate dependent on the diffusion coefficient of the small molecules or macromolecule through the gel network [3]. Hydrogels of copolymers of acrylic acid (AAc) with acrylamide (AAm) derivatives have been reported for various drug release such as, gentamicin sulphate [4], theophylline release [5], bovine serum albumin (BSA) [6], ascorbic acid [7], fluorescein isothiocyanate labelled bovine serum albumin (FITC-BSA) [8] and 5-fluorouracil (5-FU) [9].

Despite many advantageous properties, hydrogels have several limitations. Hydrogels exhibit very low mechanical strength while in contact with water. The low tensile strength of hydrogels limits their use in load-bearing applications and can results in the premature dissolution or flow away of the hydrogel from target local site [3]. In order to eliminate this disadvantage, recent trends have come up in the form of composite dressings, where a textile material is coated with the hydrogel [10,11]. The fabric reinforcement provides strength to the hydrogel and drug loaded dressings offer precise control of the release behaviour [12,13].

In this study an attempt is being made to prepare composite wound dressing material by grafting hydrogel on cotton fabric for drug release. Polyacrylamide-co-acrylic acid hydrogel is grafted on cotton fabric by free radical graft polymerisation using APS as a chemical initiator and PEG as a crosslinker. The process parameters such as concentration of monomer & initiator, temperature, addition time of crosslinking agent on grafting yield of hydrogel on cotton fabric are optimized. The composite wound dressing material is loaded with model drug bovine serum albumin and drug release behaviour is studied at different pH.

Experimental

Materials

Reagent grade of acrylamide (AAm) from Sisco Research laboratories (Mumbai, India), acrylic acid (AAc) from Central Drug House (Delhi, India), ammonium per sulphate (APS) from Central Drug House (Delhi, India), ferrous ammonium sulphate from Central Drug House (Delhi, India), polyethylene glycol (PEG 6000) from LOBA CHEMI (Mumbai, India), bovine serum albumin (BSA Or fraction-v) from HIMEDIA Laboratories Pvt. Ltd. (India) and cotton fabric (139 g/m^2) were used as received. All the experiments were carried out in distilled water.

Methods

Preparation of Composite Wound Dressing Material

Treatment of Cotton Fabric with Ammonium Per Sulphate

Woven cotton fabric with the thickness of (0.22) mm was

*Corresponding author: roli.purwar@dce.edu

cut into pieces (3.5×3.5 cm^2) and immersed in solution of different concentration of APS ranging from 1 % to 5 % (w/v) for 24 hours. The samples were thoroughly washed with distilled water several times and squeezed between two filter papers to remove excess solution.

Graft Polymerization

APS treated fabric first grafted with different concentration of acrylamide and acrylic acid monomers (monomer ratio 1:1 wt/wt) ranging from 5 to 15 % (w/v). The grafting reaction was carried out in three neck flask under nitrogen atmosphere for 15 to 45 min at varied temperature range from 30 to 60 °C. After grafting of poly (acrylamide-co-acrylic acid) on cotton fabric PEG (0.1 % wt. of the monomer) was added. The time of PEG addition was varied from 15 to 45 min. Samples were washed with water to extract homopolymer as well as unreacted monomers. The grafted samples were dried under vacuum to a constant weight.

Characterization

Grafting Yield (%)

The grafting yield was determined as the ratio of the dry weight of poly (AAm-co-AAc) hydrogel grafted cotton fabric to the dry weight of the cotton fabric as shown below:

$$\text{Grafting yield (\%)} = (W_g - W_d)/W_d \times 100 \quad (1)$$

Where W_g is the total weight of the hydrogel grafted cotton fabric and W_d is the dry weight of the cotton fabric.

Fourier Transformed Infrared spectroscopy (FTIR)

FTIR of grafted cotton fabric was carried out with Scientific Nicolet 380 spectrophotometer, USA using transmittance mode. Scanning was carried out using KBr pellet in frequency range of 500 cm^{-1} to 4000 cm^{-1}. KBr pellet was prepared by 1 part of fine powder of fabric sample with 20 part of KBr.

Scanning Electron Microscopy (SEM)

The morphology of hydrogel grafted on cotton fabric was examined by SEM (Hitachi S-3700N, Germany). Samples were gold-sputter coated to render them electrically conductive and fixed by adhesive tape in the sample stage.

BSA Release Studies

The drug release studies of hydrogel grafted cotton fabric were examined by Cary 300 UV-Visible spectrophotometer (Agilents Technologies). Dried samples of weight 30 mg were placed in test tubes containing 10 m*l* of aqueous solutions of BSA (1 %) for 3 days at 37 °C. After 3 days, hydrogels were separated from the solutions and dried. The BSA loading in hydrogels was determined from the difference in the solution concentration before and after drug loading. Release of BSA was carried out at different pH 5.5, pH 7 and pH 8.5 phosphate buffer solutions. For release studies the BSA loaded composite dressing were placed in 10 mL of these solutions at 37 °C. The amount of drug released at different time interval was determined spectrophotometrically at 280 nm. The value at each time point was added to the value at all previous point to obtained cumulative release amount. The distribution of the drug molecules in the hydrogel was assumed to be homogeneous.

Mechanical Properties

The tensile properties of composite dressing and hydrogel film (50×10×0.4 mm) were measured after immersing in water for 24 hours on Universal Testing Machine (Instron 3369) at a crosshead speed of 5 mm min^{-1}. Average tensile properties from five specimens were measured.

Results and Discussion

For the development of composite wound dressing, the fabric was first immersed in the initiator solution. APS was used as an initiator to create the active sites on fabric. The initiator treated fabric was graft copolymerised with acrylic acid and acrylamide monomers. After graft copolymerization, crosslinking agent was added for the formation of hydrogel on cotton fabric. The mechanism of initiation on cotton fabric, graft copolymerization of monomers and crosslinked hydrogel formation is shown by schematic diagram in Figure 1.

Grafting Yield (%)

The effect of monomer concentration, initiator concentration, temperature of reaction and addition time of PEG was optimized with maximum grafting yield of hydrogel.

Effect of Ammonium Per Sulphate Concentration

The active sites were generated by soaking cotton fabric in different concentration of APS solution for 24 hours. This process was adopted to avoid formation of homopolymer or copolymer of acrylic acid and acrylamide during graft copolymerization reaction. APS was present only on the surface of the fabric not in the monomer solution. Effect of APS concentration on grafting yield of hydrogel was studied and the results are shown in Figure 2. With increase in APS concentration from 1 % to 5 % (w/v) the grafting yield of hydrogel increases. At 5 % (w/v) of APS concentration, the grafting yield of hydrogel was found to be 420 %. The

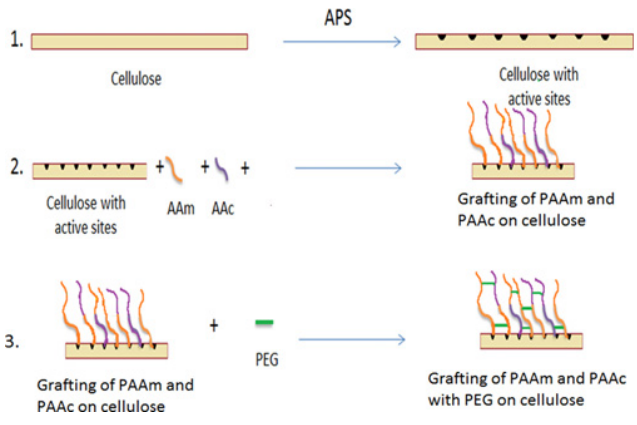


Figure 1. Schematic diagram for formation of composite dressing.

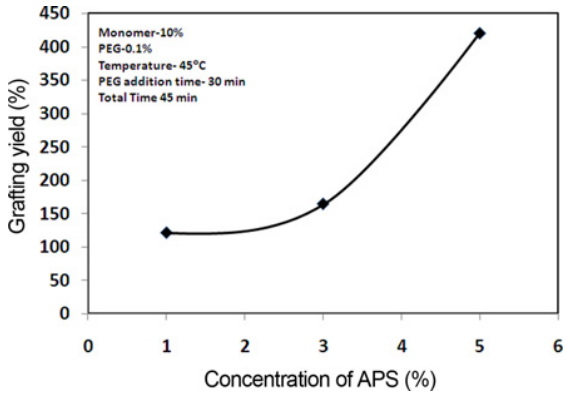


Figure 2. Effect of APS concentration on degree of grafting of hydrogel.

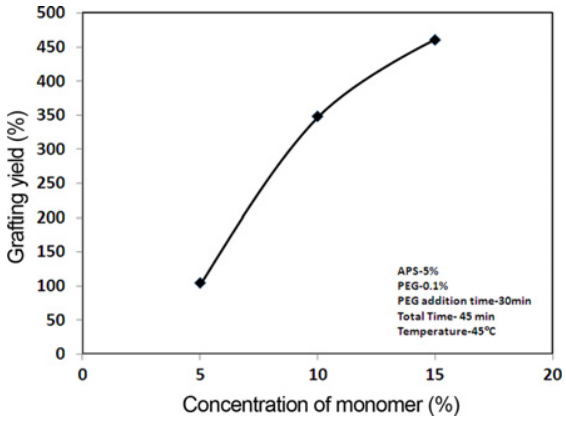


Figure 3. Effect of monomer concentration on degree of grafting of hydrogel.

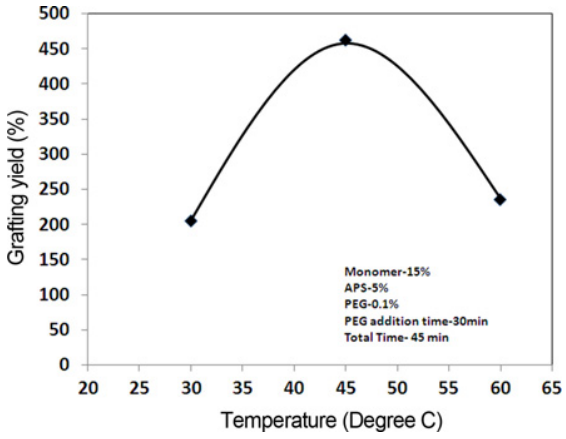


Figure 4. Effect of temperature on degree of grafting of hydrogel.

increasing trend of the grafting yield indicates that APS participated in the formation of active sites on the surface of cotton fabric. Higher the concentration of APS on the fabric surface higher is the generation of active sites. Different chemical initiator system such as cerium ammonium sulphate [14], potassium per sulphate and ferrous ammonium per sulphate [15], $KMnO_4$-HNO_3 redox [16] etc. have been used for grafting of vinyl monomers on cotton fabric and its derivatives. It was observed with all reported chemical initiator systems, with increase in concentration of initiator the grafting yield increases and after certain initiator concentration it decreases. The grafting yield depends on the chemical nature of initiator. The decrease in grafting yield is attributed to formation of more homopolymer at higher concentration of initiator. In our case the initiator was present only on the surface of the fabric not in reaction solution; therefore, it was participated more in graft copolymerization reaction. Very less homopolymer or copolymer of acrylamide and acrylic acid was formed. For further studies the initiator concentration 5 % (w/v) was taken as it had given sufficient amount of grafting of hydrogel on cotton fabric.

Effect of Monomer Concentration

Two different monomers acrylamide and acrylic acid were grafted on cotton fabric. The ratio of acrylamide/acrylic acid was taken 1:1 w/w. The effect of monomer concentration on grafting yield of hydrogel is shown in Figure 3. The results show that with increase in monomer concentration from 5 % to 15 % (w/v), the grafting yield of hydrogel increases. Increase in monomer concentration leads to increase in availability of the monomer to reach the reaction sites. Similar results were observed when polypropylene films were grafted with mixture of acrylic acid and acrylamide monomers [17] and cotton fabric grafted with hydrogel of acrylic acid and itaconic acid [18,19]. The grafting yield of hydrogel was observed 460 % at 15 % (w/v) monomer concentration. At 15 % (w/v) monomer concentration 0.22 mm hydrogel layer was formed similar to thickness of fabric. Therefore, for further studies 15 % (w/v) monomer concentration was taken.

Effect of Temperature

The grafting reactions were carried out at different temperatures (30-60 °C) keeping the other variables constant. The effect of temperature on grafting yield is shown in Figure 4. As the temperature of grafting increases the grafting yield of hydrogel increases up to 45 °C then decreases. The dependence of grafting yield on temperature can be ascribed to higher rate of dissociation of initiator as well as the diffusion and mobility of monomer from the aqueous phase to fabric phase, resulting in considerable improvement in the grafting yield. With further increase of temperature beyond 45 °C, the radical termination reaction might be accelerated, leading to decrease of grafting yield. These findings are in agreement to those reported in literature [14-16].

Effect of the PEG Addition Time

PEG was added to form crosslinks between the grafted chains. Initially grafted chains of poly acrylic acid or polyacrylamide or poly (acrylamide-co-acrylic acid) were allowed to grow on cotton fabric, then after specified time PEG was added to form crosslink network on grafted chains.

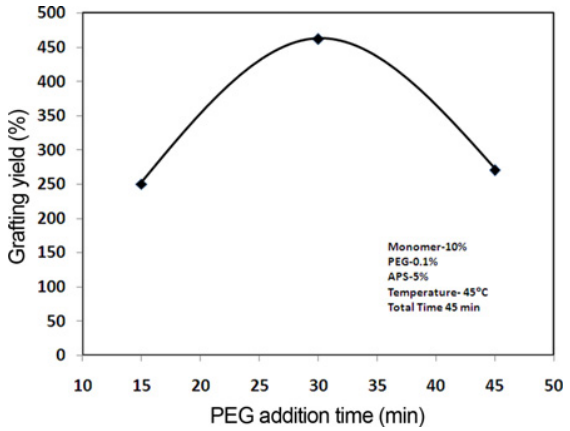
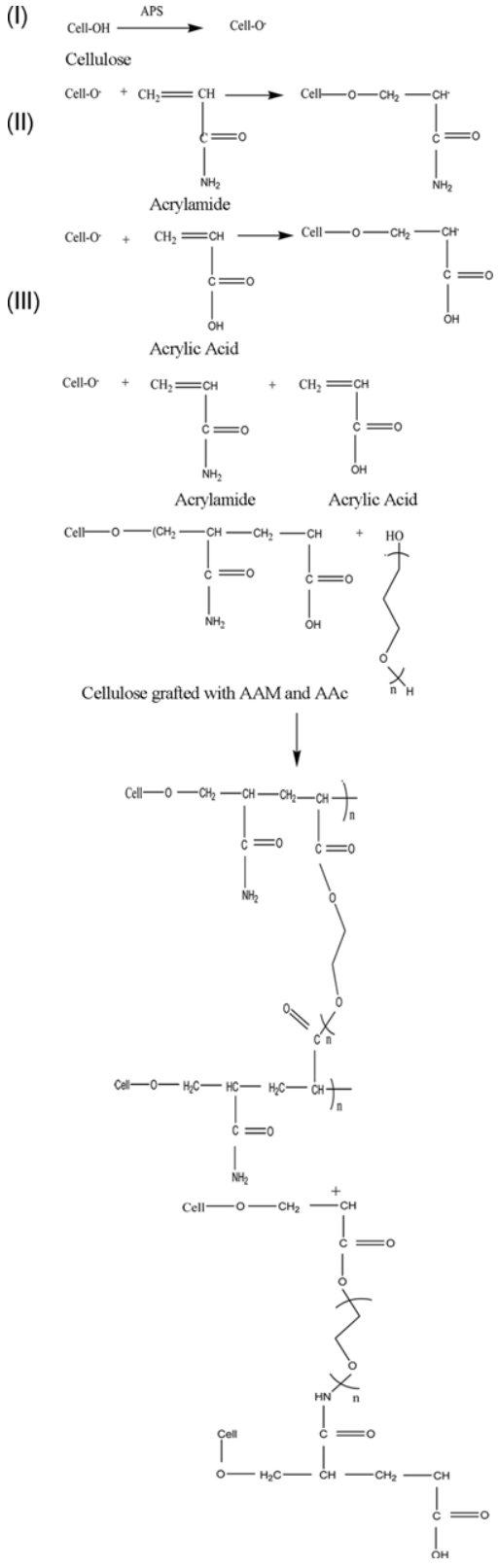


Figure 5. Effect of PEG addition time on degree of grafting of hydrogel.

The effect of PEG addition time on grafting yield is shown in Figure 5. PEG was added at different time interval from 15-45 min. The total time of grafting reaction was kept 45 min. It was observed that grafting yield of hydrogel increases with an increase in the PEG addition time, but reaches maximum at 30 min. Further increase in PEG addition time is accompanied by a decrease in the grafting yield of hydrogel. This may be due to that apart from acting as crosslinker; PEG may also be acting as chain terminating agent. At initial stage of grafting if PEG added to the polymerization reaction flask it acts as chain terminator agent which arrest the growth of the chains finally grafting yield of hydrogel. When PEG added to polymerization flask at 30 min sufficient length of polyacrylic acid or polyacrylamide or poly (acrylamide-co-acrylic acid) chain growth takes place on the surface of the fabric. PEG forms crosslinked network of hydrogel with the grafted chains of polyacrylamide, polyacrylic acid, poly (acrylamide-co-acrylic acid). Increase in addition time of PEG from 30 to 45 min, it was observed that hydrogel grafting on fabric decreases. This may be due to the total time of grafting reaction was taken 45 min; it may be possible that PEG not get sufficient time for crosslinking.

Fourier Transform Infrared Spectroscopy (FTIR)

FTIR was performed to determine the structure of the composite dressing and to identify the presence of specific functional groups within a sample. Chemical reactions involved in each step of graft copolymerization of hydrogel on cotton fabric are shown in Scheme 1. APS produces cellulose macroradicals via direct abstraction of hydrogen atom from cellulose molecules. Cellulose free radical molecules are reacted with vinyl monomer (i.e. acrylic acid or acrylamide) formed a covalent bond between monomer and cellulose with creation of free radical on the monomer i.e. a chain reaction is initiated. Subsequent addition of monomer molecules to the initiated chains propagates the grafting reaction onto cellulose.



Scheme 1. (I) Initiation reactions, (II) propagation reactions, and (III) cross-linking reactions.

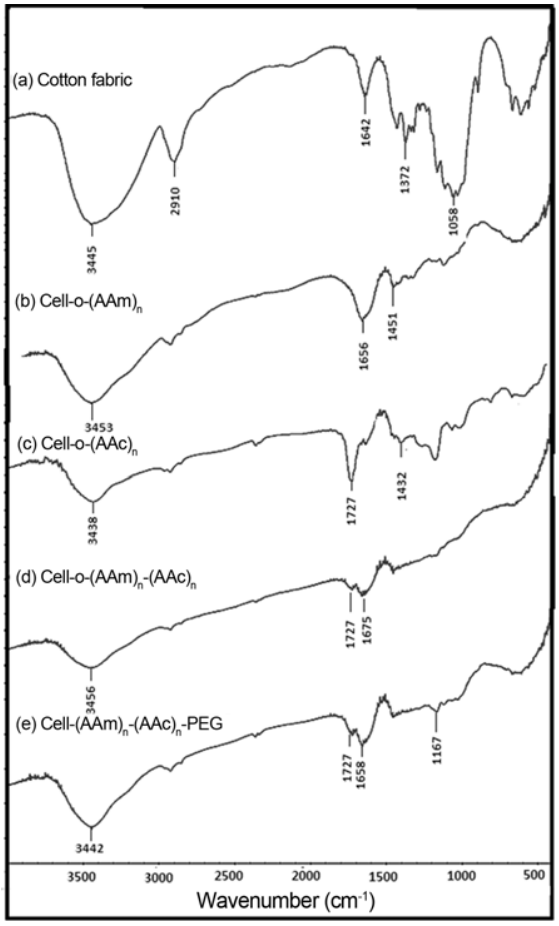


Figure 6. FTIR spectra of (a) un-grafted, (b) polyacrylamide grafted, (c) polyacrylic acid grafted, (d) polyacrylamide-co-acrylic acid grafted, and (e) polyacrylamide-co-acrylic acid-PEG grafted, cotton fabric.

Termination of the growing grafted chains may occur via reaction with the initiator, coupling or combination or by reacting with PEG and disproportionation. After grafting reaction PEG is added which make crosslinks between grafted chains of acrylic acid and acrylamide. A comparative depiction of FTIR spectra of ungrafted (Figure 6(a)), poly (AAm) grafted (Figure 6(b)), poly (AAc) grafted (Figure 6(c)), poly (AAm-co-AAc) grafted (Figure 6(d)) and poly (AAm-co-AAc-PEG) grafted (Figure 6(d)) cotton fabric is shown in Figure 6. Figure 6(a) shows characteristic cellulose peaks around 1000-1200 cm^{-1}. Other characteristic bands related to the chemical structure of cellulose are H-bonded O-H stretching at 3445 cm^{-1}, the C-H stretching at 29102 cm^{-1}, the asymmetrical COO^- stretching at 1642 cm^{-1}, and the C-H wagging at 1372 cm^{-1} and the C-O stretching at 1058 cm^{-1} are observed. Figure 6(b) shows the characteristic peaks of polyacrylamide. N-H stretching at 3453 cm^{-1}, C=O (C=O of amide group) stretching at 1656 cm^{-1}. Figure 6(c) shows the characteristic peaks of polyacrylic acid O-H stretching at 3438 cm^{-1}, C=O (C=O of acidic group) stretching at 1727 cm^{-1}. Figure 6(d) shows the characteristic peaks of polyacrylic acid and Polyacrylamide. N-H stretching at 3456 cm^{-1}, C=O (C=O of acidic group) stretching at 1727 cm^{-1}, C=O (C=O of acrylamide group) stretching at 1659 cm^{-1}. Figure 6(e) shows the characteristic peaks of polyacrylic acid, acrylamide and PEG. N-H stretching at 3442 cm^{-1}, C=O (C=O of acidic group) stretching at 1727 cm^{-1}. C=O (C=O of acrylamide group) stretching at 1658 cm^{-1}. The main characteristic peak of C-O-C stretching at 1167 cm^{-1} is found which shows the presence of PEG crosslinking in hydrogel. Observed peaks are in close relation with literature [11-19].

Scanning Electron Microscopy (SEM)

The surface of the ungrafted cotton fabric and the grafted cotton fabric was examined by SEM and the results are shown in Figure 7. Figure 7(a), (b) shows the SEM micrograph of un-grafted cotton fabric. Cotton fibre convolutions are shown in the picture. Surface of the fibre is observed very smooth and ribbon like. Figure 7(c), (d) shows the SEM micrographs of hydrogel grafted fabric. It is evident from the micrographs that the considerable thick layer of hydrogel is grafted on the surface of the fabric. The grafted surface of the fabric shows markedly bumpy texture. Similar findings observed when cotton fabric grafted with polyacrylic acid-co-itaconic acid hydrogel [11,18]. SEM photographs clearly show the layer structure of composite dressing where core is made of cotton fabric and outer layer is made of hydrogel.

BSA Drug Release

Wound healing is a complex, multifaceted process which is influenced by both intrinsic and extrinsic factors. The pH of the wound can affect by many factors including oxygen, angiogenesis, protease activity and bacterial toxicity. The pH environment of chronic wounds had been recorded within the range of 7.1-8.9. As the wound progress towards healing the pH moves to neutral and then becomes acidic up to 5.4-5.6. Wound healing takes place faster in acidic environment as compared to alkaline environment [21]. Therefore, in this study, the release of BSA from composite wound dressing was performed by immersing the drug loaded samples in different pH 5.5, pH 7 and pH 8.5 buffer solutions. The release profiles of BSA from composite dressing at 37 ^oC are shown in Figure 8. It is observed that BSA releases at all pH 5.5, pH 7 and pH 8.5. The rate of release of BSA was high initially and with increase in time release rate decreases. It is dependent upon the swelling behaviour of hydrogel at different pH. At pH 5.5, pH 7 and pH 8.5 the carboxylic groups of acrylic acid are dissociated (pKa=4.7) and the consequent expansion of the gels together with the electrostatic repulsive force between the COO^- charged site of acrylic acid and BSA (pKa=4.8) favours protein release [6]. With increase in pH from 5.5 to 8.5 the amount of protein release decreases. This is dependent on swelling and the size of the

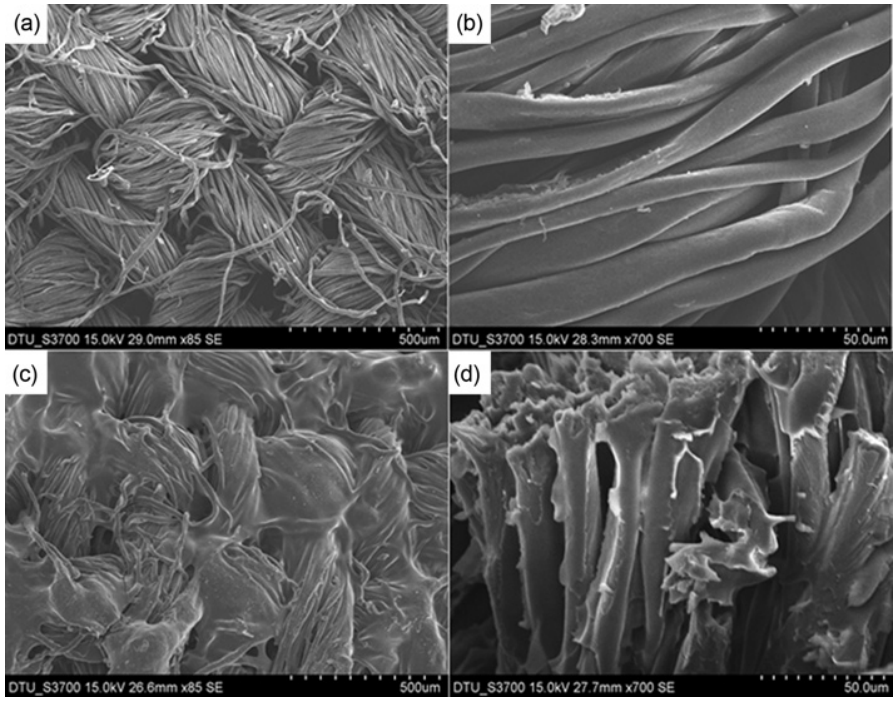


Figure 7. SEM photographs of (a)-(b) un-grafted and (c)-(d) hydrogel grafted cotton fabric.

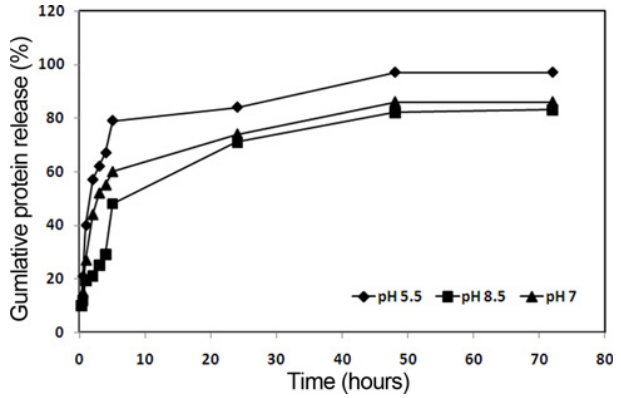


Figure 8. BSA drug release profile from composite wound dressing materials.

pore opening at different pH. Presence of different functional groups -COOH, -$CONH_2$, and -OH affects the swelling of hydrogel at different pH. To further investigate this behaviour, scanning electron microscopy of composite dressing samples was performed after immersing them at different pH for 3 days. The SEM photographs are shown in Figure 9. It is observed that the composite dressing sample immersed at pH 5.5 showed smooth texture of hydrogel with large pores (Figure 9(a)). The composite dressing samples immersed at pH 7 and pH 8.5 show rough surfaces with small pore size (Figure 9(b), (c)). The pore size decreases with increase in pH. Therefore, the amount of drug release also decreases

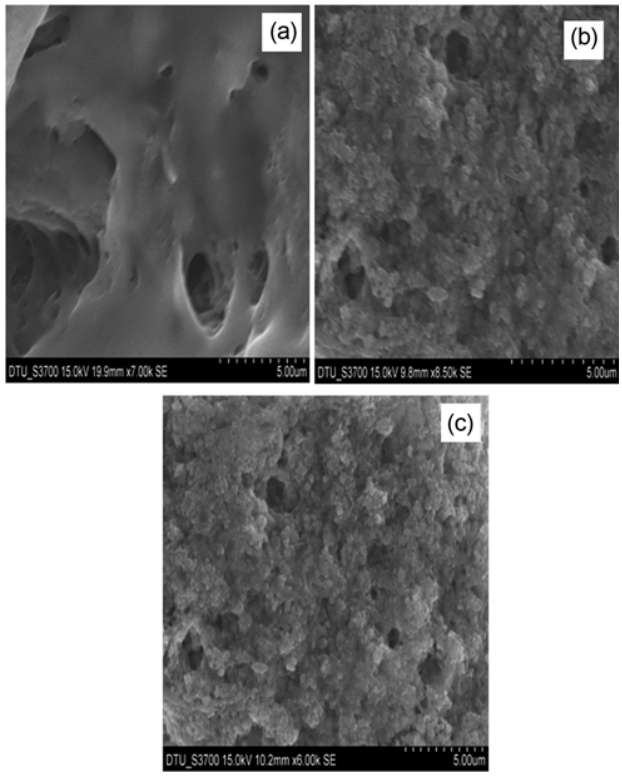


Figure 9. SEM photographs of hydrogel after immersing in (a) pH 5.5, (b) pH 7, and (c) pH 8.5 for 3 days.

Table 1. Mechanical properties of composite wound dressing

Materials	Tensile strength (MPa)	Tensile modulus (MPa)	Extension at break (mm)
Hydrogel film	0.43±.05 (.03)	0.22±.03 (.07)	305±5 (.01)
Wound dressing	11.7±0.7 (.03)	97.5±.7 (.01)	22.19±.06 (.01)

Values in the bracket is denoting coefficient of variation (CV).

with increase in the pH. In this study, within first 5 hours, 79 %, 60 % and 48 % BSA was released from the composite dressing at pH 5.5, pH 7 and pH 8.5, respectively. After that, all the samples gave a slow drug release up to 36 hours. Such type of release behaviour favour the wound treatment as initial high amount of drug release provides immediate relief followed by prolonged release to promote gradual healing [22].

Mechanical Properties

The mechanical properties of composite dressing in wet condition were evaluated and compared with the pure hydrogel films. The mechanical testing was performed after immersing the samples in water for 24 hours. The results are shown in Table 1. The tensile strength and tensile modulus of hydrogel film are much lower as compared to that of composite dressing. The cotton fabric provides reinforcement to hydrogel in composite dressing.

Conclusion

A composite wound dressing with core layer of cotton fabric and outer layer with drug loaded poly (acrylic acid-co-acrylamide) hydrogel was developed in this study. Hydrogel layer was developed on fabric by grafting AAm and AAc monomer on cotton fabric using APS as initiator and PEG as crosslinker. The optimum reaction conditions obtained for grafting of AAm and AAc onto cotton fabric were: APS concentration 5 % (w/v), monomers concentration 15 % (w/v), temperature of reaction 45 ^{o}C, polymerization time 45 min and PEG addition time 30 min. The grafting yield for optimized samples is at achieved 462 %. The samples are characterized by FTIR and SEM techniques. The FTIR spectra shows the acrylic acid and acrylamide is grafted onto the cotton fabric and PEG forms crosslinked network between the polymer chains. Composite dressing is loaded with model drug BSA and release behaviour of the drug was studied at different pH. Within first 5 hours, 79 %, 60 % and 48 % BSA was released from the composite dressing at pH 5.5, pH 7 and pH 8.5, respectively. After that all the samples gave a slow drug release up to 36 hours. The composite dressing showed very good tensile strength and modulus in wet condition.

References

1. P. S. Murphy and G. R. D. Evans, *Plast. Surg. Int.*, **2012**, 1 (2012).
2. J. S. Boating, K. H. Matthews, H. N. E. Stevens, and G. M. Eccleston, *J. Pharm. Sci.*, **97**, 2892 (2008).
3. T. R. Hoare and D. S. Kohane, *Polymer*, **49**, 1993 (2008).
4. A. Thakur, R. K. Wanchoo, and P. Singh, *Chem. Biochem. Eng.*, **25**, 471 (2011).
5. I. Katime, R. Novoa, E. Díaz de Apodaca, and E. Mendizábal, Puig, *J. Polym. Test.*, **18**, 559 (1999).
6. M. B. Poveal, W. A. Monal, J. V. C. Rodríguez, A. M. Pat, N. B. Rivero, and C. P. Covas, *Mater. Sci. Appl.*, **2**, 509 (2011).
7. F. Becerra-Bracamontes, J. C. Sánchez-Díaz, A. González-Álvarez, P. Ortega-Gudiño, E. Michel-Valdivia, and A. Martínez-Ruvalcaba, *J. Appl. Polym. Sci.*, **106**, 3939 (2007).
8. C. Jin-lei, Z. Wen-wen, Q. Yu-qin, and G. A. O. Yun-hua, *Imaging Sci. Photochem.*, **29**, 336 (2011).
9. D. Ray, D. K. Mohapantra, G. P. Mohapantra, G. P. Mohanta, and P. K. Sahoo, *J. Biomater. Sci. Poly. Ed.*, **19**, 1487 (2008).
10. B. Gupta, R. Aggarwal, and M. S. Alam, *Ind. J. Fibre Text.*, **35**, 174 (2010).
11. B. Liu and J. Hu, *Fibres Text. East. Eur.*, **13**, 45 (2005).
12. C. Ko-Shao, K. Yuan-An, L. Chi Han, L. H. Ru, L. F. Huei, and C. T. Mo, *Mater. Sci. Eng.*, **25**, 472 (2005).
13. B. Gupta, S. Mishra, and S. Saxena, *Radiat. Phys. Chem.*, **77**, 553 (2008).
14. R. Khullar, V. K. Varshney, S. Naithani, and P. L. Soni, *Exp. Polym. Lett.*, **2**, 12 (2008).
15. A. Bhattacharya and B. M. Mishra, *Prog. Polym. Sci.*, **29**, 767 (2004).
16. K. M. Mostafa, *J. Appl. Sci.*, **5**, 341 (2005).
17. H. J. Chun, S. M. Chao, Y. M. Lee, H. K. Lee, T. S. Suk, and K. S. Shim, *J. Appl. Polym. Sci.*, **72**, 251 (1999).
18. H. Hosseinzadeh and S. Mohammadi, *Current Chem. Lett.*, **2**, 109 (2013).
19. P. Gupta, M. Bajpai, and S. K. Bajpai, *J. Macromol. Sci., Pure Appl. Chem.*, **45**, 179 (2008).
20. H. Kamogawa and T. Sekiya, *Text. Res. J.*, **31**, 585 (1961).
21. G. Gethein, *Wound UK.*, **3**, 52 (2007).
22. X. Huang and U. S. Brazel, *J. Controlled Release*, **73**, 121 (2001).

Detecting Computer Viruses

Manju Khari, Chetna Bajaj

***Abstract*— Virus (in biology) refers to microorganism, means very small creatures. Likewise, Virus is a small sized program in computer world but can cause severe destructive actions to computer(s). Virus can result in poor performance, loss of data, loopholes in system. Because of it, everyone who uses computers have a fear of losing data. Resultant, virus developer becomes powerful by holding an exotic power to attack. High losses become an important concern for sober computer users. To restrict them, virus must be detected and observed to know how they produce severe destruction. Various virus detection techniques, which are beneficial in virus prevention, are described in paper. They are also often used in development of antivirus systems to automate virus detection, resulting in a security mechanism which has power to restrict virus i.e. does not allow virus to infect other files on system.**

***Index Terms*—Malware, Virus, Virus Detection Techniques.**

I. INTRODUCTION

Malware is a program code which has an extensive capability to infect system. It can perform malicious actions on system as well as on network(s) of systems. It can propagate over the network. It can produce severe effects which lead to attack. It can also perform activities that facilitate malware for its operation i.e. disables the installed malware detector [1] [2]. Malware has grown rapidly in past few years and most of them come from well known websites. Malwares can be classified into four generations based on their payload, enabling vulnerability and propagation mechanism [2] [3]. Table 1 shows Generations of malware with, its example and propagation method.

Organization of the paper is as follows: We have described various types of malwares, their basic characteristics with detailed description and examples, in section 2. Concentrating on virus, in section 3, Virus's evolution in different phases, is illustrated. Each phase has its own characteristics and consequently, virus has evolved into more complex form to prevent its detection. Due to destructive action of virus, its detection has become an important vertical in computer world. So, various detection techniques are outlined in section 4. Section 5 through some light on analysis techniques like Static Analysis, Dynamic Analysis and Hybrid Analysis, and also describes the relationship among analysis techniques and detection techniques. Some more and efficient virus detection techniques which use machine learning technique are described in section 6. At the end, we have concluded the paper with its future scope discussion continued with references list.

TABLE I. GENERATIONS OF MALWARE, IT'S EXAMPLE WITH PROPAGATION METHOD

Generations	Example	Propagation Method
First (1980)	Virus	Replicate and propagate by human's intervention, emails and file sharing.
Second (1995)	Worms and Trojan horse	Hybrid in nature. Propagates itself on network, does not require human intervention.
Third (2000)	Specific to organization or geographical region	It employs multiple attack vectors and attacks on security technologies and products.
Fourth (2000 onwards)	Specific to particular application and websites that are used massively	Employs infection through already infected computers and by installing malicious programs to infect application like Facebook, Skype and Operating System like Linux.

II. TYPES OF MALWARES

Different types of malwares are diagrammed in Figure 1:

A. Virus

Virus is a computer program which replicates itself byte-by-byte to create a new executable file, and infect files on system. It is a self replicating program and need some host

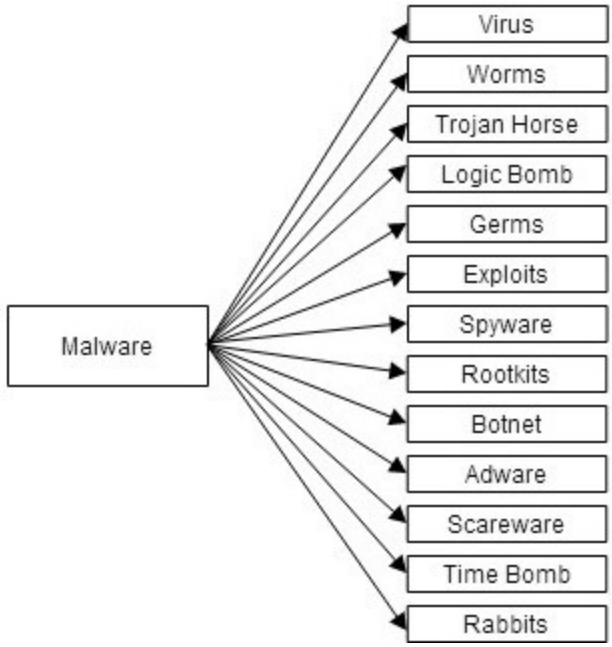


Fig. 1. Various types of Malwares

***Manuscript received July, 2014*.**

***Manju Khari**, Department of Computer Science & Engineering, Ambedkar Institute of Advanced Communication Technologies and Research, Delhi, India, Mobile No. 9899296110,*

***Chetna Bajaj**, Department of Computer Science & Engineering, Ambedkar Institute of Advanced Communication Technologies and Research, Delhi, India, Mobile No. 9213730027,*

 All Rights Reserved © 2014 IJARCET

or human intervention for its propagation. Virus gets attach to host program to be able to replicate. Its main target is to infect files on system, which ensures their presence on system for long time and then these files propagates to other computer through some communication medium i.e. as an email attachment, trade program or diskette, coping files to/from server and then again replicates and propagates in same fashion on other machines as well [4].

Example: ILOVEYOU, Melissa, Christmas Tree.

B. Worms

Worms are self replicating and self propagating computer program. It mainly communicates to others systems on network. Its main target is to infect systems on the network unlike a virus, which wants to infect files on system [5] [6].

Example: Blaster, Morris, Code Red I and II.

C. Trojan horse

Trojan horse is a software program. It appears legitimate, but can easily create backdoor to application which helps to gain control of the entire system remotely without any knowledge and permission of the legitimate user [7].

Example: Netbus, Back Orifice, SubSeven and AIDS TROJAN DISK, Nuker.

D. Logic Bomb

Logic Bomb is developed for a specific legitimate application. It is inserted or linked with the application in such a way that user will not be able to observe or locate its presence. Means, it remains hidden but whenever application executes, user can observe its damaging effects. Logic bomb has a flaw that it doesn't replicate on other application. It only works for a application for which it has been designed [7].

Example: Jerusalem, SOBIG worm, Michelangelo.

E. Germs

Germs are considered as the first generation virus. It does not have any host program. It exists in its own form when it gets compiled for the first time. It has problem that it does not generate prominent effect of infection process. It infects file but does not leave any sign or mark of infection on that file resulting virus again start to infect already infected file which consumes resources that can be used to infect uninfected files. This problem gets overcome in second generation virus which leaves a flag on infected files to avoid their reinfection [3] [7].

Example: Germ was written for book sector or the diskette in the form of dropper.

F. Exploits

Exploits occur due to flaws or vulnerabilities. Vulnerabilities are exploited to create security hole to get into system. Attacker executes a program to locate system's problems and that can be used to make a hidden path to access important and confidential data and operations. Exploits can be executed remotely or by connecting machine to network [7].

Example: 'White hat' hacker's Exploit code is used for application's penetration testing. Exploits can also be developed to execute command prompt (cmd.exe on Windows or /bin/sh on Unix) on remote system.

G. Spyware

Spyware gets installed on system without the knowledge and permission of legitimate user. It usually installed as a background process. It collects user's personal and confidential information and uses it against him [2]. It can cause monetary losses as well by accessing and using user's bank details.

Example: Spyware Quake, Spyware cleaner, Security toolbar.

H. Rootkits

Rootkits usually get installed on already infected machines (by virus). It is used to gain system's administrator access by compromising it. It is named after term root in UNIX [2].

Example: Adore, svchost.exe, PDCOMP, Hacker Defender, Knark, LRK5.

I. Botnet

Botnet is an autonomous software program, remotely controlled by attacker. It is usually a zombie program which can be controlled for any network [2].

Example: Boatnet, Zer0n3t, Kelihos, LowSec, Rbot.

J. Adware

It is used in context of advertisements. It is advertising supported software. Its functionality is to display and download advertisements to an already infected system and through these advertisements, other malicious or controlling program can easily be executed on system to acquire its full access [2].

Example: DeskAd, Flipopia, iAdware for MAC, AdBlaster, Clickbank.

K. Scareware

Scareware usually comes unknowingly from unreliable internet sources like malicious or hacked websites and applications, or hacker's trap. Innocent users download some programs that appear useful as they primarily claim to provide security to system, resulting in producing vulnerable results. A free or trial version of antivirus program or any free online scam can be considered as scareware program. User gets attracted toward exciting offers and downloads false security software. When user opens attachment, malicious code gets executed and makes system prone to attacks. Some scarewares even try to collect E-commerce related information like bank details, personal information and can cause great losses [8].

Example: Smart Fortress, Android Defender. Ramsomware, System Security (blue screen of death).

L. Time Bomb

Time Bomb is a malware, similar to logic bomb. The time in its name specifies the property of occurrence of malware i.e. the particular event or time at which malware will execute to reflect its destructive effects on system and network. Time bombs are programmed to get executed at scheduled time or when some specific condition is met, till

 All Rights Reserved © 2014 IJARCET

the time it remains dormant or inactive [9]. Time bomb like Jerusalem virus i.e. Friday the 13th or April fool's Day, deletes files on infected computer, on every Friday the 13th. Time bomb can be used by an insider, who wishes to destroy the data of organization upon his termination. The employee will set the time of time bomb and it will burst out after his termination. For example, employee may insert malicious code in payroll system and program it to delete all files if in case his name is not present in list. It means, all important files will get deleted if employee gets removed or terminated from organization's payroll system. An organization named Omega Engineering has lost millions of dollars due to a time bomb installed by a former employee.

Examples: The Christmas or Valentine's Day, Conficker.

M. Rabbits

Rabbits appeared around 1974. It remains on network but caters itself from one point to other. Rabbits replicate and propagate itself, but deletes its original copy keeping only one copy on network. The feature of replication refers to fork (creating its own copy). So, it is also called as Fork Bombs. Rabbits, being a malicious program, do not cause significant destruction but execute itself recursively and infinitely on system without any restriction. It gradually occupies system's whole memory with multiple copies of recursively executed same program code and slow down the processing thus increase CPU computing time [10]. In short, they monopolize CPU, memory or disk space and can even result in DOS attack [4]. Resultant, it restricts execution of programs which require large amount of resources like processing time and memory. Rabbit worm is effective in evading its detection through antivirus resulting in difficulty in its removal from system.

Example: Fork Bombs, cmd.exe, rabbits written in Perl, JavaScript.

III. Evolution of Virus

Virus has various variant according to their structure and impact on system [1] [3]. Origin of Virus is categorized into:

A. Initial Stage

In initial stage, virus was developed to infect system's files and data. It was developed for corrupting disk, email accounts, private networks, etc. It infects systems, and spread across others. Initial stage viruses can be easily detected by antivirus i.e. by using their signatures or pattern.

B. Stealth Virus

As earlier viruses are easy to detect, virus developers coded stealth virus to elude virus detection system. Stealth virus takes the charge of file management system and conceals the changes it has made to infected files. It can corrupt and encrypt data files. Stealth virus resides in memory and remains hidden from virus detection system. Whenever antivirus scans system for malicious programs, it automatically renders the search for non-malicious data and antivirus fails to detect it. To detect stealth virus, detection system should scan active memory, compact disc or floppy disk.

Example: Brain, Frodo and Whale.

C. Polymorphic Virus

Polymorphic virus challenges virus detection system. It uses a polymorphic generator to mutate code without changing original program or algorithm. The simplest method for mutation is self-encryption. It encrypts virus's body and hides its signature, and makes it difficult for detection. Each time, a different key is used in self-encryption process to produce different viruses. After propagation, polymorphic virus decrypts itself by its own decryption algorithm attach to it and virus get executed on host. To further restrict its detection, polymorphic virus goes through multiple encryption-decryption process. Polymorphic virus can be detected using Emulation based detection system [2].

Example: 1260 was the first polymorphic virus, used different encryption and decryption process to evade detection, HPS, Marburg.

D. Metamorphic virus

Metamorphic virus modifies or manipulates itself during propagation across network. It changes its code or internal structure and generates a new virus which functions as original, but does not appear same i.e. signatures do not match [3] [11]. After propagation, metamorphic virus resumes its original structure and again modifies itself to a new virus to evade its detection [2]. Modification to the virus's program code can be done by Code obfuscation techniques like swapping interchangeable instructions, inserting garbage instruction and introducing conditional jumps to generate new virus. Code obfuscation may also include change in instruction order without altering control flow. Code obfuscation technique breaks virus's signature and make it difficult for signature based detectors to detect metamorphic virus. Metamorphic virus translates its new code according to corresponding host's operating system. Other techniques which can be used to create metamorphic virus are Expansion, Permutation, Assembling, Transformation, Disassembly-Depermutation/Shrinking [2].

Along with code obfuscation, packing also restrict malware detection. It encrypts and compresses program code. Packed code or executable is difficult to analyze for detection. So, packed code must be unpacked to get malware's actual code,

By breaking virus's signature by ordering virus's code instructions, signature based detector would not be able to detect metamorphic viruses. So, these viruses must be detected by a system which can extract essential instructions that resemble virus's presence. Therefore, machine learning technique can be used to detect them.

IV. Virus Detection Techniques

Virus detection is important to rescue system(s) or network(s) from their adverse effect. Detection comes in

 All Rights Reserved © 2014 IJARCET

mind when a normal user looks for virus's erroneous effect, which could be very destructive ranging from corruption of files to destruction of whole network. To protect system from virus, it is important to detect them and void their effect. For detection, users may look for virus's execution behavior. User may also observe program's correctness to identify it as benign or malicious activity. Detection method must be able to understand obfuscation technique applied to code and identify malicious code from obfuscated code.

Different detection techniques are used to detect different viruses (with varied characteristics) as a single detection technique would not be able to detect all types of viruses [3]. Antivirus (software program used to detect malwares/virus) incorporates a combination of different detection techniques so that it wouldn't miss any virus being detected. To elaborate further about detection techniques, some of them are explained:

A. Signature based detection technique

Signature based detection technique is a traditional, simple and efficient method for detecting viruses. This technique scans files for virus's signatures. Signature resembles the instruction pattern or a specific string of byte from virus's program code [3]. Signatures can be extracted by examining disassembled code of malware. Antivirus developer must look virus program code carefully to extract virus signature pattern. If there's new virus comes, whose signature pattern is not available then developer must analyze infected file to find its signature. After collecting signatures of viruses, a signature database is created which facilities in virus detection. During detection process, whole computer system including executable files, boot records, document files etc. are checked for viruses. Matching of database's signatures with any file's signature resembles virus's presence [3]. After identifying virus, signature based detection procedure raises alarm for files immediate remedy. Figure 2 describes diagrammatic review of Signature based detection technique.

Signature based detection technique is used for the detection of known viruses, which has been identified earlier i.e. their pattern or signatures are already captured in database. The technique requires signature database to be regularly updated for better results. Higher the signatures present in database, more will be the virus detection rate. This technique produces fast and accurate results. That's why, this technique is used in almost every antivirus system [12].

But problem come when it is required to detect a new virus, which become next to impossible for signature based detection technique as its database does not have any signature for a new virus. As a solution, other methods can be used, tools like disassemblers and debuggers are available in market which can help in extracting signatures from program code. The code gets disassembled, analyzed and then signature extraction is performed [2].

B. Anomaly based detection

Anomaly based detection technique covers problems related to signature based detection technique. It can detect

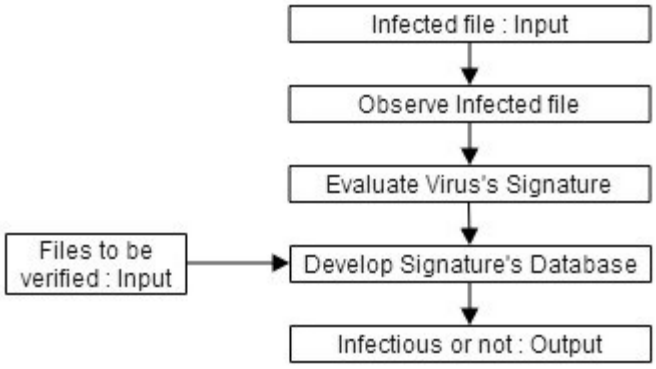


Fig. 2. Diagrammatic review of Signature based detection technique.

unknown viruses which make it more reliable than signature based detectors [12]. It monitors processes on host machine and looks for abnormal activities. It considers rules or heuristics, and most importantly, learning in training period to differentiate between normal or abnormal activities. Upon finding any abnormal activity on machine, it blocks the activity and raises alarm indicating virus's presence. With advantages, it has disadvantage of high rate of raising false alarms and of being costly.

C. Emulation based detection technique

Emulation based detection technique an effective way of virus detection. In this technique, a virtual environment is set, and virus is executed by emulating virus's instructions. During virus execution, instruction sequence and its behavior are identified. Along with virtual environment, code optimization technique can be used to optimize detection time [11].

D. Generic Signature scanning

Generic Signature scanning method is used to detect viruses belonging to same family. It is also known as heuristic signature scanning. It is possible to have a little difference in signatures of one virus family. Signature based detection does not produce good results in detecting similar signature viruses, but Generic Signature scanning provides. It uses patterns, wildcards to detect different viruses or variants from one family. Variants are formed with some minor changes performed in actual source code of virus program. Moreover, It is very fast method and also capable of detecting new and upcoming future viruses belonging to same family [3] [13].

E. Integrity checking

Integrity checking is a simple, efficient and time saving detection technique. Basic approach of the technique is hash value comparison i.e. comparison of hash value of infected file to that of an uninfected file. If there is not any difference in both hash values then there's no virus in system files [13].

Integrity checker can also use checksum/snapshot/ fingerprints of files as well apart from hash value. File's hash is computed when it is uninfected and stored in database or file to keep it safe. Integrity checker computes hash value of all important files like executable, boot records, system files, etc.

While scanning for virus in system, Integrity checker

 All Rights Reserved © 2014 IJARCET

again calculate hash. The new calculated hash must match earlier calculated hash, stored in database to assure that the file does not get infected. It facilitates detector by not investigating those files whose hash matches and to put its efforts to detect virus in rest of the files. This way, Integrity checking restricts the virus detection space, thus saves measurable amount of time.

F. Heuristic scanning

Heuristic scanning is used to detect new/unknown viruses. It examines application program code and looks for particular commands to relate it with malicious programs. The process scans various programs i.e. boot record, macro files, executable files for virus-like instructions. Virus-like instructions could be malicious program's payload, worm propagation routine, virus replication routine, etc. If scanning detects virus-like instructions, then heuristic scanner informs users about it.

Heuristic scanning can be of two forms: Static scanning and Dynamic scanning. The former includes the scanning of program code and later includes the execution of program code on emulators to locate virus's presence. Heuristic scanning can be done by three techniques which are illustrated in Table 2:

- Code Anomaly Detection
- Protocol Anomaly Detection
- Mixed Heuristic Detection

G. Behavior based detection technique

Behavior based virus detection technique observes behavior of known and unknown malwares. It checks source and destination from/to malware is propagating, attachment's type and size, etc. On observing, it can also predict that a particular source will send only malicious codes to attack the system.

V. ANALYSIS TECHNIQUES

Paper [2] and [8] have categorized detection technique in three categories and figure 3 describes relationship between detection and analysis techniques. Categories are:

- Static Analysis
- Dynamic Analysis
- Hybrid Analysis

A. Static Analysis

Static analysis is a process of analyzing program's source code. It does not execute program code. It reveals program structure and can locate executable and non-executable parts of program. It uses disassembler tool for acquiring disassembled and decompiled code to extract low level

TABLE II. HEURISTIC DETECTION TECHNIQUES

Heuristic Detection	Process
Code Anomaly	Looks program code for detection of malware.
Protocol Anomaly	Looks for protocol like TCP/IP and any deviation from its standard for detection of malware.
Mixed Heuristic	It includes the combination of above two and can also combine other detection techniques like generic detection methods to validate results.

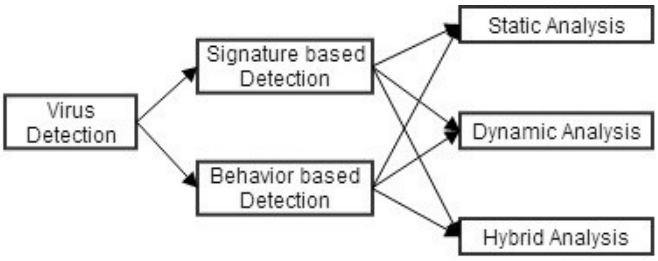


Fig. 3. Relationship between the detection and analysis techniques

information from program code. It can also use program analyzer and debugger. Static analyzers must possess good knowledge of assembly language and Operating system's working. It can also use some other tools like program analyzer, disassemble, debugger. It is advantageous as it is very easy to perform and secondly, it does not require executing program code, so as respective execution environment.

B. Dynamic Analysis

Dynamic analysis is a good approach. It facilitates actual behavior by executing virus's program code and monitoring its behavior, system interaction and its vulnerable effect on system. Malware's behavior is analyzed through simulating infected files in special environment like a virtual machine, simulator, emulator, sandbox etc. As dynamic analyzers look for dynamic or behavior component, this analysis is referred as behavioral analysis. It shows problems in executing malware by not detecting an event which shows behavioral changes in code by different trigger conditions.

Static and dynamic analysis techniques are compared in table 3 with respect to their advantages and disadvantages [2] [8].

C. Hybrid Analysis

Hybrid analysis considers benefits of both two i.e. static and dynamic analysis and overcome their limitations. It provides enhanced protection as compared to earlier two. It first looks for malware's signatures and then applies behavioral constructs on it for analysis.

VI. VIRUS DETECTION USING MACHINE LEARNING

Machine learning can be used to detect viruses. It detects the similarities in virus instances. It is beneficial for detecting metamorphic viruses. Machine learning techniques used for virus detection are [11]:

- Neural Networks
- Data Mining techniques
- Hidden Markov Models

A. Neural network

Neural network technique is best for detecting viruses with similar set of features. In process, virus's features are analyzed first. Analyzed features are modeled in neural network model and trained periodically. Network model detects viruses whose features are modeled in it. It detects viruses with similar features, but they may or may not belong

 All Rights Reserved © 2014 IJARCET

TABLE III. VARIOUS VIRUS DETECTION TECHNIQUES ILLUSTRATING -- FEATURES, ADVANTAGES, DISADVANTAGE AND APPLICATIONS

Detection Technique	Features	Advantages	Disadvantages	Applications
Signature based	1. Scans files for virus's signatures. 2. Used for detecting known viruses. 3. Doesn't require knowledge of normal traffic.	1. Simple and efficient method. 2. Does not consume much time.	1. Cannot detect new viruses. 2. Large signature database is required to store virus's signatures, which is very costly to maintain. 3. Resource-consuming as every signature requires an entry in database. 4. Not reliable as a little change in signature will not detect virus.	1. Used in various basic anti-viruses to facilitate virus detection.
Anomaly based	1. Used for detecting unknown viruses. 2. Check for headers and payload of packets on network. 3. Observes network traffic and monitor host's behavior. 4. Detects abnormal behavior. 5. Notifies users about malicious content by generating alarms.	1. Keeps knowledge of normal traffic to track abnormal activities. 2. Checks packet's headers, connection type, packet payload, etc. to detect virus. 3. Suitable for unknown attacks. 4. Reliable as compared to Signature based detection.	1. Confusing to define what a normal behaviour (threshold) is or what is to be considered as abnormal behaviour. 2. A significant training period is required to define abnormal activity. So, it requires resources. 3. Time consuming, 4. May provide high false positives. 5. Costly to implement	1. Used for creating and defining signatures for new and unknown viruses.
Emulation based	1. Virtual environment is set to emulate instructions. 2. Program code's Instruction sequence and its behaviour are identified. 3. Code optimization technique can be used to optimize time required for virus detection. 4. Trail-and-error detection method.	1. Best for detecting polymorphic and metamorphic viruses, also for encrypted viruses. 2. Fast detection technique. 3. Simulate virus's behaviour to understand its remedy	1. Costly to implement, Time consuming. 2. May require extensive emulation i.e. need to execute virus program of thousands of line of code, and results in slow down the antivirus operation. 3. Does not detect virus that does not show their behavior while emulation. 4. May not provide good result for detecting memory resident programs.	1. Used to detect metamorphic viruses. 2. Used in Skulason's F-PROT antivirus program.
Generic Signature Scanning	1. Uses patterns and wildcards to detect different viruses. 2. Also known as heuristic signature scanning	1. Fast detection method. 2. Capable of detecting new and upcoming future viruses.	1. Cannot detect new viruses. 2. Not suitable for detecting complex virus like polymorphic and metamorphic viruses. 3. Require a highly skilled researcher for extracting virus's patterns.	1. Used to detect viruses belonging to same family.
Integrity Checking	1. Based on hash value of files on the system. 2. Compares hash function of files. 3. Maintains a hash (i.e. Checksum, snapshot, fingerprint) in database. 4. Restricts the virus detection space.	1. Simple and efficient method. 2. Does not consume much time. 3. Fast result producing method as we just need to check the integrity of the file. 4. Can be used to detect any viruses as it doesn't use the concept of virus's signatures.	1. Costly and resource consuming. 2. Tedious for user to update and maintain a huge hash database regularly. 3. Wouldn't have any advantage if system is already virus infected. 4. Does not provide benefit if program is from floppy disk or CD. 5. May raise alarm even on a legitimate change in program. 6. Not suitable for files that rapidly changes.	1. Used for restricting virus detection space. 2. Adopted in virus scanners and many security systems. 3. Implemented as System File Checker (SFC) in Window 2000 and XP systems to check files for change during booting.
Heuristic scanning	1. Examines program code for viruses and worm. 2. Looks for specific commands which signify the presence of malicious code. 3. User observes various programs like boot record, macro files, executable files for virus-like commands like malicious program's payload, worm propagation routine, virus replication routine, etc.	1. Used to detect new and unknown viruses. 2. Not based on virus's signatures, eliminating their drawbacks. 3. Look for protocol used in communication for detection.	1. If the program code to be detected is not updated, then new viruses may go undetected. 2. The potential for false alarms and not detecting a known virus is greater with heuristic scanners as compared to others. 3. May generate a lot of false alarms and may either scare novice users or give them a false sense of security. 4. Time consuming.	1. Used in Kaspersky Anti-Virus to facilitate virus detection.
Behavior based	1. Observes behavior and characteristics of known and unknown malwares. 2. Considers source and destination of the communication, type and size of attachments.	1. Facilitates successful detection of known and unknown viruses from several classes and under several execution conditions. 2. Provides minimal false positives and false negatives.	1. Problem is to define virus behaviour that assures detection of known and unknown viruses while not incorrectly detect benign process as virus. 2. Must be performed by knowledge experts whom are hard to find. 3. Produces false positives and false negatives.	1. Used in detection of virus with self reference replication behaviour. 2. Used for detecting virus in Smart terminal like mobile phones and PCs.
Neural Networks	1. Model is developed and trained over features. 2. Model must be trained with more features for better detection.	1. Best method for detection of viruses with similar features. 2. An efficient technique. 3. Provide low false positive rate if multiple features are used for training.	1. Efficiency depends on threshold values of the features, so maximum number of features must be considered for model. 2. Less number of features in model may result in high value of false positive.	1. Implemented for detection of boot sector viruses in IBM Antivirus program.
Data Mining	1. Rule based method. 2. Develop a model, based on virus's functionality.	1. Provides best results if multiple data mining model get combined.	1. Provides high false positive results.	1. Used for pattern detection in large set of data.

 All Rights Reserved © 2014 IJARCET

Hidden Markov Model	1. State machine based model, depends on current state and input. 2. It is based on Markov model.	1. Based on statistical model, so results can be analyzed easily. 2. Hides complexity and provides output directly.	1. Modeling process is time consuming and complex.	1. Used to detect metamorphic viruses.

to same family. A network model is efficient too. Its efficiency depends on threshold values for a minimum number of features, presented or trained in network model. Higher threshold value allows it to detect specific virus's families, but in contrast, a lower threshold value could create high false positive.

Neural Networks was implemented for detecting boot sector viruses in IBM Antivirus program. It works very efficiently and has low false positive rate as network model cover almost all features of boot sector virus [14].

A. Data mining techniques

Data mining techniques are rule based methods which create a model and train it with the functionality of the viruses. This created model detects the virus based on their functionality. This technique provides best result if multiple data mining model get combined. It provides high false positive results. It is widely used for pattern detection in a large set of data [15] [16].

B. Hidden markov models

Hidden markov model is mainly used to detect metamorphic viruses. The model is a statistical model, used to analyze markov process and provide results on the related observations. These results are used to make proper decisions. It is a state machine based model, which completely dependent on the current state and input's observation [17].

As far, we have studies various virus detection methods which are illustrated in Figure 4 and are summarized in Table 4. Among all these techniques, every detection technique does not provide full proof detection of all types of viruses, but yes they have their special field to serve. For the purpose of better detection, a user can even combine two to three techniques to protect his system.

VII. CONCLUSION

In this paper, Malwares are described which are involved in destruction of computer data and programs. There are various types of malwares including virus, worms, etc. Each malware has its own characteristic and process of infection. We have described virus, its definition, its evolution in different phases. As virus detection is very important for keeping data and programs safe, various detection techniques have been described in detail. Along with it some analysis techniques for virus detection, are also described. Some machine learning virus detection techniques are also explained to enhance the detection capability of detectors, which is evaded by the invention of various complex viruses like polymorphic viruses.

Moving forward, the paper would be helpful for new learners, who can learn and understand virus and its evolution, and their detection techniques can be easily understood. Moreover, these techniques can be used to develop antivirus software to detect viruses for protecting data on system, network, etc.

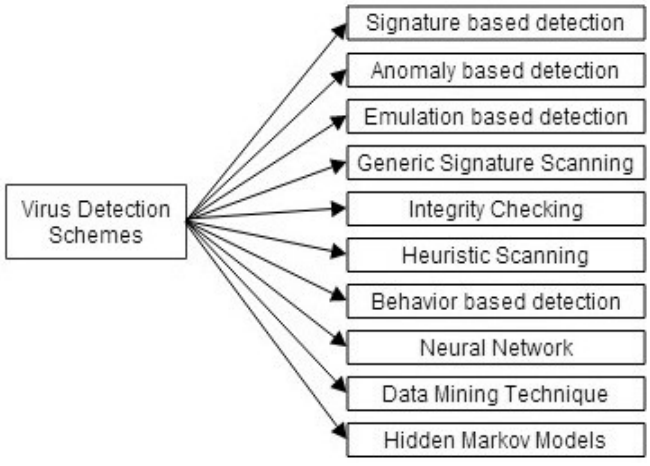


Fig. 4. Various virus detection techniques

REFERENCES

[1] S. Venkatachalam, "Detecting Undetectable Computer Viruses". Master's Projects. Paper 156. 2010. Available: http://scholarworks.sjsu.edu/etd_projects/156.

[2] K. Mathur, S. Hiranwal, "A Survey on Techniques in Detection and Analyzing Malware Executables", International Journal of Advanced Research in Computer Science and Software Engineering, ISSN: 2277 128X, Vol. 3, Issue 4, April 2013.

[3] Hossein Bidgoli, Handbook of Information Security, Volume 3,1st Edition, John Wiley & Sons, ISBN-10: 0471648337, ISBN-13: 978-0471648338, December, 2005.

[4] Peter Szor, The Art of Computer Virus and Defense, Harlow, England: Addison Wesely Professional, February, 2005, ISBN-10: 0321304543, ISBN-13: 978-0321304544.

[5] V. Sharma, "An Analytical Survey of Recent Worm Attacks", International Journal of Computer Science and Network Security, Vol.11, No.11, pp 99-103, November 2011.

[6] Craig Fosnock, "Computer Worms: Past, Present, and Future", East Carolina University, 2005

[7] H. Shravan Kumar, "Seminar Report on Study of Viruses and Worms", Indian Institute of Technology Bombay, 2005.

[8] J. Landage, M.P. Wankhade, "Malware and Malware Detection Techniques : A survey", International Journal of Engineering Research & Technology, ISSN : 2278-0181, Vol. 2, Issue 12, December 2013.

[9] Online documentation: http://antivirus.about.com/od/combinations/a/What-Is-A-Logic-Bomb.htm, Available on March, 2014.

[10] Online documentation: http://cecs.wright.edu/~pmateti/InternetSecurity/Lectures/Viruses/, Available on March, 2014

[11] S. Venkatachalam, M. Stamp, "Detecting Undetectable Metamorphic Viruses", Proceedings of the 2011 International Conference on Security & Management (SAM 2011), pp. 340-345, 2011, ISBN-10: 1-60132-196-1.

[12] Pele Li, Mehdi Salour, And Xiao Su, "A Survey of Internet worm detection And containment", IEEE Communications Surveys & Tutorials, 1st Quarter 2008, Vol. 10, NO. 1.

[13] Mishra, Umakant, "Methods of Virus Detection and Their Limitations", Available at SSRN: http://ssrn.com/abstract=1916708 or http://dx.doi.org/10.2139/ssrn.1916708, August 25, 2010.

[14] Tesauro G.J., Kephart J.O., Sorkin G.B., "Neural networks for computer virus recognition", IEEE Expert, Vol. 11, No. 4, pp 5-6, Aug 1996.

[15] J. Dai, R. Guha, J. Lee, "Feature set selection in data mining techniques for unknown virus detection - A comparison study", ACM International Conference Proceeding Series, 2009.

 All Rights Reserved © 2014 IJARCET

[16] O. Henchiri, N. Japkowicz, "A feature selection and evaluation scheme for computer virus detection", Proceedings – Sixth IEEE International Conference on Data Mining, ICDM, pp 891-895, December, 2006.
[17] S. Attaluri, S. McGhee, M. Stamp, "Profile hidden Markov models and metamorphic virus detection", Journal in Computer Virology, Vol. 5, No. 2, pp 151-169, May 2009.



Manju Khari (manjukhari@yahoo.co.in) is a research scholar with Delhi Technological University (formerly Delhi College of Engineering), Delhi, India. She is an Assistant Professor in Ambedkar Institute of Advanced Communication Technoloies and Research, Guru Gobind Singh Indraprastha University, Delhi, India. She received her Masters degree in Information Security from Ambedkar Institute of Technology, Guru Gobind Singh Indraprastha University, Delhi, India. Her research interests are software testing, software quality, software metrics and artificial intelligence. She has published several papers in international journals and conference.



Chetna Bajaj (chetnabajaj7@gmail.com) is a research scholar, pursuing Masters of Technology in Information Security from Ambedkar Institute of Advanced Communication Technologies and Research, Guru Gobind Singh Indraprastha University, Delhi, India. She has completed her B.Tech in Computer Science & Engineering from Guru Premsukh Memorial college of Engineering, Guru Gobind Singh Indraprastha University, Delhi, India. Her research interests are Near Field Communcation, software security testing and their tools, Mobile Ad-hoc Network, and Virus Detection.

 All Rights Reserved © 2014 IJARCET

Plasma Science and Applications (ICPSA 2013)
International Journal of Modern Physics: Conference Series
Vol. 32 (2014) 1460350 (10 pages)
© The Author
DOI: 10.1142/S2010194514603500

Int. J. Mod. Phys. Conf. Ser. 2014.32. Downloaded from www.worldscientific.com
by 14.139.251.100 on 08/18/14. For personal use only.

Effect of dust charge fluctuations on upper hybrid wave instabilities in magnetized dusty plasma

Jyotsna Sharma

Physics Group, School of Environmental Sciences, Jawaharlal Nehru University, New Delhi-110067, India
bjyotsna28@yahoo.com

Ajay Gahlot

Department of Physics, Maharaja Surajmal Institute of Technology, C-4, New Delhi-110058, India
drajaygahlot@gmail.com

Suresh C. Sharma

Department of Applied Physics, Delhi Technological University, Shahbad Daulatpur, Delhi-110042, India
suresh321sharma@gmail.com

V. K. Jain

Physics Group, School of Environmental Sciences, Jawaharlal Nehru University, New Delhi-110067, India
vkj0400@mail.jnu.ac.in

Published 13 August 2014

The decay instability of an upper hybrid electrostatic wave into an upper hybrid sideband wave and lower hybrid wave is studied in magnetized dusty plasma. A local theory of this process has been developed. The growth rate and mode frequencies of the unstable wave were evaluated based on existing dusty plasma parameters and it is found that the unstable mode frequency and growth rate increases with δ (ion-to-electron density ratio) in the presence and absence of dust charge fluctuations in addition to dust dynamics.

Keywords: Upper hybrid waves; charge fluctuations; decay instability.

1. Introduction

The first experimental observations of upper hybrid waves in laboratory plasma were reported by Idehara et *al*[1]. The study of parametric instabilities[2-5] of large-amplitude electrostatic[6-10] and electromagnetic[11-14] waves has been an active field of research for the last several decades. Barkan et *al.*[15] have found experimentally that the presence of negatively charged dust grains enhanced the growth rate of the instability of current driven electrostatic ion-cyclotron (EIC) wave in dusty plasma. Chow et *al.*[16-17] have

This is an Open Access article published by World Scientific Publishing Company. It is distributed under the terms of the Creative Commons Attribution 3.0 (CC-BY) License. Further distribution of this work is permitted, provided the original work is properly cited.

studied the effect of dust charged fluctuations on the collisionless EIC instability using Vlasov theory. They have found that the critical electron drift velocity (V_{de}) for the excitation of wave decreased in presence of negatively charged dust grains as the ratio of positive ion density to electron density increased showing that the mode was more easily destabilized in plasma containing negatively charged dust grains. The dust has been noted to influence a three-wave parametric process in unmagnetized[18-19] and magnetized plasmas[20]. Parametric instabilities of an upper hybrid wave without dust grains in plasmas have been studied earlier[21-23].

In this paper, we study the effect of dust charge fluctuations and dust dynamics on parametric decay instability of an upper hybrid electrostatic wave into low frequency lower-hybrid and high frequency upper hybrid waves in a magnetized plasma.

Int. J. Mod. Phys. Conf. Ser. 2014.32. Downloaded from www.worldscientific.com
by 14.139.251.100 on 08/18/14. For personal use only.

2. Dispersion Relation

Consider a magnetized dusty plasma with equilibrium electrons, ions and dust grains densities, charges, masses, and temperatures as ($n_{e0}, -e, m_e, T_e$), (n_{i0}, e, m_i, T_i) and ($n_{d0}, -Q_{d0}, m_d, T_d$), respectively. The static magnetic field B_s is parallel to z-axis. An upper hybrid pump wave $\left(\omega_0, \vec{k}_0\right)$ propagates through the plasma with electrostatic potential

$$\phi_0 = \phi_0 e^{-i\left(\omega_0 t - k_0 .x\right)},$$

$$\omega_0^2 = \frac{1}{2}\left[\left(\omega_{pe}^2 + \omega_{ce}^2\right) + \sqrt{\left(\omega_{pe}^2 + \omega_{ce}^2\right)^2 - 4\omega_{pe}^2\omega_{ce}^2 \frac{k_{z0}^2}{k_{\perp 0}^2 + k_{z0}^2}}\right], \tag{1}$$

where

$\omega_{pe}\left(=\sqrt{\frac{4\pi n_{e0}e^2}{m_e}}\right)$, $\omega_{ce}\left(=\frac{eB_s}{m_e c}\right)$ and ω_0 are the plasma, electron cyclotron and pump wave frequencies, respectively. The upper hybrid pump wave may excite a parametric decay instability involving a lower hybrid wave $\phi(\omega, \vec{k})$ and an upper hybrid sideband $\phi_1(\omega_1, \vec{k_1})$ with electrostatic potential $\phi = \phi e^{-i\left(\omega t - k.x\right)}$ and $\phi_1 = \phi_1 e^{-i\left(\omega_1 t - k_1 .x\right)}$, respectively. (2)

The response of plasma electrons to the pump wave is governed by the equation of motion and by solving that we get the electron density as

$$n_0 = -\frac{n_{e0} e\phi_0}{m_e}\left[\frac{k_{x0}^2}{\omega_0^2 - \omega_{ce}^2} + \frac{k_{z0}^2}{\omega_0^2}\right]. \tag{3}$$

The pump and sideband waves exert a low frequency ponderomotive force on the electrons given by

$$\overrightarrow{F_p}\left(\omega, \vec{k}\right) = -\frac{m_e}{2}\left[\left(\overrightarrow{v_0}.\nabla\right)\overrightarrow{v_1} + \left(\overrightarrow{v_1}.\nabla\right)\overrightarrow{v_0}\right]. \tag{4}$$

The response of the electrons at $\phi(\omega, \vec{k})$ due to $\overrightarrow{F_p}$ and the self-consistent field $-\nabla\phi$ is obtained by solving the equation of motion and we get the perturbed electron density as

$$n_{e1} = \frac{n_{e0}}{\omega}\left\{-\frac{ek_x^2\phi\omega}{m_e\left(\omega^2 - \omega_{ce}^2\right)} + \frac{k_x\omega}{2i\left(\omega^2 - \omega_{ce}^2\right)}\left[\left(\overrightarrow{v_0}.\nabla\right)v_{1x} + \left(\overrightarrow{v_1}.\nabla\right)v_{0x}\right]\right.$$

$$\left. -\frac{k_x\omega_{ce}}{2\left(\omega^2 - \omega_{ce}^2\right)}\left[\left(\overrightarrow{v_0}.\nabla\right)v_{1y} + \left(\overrightarrow{v_1}.\nabla\right)v_{0y}\right] - \frac{ek_z^2\phi}{m_e\omega} + \frac{k_z}{2i\omega}\left[\left(\overrightarrow{v_0}.\nabla\right)v_{1z} + \left(\overrightarrow{v_1}.\nabla\right)v_{0z}\right]\right\},$$

Which, on further simplification gives

$$n_{e1} = n_{e0}R \tag{5}$$

where

$$R = \left\{\frac{-ek_x^2\phi}{m_e\left(\omega^2 - \omega_{ce}^2\right)} - \frac{ek_z^2\phi}{m_e\omega^2} + \frac{e^2k_x^2k_{0x}k_{1x}\phi_0\phi_1\omega_0\omega_1}{2m_e^2\left(\omega_1^2 - \omega_{ce}^2\right)\left(\omega_0^2 - \omega_{ce}^2\right)\left(\omega^2 - \omega_{ce}^2\right)} + \right.$$

$$\frac{e^2k_xk_{1z}k_{0z}\phi_0\phi_1}{2m_e^2\left(\omega^2 - \omega_{ce}^2\right)}\left[\frac{k_{1x}\omega_1}{\omega_0\left(\omega_1^2 - \omega_{ce}^2\right)} + \frac{k_{0x}\omega_0}{\omega_1\left(\omega_0^2 - \omega_{ce}^2\right)}\right] +$$

$$\frac{e^2\omega_{ce}^2k_xk_{1x}\phi_0\phi_1\omega_0}{2m_e^2\left(\omega_1^2 - \omega_{ce}^2\right)\left(\omega^2 - \omega_{ce}^2\right)\omega}\left[\frac{k_{1x}k_{0x}}{\left(\omega_0^2 - \omega_{ce}^2\right)} + \frac{k_{0z}k_{1z}}{\omega_0^2}\right] +$$

$$\frac{e^2\omega_{ce}^2k_xk_{1x}\phi_0\phi_1\omega_1}{2m_e^2\left(\omega_0^2 - \omega_{ce}^2\right)\left(\omega^2 - \omega_{ce}^2\right)\omega}\left[\frac{k_{0x}^2}{\left(\omega_1^2 - \omega_{ce}^2\right)} + \frac{k_{0z}k_{1z}}{\omega_1^2}\right] +$$

$$\left.\frac{e^2k_zk_{1x}\phi_0\phi_1}{2m_e^2\omega^2}\left[\frac{k_{0x}k_{1x}\omega_0}{\omega_1\left(\omega_0^2 - \omega_{ce}^2\right)} + \frac{k_{0z}k_{0x}\omega_1}{\omega_0\left(\omega_1^2 - \omega_{ce}^2\right)}\right] + \frac{e^2k_z^2k_{1z}k_{0z}\phi_0\phi_1}{2m_e^2\omega^2\omega_0\omega_1}\right\}.$$

The ion response can be written as

$$n_{i1} = \frac{n_{i0}e\phi}{m_i}\left[\frac{k_x^2}{\omega^2 - \omega_{ci}^2} + \frac{k_z^2}{\omega^2}\right], \tag{6}$$

where $\omega_{ci}\left(=\frac{eB_s}{m_ic}\right)$ is the ion cyclotron frequency.

Int. J. Mod. Phys. Conf. Ser. 2014.32. Downloaded from www.worldscientific.com
by 14.139.251.100 on 08/18/14. For personal use only.

Similarly the dust density perturbation is given by

$$n_{d1} = -\frac{n_{d0} Q_{d0} k^2 \phi}{m_d \omega^2}. \tag{7}$$

Following Whipple et *al.* [25], Jana et *al.* [22] and Varma et *al.* [24], we obtain the dust charge fluctuation

$$Q_{d1} = \frac{|I_{e0}|}{i(\omega + i\eta)} \left[\frac{e\phi}{m_i} \left(\frac{k_x^2}{\omega^2 - \omega_{ci}^2} + \frac{k_z^2}{\omega^2} \right) - R \right], \tag{8}$$

Using Eqs. (5), (6), (7) and (8) in the Poisson's equation,

$$\nabla^2 \phi = 4\pi \left[n_{e1} e - n_{i1} e + n_{d1} Q_{d0} + n_{d0} Q_{d1} \right],$$

we obtain

$$\left[1 - \frac{\omega_{pe}^2 k_x^2}{(\omega^2 - \omega_{ce}^2) k^2} - \frac{\omega_{pe}^2 k_z^2}{\omega^2 k^2} - \frac{\omega_{pi}^2 k_x^2}{(\omega^2 - \omega_{ci}^2) k^2} - \frac{\omega_{pd}^2}{\omega^2} - \frac{i\beta \omega_{pe}^2 k_x^2}{(\omega + i\eta)(\omega^2 - \omega_{ce}^2) k^2} - \frac{i\beta \omega_{pe}^2 k_z^2}{(\omega + i\eta)\omega^2 k^2} \right] \phi =$$
$$- \left(\frac{\omega_{pe}^2 e \phi_0 \phi_1}{2 m_e \omega k^2} \right) \left(1 + \frac{i\beta}{\omega + i\eta} \right) P, \tag{9}$$

where

$$P = \frac{k_x^2 k_{0x} k_{1x} \omega_0 \omega_1 \omega}{(\omega^2 - \omega_{ce}^2)(\omega_0^2 - \omega_{ce}^2)(\omega_1^2 - \omega_{ce}^2)} + \frac{k_x k_{0z} k_{1z} \omega}{(\omega^2 - \omega_{ce}^2)} \left[\frac{k_{1x} \omega_1}{\omega_0 (\omega_1^2 - \omega_{ce}^2)} + \frac{k_{0x} \omega_0}{\omega_1 (\omega_0^2 - \omega_{ce}^2)} \right] +$$
$$\frac{k_x k_{1x} \omega_0 \omega_{ce}^2}{(\omega^2 - \omega_{ce}^2)(\omega_1^2 - \omega_{ce}^2)} \left[\frac{k_{0x} k_{1x}}{(\omega_0^2 - \omega_{ce}^2)} + \frac{k_{0z} k_{1z}}{\omega_0^2} \right] + \frac{k_x k_{1x} \omega_1 \omega_{ce}^2}{(\omega^2 - \omega_{ce}^2)(\omega_0^2 - \omega_{ce}^2)} \left[\frac{k_{0x}^2}{(\omega_1^2 - \omega_{ce}^2)} + \frac{k_{0z} k_{1z}}{\omega_1^2} \right] +$$
$$\frac{k_z k_{1x}}{\omega} \left[\frac{k_{0x} k_{1x} \omega_0}{\omega_1 (\omega_0^2 - \omega_{ce}^2)} + \frac{k_{0z} k_{0x} \omega_1}{\omega_0 (\omega_1^2 - \omega_{ce}^2)} \right] + \frac{k_z^2 k_{1z} k_{0z}}{\omega \omega_0 \omega_1},$$

$\omega_{pi} \left(= \sqrt{\frac{4\pi n_{i0} e^2}{m_i}} \right)$, $\omega_{pd} \left(= \sqrt{\frac{4\pi n_{d0} Q_{d0}^2}{m_d}} \right)$ are the ion and dust plasma frequencies, respectively and $\beta = \frac{|I_{e0}| n_{d0}}{e n_{e0}}$ is the coupling parameter.

The nonlinear response of electrons at the sideband wave is governed by the equation of continuity and which on linearization yields the perturbed electron density as

$$n_{e1} = -\frac{n_{e0} e \phi_1}{m_e} \left[\frac{k_{1x}^2}{(\omega_1^2 - \omega_{ce}^2)} + \frac{k_{1z}^2}{\omega_1^2} \right] - \frac{n_{e0} e^2 \phi \phi_0 \omega_0}{2 m_e^2 \omega_1} \left[\frac{k_x^2}{(\omega^2 - \omega_{ce}^2)} + \frac{k_z^2}{\omega^2} \right] \left[\frac{k_{0x} k_{1x}}{(\omega_0^2 - \omega_{ce}^2)} + \frac{k_{0z} k_{1z}}{\omega_0^2} \right]. \tag{10}$$

Int. J. Mod. Phys. Conf. Ser. 2014.32. Downloaded from www.worldscientific.com
by 14.139.251.100 on 08/18/14. For personal use only.

Int. J. Mod. Phys. Conf. Ser. 2014.32. Downloaded from www.worldscientific.com
by 14.139.251.100 on 08/18/14. For personal use only.

In the high frequency regime, the typical time scale is such that the density perturbation of ions can be ignored i.e.,

$$n_{i0} \approx 0. \tag{11}$$

Thus the dust charge fluctuation is given by $Q_{d1} = -\frac{|I_{e0}|}{i(\omega + i\eta)} \frac{n_{e1}}{n_{e0}}.$

Substituting the value of n_{e1} and n_{i1} from Eqs. (10) and (11) in above equation, we obtain

$$Q_{d1} = \frac{|I_{e0}|}{i(\omega+i\eta)} \left[\frac{e\phi_1}{m_e} \left(\frac{k_{1x}^2}{\left(\omega_1^2 - \omega_{ce}^2\right)} + \frac{k_{1z}^2}{\omega_1^2} \right) + \frac{e^2 \phi \phi_0 \omega_1}{2 m_e^2 \omega_1} \left(\frac{k_x^2}{\omega^2 - \omega_{ce}^2} + \frac{k_z^2}{\omega^2} \right) \left(\frac{k_{0x} k_{1x}}{\omega^2 - \omega_{ce}^2} + \frac{k_{0z} k_{1z}}{\omega_0^2} \right) \right]. \tag{12}$$

Using Eqs. (10) , (11) and (12) in the poisson's equation , we obtain

$$\left[1 - \frac{\omega_{pe}^2}{\left(\omega_1^2 - \omega_{ce}^2\right)} \frac{k_{1x}^2}{k_1^2} - \frac{\omega_{pe}^2}{\omega_1^2} \frac{k_{1z}^2}{k_1^2} - \frac{i\beta}{(\omega+i\eta)} \frac{\omega_{pe}^2}{\left(\omega_1^2 - \omega_{ce}^2\right)} \frac{k_{1x}^2}{k_1^2} - \frac{i\beta}{(\omega+i\eta)} \frac{\omega_{pe}^2}{\omega_1^2} \frac{k_{1z}^2}{k_1^2} \right] \phi_1 \tag{13}$$

$$= \frac{\omega_{pe}^2 e \phi \phi_0 \omega_0}{2 m_e \omega_1 k_1^2} \left[\frac{k_x^2}{\left(\omega^2 - \omega_{ce}^2\right)} + \frac{k_z^2}{\omega^2} \right] \left[\frac{k_{0x} k_{1x}}{\left(\omega_0^2 - \omega_{ce}^2\right)} + \frac{k_{0z} k_{1z}}{\omega_0^2} \right] \left[1 + \frac{i\beta}{(\omega+i\eta)} \right]$$

Combining Eqs. (9) and (13), we obtain the nonlinear dispersion relation as

$$\varepsilon_1(\omega_1)\varepsilon(\omega) = -\frac{\omega_{pe}^4 e^2 \phi_0^2 \omega_0}{4 m_e^2 \omega \omega_1 k_1^2 k^2} \left[\frac{k_x^2}{\left(\omega^2 - \omega_{ce}^2\right)} + \frac{k_z^2}{\omega^2} \right] \left[\frac{k_{0x} k_{1x}}{\left(\omega_0^2 - \omega_{ce}^2\right)} + \frac{k_{0z} k_{1z}}{\omega_0^2} \right] \left[1 + \frac{i\beta}{(\omega+i\eta)} \right]^2 P \tag{14}$$

where

$$\varepsilon_1(\omega_1) = 1 - \frac{\omega_{pe}^2}{\left(\omega_1^2 - \omega_{ce}^2\right)} \frac{k_{1x}^2}{k_1^2} - \frac{\omega_{pe}^2}{\omega_1^2} \frac{k_{1z}^2}{k_1^2} - \frac{i\beta}{(\omega + i\eta)} \frac{\omega_{pe}^2}{\left(\omega_1^2 - \omega_{ce}^2\right)} \frac{k_{1x}^2}{k_1^2} - \frac{i\beta}{(\omega + i\eta)} \frac{\omega_{pe}^2}{\omega_1^2} \frac{k_{1z}^2}{k_1^2},$$

$$\varepsilon(\omega) = 1 - \frac{\omega_{pe}^2}{\left(\omega^2 - \omega_{ce}^2\right)} \frac{k_x^2}{k^2} - \frac{\omega_{pe}^2}{\omega^2} \frac{k_z^2}{k^2} - \frac{\omega_{pi}^2}{\left(\omega^2 - \omega_{ci}^2\right)} \frac{k_x^2}{k^2} - \frac{\omega_{pd}^2}{\omega^2} - \frac{i\beta}{(\omega + i\eta)} \frac{\omega_{pe}^2}{\left(\omega^2 - \omega_{ce}^2\right)} \frac{k_x^2}{k^2} -$$

$$\frac{i\beta}{(\omega + i\eta)} \frac{\omega_{pe}^2}{\omega^2} \frac{k_z^2}{k^2}.$$

In the absence of pump wave, we have $\varepsilon_1(\omega_1)\varepsilon(\omega) = 0$, i.e $\varepsilon_1(\omega_1) = 0$ or $\varepsilon(\omega) = 0.$

Let $\omega_1 = \omega_{1r}$ and $\omega = \omega_r$ i.e.,

$$\varepsilon_1(\omega_{1r}) = 0 \text{ and } \varepsilon(\omega_r) = 0.$$

Or

$$\varepsilon(\omega_r) = 1 - \frac{\omega_{pe}^2}{(\omega_r^2 - \omega_{ce}^2)}\frac{k_x^2}{k^2} - \frac{\omega_{pe}^2}{\omega_r^2}\frac{k_z^2}{k^2} - \frac{\omega_{pi}^2}{(\omega_r^2 - \omega_{ci}^2)}\frac{k_x^2}{k^2} - \frac{\omega_{pd}^2}{\omega_r^2} - \frac{i\beta}{(\omega + i\eta)}\frac{\omega_{pe}^2}{(\omega_r^2 - \omega_{ce}^2)}\frac{k_x^2}{k^2} - \frac{i\beta}{(\omega + i\eta)}\frac{\omega_{pe}^2}{\omega_r^2}\frac{k_z^2}{k^2}. \quad (15)$$

We obtain the growth rate as

$$\gamma = \frac{\omega_{pe}^2 v_{osc}}{4kk_1}\left[1 + \frac{i\beta}{(\omega + i\eta)}\right]\left\{\left[\frac{k_x^2}{(\omega_r^2 - \omega_{ce}^2)} + \frac{k_z^2}{\omega_r^2}\right]\frac{P}{MN\omega_r}\right\}^{1/2}, \quad (16)$$

where

$$v_{osc} = \frac{e\phi_0 k_{0x}}{m_e \omega_0}$$

is the oscillatory velocity of plasma electrons due to pump wave in the x-direction.

$$M = \frac{\omega_{1r}\omega_{pe}^2}{(\omega_{1r}^2 - \omega_{ce}^2)^2}\frac{k_{1x}^2}{k_1^2} + \frac{\omega_{pe}^2}{\omega_{1r}^3}\frac{k_{1z}^2}{k_1^2} + \frac{i\beta}{(\omega + i\eta)}\frac{\omega_{1r}\omega_{pe}^2}{(\omega_{1r}^2 - \omega_{ce}^2)^2}\frac{k_{1x}^2}{k_1^2} + \frac{i\beta}{(\omega + i\eta)}\frac{\omega_{pe}^2}{\omega_{1r}^3}\frac{k_{1z}^2}{k_1^2},$$

and

$$N = \frac{\omega_{pe}^2}{\omega_r^3}\frac{k_z^2}{k^2} + \frac{\omega_{pi}^2}{\omega_r^3}\frac{k_x^2}{k^2} + \frac{i\beta}{(\omega + i\eta)}\frac{\omega_{pe}^2}{\omega_r^3}\frac{k_z^2}{k^2} + \frac{i\beta}{(\omega + i\eta)^2}\frac{\omega_{pe}^2}{2\omega_r^2}\frac{k_z^2}{k^2} + \frac{\omega_{pd}^2}{\omega_r^2}.$$

Case I: In the presence of dust charge fluctuations (i.e., dust charging rate η is finite) and dust dynamics.

Case II: In the absence of dust charge fluctuations (i.e., $Q_{d_1} = 0$ when dust charging rate $\eta \to \infty$) and with dust dynamics (i.e, ω_{pd} is finite)

Case III: In the presence of dust charge fluctuations (i.e., η is finite) and in the absence of dust dynamics (i.e, $\omega_{pd} = 0$ when dust grain mass $m_d \to \infty$)

Int. J. Mod. Phys. Conf. Ser. 2014.32. Downloaded from www.worldscientific.com
by 14.139.251.100 on 08/18/14. For personal use only.

Int. J. Mod. Phys. Conf. Ser. 2014.32. Downloaded from www.worldscientific.com
by 14.139.251.100 on 08/18/14. For personal use only.

3. Numerical Results

To estimate the numerical values of the real frequency and growth rate, we use typical dusty plasmas parameters. Figure 1, illustrates the numerical solutions to Eq. (15) for the following parameters: dust density $n_{d0} = 1\times10^{4}$ cm^{-3}, ion and electron temperatures are assumed to be $T_e \approx T_i = 0.2$eV, static magnetic field B_s =10^{3}G, m$_i$/m$_e$ ≈ 7.16x10^4 (Potassium), average dust grain size a=1μm, k_z =0.01cm^{-1}, k_x =6cm^{-1}, k_1 =6.5cm^{-1}, v_{osc} =10^{6}cm/sec and $\omega_0 = 2\times10^{10}\, rad./\sec$. We vary δ (=n_{i0}/n_{e0}) from 1 to 5 for a fixed value of dust grain density, n$_{i0}$ is varied from 10^{11} to 9.0 × 10^{11} while n$_{e0}$ is varied from 10^{11} to 1.8 ×10^{11}. Such a model is reasonable valid in the limit $a \ll \lambda_{De} \ll \lambda$, where λ is the wavelength of the fluctuation fields. Jana *et al.* [22] have given the limits of the OML approximation for magnetized dusty plasma. According to Jana et al. the charging equation can be valid if a$\ll \rho_L$. Using the same parameters as defined earlier we have found in Fig. 1 that the above mentioned condition is satisfied.

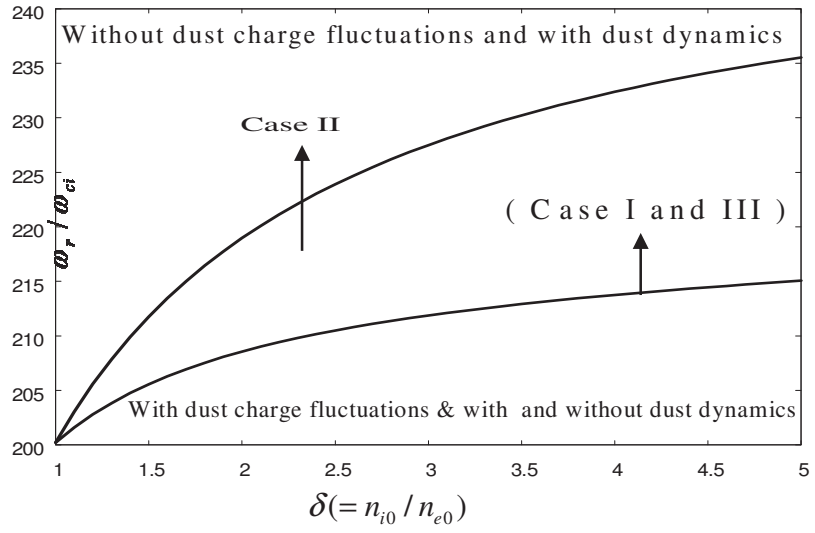


Fig. 1 Normalized real frequency ω_r/ω_{ci} of the lower hybrid waves as a function of the density ratio of negatively charged dust grains to electron $\delta\left(=n_{i0}/n_{e0}\right)$ [with and without dust charge fluctuations in addition to dust dynamics].

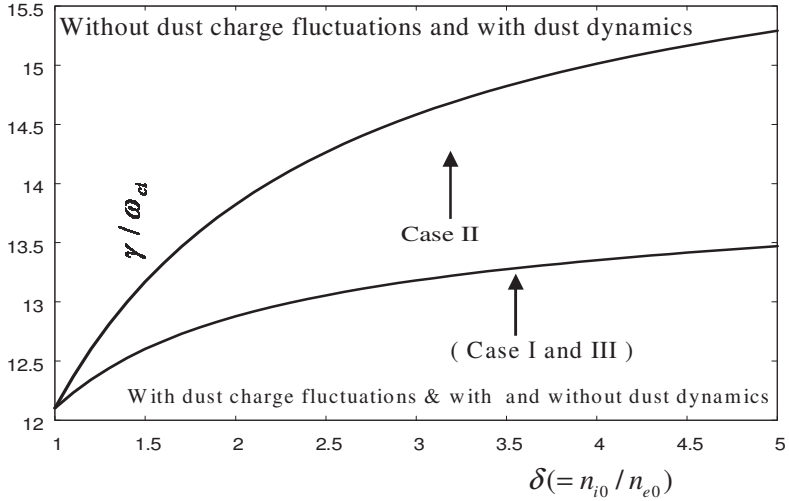


Fig. 2 Normalized growth rate γ/ω_{ci} of the lower hybrid waves as a function of the δ [with and without dust charge fluctuations in addition to dust dynamics].

4. Results and discussions

In Fig.1 it can be seen that the normalized wave frequency ω_r/ω_{ci} increases 6.5 % when δ changes from 1 to 4 if dust charge fluctuations (with and without dust dynamics) are taken into account and 16 % in the absence of dust charge fluctuations and with dust dynamics under the plasma parameters listed above. Moreover, the normalized wave frequency is getting saturated at higher values of δ in all the three cases. Barkan *et al.*[15] have found that the wave frequency was about 10-20% larger than the ion-cyclotron frequency in the presence of dust. Chow and Rosenberg [16] have shown that, in their kinetic analysis on the effects of charged dust on the collisionless EIC instability, the wave frequency ω_r/ω_{ci} increases about 11% when δ is changed from 1 to 4 under similar conditions. From Fig. 2, it can be seen that the normalized growth rate γ/ω_{ci} increases by a factor 1.1 when δ changes from 1 to 4.0 if dust charge fluctuations (with and without dust dynamics) are taken into account and by a factor 1.24 in the absence of dust charge fluctuations and with dust dynamics. Thus the increase is more drastic in the absence of dust charge fluctuations. That is, the dust charge fluctuations can play a significant role in suppression of three wave interaction process.

Int. J. Mod. Phys. Conf. Ser. 2014.32. Downloaded from www.worldscientific.com
by 14.139.251.100 on 08/18/14. For personal use only.

Int. J. Mod. Phys. Conf. Ser. 2014.32. Downloaded from www.worldscientific.com
by 14.139.251.100 on 08/18/14. For personal use only.

5. Conclusion

In conclusion, a local theory of three wave interactions have been developed to examine the instability of lower hybrid waves in a magnetized dusty plasma in presence and absence of dust charge fluctuations in addition to dust dynamics. The growth rate and mode frequencies were evaluated based on existing dusty plasma parameters and it is found that the unstable mode frequency increases with δ in all the three cases. However, the increase in normalized unstable wave frequency ω_r/ω_{ci} with δ is more in the absence of dust charge fluctuations (cf. case II) than the corresponding value of ω_r/ω_{ci} in the presence of dust charge fluctuations and with dust dynamics (cf. case I). Dust charge fluctuations increases the damping effect in the present case and the growth rate is also sensitive to the frequency and phase velocity of the lower hybrid wave. From the above results, we can also say that the term containing dust dynamics effect does not contribute significantly because of dust grain mass.

References

1. T. Idehara, M. Takedo and Y. Ishida, *Phys. Lett*. **46A**, 409 (1974).
2. C.S. Liu and V.K. Tripathi, *Phys. Reports* **130**, 143 (1986).
3. L. Stenflo and P.K. Shukla, *Planet Space Sci.* **40**, 473 (1992).
4. C. Grebogi, C.S. Liu and V.K. Tripathi, *Phys. Rev. Lett.* **39**, 338 (1977).
5. S.C. Sharma, *J. Plasma Phys.* **57**, 545 (1977).
6. N.S. Wolf, R. Majeski, H. Lashinky, V.K. Tripathi and C.S Liu, *Phys. Rev. Lett.* **45**, 799 (1986).
7. C.S. Liu, V.S. Chan, D.K. Bhandari and R.W. Harvey, *Phys. Fluids* **48**, 1479 (1982).
8. C.S. Liu, V.K. Tripathi, V.S. Chan and V. Stefan, *Phys. Fluids* **27**, 1709 (1984).
9. K. Akimoto, *Phys. Fluids* **B1**, 1998 (1989).
10. L. Stenflo, *Physica Scripta* **T50**, 15 (1994).
11. R.P. Sharma, K. Ramamurthy and M.Y. Yu, *Phys. Fluids* **27**, 399 (1984).
12. H. Saleem and G. Murtaza, *J. Plasma Phys.* **36**, 295 (1986).
13. A.N. Kaufman and L. Stenflo, *Phys. Scripta* **11**, 269 (1975).
14. P.K. Shukla, B. Elisson and L. Stenflo, *Phys. Rev. E* 68, 067401 (2003).
15. A. Barkan, N. D' Angelo and R. L. Merlino, *Planet. Space Sci.* **43**, 905 (1995).
16. V. W. Chow and M. Rosenberg, *Planet. Space Sci.* **43**, 613 (1995).
17. V. W. Chow and M. Rosenberg, *Planet. Space Sci.* **44**, 465 (1996).
18. J.X. Ma and P.K. Shukla, *Phys. Plasmas* **2**, 1506 (1995).
19. P.K. Shukla and S.V. Vladimirov, *Phys. Plasmas* **2**, 3179 (1995).
20. R. Annou and V.K. Tripathi, *Phys. Plasmas* **5**, 60 (1998).
21. S.C. Sharma and V.K. Tripathi, *IEEE Trans. Plasma Sci.* **23**, 792 (1995).
22. M. R. Jana, A. Sen and P. K. Kaw, *Phys. Rev. E* **48**, 3930 (1993).

23. S. Konar, V.K. Jain and V.K. Tripathi, *J. Appl. Phys.* **65**, 4612 (1989).
24. R.K. Varma, P.K. Shukla and V. Krishan, *Phys. Rev. E* **47**, 3612 (1993).
25. E. C. Whipple, T. G. Northdrop and D. A. Mendis, *J. Geophys. Res.* **90**, 7405 (1985).

Int. J. Mod. Phys. Conf. Ser. 2014.32. Downloaded from www.worldscientific.com
by 14.139.251.100 on 08/18/14. For personal use only.

Scientific Online

OPEN JOURNAL OF WATER POLLUTION AND TREATMENT
In Press

OPEN JOURNAL OF WATER POLLUTION AND TREATMENT

Effluent Treatment for Sago Industry Using Zeolite and Activated Carbon

S. Anbukumar[1], Narad Muni Prasad[1], M. Ashok Kumar[2]

[1] *Department of Civil Engineering, Delhi Technological University, Formerly Delhi College of Engineering, Delhi-110042, India*
[2] *Project Head, DeepWater Consortium for Engineering Solutions, Namakkal, Tamil Nadu*

Abstract:
Sago industry is an important component of small scale sector in the developing countries of the tropical region, like India. Being small scale industries, they suffer a lot to overcome the menace of treating the high strength effluent, from the sago processing, containing a large amount of organic material which has a potential to cause high level of water pollution in the surrounding environment. With an objective to minimise the effects of water pollution from the sago industries, we took up a study to increase the efficiency of effluent treatment, by using a complex filter comprising activated carbon and zeolite. The study shows that this method can prove to be an improvement over other methods by enhancing the efficiency of the pollutant reduction process in the sago effluent treatment as the result has shown considerable reduction in TDS, BOD_5 and COD of the effluent.

Keywords:
Activated Carbon; Effluent Treatment; Pollutant Reduction; Sago Effluent; Water Pollution; Zeolite

1. INTRODUCTION

Sago industry, an important small scale industry in India, is basically seasonal in nature, operating for only six months of the calendar year from September to March. In this industry, the cassava/tapioca tubers are the raw material and it is converted into commercial sago through indigenous technology that uses huge amount of water. As a normal procedure, sago factory produces sago starch through debarking and processing of sago trunk, which generate high organic content effluent (sago starch factory wastewater). In this process, a medium sago processing unit release about 5000-6000 litres of sago effluent per day as outlet.

This high requirement of water in sago industry is mainly for washing roots and separation of free starch from fibrous pulp. Thus this effluent is characterised with a very high content of organic solid in dissolved and suspended state. This effluent with high content of organic load, when stored for some days results in obnoxious odours, irritating colour, lower pH and higher BOD and COD. When the effluent is released into the environment without proper treatment, it alters the characteristics of ecosystem. Farmers are using these effluents for irrigation and found that the growth, yield and soil health are reduced [1].

The effluent resulting from sago debarking and processing are often used for irrigating the nearby farm fields or discharged to nearby water bodies. This inevitably contributes to infertility of the farm land, in

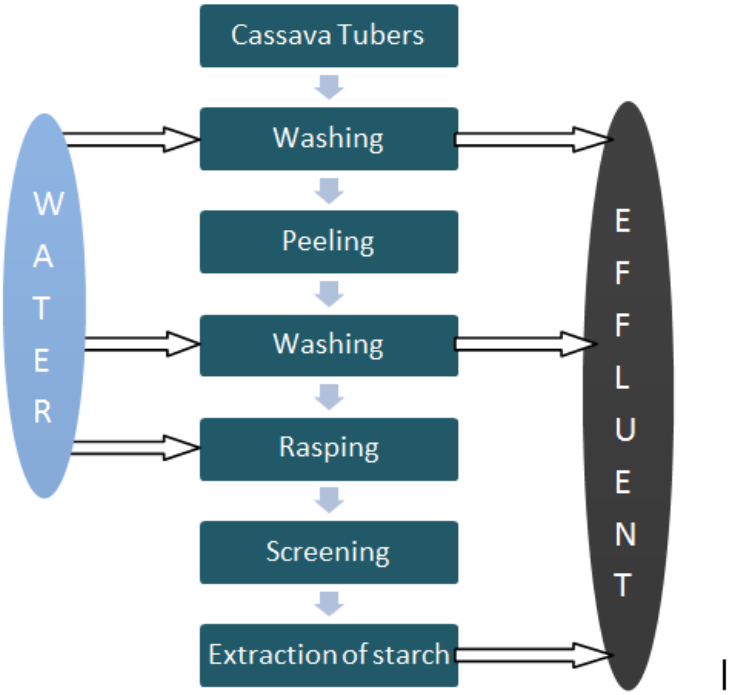


Figure 1. Typical stages and activities involved in a Sago processing industry

case of irrigating it with the untreated effluent, and to water pollution, when discharged into water bodies. This high concentration effluent requires systematic treatment to reduce the pollutants content before disposal.

Any industrial effluent treatment method can be improved through two different ways, like: one by enhancing the efficiency of the pollutant reduction process and another by increasing the retention time of the wastewater in the treatment facility. The aim of this study was to examine the efficiency of the pollutant reduction process in the effluent treatment using a complex filter made of zeolite and activated carbon. In addition, the future scopes for further reduction of pollutant and its reuse also been studied.

2. PROBLEMS OF SAGO INDUSTRY EFFLUENT

The sago industry is a water-intensive industry, as the processing of sago requires several washing cycles and generates 30,000–35,000 litres of effluent per tonne of sago produce. This effluent is acidic and highly organic in nature with chemical oxygen demand (COD) of 5,000–7,000 mg per litre during the season and 1,000–5,000 mg per litre during the off-season. The major environmental concern is, therefore, the amount of wastewater produced and its pollutant load. Those major pollutants specific for this sago effluent are higher amounts of dissolved organic solids, suspended organic solids, BOD and COD. Thus, these effluents pose a serious threat to the environment and quality of life in the rural area, especially. In rural areas, it contributes to infertility of the farm land, in case of leaving the untreated effluent in agricultural fields, and to water pollution, when discharged into water bodies. Thus, Pollution-control is becoming a major problem for the sago industry. Also, there is no standardised cost effective design developed for the sago manufacturers; neither by any institution and nor by the pollution control board

itself. Problem posed by pollution and high cost of effluent treatment plants needs to be rectified for the betterment of both economy and environment.

3. CHARACTERISTICS OF SAGO EFFLUENT

The Characterisation of effluent from sago processing industry indicates that the effluents arising are very acidic in nature with BOD/COD ratio in the range of 0.77 0.88. Because of its high organic content, it is highly biodegradable. From the literature review, the following characteristics been identified for the sago factory effluent. They are:

Wastewater generated: 200 to 600 cum/d
Colour: Pale white - Black
pH: 5.0-5.7 (Acidid)
BOD: very high, range 400 mg/l
COD: very high, range 5500 mg/l
Total solids: 3100 mg/l
Total dissolved solids: 2950 mg/l
Calcium: 42 mg/l
Magnesium: 105 mg/l
Sodium: 12 mg/l
Potassium: 90.5 mg/l
Chloride: 487 mg/1

The above characteristics of Sago wastewater is a general abstract from different sources and studies. Thus, the pollution loads of the effluent vary depending on the nature of raw materials, chemicals used, at the time of tuber Pulping and Starch Extraction.

A sample of raw effluent from a sago factory, in the Namakkal District of Tamil Nadu, was collected and analysed with the help of an NGO, Thulihal – An Organisation for Societal and Environmental Rejuvenation, working for the betterment of rural environment. The raw effluent was collected in a 10 litre sterilized plastic can from the effluent disposal system of the sago unit. And the sample has been analysed for physicochemical parameters using the standard methods in a lab. The **Table 1** below shows the results obtained out of the performed characteristic analysis of the collected effluent.

3.1 Methodologies Adopted in Effluent Analysis

1. *Colour*: The colour of the effluent sample was observed visually.
2. *Odour*: Odour of the sample was recognised as objectionable or non-objectionable by smelling the sample.
3. *pH*: The pH of the effluent sample was determined by pH meter using a glass electrode.
4. *Total solids:* Total solids were determined by taking 100 ml sample in a Pre-weighed evaporation disc and the sample was evaporated to dryness at 103°C for one hour, and the total solids in mg/litre is calculated.
5. *Dissolved solids:* The dissolved solids were estimated by filtering a known volume (100 ml) of well mixed sample through a stand glass fiber filter, the filtrate is then evaporated to dryness.

Table 1. Characteristics of collected raw sago effluent

S.No.	Pollutant/Parameter	Level
1	Colour	Greyish Hue
2	Odour	Pungent
3	pH	5.20
4	Total Solids	2096 mg/l
5	TSS	86.0 mg/l
6	TDS	2010.0 mg/l
7	BOD_5	531.0 mg/l
8	COD	2080 mg/l
9	Turbidity	22 NTU
10	Calcium	335 mg/l
11	Magnesium	181.2 mg/l
12	Silica	36 mg/l
13	Potassium	90 mg/l
14	Chloride	545.93 mg/l
15	Shulphate	510 mg/l
16	Carbonate	960 mg/l
17	Non-carbonate	130 mg/l

6. *Suspended solids:* The suspended solids were estimated by filtering 100 ml of well mixed sample through Whatmann No. 4 filter paper, the residue obtained was dried to constant weight at 104-105°C. It is only the difference between total solids and dissolved solids.

7. *Biological Oxygen Demand (BOD):* BOD of the effluent was determined by incubating BOP bottles containing the samples kept at 20°C for five day. The pH of the sample was diluted with distilled water, 1 ml of each phosphate buffer, magnesium, sulphate, calcium chloride and ferric chloride were added to aerated distilled water. The dissolved oxygen constant of one set was estimated immediately following the Winkler's method of dissolved oxygen, and another set was incubated for 5 days in a BOD incubator and estimated for dissolved oxygen.

8. *Chemical Oxygen Demand (COD):* In a 500 ml COD flask, 10 ml of 0.1 N potassium dichromate, 1g silver sulphate and mercuric sulphate were added besides 30 ml of concentrated sulphuric acids, the mixtures were kept for 2 hours in a water bath. After cooling, the solution was made upto 140 ml by adding distilled water, 0.5 ml was added and mixed thoroughly. Then the solution was titrated against 0.1 N ferrous ammonium sulphate. For each experiment appropriate blank was used.

4. PROPOSED TREATMENT PROCESS

To investigate the viability of treatment of sago effluent, a laboratory scale apparatus was made with alternative layers of zeolite and activated carbon, for 45cm each, in two successive terms. The following design parameters were adopted, based on the plant operation parameters of:

1. Total contact time (empty bed volume) 25 minutes

2. Hydraulic Loading (approach velocity) 440 cu.m. day /sq.m

The combination of these factors resulted in a filter complex diameter of 2.4m and a bed depth of 1.8m. Thus, the filter complex is made of alternative layers of zeolite and activated carbon, for 45cm each, in

two successive terms.

4.1 Properties of Zeolite

Natural zeolite is the best natural filter medium available for the filtration of water. It's highly porous structure captures particulate contamination down to 4 microns in size. It has a natural negative charge which gives it the capacity to adsorb cations, such as heavy metals and ammonium. It also absorbs some organic contaminants and undesirable odours. Natural zeolite particles also act as seeds to boost bacterial flocs by attracting and increasing bacterial action per unit volume. The Research work done in this field has made the certain conclusions, like:

(Andrews, 1993) The replacement of the top 20 cm of a 1 metre thick bed of finely graded silica sand with zeolite result in:

1. Higher throughput rate of up to $0.75m^3/hr/m^2$ versus $0.15m^3/hr/m^2$ whilst maintaining water quality (measured in turbidity).
2. Up to 3 to 5 times more water processed between maintenance scrapings.
3. Up to 50% longer runs, even at higher loadings.

(Burtica *et al*., 1997) The Zeolite reduced turbidity and organic charge (second filtering cycle) by 30% as opposed to 10% with sand.

4.2 Properties of Activated Carbon

Activated carbon has been recognised as a highly effective adsorbent for the treatment of heavy metals in waste water. Activated carbon is a particularly good adsorbent medium due to its high surface area to volume ratio. One gram of a typical commercial granular activated carbon will have a surface area equivalent to 1,000 square meters. This high surface area permits the accumulation of a large number of contaminant molecules. The properties of Activated carbon in relation to effluent treatment are:

1. Very effective in removing non-polar organic chemicals from water.
2. Effective to a wide variety of organic compounds
3. Very effective in removing colours from effluents.
4. Effective at removing low levels (ppb range) of inorganic pollutants.
5. Very flexible system allows rapid start-up and shut down as needed.

If we go with the above studies, the proposed effluent treatment process, generally improve the quality of effluent water both by enhancing the efficiency of the pollutant reduction process and by increasing the retention time of the wastewater in the treatment process system. Because, the high surface area to volume ratio of the activated carbon will increase the contact time of the effluent with the treatment system and the highly porous structure of zeolite increase the efficiency of reduction of particulate contamination. In case of other systems like oxidation ponds or aerobic treatment systems, the retention time can be increased easily. However, it need larger aeration basin and at higher operation cost, which is not the case in this proposed complex filter system. Because, one of the most promising approaches to improve the efficiency and increase the capacity of wastewater treatment plants without increasing size is based

Table 2. Characteristics of sago effluent treated through the complex filter system

S.No.	Pollutant/Parameter	Level
1	Colour	Pale White
2	Odour	Pungent
3	pH	6.1
4	Total Solids	662 mg/l
5	TDS	590 mg/l
6	BOD_5	164 mg/l
7	COD	560 mg/l

upon application of granular activated carbon in the system. Also the zeolite particles are good carriers of bacteria, which adsorb on the zeolite surface resulting in increased sludge activity. However, there is a drawback to the application of the zeolite. That is, the formation of the bacteria layer on the zeolite surface is a slow process and becomes effective only after approximately a week.

Still the zeolite modification method can be used to accelerate the interaction between zeolites and activated sludge, which further increases the sludge activity. In this study, nothing of this modified kind is used and hence the sample for the treated effluent is taken after 12 days working of this complex filter.

The filter complex modelled for this study combines the advantages of both Physical Treatment Unit (PTU) and Biological Treatment Unit (BTU) for the treatment of sago wastewater in the reduction of pollutants especially, TDS, TSS, BOD and COD. Because the activated carbon work as PTU and the zeolite part work as BTU in this system.

In this investigation, simply the effluent water was made to flow through the filter complex for 12 days, at a Surface Loading Rate of 440 cu.m. day /sq.m and then the treated effluent sample was taken for analysis.

The analysis result, comparing the characteristics of sago effluent before and after treatment through the complex filter system tabulated in **Table 1** and **Table 2** respectively, shows that the COD removal varied from 80 to 70%, while the removal of BOD_5 was of 60 to 70%, the removal of total solids was in the range of 65 - 69% and that of dissolved solids varied from 65 - 75%.

According to a study conducted by Ravi Mycin *et al* [2], it was suggested that wastewater have to be diluted before it is used for irrigation. After dilution, the effluent characteristics will become within the prescribed limits and pollution load of the effluent. The effluent at lower concentration can serve as a liquid fertilizer for the cultivation of agricultural crops (Ravi Mycin *et al*). Based on the above suggestion, the treated effluent was analysed for reuse in the agricultural fields to ensure an alternative sustainable water resource management. In general, the reduction in fertility level was not visible; however, the pungent smell makes it problematic in reuse. Hence, the scope for reuse in other utilities needs to be studied further to provide for a sustainable water resource management, in the localities of the sago industries.

5. RESULT AND CONCLUSION

5.1 Expected Results

1. Higher effluent quality by reducing nutrients level

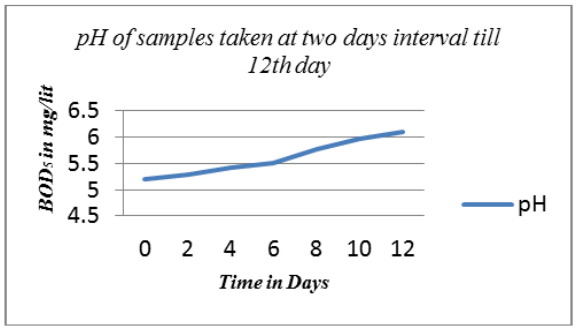


Figure 2. Chart showing the change in pH over the 12 days course of treatment through the filter

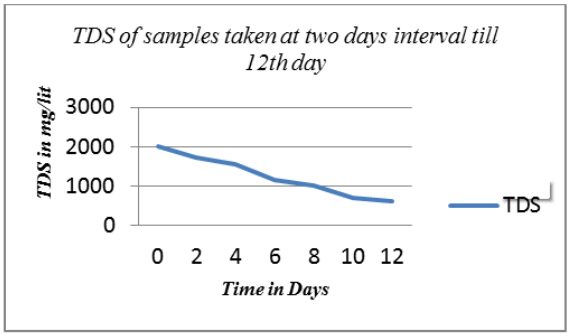


Figure 3. Chart showing the reduction in TDS over the 12days course of treatment through the filter

2. Reduce odours and gases emission
3. Increase sediment removal
4. Reduce chemical costs (like, alum used in coagulation)
5. Improve sludge dewatering
6. Lower ammonia content

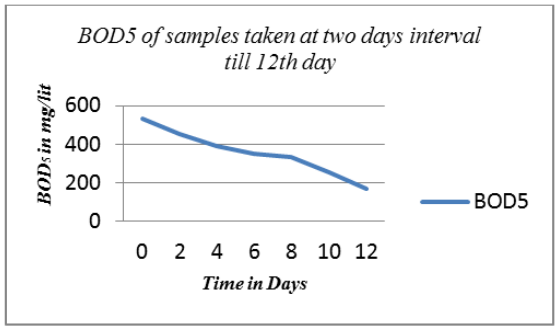


Figure 4. Chart showing the reduction in BOD_5 over the 12days course of treatment through the filter

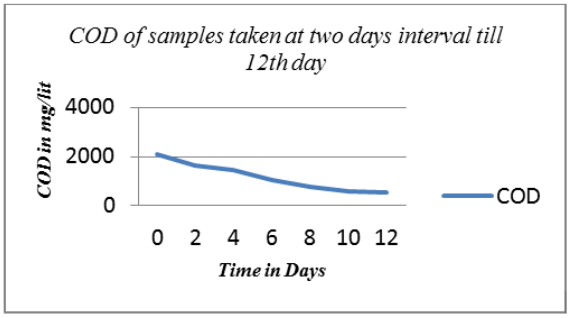


Figure 5. Chart showing the reduction in COD over the 12days course of treatment through the filter

Table 3. Observed change in the characteristics of sago effluent, treated through the complex filter system, in the 12 days course of time

	pH	*TDS (mg/l)*	*BOD5 (mg/l)*	*COD (mg/l)*
Day 0	5.20	2010	531	2080
Day 2	5.29	1724	451	1642
Day 4	5.42	1535	386	1436
Day 6	5.51	1155	361	1056
Day 8	5.78	1012	333	777
Day 10	5.97	681	252	612
Day 12	6.10	590	164	560

5.2 Obtained Results

In the investigation of treatment of sago industry effluent in the filter complex made of zeolite and activated carbon under experimental condition, the results obtained are given in the **Table 3**.

The working efficiency of this proposed complex filter can be better observed from the following 4 charts **Figures 2- 5**:

From the above graphs, it is clear that the maximum efficiency of treatment of this filter is reached only after the 12^{th} day of its working, from then the filter will yield the effluent standard given in **Table 2**.

The result obtained can be summarised as below:

1. Reduced organic content, with lower BOD and COD levels
2. Increased Sediment removal, with lower TDS and TSD
3. Reduced chemical cost

5.3 Conclusion

As a conclusion the complex filter comprising of zeolite and activated carbon, proves to be an inexpensive, environmentally friendly solution that can improve the effectiveness of effluent treatment for sago

industries. However, the reuse potential of treated effluent needs to be further studied in detail to develop a completely sustainable water management system.

References

[1] T. Nandy and S. Kaul, "WASTEWATER MANAGEMENT FOR TAPIOCA BASED SAGO INDUSTRY," *Indian Journal of Environmental Protection*, vol. 14, pp. 721–728, 1994.

[2] T. R. Mycin and M. Lenin, "MORPHOMETRICAL AND BIOCHEMICAL CHANGES ON SUNFLOWER (Helianthus annuus L.) UNDER SAGO FACTORY EFFLUENT," *International Journal of Environmental Biology*, vol. 2, no. 3, pp. 114–120, 2012.

Wiley Online Library

Early View publication on www.wileyonlinelibrary.com
(issue and page numbers not yet assigned;
citable using Digital Object Identifier – **DOI**)

Phys. Status Solidi A, 1–4 (2014) / **DOI** 10.1002/pssa.201400020

physica status solidi a
www.pss-a.com
applications and materials science

Energy transfer and NIR emission in rare earth tri-doped barium lanthanum fluoro tellurite glasses

J. Suresh Kumar[1], K. Pavani[1], G. Venkataiah[2], M. Jayasimhadri[3], M. P. F. Graça*[,1], and M. J. Soares[1]

[1] Department of Physics and I3N, University of Aveiro, Aveiro 3810-193, Portugal
[2] Department of Physics, Sri Venkateswara University, Tirupati 517502, India
[3] Department of Applied Physics, Delhi Technological University, Delhi 110042, India

Received 2 March 2014, revised 30 May 2014, accepted 3 July 2014
Published online 26 August 2014

Keywords energy transfer, NIR emission, optical communciation, rare earth doped glasses

* Corresponding author: e-mail mpfg@ua.pt, Phone: +351 234378113, Fax: +351 234378197

Barium lanthanum fluoro tellurite (BLFT) glasses doped with rare earth ions (ErF_3, PrF_3 and YbF_3) both singly or in combinations were prepared by melt-quench technique and analysed spectroscopically. The prepared glasses were found to be mechanically strong and transparent. Optical absorption and NIR fluorescence were measured to the highly transparent and stable glass samples. Judd–Ofelt parameters and radiative properties were estimated for the single rare earth doped BLFT glasses using the optical absorption spectra. NIR fluorescence is measured using laser excitation. From the NIR emission spectra, energy transfer among the rare earth ions is analysed in the rare earth tri-doped BLFT glasses. These rare earth tri-doped BLFT glasses are found to be highly useful for the multi- wavelength emission in the NIR region for opto-electronic applications.

© 2014 WILEY-VCH Verlag GmbH & Co. KGaA, Weinheim

1 Introduction The rare earth (RE) incorporation in tellurite based glass matrices is being reported extensively in the literature [1]. Adding of fluorine ions is an asset to the properties of tellurite-based glasses due to the phonon reducing nature of the fluoride ions [2, 3]. These materials exhibit better photoluminescence phenomena and are known for efficient down and upconversion processes. As the base matrix can yield excellent properties for the up and down conversions, three ions were doped simultaneously to test the collective photoluminescence properties. The couple Er^{3+} and Yb^{3+} is already well known for the upconversion as well as for the development of optical amplifiers, because of erbium's large emission band around 1.54 μm and the efficient energy transfer process between Yb^{3+} and Er^{3+} ions acting as sensitiser and activators, respectively [4, 5]. The addition of Pr^{3+} may improve the 1.54 μm band of erbium expanding its span of operation.

Hence, in this work, barium lanthanum fluoro tellurite (BLFT) glasses are tri-doped with Er^{3+}, Yb^{3+} and Pr^{3+} ions and spectroscopic properties were investigated.

2 Experimental details The molar composition of rare earth doped BLFT glasses investigated in this work is $(60-(x+y+z))\ TeO_2 + 20\ BaF_2 + 10\ LaF_3 + 10\ SiO_2 + x\ ErF_3 + y\ YbF_3 + z\ PrF_3$. The combination of dopant ions with their nomenclature is shown in Table 1. Glasses were prepared by the melt quenching technique. All the above weighed chemicals were well mixed and heated for 30 min in a platinum crucible at 900 °C in an electric furnace. The glasses were obtained by pouring the melt onto a preheated stainless steel plate and then annealed at 350 °C for 5 h to eliminate mechanical and thermal stress. The refractive indices n were measured by Brewster's angle method with He–Ne (632.8 nm) laser source. Densities were measured by the Archimedes's method using distilled H_2O as an immersion liquid. The optical absorption spectra were recorded in the UV–Vis–NIR regions on a double beam spectrophotometer (UV-2101/3101PC, Shimadzu Scientific Instruments Inc. USA). Fluorescence spectra were obtained by exciting the samples with 980 nm diode laser. The fluorescence was detected by passing through monochromator equipped with a InGaAs detector. For lifetime measurements, a mechanical chopper in conjunction with a Lecroy oscilloscope was employed.

3 Results and discussion Figure 1 shows the optical absorption spectra of single Er^{3+}, Er^{3+}–Yb^{3+} and Er^{3+}–

© 2014 WILEY-VCH Verlag GmbH & Co. KGaA, Weinheim

Table 1 Nomenclature and molar composition of the rare earth doped BLFT glasses.

glass nomenclature	TeO_2	BaF_2	LaF_3	SiO_2	ErF_3	YbF_3	PrF_3
BLFT (host)	60.0	20	10	10	0.0	0.0	0.0
BLFTEr01	59.9	20	10	10	0.1	0.0	0.0
BLFTEr02	59.8	20	10	10	0.2	0.0	0.0
BLFTEr05	59.5	20	10	10	0.5	0.0	0.0
BLFTEr10	59.0	20	10	10	1.0	0.0	0.0
BLFTEr05Yb05	59.0	20	10	10	0.5	0.5	0.0
BLFTEr05Yb10	58.5	20	10	10	0.5	1.0	0.0
BLFTEr05Yb20	57.5	20	10	10	0.5	2.0	0.0
BLFTEr05Yb20Pr01	57.4	20	10	10	0.5	2.0	0.1
BLFTEr05Yb20Pr02	57.3	20	10	10	0.5	2.0	0.2
BLFTEr05Yb20Pr05	57.0	20	10	10	0.5	2.0	0.5

Yb^{3+}–Pr^{3+} doped BLFT glasses. In the absorption spectrum of BLFTEr05 glass, ten absorption bands were found at 406.2, 442.2, 451.0, 456.0, 488.6, 520.8, 652.2, 799.4, 977.0 and 1531.0 nm. These absorption bands belong to f–f transitions in Er^{3+} ions and can be assigned to $^2H_{9/2}$, $^4F_{3/2}$, $^4F_{5/2}$, $^4F_{7/2}$, $^2H_{11/2}$, $^4S_{3/2}$, $^4F_{9/2}$, $^4I_{9/2}$, $^4I_{11/2}$ and $^4I_{13/2}$, respectively. Judd–Ofelt (J–O) parameters for BLFTEr05 glass were calculated from areas of the individual peaks. As the absorption spectra of co-doped and tri-doped BLFT glasses are complicated, J–O analysis for individual ions has not been performed. The thickness (0.253 cm), refractive index (2.016) and concentration (1.58×10^{20} ions/cm^3) of BLFTEr05 were used to calculate the J–O parameters and are found to be $\Omega_2 = 1.97 \times 10^{-20}$, $\Omega_4 = 0.82 \times 10^{-20}$ and $\Omega_6 = 1.06 \times 10^{-20}$ cm^2. The radiative transition probability (A_R) and radiative lifetime (τ_R) for the transition $^4I_{13/2} \rightarrow {}^4I_{15/2}$ are estimated from the J–O parameters and are found to be 321 s^{-1} and 1.32 ms, respectively. In the Er^{3+}-Yb^{3+} co-doped BLFT glass, apart from the Er^{3+} absorption bands, the Yb^{3+} absorption band corresponding to $^2F_{7/2} \rightarrow {}^2F_{5/2}$ is found at 976.8 nm. The presence of Yb^{3+} ions will enhance the NIR photoluminescence spectrum of Er^{3+} ions. The absorption spectrum of Er^{3+}–Yb^{3+}–Pr^{3+} tri-doped BLFT glass apart from absorption bands of Er^{3+} and Yb^{3+}, the absorption bands of Pr^{3+} ions were also present. The absorption bands pertaining to Pr^{3+} ions at 444.0, 470.2, 482.6, 591.4, 1010.6, 1435.8, 1522.8, 1924.4 and 2379.8 nm and belong to $^3H_4 \rightarrow {}^3P_2$, $^3P_1$, $^3P_0$, $^1D_2$, $^1G_4$, $^3F_4$, $^3F_3$, $^3F_2$ and $^3H_6$, respectively. As the absorption spectrum of co-doped (BLFTEr05Yb20) and tri-doped (BLFTEr05Yb20Pr05) BLFT glasses shown in Fig. 1 are convolutions of the absorption of more than one ion, J–O analysis has not been carried out.

Figures 2–4, show the NIR photoluminescence spectra of single Er^{3+}, Er^{3+}–Yb^{3+} co-doped and Er^{3+}–Yb^{3+}–Pr^{3+} tri-doped BLFT glasses. In Fig. 2, it is observed that as the concentration of the Er^{3+} ions increases, the intensity of 1531 nm peak ($^4I_{13/2} \rightarrow {}^4I_{15/2}$) increases. 0.5 mol% Er^{3+} concentration is chosen for co-doping. Figure 3 shows the emission spectra of Er^{3+}–Yb^{3+} co-doped samples. The intensity of the NIR emission peak at 1531 nm is found to increase with the increase of Yb^{3+} concentration. Further, in Fig. 4, NIR photoluminescence spectra of Er^{3+}–Yb^{3+}–Pr^{3+} tri-doped BLFT glasses are shown. Here, as the Pr^{3+} concentration increases, the intensity of NIR peak pertaining to Er^{3+} emission decreases. On the other hand, there is an increase in NIR emission of Pr^{3+} ion at 1351 nm pertaining to $^1G_4 \rightarrow {}^3H_5$ transition. To understand the excitation and emission processes along with energy transfer mechanism between the three ions, the energy level diagram is shown in Fig. 5.

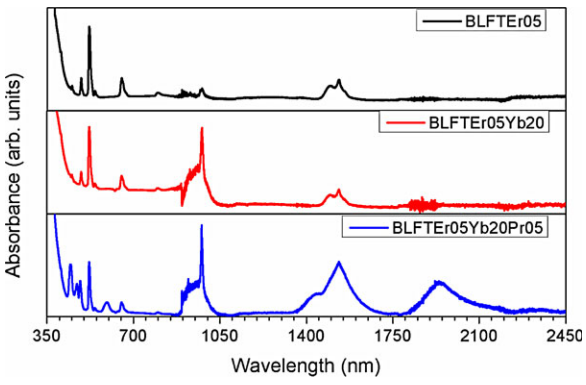


Figure 1 Optical absorption spectra of RE^{3+} doped BLFT glasses.

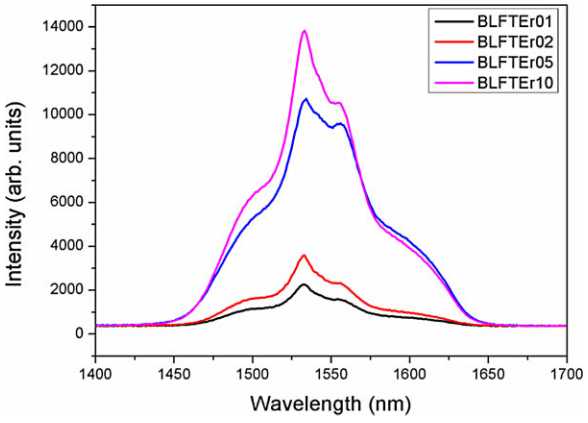


Figure 2 NIR Photoluminescence spectra of Er^{3+} doped BLFT glasses.

© 2014 WILEY-VCH Verlag GmbH & Co. KGaA, Weinheim

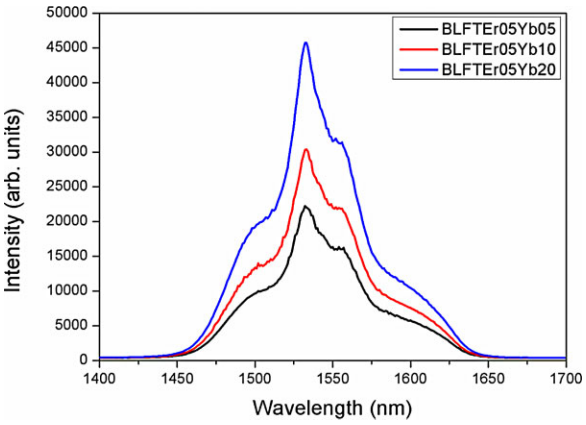


Figure 3 NIR photoluminescence spectra of Er^{3+}–Yb^{3+} co-doped BLFT glasses.

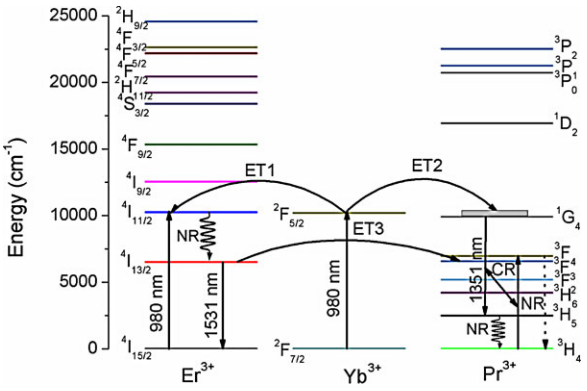


Figure 5 Energy level diagram of Er^{3+}–Yb^{3+}–Pr^{3+} tri-doped BLFT glasses.

From the energy level diagram it is observed that the Er^{3+} and Yb^{3+} ions excite individually with 980 nm laser radiation. In single Er^{3+} doped BLFT glasses, the ions are excited to $^4I_{11/2}$ from the ground $^4I_{15/2}$ after which they de-excite to $^4I_{13/2}$ level through non-radiative relaxation (NR). The ions in $^4I_{13/2}$ level then de-excite radiatively emitting 1531 nm radiation. In Er^{3+}–Yb^{3+} co-doped BLFT glasses, Er^{3+} and Yb^{3+} excite individually and the energy of Yb^{3+} is also transferred to Er^{3+} ions through energy transfer (ET1) process. Hence, the increase in Yb^{3+} ion concentration leads to an increase in Er^{3+} NIR emission. Whereas in the case of Er^{3+}–Yb^{3+}–Pr^{3+} tri-doped BLFT glasses, Yb^{3+} ions transfer their excited energy to both Er^{3+} and Pr^{3+} ions through energy transfers (ET1 and ET2) processes, respectively. In the energy transfer (ET2) process, there is a mismatch in the energies of excited levels $^2F_{5/2}$ (Yb^{3+}) and $^1G_4$ (Pr^{3+}). The mismatch in the energies is compensated by the assistance of a phonon from the host matrix. Hence, the energy transfer (ET2) is a phonon-assisted energy transfer, which is less efficient than the Er^{3+}–Yb^{3+} energy transfer (ET1). The energy transferred to $^1G_4$ is de-excited to $^3H_5$ emitting a photon with wavelength 1351 nm. It is observed from Fig. 4 that as the concentration of Pr^{3+} increases, the intensity of NIR emission of Er^{3+} decreases and that of Pr^{3+} increases. This is due to increase of energy transfer to Pr^{3+} from Yb^{3+} ions. Figures 6 and 7 depict the decay curves of Er^{3+} (1531 nm) and Pr^{3+} (1351 nm) NIR photoluminescence in the tri-doped BLFT glasses. From Fig. 6, it is observed that the lifetimes of $^4I_{13/2}$ level of Er^{3+} ions decreased with increase of Pr^{3+} concentration due to the energy transfer (ET3) resulting from increase of the energy transfer from Er^{3+} to Pr^{3+} ions. This may be one of the causes of decrease of emission intensity of Er^{3+} ions in Fig. 4. The transferred energy is lost by NR of Pr^{3+} ions.

From Fig. 7, it is also observed that the lifetime of $^1G_4$ decreased with increase of Pr^{3+} concentration though there is energy transfer from both Er^{3+} and Yb^{3+} ions. This is due to the cross-relaxation (CR) processes sustaining within the Pr^{3+} ions and not due to the energy back transfer. The CR process is clearly depicted in Fig. 5. The Pr^{3+} ions which are excited to $^1G_4$ level are de-excited by cross-relaxation mechanism ($^1G_4$:$^3H_4$) → ($^3H_5$:$^3F_4$). One excited Pr^{3+} ion at $^1G_4$ level de-excites to $^3H_5$ level and the energy is used by another Pr^{3+} ion, which is excited from ground $^3H_4$ level to

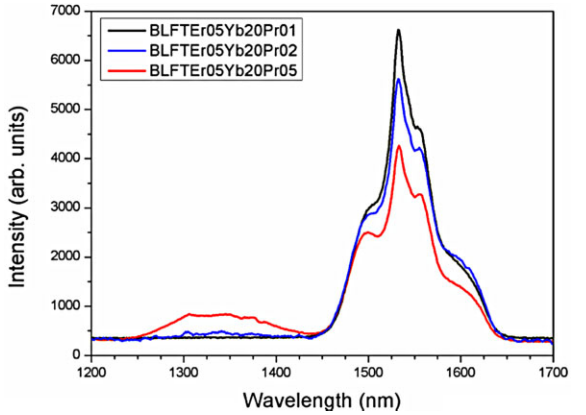


Figure 4 NIR photoluminescence spectra of Er^{3+}–Yb^{3+}–Pr^{3+} tri-doped BLFT glasses.

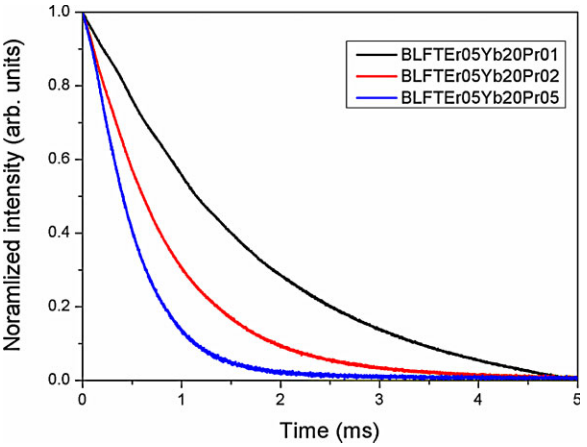


Figure 6 Decay curves of NIR photoluminescence spectra at 1.53 μm peak of Er^{3+} ions.

© 2014 WILEY-VCH Verlag GmbH & Co. KGaA, Weinheim

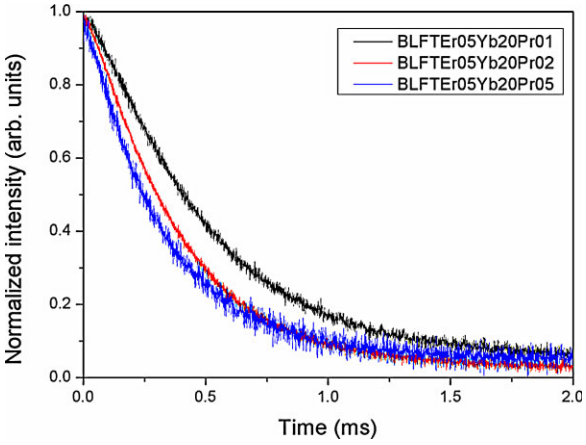


Figure 7 Decay curves of NIR photoluminescence spectra at 1.35 μm peak of Pr^{3+} ions.

intermediate $^3F_4$ level. This energy transfer is followed by simultaneous de-excition of the two Pr^{3+} ions to the ground level due to non-radiative multi-phonon relaxation with total energy loss. Hence, there is decrease in the lifetimes of $^1G_4$ level with increase of Pr^{3+} ion concentration.

Though there is decrease in lifetimes of both the Er^{3+} and Pr^{3+} NIR photoluminescence spectra, there is an extension of NIR band due to the tri-doping of Pr^{3+} ions along with Er^{3+} and Yb^{3+} ions in BLFT glasses. In the present study BLFTEr05Yb20Pr05 is found to be useful for broadband NIR applications, which are used in fiber telecommunications.

4 Conclusions Low phonon energy BLFT glasses doped with Er^{3+}, Yb^{3+} and Pr^{3+} ions have been prepared successfully. Optical absorption, NIR photoluminescence and decay spectra have been recorded for the prepared glasses. The NIR emission band of Er^{3+} ions at 1.53 μm (1531 nm) increased with increase of Yb^{3+} ions due to an effective energy transfer between the dopant ions. The NIR emission band of Pr^{3+} ions at 1.35 μm (1351 nm) is possible only because of the energy transfer from Yb^{3+} to Pr^{3+} ions. Decrease of Er^{3+} band intensity is due to energy transfer through cross-relaxation between Er^{3+} and Pr^{3+} ions. The decay times of 1.53 μm NIR emission from Er^{3+} ions decreased due to energy transfer from Er^{3+} to Pr^{3+} ions. The decay times of 1.35 μm emission from Pr^{3+} ions decreased due to self-quenching mechanisms in Pr^{3+} ions and not due to energy back transfer. The studies concluded that optimum concentrations of Er^{3+}, Yb^{3+} and Pr^{3+} tri-doped in low phonon glass matrix may increase the bandwidth in the NIR fibre telecommunications.

Acknowledgement The author Dr. JSK acknowledges the Fundação para a Ciência e Tecnologia – Portugal, for the financial funding through SFRH/BPD/75857/2011 post-doc fellowship.

References

[1] M. Irannejad, T. Fernandez, P. Joshi, Z. Zhao, J. Lousteau, B. Richards, G. Jose, and A. Jha, Int. J. Appl. Glass Sci. **4**, 202 (2013)
[2] B.C. Jamalaiah, J. Suresh, T. Kumar, K. Suhasini, H.S. Jang, H. Lee, L. Choi, and Rama Moorthy, J. Alloys. Compd. **474**, 382 (2009)
[3] S.J.L. Ribeiro, P. Goldner, and F. Auzel, J. Non-Cryst. Solids **219**, 176 (1997)
[4] Q. Cheng, J. Sui, and W. Cai, Nanoscale **4**, 779 (2012)
[5] J. Suresh Kumar, K. Pavani, M.P.F. Graça, M.J. Soares, and M.A. Valente, Phys. Status. Solidi B **250**, 837 (2013)

© 2014 WILEY-VCH Verlag GmbH & Co. KGaA, Weinheim

datasets, Apache Ivy and JEdit. To demonstrate the effectiveness of the proposed methodology, interproject validation has also been carried out on three open source datasets, Apache Ant and Apache Tomcat and Sakura. Interproject validation refers to using different datasets for testing and training. Training and testing performed on the same dataset may lead to very optimistic results. But this may not always be true as it is seen that in some cases, using training set different from test set lead to better prediction results as compared with using single training and test set (He *et al.*, 2012).

We have validated the threshold values of Ivy on Apache datasets (Ant, Tomcat) and the threshold values of JEdit on Sakura dataset. In other words, we performed interproject validation on the projects of similar nature. Ivy, Ant and Tomcat are apache software, and all are implemented in Java programming language, whereas JEdit and Sakura are test editors. We obtained comparative and competitive results. The results give us stronger confirmation and proof of the effectiveness of our proposed methodology. The study has analyzed the performance of various machine learning methods (BayesNet, NaïveBayes, random forest, support vector classifier and multilayer perceptron) in order to predict fault prone classes. The validation technique used for this purpose is *K*-cross validation, and the performance is evaluated using receiver operating characteristics (ROC) curve (El Emam *et al.*, 1999).

The paper is organized as follows: in the next section, we have explained the related work carried out in the area of fault proneness. Section 3 explains the background of the research, that is, the dependent and independent variables used along with description of the dataset. Section 4 explains the basic methodology followed in this study. The concept and usage of 'threshold values' is also explained in this section. Next, Section 5 summarizes the univariate and threshold analysis. The results of validation are discussed in Section 6, along with the results of interproject validation. The model application is explained in Section 7. The threats to validity are presented in Section 8. Finally, the work is concluded in Section 9.

2. Related work

As the complexity and size of every software is increasing everyday, it is becoming very essential to predict various quality attributes that affect the quality of the system. The prediction of quality attributes in early stages of software development will help in effective utilization of resources. There are various software metrics (Chidamber & Kemerer, 1991, 1994; Li & Henry, 1993; Lorenz & Kidd, 1994; Bieman & Kang, 1995; Lee *et al.*, 1995; Briand *et al.*, 1998, 1999; Cartwright & Shepperd, 1999; Aggarwal *et al.*, 2005) that can be used in predicting these quality attributes. Among all the metrics, object-oriented metrics suite given by Chidamber and Kemerer is most widely used in various studies (El Emam *et al.*, 2001; Gyimothy *et al.*, 2005; Cruz & Ochimizu, 2009; Singh *et al.*, 2010; Glasberg *et al.*, 2000). We need to develop prediction models that can be used to identify classes that are prone to faults. The researchers and software practitioners can use the predicted model to focus their testing resources on the classes that are likely to be fault prone. An exhaustive survey of fault prediction studies till 2008 is provided by C. Catal and Diri (2009). The important concept of threshold values for the metrics have been discussed in very few papers (El Emam *et al.*, 2000, 2002; Shatnawi, 2010; Herbold *et al.*, 2011). We have briefly discussed these papers in this section.

There are broadly two categories of data analysis methods, that is, machine learning and statistical methods. Although the trend is shifting towards modern machine learning methods, we have observed, much of the past work (Ohlsson *et al.*, 1998; El Emam & Melo, 1999; El Emam *et al.*, 1999; Tang *et al.*, 1999) is carried out in the area of statistical methods such as univariate and multivariate logistic regression. Some of the selected papers have been discussed in this section. The paper (El Emam & Melo, 1999) has constructed a model to predict fault classes using object-oriented design metrics. Tang *et al.* (Tang *et al.*, 1999) has worked on three industrial projects and concluded that among Chidamber and Kemerer (CK) metrics, weighted methods per class (WMC) and response for a class (RFC) are effective predictors of fault proneness. Confounding effect of size is taken into account by various studies (Cartwright & Shepperd, 1999; Gyimothy *et al.*, 2005; Briand *et al.*, 1997) and they concluded that class size is associated with many contemporary object-oriented metrics. Thus, the results should be revalidated after considering the effect caused by metrics. The work by M. Cartwright and Shepperd (1999) has worked on object-oriented constructs such as inheritance and polymorphism and concluded that the classes using high inheritance have shown more defect densities. Briand *et al.* (2000, 2001) have empirically validated a set 49 metrics and used univariate and multivariate analysis to find the individual and combined effect of metrics on fault proneness. The paper (Briand *et al.*, 2000) has found all the metrics to be significant except number of children (NOC), whereas paper (Briand *et al.*, 2001) have found WMC, RFC, and coupling between objects (CBO) strong predictors.

As there are various machine learning methods such as artificial neural network (ANN), Bayesian network (BN), decision tree (DT), and multilayer perceptron (MLP), we need to compare the results of various machine learning methods. The paper by Gyimothy *et al.* (2005) has DT and ANN and concluded NOC to be insignificant, whereas all the other metrics to be significant. A comparison between ANN and support vector machine (SVM) is carried out by I. Gondra (2008). Some authors (Fenton & Ohlsson, 2000; Kanmani *et al.*, 2007; Pai, 2007) have constructed various machine learning models. The paper by S. Kanmani *et al.* (2007) has introduced neural network based prediction models, whereas papers by Fenton and Ohlsson (2000) and G. J. Pai (2007) have introduced Bayesian belief networks to predict faulty classes. Few

© 2014 Wiley Publishing Ltd

papers (Zhou & Leung, 2006; Shatnawi & Li, 2008; Singh *et al.*, 2010) have discussed and taken into account the severity of faults to predict faulty classes.

Less work has been carried out to study the effect of threshold values of metrics on fault proneness. Thresholds help to identify the risk levels in a class. Some of the papers (Daly *et al.*, 1996; Cartwright, 1998; Harrison *et al.*, 2000; Prechelt *et al.*, 2003) have worked on levels of inheritance depth and how they affect maintenance. Daly *et al.* (1996) compared the performance of the program with three and five levels of depth. They concluded that program with three levels of depth performed the tasks much quicker than the program with no inheritance, whereas, programs with five levels took longer. On the other hand, Cartwright (1998) concluded that making changes in a program with three levels of depth require more effort than the program with no inheritance. Similarly L. Prechelt *et al.* (2003) also concluded that programs with three or five levels of inheritance did not show good performance when compared with programs with no inheritance. According to a paper (Prechelt *et al.*, 2003), inheritance depth is not related to maintenance. Thus, we cannot say anything about the effect of inheritance depths on maintenance. The threshold values of OO metrics are calculated by S. Benlarbi *et al*. (2000) and El Emam *et al*. (2002). They found that there was no statistical difference between the model predicted with threshold values and model predicted without threshold values. A new model was proposed by R. Shatnawi (2010), which can be used to find the risk level for any arbitrary threshold value.

3. Research background

In this section, we present independent and dependent variables used in this study. The details of the datasets and their descriptive statistics are also provided.

3.1. Dependent and independent variables

A single metric alone is not sufficient to explain all characteristics of a software under development. Several metrics must be used together to have better assessment of the software.

We have used object-oriented software metrics as independent variables in our study. There are various software metrics proposed in literature (Chidamber & Kemerer, 1991, 1994; Li & Henry, 1993; Lorenz & Kidd, 1994; Bieman & Kang, 1995; Lee *et al.*, 1995; Briand *et al.*, 1998, 1999; Cartwright & Shepperd, 1999; Aggarwal *et al.*, 2005). Among all the metrics, object-oriented metrics suite given by CK is most popular and widely used in various studies (El Emam *et al.*, 2001; Gyimothy *et al.*, 2005; Cruz & Ochimizu, 2009; Singh *et al.*, 2010; Glasberg *et al.*, n.d.). Also, metrics in CK suite cover various dimensions of object-oriented design such as coupling, cohesion, inheritance and size. Therefore, we decided to use CK metrics suite as independent variables. In addition to CK metrics, lines of code (LOC) metric is also included as it is the most common metric to measure size of the software.

The binary dependent variable in our study is fault proneness. Fault proneness is defined as the probability of occurrence of fault in a class (Briand *et al.*, 2000; Pai, 2007; Aggarwal *et al.*, 2009).

The following seven metrics used as independent variables are summarized in the succeeding text.

(i) Response for a class (RFC): RFC is the number of methods in the class including the methods that are called by class's methods.
(ii) Coupling between objects (CBO): CBO for a class is a count of the number of classes that are coupled to the other classes and vice versa.
(iii) Lack of cohesion (LCOM): For each data field in a class, the percentage of the methods in the class using that data field; the percentages are averaged then subtracted from 100%.
(iv) Number of children (NOC): NOC is the number of immediate subclasses of a class.
(v) Depth of inheritance (DIT): DIT is the maximum number of steps from the class node to the root of the tree in the inheritance hierarchy.
(vi) Weighted methods per class (WMC): WMC is a count of sum of complexities of all methods in a class
(vii) Source Lines of Code (LOC): LOC is the number of lines of code

3.2. Empirical data collection

We have used various data sets from Promise data repository, namely KC1, Ivy, Tomcat, Ant, and JEdit. Besides these datasets obtained from Promise data repository, Sakura editor is also used. KC1 is the proprietary data set obtained from the NASA Metrics Data Program (NASA 2004, PROMISE) (NASA, 2000), whereas Ivy, Tomcat, Ant, JEdit and Sakura are open source datasets. To show the effectiveness of the proposed methodology, generalization and comparison of results is very important, which is conducted using the open source datasets.

KC1 is implemented in C++ programming language and consists of 145 classes, 2107 methods and 40K lines of code. It consists of both the class level and the method level static metrics. We have used KC1 for class level metrics. The system consists of seven class level metrics including six CK metrics, which is collected and validated by the Metrics Data Program (MDP 2006, http://sarpresults.ivv.nasa.gov/ViewResearch/107.jsp). We extracted the defect data from KC1 using information contained in error reports. An error either could be from the source code, COTS/OS, design or is actually not a fault. We found total number of faults to be 669. We considered only those defects that are

© 2014 Wiley Publishing Ltd

produced from the source code, COTS/OS and design and removed all the faults that had 'not a fault' keyword used as the reason of closure of error report. This reduced the total number of faults to 642. The number of classes found to be faulty is 58 out of 145 classes. The details about the dataset can be obtained from Singh *et al.* (2010).

Given in the succeeding text are the important details regarding the data:

- Total number of classes: 145
- Number of faulty classes in the system: 58
- Number of faults in the system: 669 (reduced to 642)
- Implementation language used: C++

Apache Ant is a Java library and command-line tool for automating software processes. The main usage of Ant is building of Java applications. Ant can also be used effectively to build non Java applications, for instance C or C++ applications (http://ant.apache.org). Apache ivy is a powerful dependency manager that manages dependencies of any kind. It is integrated with Apache Ant and thus follows same design principles as Apache Ant (http://ant.apache.org/ivy). Apache Tomcat is a software implementation of Java Servlet and the JavaServer Pages (JSP) specifications from Sun Microsystems. It provides a 'pure Java' HTTP web server environment for Java code to run in (http://tomcat.apache.org). JEdit and Sakura, both are text editors for programmers. Sakura is available under the GNU General Public License 2.0 and implemented in Java programming language, whereas Sakura is available under Shareware license and is implemented in C++. All these datasets (except Sakura) are from Promise data repository collected by Jureczko and Madeyski (2010), and Jureczko and Spinellis (2010) using ckjm tool. The data for Sakura is collected using metric tool family, Understand for C and Understand for Java (Watanabe *et al.*, 2008; Scitools, 1996-2013).

The details of open source datasets, which include the version of the dataset we have used, number of instances (data points) and the number of faulty instances in the dataset is provided in the Table 1. An instance or a data point refers to a class in the dataset. Therefore, the number of instances in a particular dataset is the number of classes. Out of 352 classes of Ivy, 40 classes are found to be fault prone. For Ant and Tomcat, the number of faulty classes is 166 and 77, respectively. JEdit and Sakura have 10 and 47 faulty classes, respectively. Figure 1 indicates the percentage of classes that are found to be actually faulty in each of the five software.

Table 1: *Brief details of open source datasets used*

Dataset	Version	No. of instances	No. of faulty instances
Ivy	2.0	352	40
Ant	1.7	745	166
Tomcat	6.0	858	77
JEdit	4.3	492	10
Sakura	2.0.2.0	80	47

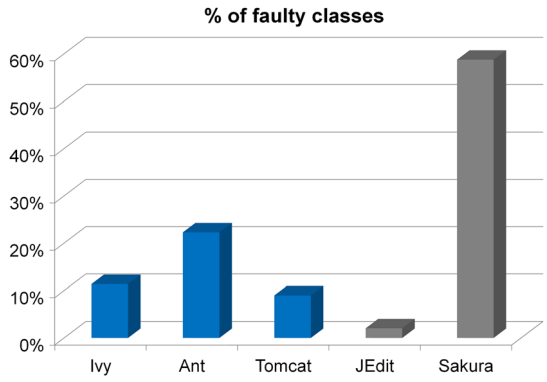


Figure 1: *Summary of faulty classes.*

3.3. *Descriptive statistics*

We have calculated various statistics including minimum (Min.), maximum (Max.), mean (Mean), median (Median) and standard deviation (SD) for metrics of all the six software which we have analyzed. Table 2 shows the descriptive statistics for KC1 dataset. We can make the following important observations regarding some of the metrics (Singh *et al.*, 2010):

- LOC: The size of a class is measured in terms of lines of source code. We can see that the minimum value for LOC is 0, whereas the maximum is 2313, which is a not a very large value.
- NOC and DIT: The NOC metric value is 0 in 75% of the classes. This shows that the number of immediate children in 75% of the classes is 0, which concludes low inheritance in the system. This is also shown by the DIT metric, the maximum DIT metric value is 6. Also, 75% of the classes do not have even two levels of inheritance.
- LCOM: cohesion in the system is not very high. Cohesion metric LCOM has the maximum value as 100, which is quite low.

Tables 3–7 show the descriptive statistics of Ivy, Ant, Tomcat, JEdit and Sakura, respectively. Following important observations can be made from these tables:

- LOC: the size of the class measured in terms of lines of code ranges from 1 to 2894 (Ivy), 0 to 4541 (Ant) and 0 to 7956 (Tomcat). We can say that although Tomcat and Ant are medium-sized software, Ivy is smaller software. But both JEdit and Sakura are large sized software with the LOC ranging from 1 to 12 535 for JEdit and 1 to 15 227 for Sakura.
- NOC and DIT: the mean values of NOC for all the software are quite low. For Ivy mean value of NOC is 0.37, for Ant it is 0.73, for Tomcat it is 0.36, JEdit and Sakura has mean values 0.45 and 0.38, respectively.

© 2014 Wiley Publishing Ltd

Table 2: *Descriptive statistics for KC1*

						Percentile	
Metric	Min.	Max.	Mean	Median	SD	0.25	0.75
WMC	0.00	100.00	17.42	12.00	17.45	8.00	235.50
DIT	0.00	6.00	1.00	1.00	1.26	0.00	1.50
NOC	0.00	5.00	0.21	0.00	0.70	0.00	0.00
CBO	0.00	24.00	8.32	8.00	6.38	3.00	14.00
RFC	0.00	222.00	34.38	28.00	36.20	10.00	44.50
LCOM	0.00	100.00	68.72	84.00	36.89	56.50	96.00
LOC	0.00	2313.00	211.25	108.00	345.55	8.00	235.50

RFC, response for a class; CBO, coupling between objects; LCOM, lack of cohesion; NOC, number of children; DIT, depth of inheritance; WMC, weighted methods per class; LOC, lines of code.

Table 3: *Descriptive statistics for Ivy*

						Percentile	
Metric	Min.	Max.	Mean	Median	SD	0.25	0.75
WMC	1.00	157.00	11.28	6.00	15.15	3.00	13.00
DIT	1.00	6.00	1.79	1.00	1.25	1.00	2.00
NOC	0.00	17.00	0.37	0.00	1.32	0.00	0.00
CBO	1.00	150.00	13.23	8.00	16.57	5.00	16.00
RFC	1.00	312.00	34.04	19.00	44.68	6.00	40.00
LCOM	0.00	11794.00	131.58	6.00	712.19	0.00	45.75
LOC	1.00	2894.00	249.34	85.50	428.26	20.00	267.00

RFC, response for a class; CBO, coupling between objects; LCOM, lack of cohesion; NOC, number of children; DIT, depth of inheritance; WMC, weighted methods per class; LOC, lines of code.

Table 4: *Descriptive statistics for Ant*

						Percentile	
Metric	Min.	Max.	Mean	Median	SD	0.25	0.75
WMC	0.00	120.00	11.07	7.00	11.98	4.00	14.00
DIT	1.00	7.00	2.52	2.00	1.40	1.00	4.00
NOC	0.00	102.00	0.73	0.00	4.80	0.00	0.00
CBO	0.00	499.00	11.05	6.00	26.34	4.00	11.00
RFC	0.00	288.00	34.36	23.00	36.03	11.00	43.00
LCOM	0.00	6692.00	89.15	6.00	349.94	0.00	53.00
LOC	0.00	4541.00	280.07	143.00	411.87	52.00	325.00

RFC, response for a class; CBO, coupling between objects; LCOM, lack of cohesion; NOC, number of children; DIT, depth of inheritance; WMC, weighted methods per class; LOC, lines of code.

Table 5: *Descriptive statistics for Tomcat*

						Percentile	
Metric	Min.	Max.	Mean	Median	SD	0.25	0.75
WMC	0.00	252.00	12.96	7.00	18.62	3.00	14.00
DIT	1.00	6.00	1.69	1.00	1.05	1.00	2.00
NOC	0.00	31.00	0.36	0.00	1.97	0.00	0.00
CBO	0.00	109.00	7.57	4.00	11.10	2.00	9.00
RFC	0.00	511.00	33.47	17.00	44.98	7.00	40.00
LCOM	0.00	29258.00	176.28	4.00	1159.19	0.00	42.00
LOC	0.00	7956.00	350.44	112.00	644.84	25.00	373.50

RFC, response for a class; CBO, coupling between objects; LCOM, lack of cohesion; NOC, number of children; DIT, depth of inheritance; WMC, weighted methods per class; LOC, lines of code.

© 2014 Wiley Publishing Ltd

Table 6: *Descriptive statistics for JEdit*

Metric	Min.	Max.	Mean	Median	SD	Percentile 0.25	Percentile 0.75
WMC	0.00	351.00	12.35	7.00	24.51	3.00	13.00
DIT	1.00	8.00	2.37	1.50	1.93	1.00	3.00
NOC	0.00	38.00	0.45	0.00	2.43	0.00	0.00
CBO	0.00	346.00	14.32	8.50	25.00	4.00	15.00
RFC	0.00	540.00	39.85	24.50	56.34	9.00	52.75
LCOM	0.00	41713.00	259.91	6.00	2184.69	1.00	36.00
LOC	1.00	12535.00	411.31	176.00	946.96	41.25	451.00

RFC, response for a class; CBO, coupling between objects; LCOM, lack of cohesion; NOC, number of children; DIT, depth of inheritance; WMC, weighted methods per class; LOC, lines of code.

Table 7: *Descriptive statistics for Sakura*

Metric	Min.	Max.	Mean	Median	SD	Percentile 0.25	Percentile 0.75
WMC	2.00	275.00	17.19	9.00	32.78	6.00	14.75
DIT	0.00	2.00	0.43	0.00	0.59	0.00	1.00
NOC	0.00	14.00	0.38	0.00	1.69	0.00	0.00
CBO	0.00	64.00	5.33	2.00	9.40	1.00	6.00
RFC	2.00	275.00	25.35	15.00	33.21	8.25	35.00
LCOM	0.00	94.00	56.13	60.00	25.56	42.00	75.00
LOC	13.00	15227.00	681.50	162.50	1873.67	66.75	351.25

RFC, response for a class; CBO, coupling between objects; LCOM, lack of cohesion; NOC, number of children; DIT, depth of inheritance; WMC, weighted methods per class; LOC, lines of code.

These low values indicate that there are very few children and inheritance is not much used in the systems. Similar results are shown by KC1 dataset

- LCOM: in contrast to the degree of cohesion in KC1, the maximum value of LCOM is 11 794 in Ivy, 6692 in Ant and 29 258 in Tomcat. This indicates that cohesion is there in the systems to a high extent.

4. Research methodology

In this section, we have explained the methodology used for analysis. The brief discussion of the statistical method (logistic regression) used in our study is given here.

The basic approach we followed in this study is shown in Figure 2. Each of these steps has been explained in detail in subsequent sections. To begin with, we conducted univariate analysis to determine the metrics that are significant in predicting fault proneness. Once the significant metrics are determined, threshold values are calculated for these metrics. Validation of these threshold values are conducted using various machine learning methods. The validation is carried on the same project for which thresholds are calculated as well as on other projects. In other words, a particular dataset is converted into binary using the threshold values of the metrics of that dataset as well as of some other similar dataset. This is termed as interproject validation of threshold values. Then, for that binary data, various models are predicted using different machine learning methods.

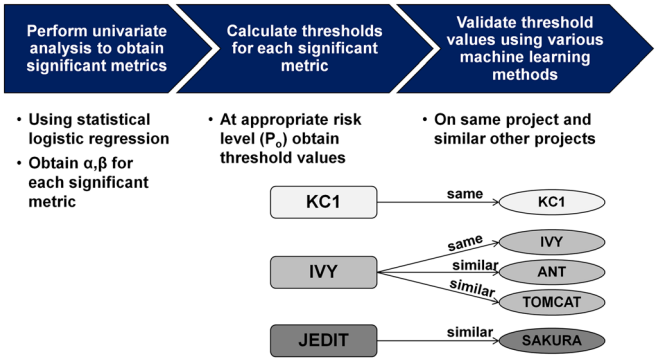


Figure 2: *Proposed methodology.*

4.1. Statistical model: logistic regression

Logistic regression (LR) is the statistical method used to predict the dependent variable from a set of independent variables (Hosmer & Lemeshow, 1989; Basili *et al.*, 1996; Aggarwal *et al.*, 2009). We have used logistic regression to find significant metrics and to find the value of thresholds. LR is of two types, univariate LR and multivariate LR. We have used univariate logistic regression to find the relationship between of each independent variable (OO metric) and the dependent variable (fault proneness). This

© 2014 Wiley Publishing Ltd

helps us to find the metrics that are significantly associated with fault proneness.

The simple logistic model is based on a linear relationship between the natural logarithm (ln) of the odds of an event and a numerical independent variable.

In our study,

$$\text{odds} = \frac{P}{1-P} \quad \ldots \tag{1}$$

where

P = probability of a class being faulty

Therefore, according to definition of simple logistic model,

$$\ln(\text{odds}) = \alpha + \beta x \quad \ldots \tag{2}$$

where

x is the independent variable, that is, an object-oriented metric

α and β are the Y-intercept and the slope, respectively

From 1 and 2, we get

$$P = \frac{e^{g(x)}}{1 + e^{g(x)}}$$

Where $g(x) = \alpha + \beta x$; $\alpha = Y$-intercept or constant and β = slope or estimated coefficient

In this study, we will use the terms, constant and coefficient for α and β, respectively. The values of α and β are used for calculating threshold values as explained in Section 4.2.

4.2. Calculation of threshold values

This section explains the methodology required to compute the threshold values.

A threshold can be defined as a benchmark or an upper bound such that the values greater than a threshold value are considered to be problematic, whereas the values lower are considered to be acceptable. We have used the Bender method (Bender, 1999) known as Value of an Acceptable Risk Level (VARL) to compute the threshold values where the acceptable risk level is given by a probability Po (e.g. $Po = 0.05$ or 0.01). Because we are calculating threshold values for the metrics of a dataset, we can say that for classes with metrics values below VARL, the risk of a fault occurrence is lower than the probability (Po).

In other words, R. Bender (1999) has suggested that the value of Po can be any probability, which can be considered as the acceptable risk level by us. We have calculated the results of the VARL at six levels of risk (between $Po = 0.01$ and $Po = 0.15$). This will help us to select the most appropriate risk level for our datasets in study.

The detailed description of VARL is given in (Bender, 1999). The formula for VARL is given as follows:

$$\text{VARL} = \frac{1}{\beta}\left[\ln\left[\frac{Po}{1-Po}\right] - \alpha\right]$$

Where

α = constant
β = estimated coefficient
Po = acceptable risk level

In this formula, α and β are obtained using the standard logistic regression formula. This formula will be used for each metric individually to find its threshold value.

For example, consider Ivy dataset and we need to calculate the threshold value of CBO metric. Referring Table 9 (univariate analysis for Ivy) to obtain the values of α and β, we get $\alpha = -2.598$ and $\beta = 0.033$.

$$\begin{aligned}\text{VARL} &= \frac{1}{\beta}\left[\ln\left[\frac{Po}{1-Po}\right] - \alpha\right] \\ &= (1/0.033)^*\left[\ln\left[\frac{Po}{1-Po}\right] - (-2.598)\right] \\ &\quad (\text{the values of } Po \text{ are taken between 0.01 to 0.15}) \\ &= (1/0.033)^*\left[\ln\left[\frac{0.07}{1-0.07}\right] - (-2.598)\right] \\ &\quad (\text{taking } Po = 0.07) = 0.34\end{aligned}$$

Thus, we say VARL for CBO metric at risk level of 0.07 is 0.34

5. Result analysis

In this section, we have explained the results obtained using univariate analysis and threshold analysis. Also, the validation of the model using ROC curve has been explained in this section.

5.1. Univariate analysis

Threshold values are calculated for the metrics of KC1, Ivy and JEdit. Therefore, we conducted univariate analysis for these software to find the effect of individual metrics on fault proneness. Tables 8–10 show the coefficient (β), constant (α), and statistical significance (sig.) for each metric of KC1, Ivy and JEdit datasets.

The 'sig' parameter tells about the association between each metric and fault proneness. If 'sig' value is below or at the significance threshold of 0.05, then the metric is said to be significant in predicting fault proneness. We can observe that for both the software (KC1 and Ivy), metrics LCOM, NOC and DIT are not significant and hence not being used for further analysis, that is, only for significant

© 2014 Wiley Publishing Ltd

Table 8: *Univariate analysis for KC1*

Metric	Sig.	β	α
WMC	**0.021**	**0.028**	**−0.886**
DIT	0.5	0.09	−0.497
NOC	0.213	−0.401	−0.332
CBO	**0.000**	**0.207**	**−2.238**
RFC	**0.037**	**0.011**	**−0.785**
LCOM	0.796	0.001	−0.488
LOC	**0.000**	**0.005**	**−1.353**

RFC, response for a class; CBO, coupling between objects; LCOM, lack of cohesion; NOC, number of children; DIT, depth of inheritance; WMC, weighted methods per class; LOC, lines of code.

Table 9: *Univariate analysis for Ivy*

Metric	Sig.	β	α
WMC	**0.000**	**0.050**	**−2.786**
DIT	0.818	−0.032	−1.997
NOC	0.460	−0.149	−2.011
CBO	**0.000**	**0.033**	**−2.598**
RFC	**0.000**	**0.023**	**−3.131**
LCOM	0.108	0.000	−2.126
LOC	**0.000**	**0.002**	**−2.874**

RFC, response for a class; CBO, coupling between objects; LCOM, lack of cohesion; NOC, number of children; DIT, depth of inheritance; WMC, weighted methods per class; LOC, lines of code.

Table 10: *Univariate analysis for JEdit*

Metric	Sig.	β	α
WMC	**0.001**	**0.041**	**−4.486**
DIT	0.696	0.061	−4.007
NOC	0.598	−0.376	−3.788
CBO	**0.012**	**0.023**	**−4.259**
RFC	**0.000**	**0.016**	**−4.698**
LCOM	**0.003**	**0.001**	**−4.066**
LOC	**0.021**	**0.001**	**−4.137**

RFC, response for a class; CBO, coupling between objects; LCOM, lack of cohesion; NOC, number of children; DIT, depth of inheritance; WMC, weighted methods per class; LOC, lines of code.

metrics, we calculate the threshold values. For JEdit, NOC and DIT are found to be insignificant. The significant metrics are shown in bold in the tables. The 'sig' parameter is basically two-tailed *p*-value whose value is determined using the Wald test. The value of Wald test for an independent variable is the ratio of its coefficient to its standard error. For example, let the coefficient of an independent variable be 0.111 and its standard error be 0.024. Then, $W = 0.111/0.024 = 4.61$, and the two tailed *p*-value ('sig' parameter) is $P(|z| > 4.61)$, where z denotes a random variable following the standard normal distribution. (For details, refer Hosmer & Lemeshow, 1989).

The coefficient 'β' shows the impact of the independent variable and its sign shows whether the impact is positive or negative.

5.2. Threshold analysis

We have calculated the VARL threshold values for the metrics that are found to be significant. The VARL values are calculated for different values of *Po*, that is, at different levels of risks (between $Po = 0.01$ and $Po = 0.15$). The threshold values at different values of *Po* for all the significant metrics are shown in Tables 11–13 for KC1, IVY and JEDIT datasets, respectively. We can make the following two important observations:

(1) VARL threshold values of all the metrics change significantly as *Po* changes. This shows *Po* plays a significant role in calculating threshold values.
(2) As we have discussed, *Po* is defined as the acceptable risk level, that is, risk level that can be acceptable to classify a class as non-faulty. Thus, low values of *Po* are desirable. The lowest value of *Po,* using which we get the threshold values within the observation range (i.e. positive values) of all the metrics, is considered to be the best value of *Po*.

5.2.1. Analysis for KC1 Table 11 shows the results of threshold analysis for KC1 dataset. We can observe from Table 11 that at all levels of risks except at $Po = 0.15$, the VARL values of metrics are out of range (i.e. negative values) for some of the metrics. For example, the threshold values at $Po = 0.05$, 0.08 and 0.1 are outside the observation range of RFC and WMC metrics, whereas threshold values at $Po = 0.01$ lay outside the range of RFC, WMC and LOC metrics. Thus, these levels of risks cannot be considered and hence are ignored. The only risk level that gives threshold values within the observation range of all the metrics is 0.15. Hence, we select $Po = 0.15$ as the appropriate value of risk level. In other words, we can say, for classes with metric value below VARL, the risk of fault occurrence is lower than the probability of 15%. The threshold values of metrics (at 0.15

Table 11: *Thresholds at different risk levels for KC1*

Metrics	VARL at 0.01	VARL at 0.05	VARL at 0.06	VARL at 0.08	VARL at 0.1	VARL at 0.15
WMC	−39.63	−14.03	−11.03	−6.24	−2.44	4.74
CBO	1.17	4.63	5.04	5.69	6.20	7.17
RFC	−110.06	−44.89	−37.27	−25.06	−15.39	2.88
LOC	−128.53	14.85	31.6	58.46	79.75	119.93

RFC, response for a class; VARL, Value of an Acceptable Risk Level; CBO, coupling between objects; WMC, weighted methods per class; LOC, lines of code.

© 2014 Wiley Publishing Ltd

Table 12: *Thresholds at different risk levels for Ivy*

Metrics	VARL at 0.01	VARL at 0.05	VARL at 0.06	VARL at 0.07	VARL at 0.08	VARL at 0.1	VARL at 0.15
WMC	−36.18	−3.17	0.69	3.99	6.87	11.78	21.03
CBO	−60.52	−10.50	−4.65	0.34	4.72	12.14	26.16
RFC	−63.66	8.11	16.50	23.67	29.94	40.60	60.71
LOC	−860.56	−35.22	61.23	143.66	215.83	338.39	569.70

RFC, response for a class; VARL, Value of an Acceptable Risk Level; CBO, coupling between objects; WMC, weighted methods per class; LOC, lines of code; LCOM, lack of cohesion.

Table 13: *Thresholds at different risk levels for JEdit*

Metrics	VARL at 0.01	VARL at 0.015	VARL at 0.02	VARL at 0.05	VARL at 0.06	VARL at 0.08	VARL at 0.1	VARL at 0.15
WMC	−2.66	7.35	14.49	37.60	42.30	49.84	55.82	67.11
CBO	−14.61	3.24	15.96	57.15	65.54	78.98	89.64	109.76
RFC	6.43	32.09	50.39	109.60	121.65	140.98	156.30	185.21
LCOM	−529.12	−118.60	174.18	1121.56	1314.47	1623.65	1868.78	2331.40
LOC	−458.12	−47.59	245.18	1192.56	1385.47	1694.65	1939.78	2402.40

RFC, response for a class; VARL, Value of an Acceptable Risk Level; CBO, coupling between objects; WMC, weighted methods per class; LOC, lines of code.

risk level) CBO, RFC, WMC and LOC at 0.15 are 7.17, 2.88, 4.74 and 119.93, respectively.

5.2.2. Analysis for IVY Table 12 shows threshold values for the metrics of Ivy at different risk levels. We can observe from Table 12 that the threshold values equal to and greater than 0.07 are within the observation range of all the metrics. Because *Po* is the acceptable risk level, we will consider the lowest considerable value, that is, 0.07 as the appropriate risk level. By definition of *Po* as given by Bender (1999), at risk level of 0.07, the risk of fault occurrence is lower than the probability 0.07 (7%). As *Po* increases, the risk of fault occurrence increases. Therefore, we have considered the lowest possible value of *Po*, that is, 0.07 and not considered the other values. The threshold values at 0.07 risk level are 3.99 for WMC, 0.34 for CBO, 23.67 for RFC and 143.66 for LOC. These values are validated on the same dataset as well as on two different open source, public datasets – Ant and Tomcat.

5.2.3. Analysis for JEdit The values of threshold for all the significant metrics of JEdit at different risk levels are shown in Table 13. We can observe that among all the risk levels between 0.01 and 0.15, the risk level 0.02 gives the threshold values within the range, that is, positive values. This means that the classes whose metrics values are below their threshold values, the risk of fault occurrence is lower than 2%. The threshold values at 0.02 risk level are 14.49, 15.96, 50.39, 174.18 and 245.18 for the metrics WMC, CBO, RFC, LCOM, and LOC, respectively.

5.3. Validation of the threshold values

We need to check the accuracy of the model constructed using threshold values. There are various measures that are used to evaluate the performance of a model:

Sensitivity and specificity: The correctness of the predicted model can be measured by sensitivity and specificity. Sensitivity is defined as the percentage of classes correctly predicted to be fault prone. Specificity is defined as the percentage of classes correctly predicted to be not faulty.
Precision or accuracy: It is defined as the percentage of classes correctly predicted to be either faulty or non-faulty.
Receiver operating characteristic analysis: our main aim is to maximize both sensitivity and specificity. The ROC curve finds the optimal cut-off point that maximizes both sensitivity and specificity (El Emam *et al.*, 1999; Shatnawi, 2010). Thus, ROC curve helps to measure the performance of the predicted model. It is plotted by taking various cut-off points between 0 and 1 and calculating sensitivity and specificity at each point. Then, ROC curve is plotted as sensitivity on the *y*-coordinate versus its (1-specificity) on the *x*-coordinate (El Emam *et al.*, 1999). The main advantage of using ROC curve is that no arbitrary decisions need to be made regarding the cut-off point, which is used in predicting probability. We calculate the area under the ROC curve (AUC) in order to compute the accuracy. The AUC is a combined measure of sensitivity and specificity.

Besides these basic performance evaluation measures, a new evaluation technique that uses the geometric mean (g-mean) was suggested by Kubat and Matwin (1997). They found that evaluation measure using g-mean is more accurate and precise than usual evaluation measures when data is imbalanced. Using g-mean, we can calculate two accuracies: accuracy of positives, denoted by a+ and accuracy of negatives, denoted by a−. When both a+ and a− are high, the calculated g-mean is also high, this is desirable. To understand the formulae for a+ and a−, we need to first construct the confusion matrix (Table 14) as given in the succeeding text:

© 2014 Wiley Publishing Ltd

Table 14: *Confusion matrix*

Observed	Predicted	
	0 (Not fault prone)	1 (Fault prone)
0 (not fault prone)	True not fault prone	False fault prone
1 (fault prone)	False not fault prone	True fault prone

$$\text{Now, } a+ = \text{TFP}/(\text{FFP} + \text{TFP})$$
$$a- = \text{TNFP}/(\text{TNFP} + \text{FNFP})$$
$$\text{g-mean} = \sqrt{(a+)^*(a-)}$$

Sensitivity and specificity can be written as:

$$\text{Sensitivity} = (\text{Number of modules correctly predicted as fault prone})/(\text{total number of actual faulty modules}) = \text{TFP}/(\text{FNFP} + \text{TFP}) \quad \ldots. \tag{3}$$

$$\text{Specificity} = (\text{Number of modules correctly predicted as non-fault prone})/(\text{total number of actual non-faulty modules}) = \text{TNFP}/(\text{TNFP} + \text{FFP}) \quad \ldots. \tag{4}$$

5.3.1. Construction of confusion matrix The diagrammatic representation showing the procedure followed to construct confusion matrix is shown in Figure 3. We have used various machine learning methods such as BayesNet, Naïve Bayes, random forest, support vector classifier and multilayer perceptron to validate the model. Our first step is to construct a binary data corresponding to our original dataset. If the metric values are below the threshold value of that metric, then the metric value is changed to 0, otherwise 1. This is carried for all the metrics and we get a binary dataset. Then, using any machine learning method, ROC curve is constructed to get an optimal cut-off point that maximizes sensitivity and specificity. Using these values of sensitivity and specificity, confusion matrix is constructed in following way:

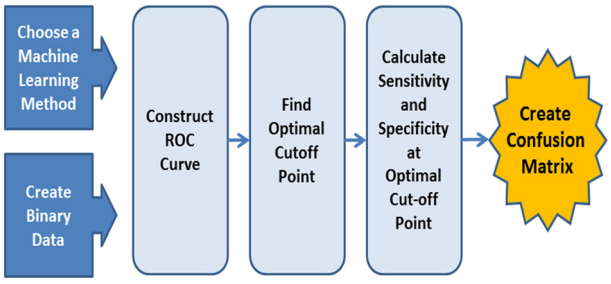


Figure 3: *Construction of confusion matrix.*

$$\text{TFP} = \text{sensitivity}^*\text{actual faulty classes} \quad \ldots(\text{from 3})$$
$$\text{FNFP} = \text{actual faulty classes} - \text{TFP}$$
$$\text{Similarly, TNFP} = \text{specificity}^*\text{actual non faulty classes} \quad \ldots(\text{from 4})$$
$$\text{FFP} = \text{actual non faulty classes} - \text{TNFP}$$

Finally, using these values of confusion matrix, g-mean is calculated for different machine learning methods.

6. Results discussion

We calculated the accuracy of the models before and after converting the data into binary. As discussed, the dataset is converted into binary using the threshold values of metrics of that dataset or some other similar dataset. We have calculated the threshold values for one proprietary dataset (KC1) and two open source datasets (Ivy and JEdit). The threshold values of KC1 and Ivy are validated on the same dataset. Besides this, the threshold values of Ivy and JEdit are also validated on two different public datasets - Ant and Tomcat. We have also used another Promise dataset, JEdit to validate its threshold values on an open source dataset, Sakura. In other words, we have conducted interproject validation on three projects/datasets (Ant, Tomcat and Sakura). This will help us to prove the effectiveness of proposed methodology more strongly and give generalized results. Interproject validation using the proprietary dataset KC1 is very difficult as we do not have access to different proprietary data. Because, as we know, KC1 is obtained from the NASA Metrics Data Program, that is, it is NASA's proprietary data, its results cannot be compared and generalized. Hence, we decided to show the strength of the proposed methodology using two open source datasets (Ivy and JEdit) and validated their results on projects of similar nature. Besides this, the results of proprietary datasets cannot be compared with that of open source datasets as their building methodology and environment are very different.

We evaluated the accuracy of the thresholds by validating combination of metrics using various machine learning techniques. Based on the threshold values, metrics are converted into a binary scale in which 0 indicates low risk and 1 indicates high risk. The results of validation are shown in Tables 15–19. The results would be optimistic if we use the same dataset for training as well as testing. Thus, we have used 10-cross validation in which the dataset is divided into 10 parts; one part is used for testing and remaining nine parts are used for training. This process is repeated for all the 10 parts.

6.1. KC1 result analysis

Table 15 shows the results when the original data has been validated along with the results of its corresponding binary data. This will allow us to analyze the effect and benefit of

© 2014 Wiley Publishing Ltd

Table 15: *Validation results for KC1*

Machine learning method	Validated model	Sensitivity	Specificity	AUC	g-mean	Cut-off point
Naïve-Bayes	Non-binary	0.690	0.667	0.769	66.52	0.134
	Binary	0.724	0.690	0.713	69.66	0.479
BayesNet	Non-binary	0.707	0.621	0.736	64.90	0.694
	Binary	0.741	0.678	0.702	69.49	0.401
Random forest	Non-binary	0.741	0.724	0.815	71.99	0.450
	Binary	0.690	0.678	0.716	67.13	0.591
Support vector	**Non-binary**	**0.630**	**0.782**	**0.693**	**69.59**	**0.500**
	Binary	**0.810**	**0.667**	**0.739**	**72.08**	**0.500**
Multilayer perceptron	Non-binary	0.690	0.690	0.803	67.77	0.441
	Binary	0.655	0.667	0.723	64.94	0.592

AUC, area under receiver operating characteristics curve.

Table 16: *Validation results for Ivy*

Machine learning method	Validated model	Sensitivity	Specificity	AUC	g-mean	Cut-off point
Naïve-Bayes	Non-binary	0.750	0.744	0.799	51.17	0.005
	Binary	0.725	0.724	0.764	49.03	0.485
BayesNet	Non-binary	0.750	0.744	0.791	51.17	0.056
	Binary	0.725	0.724	0.763	49.03	0.505
Random forest	**Non-binary**	**0.725**	**0.683**	**0.735**	**46.46**	**0.050**
	Binary	**0.725**	**0.724**	**0.776**	**49.03**	**0.044**
Support vector	Non-binary	—	—	0.500	—	—
	Binary	—	—	0.500	—	—
Multilayer perceptron	**Non-binary**	**0.725**	**0.721**	**0.794**	**48.81**	**0.086**
	Binary	**0.725**	**0.728**	**0.773**	**49.23**	**0.236**

AUC, area under receiver operating characteristics curve.

Table 17: *Interproject Validation Results for Ant*

Machine learning method	Validated model	Sensitivity	Specificity	AUC	g-mean	Cut-off point
Naïve-Bayes	**Non-binary**	**0.759**	**0.699**	**0.788**	**61.82**	**0.012**
	Binary	**0.717**	**0.708**	**0.742**	**60.65**	**0.629**
BayesNet	Non-binary	0.753	0.753	0.803	65.26	0.113
	Binary	0.717	0.708	0.745	60.65	0.631
Random forest	**Non-binary**	**0.719**	**0.758**	**0.786**	**64.38**	**0.250**
	Binary	**0.729**	**0.699**	**0.745**	**60.75**	**0.407**
Support vector	Non-binary	—	—	0.636	—	—
	Binary	—	—	0.717	—	—
Multilayer perceptron	Non-binary	0.753	0.753	0.812	65.26	0.194
	Binary	0.645	0.729	0.743	59.61	0.385

AUC, area under receiver operating characteristics curve.

Table 18: *Interproject Validation Results for Tomcat*

Machine learning method	Validated model	Sensitivity	Specificity	AUC	g-mean	Cut-off point
Naïve-Bayes	**Non-binary**	**0.779**	**0.659**	**0.772**	**42.20**	**0.003**
	Binary	**0.688**	**0.738**	**0.740**	**44.36**	**0.408**
BayesNet	Non-binary	0.753	0.713	0.777	44.63	0.019
	Binary	0.714	0.708	0.718	43.19	0.309
Random forest	**Non-binary**	**0.714**	**0.711**	**0.736**	**43.42**	**0.050**
	Binary	**0.792**	**0.711**	**0.705**	**45.50**	**0.200**
Support vector	Non-binary	—	—	0.500	—	—
	Binary	—	—	0.500	—	—
Multilayer perceptron	Non-binary	0.740	0.740	0.801	46.02	0.065
	Binary	0.792	0.704	0.752	45.07	0.126

AUC, area under receiver operating characteristics curve.

© 2014 Wiley Publishing Ltd

Table 19: *Interproject validation results for Sakura*

Machine learning method	Validated model	Sensitivity	Specificity	AUC	g-mean	Cut-off point
Naïve-Bayes	Non-binary	0.574	0.576	0.617	56.67	0.008
	Binary	0.617	0.606	0.62	60.24	0.331
BayesNet	Non-binary	0.617	0.364	0.459	48.17	0.554
	Binary	0.255	0.636	0.446	43.30	0.589
Random forest	Non-binary	0.574	0.606	0.615	58.09	0.65
	Binary	0.574	0.545	0.581	55.20	0.485
Support vector	Non-binary	0.83	0.303	0.566	59.08	0.5
	Binary	0.617	0.515	0.566	55.94	0.5
Multilayer perceptron	**Non-binary**	**0.553**	**0.576**	**0.459**	**54.48**	**0.554**
	Binary	**0.617**	**0.545**	**0.586**	**57.40**	**0.482**

AUC, area under receiver operating characteristics curve.

using thresholds. We can observe from the table that the binary model predicted using BayesNet, Naive Bayes and support vector classifier show high g-mean values as compared with their equivalent non-binary models. The models predicted using other machine learning methods, that is, random forest and multilayer perceptron also showed comparable results. Significant difference between binary model and its corresponding non-binary model are shown in the values of g-mean and AUC when support vector classifier is used. The ROC curves for both the binary and non-binary models predicted using support vector classifier are shown in Figure 4. The g-mean of the model obtained when validating binary data using support vector classifier is 72.08, whereas g-mean of the model obtained when validating non-binary data is 69.59, which is quite a significant difference. Besides this, observable difference is also seen in the values of AUC of binary (0.739) and non-binary (0.693) model. Thus, we can conclude that thresholds are quite effective and can be used by researchers and practitioners for alarming the classes that are at high-risk. Also, the best machine learning method that can be used by researchers for validating future projects is support vector classifier.

6.2. *Results of validation using open source datasets*

Tables 16–19 show the results of validation on different open source datasets. Table 16 shows the results of

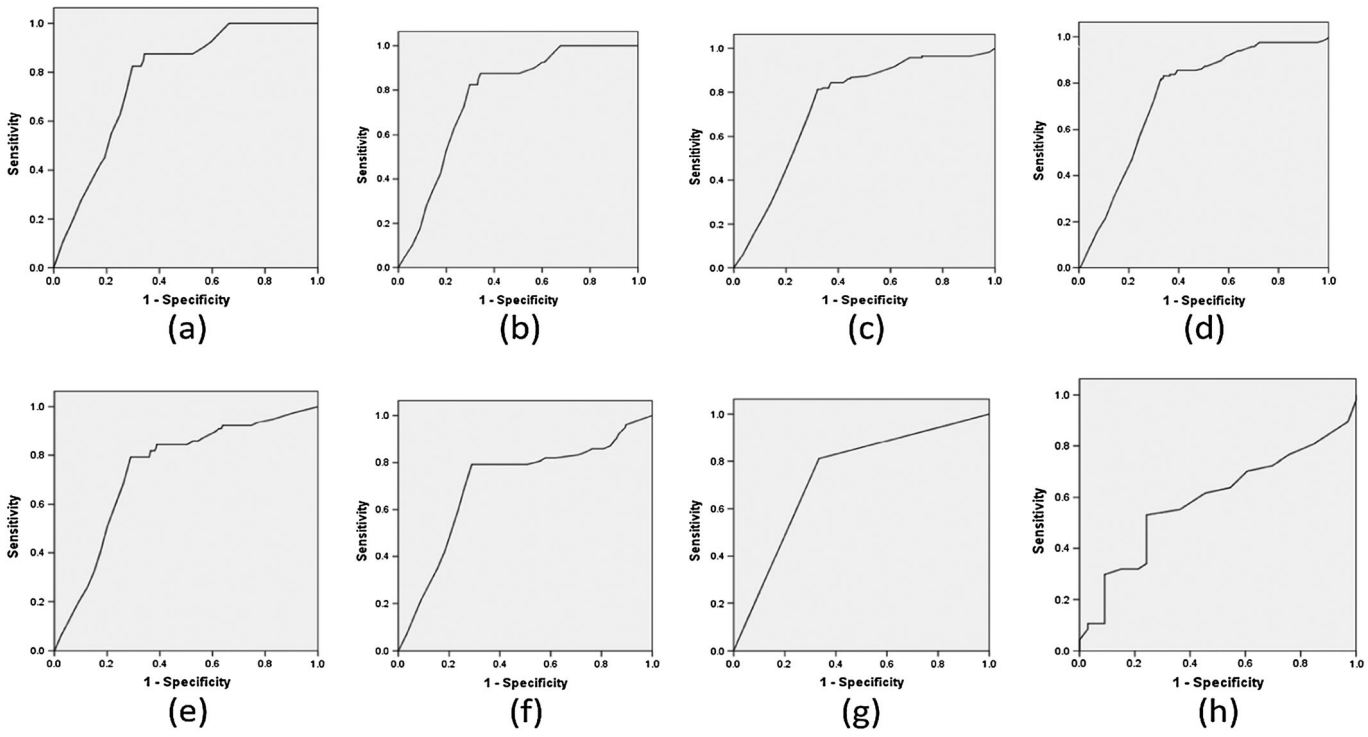


Figure 4: *Receiver operating characteristic curves for binary models: (a) Ivy: random forest; (b) Ivy: multilayer perceptron; (c) Ant: Naïve Bayes; (d) Ant: Random forest; (e) Tomcat: Naïve Bayes; (f) Tomcat: random forest; (g) KC1: support vector; (h) Sakura: multilayer perceptron.*

© 2014 Wiley Publishing Ltd

validation when the thresholds of the metrics of Ivy are validated on the same dataset, whereas Tables 17–19 show the results of interproject validation.

6.2.1. Ivy result analysis Various models are predicted using different machine learning methods such as BayesNet, Naïve Bayes, random forest, support vector classifier and multilayer perceptron. Table 16 shows the results of validation on Ivy dataset as well as results of validation when the dataset is converted into binary (using threshold values of metrics of Ivy). We can observe that the results are comparative for binary and non-binary datasets.

Among the models predicted using non-binary dataset, Naïve Bayes and BayesNet have shown the best results with the highest (same) values for sensitivity (0.75), specificity (0.744) and g-mean (51.17). The AUC for Naïve Bayes, BayesNet and multilayer perceptron are quite high. For multilayer perceptron, the values of sensitivity (0.725) and specificity (0.721) are also reasonably high.

Among the models predicted using the binary dataset, we can see that random forest and multilayer perceptron have outperformed their corresponding non-binary models with higher values for specificity, AUC and g-mean, whereas same values for sensitivity. The values of specificity, AUC and g-mean for the binary model of random forest are 0.724, 0.776 and 49.03, respectively, whereas for binary model of multilayer perceptron, the values are 0.728, 0.773 and 49.23, respectively. These values are reasonably high when compared with the values of their corresponding non-binary models. Their ROC curves are shown in Figure 4. Other binary models have shown comparative results when compared with their corresponding non-binary models, and no model (except support vector) has shown significantly low results. Hence, we can conclude that our proposed methodology of using threshold values stands strong for Ivy dataset as well, in addition to KC1.

6.2.2. Interproject validation We conducted interproject validation (threshold values of metrics obtained from one dataset is applied on other dataset) on the projects of similar nature or having similar characteristics. This helps us to prove the effectiveness and strength of the proposed methodology.

Therefore, as discussed, we considered five open source projects, namely, Ivy, Ant, Tomcat, JEdit and Sakura belonging to two different categories having similar characteristics. We selected these datasets as they are large enough to perform cross validation and also their source code is available in the open source project repositories. Figure 2 clearly demonstrates the projects used for interproject validation.

Category 1: the three projects, namely Ivy, Ant and Tomcat, are categorized together as they have certain features that are common amongst them. Thus, we have validated the threshold results obtained from Ivy software on Ant and Tomcat. In other words, Ant and Tomcat are converted into binary using threshold values of metrics of Ivy.

Similarities: all these are open source software, obtained from Promise data repository. They are released under the Apache Software License. They are written in Java programming language, that is, they have been developed in same environment. Their similarities are summarized in the succeeding text:

Common features
Developer: Apache software Foundation Written in: Java Operating system: cross-platform License: Apache License 2.0

Tables 17 and 18 show the results of validation on Ant and Tomcat dataset, respectively.

For non-binary models of Ant, we can observe that the best results are shown by multilayer perceptron and BayesNet with nearly highest values of sensitivity (0.753) along with highest values for specificity (0.753) and g-mean (65.26). The AUC for multilayer perceptron is highest (0.812), followed by AUC of BayesNet (0.803). The models of Naïve Bayes and BayesNet predicted using binary dataset have shown exactly the same and quite high results. Among all the binary models, random forest has shown the highest specificity (0.729), which is also higher than the specificity of its corresponding non-binary model. Similarly, specificity of binary naïve bayes model (0.708) is also higher than its non-binary model. Thus, overall, we can say that the binary models of Naïve Bayes and random forest have outperformed their corresponding non-binary models and other binary machine learning models have shown comparable performance. Their ROC curves are shown in Figure 4.

For Tomcat non-binary models, all the models have shown good results (except support vector classifier), the best being of BayesNet and multilayer perceptron. The model predicted using BayesNet has shown the highest sensitivity (0.753) along with reasonably high AUC (0.777) and g-mean (44.63). The model predicted using multilayer perceptron has shown highest specificity (0.74), AUC (0.801) and g-mean (46.02). Among the binary models, Naïve Bayes and random forest have shown better performance than their non-binary models with higher values of specificity (0.738) and g-mean (44.36) for Naïve Bayes model, whereas higher values of sensitivity (0.792), g-mean (45.5) and same value of specificity (0.711) for binary random forest model. The ROC curves are shown in Figure 4, for both binary and non-binary models predicted using Naïve Bayes and random forest.

Overall, we can conclude that the binary models predicted using random forest**,** followed by Naïve Bayes (for all the three datasets; Ivy, Ant and Tomcat) have outperformed their non binary models. Thus, validating the threshold values of Ivy on Ant, Tomcat and obtaining significantly

© 2014 Wiley Publishing Ltd

good results give us stronger confirmation and proof of the effectiveness of our proposed methodology.

Category 2: the two projects, namely JEdit and Sakura, are categorized together as they have certain common characteristics. Thus, thresholds obtained using JEdit software have been validated on Sakura.
Similarities: the target domain of these software is same, that is, they are text editors for programmers. The LOC for both these software is also similar (15 227 for Sakura editor and 12 535 for JEdit).

Table 19 shows the results of interproject validation on Sakura dataset using the threshold values of JEdit. We can observe that the results on Sakura dataset (i.e. non binary models) are not so well appreciating as some of the values of sensitivity and specificity are quite low. After converting the dataset into binary (using threshold values of JEdit), we can see comparable results are obtained as are the results of non-binary models. Some of the models have also shown better sensitivity and specificity. As discussed, using thresholds will lead to saving lots of resources (in terms of cost, manpower and time) by helping developers in knowing the classes that fall outside a specified risk level (application/advantage of using threshold methodology is explained in Section 7), thus, we can comment that we should use threshold methodology for obtaining atleast comparable results, if not better.

To summarize, we have carried out interproject validation and concluded that the proposed methodology can be used on the projects having similar characteristics.

7. Application of the work

The most important aim of this work is to study the effect of thresholds on object-oriented metrics. A threshold can be defined as an upper bound such that a metric value greater than its threshold value can be considered problematic and the value lower than threshold value can be considered acceptable. At the design phase of the software development life cycle, when we have metrics available with us, we can compare the values of the metrics with their threshold values and identify the metrics whose value is more than its threshold. Thus, at the design phase, we can suggest alternative design structure and take corrective actions for the classes whose metric values are above the threshold values. In other words, we can predict which classes need careful attention in the development of software. For example, if the value of CBO metric for a particular class is found to be above its threshold value, this means there is high coupling between classes and we can redesign the class to obtain the desired value. This will help in reducing the number of classes that can be prone to faults at a later stage (during testing) in software development life cycle. Thus, lot of resources in terms of money, manpower and time will be saved and will ensure better quality product.

The proposed methodology can be used on different types of datasets like proprietary, private or open source/public datasets. The results must be validated on different datasets in order to obtain generalizable and universally acceptable findings. We have applied the methodology on one proprietary dataset and two public datasets. We have also showed that the methodology gives good results on similar nature of the projects/datasets. Once the thresholds are found for a particular type of dataset, then these thresholds can also be applied on any other dataset of similar nature or having similar characteristics. We have validated the threshold values obtained from one dataset on other datasets of similar nature and obtained comparable and competitive results. These design measurements (values of thresholds of metrics) can be used as quality benchmark to assess and compare products once we know the metrics to be measured (CBO, DIT, LOC, NOC, etc). Thus, we can set quality benchmarks across organizations by conducting more such studies.

8. Threats to validity

We will explain the most important threats to validity. We have used CK object-oriented metrics in our study as independent variables. These metrics have already been validated by various studies (El Emam *et al.*, 2001; Gyimothy *et al.*, 2005; Cruz & Ochimizu, 2009; Singh *et al.*, 2010; Glasberg *et al.*, 2000.) to judge the effectiveness of the these metrics in measuring the concepts they represent. To calculate the metrics for the classes of the datasets, various tools ('ckjm', 'Understand for Java', 'Understand for C') are being used. These tools do not explain the procedure as to how they calculate the values, which is important for accurate estimation of their validity. We have calculated threshold values for the metrics used in this study. But these threshold values cannot be generalized to every organization. This means a threshold value that may be good in one scenario does not imply that it is good for every scenario. Thus, good thresholds depend on various factors such as type of organization, programming language used, and project dependent factors. These are possible threats to construct validity, which is defined as the degree to which the independent and independent variables measure the concepts they propose to measure (Zhou & Leung, 2006). Next, we will report some threats to internal validity, which is based on the casual effect of independent variables on dependent variables. Despite exploring the relationship between OO metrics and fault proneness, we are not focusing on the relationship of various attributes like inheritance, coupling and cohesion on fault proneness in this study. Such relationships can only be evaluated by conducting controlled experiments, in which one of the many measures is varied and other measures are kept constant. Such controlled experiments are difficult to be conducted. Lastly, the threats to external validity are related to the act of generalizing the results of the study to various other products. We cannot

© 2014 Wiley Publishing Ltd

claim that our results can be generalized as we have used only few datasets, that is, we cannot account for various programming languages and working environments. This threat can be removed by replicating our study across different platforms and environments.

9. Conclusion

Object-oriented metrics are being widely used to assure the quality of the software product. Determining the threshold values of object-oriented metrics will help in identification of risky classes earlier in software development life cycle. Threshold can be defined as a value above which risk is high and below which risk is low. In this paper, we have predicted the occurrence of fault prone classes so that focussed attention can be laid on them. The classes predicted to be fault prone can be selected for more and focussed testing by the developers to improve the quality. Thresholds help in early detection of fault prone classes as soon as the values of object-oriented metrics are available. The classes that are predicted to be fault prone can be redesigned or modified so as to bring them within the non-risky category. We have used a methodology based on logistic regression to calculate the threshold values of CK object-oriented metrics. We have used a proprietary NASA dataset, KC1 and two open source Promise datasets, Ivy and JEdit for validation of threshold values. Thresholds are calculated for the metrics of KC1, Ivy and JEdit at different risk levels between 0.01 to 0.15, and results are compared to conclude one of the risk level as the best one. Using the threshold values obtained at the best risk level, binary models are constructed, which are validated using various machine learning methods, that is, BayesNet, NaïveBayes, random forest, support vector classifier and multilayer perceptron. The validation technique used is *K*-cross validation, with the value of *K* as 10. Besides this, interproject validation is also carried out using three open source datasets, Apache Ant, Apache Tomcat and Sakura. We concluded the following from our study:

(1) Univariate logistic regression is conducted to find the metrics significant to fault proneness. As threshold values are calculated for the metrics of KC1, Ivy and JEdit, univariate logistic regression is applied on these datasets. We found CBO, RFC, WMC and LOC metrics to be significant to fault proneness for both KC1 and Ivy datasets. In addition to these metrics, LCOM is also found to be significant for JEdit dataset. These metrics can be used by researchers in their studies to bring out effective results.
(2) For KC1, the best risk level that gave threshold values of all the metrics within the observation range (i.e. positive values) is 0.15. This means for classes with metric values lower than corresponding threshold values, the probability of fault occurrence is lower than 15%. The threshold values of object-oriented metrics at risk level 0.15 are 7.17 for CBO metric, 2.88 for RFC metric, 4.74 for WMC metric and 119.93 for LOC metric.
    For Ivy, the threshold values at the risk level 0.07 and higher are within the observation range of all the metrics. But we selected the lowest considerable value, that is, 0.07 as the appropriate risk level. This is because at risk level of 0.07, the risk of fault occurrence is lower than the probability of 7%. As the value of risk level increases, risk of fault occurrence also increases. Hence, lowest possible value is appropriate to be considered.
    For JEdit, we can observe the lowest risk level for which all the threshold values are within the range is 0.02. The threshold values at 0.02 risk level are 14.49, 15.96, 50.39, 174.18 and 245.18 for the metrics WMC, CBO, RFC, LCOM and LOC, respectively.
(3) Results of validation on KC1 dataset concluded support vector classifier to be the best machine learning method that can be used by researchers and practitioners for validating other projects. The results of support vector classifier showed high g-mean (69.59) and AUC (0.693). When the data is converted to binary using threshold values of KC1, the model showed higher g-mean (72.08) and AUC (0.739). Results of validation on Ivy dataset concluded that the binary models predicted using random forest and multilayer perceptron have outperformed their corresponding non-binary model. The models predicted using other machine learning methods have shown comparative results.
(4) Interproject validation carried out by validating the threshold values of Ivy on Ant and Tomcat, whereas threshold values of JEdit on Sakura concluded that the proposed threshold methodology can be used on the projects of similar characteristics or similar nature.

Overall, we concluded that calculating threshold values of metrics and then validating the model is an effective methodology.

References

AGGARWAL, K.K., Y. SINGH, A. KAUR and R. MALHOTRA (2005) Software reuse metrics for object-oriented systems. in *Proceedings of the Third ACIS Int'l Conference On Software Engineering Research, Management and Applications (SERA '05)*, Michigan, USA: IEEE, 48–55.

AGGARWAL, K.K., Y. SINGH, A. KAUR and R. MALHOTRA (2009) Empirical analysis for investigating the effect of object-oriented metrics on fault proneness: a replicated case study, *Software Process: Improvement and Practice*, **16**, 39–62. DOI: 10.1002/spip.389s

BASILI, V., L. BRIAND and W. MELO (1996) A validation of object-oriented design metrics as quality indicators, *IEEE Transactions on Software Engineering*, **22**, 751–761. DOI: 10.1109/32.544352

BENDER, R. (1999) Quantitative risk assessment in epidemiological studies investigating threshold effects, *Biometrical Journal*, **41**, 305–319.

BIEMAN, J. and B. KANG (1995) Cohesion and reuse in an object-oriented system, in *Proceedings of the ACM Symposium on Software Reusability (SSR'94)*, ACM, 259–262.

BRIAND, L., W. DALY and J. WUST (1998) Unified framework for cohesion measurement in object-oriented systems, *Empirical Software Engineering*, **3**, 65–117. DOI: 10.1023/A:1009783721306

© 2014 Wiley Publishing Ltd

BRIAND, L., W. DALY and J. WUST (1999) A unified framework for coupling measurement in object-oriented systems, *IEEE Transactions on Software Engineering*, **25**, 91–121. DOI: 10.1109/32.748920

BRIAND, L., W. DALY and J. WUST (2000) Exploring the relationships between design measures and software quality, *Journal of Systems and Software*, **51**, 245–273. DOI: 10.1016/S0164-1212(99)00102-8

BRIAND, L., J. WÜST and H. LOUNIS (2001) Replicated case studies for investigating quality factors in object-oriented designs. Empirical software engineering, *International Journal (Toronto, Ontario)*, **6**, 11–58.

BRIAND, L., P. DEVANBU and W. MELO (1997) An investigation into coupling measures for C++, in *Proceedings of the 19th International Conference on Software Engineering*, Boston: ACM, 412–421.

CARTWRIGHT, M. (1998) An empirical view of inheritance, *Information and Software Technology*, **40**, 795–799.

CARTWRIGHT, M. and M. SHEPPERD (1999) An empirical investigation of an object-oriented software system, *IEEE Transactions on Software Engineering*, **26**, 786–796. DOI: 10.1109/32.879814

CATAL, C. and B. DIRI (2009) A systematic review of software fault prediction studies, *Expert Systems with Applications*, **36**, 7346–7354.

CHIDAMBER, S. and C. KEMERER (1991) Towards a metrics suite for object oriented design, in *Proceedings of the Conference on Object-Oriented Programming: Systems, Languages and Applications (OOPSLA'91)*, SIGPLAN Notices, Phoenix, Arizona: ACM, **26**, 197–211.

CHIDAMBER, S. and C. KEMERER (1994) A metrics suite for object-oriented design, *IEEE Transactions on Software Engineering*, **20**, 476–493. DOI: 10.1109/32.295895

CRUZ, A.E.C. and K. OCHIMIZU (2009) Towards logistic regression models for predicting fault-prone code across software projects, Third International Symposium on Empirical Software Engineering and Measurement, Lake Buena Vista, FL: IEEE, 460–463.

DALY, J., A. BROOKS, J. MILLER, M. ROPER and M. WOOD (1996) Evaluating inheritance depth on the maintainability of object-oriented software, *Empirical Software Engineering*, **1**, 109–132.

EL EMAM, K. and W. MELO (1999) The prediction of faulty classes using object-oriented design metrics, Technical report: NRC 43609.

EL EMAM, K., S. BENLARBI, N. GOEL and S. RAI (1999) A validation of object-oriented metrics, Technical report ERB-1063, NRC.

BENLARBI, S., K. EL EMAM, N. GOEL and S. RAI (2000) Thresholds for object-oriented measures, in *Proc. 11th Int'l Symp. Software Reliability Eng*, San Jose, CA: IEEE, 24–38.

EL EMAM, K., W. MELO and J.C. MACHADO (2001) The prediction of faulty classes using object-oriented design metrics, *The Journal of Systems and Software*, **56**, 63–75.

EL EMAM, K., S. BENLARBI, N. GOEL, W. MELO, H. LOUNIS and S. RAI (2002) The optimal class size for object-oriented software, *IEEE Trans. Software Eng*, **28**, 494–509.

FENTON, N. and N. OHLSSON (2000) Quantitative analysis of faults and failures in a complex software system, *IEEE Transactions on Software Engineering*, **26**, 797–814.

GLASBERG, D., K. EL EMAM, W. MELO and N. MADHAVJI (2000) Validating object-oriented design metrics on a commercial java application, Technical report: NRC 44146.

GONDRA, I. (2008) Applying machine learning to software fault-proneness prediction, *The Journal of Systems and Software*, **81**, 186–195.

GYIMOTHY, T., R. FERENC and I. SIKET (2005) Empirical validation of object-oriented metrics on open source software for fault prediction, *IEEE Transactions on Software Engineering*, **31**, 897–910.

HARRISON, R., S. COUNSELL and R. NITHI (2000) Experimental assessment of the effect of inheritance on the maintainability of object-oriented systems, *Journal of Systems and Software*, **52**, 173–179.

HE, Z., F. SHU, Y. YANG, M. LI and Q. WANG (2012) An investigation on the feasibility of cross-project defect prediction, *Automated Software Engineering*, **19**, 167–199. DOI: 10.1007/s10515-011-0090-3

HERBOLD, S., J. GRABOWSKI and S. WAACK (2011) Calculation and optimization of thresholds for sets of software metrics, *Empirical Software Engineering*, **16**, 812–841. DOI: 10.1007/s10664-011-9162-z

HOSMER, D. and S. LEMESHOW (1989) Applied Logistic Regression, New York: Wiley.

JURECZKO, M. and L. MADEYSKI (2010) Towards identifying software project clusters with regard to defect prediction, in *Proceedings of the 6th International Conference on Predictive Models in Software Engineering,* Timisoara, Romania: ACM, 9. DOI: 10.1145/1868328.1868342

JURECZKO, M. and D. SPINELLIS (2010) Using object-oriented design metrics to predict software defects, *Models and Methods of System Dependability*, *Proceedings of RELCOMEX 2010: Fifth international Conference on Dependability of Computer Systems, Monographs of System Dependability*, Wroclaw, Poland, 69–81.

KANMANI, S., V.R. UTHARIARAJ, V. SANKARANARAYANAN and P. THAMBIDURAI (2007) Object-oriented software prediction using neural networks, *Information and Software Technology*, **49**, 482–492.

KUBAT, M. and S. MATWIN (1997) Addressing the curse of imbalanced training sets: one-sided selection, in *Proc. 14th Int'l Conf. Machine Learning*, Nashville, USA: Morgan Kaufmann, 179–186.

LEE, Y., B. LIANG, S. WU and F. WANG (1995) Measuring the coupling and cohesion of an object-oriented program based on information flow, in *Proceedings of the International Conference on Software Quality*, Maribor, Slovenia.

LI, W. and S. HENRY (1993) Object-oriented metrics that predict maintainability, *Journal of Systems and Software*, **23**, 111–122. DOI: 10.1016/0164-1212(93)90077-B

LORENZ, M. and J. KIDD (1994) Object-Oriented Software Metrics, Englewood Cliffs, NJ: Prentice-Hall.

NASA. (2000) Metrics data repository, http://www.mdp.ivv.nasa.gov. (accessed on May, 2013)

OHLSSON, N., M. ZHAO and M. HELANDER (1998) Application of multivariate analysis for soft ware fault prediction, *Software Quality Journal*, **7**, 51–66.

PAI, G. (2007) Empirical analysis of software fault content and fault proneness using Bayesian methods, *IEEE Transactions on Software Eng*, **33**, 675–686.

PRECHELT, L., B. UNGER, M. PHILIPPSEN and W. TICHY (2003) A controlled experiment on inheritance depth as a cost factor for code maintenance, *Journal of Systems and Software*, **65**, 115–126.

Scitools (1996-2013) http://www.scitools.com/index.php. (accessed May, 2013)

SHATNAWI, R. (2010) A quantitative investigation of the acceptable risk levels of object-oriented metrics in open-source systems, *IEEE Transactions on Software Engineering*, **36**, 216–225.

SHATNAWI, R. and W. LI (2008) The effectiveness of software metrics in identifying error-prone classes in post release software evolution process, *The Journal of Systems and Software*, **81**, 1868–1882.

SINGH, Y., A. KAUR and R. MALHOTRA (2010) Empirical validation of object-oriented metrics for predicting fault proneness models, *Software Quality Journal*, **18**, 3–35.

TANG, M.H., M.H. KAO and M.H. CHEN (1999) An empirical study on object-oriented metrics, in *Proceedings of the 6th International Symposium on Metrics*, Boca Raton, FL: IEEE, 242–249.

WATANABE, S., H. KAIYA and K. KAIJIRI (2008) Adapting a fault prediction model to allow inter language reuse, in *Proceedings of the 4th international workshop on Predictor*

 © 2014 Wiley Publishing Ltd

models in software engineering, Leipzig, Germany: ACM, 19–24. DOI: 10.1145/1370788.1370794

ZHOU, Y. and H. LEUNG (2006) Empirical analysis of object-oriented design metrics for predicting high and low severity faults, *IEEE Transactions on Software Engineering*, **32**, 771–789.

The authors

Ruchika Malhotra

Ruchika Malhotra is an assistant professor at the Department of Software Engineering, Delhi Technological University (formerly known as Delhi College of Engineering), Delhi, India. She was an assistant professor at the University School of Information Technology, Guru Gobind Singh Indraprastha University, Delhi, India. Prior to joining the school, she worked as full-time research scholar and received a doctoral research fellowship from the University School of Information Technology, Guru Gobind Singh Indraprastha, Delhi, India. She received her master's and doctorate degrees in software engineering from the University School of Information Technology, Guru Gobind Singh Indraprastha University, Delhi, India. Her research interests are in software testing, improving software quality, statistical and adaptive prediction models, software metrics, neural nets modeling, and the definition and validation of software metrics. She has published more for than 50 research papers in international journals and conferences.

Ankita Jain Bansal

Ankita Jain Bansal is a research scholar with the Delhi Technological University (formerly Delhi College of Engineering), Delhi, India. She received her master's degree in computer technology and applications (CTA) from Delhi Technological University. Her research interests are software quality, software metrics, and statistical and machine learning models. She has published several papers in international journals and conferences.

© 2014 Wiley Publishing Ltd

3 Biotech
DOI 10.1007/s13205-014-0247-4

ORIGINAL ARTICLE

In silico analysis and modeling of putative T cell epitopes for vaccine design of Toscana virus

Amisha Jain · Pranav Tripathi · Aniket Shrotriya · Ritu Chaudhary · Ajeet Singh

Received: 20 May 2014 / Accepted: 6 August 2014
© The Author(s) 2014. This article is published with open access at Springerlink.com

Abstract The sandfly fever Toscana virus is an important etiological agent known to cause human neurological infections in endemic Mediterranean countries during summer season. In the present study, prediction and modeling of T cell epitopes of Toscana virus (TOSV) antigenic proteins followed by the binding simulation studies of predicted highest binding scorers with their corresponding MHC class II alleles were done. Immunoinformatics was applied in computational vaccinology to analyze the viral proteins which generate possible outcomes to elicit vaccine for TOSV. Here, immunoinformatic tool ProPred was used to predict the promiscuous MHC class II epitopes of viral antigenic proteins. The molecular modeling of the selected epitopes as well as MHC alleles was done at CPH model 3.2 server. Molecular dynamics (MD) simulation studies were performed through the NAMD graphical user interface embedded in visual molecular dynamics. The epitope/peptide VKMMIVLNL of viral nucleoprotein as well as VMILGLLSS of viral glycoprotein has shown the highest binding score with the same DRB1*1104 MHC II allele. These two predicted peptides are highly potential to induce T cell-mediated immune response and are expected to be useful in designing epitope-based vaccines after further testing. The results signify that the nucleoprotein, glycoprotein or the combination of both could be useful for future development of a vaccine controlling the spread of this emerging virus that could pose a new threat for humans.

A. Jain · P. Tripathi · R. Chaudhary · A. Singh (✉)
Department of Biotechnology, G B Pant Engineering College, Pauri Garhwal, Uttarakhand, India
e-mail: ajeetsoniyal@gmail.com

A. Shrotriya
Department of Biotechnology, Delhi Technological University, Delhi, India

Published online: 26 August 2014

Keywords Toscana virus · ProPred · Structural modeling · Docking · Molecular dynamics · Vaccine design

Introduction

Toscana virus (TOSV) is an arbovirus (arthropod-borne virus), which belongs to the family *Bunyaviridae* and genus *Phlebovirus* (Bishop et al. 1990; Elliott et al. 1991). There are at least 45 members of the Phlebovirus genus, which are mostly transmitted to vertebrates by phlebotomine sandflies. Its genome is comprised of an enveloped negative-strand RNA that consists of three segments, designated as large (L), medium (M) and small (S), which encodes the viral RNA polymerase, the envelope glycoprotein and the nucleoprotein, respectively (Olal et al. 2014). The segment L is the largest about 6,400 nucleotides, M is about 4,200 nucleotides and S about 1,900 nucleotides in length. TOSV is among the three most prevalent viruses associated with meningitis during the warm seasons and, therefore, must be considered as an emerging pathogen. Currently, there is no effective antiviral treatment or vaccine for the infection caused by TOSV; the best prevention will likely to come by development of effective and safe vaccine.

Naples and *Sicilian* serocomplexes are the two main serocomplexes of sandfly fever viruses associated with human diseases. Sandfly fever Toscana virus (SFTV) belongs to *Naples* serocomplex and is endemic in Mediterranean countries like Italy, Portugal, Spain, and Cyprus. Within the group of sandfly-transmitted *phleboviruses*, TOSV is the only virus known to cause Central Nervous System (CNS) manifestations (Braito et al. 1998; Cusi et al. 2010). Data from Italy, France and Spain indicate that it is among the three leading causes of aseptic meningitis during periods of sandfly activity (Charrel et al. 2005). The

other viruses are associated with systemic febrile illness, but not CNS infections. TOSV is the most important etiologic agent of meningitis, meningoencephalitis, or encephalitis associated with fever, severe frontal headache, vomiting, myalgia, ocular pain and, nuchal rigidity (Braito et al. 1998; Dionisio et al. 2001; Nicoletti et al. 1991; Valassina et al. 1998; 2000).

Vaccination is generally considered as a cost-effective weapon for preventing life-threatening infectious diseases. Awareness of differences in epitopes recognized by T cells and B cells has enabled immunologists to begin designing vaccine candidates to maximize activation of both arms of the immune system. Major histocompatibility complex (MHC) plays an important role in intercellular recognition of foreign antigenic peptides and thus participates in the development of both humoral and cell-mediated immune responses. T cells are present on the surface of antigen-presenting cells (APCs) and they recognize antigenic fragments only when they are combined with MHC molecules exposed on the surface of all vertebrate cells (Shekhar et al. 2012; Mohabatkar and Mohammadzadegan 2007). MHC molecules are heterodimeric glycoproteins which present a highly diverse set of peptides on the surface of a cell and thus induce T cell activation, hence play a profound role in immune response regulation (Viret and Janeway 1999; Tambunan and Parikesit 2011). As they are highly polymorphic in nature, the binding region for one allele may not induce an immune response in a population with different alleles. This raises the need for the identification of promiscuous viral peptides which can bind to multiple MHC alleles (Jiao et al. 2012).

Epitope- or peptide-based vaccines offer several advantages over conventional vaccines as they are more specific, easy to produce, cost-effective, less time-consuming and also safe. Apart from these, the main advantage of epitope- or peptide-based vaccine is the ability to deliver high doses of potential immunogen at low cost (Von Hoff et al. 2005; Tang et al. 2012). The viral protein that could act as a vaccine candidate must be antigenic and responsible for pathogenicity (Cerdino-Tarraga et al. 2003; Verma et al. 2011).

Materials and methods

Retrieval of Toscana virus antigenic proteins

The complete sequences of viral nucleoprotein (NP) and glycoprotein (GP) were retrieved from National Center for Biotechnology Information (NCBI), having accession code, ABY19521 and AGP51529, with length 253 and 1,339 amino acids, respectively (http://www.ncbi.nlm.nih.gov/protein).

T cell epitope prediction by ProPred

Several different prediction methods have been employed for the identification of promiscuous T cell epitopes. Identification of various T cell epitopes by more than one MHC allele and their recognition by more than one T cell clone are known as "promiscuous" epitopes. ProPred, the graphical web-based tool was used in this study to predict MHC class II binding regions in an antigenic sequence, using quantitative matrices that assist in locating promiscuous binding regions that are useful in selecting vaccine candidates (Sturniolo et al. 1999). In ProPred, the NP and GP sequences were analyzed, taken into consideration a total of 51 MHC class II alleles. Each nonamer comprises an anchor or starting residue that helps to identify those antigenic determinants in NP and GP which binds to several Human Leukocyte Antigen (HLA) class II molecules with good binding affinity. The predicted binders can be visualized either as peaks in graphical interface or as colored residues in HTML interface. Peptides displaying highest score were selected for immunoinformatic analysis.

Modeling and validation of favored MHC II alleles and epitopes

The NP epitope (VKMMIVLNL) and GP epitope (VMILGLLSS) of TOSV were modeled at CPH model 3.2 server. The 3-D structure of DRB1*1104 MHC allele was unavailable in the Protein Data Bank (PDB) server, therefore, CPH model 3.2 server was used to acquire its three-dimensional coordinate files employing its respective structural template (1A6A.B). The structure of MHC allele was then validated using various online structural analysis and verification servers, viz., Errat, ProQ, ProSA, RAMPAGE, etc. Errat (Colovos and Yeates 1993), a protein structure verification algorithm was especially used to analyze the statistics of non-bonded interactions between different atom types. The quality of a protein model was predicted by a protein quality predictor tool, ProQ (Wallner and Elofsson 2003) on the basis of two quality measures, LG score and MaxSub. A web-based Protein Structure Analysis tool ProSA (Wiederstein and Sippl 2007) calculates an overall quality score of specific protein structure by determining the overall model quality (Z-score) and local model quality. RAMPAGE (Lovell et al. 2002) was used for Ramachandran Plot Assessment of protein model.

Binding simulation of epitopes with the alleles

After structural modeling, rigid docking of selected peptides and alleles was accomplished with the help of Hex 8.0 (Ritchie et al. 2008) followed by semi-flexible docking using AutoDock Vina (Trott and Olson 2010) to determine

the energy minimization values. In Hex, the prediction of energy minimization is based on various parameters including correlation type of shape only, 3-D FFT mode, Grid dimension of 0.6, receptor range of 180 with step size 7.5 and ligand range of 180 with step size 7.5. Semi-flexible docking was achieved using AutoDock Vina which involves choosing of macromolecule, adding polar H-bonds, computing Gasteiger, and Kollman charges for the receptor. Then, for ligand all bonds, except amide bonds, were made rotatable. The docked complexes were finally visualized and analyzed using Autodock Tools.

Molecular dynamics simulation of epitope and HLA allele complex

Molecular dynamics simulation was done using NAMD graphical interface module (James et al. 2005) incorporated visual molecular dynamics (VMD) (Humphrey et al. 1996). Automatic PSF builder tool of VMD was used to make the PSF file and by accessing PSF and PDB files, NAMD generated the trajectory DCD file. Root Mean Square Deviation (RMSD) of the complex was completed using rmsd.tcl source file from the Tk console and finally rmsd.dat was saved and accessed in Microsoft office excel 2007.

Results

Prediction and analysis of MHC Class II binding peptides

The NP peptide VKMMIVLNL at position 58–66 showed maximum binding score of 62.65 with DRB1*1104 MHC II allele. The GP peptide VMILGLLSS at position 824–832 showed maximum binding score of 73.49 with the same DRB1*1104 allele. ProPred scores and the no. of MHC II alleles showing binding affinities for epitopes are shown below (Table 1).

Modeling and validation of target peptides and MHC allele

3-D coordinate files of preferred peptides and allele were obtained through CPH model server. The structure of DRB1*1104 allele was validated using Errat, ProQ, ProSA, and RAMPAGE web-based tools. The overall quality factor of allele as determined by Errat was found to be 67.039. Quality of a model as predicted by ProQ was 'fairly good' with LG score of 2.096 and MaxSub of 0.131. Using ProSA, the calculated Z-score of above-mentioned allele was −5.52 (Fig. 1) and the local model quality was also good to consider. Through RAMPAGE analysis, the number of amino acid residues in favored region was 177 (95.7 %) out of 187 amino acid residues.

Binding energy determination by Hex 8.0 and AutoDock Vina

Binding simulation studies of NP epitope VKMMIVLNL with DRB1*1104 allele as well as GP epitope VMILGLLSS with DRB1*1104 allele formed stable HLA–peptide complexes with the energy minimization values of −5.5 and −6.0 kcal/mol, respectively (Table 2). After docking studies, we determined the number of H-bonds present in the stable complex formed. Using AutoDock Vina, it was found that two H-bonds were present in NP-DRB1*1104 complex at positions CYS44:HN1 and GLY154:HN1 (Fig. 2), whereas two H-bonds were present in GP-DRB1*1104 complex at positions CYS44:HN1 and PHE46:HN1 (Fig. 3). While using Hex 8.0, the predicted number of H-bond was 1 in both the complexes with good E-total values. Thus, it shows maximum probability of proper binding as there is possibility of formation of H-bonds.

Molecular dynamics simulation of peptide–allele complex through NAMD

The peptide–allele complexes formed by Hex 8.0 were subjected to molecular dynamics simulation and RMSD. NP peptide VKMMIVLNL-DRB1*1104 allele complex displayed the highest peak at RMSD value of 6.8 Å (Fig. 4). On the other hand, GP peptide VMILGLLSS-DRB1*1104 allele complex resulted in highest peak at RMSD value of 11 Å (Fig. 5). As displayed by the graph, the NP–allele complex runs till 10,500 picoseconds, while the GP–allele complex runs till 6,000 picoseconds which is lesser than the time value of NP–allele complex.

Table 1 Scores generated by ProPred

Protein	Position	Peptide/epitope	ProPred Score	HLA alleles	No. of reactivated MHC alleles
NP	58–66	VKMMIVLNL	62.65	DRB1*1104	51
GP	824–832	VMILGLLSS	73.49	DRB1*1104	49

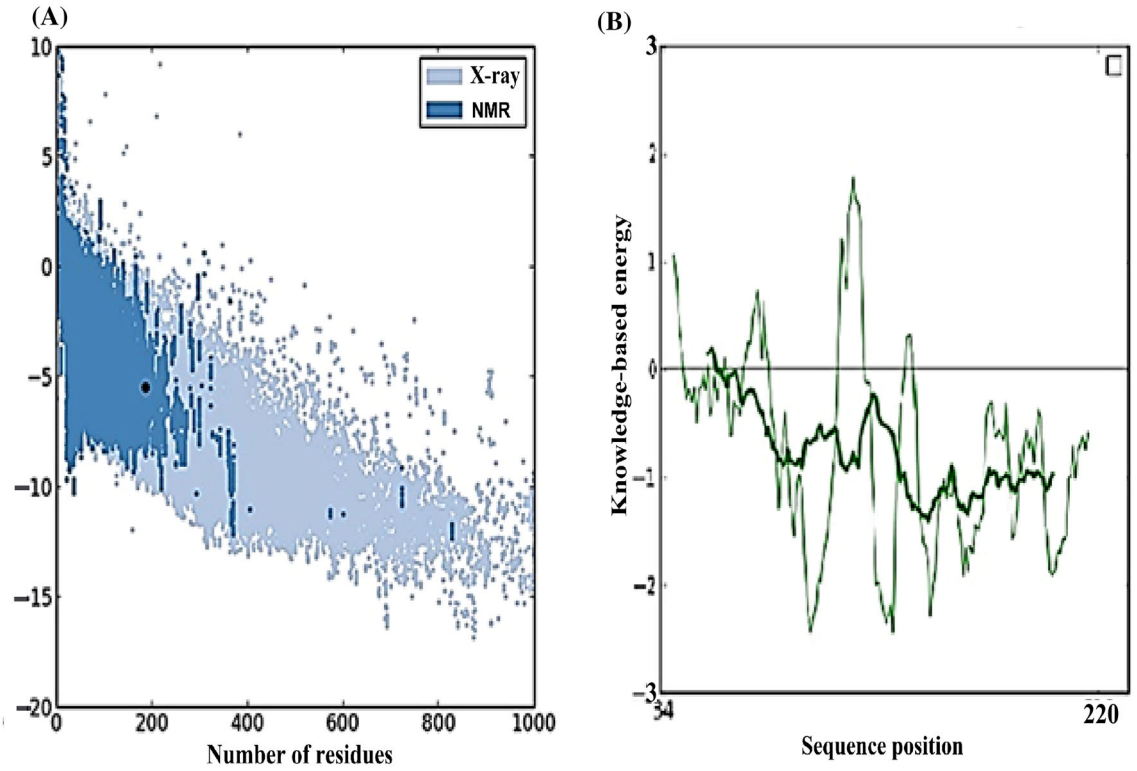


Fig. 1 ProSA analysis. **a** Z-score plot of DRBI*1104 allele. **b** Graphical plot of residue scores of allele structure

Table 2 Energy minimization results of docking studies with Hex 8.0 and Autodock Vina followed by the identification of H-bonds

Protein	Peptide/Epitope	Hex 8.0		Autodock Vina		HLA alleles
		E-total	H-bonds	Energy	H-bonds	
NP	VKMMIVLNL	−446.19	1	−5.5	2	DRB1*110
GP	VMILGLLSS	−301.04	1	−6.0	2	DRB1*1104

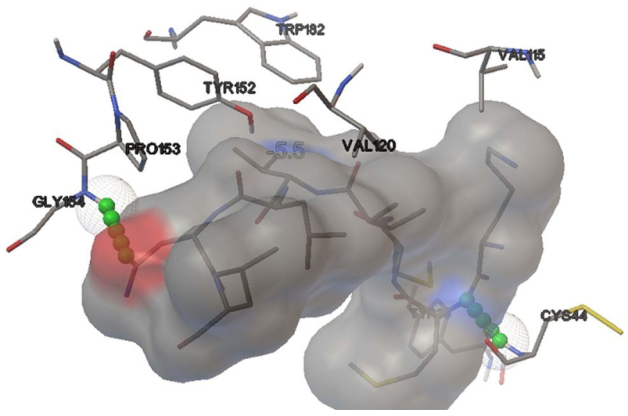


Fig. 2 Docked NP peptide VKMMIVLNL-DRB1*1104 allele complex by Autodock Vina depicting detailed position of amino acids along with formation of 2 H-bonds with CYS44 and GLY154

Discussion

The pathogenic activity of Toscana virus creates a challenge to develop novel vaccines. Addressing these challenges involves a time-consuming battery of in vivo and in vitro experiments. The growth of virus and isolation of peptides on a large array of experiments is also a huge and valid constraint. The current study incorporates immunoinformatics approach for reducing the time consumed in the long array of experiments to avoid hit and trial sets. Valassina et al. 2003 reported the antigenic properties of the viral proteins (NP and GP) to better understand their immunogenic role. It has been also reported that the viral NP is highly immunogenic for many members in the genus of *Phlebovirus* and is a major antigen that acts as a scaffold for packing of virus (Martin-Folgar et al. 2010; Magurano et al. 1999). A glycoprotein of length 1,339 amino acids

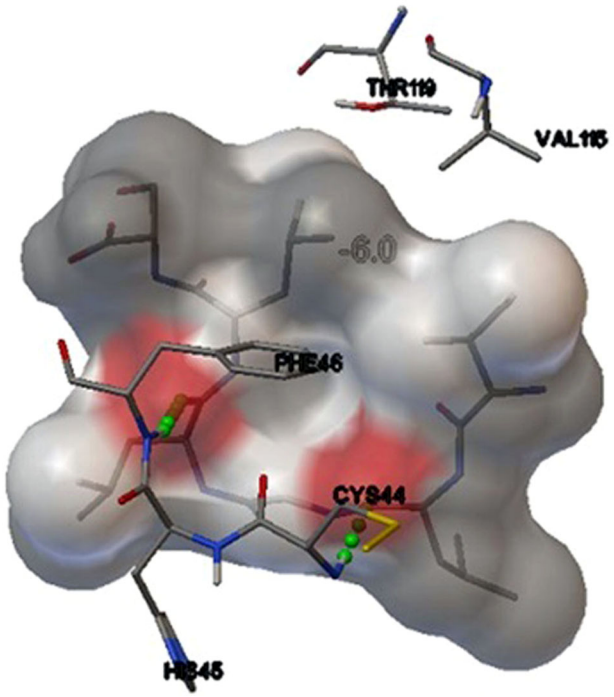


Fig. 3 Docked GP peptide VMILGLLSS-DRB1*1104 allele complex depicting position of amino acids along with formation of 2 H-bonds with CYS44 and PHE46

has possibility of holding large number of epitopes. So, two proteins, one 253 amino acids long (NP) and the other 1,339 amino acids long (GP), was taken into consideration, so that T cell bound MHC II epitopes can be predicted. Only one sequence variant for each of the two proteins was studied because NP is highly conserved and according to Collao et al. 2009 geographic differences in genotype distribution relate to differences in vector distribution only. For nucleoprotein, VKMMIVLNL peptide was predicted with the highest score of 62.65 % with DRB1*1104 allele. The homology modeling of the above-mentioned allele was satisfactorily validated with an Errat score of 67.039, LG score of 2.096 by ProQ, Z-score of −5.52 by ProSA. Ramachandran plot analysis through RAMPAGE resulted in 177 (95.7 %) amino acids in favored region. The rigid docking approach was carried out successfully by Hex 8.0 on a correlation type of shape in 3-D FFT mode. The E-total value of the predicted peptide was −446.19 using Hex 8.0. Semi-flexible approach used AutoDock Vina at default parameters which resulted in binding affinity of −5.5 kcal/mol along with two H-bonds. First H-bond was detected with CYS44:HN1 and second was predicted with GLY154:HN1. The molecular dynamics simulation showed that complex formed between a peptide and allele was attaining proper stability by creating a parallelism in

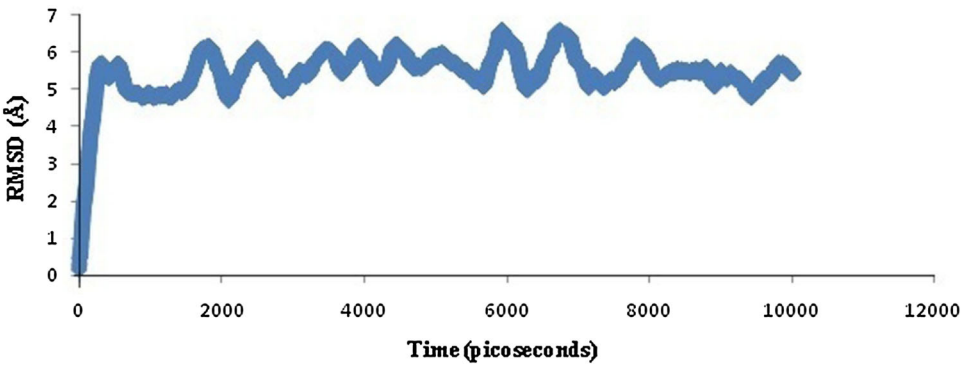


Fig. 4 Graph displaying molecular dynamic simulation of NP–allele complex, resulted in highest peak at 6.8 Å

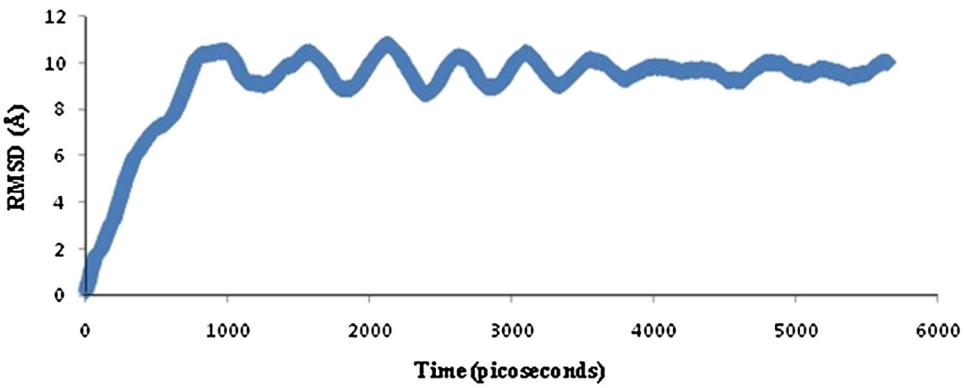


Fig. 5 Graph displaying molecular dynamic simulation of GP–allele complex, resulted in highest peak at 11 Å

RMSD over a time window of 10,500 picoseconds, with the highest peak at 6.8 Å.

For glycoprotein, VMILGLLSS peptide was predicted with highest score of 73.49 % and activating same allele as by the nucleoprotein. The homology modeling of above-mentioned allele was already completed satisfactorily, so rigid docking approach was initiated by Hex 8.0 on a correlation type of shape in 3-D FFT mode. E-total value of the predicted peptide was −301.04. Autodock Vina at default parameters resulted into binding affinity of −6.0 kcal/mol along with two H-bonds, first with CYS44:HN1 and second was predicted with PHE46:HN1. The molecular dynamics simulation here also showed proper stability over a time window of 6000 picoseconds in all the frames, with the highest peak at 11 Å.

It is observed that peptides from NP as well as GP activating the same allele were providing a solid base to the prediction for vaccine design. The mentioned peptides can be either isolated or formulated for further in vitro and in vivo testings.

Conclusion

The conclusion drawn from present study is that the two nonameric epitopes VKMMIVLNL and VMILGLLSS of NP and GP, respectively, have considerable binding with DRB1*1104 MHC class II allele and low-energy minimization values providing stability to the peptide–MHC complex. These peptide constructs may further be undergone wet lab studies for the development of targeted vaccine against Toscana virus. This would reduce the time and expenses of in vivo and in vitro experiments.

Acknowledgments This study was conducted in the Department of Biotechnology, G.B. Pant Engineering College (GBPEC), Pauri Garhwal (Uttarakhand). Authors gratefully acknowledge the necessary computational facilities and constant supervision provided by the Department of Biotechnology, GBPEC. Amisha Jain is thankful to AICTE (All India Council for Technical Education, New Delhi, India) for fellowship.

Conflict of interest Authors have no conflict of interest regarding the publication of paper.

Open Access This article is distributed under the terms of the Creative Commons Attribution License which permits any use, distribution, and reproduction in any medium, provided the original author(s) and the source are credited.

References

Bishop DHL, Knipe BN, Chanock RM, Hirsch MS, Melnick JL, Monath TP, Roizman B (1990) *Bunyaviridae* and their replication, Part 1: *Bunyaviridae*. In: Fields virology, 2nd edn, vol 1. Raven Press, New York, pp 1155–1173

Braito A, Corbisiero R, Corradini S, Fiorentini C, Ciufolini MG (1998) Toscana virus infections of the central nervous system in children: a report of 14 cases. J Pediatr 132:144–148

Cerdino-Tarraga AM, Efstratiou A, Dover LG, Holden MTG, Pallen M (2003) The complete genome sequence and analysis of *Corynebacterium diphtheria* NCTC13129. Nucleic Acids Res 31:6516–6523

Charrel RN, Gallian P, Navarro-Mari JM, Nicoletti L, Papa A, Sanchez-Seco MP, Tenorio A, De Lamballerie X (2005) Emergence of Toscana virus in Europe. Emerg Infect Dis 11:1657–1663

Collao X, Palacios G, Sanbonmatsu-Gámez S, Pérez-Ruiz M, Negredo AI, Navarro-Marí J, Grandadam M, Aransay AM, Lipkin WI, Tenorio A, Sánchez-Seco M (2009) Genetic diversity of Toscana virus. Emerg Infect Dis 15:574–577

Colovos C, Yeates TO (1993) Verification of protein structures: patterns of non-bonded atomic interactions. Protein Sci 2:1511–1519

Cusi MG, Savellini G, Zavelli G (2010) Toscana virus epidemiology from Italy to beyond. Open virol I 4:22–28

Dionisio D, Valassina M, Ciufolini MG, Vivarelli A, Esperti F, Cusi MG, Mazzoli F, Lupi C (2001) Encephalitis without meningitis due to sandfly fever virus serotype Toscana. Clin Infect Dis 32:1241–1248

Elliott RM, Schmaljohn CS, Collett MS (1991) *Bunyaviridae* genome structure and gene expression. Curr Top Microbiol Immunol 169:91–114

Humphrey W, Dalke A, Schulten K (1996) VMD—visual molecular dynamics. J Mol Graphics 14:33–38

James CP, Braun R, Wang W, Gumbart J, Tajkhorshid E, Villa E, Chipot C, Skeel RD, Kale L, Schulten K (2005) Scalable molecular dynamics with NAMD. J Comput Chem 26:1781–1802

Jiao W, Yin W, Li X, Liu J (2012) Research advancement in RV novel vaccine. Asian J Anim Vet Adv 7:1234–1244

Lovell SC, Davis IW, Arendall WB III, De Bakker PIW, Word JM, Prisant MG, Richardson JS, Richardson DC (2002) Structure validation by Calpha geometry: phi, psi and Cbeta deviation. Proteins 50:437–450

Magurano F, Nicoletti L (1999) Humoral response in Toscana virus acute neurologic disease investigated by viral-protein-specific immunoassays. Clin Diagn Lab Immunol 6:55–60

Martin-Folgar R, Lorenzo G, Boshra H, Iglesias J, Mateos F (2010) Development and characterization of monoclonal antibodies against Rift Valley fever virus nucleocapsid protein generated by DNA immunization. MAbs 2:275–284

Mohabatkar H, Mohammadzadegan R (2007) Computational comparison of T-cell epitopes of GP 120 of Iranian HIV-1 with different subtypes of the virus. Pak J Biol Sci 10:4295–4298

Nicoletti L, Verani P, Caciolli S, Ciufolini MG, Renzi A, Bartolozzi D, Paci P, Leoncini F, Padovani P, Traini E (1991) Central nervous system involvement during infection by Phlebovirus toscana of residents in natural foci in central Italy (1977–1988). Am J Trop Med Hyg 45:429–434

Olal D, Dick A, Woods VL, Liu T, Li S, Devignot S, Weber F, Saphire EO, Daumke O (2014) Nucleic Acids Res 42:6025–6037

Ritchie DW, Kozakov D, Vajda S (2008) Accelerating Protein–Protein docking correlations using a six-dimensional analytic FFT generating function. Bioinform 24(17):1865–1873

Shekhar C, Dev K, Verma SK, Kumar A (2012) In-silico: screening and modeling of CTL binding epitopes of Crimean congo hemorrhagic fever virus. Trends Bioinform 5:14–24

Sturniolo T, Bono E, Ding J, Raddrizzani L, Tuereci O, Sahin U, Braxenthaler M, Gallazzi F, Protti MP, Sinigaglia F, Hammer J (1999) Generation of tissue-specific and promiscuous HLA ligand database using DNA microarrays and virtual HLA class II matrices. Nat Biotechnol 17:555–561

Tambunan USF, Parikesit AA (2011) Insilico design of drugs and vaccines for dengue disease. Trends Bioinform 4:1–9

Tang H, Liu XS, Fang YZ, Pan L, Zhang ZW et al (2012) The epitopes of foot and mouth disease. Asian J Anim Vet Adv 7:1261–1265

Trott O, Olson AJ (2010) Autodockvina: improving the speed and accuracy of docking with a new scoring function, efficient optimization and multithreading. J Comput Chem 31:455–461

Valassina M, Cuppone AM, Bianchi S, Santini L, Cusi MG (1998) Evidence of Toscana virus variants circulating in Tuscany, Italy, during the summers of 1995–1997. J Clin Microbiol 36:2103–2104

Valassina M, Meacci F, Valensin PE, Cusi MG (2000) Detection of neurotropic viruses circulating in Tuscany: the incisive role of Toscana virus. J Med Virol 60:86–90

Valassina M, Cusi MG, Valensin PE (2003) A Mediterranean arbovirus: the Toscana virus. J Neurovirol 9:577–583

Verma SK, Yadav SSP, Kumar A (2011) Insilico T cell antigenic determinants from proteome of H1N2 swine influenza A virus. Online J Bioinform 12:371–378

Viret C, Janeway CA (1999) MHC and T cell development. Rev Immunogenet 1:91–104

Von Hoff DD, Evans DB, Hruban RH (2005) Pancreatic cancer. Jones and Bartlett, Sudbury

Wallner B, Elofsson A (2003) Can correct protein models be identified. Protein Sci 12:1073–1086

Wiederstein M, Sippl MJ (2007) ProSA-web: interactive web service for the recognition of errors in three-dimensional structures of proteins. Nucleic Acids Res 35:407–410

J Polym Res (2014) 21:550
DOI 10.1007/s10965-014-0550-0

ORIGINAL PAPER

In situ grafted nanostructured ZnO/carboxymethyl cellulose nanocomposites for efficient delivery of curcumin to cancer

Laxmi Upadhyaya · Jay Singh · Vishnu Agarwal · A.C. Pandey · Shiv P. Verma · Parimal Das · R. P. Tewari

Received: 27 May 2014 / Accepted: 24 July 2014
© Springer Science+Business Media Dordrecht 2014

Abstract In this present manuscript, zinc oxide (ZnO) nanoparticles embedded carboxymethyl cellulose (CMC) bionanocomposite were prepared by in situ grafting and the hydrophobic anticancer drug curcumin (Cur) was loaded into it. Structural, morphological, and physiochemical behavior of prepared curcumin-loaded CMC/ZnO nanocomposites (NCs) were characterized by FTIR, XRD, SEM, TEM, TGA, and DTA. The drug entrapment efficiency was evaluated and the in vitro efficacy as anticancer drug delivery vehicle was analyzed. The potential toxicity of curcumin-loaded ZnO/CMC NCs (Cur/ZnO/CMC NCs) was studied by using L929 and MA104 cell lines via MTT assay. The cellular uptake study of Cur/ZnO/CMC NCs by normal (L929) and cancer (MA104) cells carried out by using ethanol extraction and by FACS analysis has been reported. The results of this investigation demonstrate that the nanomatrix synthesized can effectively deliver the anticancer drug curcumin, and hence appears to be a promising nanoformulation for anticancer therapy and other biomedical applications.

L. Upadhyaya · R. P. Tewari
Department of Applied Mechanics, MotiLal Nehru National Institute of Technology, Allahabad 211004, India

V. Agarwal
Department of Biotechnology, MotiLal Nehru National Institute of Technology, Allahabad 211004, India

J. Singh (✉)
Department of Applied Chemistry, Delhi Technological University, ShahbadDaulatpur, Main Bawana RoadDelhi 110 042, India
e-mail: jay_singh143@yahoo.co.in

A. Pandey
Nanotechnology Application Centre, University of Allahabad, Allahabad 211002, India

S. P. Verma · P. Das
Centre for Genetic Disorders, Faculty of Science, Banaras Hindu University, Varanasi 221 005, India

Keywords Carboxymethyl cellulose · ZnO nanoparticles · Curcumin · Cancer therapy

Introduction

During the last decade, nanomaterials have attracted considerable interest of researchers and scientists due to the functionalities unavailable to bulk materials [1]. As a new generation of nanomaterials, nanocomposites signify an emerging area in the frontier between the fields of materials science, life science, and nanotechnology. Biodegradable polymers have gained much attention as a matrix for drug delivery as they offer promising increased bioavailability, solubility, and retention time, thereby providing enhanced therapeutic efficacy of many hydrophobic anticancer drugs [2–6]. These nanoformulations exhibit merit over traditional medicines with respect to controlled release, targeted delivery, and therapeutic impact. Carboxymethyl cellulose (CMC) is a water soluble cellulose derivatives produced by heterogeneous etherification of solid cellulose with monochloroacetic acid [7]. It is a long-chain, linear-anionic polysaccharide with ubiquitous distribution, comprising the fibrous tissue of plants, and has wide application in the field of cosmetics, food, detergents, paper, textiles, paint, and pharmaceutical industries [8–11]. The presence of a number of sodium carboxymethyl groups (CH_2COONa) in the cellulose molecule promotes the water solubility of CMC [9]. Also, among these, polysaccharides are very cheap and easily available.

Among several natural dietary compounds exhibiting therapeutic effects with no or minimal side effects to normal organs in cancer treatment, curcumin has received considerable attention. Curcumin is an orange-yellow colored polyphenolic isolate from the herb *Curcuma longa* with anticarcinogenic effects. Extensive research on this compound over the past five decades has well established the excellent anticarcinogenic [12], anti-HIV [13], anti-inflammatory [14],

Published online: 08 August 2014

antioxidant [15], and antimicrobial [16] potential of this marvelous pigment. A major limiting factor of curcumin is its low solubility in water (i.e. 0.0004 mg/mL at pH 7.3), and soluble curcumin molecules are extremely sensitive at physiological pH [17, 18]. A simple way of solving the limiting factors of curcumin is to improve its bioavailability, protect it from degradation and metabolism, and increase its targeting capacity to cancerous tumors. Various types of nanoparticle, such as polymer NPs, polymeric micelles, liposome/phospholipid, nano-/microemulsions, nanogels, solid lipid nanoparticles, polymer conjugates, and self-assemblies, are suitable for the delivery of an active form of curcumin to tumors [19–21]. In this context, biodegradable polymer and metal oxide nanocomposites have been of the most interest in drug delivery applications. Among them, nanostructured zinc oxide (ZnO), basically an n-type semiconductor, is a fascinating, multifunctional material as it has wide applications in the area of solar cells, varistors, sensors, gas sensors, displays, piezoelectric devices, photodiodes, electro-acoustic transducers, and UV light-emitting devices [22, 23]. ZnO nanowires have been shown to be biodegradable and to dissolve eventually into ions that can be absorbed by the body and become part of the nutritional cycle, and therefore, they are proposed for in vivo biosensing and biodetection applications [23]. The ability to synthesize ZnO into hollow nanotube-type structures also makes them reasonable choices for drug delivery, particularly slow drug release applications [24]. One of the primary advantages for considering ZnO nanoparticles for use in cancer is the inherent preferential cytotoxicity against cancer cells in vitro [25–28]. Also, the ease of the synthesis of ZnO nanoparticles and its high drug loading efficiency make it suitable for anticancer drug delivery [29]. In this regard, the present paper reports on the synthesis and characterization of an efficient, water-soluble nanodrug system containing carboxymethyl cellulose (CMC), ZnO, and curcumin. Also, a drug entrapment efficiency evaluation and in vitro drug release study of the prepared nanoformulation was performed. The effect of curcumin-loaded ZnO/CMC nanocomposite (Cur/ZnO/CMC NCs) on MA104 cancer cell lines and cellular uptake study by FACS analysis has been reported as well.

Materials

Carboxymethyl cellulose (CMC average Mw=90,000) was purchased from Sigma–Aldrich (USA). NaOH, zinc nitrate hexahydrate, and curcumin were purchased from Merck (India). Cell culture media like minimum essential medium (MEM), Dulbecco's modified eagle medium (DMEM), and MTT [3-(4,5-Dimethylthiazole-2-yl)-2,5-diphenyl tetrazolium] were obtained from Sigma–Aldrich (USA).

Methods

Preparation of ZnO/CMC and Cur/ZnO/CMC nanocomposites

First, 1.5 g CMC was added to 250 mL distilled water. For the complete dissolution of CMC, the mixture was heated at 90 °C for approximately 10 min with constant stirring. The solution was cooled at room temperature. To this solution, 7.44 g zinc nitrate hexahydrate was added in to the solution. Then 0.2 M of sodium hydroxide solution was added to the mixture, drop-wise with constant stirring. The transparent solution turned milky white without any precipitation. After the complete addition of sodium hydroxide, the reaction was continued for 2 h. Subsequently, the solution was centrifuged at 8,000 rpm for 20 min. The precipitated ZnO/CMC was washed thrice using distilled water to remove excess CMC and the by-products. Finally, ZnO/CMC was dried at 80 °C for 3 h for complete conversion of the remaining zinc hydroxide to zinc oxide.

Initially, a stock solution of curcumin was prepared in ethanol at a concentration of 2 mg/mL. Then an aqueous solution was prepared by dissolving 10 mg of ZnO/CMC NCs in 20 mL ultrapure water (Millipore Corp.) under constant stirring. Subsequently, to this solution, the required volume of ethanolic curcumin was added drop-wise under continuous stirring for 48 h in a closed flask in order to load curcumin into ZnO/CMC NCs. Finally, the solution was stirred in open air for a further 24 h to evaporate ethanol completely, resulting in the formation of curcumin-loaded ZnO/CMC NCs (Cur/ZnO/CMC NCs). Fig. 1 shows the schematic representation for the preparation of curcumin loaded ZnO/CMC NCs.

Characterizations

Fourier transform infrared (FT-IR) spectroscopy spectra of the prepared ZnO/CMC and Cur/ZnO/CMC NCs were recorded on a Perkin Elmer SPECTRUM GX-Raman spectrophotometer using KBr disc in the frequency range from 400–4,000 cm^{-1}. The crystalline nature of prepared NCs were recorded on X-ray diffractometer (Phillips X-pert model) with CuKα radiation at λ=1.5406 Å. The morphology was studied using scanning electron microscopy (SEM) with JEOL JSM-5200 at 15 kV. The structural morphology and crystalline size of the synthesized nanocrystals is investigated by TEM measurements using Tecnai G2 S-Twin electron microscope. The thermal behavior of ZnO/CMC and Cur/ZnO/CMC NCs were studied through thermo-gravimetric and differential thermal analysis using a Perkin-Elmer Pyris Diamond TG/DTA/DSC 8.0 series instrument at a heating rate of 10 °C under N_2 atm.

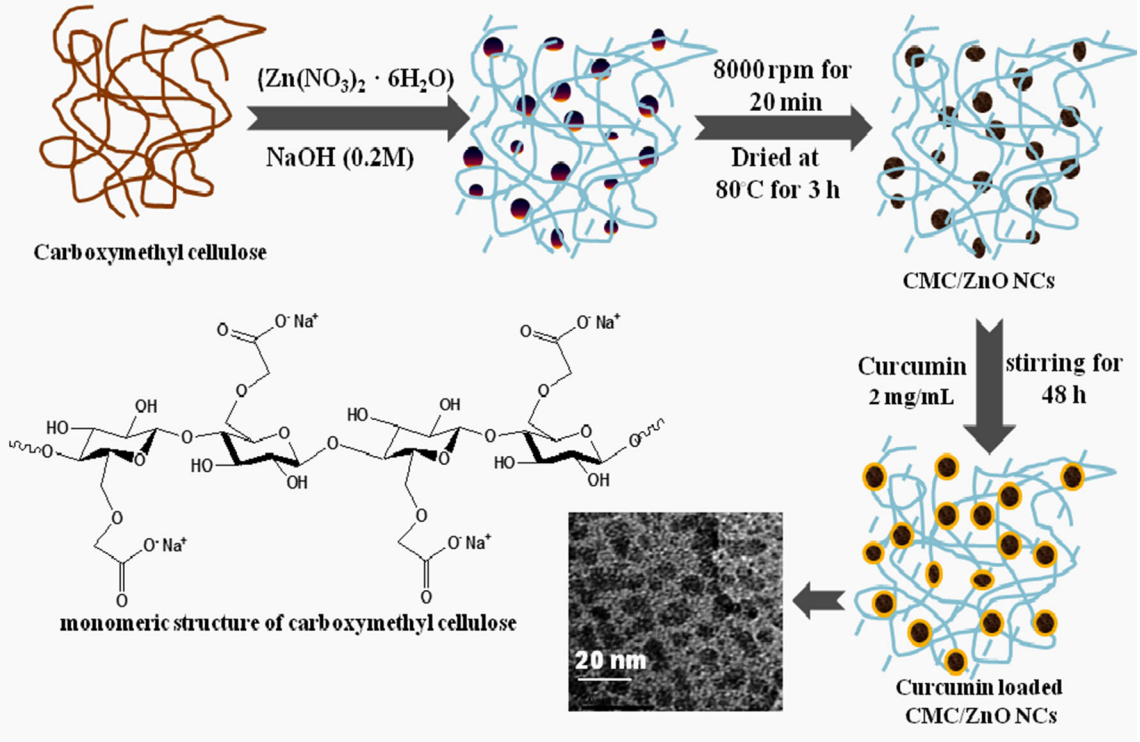


Fig. 1 Schematic representation for in situ preparation of curcumin-loaded ZnO/carboxymethyl cellulose nanocomposites

Entrapment efficiency and loading efficiency

In order to evaluate the entrapment efficiency of curcumin within the prepared ZnO/CMC NCs, the sample was pelletized by ultracentrifugation at 20,000 rpm at 4 °C for 45 min from the aqueous medium containing free curcumin. Then the pellet obtained was washed thrice with distilled water. This pellet was dispersed again in ethanol (2 mg pellet in 10 mL ethanol), vortexed well for 5 min, and subsequently centrifuged at 20,000 rpm for 10 min. Finally, the amount of drug within the supernatant collected was quantified spectrophotometrically at 429 nm. Loading efficiency of the drug loaded NCs was also calculated with respect to the weight of the NCs obtained after centrifugation [30, 31].

$$\text{Entrapment efficiency} = \frac{(\text{Amount of curcumin in the pellet})\text{X } 100\%.}{\text{Initial amount of curcumin}} \quad (1)$$

$$\text{Loading efficiency} = \frac{(\text{Totalamount of curcumin})\text{X } 100\%}{\text{Yield of nanocomposite}} \quad (2)$$

In vitro drug release studies

The evaluation of in vitro drug release profile of curcumin from the synthesized drug-loaded ZnO/CMC NCs was carried out by direct dispersion for a period of 1 week at two different pH values (7.4 and 4.5) as per the method reported in the literature [32]. For this, the prepared NCs suspension was centrifuged at 20,000 rpm for a period of 30 min. Then, the pellet collected was dispersed again in 10 mL PBS (pH 7.4 and 4.5) at a final concentration of 0.2 mg/mL. After this, the whole mixture was divided into 20 Eppendorf tubes with 0.5 mL each for a time-dependent release study at time intervals of 1, 6, 12, 24, 48, 72, 96, 102, and 126 h. And these tubes were incubated at 37 °C under gentle shaking. Subsequently, at proper time intervals, curcumin in ZnO/CMC NCs were first extracted in ethanol and then quantified spectrophotometrically. Drug release was quantified as follows in Eq (3) [31]:

$$\text{Release (\%)} = \frac{(\text{Releasedcurcumin})\text{X } 100\%}{\text{Total curcumin}} \quad (3)$$

Cell culture and cytotoxicity studies

Before performing the cytotoxicity test by MTT assay, the MA104 cell line was grown in Dulbecco's modified Minimum Essential Medium (DMEM) (Sigma) supplemented with 10 % fetal bovine serum (FBS) (Sigma) and antibiotics (penicillin and streptomycin) (Sigma) in 96-well tissue culture plates. Then the potential cytotoxicity effects of pure curcumin, ZnO/CMC, and Cur/ZnO/CMC NCs were determined via standard MTT assay. Basically, it is a colorimetric test based on the principle of selective ability of viable cells to reduce the tetrazolium component of MTT to purple-coloured

formazan crystals. For this, initially, in a 96-well plate, MA104 cells were seeded at a density of 10,000 cells/well and kept in a CO_2 incubator under standard culturing conditions. Then five different concentrations of pure curcumin, ZnO/CMC and Cur/ZnO/CMC NCs (1, 2, 3, 4, and 5 mg/mL) were prepared by dilution with the media. After this, the cells were incubated with different concentrations of the NCs (100 μL) for a period of 24 h after reaching 90 % confluency. Cells in media alone, devoid of NCs (untreated cells), were used as a negative control (i.e., 100 % viable), and the cells treated with the toxin Triton were used as positive control. Subsequently, MTT reagent was added in each well 4 h before the end of the experiment and kept at 37 °C in a CO_2 incubator followed by 1 h incubation with solubilization buffer. Finally, at a wavelength of 570 nm, the optical density of the solution was measured and % cell viability was determined. Triplicate samples were analyzed for each experiment.

Cell uptake study by flow cytometry

First, 10^5 ACHN cells were seeded in a 12-well plate and grown in DMEM supplemented with 10 % foetal bovine serum (FBS) at 37° and 5 % CO_2. After 24 h of growth, cells were treated with 5 mg/mL Cur/ZnO/CMC NCs and respective NCs as control. Finally, intracellular curcumin fluorescence of 10,000 cells was analyzed by FACS Calibur (Beckton Dickinson) flow cytometer after excitation with a 488 nm argon laser.

Statistical analysis

All experimental values are presented as means±SD. The FACS data are analyzed using Calibur (Beckton Dickinson), and then a cytotoxicity test was used to analyze multiple differences between the groups using Origin Pro software, version 7.

Results and discussions

FTIR

Figure 2A shows the FTIR spectra of CMC, pure curcumin, ZnO/CMC NCs, and curcumin-loaded ZnO/CMC NCs in the range of 400 to 4,000 cm^{-1}. As shown in the FTIR spectra of CMC (curve a), characteristic peak assignment of CMC is 3,400–3,600 cm^{-1} for hydroxyl groups, and the peak at 1,492 cm^{-1} is due to the $–COO^-$ symmetric stretch [33]. In addition, the bands in the region 1,326 cm^{-1} are due to symmetrical deformations of CH_2 and COH groups. The small band appears at 1,085 and 997 cm^{-1} and is due to

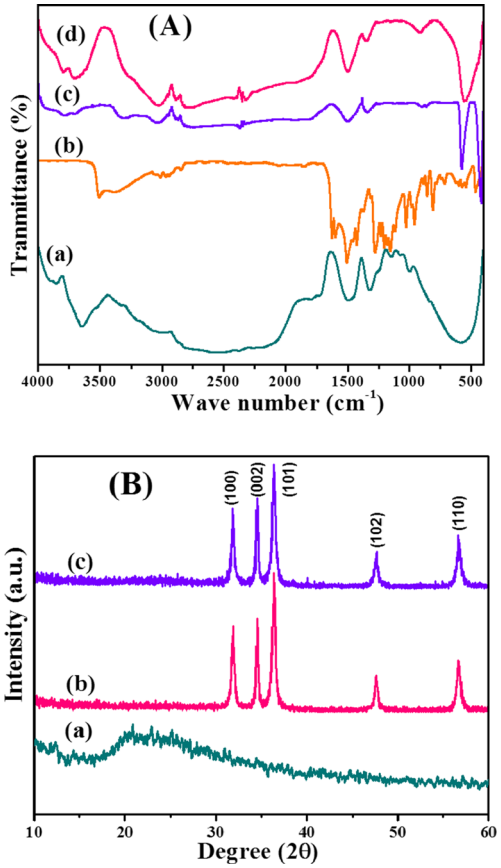


Fig. 2 (**A**) FTIR spectra of (a) carboxymethyl cellulose, (**b**) pure curcumin, (**c**) ZnO/carboxymethyl cellulose nanocomposite, (**d**) curcumin loaded ZnO/CMC nanocomposite, (**B**) X-ray diffraction pattern of (**a**) carboxymethyl cellulose, (**b**) ZnO/carboxymethyl cellulose nanocomposite, and (**c**) curcumin/ZnO/carboxymethyl cellulose nanocomposites

primary alcoholic $–CH_2OH$ stretching mode and CH_2 twisting vibrations, respectively. The broad bands at around 595 cm^{-1} are due to ring stretching and ring deformation of α-D-(1–4) and α-D-(1–6) linkages. The characteristic peaks observed in the FTIR of pure curcumin (curve b) are an absorption band at 3,508 cm^{-1} (phenolic O–H stretching vibration), peaks 1,620 (stretching vibrations of benzene ring), 1,506 (C=O and C–C vibrations), 1,420 (olefinic C–H bending vibration), and 1,280 cm^{-1} (aromatic C–O stretching vibration) [34]. The IR spectrum of ZnO/CMC NCs (curve c) confirms the bonding between CMC and ZnO forming nanocomposites as it shows different characteristic peaks of CMCs along with a sharp peaks at 414 and 570 cm^{-1} which corresponds to the presence of a metal oxide bond (Zn-O). Because of the complexation of curcumin with CMC/ZnO NCs, the wave numbers corresponding to the characteristic peaks of CMC were shifted. Comparing ZnO/CMC and Cur/ZnO/CMC NCs (curve d), peak shifts were observed from 3,496 to 3,445 cm^{-1} and 1,636 to 1,622 cm^{-1}. This observed result confirmed that the presence of curcumin in the CMC matrices is successfully incorporated into the NCs.

XRD

Figure 2B shows the X-ray diffraction pattern of CMCS, ZnO/CMC NCs, and curcumin-loaded ZnO/CMC NCs. The CMC is typically a non-crystalline polymer and shows a broad diffraction peak appearing at around 2θ=20°–25° which indicates the amorphous nature (curve a). From the X-ray diffraction pattern, the positions and relative intensities of the reflection peak of the ZnO/CMC NCs (curve b) and curcumin-loaded ZnO/CMC NCs (curve c) are in agreement with each other. The diffraction peaks can be indexed to the wurtzite type structure of bulk hexagonal ZnO (JCPDS-card No. 36–1451) crystal [35]. The diffraction peaks (2θ) at 31.73°, 34.52°, 36.33°, 47.74 °, and 56.78° correspond to (100), (002), (101), (102), and (110) planes, respectively. In the ZnO nanoparticle stabilization process, the presence of carboxylate (−COO-) and hydroxyl (−OH) functional groups in CMC provides a net negative surface charge which ensures nanocrystal stability through electrostatic interaction. The average crystallite size of ZnO/CMC NCs and curcumin-loaded ZnO/CMC NCs are determined by the Debye Scherrer equation, $d=0.941\ \lambda/\beta \cos\theta$, where λ is the wavelength, β is the full width at half maximum (FWHM) of four most intense diffraction peaks (101), and θ is the Bragg angle. The average crystalline size of the ZnO/CMC NCs and curcumin-loaded ZnO/CMC NCs are found to be ~18 and ~23 nm, respectively. During the formulation of curcumin, crystallinity of CMC/ZnO NCs was well-maintained with increasing the crystalline size (up to ~5 nm). This result indicates the successful formulation of drug onto the surface of O ZnO/CMC matrix.

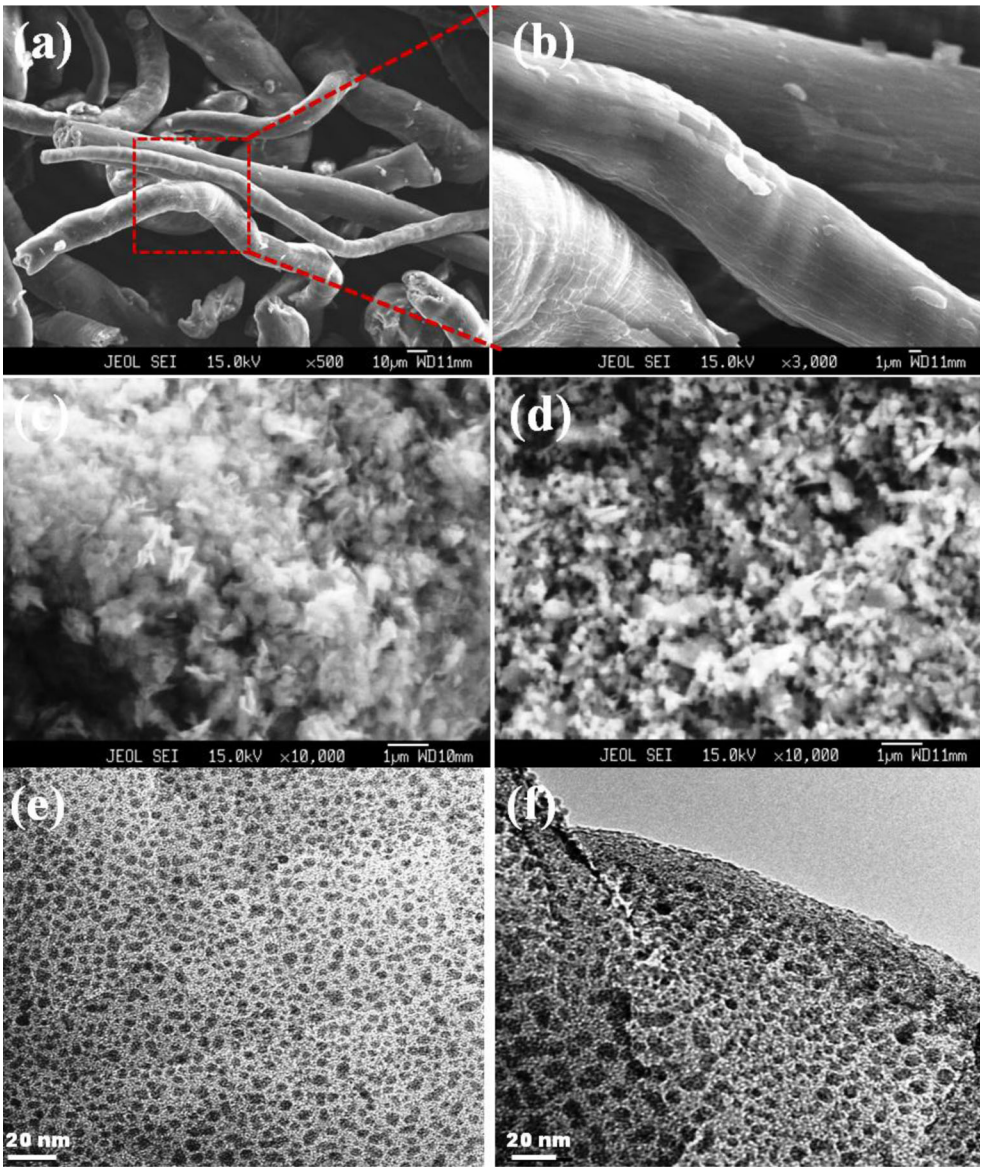


Fig. 3 (**a** and **b**) SEM micrographs of pure carboxymethyl cellulose, (**c**) ZnO/carboxymethyl cellulose nanocomposite, (**d**) curcumin/ZnO/carboxymethyl cellulose nanocomposites, (**e** and **f**) TEM micrograph of ZnO/carboxymethyl cellulose nanocomposites, (**f**) curcumin/ZnO/carboxymethyl cellulose nanocomposites

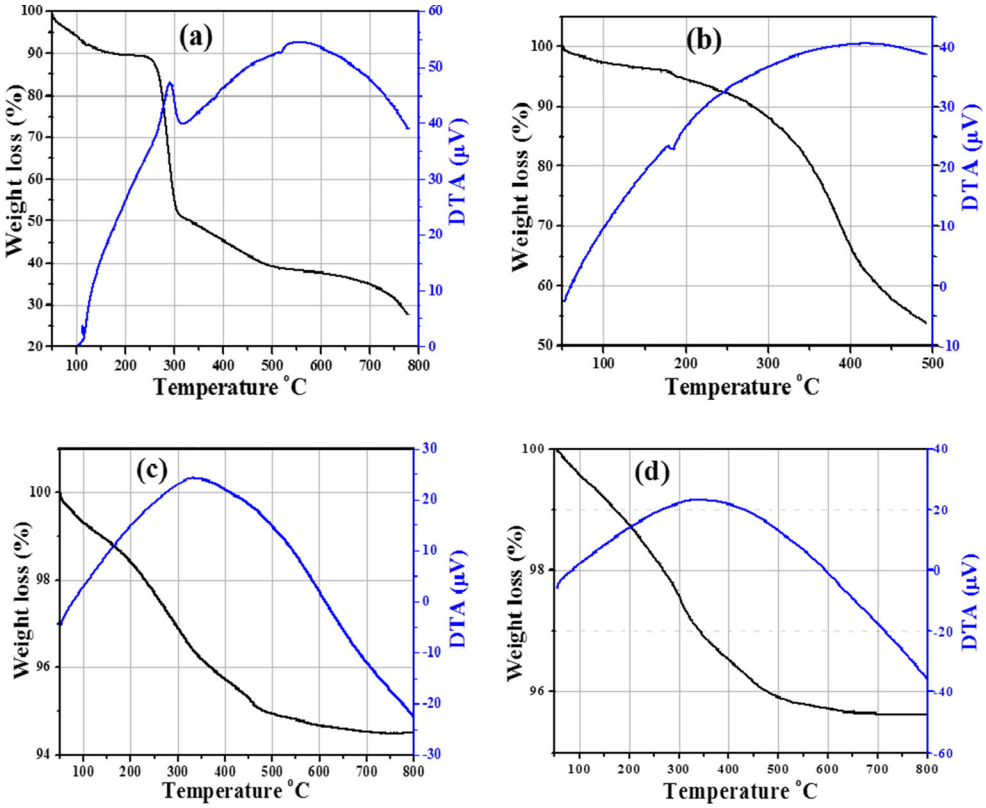


Fig. 4 TGA and DTA spectra of (**a**) carboxymethyl cellulose, (**b**) pure curcumin, (**c**) ZnO/carboxymethyl cellulose nanocomposite, (**d**) curcumin-loaded ZnO/CMC nanocomposite

Scanning electron microscopy (SEM) analysis

Figure 3a and b) shows the SEM micrographs of pure CMC with fibrous surface structure arranged in a woven network. On the other hand, smooth nanofibrillar structures can be observed as shown in the SEM micrograph of ZnO/CMC NCs in (image c). In addition, in the encapsulation of curcumin, the Cur/ZnO/CMC NCs (image d) obtained displayed aggregates composed of spherical particles.

Transmission electron microscopy (TEM) analysis

Figure 3e and f shows the TEM image of ZnO/CMC and Cur/ZnO/CMC NCs, respectively. It is shown by Fig. 3e that the ZnO nanoparticles (black dots) embedded in the CMC matrix seem to be spherical in shape, homogenous, and the NPs are found to be dispersed well with an average particle size of ~12 nm. Upon the encapsulation of curcumin, the Cur/ZnO/CMC NCs obtained had nearly the same size. However, unlike others, in the case of Cur/ZnO/CMC NCs, agglomeration could not be observed and was of isolated particles. The average particle size is of ~15 nm.

Thermal studies

The TGA and DTA studies to analyze the degradation of CMC, pure curcumin, ZnO/CMC, and Cur/ZnO/CMC NCs

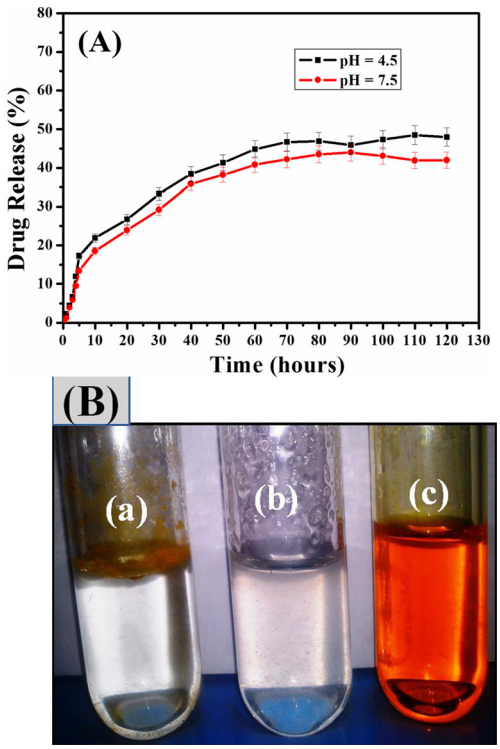


Fig. 5 (**a**) Drug release profile of curcumin from curcumin-loaded ZnO/carboxymethyl cellulose nanocomposite in pH 4.5 and 7.5 at 37 °C (values with error bars of ±3). (**b**) Water solubility of curcumin (**a**), CMC/ZnO nanocomposites, (**b**) curcumin-loaded ZnO/CMC NCs nanocomposites (**c**)

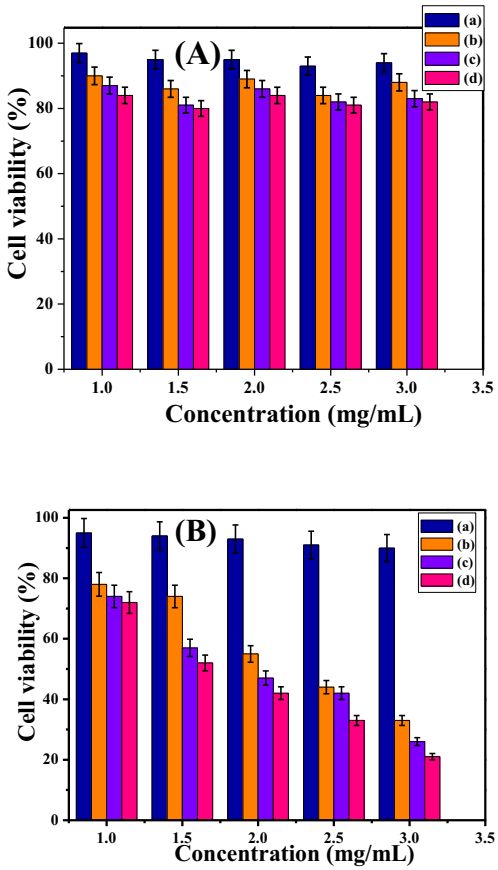


Fig. 6 Cell viability of (**A**) L929 normal cells and (B) MA104 cancer cells for carboxymethyl cellulose (**a**), ZnO/carboxymethyl cellulose nanocomposite (**b**), curcumin/ZnO/carboxymethyl cellulose nanocomposites (**c**), and pure curcumin (**d**)

with temperature by TGA is shown in Fig. 4a-d, respectively. Within 100 °C, weight reduction can be due to moisture loss. The TG curve clearly shows that at 400 °C, CMC is degraded to 45 %, curcumin to 66 %, and ZnO/CMC and Cur/ZnO/CMC NCs to 95 %, respectively. Therefore, although the nanocomposites prepared (ZnO/CMC and Cur/ZnO/CMC NCs) exhibit higher thermal stability than CMC and pure curcumin, no significant difference has been observed between ZnO/CMC and Cur/ZnO/CMC NCs. In the DTA analysis (Fig. 4a-d), due to the crystalline nature of curcumin, an endothermic peak is observed at a temperature around 185 °C, while there is no such peak observed in the DTA graph of Cur/ZnO/CMC NCs. This confirms the disordered-crystalline phase, i.e. amorphous nature of curcumin in the ZnO/CMC NCs. In general, the complexation of a drug and a polymer causes either absence or shifting of endothermic peaks which indicates a change in the crystal lattice, melting, boiling, or sublimation points [34]. Hence, the nanoformulation prepared Cur/ZnO/CMC NCs appear to be amorphous in nature.

Entrapment efficiency and in vitro drug release study

Entrapment and loading efficiency of Cur/ZnO/CMC NCs have been found to be 67 % and 44 %, respectively. The results indicated that the amount of the ZnO/CMC matrix and curcumin had critical effects on the drug absorption. Higher amounts of O ZnO/CMC NCs facilitate more loading and entrapment, but resulted in large sized particles. However, at higher curcumin concentration, entrapment efficiency has been reduced where the drug tends to precipitate. In considering all these parameters, concentration of ZnO/CMC NCs and curcumin was optimized so as to give better entrapment, loading efficiency, and desired size. The in vitro drug release profile of curcumin from Cur/ZnO/CMC NCs at two different pHs (4.5 and 7.5) is shown in Fig. 5A. In the initial 4 h, a burst release was observed which was followed by slow and controlled release of curcumin over a period of 1 week. Approximately 48 and 42 % of the drug was released at ph 4.5 and 7.4, respectively, in this duration of 1 week. The reason for the initial burst release of the drug might be the curcumin entrapped near the surface and the drug adsorbed onto the NCs. Since the dissolution rate of polymers near the surface is high, the amount of drug released will also be high. Also, the faster drug release was observed in acidic pH than in neutral and can be attributed to the swelling of polymer matrix in acidic pH, thereby facilitating higher drug elution. Figure 5B demonstrates that the water solubility of curcumin (a), CMC/ZnO nanocomposites, (b) curcumin-loaded ZnO/CMC NCs

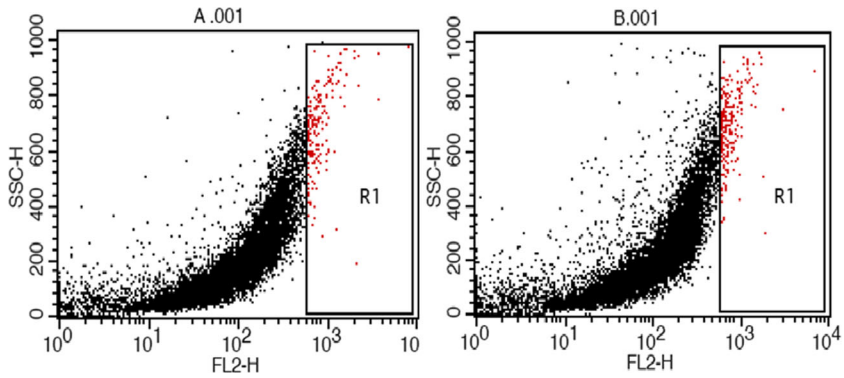


Fig. 7 Cellular uptake study of curcumin loaded ZnO/CMC nanocomposite by FACS cells in MA104 cancer cells

nanocomposites (c). While curcumin as such is insoluble in water, curcumin loading into CMC/ZnO NCs enhanced the drug solubility in water. As a result, loading of curcumin into CMC/ZnO NCs enhanced the aqueous solubility of curcumin.

Cytotoxicity test by MTT assay

Cell viability of CMC, CMC/ZnO NCs, Cr/O-CMCS/ZnO NCs, and pure curcumin on L929 and MA104 cell lines were analyzed using MTT assay as shown in Fig. 6. The study demonstrated that when L929 cells (Fig. 6A) were exposed to CMC, the cells showed high viability, whereas when the same cells were exposed to CMC/ZnO NCs, Cr/O-CMCS/ZnO NCs, and pure curcumin in the concentration range of 1–3 mg/mL, the viability of the cells reduced. However, the non-toxicity of CMC, CMC/ZnO NCs, Cr/O-CMCS/ZnO NCs, and pure curcumin was depicted by the viability of 80 % of the L929 cells. On the other hand, in the case of cancer (MA104) cell line, although CMC showed no toxicity, considerable toxicity was revealed by CMC/ZnO NCs, Cr/O-CMCS/ZnO NCs, and pure curcumin. Both the higher toxicity of CMC/ZnO NCs and Cr/O-CMCS/ZnO NCs than CMC and preferential toxicity of the nanoformulation prepared (Cr/O-CMCS/ZnO NCs) can be attributed to the presence of ZnO NPs in the hybrid nanocomposites formed. As reported in the literature, when reduced from bulk to nanoscale, ZnO has been shown to exhibit inherent preferential cytotoxicity against cancer cells in vitro [27, 28]. Therefore, the MTT assay demonstrated significant toxicity of the Cr/O-CMCS/ZnO NCs against MA104 cells, because of which, at a concentration of 3 mg/mL, the cell viability reduced to 20 %, thereby confirming its anticancer effect. The images of the cells after treatment with CMC, CMC/ZnO NCs, Cr/O-CMCS/ZnO NCs, and pure curcumin are shown in Fig. 6B.

In vitro cell uptake study by FACS analysis

The in vitro cellular uptake study of Cr/O-CMCS/ZnO NCs by ACHN cells was performed by flow cytometry. Figure 7 shows the cell uptake profile of Cr/O-CMCS/ZnO NCs (A) by ACHN cells which clearly demonstrates an increase in the uptake of the nanoformulation prepared with concentration by the cancer cell line (MA104). Therefore, the cell uptake study clearly shows that the cell uptake of the curcumin-loaded ZnO/CMC NCs (B) is concentration dependent.

Conclusions

The results of this study demonstrated that the NCs prepared exhibit physicochemical and biological properties that recommend them for further applications in cancer treatment. The IR spectra showed the presence of ZnO in Cur/ZnO/CMC NCs along with the confirmation of bonding between curcumin and the ZnO/CMC NCs. The XRD analysis and thermal study confirmed the amorphous nature of the nanoformulation prepared. The resultant NCs possessed desirable particle size and surface charge required for anticancer drug delivery. The in vitro drug release study demonstrated the slow and controlled release of curcumin from the NCs prepared which is desirable in the field of cancer therapy. Moreover, the cellular uptake study by FACS analysis showed that the uptake profile is concentration dependent and increases with the increase in the concentration of the nanoformulation prepared. Hence, the nanoformulation prepared appears to be promising anticancer drug delivery biomaterial.

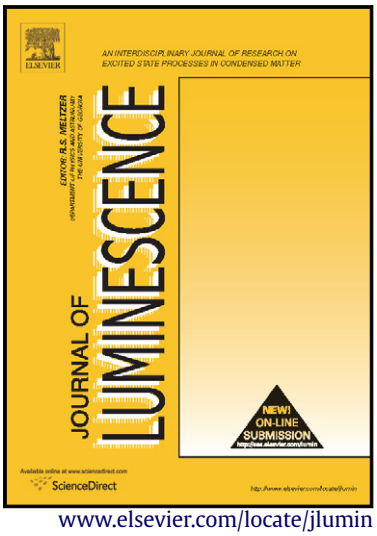
Acknowledgments We thank Prof. P. Chakrabarti, Director, Motilal Nehru National Institute of Technology, Allahabad, India for providing other necessary facilities for research work. The author LU kindly acknowledges the Ministry of Human Resource Development (MHRD), Govt. of India for providing senior research fellowship (SRF) for research. JS kindly acknowledges Department of Science and Technology, New Delhi, India for awarding the INSPIRE FACULTY AWARD [IFA-13-CH-105].

References

1. Di Sia P (2012) THz spectroscopy and nanostructures: a short interesting review. Lett Appl Nanobiosci 1:8
2. Jude IN, Luke MG, John K, Clement LH (2013) Development of novel chitosan-poly(N, N-diethylacrylamide) IPN films for potential wound dressing and biomedical applications. J Polym Res 20:1
3. Ionela A, Gheorghe F, Mariana C, Valeria H, Marieta C (2013) Thermo- and pH-sensitive interpenetrating poly(N-isopropylacrylamide)/carboxymethyl pullulan network for drug delivery. J Polym Res 20:293
4. Xiu-Li W, Yan-Li Z, Dao-Lu T, Gui-Ying L, Yu-Zhong W (2012) Self-assembly, drug-delivery behavior, and cytotoxicity evaluation of amphiphilic chitosan-graft-poly(1,4-dioxan-2-one) copolymers. J Polym Res 19:1–9
5. Shi L, Tang C, Yin C (2012) Glycyrrhizin-modified-O-carboxymethyl chitosan nanoparticles as drug vehicles targeting hepatocellular carcinoma. Biomaterials 33:7594
6. Rejinold NS, Muthunarayanan M, Divyarani VV, Sreerekha PR, Chennazhi KP, Nair SV, Tamura H, Jayakumar R (2011) Curcumin loaded biocompatible thermoresponsive polymeric nanoparticles for cancer drug delivery. J Coll Interf Sci 360:39
7. Jiugao Y, Jingwen Y, Baoxiang L, Xiaofei M (2009) Preparation and characterization of glycerol plasticized-pea starch/ZnO–carboxymethylcellulose sodium nanocomposites. Bioresour Technol 100: 2832–41
8. Bayarri S, Gonzalez-Tomas L, Costell L (2009) Viscoelastic properties of aqueous and milk systems with carboxymethyl cellulose. Food Hydrocoll 23:441
9. Biswal DR, Singh RP (2004) Characterisation of carboxymethyl cellulose and polyacrylamide graft copolymer. Carbohydr Polym 57:379
10. Pushpamalar V, Langford SJ, Ahmad M, Lim YY (2006) Optimization of reaction conditions for preparing carboxymethyl cellulose from sago waste. Carbohydr Polym 64:312–8
11. Ueno T, Yokota S, Kitaoka T, Wariishi H (2007) Conformational changes in single carboxymethyl-cellulose chains on a highly

oriented pyrolytic graphite surface under different salt conditions. Carbohydr Res 342:954–60
12. Kuttan R, Bhanumathy P, Nirmala K, George MC (1985) Potential anticancer activity of turmeric (Curcuma longa). Cancer Lett 29:197
13. Jordan WC, Drew CR (1996) Curcumin—a natural herb with anti-HIV activity. J Natl Med Assoc 88:33
14. Srimal RC, Dhawan BN (1973) Pharmacology of diferuloyl methane (curcumin), a non-steroidal anti-inflammatory agent. J Pharm Pharmacol 25:447
15. Sharma OP (1976) Antioxidant activity of curcumin and related compounds. Biochem Pharmacol 25:1811
16. Kim MK, Choi GJ, Lee HS (2003) Fungicidal property of Curcuma longa L. rhizome-derived curcumin against phytopathogenic fungi in a greenhouse. J Agric Food Chem 51:1578
17. Tonnesen HH (2002) Solubility, chemical and photochemical stability of curcumin in surfactant solutions. Studies of curcumin and curcuminoids. Pharmazie 57:820
18. Yallapu MM, Jaggi M, Chauhan SC (2012) Curcumin nanoformulations: a future nanomedicine for cancer. Drug Discov Today 17:71
19. Muqbil I, Masood A, Sarkar FH, Mohammad RM, Azmi AS: Progress in nanotechnology based approaches to enhance the potential of chemopreventive agents Cancers 3:428 (2011)
20. Yallapu MM, Jaggi M, Chauhan SC (2010) Poly(beta-cyclodextrin)/curcumin self-assembly: A novel approach to improve curcumin delivery and its therapeutic efficacy in prostate cancer cells. Macromol Biosci 10:1141
21. Yallapu MM, Othman SF, Curtis ET, Gupta BK, Jaggi M, Chauhan SC (2011) Multi-functional magnetic nanoparticles for magnetic resonance imaging and cancer therapy. Biomaterials 32:1890
22. Chandramouleeswaran S, TMhaske S, Kathe AA, Varadarajan PV, Prasad V, Vigneshwaran N (2007) Functional behaviour of polypropylene/ZnO–soluble starch nanocomposites. Nanotechnology 18: 385702
23. Zhou J, Xu N, Wang ZL (2006) Dissolving behavior and stability of Zno wires in biofluids: A study on biodegradability and biocompatibility. Adv Mater 18:2432
24. Nie L, Gao L, Feng P, Zhang J, Fu X, Liu Y, Yan X, Wang T (2006) Three-dimensional functionalized tetrapod-like ZnO nanostructures for plasmid DNA delivery. Small 2:621
25. Zhang LL, Jiang YH, Ding YL (2010) Mechanistic investigation into antibacterial behaviour of suspensions of ZnO nanoparticles against *E. coli*. J Nanopart Res 12:1625
26. Huang ZB, Zheng X, Yan DH (2008) Toxicological effect of ZnO nanoparticles based on bacteria. Langmuir 24:4140
27. Hanley C, Layne J, Punnoose A (2008) Preferential killing of cancer cells and activated human T cells using ZnO nanoparticles. Nanotechnology 19:295103
28. Wang H, Wingett D, Engelhard MH (2009) Fluorescent dye encapsulated ZnO particles with cell- specific toxicity for potential use in biomedical applications. J Mater Sci Mater Med 20:11
29. Rasmussen JW, Martinez E, Louka P, Wingett DG (2010) Zinc oxide nanoparticles for selective destruction of tumor cells and potential for drug delivery applications. Expert Opin Drug Deliv 7:1063
30. Kim DG, Jeong YI, Choi C, Roh SH, Kang SK, Jang MK (2006) Retinol-encapsulated low molecular water-soluble chitosan nanoparticles. Int J Pharmaceut 319:130
31. Das RK, Kasoju N, Bora U (2010) Encapsulation of curcumin in alginate-chitosan-pluronic composite nanoparticles for delivery to cancer cells Nanomed. Nanotechnol Biol Med 6:153
32. Bisht S, Feldmann G, Soni S, Ravi R, Karikar C, Maitra M (2007) Polymeric nanoparticle-encapsulated curcumin ("nanocurcumin"): A novel strategy for human cancer therapy. J Nanobiotechnol 5:3
33. Su JF, Huang Z, Yuan XY, Wang XY, Li M: Structure and properties of carboxymethyl cellulose/soy protein isolate blend edible films crosslinked by Maillard reactions Carbohydr Polym 79: 145–53 (2010)
34. Yallapua MM, Jaggi M, Chauhana SC: Cyclodextrin-curcumin selfassembly enhances curcumin delivery in prostate cancer cells Colloids Surfaces B 79:113 (2010)
35. Chen C, Yu B, Liu P, Liu JF, Wang L (2011) Investigation of nano-sized ZnO particles fabricated by various synthesis routes. J Ceramic Processing Res 12:420

Author's Accepted Manuscript



www.elsevier.com/locate/jlumin

Luminescence characterization of Eu^{3+} doped Zinc Alumino Bismuth Borate Glasses for Visible Red Emission Applications

K. Swapna, Sk. Mahamuda, A. Srinivasa Rao, T. Sasikala, P. Packiyaraj, L. Rama Moorthy, G. Vijaya Prakash

PII: S0022-2313(14)00424-4
DOI: http://dx.doi.org/10.1016/j.jlumin.2014.07.022
Reference: LUMIN12810

To appear in: *Journal of Luminescence*

Received date: 19 March 2014
Revised date: 17 June 2014
Accepted date: 25 July 2014

Cite this article as: K. Swapna, Sk. Mahamuda, A. Srinivasa Rao, T. Sasikala, P. Packiyaraj, L. Rama Moorthy, G. Vijaya Prakash, Luminescence characterization of Eu^{3+} doped Zinc Alumino Bismuth Borate Glasses for Visible Red Emission Applications, *Journal of Luminescence,* http://dx.doi.org/10.1016/j.jlumin.2014.07.022

This is a PDF file of an unedited manuscript that has been accepted for publication. As a service to our customers we are providing this early version of the manuscript. The manuscript will undergo copyediting, typesetting, and review of the resulting galley proof before it is published in its final citable form. Please note that during the production process errors may be discovered which could affect the content, and all legal disclaimers that apply to the journal pertain.

ACCEPTED MANUSCRIPT

Luminescence Characterization of Eu^{3+} doped Zinc Alumino Bismuth Borate Glasses for Visible Red Emission Applications

K.Swapna[1], Sk.Mahamuda[1], A. Srinivasa Rao[*1, 2], T. Sasikala[3], P. Packiyaraj[4], L. Rama Moorthy[3] and G. Vijaya Prakash[4].

[1]*Department of Physics, K L University, Green Fields, Vaddeswaram- 522 502, Guntur (Dt.), A P, India.*

[2]*Department of Applied Physics, Delhi Technological University, Bawana Road, New Delhi-110 042, India.*

[3] *Department of Physics, SV University, Tirupathi-517 502,A.P, India.*

[4]*Nanophotonics Laboratory, Department of Physics, Indian Institute of Technology-Delhi, Hauz Khaz, New Delhi-110 016, India.*

Corresponding author* ***E-mail: drsrallam@gmail.com, Tel: +91-85860 39007,Fax:+91 01127871023*

Accepted manuscript

ABSTRACT

Zinc Alumino Bismuth Borate (ZnAlBiB) glasses doped with different concentrations of Eu^{3+} ions have been prepared by rapid melt quenching technique and characterized for their luminescence behavior through various spectroscopic techniques such as absorption, excitation, emission, decay profiles and confocal image measurements at room temperature. From the measured absorption spectra, the bonding parameters (δ) were evaluated to find the nature of bonding between Eu^{3+} ions with its surrounding ligands in these ZnAlBiB glasses. The emission spectra of Eu^{3+} ions in ZnAlBiB glasses excited at 410 nm (CW laser) show the characteristic of Eu^{3+} ions with more intense visible red emission corresponding to $^5D_0 \rightarrow {}^7F_2$ transition. This intense visible red emission is further confirmed by the confocal luminescence images recorded for all the ZnAlBiB glasses. Judd-Ofelt (J-O) parameters are estimated from the emission spectral information are used to estimate the important radiative properties such as transition probability (A_R), branching ratios (β_R) and emission-cross sections for the prominent emission levels. The large stimulated emission cross-sections and branching ratios observed for ZnAlBiB glasses suggest the utility of these glasses in visible red region of the electromagnetic spectrum. The CIE chromaticity coordinates evaluated from the emission spectra and the confocal images recorded for all the ZnAlBiB glasses also indicates that, these glasses at higher concentration of Eu^{3+} ions are aptly suitable for intense red emission at 613 nm corresponding to $^5D_0 \rightarrow {}^7F_2$ transition.

Keywords: *Glasses, Optical properties, JO Parameters, Photo luminescence spectroscopy.*

ACCEPTED MANUSCRIPT

1. Introduction

The characterization of luminescence materials emerged as a fascinating field of research that encompasses a wide variety of scientific applications in the design and development of new optical devices such as solid state lasers, white light emitting diodes (LEDs) and other flat panel technologies like plasma display panels (PDP) [1-4]. Glassy materials doped with rare earth and transition metals have attracted many researches because of their memory and photo conducting properties. They also find potential applications in diversified fields such as lasers, solar energy concentrators and optoelectronic devices [5-8]. Effective development of devices for the aforementioned applications needs a glassy system with low phonon energies besides having some novel characteristic futures such as good transparency, high solvability of the doped ions and chemically more stable. It is well known that, a glassy host with low phonon energies can enhance radiative transition rates very much and are much useful as luminescent materials [9-13]. Since luminescence efficiency and emission transition band widths of the doped ions depends on the structural changes of the host matrix, apt selection of a suitable host matrix is crucial in order to obtain better luminescent efficiency [8, 14-17]. Among various glassy materials available, oxide based glassy systems are found to be chemically stable host matrices. Among the oxide glasses, particularly borate glasses are known to be the best choice because of their high transparency, good rare earth ion (RE) solubility. But borate glasses possess high phonon energies which are responsible for the non radiative transitions and lead to low quantum efficiencies. The high phonon energies observed in borate glasses can be suppressed to enhance the luminescence efficiency by adding the heavy metal oxides (HMO) like Bi_2O_3. When compared with conventional silicate glasses, borates glasses containing heavy metals have high linear and non-linear refractive index with broad transparent range over a wide spectral region extended from 0.4 to 8μm [18-20]. The broad transparent range in the mid-IR is related to the lowest phonon energy among all the oxide glasses [21]. All these properties make HMO glasses very attractive for photonic applications such as optical wave guides in the 2.5-3.0μm range and more efficient gain or non-linear optical devices [18-20]. Bismuth in glasses plays a dual role as a glass network former at high concentration and a network modifier at low concentration [22]. Aluminium trioxide (Al_2O_3) is often added to borate glasses to enhance the physical properties and chemical stability [23]. The aluminium based glasses are considered as potential candidates for various applications ranging from transparent ballistic protectors through infrared transparent windows to solid state lasers [24]. The ZnO in a glass can acts as a network former/modifier by imparting better chemical durability, low glass transition temperature and

Accepted manuscript

ACCEPTED MANUSCRIPT

wide glass forming compositional range. Considering the above mentioned scientific patronages offered by chemicals such as B_2O_3, ZnO, Bi_2O_3 and Al_2O_3, we recently prepared one good optical system namely Zinc Alumino Bismuth Borate (ZnAlBiB) glasses taking the aforementioned elements as the constituent elements. Quite recently we have reported the luminescence efficiency of these glassed doped with different rare earth ions [9-10, 13, 15]. In continuation to this, in the present paper we are reporting the preparation and luminescence characterization of the ZnAlBiB glasses doped with Eu^{3+} ions with an aim to understand their possible use for visible red emission applications.

Among the various lanthanide doped materials, Eu^{3+} doped borate materials are preferred as red luminophores for display applications as well as for red-LEDs, due to the host matrix chemical, mechanical durability and wide spectral transparency [25]. Further, the trivalent europium ions are well-established as a spectroscopic probe to get an insight into the structure and nature of the chemical bonds [26, 27]. This is mainly because of the simple energy level scheme of Eu^{3+} ions and the site selective nature of intensities between ^7F_J and $^5D_0$ energy levels [28]. Also, the relative variation of emission intensities within the orange-red region due to site selective nature of hypersensitive and non-hypersensitive $^5D_0 \rightarrow {}^7F_1$ and $^7F_2$ transitions are of particular interest for device applications.

2. Experimental

ZnAlBiB glasses doped with europium ions were prepared by rapid melt quenching technique with the composition of $20ZnO\text{-}8Al_2O_3\text{-}(12\text{-}x)Bi_2O_3\text{-}60B_2O_3\text{-}xEu_2O_3$ (x= 0.1, 0.5, 1.0, 2.0 and 2.5 mol%). Starting powders ZnO, Al_2O_3, Bi_2O_3, B_2O_3 and Eu_2O_3 were weighted, mixed in an agate mortar and melted in an alumina crucible at 1200°C for 50 min in an electric furnace. The resultant bubble free melt was then poured onto a brass mould and subsequently annealed at 400°C temperature for two hours to avoid thermal gradient induced mechanical stress. The final glass was slowly cooled to room temperature and polished for characterization. All the glass samples prepared are circular in shape with uniform thickness 1.5-1.7 mm and diameter 1.5-2.0 cm. These glasses are entitled as E1 to E5 based on the europium content from 0.1 to 2.5 mol% respectively in these glasses. The refractive index of ZnAlBiB glasses were measured with Brewster's angle method using He-Ne laser of wavelength λ=650 nm. With help of Archimedes' principle using water as an immersion liquid, the densities of ZnAlBiB glasses were measured with an accuracy of ± 0.01.The optical absorption spectra of these glasses have been recorded with UV-vis-NIR spectrophotometer (model V-670 of JASCO, with a spectral resolution of 0.1nm) in a wavelength range 350-2250 nm. The room temperature excitation and

Accepted manuscript

ACCEPTED MANUSCRIPT

Photoluminescence (PL) spectra of the titled glasses have been recorded using Schimadzu RF-5301 PC Spectrofluorophotometer. For time-resolved and steady-state photoluminescence measurements, 410nm (<20mW) diode (CW) laser as excitation, frequency generator (5Hz), lock-in amplifier, digital storage oscilloscope and a monochromator (Acton SP2300) coupled to a photomultiplier tube (PMT) were employed. The high-resolution PL images were obtained from confocal microscope (Olympus, BX51) equipped with XY-piezo stage and coupled with a 410 nm CW diode laser.

3. Result and Discussion

3.1. Physical Properties

Using the measured values of density and refractive index, various other physical properties of titled glasses have been determine by adopting the relevant expressions available in literature [29] and are presented in Table 1. From Table 1, it can be seen that, the present glasses possess low reflection losses which are helpful in the measurement of surface coating uniformity and the light transmission characteristics of various colors of glasses. For the present glasses, molar refraction decreases with the increase of Eu^{3+} concentration. The molar refractivity is considered as the sum of the contributions of the cationic refraction and oxygen ion reaction and it is also a measure of bonding condition in the glass [30]. The polaron radius in titled glasses decreases with increase in the Eu^{3+} concentration and these results are in good agreement with the results in literature [31]. Interionic distance decreasing with increase in Eu^{3+} concentration indicates that the atoms are more densely packed in these glasses. The present glasses give low field strength values, which indicate good solubility of the doped rare earth ions. The stability of the titled glasses can be confirmed from the low molecular electronic polarizability values. The increase in optical basicity values of these glasses with increase in Eu^{3+} concentration indicates the increase in the ability of oxide ions to contribute negative charge to the glass matrix i.e., the electron donating power of the oxygen in the titled glasses.

3.2. Optical Absorption Spectra

The optical absorption spectrum of Eu^{3+} doped ZnAlBiB glass (E5) recorded in NIR regions is shown in Fig.1, with the assignments of the bands originating from $^7F_0$ and $^7F_1$. The strong absorption of the host glass in UV region has resulted in the disappearance of some of the absorption bands of Eu^{3+} in the host glass in that region. The assignment of the energy levels in Fig.1 is done in accordance with the procedure outlined by Carnall et al [32].The absorption spectrum shown in Fig. 1, gives only two transitions in NIR regions ($^7F_0 \rightarrow {}^7F_6$ and $^7F_1 \rightarrow {}^7F_6$). The close absorption band positions of $^7F_0 \rightarrow {}^7F_6$ and $^7F_1 \rightarrow {}^7F_6$ reveals that the energy gap between $^7F_0$ & $^7F_1$ levels are 236 cm^{-1}, which is comparable

Accepted manuscript

ACCEPTED MANUSCRIPT

to the other Eu^{3+} doped systems [33]. Due to this small energy gap, first excited state $^7F_1$ also gets populated along with ground state $^7F_0$. Generally, the bands in the absorption spectra of rare earth ions occur due to intra-configurational f-f transitions. The band positions of the absorption transitions for the titled glasses are at the same wavelength for all the glasses with significant difference in their intensities with Eu^{3+} ion concentration. The bonding parameters for the titled glasses have been evaluated by using the expressions given in our previous paper [13]. The bonding parameters (δ) for the titled glasses are found to be 0.014, 0.015, 0.015, 0.015 and 0.017 for E1 to E5 respectively. The bonding parameter (δ) may be positive or negative, which indicates the nature of bonding (covalent or ionic).The evaluated δ value for the titled glasses are found to be positive, indicating the bonding between Eu-O is more covalent in nature. The J-O intensity parameters for Eu^{3+} doped glasses can be estimated in two different approaches [34, 35]. One is from the optical absorption spectra by considering the selective transitions and the other one is from the analysis of luminescence spectra at room temperature. In the present work, due to the availability of limited number of absorption bands, the J-O parameters are obtained from the luminescence spectral analysis which will be discussed in the following sections.

3.3. Excitation Spectra, Photoluminescence Spectra and J-O analysis

The excitation spectra for all the ZnAlBiB glasses were recorded from 350-550 nm at an emission wavelength 613 nm and are shown in Fig. 2. It shows various excitation transitions populated from $^7F_0$ and $^7F_1$ ground states. Several excitation bands observed in the excitation spectra for the titled glasses suggests the feasibility of using many commercially available UV-green LEDs for excitation. The excitation spectra show characteristic features of Eu^{3+} excitation without any spectral shifts in all the samples under 613 nm emission. Among all excitation spectra, 2.5mol % of Eu^{3+} concentration shows relatively high intense emission peaks at 364, 383, 395, 413, 467, 528 and 532nm, corresponding to $^7F_0 \rightarrow {}^5D_4$, $^5G_2$, $^5L_6$, $^5D_3$, $^5D_2$, $^7F_1 \rightarrow {}^5D_1$ and $^7F_0 \rightarrow {}^5D_1$ transitions of Eu^{3+} ion, respectively. Among all the excitation bands, a band observed at 395 nm is sharper than other bands in all the glasses. It is well known fact that a sharp excitation wavelength can give intense emissions. Though the excitation band at 395 nm is more intense in all the glasses, the emission spectra in the present work were recorded at 410 nm using CW laser source because a laser source can excite more number of atoms to the desired level than the conventional excitation sources. The non-availability of a laser source at 395 nm made us to record the emission spectra by fixing the nearest CW laser source wavelength (410 nm) for excitation. Fig.3 shows the emission spectra recorded for all the ZnAlBiB

Accepted manuscript

glasses doped with Eu^{3+} ions at room temperature using 410 nm CW laser excitation source. As shown in Fig.3 the emission spectra consists of five emission bands at 579, 590, 613, 646 and 702nm related to the $^5D_0 \rightarrow {}^7F_J$ (J = 0, 1, 2, 3, 4) transitions respectively. We have also recorded the emission spectra for Eu^{3+} ions in ZnAlBiB glasses by fixing the excitation wavelength at 395 nm using a commercial spectrofluorophotometer to know the difference between the emission spectra given by 395 nm (conventional source) and 410 nm (CW laser) excitation sources. The inset in Fig.3 shows the emission spectra of Eu^{3+} ions in ZnAlBiB glasses at an excitation wavelength 395 nm. The emission spectra shown in Fig.3 and its inset give the same emission bands with slight difference in their intensities. The intensity of the emission bands produced by 410 nm CW laser excitation source is slightly more than its counterparts produced at 395 nm conventional excitation source. Overall, the emission intensities were found to increase with the increase of Eu^{3+} concentration in these glasses and no concentration quenching is observed. The increase in intensity of the photoluminescence and excitation spectra confirms the increase in Eu^{3+} ions luminescence centers with the increase in Eu^{3+} ion concentration. The PL intensity of $^5D_0 \rightarrow {}^7F_J$ transition and the Stark-crystal field splitting is strongly dependent on the local symmetry crystal field of Eu^{3+} ions [36]. Among all the emission spectral lines, $^5D_0 \rightarrow {}^7F_0$, $^5D_0 \rightarrow {}^7F_2$ and $^5D_0 \rightarrow {}^7F_3$ transitions originate from C_2 sites by electric dipole transition and $^5D_0 \rightarrow {}^7F_1$ by magnetic dipole transition positioned at both S_6 and C_2 sites [35, 37-38]. Among all the emission transitions, an intense emission peak at 613 nm due to $^5D_0 \rightarrow {}^7F_2$ transition is hypersensitive forced electric dipole transition. The second strongest at 590 nm is in the orange region corresponding to the magnetic dipole transition $^5D_0 \rightarrow {}^7F_1$. To understand the visible emission of these glasses we have recorded the confocal photoluminescence images and are shown in Fig. 3. These images show dominant red color luminescence, as visible to the naked eye. From these images, it has can be observed that (Fig 3) 2.5 mol% of Eu^{3+} ions in these glasses gives highest red emission among all the glasses.

For the titled glasses, the lower asymmetry of Eu^{3+} ions is confirmed by the splitting of $^5D_0 \rightarrow {}^7F_1$ transition into three components, which is further supported by the red to orange luminescence intensity ratio (R/O) of $^5D_0 \rightarrow {}^7F_2$ to $^5D_0 \rightarrow {}^7F_1$transition. The R/O ratio also known as asymmetric ratio is used as an indication to assess the chemical bond strengths around Eu^{3+} ions [39]. The R/O emission intensity ratio measured for the color transitions corresponding to $^5D_0 \rightarrow {}^7F_2$ and $^5D_0 \rightarrow {}^7F_1$ for different Eu^{3+}doping ZnAlBiB glasses are listed in Table 2. The relatively higher R/O ratio (2.78) obtained for the present ZnAlBiB glasses clearly shows that red color emission is more intense when compared with

Accepted manuscript

ACCEPTED MANUSCRIPT

orange color emission. From Table 2, it can be observed that the R/O values goes on increasing with increase in the concentration of Eu^{3+} ions. The highest value of R/O for E5 glass suggests that Eu^{3+} ions possess lower symmetry and a higher Eu-O covalence. Further these results are in consistent with aforementioned bonding parameters evaluated from nephelauxetic ratios. In general, the dominant red $^5D_0 \rightarrow {}^7F_2$ transition and enhanced emission intensities indicates the strong covalent nature of the bonds between the Eu^{3+} ions and other constituents [40]. The richness in red color emission is further confirmed by the measurements of CIE chromaticity coordinates, which are highly useful in developing luminescent optical systems [41, 42].

As mentioned earlier, in the present work for the present glasses we have measured the J-O intensity parameters from the emission spectra. In Eu^{3+} ions, the $^5D_0 \rightarrow {}^7F_1$ transition is magnetic dipole allowed, and other emission transitions $^5D_0 \rightarrow {}^7F_J$ (J =2, 4 and 6) are from allowed electric dipole induced transitions. It is also known that, the magnetic dipole allowed transitions are independent of the host matrix whereas the electric dipole allowed transitions are depend on host matrix i.e., on J-O parameters Ω_λ (λ = 2, 4 and 6). Thus the J-O parameters Ω_λ (λ = 2, 4 and 6) for Eu^{3+} ions can be evaluated by taking the ratio of the intensity of the $^5D_0 \rightarrow {}^7F_J$ (J=2, 4 and 6) transitions [$\int I_J d\vartheta$] to the intensity of $^5D_0 \rightarrow {}^7F_1$ transition [$\int I_1 d\vartheta$] using the following equation [43]

$$\frac{\int I_J d\vartheta}{\int I_1 d\vartheta} = \frac{A_J}{A_1} = \frac{e^2}{S_{md}} \frac{\vartheta_J^3}{\vartheta_1^3} \frac{n(n^2+2)^2}{9n^3} \Omega_\lambda < \Psi_J U^\lambda \Psi_{J'} >^2 \text{ -------- (3)}$$

where ϑ_1 is the wavenumber (cm^{-1}) of the $^5D_0 \rightarrow {}^7F_1$ transition and ϑ_J is the wavenumber of $^5D_0 \rightarrow {}^7F_J$ (J = 2, 4 and 6) transitions, S_{md}, is the magnetic dipole line strength of the $^5D_0 \rightarrow {}^7F_1$ transition of the Eu^{3+} ions which is independent of the host matrix. In the present work the value of J-O parameter Ω_6 has been neglected in evaluating the radiative properties as its influence is negligible [44-46]. The J-O parameters thus evaluated are given in Table 2. From Table 2, it can be seen that the J-O parameters are following the same trend ($\Omega_2 > \Omega_4$) for all the ZnAlBiB glasses. From Table 2, it can also be seen that E5 glass has highest Ω_2 values than the other glasses indicating the stronger covalence and lower symmetry in that glass. This information is also in consistent with the estimated red-orange (R/O) intensity ratios as well as bonding parameter value observed for the E5 glass.

3.4. Radiative Properties

The phenomenological J-O parameters have been used to derive the most important radiative properties such as transition probability (A), total transition probability (A_T), radiative lifetime (τ_R) and branching ratio (β_R). These radiative properties are useful in predicting the lasing potentiality for the electric

Accepted manuscript

ACCEPTED MANUSCRIPT

dipole transitions between an excited level to its lower lying levels. The radiative transition probability A can be expressed from initial a_J to final a_J' [4, 47] as

$$A = \frac{64\pi^4\lambda_0{}^3}{3h(2J+1)}\left[\frac{n(n^2+2)^2}{9}S_{ed} + n^3 S_{md}\right] \quad \text{---------- (4)}$$

Where λ_0 is the peak wavelength of the emission band, S_{ed} and S_{md} are the electric and magnetic dipole line strengths respectively.

The summation of radiative transition probability from a higher energy level to all the lower energy levels gives total radiative transition probability A_T.

$$A_T = \sum A \quad \text{---------- (5)}$$

The radiative lifetime (τ_R) of an excited state can be determined by using the formula

$$\tau_R = \frac{1}{A_T} \quad \text{---------- (6)}$$

The fluorescence branching ratio (β_R) is another important radiative parameter used to understand the optical potentiality of the titled glasses and can be determined by

$$\beta_R = \frac{A}{A_T} \quad \text{---------- (7)}$$

Table 3 represents spontaneous transition probability (A_R) and total transition probability (A_T) for all the Eu^{3+} ions in ZnAlBiB glasses. From Table 3, it is observed that spontaneous transition probability (A_R) and total transition probability (A_T) are increasing from glass E1 to E5 for all transitions. Among all the glasses, glass E5 possesses maximum values of spontaneous transition probability (A_R) and total transition probability (A_T) for the transition $^5D_0 \rightarrow {}^7F_2$.

It is well know that a good laser host possesses larger stimulated emission of cross-section and can be calculated for transition from an initial manifold to final manifold using the expression [33]

$$\sigma_{se} = \frac{\lambda_p^4}{8\pi c n^2 \Delta\lambda_p} A \quad \text{---------- (8)}$$

Table 4 presents emission peak wavelength (λ_p),effective bandwidths ($\Delta\lambda_p$), peak stimulated emission cross section (σ_{se}), branching ratio (β_{exp} & β_{cal}), gain bandwidth (σ_{se} x $\Delta\lambda_P$), and Optical gain (σ_{se} x τ_R)

Accepted manuscript

ACCEPTED MANUSCRIPT

values measured for all the emission transitions of Eu^{3+} ions in E5 glass. The experimental branching ratio (β_{exp}) measured by using the relative areas under the emission peaks are found to be in good agreement with radiative branching ratio (β_R) values measured from J-O theory. The β_{exp} value is found to be high for $^5D_0 \rightarrow {}^7F_2$ transition in E5 glass with its value 0.56. The Branching ratio characterizes the lasing power of an emission transition if its values are ≥ 0.50 [48]. The laser performance of the material can be decided from the stimulated emission cross-section (σ_{se}). From Table 4 it was found that the σ_{se} values are high for $^5D_0 \rightarrow {}^7F_2$ transition of Eu^{3+} in E5 glass than other ZnAlBiB glasses. Table 5 gives the measured and calculated lifetimes (τ_{mes} & τ_{cal}). The measured lifetimes were evaluated from the decay curves which are shown in Fig. 4. From Table 5 it is observed that the measured lifetimes are decreasing with the increasing concentration. This decrease in lifetime is mainly due to the resonant energy transfer or the cross-relaxation processes.

Quantum efficiency (η) is another important characteristic parameter for lasers to predict efficiency of a laser media [14].

$$\eta = \frac{\tau_{mes}}{\tau_{cal}} \quad \text{---------- (9)}$$

It is usually taken as the ratio for the number of photons emitted from an energy level to the number of photons absorbed to that level. Such quantum efficiency values measured for all the ZnAlBiB glasses are also given in Table 5. From Table 5, it is observed that quantum efficiency increases from glass E1 to E5 and found to be maximum for the glass E5. From all the spectroscopic parameters i.e. branching ratio, stimulated emission cross-section and quantum efficiencies it is suggested that the glass E5 is more suitable to give bright red emission at a wavelength 613 nm.

3.5. Evaluation of color coordinates

The assessment and quantification of color emitted by a substance is referred to as colorimetry or the "science of color". Colorimetry is closely associated with human color vision. Mixing of two colors will appear to the human eye as one color and the eye is unable to recognize the original dichromatic composition of that color [49]. The science of mixing of colors and the resultant to the vision of eye are given by the mathematical functions called color matching functions represented by the CIE chromaticity diagram.

Accepted manuscript

ACCEPTED MANUSCRIPT

The color possessed by a light source can be characterized by three variables $\bar{x}(\lambda)\bar{y}(\lambda) and\, \bar{z}(\lambda)$ color matching functions), which are dimensionless [49]. For a given power-spectral density P(λ), the degree of stimulation required to match the color of P(λ) is given by

$$X = \int_{\lambda} \bar{x}(\lambda)P(\lambda)d\lambda$$

$$Y = \int_{\lambda} \bar{y}(\lambda)P(\lambda)d\lambda$$

$$Z = \int_{\lambda} \bar{z}(\lambda)P(\lambda)d\lambda$$

Where *X, Y* and *Z* are the tristimulus values used to get stimulation (i.e. power) for each of the three primary colors such as red, green and blue colors required to match the color P(λ).

The chromaticity coordinates *x* and *y* are calculated from the tristimulus values according to equations

$$x = \frac{X}{X+Y+Z} \quad \text{---------- (10)}$$

$$y = \frac{Y}{X+Y+Z} \quad \text{---------- (11)}$$

The chromaticity coordinates of Eu^{3+} ions in ZnAlBiB glasses at different concentrations when excited at 410 nm using CW laser have been calculated using the above said procedure and depicted in Fig.5. From Fig.5, it can be seen that irrespective of Eu^{3+} ion concentration the color coordinates measured for all the glasses falls in red region. From Fig.5, it can also be observed that in the samples prepared at relatively lower concentration of Eu^{3+} ion, the red color emission is significantly less compared with the E5 (2.5 mol%) glass. Thus it can be confirmed that the E5 glass can act as a potential red emitting material, upon excitation at 410 nm CW laser.

4. Conclusion

Zinc Alumino Bismuth Borate (ZnAlBiB) glasses with different concentrations of Eu^{3+} ions were prepared using rapid melt quenching technique to characterize their effective usage for visible red emission applications using spectroscopic techniques such as absorption, excitation, emission and confocal photoluminescence. Very limited absorption bands observed for the titled glasses constrained us to calculate J-O parameters needed to evaluate the radiative properties. Several excitation bands

Accepted manuscript

ACCEPTED MANUSCRIPT

observed in the excitation spectra suggests the feasibility of using commercially available UV green LEDs for excitation. The emission spectra recorded for all these glasses give five emission bands at 579, 590, 613, 646 and 702nm related to the $^5D_0 \rightarrow {}^7F_J$ (J = 0, 1, 2, 3, 4) transitions respectively. Red to orange luminescence intensity (R/O) ratio increases with Eu^{3+} ion concentration in these glasses indicates that the symmetry of Eu^{3+} decreases whereas the covalency increases. This result is also in consistent with the bonding parameters measured from the absorption spectra. The J-O parameters derived from the luminescence intensity ratios of $^5D_0 \rightarrow {}^7F_J$ (J = 2, 4 and 6) to $^5D_0 \rightarrow {}^7F_1$ transitions were used to calculate various radiative properties. Among various emission transitions, $^5D_0 \rightarrow {}^7F_2$ transition possesses maximum J-O parameter (Ω_2) and stimulated emission cross-section (σ_{se}) indicating red color richness in these glasses. The CIE chromaticity co-ordinates measured from the emission spectra and confocal photoluminescence images recorded for the present glasses indicates that these glasses at higher concentration of Eu^{3+} ions are most suitable for intense red emission corresponding to $^5D_0 \rightarrow {}^7F_2$ transition. Various radiative properties measured for Eu^{3+} doped ZnAlBiB glasses also speaks that these glasses at higher concentration of Eu^{3+} ions are most suitable for intense red emission. From the evaluated emission cross-sections, branching ratios, confocal photoluminescence images and CIE chromaticity co-ordinates, it was concluded that 2.5 mol% of Eu^{3+} doped ZnAlBiB glass (E5) is quite suitable for visible red emission applications.

Acknowledgements

Two of the authors, **Swapna Koneru** (File No: SR/WOS-A/PS-35/2011) and **Mahamuda Shaik**, (File No: SR/WOS-A/PS-53/2011) are highly grateful to Department of Science and Technology (DST) Govt. of India, New Delhi, for providing financial assistance to them under DST, WOS-A programme to carry out their research work. This work is also partly supported by High-impact Research initiative of IIT Delhi, UK-India Education Research Initiative (UKIERI) and DST, Govt. of India, New Delhi.

References:

[1] H. M. Yang, J. X. Shi, and M. L. Gong. J. Solid State Chem. 178 (3) (2005) 917-920.

[2] M. K. Chong , K. Pita, and C. H. Kam, J. Phys. Chem. Solids 66(1) (2005) 213-217.

[3] E. J. Nassar, L. R. Avila, P. F. S. Pereira, C. Mello, O. J. de Lima, K. J. Ciuffi, C. Mello and L. D. Carlos, J. Lumin. 111 (2005) 159-166.

[4] V. Lavin, P. Babu, C. K. Jayasankar, I. R. Martin, V. D. Rodriguez, J. Chem. Phys 115 (23) (2001) 10935-10944.

[5] R. Rama Kumar, A. S. Rao, B.C. Venkata Reddy, Optical Materials 4(6) (1995)723-728.

Accepted manuscript

ACCEPTED MANUSCRIPT

[6] A. Srinivasa Rao, J. Lakshmana Rao, R. Ramakrishna Reddy, T.V. Ramakrishna Rao, Optical Materials 4(6) (1995) 717-721.

[7] M. Sreenivasulu, A. S. Rao, J. Mater.Science. Letter 20(8) (2001)737-740.

[8] M. Venkateswarlu, M.V.V.K.S. Prasad, K. Swapna, Sk. Mahamuda, A. Srinivasa Rao, A. Mohan Babu, D. Haranath, Ceramic International 40 (2014)6261-6269.

[9] K. Swapna , Sk. Mahamuda , A. Srinivasa Rao, M. Jayasimhadri, T. Sasikala, L. Rama Moorthy J. Lumin.139 (2013) 119–124.

[10] K. Swapna, Sk. Mahamuda, A. SrinivasaRao, T. Sasikala, L. RamaMoorthy, J. Lumin (2014)288– 294

[11] Sk. Mahamuda, K. Swapna , P. Packiyaraj , A. Srinivasa Rao, G. Vijaya Prakash, Opt. Materials 36 (2013) 362–371.

[12] Sk. Mahamuda, K. Swapna, P. Packiyaraj, A. Srinivasa Rao ,G. Vijaya Prakash, J. Lumin 153 (2014) 382-392.

[13] Sk. Mahamuda , K. Swapna , A. Srinivasa Rao , M. Jayasimhadri , T. Sasikala ,K. Pavani , L. Rama Moorthy, J. Phys. Chem. Solids 74 (2013) 1308–1315

[14] K. Swapna, Sk. Mahamuda, A. SrinivasaRao, M. Jayasimhadri, T. Sasikala, L. RamaMoorthy, ceramic international 39 (2013) 8459- 8465.

[15] Sk. Mahamuda , K. Swapna , A. Srinivasa Rao , M. Jayasimhadri , T. Sasikala, L. Rama Moorthy, Physica B, 428 (2013) 36-42

[16] K. Swapna, Sk. Mahamuda, A. Srinivasa Rao ,S. Shakya, T. Sasikala, D. Haranath, G. Vijaya Prakash, Spectrochimi. Acta Part A 125 (2014) 53– 60.

[17] Sk. Mahamuda, K. Swapna, M. Venkateswarulu, A. Srinivasa Rao ,Suman latha Shakya, G. Vijaya Prakash,J. Lumin (in press).

[18] W. H. Dumbaugh, J.C. Lapp, J. Am. Ceram. Soc. 75 (1992) 2315-2326

[19] D. W. Hall, M. A. New House, N.F. Borelli, W. H. Dumbaugh, D.L. Weidman, Appl. Phys. Lett. 54 (1989) 1293-1295.

[20] J.E. Shielby, J. Am. Ceram. Soc. 71 (1998) C254-256.

[21] A.A. Kharlamov, R.M. Almeida, J. Heo, J. Non-Cryst. Solids 202 (1996) 233-240.

[22] Atul D. Sontakke, Anal Tarafdes, kaushik Biswas, K. Annapurna. Physica B 404 (2009) 3525-3529.

[23] S. Surendra Babu, P. Babu, C. K. Jayasankar, W. Sievers, Th. Troster, G. Wortmanm,

Accepted manuscript

ACCEPTED MANUSCRIPT

J. Lumin 126 (2007) 109-120.

[24] Prnova, Anna-Karell, Radovan- Gulusek, Dugan Ceramics Silicate 52 (2) (2008) 109-114.

[25] Y. Wang, T. Endo, L. He, Ch. Wu, J. Cryst. Growth 268 (2004) 568- 574.

[26] H. Ebendroff- Heidepriem and D. Ehrt, J. Non- Cryst. Solids 208 (1996) 205-216.

[27] R. Rolli, G. Samoggia, M. Bettinelli, A. Speghini, M. Wachtler, J. Non-Cryst. Solids. 288 (2001) 114 - 120.

[28] J. Mendez- Ramos, V. Lavin, I. R. Martin, U. R. Rodriguez-Mendoze, V. D. Rodriguez, A. D. Lozano- Gorrin, P. Nunez, J. Appl. Phys. 89 (2001) 5307-5310.

[29] G. V. Prakash, R. Jagannathan, D. N. Rao, Mater. Lett. 57 (2002) 134-140.

[30] Kreidl N J, Glastech Ber 62 (1989) 213-218.

[31] Agus Setyo Budi, Rosli Hussin, Md. Rahim Sahar, Jabatan Fizik, Fakulti Sains, Proceedings ICSE 19 (2002) 247-250.

[32] W. T. Carnall, P. R. Fields, K. Rajnak, J. Chem. Phys. 49 (1968) 4450-4455.

[33] B. Deva Prasad Raju, C. Madhukar Reddy, Opt. mat. 34 (2012) 1251-1260.

[34] G. Tripathi, V. K. Rai, S. B. Rai, Opt. Commun. 264 (2006) 116-122.

[35] R. Van Deun, K. Binnemans, C. Gorller- Walrand, J. L. Adam, J. Phys. Chem. Matter. 10 (1998) 7231-7241.

[36] A. Amarnath Reddy, Subrata Das, Shahab Ahmad, S. Surendra Babu, Jose, M. F. Ferreira, G. Vijaya Prakash, RSC advances 2 (2012) 8768-8776.

[37] H. Ishibashi, K. Shimomoto, K. Nakahigashi, J. Phys. Chem.Solid 55 (1994) 809-814.

[38] G. Mialon, S. Turkcan, A. Alexandrou, T. Gacoin, J. P Boilot, J. Phys.Chem. 113 (2009)18699-18706.

[39] R. Reisfeld, E. Zigansky, M. Gaft, J. Mol. Phys. 102 (2004) 1319-1330.

[40] Nogami M, Umehara N, Hayakawa T. Phys. Rev.B 58 (1998) 6166-6171.

[41] W. R. Liu, C. C. Lin, Y. C. Chiu, Y. T. Yeh, S. M. Jang, R. S. Liu, Opt. Express, 18 (3) (2010) 2946-2951.

[42] G. Kaur, S.K. Singh, S.B. Rai, J. Appl. Phys. 107 (2010) 073514- 073514-6.

[43] B. Peng, T. Izumitani, Rev. Laser Eng. 22 (1994) 16-27.

[44] K. Marimuthu, R.T. Karunakaran, S. Surendra Babu, G. Muralidharan, S. Arumugam, C. K. Jayasankar, Sol. State Sci. 11 (2009) 1297 -1302.

[45] Y. Nageno, H. Takebe, K. Morinaga, T. Izumitani, J. Non-Cryst. Solids 169 (3) (1994) 288-

Accepted manuscript

ACCEPTED MANUSCRIPT

294.

[46] Gao Tang, Jiqian Zhu, Yumei Zhu, Chaoyin Bai J. Alloys. Compd. 453 (2008) 487-492.

[47] R.D. Peacock, Struct. Bond 22 (1975) 83-122.

[48] K. Linganna, C.K. Jayasankar, Spectrochimi. Acta Part A 97 (2012) 788-797.

[49] E. Fred Schubert, Light-Emitting Diodes, 2nd edition, Cambridge University Press, 2006, (Chapter 17) p. 292 - 298.

Accepted manuscript

ACCEPTED MANUSCRIPT

Table 1. Physical properties of Eu^{3+} doped ZnAlBiB glasses

Physical Properties	**E1**	**E2**	**E3**	**E4**	**E5**
Refractive index (n_d)	1.798	1.8	1.802	1.804	1.807
Density (d) (g/cc)	4.034	4.028	4.020	4.000	3.998
Average molecular weight ($\bar{M}$)(g)	122.0	121.5	120.9	119.8	119.2
Eu^{3+} ion concentration (x10^{22} ions/cm^3)	0.199	0.997	2.001	4.020	5.047
Mean atomic Volume (g/cm^3/atom)	6.873	6.858	6.838	6.809	6.779
Dielectric Constant (ϵ)	3.232	3.24	3.247	3.254	3.265
Optical Dielectric constant ($\epsilon - 1$)	2.232	2.24	2.247	2.254	2.265
Reflection losses (R %)	0.0813	0.0816	0.0819	0.0822	0.0826
Molar Refraction (R_m)(cm^{-3})	12.90	12.89	12.88	12.85	12.83
Polaron radius (r_p) (Å)	3.256	1.903	1.510	1.197	1.109
Interionic distance (r_i) (Å)	8.079	4.724	3.746	2.970	2.753
Molar electronic polarizability α (x$10^{-23}$$cm^3$)	5.118	1.023	0.511	0.254	0.203
Field Strength (x $10^{15}$$cm^{-2}$)	2.829	8.276	13.15	20.93	24.36
Optical basicity (Δ_{th})	0.435	0.436	0.439	0.455	0.457

Accepted manuscript

ACCEPTED MANUSCRIPT

Table 2. Judd- Ofelt Parameters Ω_λ (λ=2, 4 and 6) (10^{-20} cm^2) estimated from emission spectral details and red to orange intensity ratio [R/O= ($^5D_0 \rightarrow {}^7F_2$) / ($^5D_0 \rightarrow {}^7F_1$)] of Eu^{3+} ions in ZnAlBiB glasses.

Host	Ω_2 a*	Ω_4 b*	Ω_6	Intensity Ratio(R)
From Emission Spectra				
E1	1.61	0.80	-	1.951
E2	1.76	1.32	-	2.139
E3	1.98	1.41	-	2.404
E4	2.19	1.49	-	2.666
E5	2.28	1.54	-	2.78
Reported Work				
BLNE [44]	5.72	2.45	-	-
BNNE [44]	4.98	2.38	-	-
BKNE [44]	5.06	2.98	-	-
KMgSi [45]	6.36	3.94	-	-
3.0 Eu-GICZps [46]	1.09	-	-	-
5.0 Eu-GICZps [46]	1.11	1.08	-	-
8.0 Eu-GICZps [46]	1.36	0.25	-	-

a* Determined from the transitions $^5D_0 \rightarrow {}^7F_2$ (emission spectra)
b* Determined from the transitions $^5D_0 \rightarrow {}^7F_4$ (emission spectra)

Accepted manuscript

ACCEPTED MANUSCRIPT

Table 3. Spontaneous transition probabilities (A_R) (s^{-1}), and total transition probabilities (A_T) (s^{-1}) of Eu^{3+} ions in ZnAlBiB glasses for the transitions $^5D_0 \rightarrow {}^7F_J$ (J=0-4)

Assignment	**E1**	**E2**	**E3**	**E4**	**E5**
	$\mathbf{A_R}$	$\mathbf{A_R}$	$\mathbf{A_R}$	$\mathbf{A_R}$	$\mathbf{A_R}$
$^5\mathbf{D_0} \rightarrow {}^7\mathbf{F_0}$	-	-	-	-	-
$^5\mathbf{D_0} \rightarrow {}^7\mathbf{F_1}$	82.76	83.04	83.31	83.59	84.01
$^5\mathbf{D_0} \rightarrow {}^7\mathbf{F_2}$	90.70	99.48	112.28	124.61	130.46
$^5\mathbf{D_0} \rightarrow {}^7\mathbf{F_3}$	-	-	-	-	-
$^5\mathbf{D_0} \rightarrow {}^7\mathbf{F_4}$	22.63	37.15	39.84	42.26	43.93
$\mathbf{A_T}$	196	219	235	250	258

Accepted manuscript

ACCEPTED MANUSCRIPT

Table 4. Emission peak wavelength (λ_P) (nm), Effective Bandwidth ($\Delta\lambda_P$) (nm), experimental and calculated branching ratios (β_{exp} & β_{cal}) , Stimulated emission cross section (σ_{se} X 10^{-22}) (cm^2) gain band width (σ_{se}x $\Delta\lambda_P$) (x10^{-28}) (cm^3) and optical gain (σ_{se} x τ_R) (x10^{-24})(s) for the respective transitions of the E5 glass

Transition $^5D_0 \rightarrow$	λ_P	$\Delta\lambda_P$	$\beta_{(exp)}$	$\beta_{(cal)}$	σ_{se}	σ_{se} x $\Delta\lambda_P$	σ_{se} x τ_R
$^7F_0$	579	2.70	0.03	0.00	0.00	0.00	0.00
$^7F_1$	590	13.5	0.19	0.32	3.10	4.19	1.23
$^7F_2$	613	12.1	0.56	0.50	6.71	7.45	2.66
$^7F_3$	646	6.76	0.05	0.00	0.00	0.00	0.00
$^7F_4$	702	13.5	0.17	0.16	3.17	4.29	1.26

Accepted manuscript

ACCEPTED MANUSCRIPT

Table 5. Measured lifetime (τ_{mes}), radiative lifetime (τ_{cal}) and quantum efficiency (η %) for the $^5D_0$ level of Eu^{3+} ions in ZnAlBiB glasses.

Host Matrix	**τ_{mes}(ms)**	**τ_{cal}(ms)**	**η (%)**
E1	1.850 ± 0.132	5.099	36
E2	1.956 ± 0.139	4.552	43
E3	2.015 ± 0.172	4.247	47
E4	2.122 ± 0.109	3.992	53
E5	2.124 ± 0.179	3.869	55

Accepted manuscript

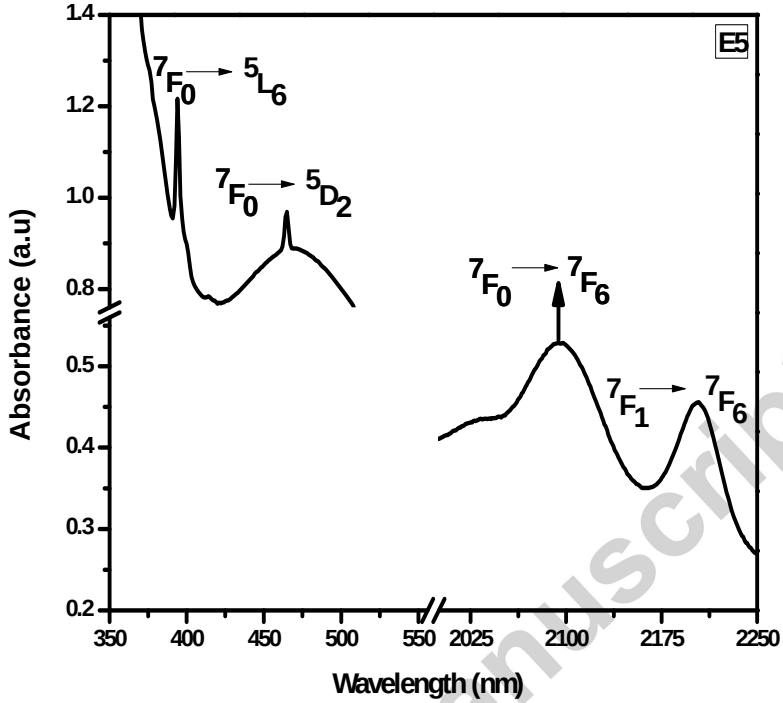


Fig 1. Optical Absorption Spectrum of E5 glass in UV-vis-NIR region.

Accepted manuscript

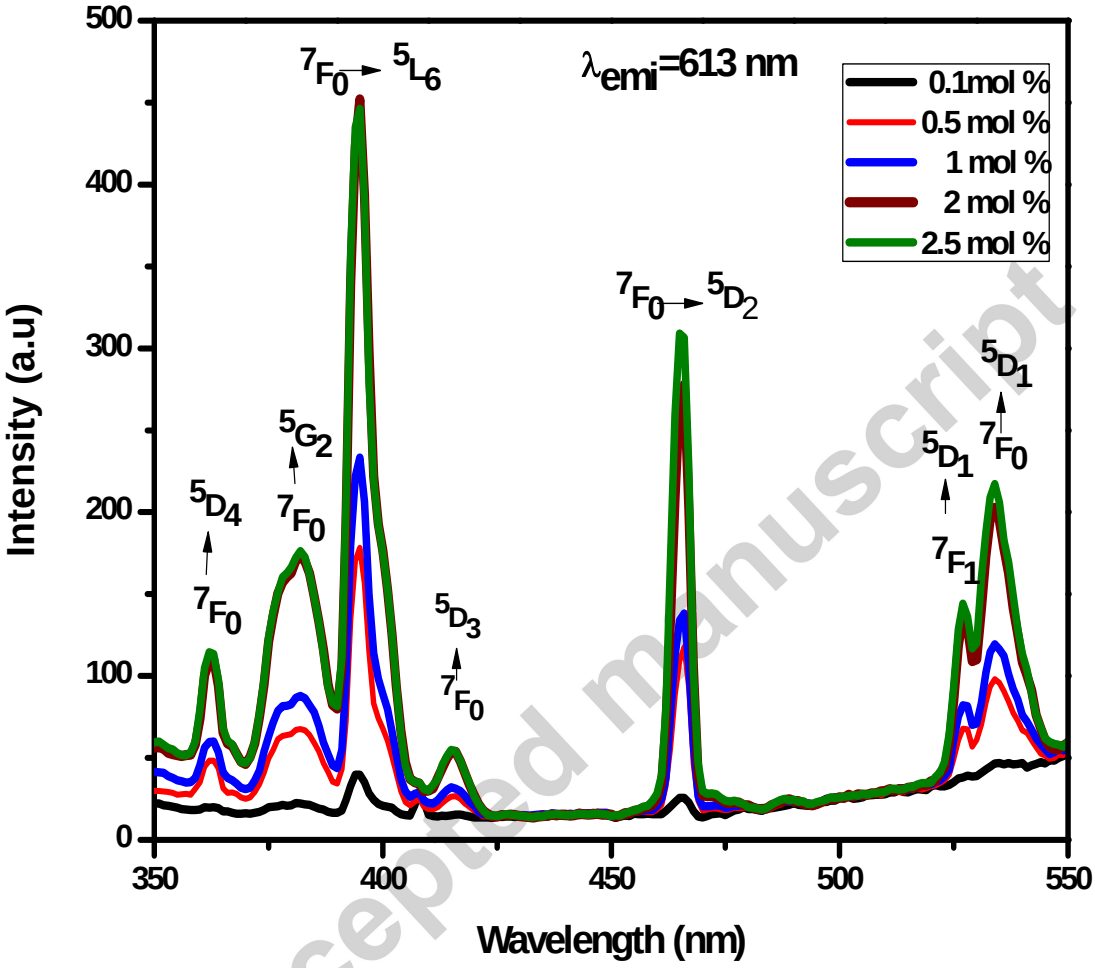


Fig 2. Excitation Spectra of Eu^{3+} doped ZnAlBiB glasses.

Accepted manuscript

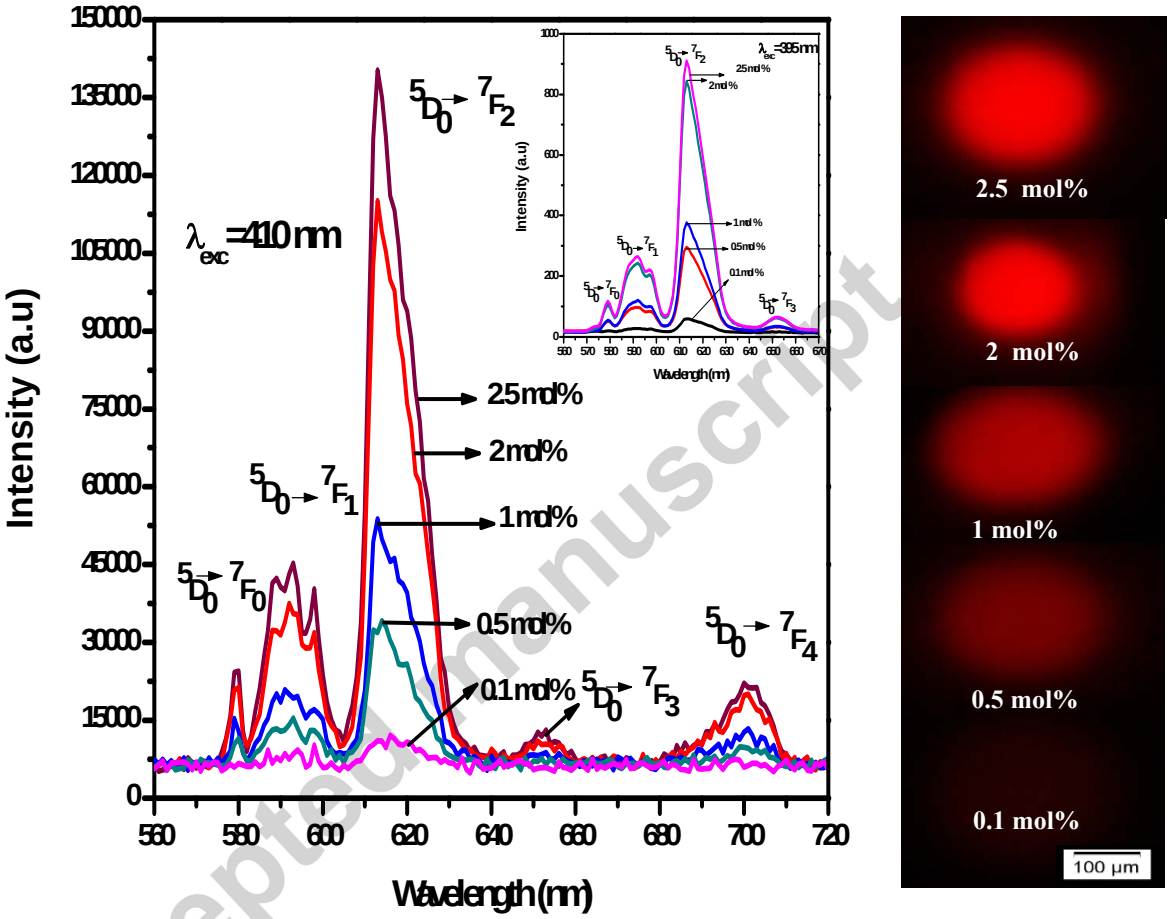


Fig 3. PL Spectra and corresponding images of Eu^{3+} doped ZnAlBiB glasses excited at 410nm CW laser. (Inset shows PL Spectra of Eu^{3+} doped ZnAlBiB glasses excited at 395nm from Xe source).

Accepted manuscript

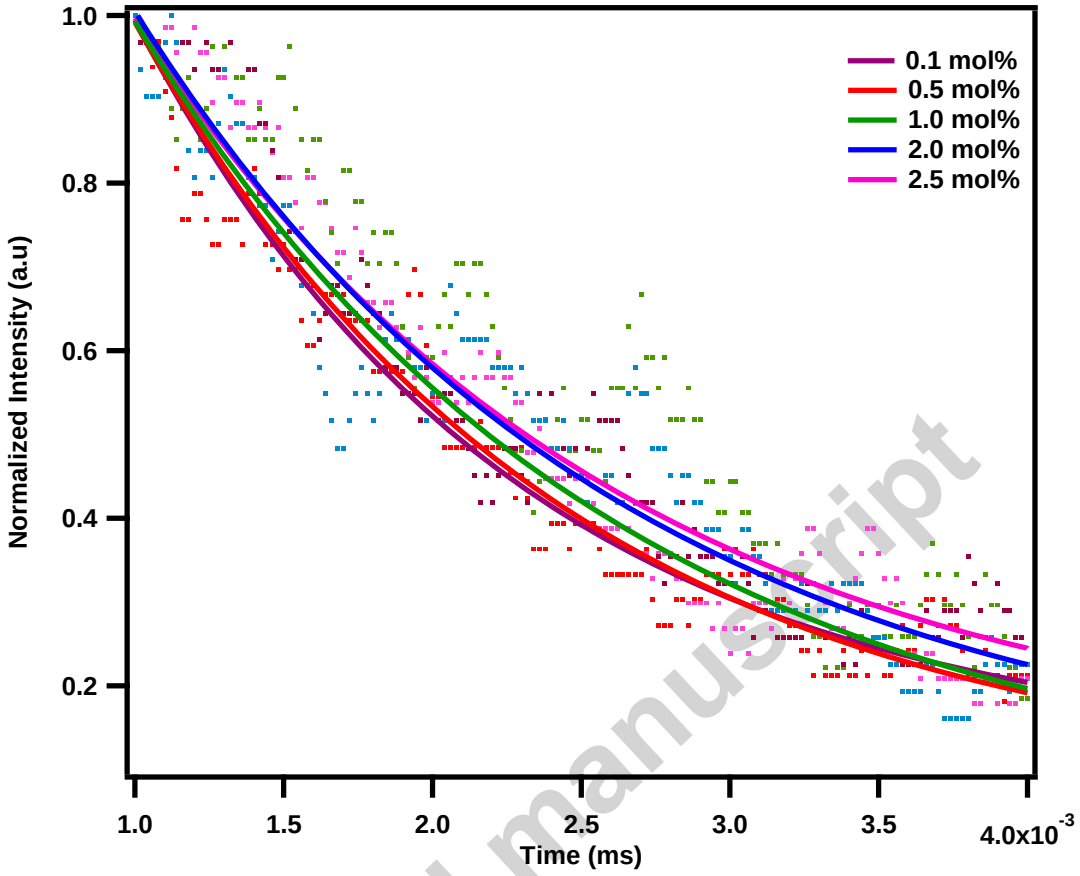


Fig 4. Decay rates for the $^5D_0$ level of Eu^{3+}: ZnAlBiB glasses for different glasses.

Accepted manuscript

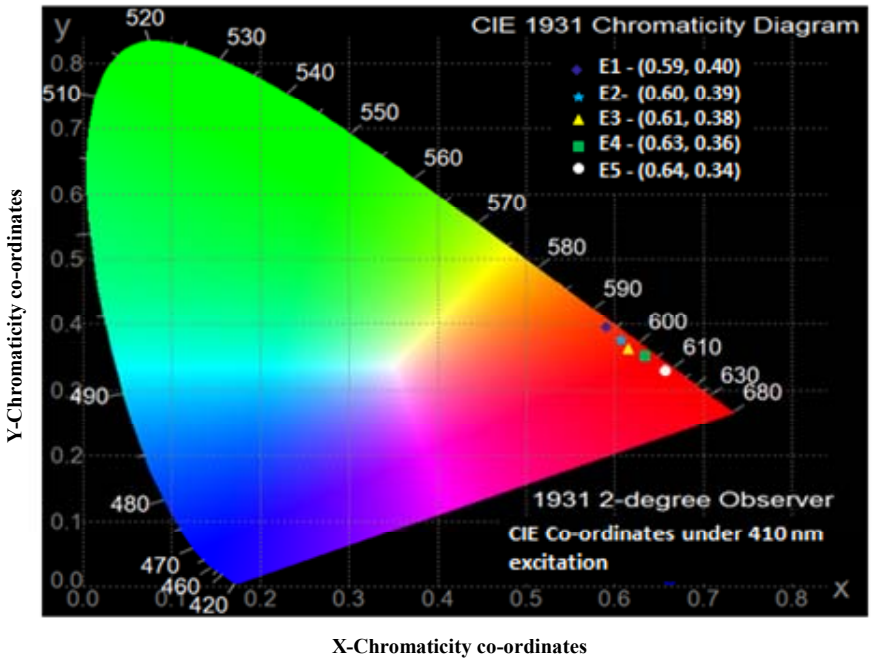


Fig 5. The color space chromaticity diagram of Eu^{3+}: ZnAlBiB glasses.

Accepted ma

ACCEPTED MANUSCRIPT

High lights

- ZnAlBiB glasses doped with Eu^{3+} ions were prepared by conventional melt quenching technique.
- Radiative properties are measured from the emission spectra.
- Quantum efficiency of the ZnAlBiB glasses is measured by using radiative and measured lifetimes.
- CIE Chromaticity coordinates are evaluated from emission spectra.

Accepted manuscript

Nature & Environment
Vol. 19 (2), 2014: 219-231
Website: www.natureandenvironment.com

ISSN (Print) : 2321-810X
ISSN (Online) : 2321-8738

RESEARCH ARTICLE

Method for Improving Thermal Performances of Vapour Compression Refrigeration Systems Using Energy and Exergy Analysis for Reducing Global Warming and Ozone Depletioning Using Ecofriendly Refrigerants

R.S. Mishra
Mechanical Engineering Department, Delhi College of Engineering (Now DTU), Delhi
Email: professor_rsmishra@yahoo.co.in

Received: 2nd June 2014, Revised: 20th June 2014, Accepted: 29th June 2014

ABSTRACT

In this paper the method for improving thermal performance of vapour compression refrigeration system using multiple evaporators and compressors with individual or multiple expansion valves have been considered by using first law and second law analysis. Numerical models have been developed for parallel and series expansion valves in the VCR. The comparison of above systems have been done in terms of first law efficiency, second law efficiency and exergy destruction ratio by using R410a, R290, R600, R600a, R1234yf, R502, R404a, R1234ze, R134a and R152a. it was observed that for the same degree of subcooling, fixed evaporators and condenser temperatures multiple evaporators and compressors with multiple expansion valves system is the best system with comparisons of system with individual expansion valves. The comparison was also done using eight ecofriendly refrigerants and it was found that R600, R600a, R290 and R152A show better performances than other refrigerants for both systems but due to inflammable property of R600 and R600a, R152a is preferred for both systems.

Key Words: *Energy and exergy analysis, thermal performance, global warming*

INTRODUCTION

Refrigeration is a technology which absorbs heat at low temperature and provides temperature below the surrounding by rejecting heat to the surrounding at higher temperature. Simple vapour compression system which consists of four major components compressor, expansion valve, condenser and evaporator in which total cooling load is carried at one temperature by single evaporator but in many applications like large hotels, food storage and food processing plants, food items are stored in different compartment and at different temperatures. Therefore there is need of multi evaporator vapour compression refrigeration system. The systems under vapour compression technology consume huge amount of electricity, this problem can be solved by improving performance of system.

Performance of systems based on vapour compression refrigeration technology can be improved by following:-

The performance of refrigerator is evaluated in term of COP which is the ratio of refrigeration effect to the net work input given to the system. The COP of vapour compression refrigeration system can be improved either by increasing refrigeration effect or by reducing work input given to the system.

It is well known that throttling process in VCR is an irreversible expansion process. Expansion process is one of the main factors responsible for exergy loss in cycle performance because of entering the portion of the refrigerant flashing to vapour in evaporator which will not only reduce the cooling capacity but also increase the size of evaporator. This problem can be eliminated by adopting multi-stage expansion with flash chamber where the flash vapours is removed after each stage of expansion as a consequence there will be increase in cooling capacity and reduce the size of the evaporator.

Work input can also be reduced by replacing multi-stage compression or compound compression with single stage compression. Refrigeration effect can also be increased by passing the refrigerant through subcooler after condenser to evaporator.

Table 1: Represents the ODP and GWP for various refrigerants.

Refrigerant		Atmospheric Lifetime (Years)	ODP	GWP (100 Year)
CFC	CFC-11 (Baseline ODP)	50	1	4000
	CFC-12	102	1	8500
CFC Blend	R-502		0.33	5260
HCFCs	HCFC-22	13.3	0.06	1700
	HCFC-123	1.4	0.02	93
	HCFC-141b	9.4	0.11	630
HFCs	HFC-134a	14.6	0	1300
	HFC-245fa	7.3	0	820
HCs	HC-290 (Propane)	-	0	3
	HC-600a (Isobutene)	-	0	3
	Cyclopentane	-	0	3
HFC Blends	R-404A	-	0	3260
	R-407A	-	0	1770
	R-407C	-	0	1530
	R-410A	-	0	1730

Vapour compression refrigeration system based applications make use of refrigerants which are responsible for greenhouse gases, global warming and ozone layer depletion. Montreal protocol was signed on the issue of substances that are responsible for depleting Ozone layer and discovered how much consumption and production of ozone depletion substances took place during certain time period for both developed and developing countries. Another protocol named as Kyoto aimed to control emission of green house gases in 1997 (Johnson 1998). The relationship between ozone depletion potential and global warming potential is the major concern in the field of GRT (green refrigeration technology) so Kyoto proposed new refrigerants having lower value of ODP and GWP. Internationally a program being pursued to phase out refrigerants having high chlorine content for the sake of global environmental problems (QiyuChen and Prasad 1999): Due to presence of high chlorine content, high global warming potential and ozone depletion potential after 90's CFC and HCFC refrigerants have been restricted. Thus, HFC refrigerants are used nowadays, showing much lower global warming potential value, but still high with respect to non-fluorine refrigerants. Research has recently been focused on development of new refrigerants to replace CFCs and HCFCs. These new working fluids are synthetic compounds-namely hydro-fluorocarbons (HFCs). Although the ozone-depletion potential (ODP) of some HFCs is zero, their global warming potential (GWP)--related to the greenhouse effect-can be large. An alternative to HFCs is the use of naturally occurring substances (refrigerants), namely; ammonia (NH3), hydrocarbons (HCs), carbon dioxide (CO2), water, air. These refrigerants have zero ODP, and the majorities also have zero GWP. However, some of them can be flammable and/or toxic. Table 1 shows the ODP and GWP for various refrigerants. From the table 1.1 It has been observed that R134a, R404A, R407A, R407C and R410C have low ODP and GWP than R12 and R22. Lots of research work has been done for replacing "old" refrigerants with "new" refrigerants (Padilla *et al.* 2010, Spauschus 1988, Ahamed *et al.* 2011, Llopis *et al.* 2010, Arora and Kaushik 2008 and Havelsky 2000).

LITERATURE REVIEW

Reddy *et al.* (2012) performed numerical computation of vapour compression refrigeration system using R134a, R143a, R152a, R404A, R410A, R502 and R507A , for finding the effect of evaporator temperature, degree of subcooling at condenser outlet, superheating of evaporator outlet, vapour liquid heat exchanger effectiveness and degree of condenser temperature on COP and exergetic efficiency using energy- exergy analysis and found that

evaporator and condenser temperature have significant effect on both COP and exergetic efficiency and also found that R134a has the better performance while R407C has poor performance in all respect. Saravanakumar and Selladurai (2013) compared the performance between R134a and R290/R600a mixture on a domestic refrigerator which is originally designed to work with R134a and found that R290/R600a hydrocarbon mixture showed higher COP and exergetic efficiency than R134a and also the highest irreversibility obtained in the compressor compare to condenser, expansion valve and evaporator in the vapour compression refrigeration system. Nikolaidis and Probert (1998) studied analytically that change in evaporator and condenser temperatures of two stage vapour compression refrigeration plant using R22 and found that there is a significant effect of plant irreversibility and suggested that there is need for optimizing the conditions imposed upon the condenser and evaporator. Kumar *et al.* (1989) carried out energy and exergy analysis of vapour compression refrigeration system by the use of exergy-enthalpy diagram and performed first law analysis (energy analysis)for calculating the coefficient of performance and exergy analysis (second law analysis) for evaluation of various losses occurred in different components of vapour compression cycle using R11 and R12 as refrigerants. Mastani Joybari *et al.* (2013) performed experiments on a domestic refrigerator originally manufactured by using of 145g of R134a. They concluded that exergetic defect occurred in compressor was highest as compare to other components and through their analysis it has been found that instead of 145g of R134a if 60g of R600a is used in the considered system gave same performance which ultimately result into economical advantages and reduce the risk of flammability of hydrocarbon refrigerants. Anand and Tyagi (2012) carried out detailed exergy analysis of two ton of refrigeration capacity window air conditioning test rig with R22 as working fluid and concluded , that irreversibility in system components will be highest when the system is 100% charged and lowest when 25% charged and irreversibility in compressor is highest among system components. Arora and Kaushik (2008) developed numerical model of actual vapour compression refrigeration system with liquid vapour heat exchanger and carried out energy and exergy analysis on the same in the specific temperature range of evaporator and condenser and concluded that R502 is the best refrigerant compared to R404A and R507A and compressor is the worst component and liquid vapour heat exchanger is best component of the system in case of exergy transfer. Ahamed *et al.* (2011) had performed experiments on domestic refrigerator with hydrocarbons (isobutene and butane) by using energy and exergy analysis and found that energy efficiency ratio of hydrocarbons comparable with R134a but exergy efficiency and sustainability index of hydrocarbons much higher than that of R134a at considered evaporator temperature. It was also found that compressors shows highest system defect (69%) among components of considered in the system. Ahamed et al. (2012) emphasized on use of hydrocarbons and mixture of hydrocarbons and R134a in vapour compression refrigeration system and found that compressor shows much higher exergy destruction as compared to rest of components in the vapour compression refrigeration system and this exergy destruction can be minimized by using of nanofluid and nanolubricants in compressor. Bolaji *et al.* (2011) had done experimentally comparative analysis of R32, R152a and R134a refrigerants in vapour compression refrigerator and concluded that R32 shows lowest performance whereas R134a and R152a showing nearly same performance but best performance was obtained of system using R152a. Yumrutas *et al.* (2002) carried out exergy analysis based investigation on VCR for effect of condensing and evaporating temperature on vapour compression refrigeration cycle in terms of pressure losses, COP, second law efficiency and exergy losses and found that the variation in temperature of condenser as well as have negligible effect on exergy losses of compressor and expansion valve, also first law efficiency and exergy efficiency increase but total exergy losses of system decrease with increase in evaporator and condenser temperature. Padilla *et al.* (2010) carried out the exergy analysis of domestic vapour compression refrigeration system with R12 and R413A and found that performance in terms of power consumption, irreversibility and exergy efficiency of R413A is better than R12, and also concluded that R12 can be replaced with

R413A in domestic vapour compression refrigeration system. Getu and Bansal (2008) optimized the design and operating parameters of like condensing temperature, subcooling temperature, evaporating temperature, superheating temperature and temperature difference in cascade heat exchanger R744-R717 cascade refrigeration system and regression analysis was also done to obtain optimum thermodynamic parameters of same system. Spatz and Motta (2004) had mainly focused on replacement of R12 with R410a through experimental investigation of medium temperature vapour compression refrigeration cycles. In terms of thermodynamic analysis, comparison of heat transfer and pressure drop characteristics, R410a gives best performance among R12, R404a and R290a. Mohanraj *et al.* (2009) concluded through experimental results of domestic refrigerator they arrived on conclusions that under different environmental temperatures COP of system using mixture of R290 and R600a in the ratio of 45.2: 54.8 by weight showing up to 3.6% greater than same system using R134a, also discharge temperature of compressor with mixture of R290 and R600a is lower in the range of 8.5-13.4K than same compressor with R134a. Han et al. (2007) Through experimental results revealed that there could be replacement of R407C under different working conditions in vapour compression refrigeration system having rotor compressor by using mixture of R32/R125/R161 showing higher COP, less pressure ratio and slightly high discharge compressor temperature without any modification in the same system. Halimic *et al.* (2003) had compared the thermal performance of R401A, R290 and R134A with R12 by using in vapour compression refrigeration system, which is originally designed for R12.Due to similar performance of R134a in comparison with R12, R134A can be replaced in the same system without any medication in the system components. But in reference to green house impact R290 presented best results.

Cabello *et al.* (2007) studied about the effect of operating parameters on first law efficiency (COP), work input and cooling capacity of single-stage vapour compression refrigeration system. There is great influence on energetic parameters due change in suction pressure, condensing and evaporating temperatures. Cabello *et al.* (2007) discussed the effect of condensing pressure, evaporating pressure and degree of superheating was experimentally investigated on single stage vapour compression refrigeration system using R22, R134a and R407C.It was observed that mass flow rate is greatly affected by change in suction conditions of compressor in results on refrigeration capacity because refrigeration capacity depended on mass flow rate through evaporator. It was also found that for higher compression ratio R22 gives lower COP than R407C. Stanciu and Alvarado (2005) carried out numerical and graphical investigation on single stage vapour compression refrigeration system for studied refrigerants (R22, R134a, R717, R507a, R404a) in terms of COP, compressor work, exergy efficiency and refrigeration effect. Effect of subcooling, superheating and compression ratio are also studied on the same system using considered refrigerants and also presented system optimization when working with specific refrigerant in the vapour compression.

Based on the literature it was observed that researchers have gone through detailed first law analysis in terms of coefficient of performance and second law analysis in term of exergetic efficiency of simple vapour compression refrigeration system with single evaporator. Researchers did not go through the irreversibility analysis or second law analysis of: Simple VCR with flash intercooler, flash chamber, water intercooler, liquid subcooler and stages in compression (double stage and triple stage) and multiple evaporators systems with multi-stage expansion and compound compression in vapour compression refrigeration systems.

To improve thermal performance of vapour compression refrigeration systems (both single and multiple evaporator system) by improving (i) First law efficiency, (ii) second law efficiency, (iii) reduction of system defect in components of system which results into reduction of work input and (iv) detailed analysis of vapour compression refrigeration systems using ecofriendly refrigerants. This paper mainly deals the energy and exergy analysis of multiple evaporators and compressors with individual expansion valves (system-1) and multiple evaporators and compressors with multiple expansion valves (system-2)

vapour compression refrigeration systems for finding irreversibility of the systems for improvement in system designs.

Models Description of Multiple Evaporators and Compressors with Individual Expansion Valves (System-1) and Multiple Evaporators and Compressors with Multiple Expansion Valves (System-2) Vapour Compression Refrigeration Systems

The multiple evaporators and compressors with individual expansion valves vapour compression refrigeration system (system-1) consists of compressors (C_1, C_2, C_3) throttle valves (TV_1, TV_2, TV_3), condenser and evaporators(EP_1, EP_2, EP_3) as shown in Fig.1(a).The pressure versus enthalpy chart for this system is shown in Fig.1(b). In this system all refrigerants coming out in point '77' from subcooler distributed by mass $\dot{m}_1$, $\dot{m}_2$, $\dot{m}_3$ to expansion valves TV_1, TV_2, and TV3 respectively. Both liquid and vapour formed by TV_1 ,TV_2 ,TV_3 represented by point '10', '9' and '8' take care the load of EP_1 ,EP_2 and EP_3 respectively. The low pressure vapours formed by EP_1 ,EP_2 and EP_3 supplied to the compressor C_1 ,C_2 and C_3 represented by point '1', '3' and '5' respectively. The high pressure vapours formed by compressor C_1 ,C_2 and C_3 respectively represented by points '2', '4' and '6' .Then high pressure vapours coming out from compressor C_1 , C_1 , C_1 collectively enter through the condenser by point '7'.

The main components of multiple evaporators and compressors with individual expansion valves vapour compression refrigeration system (system-2) are compressors (C_1, C_2, C_3) throttle valves (TV_1, TV_2, TV_3), condenser and evaporators (EP_1, EP_2, EP_3) as shown in Fig. 2(a).The corresponding pressure versus enthalpy chart for this system is shown in Fig. 2(b).In this system all the refrigerant from the condenser at point 'g' followed by the subcooler exit at point 'gg' flows through the throttle valve TV3 where its pressure is reduced from the condenser pressure of the third evaporator. All the vapours formed after leaving the expansion valve TV3 at point 'h' plus enough liquid to take care of the load of evaporator EP3.The remaining refrigerant then enter at point 'i' through the expansion valve TV2 where its pressure is reduced from the pressure of the third evaporator to the pressure of the second evaporator. Again all the vapour formed after leaving the expansion valve TV_2 at point 'j'plus enough liquid to take care of the load of evaporator EP_2 passes through this evaporator. The remaining liquid now enters at point 'k' through the expansion valve TV_1 and exit at point 'l'which supplied it to the first evaporator EP_1. The vapours formed by EP_1, EP_2, EP_3 supplied to compressors C_1, C_2 and C_3 shown by point 'a', 'c' and 'e' respectively. High pressure vapours formed by compressors C_1, C_2 and C_3 as is shown by points 'b', 'd' and 'f' respectively supplied to the condenser.

First Law Analysis (COP & Work Input Analysis) of Multiple Evaporators and Compressors with Individual or Multiple Expansion Valves Vapour Compression Refrigeration Systems

The multiple evaporators and compressors with individual or multiple expansion valves vapour compression refrigeration system as shown in Fig. 1 and Fig. 2 respectively. From the energy analysis point of view first law of thermodynamics, evaluate the performance of the vapour compression systems as given below:-

System-1

$\dot{m}_{e1} = \dot{m}_{c1}$ ..... (1)

$\dot{m}_{e2} = \dot{m}_{c2}$ ..... (2)

$\dot{m}_{e3} = \dot{m}_{c3}$ ..... (3)

$\dot{Q}_{e_1} = \dot{Q}_{e1} + \dot{Q}_{e2} + \dot{Q}_{e3}$ ..... (4)

$\dot{W}_{comp1} = \dot{m}_{c1}(\psi_2 - \psi_1)$ ..... (5)

$\dot{W}_{comp2} = \dot{m}_{c2}(\psi_4 - \psi_3)$ ..... (6)

$\dot{W}_{comp3} = \dot{m}_{c3}(\psi_6 - \psi_5)$ ..... (7)

$\dot{W}_{comp_1} = \dot{W}_{comp1} + \dot{W}_{comp2} + \dot{W}_{comp3}$ ..... (8)

$$COP_1 = \frac{\dot{Q}_{e_1}}{\dot{W}_{comp_1}} \quad \text{..... (9)}$$

System-2

$$\dot{m}_{c1} = \dot{m}_{e1} \quad \text{..... (10)}$$

$$\dot{m}_{c2} = \dot{m}_{e2} = \dot{m}_2 + \dot{m}_{e1}\left(\frac{\varphi_j}{1-\varphi_j}\right) \quad \text{..... (11)}$$

$$\dot{m}_2 = \left(\frac{\dot{Q}_{e2}}{\psi_c - \psi_j}\right) \quad \text{..... (12)}$$

$$\dot{m}_{c3} = \dot{m}_{e3} = \dot{m}_3 + (\dot{m}_{e1} + \dot{m}_{e2})\left(\frac{\varphi_h}{1-\varphi_h}\right) \quad \text{..... (13)}$$

$$\dot{m}_3 = \left(\frac{\dot{Q}_{e3}}{\psi_e - \psi_h}\right) \quad \text{..... (14)}$$

$$\dot{Q}_{e_2} = \dot{Q}_{e1} + \dot{Q}_{e2} + \dot{Q}_{e3} \quad \text{..... (15)}$$

$$\dot{W}_{comp1} = \dot{m}_{c1}(\psi_b - \psi_a) \quad \text{..... (16)}$$

$$\dot{W}_{comp2} = \dot{m}_{c2}(\psi_d - \psi_c) \quad \text{..... (17)}$$

$$\dot{W}_{comp3} = \dot{m}_{c3}(\psi_f - \psi_e) \quad \text{..... (18)}$$

$$\dot{W}_{comp_2} = \dot{W}_{comp1} + \dot{W}_{comp2} + \dot{W}_{comp3} \quad \text{..... (19)}$$

$$COP_2 = \frac{\dot{Q}_{e_2}}{\dot{W}_{comp_2}} \quad \text{..... (20)}$$

Fig. 1 (a): Schematic diagram of multiple evaporators at different temperatures with individual compressors and individual expansion valves

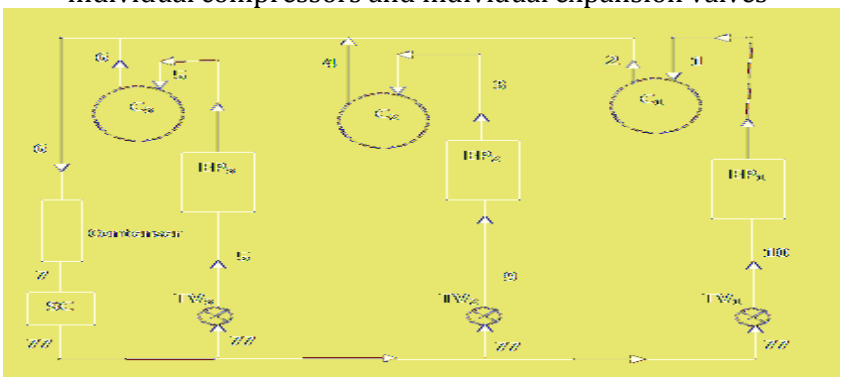


Fig. 1 (b): Pressure enthalpy diagram of multiple evaporators at different temperatures with individual compressors and individual expansion valves

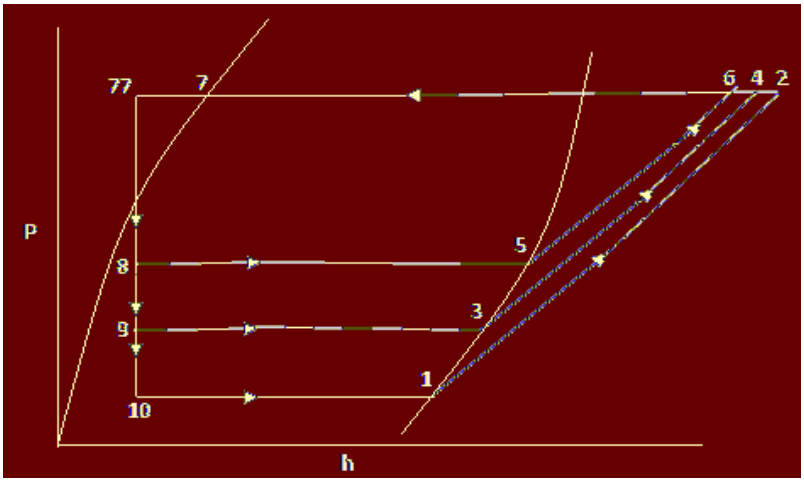


Fig. 2 (a): Schematic diagram of multiple evaporators at different temperatures with individual compressors and multiple expansion valves

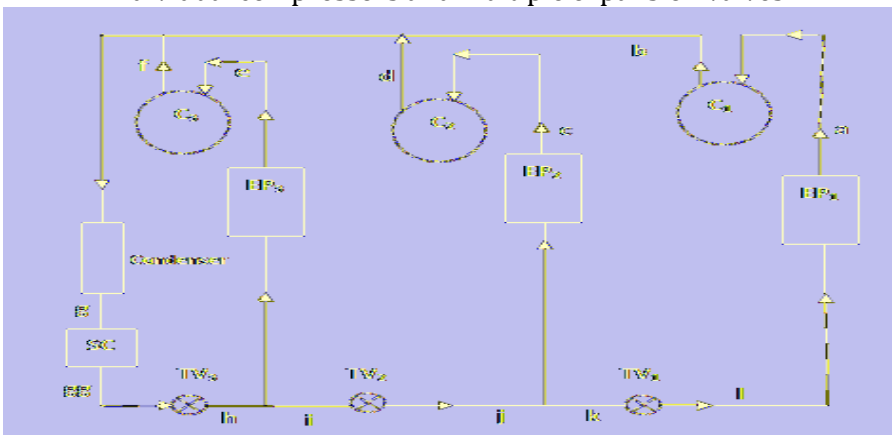
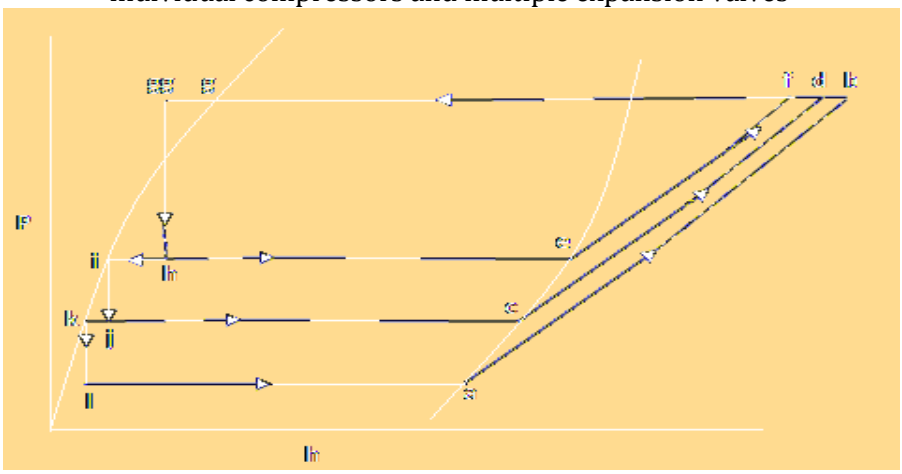


Fig. 2 (b): Pressure enthalpy diagram of multiple evaporators at different temperatures with individual compressors and multiple expansion valves



Second Law Analysis of Multiple Evaporators and Compressors with Individual or Multiple Expansion Valve Vapour Compression Refrigeration System

The concept of exergy was given by Second law of thermodynamics. Exergy is the measure of usefulness, quality or potential of a stream to cause change and an effective measure of the potential of a substance to impact the environment (12).

1. EXERGY DESTRUCTION (ED)

Exergy destruction in each component of the multiple evaporators and compressors with individual expansion valves vapour compression refrigeration system (System-1) is evaluated as per Eqs. (21)– (32) given below:-

Evaporators

$(EP_1)_{\text{System-1}}$

$$\dot{E}D_{e1} = \dot{E}_{x10} + \dot{Q}_{e1}\left(1 - \frac{T_0}{T_{r1}}\right) - \dot{E}_{x1}$$

$$= \dot{m}_{e1}(\psi_{10} - T_0 s_{10}) + \dot{Q}_{e1}\left(1 - \frac{T_0}{T_{r1}}\right) - \dot{m}_{e1}(\psi_1 - T_0 s_1) \quad \ldots\ldots\ldots\ldots (21)$$

$(EP_2)_{\text{System-1}}$

$$\dot{E}D_{e2} = \dot{E}_{x9} + \dot{Q}_{e2}\left(1 - \frac{T_0}{T_{r2}}\right) - \dot{E}_{x3}$$

$$= \dot{m}_{e2}(\psi_9 - T_0 s_9) + \dot{Q}_{e2}\left(1 - \frac{T_0}{T_{r2}}\right) - \dot{m}_{e2}(\psi_3 - T_0 s_3) \quad \ldots\ldots\ldots\ldots (22)$$

$(EP_3)_{\text{System-1}}$

$$\dot{E}D_{e3} = \dot{E}_{x8} + \dot{Q}_{e3}\left(1 - \frac{T_0}{T_{r3}}\right) - \dot{E}_{x5}$$
$$= \dot{m}_{e3}(\psi_8 - T_0 s_8) + \dot{Q}_{e3}\left(1 - \frac{T_0}{T_{r3}}\right) - \dot{m}_{e3}(\psi_5 - T_0 s_5) \quad \text{..... (23)}$$

Compressors

(C_1) System-1

$$\dot{E}D_{comp1} = \dot{E}_{x1} + \dot{W}_{comp1} - \dot{E}_{x2} = \dot{m}_{c1}(T_0(s_2 - s_1)) \quad \text{..... (24)}$$

(C_2) System-1

$$\dot{E}D_{comp2} = \dot{E}_{x3} + \dot{W}_{comp2} - \dot{E}_{x4} = \dot{m}_{c2}(T_0(s_4 - s_3)) \quad \text{..... (25)}$$

(C_3) System-1

$$\dot{E}D_{comp3} = \dot{E}_{x5} + \dot{W}_{comp3} - \dot{E}_{x6} = \dot{m}_{c3}\big(T_0(s_6 - s_5)\big) \quad \text{..... (26)}$$

Condenser

(Condenser) System-1

$$\dot{E}D_c = (\dot{E}_{x2} - \dot{E}_{x7}) + (\dot{E}_{x4} - \dot{E}_{x7}) + (\dot{E}_{x6} - \dot{E}_{x7})$$
$$= \dot{m}_{c1}\big((\psi_2 - T_0 s_2) - (\psi_7 - T_0 s_7)\big) + \dot{m}_{c2}\big((\psi_4 - T_0 s_4) - (\psi_7 - T_0 s_7)\big)$$
$$+\dot{m}_{c3}\big((\psi_6 - T_0 s_6) - (\psi_7 - T_0 s_7)\big) \quad \text{..... (27)}$$

Subcooler

(SC) System-1

$$\dot{E}D_{sc} = \dot{E}_{x7} - \dot{E}_{x77}$$
$$= (\dot{m}_{c1} + \dot{m}_{c2} + \dot{m}_{c3})((\psi_7 - T_0 s_7) - (\psi_{77} - T_0 s_{77})) \quad \text{..... (28)}$$

Throttle valves

(TV_1) System-1

$$\dot{E}D_{TV_1} = \dot{E}_{x77} - \dot{E}_{x10} = \dot{m}_{c1}(T_0(s_{10} - s_{77})) \quad \text{..... (29)}$$

(TV-2) System-1

$$\dot{E}D_{TV_2} = \dot{E}_{x77} - \dot{E}_{x9} = \dot{m}_{c2}(T_0(s_9 - s_{77})) \quad \text{..... (30)}$$

(TV-3) System-1

$$\dot{E}D_{TV_3} = \dot{E}_{x77} - \dot{E}_{x8} = \dot{m}_{c3}(T_0(s_8 - s_{77})) \quad \text{..... (31)}$$

The total irreversibility in the system-2 is the sum of irreversibility in each component of the system and is given by-

$$\sum \dot{E}D_k = \dot{E}D_{e1} + \dot{E}D_{e2} + \dot{E}D_{e3} + \dot{E}D_{comp1} + \dot{E}D_{comp2} + \dot{E}D_{comp3}$$
$$+\dot{E}D_c + \dot{E}D_{sc} + \dot{E}D_{TV_1} + \dot{E}D_{TV_2} + \dot{E}D_{TV_3} \quad \text{..... (32)}$$

Similarly exergy destruction in each component of the multiple evaporators and compressors with multiple expansion valves vapour compression refrigeration system (System-2) is evaluated as per Eqs. 33–44 given below:-

Evaporators

(EP1) System-2

$$\dot{E}D_{e1} = \dot{E}_{xl} + \dot{Q}_{e1}\left(1 - \frac{T_0}{T_{r1}}\right) - \dot{E}_{xa}$$
$$= \dot{m}_{e1}(\psi_l - T_0 s_l) + \dot{Q}_{e1}\left(1 - \frac{T_0}{T_{r1}}\right) - \dot{m}_{e1}(\psi_a - T_0 s_a) \quad \text{..... (33)}$$

(EP2) System-2

$$\dot{E}D_{e2} = \dot{E}_{xj} + \dot{Q}_{e2}\left(1 - \frac{T_0}{T_{r2}}\right) - \dot{E}_{xc}$$
$$= \dot{m}_{e2}(\psi_j - T_0 s_j) + \dot{Q}_{e2}\left(1 - \frac{T_0}{T_{r2}}\right) - \dot{m}_{e2}(\psi_c - T_0 s_c) \quad \text{..... (34)}$$

$(EP3)_{System\text{-}2}$

$$\dot{E}D_{e3} = \dot{E}_{xh} + \dot{Q}_{e3}\left(1 - \frac{T_0}{T_{r3}}\right) - \dot{E}_{xe}$$
$$= \dot{m}_{e3}(\psi_h - T_0 s_h) + \dot{Q}_{e3}\left(1 - \frac{T_0}{T_{r3}}\right) - \dot{m}_{e3}(\psi_e - T_0 s_e) \quad \text{..... (35)}$$

Compressors

$(C\text{-}1)_{System\text{-}2}$

$$\dot{E}D_{comp1} = \dot{E}_{xa} + \dot{W}_{comp1} - \dot{E}_{xb} = \dot{m}_{c1}(T_0(s_b - s_a)) \quad \text{..... (36)}$$

$(C\text{-}2)_{System\text{-}2}$

$$\dot{E}D_{comp2} = \dot{E}_{xc} + \dot{W}_{comp2} - \dot{E}_{xd} = \dot{m}_{c2}(T_0(s_d - s_c)) \quad \text{..... (37)}$$

$(C\text{-}3)_{System\text{-}2}$

$$\dot{E}D_{comp3} = \dot{E}_{xe} + \dot{W}_{comp3} - \dot{E}_{xf} = \dot{m}_{c3}(T_0(s_f - s_e)) \quad \text{..... (38)}$$

Condenser

$(Condenser)_{System\text{-}2}$

$$\dot{E}D_{cond} = (\dot{E}_{xb} - \dot{E}_{xg}) + (\dot{E}_{xd} - \dot{E}_{xg}) + (\dot{E}_{xf} - \dot{E}_{xg})$$
$$= \dot{m}_{c1}\left((\psi_b - T_0 s_b) - (\psi_g - T_0 s_g)\right) + \dot{m}_{c2}\left((\psi_d - T_0 s_d) - (\psi_g - T_0 s_g)\right)$$
$$+\dot{m}_{c3}\left((\psi_f - T_0 s_f) - (\psi_g - T_0 s_g)\right) \quad \text{..... (39)}$$

$(SC)_{System\text{-}2}$

$$\dot{E}D_{sc} = \dot{E}_{xg} - \dot{E}_{xgg}$$
$$= (\dot{m}_{c1} + \dot{m}_{c2} + \dot{m}_{c3})\left((\psi_g - T_0 s_g) - (\psi_{gg} - T_0 s_{gg})\right) \text{..... (40)}$$

Throttle valves

$(TV\text{-}1)_{System\text{-}2}$

$$\dot{E}D_{TV_1} = \dot{E}_{xk} - \dot{E}_{xl} = \dot{m}_{c1}(T_0(s_l - s_k)) \quad \text{..... (41)}$$

$(TV\text{-}2)_{System\text{-}2}$

$$\dot{E}D_{TV_2} = \dot{E}_{xi} - \dot{E}_{xj} = (\dot{m}_{c1} + \dot{m}_{c2})(T_0(s_j - s_i)) \quad \text{..... (42)}$$

$(TV\text{-}3)_{System\text{-}2}$

$$\dot{E}D_{TV_3} = \dot{E}_{xgg} - \dot{E}_{xh}$$
$$= (\dot{m}_{c1} + \dot{m}_{c2} + \dot{m}_{c3})(T_0(s_h - s_{gg})) \quad \text{..... (43)}$$

The total irreversibility in the system-2 is the sum of irreversibility in each component of the system and is given by-

$$\sum \dot{E}D_k = \dot{E}D_{e1} + \dot{E}D_{e2} + \dot{E}D_{e3} + \dot{E}D_{comp1} + \dot{E}D_{comp2} + \dot{E}D_{comp3}$$
$$+\dot{E}D_c + \dot{E}D_{sc} + \dot{E}D_{TV_1} + \dot{E}D_{TV_2} + \dot{E}D_{TV_3} \quad \text{..... (44)}$$

2. EXERGETIC EFFICIENCY

$$\eta_{ex} = \frac{\text{Exergy in product}}{\text{Exergy of fuel}} = \frac{\dot{E}P}{\dot{E}F} \quad \text{..... (45)}$$

For the multi evaporator vapour compression refrigeration system, the product is the exergy of the heat abstracted in to the evaporators' i.e.$Q_e = Q_{e1} + Q_{e2} + Q_{e3}$ from the space to be cooled at temperature T_r, and exergy of fuel is actual compressor work input. Hence, exergetic efficiency is given by-

$$\dot{E}P = \dot{Q}_{e1} + \dot{Q}_{e2}\left|\left(1 - \frac{T_0}{T_{r2}}\right)\right| + \dot{Q}_{e3}\left|\left(1 - \frac{T_0}{T_{r3}}\right)\right| \quad \text{..... (46)}$$

$$\eta_{ex} = \frac{\dot{Q}_{e1}\left|\left(1-\frac{T_0}{T_{r1}}\right)\right|+\dot{Q}_{e2}\left|\left(1-\frac{T_0}{T_{r2}}\right)\right|+\dot{Q}_{e3}\left|\left(1-\frac{T_0}{T_{r3}}\right)\right|}{(\dot{W}_{comp1}+\dot{W}_{comp2}+\dot{W}_{comp3})} \quad \text{..... (47)}$$

3. EXERGY DESTRUCTION RATIO (EDR)

EDR is the ratio of total exergy destruction in the system to exergy in the product (9) and it is given by Eq. (48). EDR is related to the exergetic efficiency by Eq. (49)-

$$EDR = \frac{\dot{E}D_{total}}{\dot{E}P} = \frac{1}{\eta_{ex}} - 1 \quad \text{..... (48)}$$

$$\eta_{ex} = \frac{1}{1+EDR} \quad \text{..... (49)}$$

RESULTS AND DISCUSSIONS

Using Engineering Equation Solver software eq. (13) a numerical model has been developed for comparison of performance parameters of systems (system 1 & system-2).

The performance parameters are evaluated by considering following specifications of the systems given below:-

1. Degree of sub cooling (ΔT_{sc}): 10K.
2. Adiabatic efficiency of compressor (η_{comp}): 75%.
3. Difference between evaporator and space temperature (T_r-T_e): 5K.
4. Temperature of evaporators EP_1, EP2 and EP3 are 263K ,273K and 283K respectively
5. Condenser temperature (T_c): 313K
6. Dead state temperature (T_0): 298K
7. Dead state enthalpy (ψ_0) and entropy (s_0) of the refrigerants have been calculated corresponding to the dead state temperature (T_0) of 298K.
8. Loads on the evaporators EP1, EP2 and EP3 are 35KW, 70KW and 105KW respectively.

Fig. 3 presents the comparison of coefficient of performance of multiple evaporators and compressors with individual expansion valves (System-1) and multiple evaporators and compressors with multiple expansion valves (System-2) for different refrigerants. COP of system-2 is better by comparison of system-1 for all considered refrigerants.R600 shows highest COP among all considered refrigerants for both systems. Though in System-1 R152a shows second highest COP among all refrigerants but as it has the lowest flammability in comparison with R600 and for system-2 R152a, R600a and R290 show almost same COP but lower than R600 and again as R152a has lowest flammability among R600, R600a and R290.The maximum difference observed between COPs of R600 and R404A is 11.65% for system-1 and 9% for system-2.

Fig.4 presents the comparison of exergetic efficiency (second law efficiency) for system-1 & system-2 for different refrigerants. It was observed that exergetic efficiency of system-2 for all refrigerants is better as comparison with system-1.As clear from the Eq.47 that exergetic efficiency is the ratio of sum of product of all evaporators to the total work input, the sum product of all evaporators in system-2 is higher with comparison to the system-1 because arrangement of expansion valves in system-2 in such a fashion that flashed vapour at the pressure of the high temperature evaporator is not allowed to go to the lower temperature evaporator and increase the products of evaporators without affecting work input, thus improving its exergetic efficiency. R404 shows lowest and R600 shows highest second law efficiency for both systems. The maximum difference observed between second law efficiency of R600 and R404A is 11% of system-1 and 9.2% of system-2. It is observed from Fig. 5 that variation of EDR and exergetic efficiency is almost opposite. This fact is also cleared from Eq. (49) that exergetic efficiency is inversely proportional to ED.

Fig. 3: Comparison of COP for system-1 &2 for different ecofriendly refrigerants

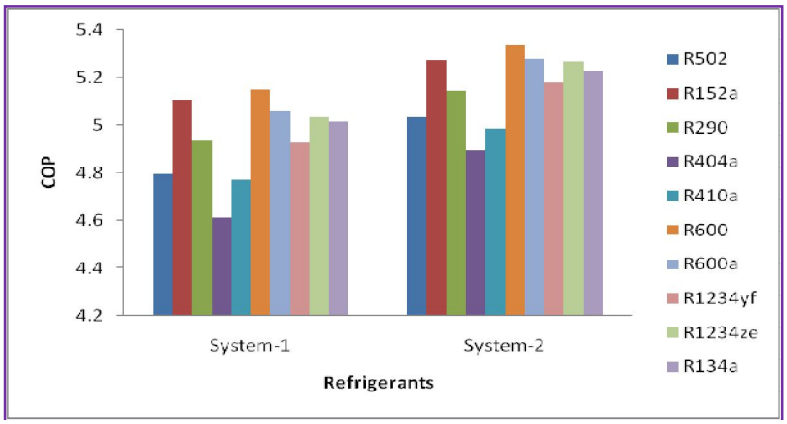


Fig. 4: Comparison of second law efficiency (η_{II}) for system-1 &2 for different ecofriendly refrigerants

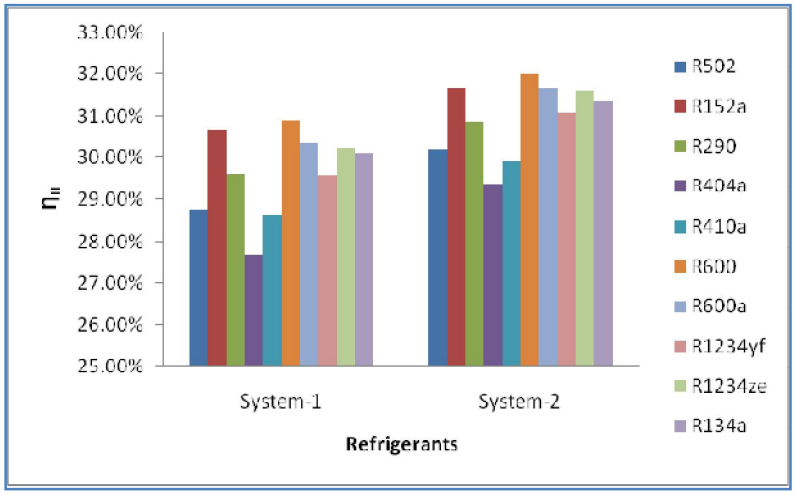
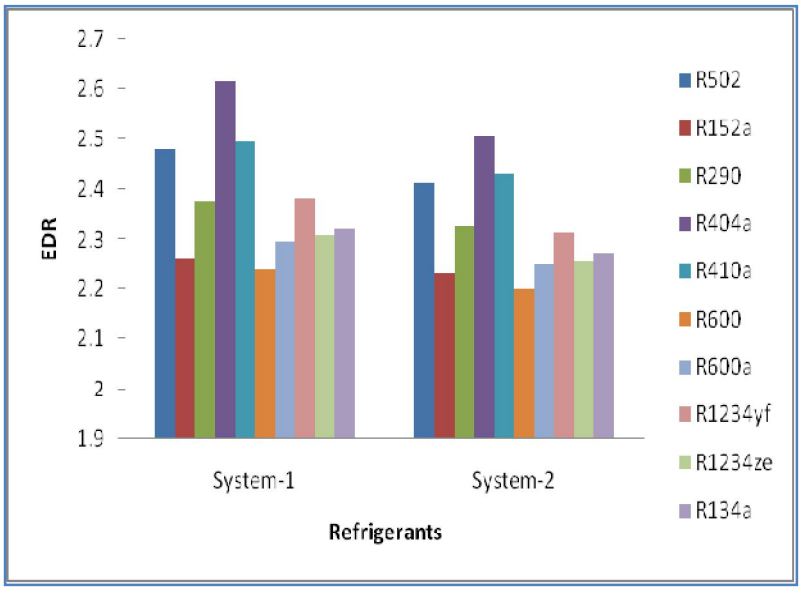


Fig. 5: Comparison of exergy destruction ratio (EDR) for system-1 &2 for different ecofriendly refrigerants



NOMENCLATURE

$\dot{E}P$	exergy rate of product (kW)	ODP	ozone depletion potential
$\dot{E}F$	exergy rate of fuel (kW)	S	specific entropy (kJ/kgK)
$\dot{Q}$	rate of heat transfer (kW)	C	compressor
$\dot{W}$	work rate (kW)	Ψ	specific enthalpy (kJ/kg)
ΔT_{sc}	degree of subcooling	K	kth component
CFC	chlorofluorocarbon	ev	expansion valve
comp	compressor	Φ	dryness fraction(non-dimensional)
cond	condenser	EP	evaporator
COP	coefficient of performance (non-dimensional)	O	dead state
E	evaporator	sc	subcooler
E_x	exergy rate of fluid (kW)	$\dot{E}D$	rate of exergy destruction (kW)
ex	exergetic	$\dot{m}$	mass flow rate (kg/s)
HCFC	hydrochlorofluorocarbon	r	refrigerant, space to be cooled
HFC	hydrofluorocarbon	H	efficiency (non-dimensional)
II	second law efficiency	GWP	global warming potential
T	temperature (K)	VCR	vapour compression refrigeration
TV	throttle valve		

CONCLUSIONS

Thermodynamic analysis in terms of energy and exergy analysis of multiple evaporators and compressors with individual expansion valves (system-1) and multiple evaporators and compressors with multiple expansion valves (system-2) have been carried out and following conclusions was drawn from present investigation. For same degree of subcooling, fixed evaporators and condenser temperatures system-2 is the best system with comparisons of system-1.

R600, R600a and R152A show better performances than other refrigerants for both systems (system-1 & system-2) but due to inflammable property of R600 and R600a, R134a is preferred for both systems. First law efficiency and second law efficiency of system-2 is 3%-6% higher than System-1.

REFERENCES

1. Ahamed J.U., Saidur R. and Masjuki H.H. (2011): A review on exergy analysis of vapor compression refrigeration system. Int J Renewable and sustainable energy reviews, 15: 1593-1600.
2. Ahamed J.U., Saidur R. and Masjuki H.H. (2011): A review on exergy analysis of vapor compression refrigeration system. Int J Renewable and sustainable energy reviews, 15: 1593-1600.
3. Ahamed J.U., Saidur R., Masjuki H.H. and Sattar M.A. (2012): An analysis of energy, exergy and sustainable development of a vapour compression refrigeration system using hydrocarbon. International journal of Green energy, 9: 707-717.
4. Anand S. and Tyagi S.K. (2012): Exergy analysis and experimental study of a vapour compression refrigeration cycle. Int J Therm Anal Calorim, 110: 961-971.
5. Arora A. and Kaushik S.C. (2008): Theoretical analysis of a vapour compression refrigeration system with R502, R404A and R507A. Int J Refrigeration, 31: 998-1005.
6. Bolaji B.O., Akintunde M.A. and Falade T.O. (2011): Comparative analysis of performance of three ozone-friends HFC refrigerants in a vapor compression refrigerator. International Journal of Sustainable Energy & Environment, 2: 61-64.
7. Cabello R., Navarro-Esbrı J., Llopis R. and Torrella E. (2007): Analysis of the variation mechanism in the main energetic parameters in a single stage vapour compression plant. International Journal of Applied Thermal Engineering, 27: 167-176.
8. Cabello R., Torrella E. and Navarro-Esbr J. (2004): Experimental evaluation of a vapour compression plant performance using R134a, R407C and R22 as working fluids. Int J Applied Thermal Engineering, 24: 1905-1917.
9. Camelia Stanciu, Adina Gheorghian, Dorin Stanciu and Alexandru Dobrovicescu (2011): Exergy analysis and refrigerant effect on the operation and performance lomits of a one stage vapour compression refrigeration system.Termotehnica, 1: 36-42.
10. Getu H.M. and Bansal P.K. (2008): Thermodynamic analysis of an R744-R717 cascade refrigeration system. Int J Refrigeration, 31: 45-54.

11. Halimic E., Ross D., Agnew B., Anderson A. and Potts I. (2003): A comparison of the operating performance of alternative refrigerants. Int J Applied Thermal Engineering, 23: 1441-1451.
12. Han X.H., Wang Q., Zhu Z.W. and Chen G.M. (2007): Cycle performance study on R32/R125/R161 as an alternative refrigerant to R407C. Int J Applied Thermal Engineering, 27: 2559-2565.
13. Havelsky V. (2000): Investigation of refrigerating system with R12 refrigerant replacements .Int J Applied Thermal Engineering, 20: 133-140.
14. Johnson E. (1998): Global warming from HFC. Environ. Impact Asses., 18: 485-492.
15. Kumar S., Prevost M. and Bugarel R. (1989): Exergy analysis of a vapour compression refrigeration system. Heat Recovery Systems & CHP, 9: 151-157.
16. Llopis R., Torrella E., Cabello R. and Sánchez D. (2010): Performance evaluation of R404A and R507A refrigerant mixtures in an experimental double-stage of vapour compression plant. Int J Applied Energy, 87: 1546-1553.
17. MastaniJoybari Md., SadeghHatamipour Md., Amir Rahimi and Fatemeh Ghadiri Modarres (2013): Exergy analysis and optimization of R600a as a replacement of R134a in a domestic refrigerator system. International Journal of refrigeration, 36: 1233-1242.
18. Mohanraj M., Jayaraj S., Muraleedharan C. and Chandrasekar P. (2009): Experimental investigation of R290/R600a mixture as an alternative to R134a in a domestic refrigerator. International Journal of Thermal Sciences, 48: 1036-1042.
19. Nikolaidis C. and Probert D. (1998): Exergy method analysis of a two-stage vapour-compression refrigeration-plants performance. Int J Applied Thermal Engineering, 60: 241-256.
20. Padilla M., Revellin R. and Bonjour J. (2010): Exergy analysis of R413A as replacement of R12 in a domestic refrigeration system. Int J Energy Conversion and Management, 51: 2195-2201.
21. Padilla M., Revellin R. and Bonjour J. (2010): Exergy analysis of R413A as replacement of R12 in a domestic refrigeration system. Int J Energy Conversion and Management, 51: 2195-2201.
22. QiyuChen and Prasad R.C. (1999): Simulation of a vapour compression refrigeration cycles HFC134A and CFC12. Int Comm.Heat Mass Transfer, 26: 513-521.
23. Reddy V.S, Panwar N.L. and Kaushik S.C. (2012): Exergy analysis of a vapour compression refrigeration system with R134a, R143a, R152a, R404A, R407C, R410A, R502 and R507A. Clean Techn Environ Policy, 14: 47-53.
24. Saravanakumar R. and Selladurai V. (2013):Exergy analysis of a domestic refrigerator using eco-friendly R290/R600a refrigerant mixture as an alternative to R134a. Int J Therm Anal Calorim.
25. Spatz Mark W. and Motta Samuel F. Yana (2004): An evaluation of options for replacing HCFC-22 in medium temperature refrigeration systems. Int J Refrigeration, 27: 475-483.

26. Spauschus H.O. (1988): HFC 134a as a substitute refrigerant for CFC 12. Int J of Refrigeration, 11: 389-392.
27. Stanciu Klein A. and Alvarado F. (2005): Engineering Equation Solver, Version 7.441. F Chart Software, Middleton, WI.2005.
28. Yumrutas R., Kunduz M. and Kanoglu M. (2002): Exergy analysis of vapor compression refrigeration systems. Exergy, an International Journal, 2: 266-272.



Microstructure and mechanical properties of thermoelectric nanostructured n-type silicon-germanium alloys synthesized employing spark plasma sintering

Sivaiah Bathula, Bhasker Gahtori, M. Jayasimhadri, S. K. Tripathy, Kriti Tyagi, A. K. Srivastava, and Ajay Dhar

Citation: Applied Physics Letters **105**, 061902 (2014); doi: 10.1063/1.4892879
View online: http://dx.doi.org/10.1063/1.4892879
View Table of Contents: http://scitation.aip.org/content/aip/journal/apl/105/6?ver=pdfcov
Published by the AIP Publishing

Articles you may be interested in

Nanocrystallization in spark plasma sintered Fe48Cr15Mo14Y2C15B6 bulk amorphous alloy
J. Appl. Phys. **114**, 054903 (2013); 10.1063/1.4817379

Heterogeneous in-situ nanostructure contributes to the thermoelectric performance of Zn4Sb3
Appl. Phys. Lett. **102**, 163902 (2013); 10.1063/1.4802780

Fabrication and Spark plasma sintering of nanostructured bismuth telluride (Bi2Te3).
AIP Conf. Proc. **1449**, 115 (2012); 10.1063/1.4731510

Thermoelectric properties of compacted Bi2-xSbxTe3 nanoplatelets with nominal composition of x = 1.5
AIP Conf. Proc. **1449**, 103 (2012); 10.1063/1.4731507

Role of oxygen on microstructure and thermoelectric properties of silicon nanocomposites
J. Appl. Phys. **110**, 113515 (2011); 10.1063/1.3658021



AIP Journal of Applied Physics

Journal of Applied Physics is pleased to announce André Anders as its new Editor-in-Chief

This article is copyrighted as indicated in the article. Reuse of AIP content is subject to the terms at: http://scitation.aip.org/termsconditions. Downloaded to IP: 14.139.251.100 On: Tue, 19 Aug 2014 06:27:48

APPLIED PHYSICS LETTERS **105**, 061902 (2014)

Microstructure and mechanical properties of thermoelectric nanostructured n-type silicon-germanium alloys synthesized employing spark plasma sintering

Sivaiah Bathula,[1,2] Bhasker Gahtori,[1] M. Jayasimhadri,[2] S. K. Tripathy,[1] Kriti Tyagi,[1] A. K. Srivastava,[1] and Ajay Dhar[1,a)]
[1]*CSIR-Network of Institutes for Solar Energy, CSIR-National Physical Laboratory, Dr. K. S. Krishnan Marg, New Delhi 110012, India*
[2]*Department of Applied Physics, Delhi Technological University, Delhi, India*

(Received 25 June 2014; accepted 29 July 2014; published online 11 August 2014)

Owing to their high thermoelectric (TE) figure-of-merit, nanostructured $Si_{80}Ge_{20}$ alloys are evolving as a potential replacement for their bulk counterparts in designing efficient radio-isotope TE generators. However, as the mechanical properties of these alloys are equally important in order to avoid in-service catastrophic failure of their TE modules, we report the strength, hardness, fracture toughness, and thermal shock resistance of nanostructured n-type $Si_{80}Ge_{20}$ alloys synthesized employing spark plasma sintering of mechanically alloyed nanopowders of its constituent elements. These mechanical properties show a significant enhancement, which has been correlated with the microstructural features at nano-scale, delineated by transmission electron microscopy. © *2014 AIP Publishing LLC*. [http://dx.doi.org/10.1063/1.4892879]

Among the several available thermoelectric (TE) materials, SiGe alloys have been identified as one of the most important material for TE power generation, due to their high TE figure-of-merit (ZT), coupled with excellent thermal stability at high temperatures ~1000 °C.[1–3] For about the past four decades, SiGe based thermoelectrics have been used as TE devices for power generation in Radio-isotope TE Generators (RTG) for deep space missions.[4] In the recent past "nanostructuring" has resulted in significantly increasing the ZT of both n-type[5] and p-type[6] $Si_{80}Ge_{20}$ and thus nanostructured $Si_{80}Ge_{20}$ are evolving as a potential replacement for their conventional bulk counterparts in designing efficient RTGs.

A vast majority of the research done[1,5–8] on SiGe TE materials has been focused on their thermal and electrical transport properties primarily aimed towards enhancing their ZT. However, their mechanical properties are equally important for the long term reliability of their TE modules, as these materials are known to be brittle with low fracture toughness. In RTGs, the individual TE elements are subjected to significant stresses under in-service conditions, due to thermal cycling as well as thermal expansion mismatch and externally applied mechanical stresses. Thus, in order to ensure the structural reliability of SiGe TE modules, it becomes important that the material must withstand numerous mechanical vibrations and thermal stresses while in-service. Thus, apart from ZT, the mechanical properties of SiGe are equally vital in order to avoid catastrophic failure of their TE modules.

In the recent past, a high ZT in both n- and p-type nanostructured $Si_{80}Ge_{20}$ alloys has been reported by several researchers,[5,6,8,9] which is far higher than their bulk counterpart,[4] currently used for RTG applications. Owing to their enhanced TE performance, these nanostructured SiGe alloys are being seriously explored for their application in RTGs, replacing the conventional SiGe bulk alloys. However, in the literature there is no comprehensive reported data on a complete set of mechanical properties of these nanostructured alloys, although there have been some sporadic reports[3,10,11] about their hardness and fracture toughness.

With this premise, we report the detailed mechanical properties of nanostructured n-type $Si_{80}Ge_{20}$ alloys, synthesized employing the Spark Plasma Sintering (SPS) of mechanically alloyed $Si_{80}Ge_{20}$ nanopowders. The results suggest that these alloys exhibited superior mechanical properties compared to state-of-the-art TE materials in terms of toughness, and more importantly, thermal shock resistance. This increase in the fracture toughness has been explained on the basis of grain boundary sliding mechanism aided by the presence of soft amorphous phase at the grain boundaries,[12,13] which has been corroborated by High Resolution Transmission Electron Microscopy (HRTEM) results. Although the hardness and elastic modulus of the SiGe nanostructured alloy, synthesized in the present study, are comparable to those reported earlier,[10] but the fracture toughness was found to be significantly higher. Further, the thermal shock resistance of the nanostructured SiGe alloys, which has not been reported earlier, exhibited a very high value compared to other TE material.

Experimental procedure for synthesis and technique used for microstructural characterization of nanostructured n-type $Si_{80}Ge_{20}$ alloys has already been described in our earlier paper.[8] It may be noted that p-type nanostructured SiGe alloys can also be synthesized by similar method[8] employing SPS of mechanically milled elemental powders of Si and Ge doped with 1.2 at. % of Boron. The Fracture toughness measurements were carried out employing the indentation-crack technique using Vickers micro-hardness tester (FM-e7) with a load of 4.9 N for 10 s of indentation time. Elastic modulus and hardness were determined using nano-indentation

a)Author to whom correspondence should be addressed. Electronic mail: adhar@nplindia.org. Tel.: +91-11-45609456, Fax: +91-11-45609310.

 © 2014 AIP Publishing LLC

This article is copyrighted as indicated in the article. Reuse of AIP content is subject to the terms at: http://scitation.aip.org/termsconditions. Downloaded to IP: 14.139.251.100 On: Tue, 19 Aug 2014 06:27:48

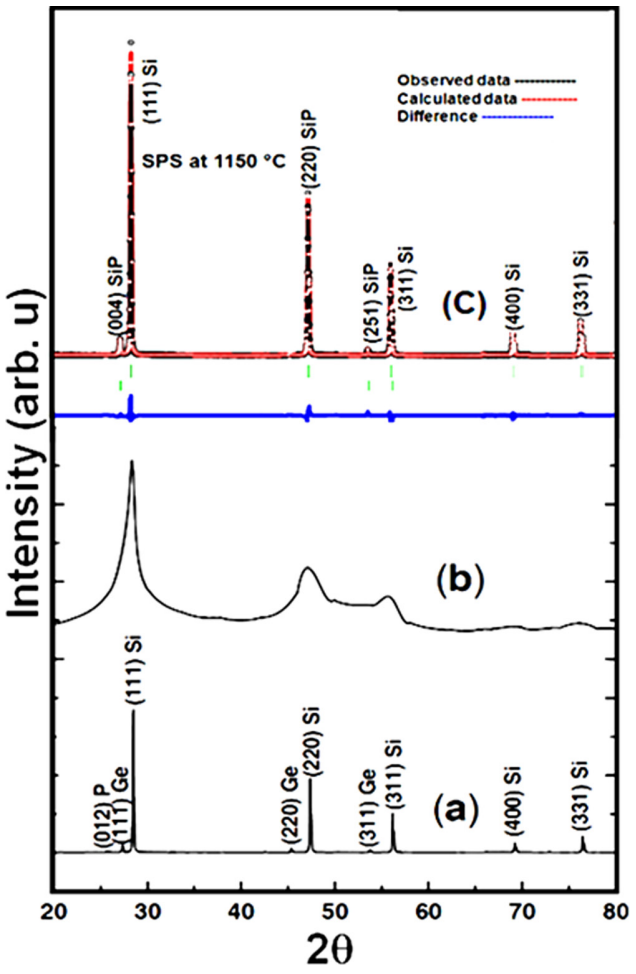


FIG. 1. X-ray powder diffraction patterns of $Si_{80}Ge_{20}$ alloy (a) unmilled powders, (b) nanopowders milled for 90 h, and (c) spark plasma sintered nanostructured alloy fitted with Rietveld refinement.

technique (M/s Fischer-Cripps, Australia) at a load of 10 mN and mechanical properties were derived from the measured load-penetration depth curves under loading/unloading through standard data analysis software. Compression tests were performed at room temperature as per ASTM standard (ASTM: E9–09) with an aspect ratio of ~2.5 under uni-axial loading with a strain rate of 2×10^{-5} s^{-1} (INSTRON 4204).

Fig. 1 elucidates the X-ray diffraction (XRD) patterns of unmilled powders, milled nanopowders, and after SPS of nanostructured $Si_{80}Ge_{20}$ alloy. The original average crystallite size of SiGe alloy powders was ~180 nm (Fig. 1(a)) and after 90 h of high energy ball milling the final crystallite size was found to be ~7 nm (Fig. 1(b)), calculated using XRD data employing Williamson-Hall method.[14] However, after SPS these crystallites slightly coarsened with an average crystallite size of ~12 nm (Fig. 1(c)). This suggests that the nano-scale features introduced during ball-milling are more-or-less retained post-sintering, which is primarily due to the high heating rates used during sintering.[8] However, Rietveld refinement of XRD data in Fig. 1(c) suggests the formation of an additional SiP phase (Fig. 2(d)) with an average crystallite size of ~4–6 nm.[8]

Fig. 2 shows the HRTEM images of nanostructured $Si_{80}Ge_{20}$ alloy. Fig. 2(a) shows a uniform microstructure with nanoscale crystallites, including some microstructural defects, which could be due to longer hours of ball-milling,[8,10,15] as shown in the inset. Further, at an atomic scale (Fig. 2(b)), an ultra-fine nano-grained microstructure with randomly oriented nanocrystallites (marked with dotted lines) with an average size of ~12 nm was delineated. Additionally, in Fig. 2(b) the presence of some amorphous region is also clearly visible. Fig. 2(c) shows the lattice scale image of nano-sized crystallite where the atomic planes hkl: 111 are marked. It can also be seen from this figure that, even at an atomic scale, the defects are clearly visible (region marked as "A").

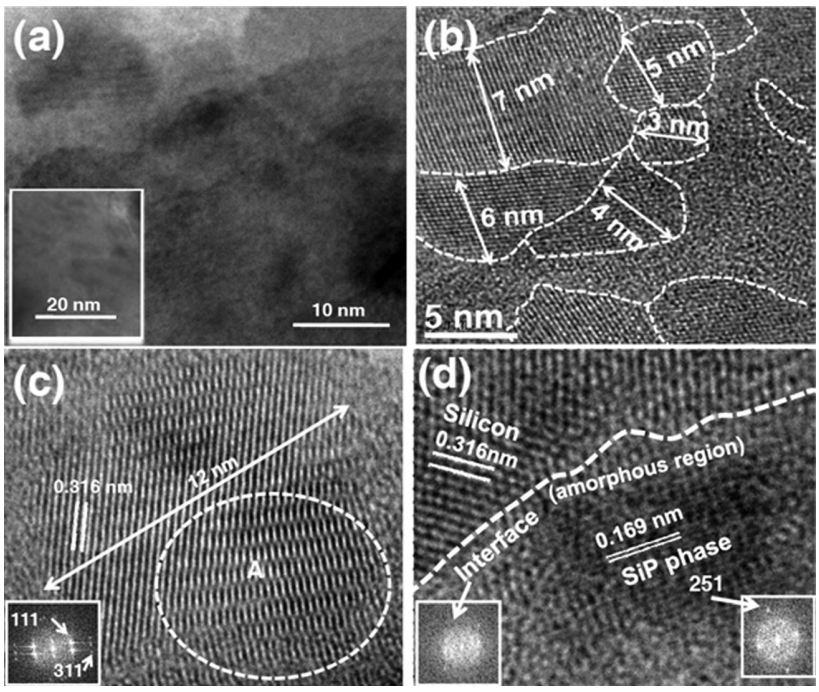


FIG. 2. HRTEM images of $Si_{80}Ge_{20}$ alloy showing (a) uniform ultra-fine densely packed microstructure, (b) distribution of different nano-grains marked with dotted white lines, and (c) a large sized nano-grain of about 12 nm with 0.316 nm inter-planar spacing and defect at lattice scale marked with dotted white line. Inset shows FFT of $Si_{80}Ge_{20}$ matrix showing the planes (111) and (311), (d) SiP phase with inter-planar spacing of 0.169 nm in the $Si_{80}Ge_{20}$ matrix. Inset shows the FFT of SiP phase showing the plane (251).

This article is copyrighted as indicated in the article. Reuse of AIP content is subject to the terms at: http://scitation.aip.org/termsconditions. Downloaded to IP: 14.139.251.100 On: Tue, 19 Aug 2014 06:27:48

A corresponding fast Fourier transform (FFT) in reciprocal space shows the presence of the planes (hkl: 111 and 311) of Si (inset in Fig. 2(c)). SiP nano precipitates are also seen near the grain boundaries with a distribution of ~4–6 nm (Fig. 2(d)). The FFT of these nano-precipitates (inset in Fig. 2(d)) and the inter-planar spacing calculated in real space (0.169 nm) confirms that these nano-precipitates correspond to a SiP phase. Further, Figure 2(d) also clearly shows the presence of amorphous regions at the grain boundaries between the nanocrystallites and a hallow Debye ring in the corresponding FFT (inset in Fig. 2(d)) confirms this amorphous structure. Also, Fig. 3 clearly shows the amorphous nature of the grain boundaries (marked as regions A and B) between nano-crystallites of varying dimensions. A corresponding FFT in reciprocal space (inset of Fig. 3) further revealed that the 111 planes are randomly oriented and exhibit amorphous region at the grain boundaries and occurrence of these amorphous regions are well known in nanostructured materials,[16] including pristine Si[17] synthesized by mechanical alloying and is due to extended hours of ball milling.

Nanoindentation tests[18,19] were performed on the nanostructured $Si_{80}Ge_{20}$ alloy samples with a load of 10 mN using Berkovich[20] indenter with a face angle (θ) of 65.27°.[21] Fig. 4 shows the typical load-displacement nano-indentation curves. The elastic modulus (E) was determined from the slope of the unloading curve (dP/dh) and the depth of the contact circle (h_c) which is initial portion of this elastic unloading response at a maximum load (P_{max}),[18,21] which yielded a value 141 ± 2.3 GPa averaged over 10 indentations. Hardness values of nanoindentation test were derived from the indentation load divided by the projected contact area ($A = 3\sqrt{3}h_c^2\tan^2\theta$),[19] which exhibited a value of 13.7 ± 0.1 GPa. Earlier reports[10] on n-type $Si_{80}Ge_{20}$ alloys, exhibited a hardness of 12.4–14.7 GPa with an elastic modulus of 137–145 GPa, which is in reasonable agreement with our present results. However, the hardness is much higher in comparison to those reported for other TE materials, Bi_2Te_3 HV = 0.62 GPa,[22] LAST HV = 0.59–0.68 GPa,[23] PbTe HV = 0.23 GPa,[23] La_3Te_4 HV = 3.28–4.3 GPa,[24] and Skutterudites HV = 2.45–5.4 GPa.[24] The observed value of E, of our samples, was in reasonable good agreement with those reported earlier,[10] as it is well known that for bulk alloys the E is primarily a material composition dependent property, although it does slightly depend on porosity and other defects.[25]

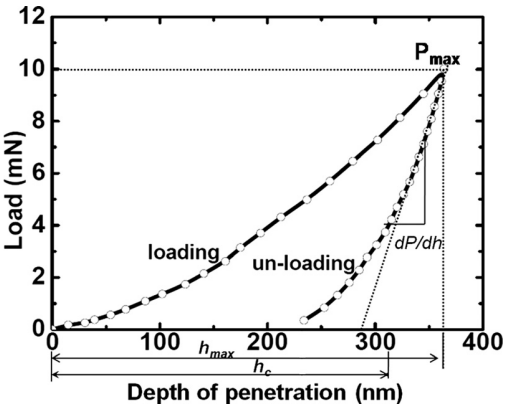


FIG. 4. Typical nanoindentation curves of nanostructured $Si_{80}Ge_{20}$ alloy during loading and un-loading.

Typical compressive stress-strain curve of nanostructured $Si_{80}Ge_{20}$ alloy as shown in Fig. 5 exhibits a strength of 1.18 ± 0.2 GPa with a strain at fracture of 6.34%. This high value of strength can be mainly associated with the strengthening due to grain refinement owing to a very small crystallite size,[13] solid-solution strengthening due to considerable difference in the atomic sizes of Si and Ge,[26,27] and strain hardening,[28] as these alloys are severely cold worked during high energy ball milling and there is always some residual strain,[27] even after sintering.[15,29] In comparison, other TE materials, such as, Skutterudite of composition $Ce_{0.5}Fe_{1.5}Co_{2.5}Sb_{12}$,[30] LAST, and LASTT[31] exhibit a compressive strength of ~1.80 GPa, 0.78–1.2 GPa, and 1.1 GPa, respectively.

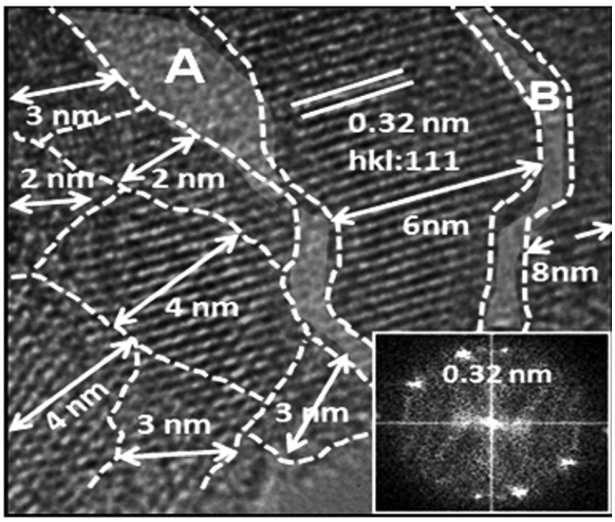


FIG. 3. HRTEM images of $Si_{80}Ge_{20}$ alloy, showing the distribution of different sized nano-crystallites with amorphous grain boundaries marked with white dotted lines marked as A and B. The inset shows the corresponding FFT in reciprocal space.

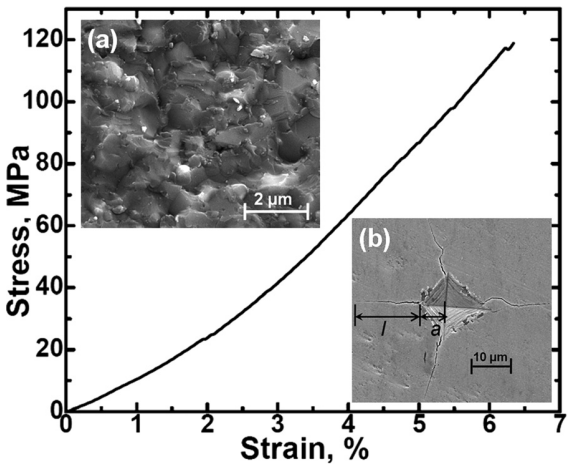


FIG. 5. Typical stress-strain curve of nanostructured $Si_{80}Ge_{20}$ alloy under uniaxial compression mode with a strain rate of 2×10^{-5} s^{-1}. Inset (a) FESEM image of fractured surface of nanostructured $Si_{80}Ge_{20}$ alloy and inset (b) FESEM images of Vickers-indentation crack developed at a load of 4.9 N. Indentation crack length (l) and the half-diagonal of Vickers indentation (a) are marked.

This article is copyrighted as indicated in the article. Reuse of AIP content is subject to the terms at: http://scitation.aip.org/termsconditions. Downloaded to IP: 14.139.251.100 On: Tue, 19 Aug 2014 06:27:48

TABLE I. Mechanical properties of nanostructured n-type $Si_{80}Ge_{20}$ alloy.

Elastic modulus (GPa)	Hardness (GPa)	Compressive strength (GPa)	Fracture toughness ($MPam^{1/2}$)	Thermal shock resistance ($W\ m^{-1}$)
141 ± 2.3	13.7 ± 0.1	1.18 ± 0.2	1.6 ± 0.05	445 ± 18

The Field Emission Scanning Electron Microscope (FESEM) micrograph of the fractured surface of nanostructured n-type $Si_{80}Ge_{20}$ alloys is shown as an inset (a) of Fig. 5, which suggests that the fractured surface exhibits a mixed morphology of shallow ductile dimples intermingled with fractured cleavage surfaces (mixed modes of brittle and ductile fracture), which is also corroborated with enhanced fracture toughness.

The fracture toughness was estimated by a method proposed by Niihara *et al.*,[32] according to which the fracture toughness (K_{IC}), as measured by Vicker's indentation-crack technique with Palmqvist crack model,[33] is given as

$$K_{IC} = 0.0089\left(\frac{E}{H}\right)^{2/5} \times \frac{P}{al^{1/2}}, \quad 2.5 \geq \frac{l}{a} \geq 0.25, \qquad (1)$$

where P is the load in Newtons, l is the crack length on the material surface after indenter removal in meters, a is the half-diagonal of Vicker's indentation mark in meters, E is the Young's modulus in GPa, and H is the Vickers hardness in GPa. In the present work, dimensions a and l were measured using SEM for better accuracy of the results (inset (b) in Fig. 5). The calculated fracture toughness was found to be 1.6 ± 0.05 MPa $m^{1/2}$ and this is value ~60% higher than that reported for similar alloy composition.[10] It has also been recently reported[34,35] that in brittle materials the presence of amorphous phase at the grain boundaries helps to increase the fracture toughness as well as the strength, which is due to the grain boundary sliding assisted by the soft amorphous phase at the grain boundaries.[34] This situation is analogous to our nanostructured SiGe alloys, where the HRTEM microstructures (Figs. 2(d) and 3) shown a clear evidence of the presence of some amorphous phase at the grain boundaries, due to extended hours of ball milling. Thus, the enhancement of fracture toughness in nanostructured $Si_{80}Ge_{20}$ alloys could be attributed to grain boundary sliding,[36] which is easy to activate owing to the presence of soft amorphous phase at the grain boundaries, which can act as a lubricant to promote grain boundary sliding.[34] In comparison, other competing TE materials,[37] such as, Co_4Sb_{12} and $In_{0.1}Co_4Sb_{12}$ shown a fracture toughness of 0.82 ± 0.11 and 0.46 ± 0.13 $MPam^{1/2}$, respectively. Furthermore, even Bi_2Te_3 and LAST, which are state-of-the-art TE materials, have a reported fracture toughness of 1.15 and 0.34 $MPam^{1/2}$, respectively.[22,38]

Thermal Shock Resistance (R_T) is an important criterion for all the TE device material, but assumes special significance in the case of SiGe alloys as these are used in RTGs which have a very high operating temperatures ~900 °C. R_T is given by the expression[39]

$$R_T = \frac{\sigma(1-\nu)\kappa}{\alpha E}, \qquad (2)$$

where ν is the Poisson's ratio, κ is the thermal conductivity, and α is the coefficient of thermal expansion. The value of R_T for nanostructured $Si_{80}Ge_{20}$ alloy samples has been calculated using Eq. (2) by substituting the experimentally determined values of σ and E from the current study, κ from our earlier reported study[8] on nanostructured sample of identical composition and α[40] and ν[41] from the literature. The value of R_T of our nanostructured $Si_{80}Ge_{20}$ alloy sample was found to be $\sim 445 \pm 18$ W m^{-1}. This value is quite high in comparison to the reported values for other state-of-the-art high ZT TE materials[38] like, $Yb_{0.20}$ $Co_4Sb_{12.4}$ (Skutterudite) is 246 W m^{-1} and for PbTe is 140 W m^{-1}. The mechanical properties obtained in the present study, are summarized in Table I.

In summary, the nanostructured n-type $Si_{80}Ge_{20}$ alloy, synthesized using high energy ball milling followed by consolidation of resulting nanopowders employing SPS technique, resulted in an enhancement of their high mechanical properties. The nanostructured $Si_{80}Ge_{20}$ alloy exhibited a hardness of $\sim 13.7 \pm 0.1$ GPa with an elastic modulus of $\sim 141 \pm 2.3$ GPa and a compressive strength of 1.18 ± 0.2 GPa. This high value of strength can be mainly associated with strengthening due to grain refinement, solid-solution, and strain hardening strengthening mechanisms. Further, the fracture toughness found to be $\sim 1.60 \pm 0.05$ $MPam^{1/2}$ which is ~60% higher than best reported value for nanostructured alloy with similar composition. The increase in fracture toughness has been attributed to the grain boundary sliding mechanism, assisted by the soft amorphous phase at the grain boundaries. The thermal shock resistance exhibited a value of 445 ± 18 W m^{-1}, which is the highest reported value for any other TE material with ZT greater than unity. This combination of good mechanical properties coupled with high reported TE figure-of-merit makes nanostructured n-type $Si_{80}Ge_{20}$ a potential candidate for TE power generation for RTG applications.

This work was supported by CSIR-TAPSUN (CSIR-NWP-54) programme entitled "*Novel approaches for solar energy conversion under technologies and products for solar energy utilization through networking*." The technical support rendered by Dr. Sushil Kumar, Mr. Radhey Shyam, and Mr. Naval Kishor Upadhyay is gratefully acknowledged.

[1]C. B. Vining, J. Appl. Phys. **69**(1), 331 (1991).
[2]C. Wood, Rep. Prog. Phys. **51**(4), 459 (1988); D. M. Rowe, V. S. Shukla, and N. Savvides, Nature **290**, 765 (1981); B. Yu, M. Zebarjadi, H. Wang, K. Lukas, H. Wang, D. Wang, C. Opeil, M. Dresselhaus, G. Chen, and Z. Ren, Nano Lett. **12**(4), 2077 (2012).
[3]D. M. Rowe and V. S. Shukla, J. Appl. Phys. **52**(12), 7421 (1981).
[4]D. M. Rowe, *CRC Handbook of Thermoelectrics* (CRC press, 1995).
[5]X. W. Wang, H. Lee, Y. C. Lan, G. H. Zhu, G. Joshi, D. Z. Wang, J. Yang, A. J. Muto, M. Y. Tang, and J. Klatsky, Appl. Phys. Lett. **93**(19), 193121 (2008).
[6]G. Joshi, H. Lee, Y. Lan, X. Wang, G. Zhu, D. Wang, R. W Gould, D. C. Cuff, M. Y. Tang, and M. S. Dresselhaus, Nano Lett. **8**(12), 4670 (2008).

This article is copyrighted as indicated in the article. Reuse of AIP content is subject to the terms at: http://scitation.aip.org/termsconditions. Downloaded to IP: 14.139.251.100 On: Tue, 19 Aug 2014 06:27:48

[7]J. Yang, H.-L. Yip, and A. K.-Y. Jen, Adv. Energy Mater. **3**(5), 549 (2013); H. Lee, D. Vashaee, D. Z. Wang, M. S. Dresselhaus, Z. F. Ren, and G. Chen, J. Appl. Phys. **107**(9), 094308 (2010).
[8]S. Bathula, M. Jayasimhadri, N. Singh, A. K. Srivastava, J. Pulikkotil, A. Dhar, and R. C. Budhani, Appl. Phys. Lett. **101**(21), 213902 (2012).
[9]H. Yin, M. Christensen, N. Lock, and B. B. Iversen, Appl. Phys Lett. **101**(4), 043901 (2012).
[10]A. C. Kallel, G. Roux, and C. L. Martin, Mater. Sci. Eng., A **564**, 65 (2013).
[11]F. Ericson, S. Johansson, and J.-Å. Schweitz, Mater. Sci. Eng., A **105**, 131 (1988).
[12]C. C. Koch, Nanostruct. Mater. **9**(1), 13 (1997); M. Gust, G. Goo, J. Wolfenstine, and M. L. Mecartney, J. Am. Ceram. Soc. **76**(7), 1681 (1993).
[13]A. A. Voevodin and J. S. Zabinski, Compos. Sci. Technol. **65**(5), 741 (2005).
[14]B. D. Cullity, *Prentice Hall* (New Jersey, USA, 2001).
[15]S. Bathula, R. C. Anandani, A. Dhar, and A. K. Srivastava, Mater. Sci. Eng., A **545**, 97 (2012).
[16]J.-F. Li, W.-S. Liu, L.-D. Zhao, and M. Zhou, NPG Asia Mater. **2**(4), 152 (2010); A. I. Hochbaum, R. Chen, R. Diaz Delgado, W. Liang, E. C. Garnett, M. Najarian, A. Majumdar, and P. Yang, Nature **451**(7175), 163 (2008).
[17]J. Tang, H.-T. Wang, D. H. Lee, M. Fardy, Z. Huo, T. P. Russell, and P. Yang, Nano Lett. **10**(10), 4279 (2010).
[18]B. Lawn, *Fracture of Brittle Solids* (Cambridge University Press, 1993).
[19]W. C. Oliver and G. M. Pharr, J. Mater. Res. **19**(1), 3 (2004).
[20]E. S. Berkovich, Ind. Diamond Rev. **11**(127), 129 (1951).
[21]A. C. Fischer-Cripps, *Nanoindentation* (Springer, 2011).
[22]L.-D. Zhao, B.-P. Zhang, J.-F. Li, M. Zhou, W.-S. Liu, and J. Liu, J. Alloys Compd. **455**(1), 259 (2008).
[23]F. Ren, E. D. Case, E. J. Timm, and H. J. Schock, J. Alloys Compd. **455**(1), 340 (2008).
[24]J. M. Ma, S. A. Firdosy, R. B. Kaner, J.-P. Fleurial, and V. A. Ravi, J. Mater. Sci. **49**(3), 1150 (2014).
[25]J. R. Gladden, G. Li, R. Adebisi, S. Firdosy, T. Caillat, and V. Ravi, Phys. Rev. B **82**(4), 045209 (2010); F. Ren, E. D. Case, E. J. Timm, and H. J. Schock, Philos. Mag. **87**(31), 4907 (2007).
[26]C. Suryanarayana, E. Ivanov, and V. V. Boldyrev, Mater. Sci. Eng., A **304**, 151 (2001); T.-Y. Chiang, H.-C. Wen, W.-C. Chou, and C.-H. Tsai, J. Cryst. Growth **390**, 92 (2014).
[27]J. Schilz, K. Pixius, W. Wunderlich, and W. A. Kaysser, Appl. Phys. Lett. **66**(15), 1903 (1995).
[28]P. B. Littlewood, Phys. Rev. B **34**(2), 1363 (1986).
[29]K. Biswas, A. Mukhopadhyay, B. Basu, and K. Chattopadhyay, J. Mater. Res. **22**(06), 1491 (2007).
[30]P. C. Zhai, W. Y. Zhao, Y. Li, L. S. Liu, X. F. Tang, Q. J. Zhang, and M. Niino, Appl. Phys. Lett. **89**(5), 052111 (2006).
[31]J. E. Ni, F. Ren, E. D. Case, and E. J. Timm, Mater. Chem. Phys. **118**(2), 459 (2009).
[32]K. Niihara, R. Morena, and D. P. H. Hasselman, J. Mater. Sci. Lett. **1**(1), 13 (1982).
[33]S. Palmqvist, Jernkontorets Ann. **141**, 300 (1957).
[34]W. J. MoberlyChan, J. J. Cao, and L. C. De Jonghe, Acta Mater. **46**(5), 1625 (1998).
[35]D. Chen, M. E. Sixta, X. F. Zhang, L. C. De Jonghe, and R. O. Ritchie, Acta Mater. **48**(18), 4599 (2000); H.-J. Kleebe, G. Pezzotti, and G. Ziegler, J. Am. Ceram. Soc. **82**(7), 1857 (1999).
[36]K. Madhav Reddy, P. Liu, A. Hirata, T. Fujita, and M. W. Chen, Nat. Commun. **4**, 2483 (2013).
[37]J. Eilertsen, M. A. Subramanian, and J. J. Kruzic, J. Alloys Compd. **552**, 492 (2013).
[38]J. R. Salvador, J. Yang, X. Shi, H. Wang, A. A. Wereszczak, H. Kong, and C. Uher, Philos. Mag. **89**(19), 1517 (2009).
[39]J. R. Salvador, J. Yang, A. A. Wereszczak, H. Wang, and J. Y. Cho, Sci. Adv. Mater. **3**(4), 577 (2011).
[40]F. Schaffler, *Properties of Advanced Semiconductor Materials GaN, AlN, InN, BN, SiC, SiGe*, edited by M. E. Levinshtein, S. L. Rumyantsev, and M. S. Shur (John Wiley & Sons, Inc., New York, 2001), p. 149.
[41]J. J. Wortman and R. A. Evans, J. Appl. Phys. **36**(1), 153 (1965).

This article is copyrighted as indicated in the article. Reuse of AIP content is subject to the terms at: http://scitation.aip.org/termsconditions. Downloaded to IP: 14.139.251.100 On: Tue, 19 Aug 2014 06:27:48

International Journal of Current Engineering and Technology
E-ISSN 2277 – 4106, P-ISSN 2347 - 5161
©2014 INPRESSCO®, All Rights Reserved
Available at http://inpressco.com/category/ijcet

Research Article

Motor Vehicle Exhaust Emissions in Delhi

Manish Jain[Á*], Shashank Mohan[Ḃ] and Amit Pal[Ḃ]

[Á]Department of Mechanical Engineering, RJIT, BSF Academy, Gwalior, India
[Ḃ]Dept. of Mechanical Engineering, Delhi College of Engineering, Delhi, 110042, India

Accepted 16 July 2014, Available online 01 Aug 2014, **Vol.4, No.4 (Aug 2014)**

Abstract

Delhi is a rapidly expanding mega city. Population and vehicle use continue to expand, with vehicles being the principal source of severe air pollution. In the present study, we attempt to resolve the complications of Delhi's transport sector, exploring what kind of a future is likely to be and how it may be altered to ensure minimum environmental pollution. In the ultimate analysis, we were able to come out with a conceptual strategy, which if implemented in its entire suggested framework, has the potential of bringing down the current environmental pollution levels drastically and promises to be commercially viable too. In this paper some novel approaches to mitigate the Delhi's vehicular pollution are discussed.

Keywords: *Public Transport, Vehicle Emissions, Environmental Pollution.*

1. Introduction

Delhi, the capital city of India, is very much plagued today by environmental degradation. Ever since its declaration as national Capital City in 1911, there has been a steady influx of people from every nook and corner of the country. Rise in population and growth in economic activities had led to increase in pollution in Delhi. Delhi is perhaps the only metropolitan city in India where the commuters are primarily dependent on a single mode of transport, i.e., the road. This has led to an enormous increase in the number of vehicle (Bose R. K., 1998). But recently under close supervision from the Indian Supreme Court, Government of Delhi has implemented a wide array of policies that are reported to have improved air quality in Delhi.

One study estimated that Delhi wastes $300,000 in fuel daily through vehicles idling at traffic lights. Air pollution levels often exceeded several folds the ambient standards set by the Central Pollution Control Board, and are increasing. Local experts, planners, policy makers, and environmental advocates indicate that a large share of the problem with the transportation system in Delhi is that too many organizations are making disjointed decisions. While a draft bill has been proposed to enable the establishment of a unified metropolitan transport authority, there appears to be no serious effort to overcome this institutional handicap.

In recent years, a series of initiatives have been launched in Delhi to reduce vehicular emission like augment public transport; adhere to progressively strength standards for fuels and vehicles; scrap old buses, taxis and auto-rickshaws; establish inspection and maintenance of in-use vehicles; and promote use of clean alternative fuels. These initiatives have come not from the legislative or executive branches of government, but by the Supreme Court of India, under a constitutional provision that warrants a certain quality of life to all the residents of India. Supreme Court heard several environmental lawsuits, a series of successful public interest litigation applications filed in 1996 and 1997 {Urvashi Narayan and Alan Krupnick, 2007). In response, the Indian Ministry of Environment and Forests created the Environment Pollution (Prevention and Control) Authority (EPCA) in January 1998. The EPCA's mission is to reduce pollution in the National Capital Region. (Bose R. K., Sperling and Daniel, October 2001). It recommended the following strategies for immediately improving air quality.

- Augment public transport
- Reduce vehicle emissions by setting standards for fuels and auto emissions
- Establish inspection and maintenance of in-use vehicles
- Use clean alternative fuel
- Improvement of road and flyover
- Increase of subsidies on public transport
- Improvement of police transport
- Use of high capacity buses
- Accelerating the metro plan
- Improve motor vehicle technologies.

Table 1 depicts the relative growth of vehicles with reference to other transport infrastructure. Table 2 gives the Average lifetime emissions of Advanced Technology Vehicles.

2. Vehicle Emissions

Motor vehicle exhaust emissions can be divided into three categories: tailpipe (or exhaust), evaporative and indirect (or fuel-cycle).

*Corresponding author: **Manish Jain**

Table 1 Growth of motor Vehicles in Delhi (Base year 1971)

Year	Population (Million)	Vehicles (Million)	Road Length(Km)	Density (Veh/Km)	(Veh/1000 person)
1971	4.07	0.18	8380	21.48	44.27
1981	6.22	0.52	14316	36.39	83.76
1991	9.42	1.81	21564	84.08	192.44
2001	13.78	3.46	28508	121.26	250.82
2011	~16.0	5.8	35084	146.34	334
Growth factor	4	34.21	4.4	7.65	8.67

Table 2 Average lifetime emissions of Advanced Technology Vehicles

Type of Emissions	SULEV, Near-Zero Evap., High Deterioration Rate	SULEV, Near-Zero Evap., Standard Deterioration Rate	PZEV	ATPZEV (GHEV)	BPEV
Tailpipe[a]					
NMOG	0.015	0.007	0.007	0.007	0
NOx	0.030	0.025	0.024	0.024	0
Evaporative[a]					
NMOG	0.032	0.032	0.020	0.020	0
Indirect[b]					
NMOG	0.031	0.031	0.031	0.021	0.002
NOx	0.016	0.016	0.016	0.011	0.003
Total					
NMOG	0.078	0.070	0.058	0.048	0.002
NOx	0.046	0.041	0.040	0.035	0.003
NMOG+NOx	0.124	0.111	0.098	0.083	0.005

[a]Estimates are from CARB, 2000b, pp. 134-137.
[b]Estimates are from Unnasch, Browning, and Montano, 1996.

Evaporative Emissions

Evaporative emission standards are set for diurnal, hot-soak, resting, and running-loss emissions. Diurnal emissions are associated with the diurnal breathing of the fuel tank as the ambient air temperature rises and falls. Hot-soak emissions occur when the fuel system is exposed to high under-hood temperatures after the vehicle is turned off. Resting losses occur when the vehicle is turned off and the hot-soak period has passed. Running losses occur when the vehicle is in operation.

Indirect Emissions

Indirect or fuel-cycle emissions are those produced during creation and distribution of the fuel that powers the vehicle. They comprise all emissions up to the point at which the fuel is in the vehicle, which means those emissions produced during

- Extraction (feedstock extraction and transport)
- Production (e.g., oil refining or electricity generation)
- Marketing (e.g., fuel bulk storage, transportation, transmission, gaseous fuel compression)
- Distribution (i.e. emissions from local fuel stations and from the process of vehicle refueling).

The components of the vehicular emissions of Delhi are shown in figure 1-5. Figure 1 shows the composition of the different pollutants vehicle sources. Highest is CO which is about 53% followed by NOx and HC which are 23% each.

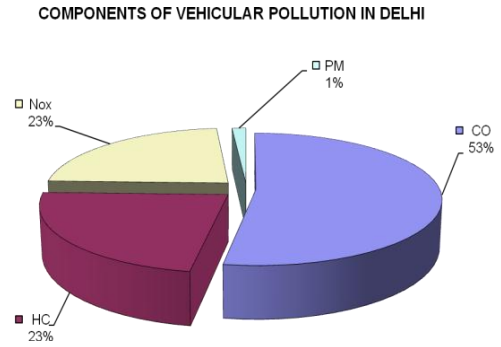


Figure 1: Composition of Vehicular exhausts Pollution in Delhi

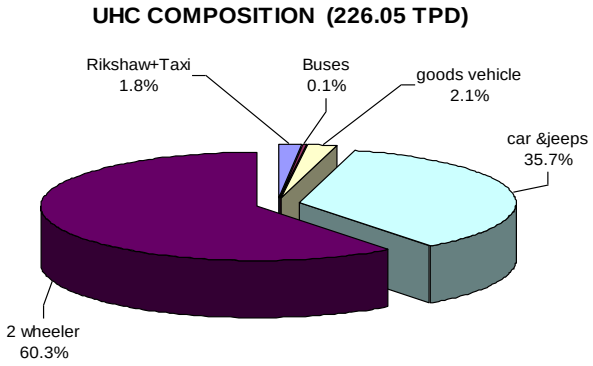


Figure 2: Composition of Vehicular Unburnt Hydrocarbon Pollution in Delhi

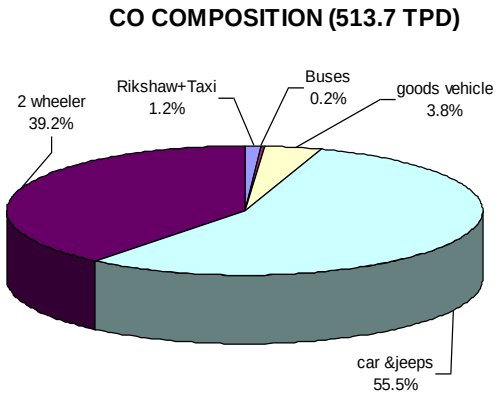


Figure 3: Composition of Vehicular Carbon MonoOxides Pollution in Delhi

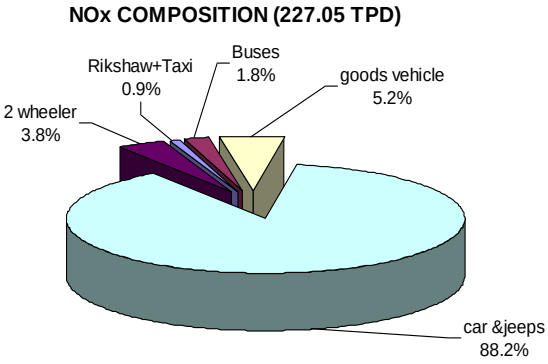


Figure 4: Composition of Vehicular Nitrogen Oxides Pollution in Delhi

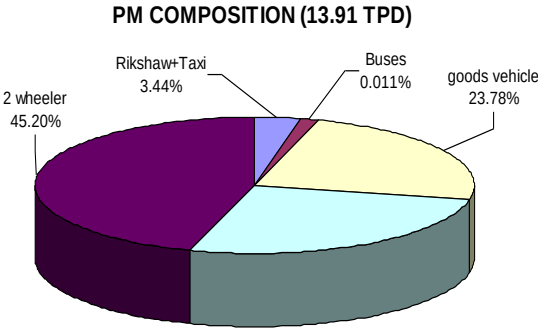


Figure 5: Composition of Vehicular Particulate Matter Pollution in Delhi

3. Main Strategic Control Options

In the ultimate analysis, we were able to come out with a conceptual strategy, which if implemented in its entire suggested framework, has the potential of bringing down the current environments pollution levels drastically and promises to be commercially viable too. Following are the appropriate actions needed for optimization of vehicle emissions in Delhi.

a. Improvement in public transport

This premised on strong local leadership that restrains vehicle use and creates a transportation system that is economically, environmentally, and socially sustainable for the long term. This is possible if ambitious initiatives are mounted in the near future to reduce vehicle and energy use.

The low emission level entails a shift away from current trends. It is a future of creativity, urban organization, efficient growth, and improved quality of life. Steps are taken to improve mass transit, in part to restrain the purchase of personal vehicles. If the planned bus ways and rail transit lines are completed on time in 2020-2021, ridership on high quality charter bus services expected to increases from 12 percent of total bus rider ship in 2000 to 18 percent in 2020, and continues to increase thereafter.

Innovative transport services are created to provide personalized transport services at less cost and greater system efficiency than cars. Ideally, they are linked to conventional transit services. Also an effort is needed to assure that vehicle owners pay their fair share of building and maintaining roads. These measures include an annual hike in registration fee tied to the size of the vehicle and engine efficiency of cleaner emissions.

b. CNG Conversion/ Vehicle Technology Improvement

The use of cleaner burning natural gas fuels by light duty vehicles is accelerated. All taxis and one-third of all personal cars are powered by CNG by 2005. By 2020, two-thirds of all cars run on CNG. All scooters switch from two-stroke to efficient four-stroke engines, and three-wheelers gradually shift to propane use (Sandhya Wakdikar,2002), (M N Karimi and B K Nath 2004). Advance vehicle technologies like CRDI, MPFI, VVT, DTSI etc. need to be used.

c. Increase the Subsidies on Public Transport

There are many ways to restrain the rapid growth in vehicle use in Delhi. Experience worldwide has shown that an approach aimed at both demand and supply is most effective. The demand approach discourages the use of personal vehicles and encourages the use of alternative modes. This can be accomplished by increasing the cost of driving to reflect the large infrastructure costs of accommodating vehicles and the costs they impose on the environment. Increased parking fees, fuel taxes, and registration fees and greater incentives for carpooling are options.

Creativity is needed in fashioning effective initiatives. One suggestion for mitigating opposition to new taxes and fees is a polluter-pays system that rewards environmentally friendly technologies and fuels while imposing charges on more polluting vehicles. Mass transit is often considered one of the best low-polluting alternatives to cars and motorcycles, and Delhi's investment in the multi-modal transit system of rail and bus ways enjoys strong support from policymakers.

d. Use of High Capacity Buses

Traffic management techniques such as downtown pedestrian zones, dedicated bus lanes, and traffic signals

that favour buses could also be successful. Because earlier attempts at making downtown areas more pedestrian friendly have failed, future attempts would likely require education programs such as outreach to downtown shop owners. Traffic managers provide special dedicated lanes for private and public buses to increase their speed relative to personal vehicles.

e. Use of Non-engined Systems

Use of Non-engined vehicles is encouragedto reduce pollution as well, mostly to serve the very poor who cannot afford even low-cost mass transit. Subsidies for bicycle use also slow the purchase and use of motorized vehicles by the more affluent. A network of protected lanes for bicycle use is provided, often separated from motorized vehicle roadways, to reduce congestion and increase the safety of bicycle riders. Subsidies for bicycle use also slow the purchase and use of motorized vehicles by the more affluent. A network of protected lanes for bicycle use is provided, often separated from motorized vehicle roadways, to reduce congestion and increase the safety of bicycle riders.

f. Promoting A/F vehicles

Compressed natural gas (CNG) and liquefied petroleum gases (LPG) and biodiesel,ethanol etc are are less expensive and environment friendly than diesel & gasoline. If vehicles are used intensively, the full lifecycle cost of owning and operating CNG and LPG vehicles will be less than for a comparable gasoline vehicle. However, the initial cost of a vehicle outfitted for these fuels, is somewhat greater due to the cost of the high-pressure tank needed to store the fuels.

g. Improvement of Roads and Flyovers

This has a special contribution to control vehicle e emissions in Delhi. Improvement of roads and flyovers results in less traffic congestion, higher mileage and less time consumed in journey and hence lesser emissions.

Conclusion

Broadly speaking, the above mentioned policies if implemented fully in Delhi, certainly will lead to lower vehicle emissions. Similarly, the policy that led to the reduction in the sulfur content of fuel appears to have helped reduce air pollution by reducing PM_{10} and SO_2 concentrations. The recent trend in Delhi toward an increase in the proportion of diesel-fueled cars also appears to be having somewhat of a mixed impact on air quality. While diesel-fueled cars have helped to reduce CO and SO_2, the latter because these cars are running on cleaner diesel, diesel cars also appear to be leading to an increase in PM_{10} and NO_2. Finally, we may conclude that no single strategy is applicable to Delhi, but an integrated approach including all above is the need of the hour.

References

Bose R. K. (1998). Automotive Energy use and Emissions Control a Simulation Model to Analyze Transport Strategies for Indian Metropolis, Elsevier, Energy Policy, vol. 26 No. 13, p 1001-1016

Towards Cleaner Air (January 1998) A Case Study of Delhi by Department of Environment, Government of NCT of Delhi & Delhi Pollution Control Committee.

Urvashi Narayan and Alan Krupnick, (February 2007) The Impact of Delhi's CNG Program on Air Quality, RFF DP 07-06.

Bose R. K., Sperling and Daniel (8-10 October 2001). Implications of Transport Policies on Local Environment & GHG Scenarios in Delhi, Workshop on Good Practices in Policies and Measures, Copenhagen, http://repositories.cdlib.org/itsdavis/UCD-ITS-REP-01-13, Institute of Transportation Studies, University of California, Davis, USA. \

M N Karimi and B K Nath, (March 13-15, 2004) Implementation of Compressed Natural Gas Technology in Delhi Transport System, Proceedings of GLOGIFT, \

Sandhya Wakdikar, (10 January 2002) Compressed Natural Gas: A Problem or a Solution? Current Science, Vol.82, No.1,

http://www.ppic.org/content/pubs/cep/EP_907LBEP.pdf

J Membrane Biol
DOI 10.1007/s00232-014-9716-2

TOPICAL REVIEW

Mutational Consequences of Aberrant Ion Channels in Neurological Disorders

Dhiraj Kumar · Rashmi K. Ambasta · Pravir Kumar

Received: 14 June 2014 / Accepted: 25 July 2014
© Springer Science+Business Media New York 2014

Abstract Neurological channelopathies are attributed to aberrant ion channels affecting CNS, PNS, cardiac, and skeletal muscles. To maintain the homeostasis of excitable tissues, functional ion channels are necessary to rely electrical signals, whereas any malfunctioning serves as an intrinsic factor to develop neurological channelopathies. Molecular basis of these disease is studied based on genetic and biophysical approaches, e.g., loci positional cloning, whereas pathogenesis and bio-behavioral analysis revealed the dependency on genetic mutations and inter-current triggering factors. Although electrophysiological studies revealed the possible mechanisms of diseases, analytical study of ion channels remained unsettled and therefore underlying mechanism in channelopathies is necessary for better clinical application. Herein, we demonstrated (i) structural and functional role of various ion channels (Na^+, K^+, Ca^{2+},Cl^-), (ii) pathophysiology involved in the onset of their associated channelopathies, and (iii) comparative sequence and phylogenetic analysis of diversified sodium, potassium, calcium, and chloride ion channel subtypes.

Keywords Neurological channelopathies · Ion channels · Nervous system · Therapeutics · Mechanisms · Pathophysiology

D. Kumar · R. K. Ambasta · P. Kumar (✉)
Molecular Neuroscience and Functional Genomics Laboratory, Department of Biotechnology, Delhi Technological University (Formerly Delhi College of Engineering), FW4TF3, Shahbad Daulatpur, Bawana Road, Delhi 110042, India
e-mail: Pravir.Kumar@tufts.edu; pravirkumar@dce.edu

P. Kumar
Neurology Department, Tufts University School of Medicine, Boston, MA, USA

Introduction

Normal functioning of neurological tissues lies in the intricate interplay among ion channels, which is responsible for the membrane excitability. Nonfunctional ion channels are accountable for special class of neurological disorders termed as neurological channelopathies. "Neurological channelopathies" are attributed to the neurological disorders which are provoked due to genetic aberration (mutation) in the ion channels (Kullmann and Hanna 2002). However, its phenotype is covering extensive areas ranging from epilepsies, migraine, and periodic paralysis to pain disorders. Eminent candidates that are responsible for aiding transient neurological disorders are found to be stress, caffeine, and ethanol (Raike et al. 2013).

Genetic neurological channelopathies possess three typical hallmarks, for instance,

- Paroxysmal in nature: It means impaired neurological functional episodes separated by periods of normality are experienced by the patient. Some of these examples include migraine and epilepsy (Kullmann and Hanna 2002; Graves and Hanna 2005; Kullmann and Waxman 2010).
- Environmental onset: Episodes are set off by environmental factors like thermal, physical, and emotional stresses.
- Genetic neurological channelopathy is prone to natural antiquity: Frequency of attack conventionally dwindles with the time, but the patient faces some neurological disability.

Clinical phenotypes include muscle disorders such as periodic paralysis and myotonia (muscle stiffness), disorders of peripheral nerve excitability such as neuromyotonia

Published online: 14 August 2014

and brain disorders like migraine and epilepsy (Graves and Hanna 2005).

Importance of Ion Channels

In an organism, ion channels play an important role for the regulation of cellular homoeostasis. The ion channels are the molecular basis of membrane excitability (synaptic transmission, action potentials, sensory transduction, Pak and Pinto 1976) that has been established for the past five decades but molecular entities are characterized only a decade back. Any alteration or malfunctioning in ion channels is incompatible with life (Graves and Hanna 2005). Ion channels are present in the plasma membrane of the cells and organelles, and monitored a critical role in cardiac, nervous, and immune systems. Several studies proved that ion channels are important target of many clinically used drugs, for instance, amitriptyline targets Na_v1 channels and ziconotide targets $Ca_v2.2$ channel (Kaczorowski et al. 2008).

Ion Channels and Underlying Genetic Diversity

Sodium Ion Channel

Sodium channel allows the inflow of Na^+ ions once excited due to potential difference across the plasma membrane of the cell. Further, depolarization activates the sodium channel which provides a passage of sodium ion into the muscle fiber or neuron, thereby forming the depolarization upstroke of the action potential. With the opening of sodium channel, membrane potential shifted from −70 mV to less negative values due to the influx of positive sodium ions thereby elevating the positive charge inside the membrane. Kariev and Green proposed and provided the evidence that protons constitute the gating current to open the channel (Kariev and Green 2012). Based on the genetic diversity, they are classified into different subtypes (i.e., $Na_v1.1$ to $Na_v1.9$) that are known to be associated with various diseases summarized in Table 1. The multiple sequence analysis of sodium channel subtypes revealed their highly conserved transmembrane regions with 34 glycine(G) and 20 cysteine(C) key residues that are responsible for anchoring in lipid bilayer while 16 highly conserved arginine(R) residues in fourth segment for imparting voltage sensitivity to the channel (Fig. 1a). Their phylogenetic analysis describes that there are two outgroups comprised (SCN5A, SCN10A) and SCN11A proteins. SCN11A protein is more distantly related with other sodium channel proteins, while SCN2A and SCN3A channel proteins are much closely related to each other based on phylogenetic relationship (Fig. 1b).

Potassium Ion Channel

Potassium channel is responsible for conducting K^+ ions level down the electrochemical gradient and involved in various functions, for instance, excitation of neuronal cells, regulation of cell volume, and secretion of hormones (Armstrong and Hille 1998). With the opening of potassium channel in response to membrane depolarization, membrane potential drops down from +30 mV to −70 mV due to the efflux of positive ion, making more negative inside the membrane and therefore proceed toward repolarization of the membrane. Different families of potassium channels exist depending upon the method of gate opening, which are ligand-gated potassium channel which requires binding of an ion and organic molecule and another one is voltage-gated potassium channel that requires voltage stimulus for pore opening (MacKinnon 2003). Mutations in these diverse potassium channel subtypes have been associated with diseases that are elaborated in Table 2. Moreover, multiple sequence alignment of these subtypes indicates that they are greatly divergent among different families proteins during evolution but selectivity filter residues and arginine residues in voltage sensor regions are highly conserved (Fig. 2a). Their phylogenetic relationship (Fig. 2b) by the help of un-weighted pair group method with arithmetic mean identified three major clusters of closely related genes.

Calcium Ion Channel

Calcium channels are responsible for mediating the flow of Ca^{2+} ions in response to either voltage or ligand and therefore designated as voltage-gated or ligand-gated calcium channel (Striggow and Ehrlich 1996). Voltage-gated calcium channel mediates the influx of Ca^{2+} ions along the electrochemical gradient across the plasma membrane and has been classified into transient (T-type), long-lasting (L-type) currents, N-, P/Q-, and R-type according to their inactivation properties (Tsien et al. 1987; Llinas et al. 1992). These diverse channel subtypes associated with diseases have been summarized in Table 3, while their multiple sequence alignment revealed that they are moderately conserved at their ion-traversing region with highly conserved 18 glycine (G) and 5 cysteine(C) key residues that are responsible for membrane attachment with 12 highly conserved arginine(R) residues for providing voltage sensitivity (Fig. 3a). Furthermore, its phylogenetic relationship has been elucidated in Fig. 3b. These calcium channels have been involved in a variety of functions that are triggering gene expression (Morgan and Curran 1989), link membrane depolarization to intracellular signaling (Westenbroek et al. 1990), excitation–contraction coupling,

Table 1 Sodium ion channel subtypes in association with various diseases

Channel name	Subtypes	Genes encoding subtypes	Tissue specificity	Subcellular location	Subunit structure	Physiological role	Involvement in disease	References
Sodium (Na_V) Channel	$Na_V1.1$	SCN1A	Adult brain, especially in Purkinje cells	Cell bodies	Na_v type-1 α-subunit (tetradomain). Each domain consists of internally repeated segments (S1–S6)	Control of action potential generation and propagation	Myoclonic epilepsy	Kalume et al. (2007), Spampanato et al. (2003)
	$Na_V1.2$	SCN2A	Central neurons, peripheral neurons	Axon initial segment of Cerebellar granule cells	Na_v type-2 α-subunit (tetradomain). Each domain consists of internally repeated segments (S1–S6)	Control of action potential generation and propagation	Inherited febrile seizures	Kearney et al. 2001), Shi et al. (2012)
	$Na_V1.3$	SCN3A	Developing CNS, peripheral neurons, and cardiac myocytes	Membrane	Na_v type-3 α-subunit (tetradomain). Each domain consists of internally repeated segments (S1–S6)	Fast activation and Inactivation Kinetics	Hyper excitability in epileptic patient	Estacion et al. (2010)
	$Na_V1.4$	SCN4A	Skeletal muscle	Membrane	Na_v type-4 α-subunit (tetradomain). Each domain consists of internally repeated segments (S1–S6)	Generation and propagation of action potentials that initiate muscle contraction	Several myotonia and periodic paralysis disorders, Arrhythmias	Anyukhovsky et al. (2011)
	$Na_V1.5$	SCN5A	Brain, cardiac muscle	Axon, Co-localized with Neurofilaments	Na_v type-5 α-subunit (tetradomain). Each domain consists of internally repeated segments (S1–S6)	Action potential generation & propagation in cardiac tissue and brain	Syncope, Seizures, Cardiac arrhythmias Long QT syndrome (LQTS), Brugada syndrome, Cardiac conduction disease	Hu et al. (2010), Tan et al. (2007)
	$Na_V1.6$	SCN8A	Cerebellar granule cells	Mature nodes along compact myelinated axons, dendrites	Na_v type-8 α-subunit (tetradomain). Each domain consists of internally repeated segments (S1–S6)	Most prominently expressed and potential generation in various types of tissues	Cognitive impairment with or without cerebellar ataxia (CIAT), Epileptic encephalopathy, early infantile, type 13 (EIEE13)	Trudeau et al. (2006), Osorio et al. (2005)
	$Na_v1.7$	SCN9A	Nociceptors (Nerves transmitting pain signals)	Membrane	Na_v type-9 α-subunit (tetradomain). Each domain consists of internally repeated segments (S1–S6)	Responsible for carrying pain signals to brain	Erythromelalgia, Paroxysmal extreme pain disorder, Congenital insensitivity to pain(CIP)	Cregg et al. (2013), Estacion et al. (2011), Klein et al. (2013)
	$Na_v1.8$	SCN10A	Peripheral sensory nervous system	Membrane	Na_v type-10 α-subunit (tetradomain). Each domain consists of internally repeated segments (S1–S6)	Transmits pain signals to CNS in cold temperature	Pain and Paresthesias	Faber et al. (2012)

Table 1 continued

Channel name	Subtypes	Genes encoding subtypes	Tissue specificity	Subcellular location	Subunit structure	Physiological role	Involvement in disease	References
	$Na_v1.9$	SCN11A	Heart and Dorsal root ganglion neurons	Trigeminal neurones and their axons	Na_v type-11 α-subunit (tetradomain). Each domain consists of internally repeated segments (S1–S6)	Involved in pain related signaling	Mechanical and Heat pain hypersensitivity	Lolignier et al. (2011)
	$Na_V\beta1$	SCN1B	Muscle and Neuronal cells	Membrane	Na_v type-1 β-subunit. Single domain. Auxiliary subunit	Modulate channel gating kinetics	Brugada syndrome, Generalized epilepsy with febrile seizures plus type 1	Audenaert et al. (2003), Patino et al. (2011)
	$Na_V\beta2$	SCN2B	White matter tracts in the cerebellum, Hippocampal, cortical pyramidal neurons, and cerebellar purkinje neurons	At the membrane of Cell bodies and Nodes of Ranvier	Na_v type-2 β-subunit. Single domain. Auxiliary subunit	Modulate channel gating kinetics	Brugada Syndrome	Riuro et al. (2013)
	$Na_V\beta3$	SCN3B	Contractile myocardium	Membrane	Na_v type-3 β-subunit. Single domain. Auxiliary subunit	Modulate channel gating kinetics	Brugada syndrome type 7	Hu et al. (2009), Carmen et al. (2010)
	$Na_V\beta4$	SCN4B	Dorsal root ganglia	Membrane	Na_v type-4 β-subunit. Single domain. Auxiliary subunit	Modulate channel gating kinetics	Long QT-syndrome type 10	Medeiros-Domingo et al. (2007)

rhythmic activity, and excitation-secretion coupling (Bergsman et al. 2000).

Chloride Ion Channel

Chloride channel is the Cl^- ion-conducting channel that can be categorized into five different types depending on the type of activators involved which are cAMP, Ca^{2+}, volume, voltage, and ligand (Suzuki et al. 2006). Presently, three well-known gene families of Cl^- ions are ClC gene family, cAMP-activated CFTR Cl^- channel gene family, and ligand-gated GABA, glycine-receptor chloride channel gene family (Jentsch et al. 2002). Different subtypes of this channel associated with diseases have been summarized in Table 4 whose multiple sequence alignment has described their very little conservation among different families during evolution (Fig. 4a). Their phylogenetic relationship showed two closely related gene families in two major clusters (Fig. 4b). These chloride channels play a variety of roles that are cell volume regulation, transepithelial transport, secretion of fluid from secretory glands, and stabilization of membrane potential (Jentsch et al. 1995).

Molecular Entities of Ion Channels

Sodium Channel Structure

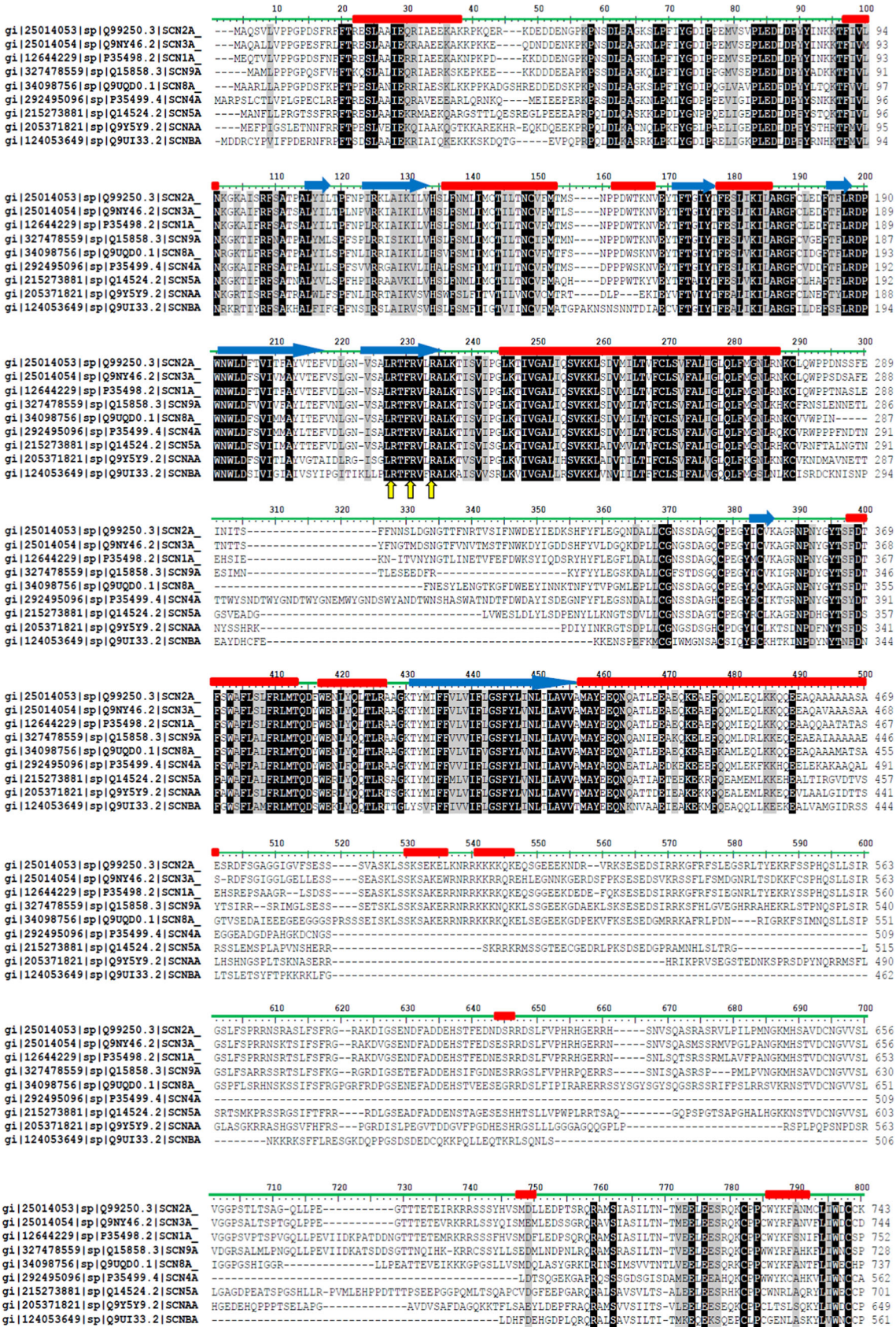
Voltage-gated sodium (Na_v) channel is a complex of a 260 kDa (α-subunit) and 33–36 kDa (β1–β4 auxiliary subunits, Casadei et al. 1986). Pore-forming single α-subunit has been associated with four β-subunits (Fig. 5a). The α-subunit has four internally repeated domains (I–IV) that mold themselves to form an ion-traversing pore. Furthermore, each domain carries six transmembrane helical segments designated as S1–S6 in which uncovered segment (S4) serves as voltage sensor along with a loop between S5 and S6 (Noda et al. 1984; Catterall et al. 2008). Apart from α-subunit that has a role in pore formation, β-subunits have an important role of modulation in the kinetics of gated channels that cause positive or negative shift upon voltage sensitivity of the channel depending on its type. Pore-forming α-subunit mutation is responsible to majority of neurological channelopathies whereas mutations in auxiliary subunit have been known to be responsible in few cases (Fontaine et al. 1990; Rojas et al. 1991; Ptacek et al. 1992).

Potassium Channel Structure

Potassium channels primarily consist of four α-subunits surrounding the central pore region frequently associated with auxiliary β-subunit (Fig. 5b). Each α-subunit of voltage-gated potassium channel (K_v) comprised six transmembrane helical segments (S1–S6) with a cytoplasmic N- and C-termini. N-terminus have T1 domain (tetramerization domain) that assembles the α-subunits into functional channel (Zerangue et al. 2000; Bocksteins et al. 2009), while S4 segment is highly positive and acts as voltage sensor along with the loop between S5–S6 (Yost 1999). Pore region contains the signature sequence GYG (Fig. 2a) which has specificity for conducting K^+ ions (Bocksteins et al. 2009). Auxiliary β-subunit assembles into tetrameric structures and interacts with α-subunit of K_v channel which provides a role in modulating channel gating kinetics (Gulbis et al. 1999). Apart from that, an additional long C-terminal extension in α-subunit has found in case of calcium-activated potassium channels, whereas inward rectifier potassium channel's α-subunit is composed of only two transmembrane segments S1 and S2 which resemble with the S5 and S6 segments of voltage-gated potassium channel (Yost 1999). The β-subunit that associates with α-subunit of calcium-sensitive potassium channel has two transmembrane segments which increases calcium sensitivity of the channel, while β-subunit that associates with α-subunit of inward rectifier potassium channel has comprised of several transmembrane segments (Benatar 2000).

Calcium Channel Structure

Calcium channel consists of a core α_1-subunit and other auxiliary subunits like β-, α_2-, δ-, and γ-subunits (Arikkath and Campbell 2003 (Fig. 5c). Ca^{2+} ion conduction is carried out by a transmembrane protein that is α1-subunit which possesses molecular mass of nearly 200–260 kDa. The α1-subunit consists of four transmembrane repeating units, where each unit is comprised six helical segments S1–S6. S4 helix serves as voltage sensor, while glutamate ions present in the linker region of S5 and S6 are the key residues responsible for providing selectivity filter role to the channel. Besides, this ion conduction tunnel is formed by the combination of S5 segment, linker region between S5–S6, and S6 segment from each of the four transmembrane units (Catterall and Curtis 1987; Campbell et al. 1988; Catterall 1988; Bergsman et al. 2000). The β-subunit is a peripheral membrane unit of nearly 60 kDa which is associated with cytoplasmic surface of membrane and is responsible for differences in major classes of calcium channel (L-, N-, P/Q-type, etc., Takahashi et al. 1987; Bergsman et al. 2000). Moreover, α_2-δ is a 175 kDa dimer which is linked by a disulfide bridge and is responsible for modulating channel gating kinetics (De Jongh et al. 1990; Klugbauer et al. 1999). Another accessory γ-subunit is known to provide the inactivating property in few cases (Eberst et al. 1997; Letts et al. 1998).


gi|25014053|sp|Q99250.3|SCN2A_
gi|25014054|sp|Q9NY46.2|SCN3A_
gi|12644229|sp|P35498.2|SCN1A_
gi|327478559|sp|Q15858.3|SCN9A_
gi|34098756|sp|Q9UQD0.1|SCN8A_
gi|292495096|sp|P35499.4|SCN4A_
gi|215273881|sp|Q14524.2|SCN5A_
gi|205371821|sp|Q9Y5Y9.2|SCNAA_
gi|124053649|sp|Q9UI33.2|SCNBA_

◀**Fig. 1** **a** Multiple sequence alignment of sodium channel subtypes: Highly conserved residues are highlighted in *black,* whereas less conserved residues are highlighted in *light gray*. Moreover, 16 highly conserved Arginine residues of segment 4 are marked with *yellow arrow*, which are responsible for providing voltage sensitivity to the channel. Secondary structure elements of SCN2A predicted by YASPIN are shown on the *top* of amino acid sequence, loop residues are shown in *green line*, α-helices are shown in *rectangles* (*red*), and β-strands are as filled arrows (*blue*). **b** Phylogenetic relationship obtained by UPGMA method using clustalW: There is single major cluster and two closely related subtypes that are SCN2A–SCN3A and SCN5A–SCNAA (SCN10A) along with SCNBA (SCN11A) as an out-group (Color figure online)

Chloride Channel Structure

Different Gene Families of Chloride Channel have Different Structures for Conducting Cl^- Ions.

ClC-chloride channel or voltage-gated Chloride channel has a double-barrel structure (Fig. 5d) (Miller and White 1984; Jentsch et al. 2002). These chloride channels are homodimers, and a pore is formed by each subunit. Each subunit exhibits an anti-parallel architecture. Each subunit contains 18 α-helices (Dutzler et al. 2002).

CFTR chloride channel is comprised two motifs. Each motif contains a membrane-spanning domain (MSD) and nucleotide-binding domain (NBD). R (regulatory) domain acts as a connecting link between these two MSD-NBD motifs (Sheppard and Welsh 1999). MSD usually comprised six transmembrane segments, and NBD has a role in interacting with ATP (Hyde et al. 1990).

Ligand-gated chloride channel consists of five subunits. Each subunit comprised long N-terminal extracellular domain, four putative transmembrane domains (TM), and a short extracellular C-terminal. N-terminal domain has conserved Cys-loop (Maricq et al. 1991; Lindstrom et al. 1995; Vannier and Triller 1997).

Ion Channels and Neurological Diseases

Action potential generation and synaptic transmission in the central and peripheral nervous system depend on the coordinated activity of voltage-gated ion channels. They are found to be present on axon hillock, node of Ranvier in case of myelinated and non-myelinated neurons as well (Debanne et al. 2011). Another salient feature of these channels is related to its highly conserved structure during the evolutionary process. However, synonymous mutation sites in transmembrane region are more conserved than the non-transmembrane region, but mutations in non-transmembrane region are also reported to be non-neutral ultimately causing channel dysfunction (Zhou et al. 2012). Nonfunctional ion channels are incompatible for the cellular entities and lead to the generation of varieties of neurological diseases.

Sodium Ion Channelopathies with Molecular Mechanism

Potassium-Aggravated Myotonia (PAM)

PAM can be categorized into three different clinical phenotypes, myotonia fluctuans, severe myotonia permanens, and acetazolamide responsive myotonia that follow autosomal dominant inheritance pattern (Orrell et al. 1998) and categorized under rare disease by the Office of Rare Diseases (ORD), National Institute of Health (NIH). Myotonia implies muscle stiffness followed by its inability to relax, while in PAM myotonia worsened in the presence of potassium ions. It begins either in childhood or adolescence and known to be caused due to alteration in $Na_v1.4$ channel α-subunit as a result of mutations in SCN4A gene (Heine et al. 1993; Orrell et al. 1998; Vicart et al. 2005). Mutated channel leads to the enhanced influx of sodium ion movement in muscle, and thus prolonged contraction has been observed in PAM. There are multiple factors responsible for its triggering, for instance, fasting, physical exercise, voluntary contraction, cold weather, fever, and potassium-rich food (Ptacek et al. 1992). However, in PAM, potassium ion promotes the muscle contraction, and therefore intake of potassium-rich food is not advisable. Severity of symptoms might be exacerbated when cramps occur in respiratory muscle which could lead to hypoxia. The affected patients exhibit same phenotype with little clinical variation which has been confirmed by electromyography (Lerche et al. 1993). Multiple reasons that have been suggested for the alteration of channel function in several myotonias are reduced fast channel inactivation, enhanced recovery rate from fast inactivation, slowed deactivation or hyperpolarizing shift in steady-state activation (Cummins and Bendahhou 2009). The above phenomenon was also reported in a recent study of $Na_v1.4$ mutation i.e., A799S (Lion-Francois et al. 2010) in a patient suffering with severe neonatal episodic laryngospasm (Simkin et al. 2011). In another study using patch clamp technique, it has been reported that heterozygous mutations (G1306V, G1306A, and G1306E) in same codon of SCN4A gene are very crucial for sodium channel inactivation (Lerche et al. 1993). Apart from fewer intakes of potassium-rich foods, other treatments like physiotherapy (stretching or massaging to aid muscle relaxation) and certain medications such as mexiletine, carbamazepine, or acetazolamide are useful.

Para Myotonia Congenita (PMC)

PMC is a myopathy condition that affects the skeletal muscle contraction and tone that result in stiffness along with sustained weakness for hours. However, the onset of

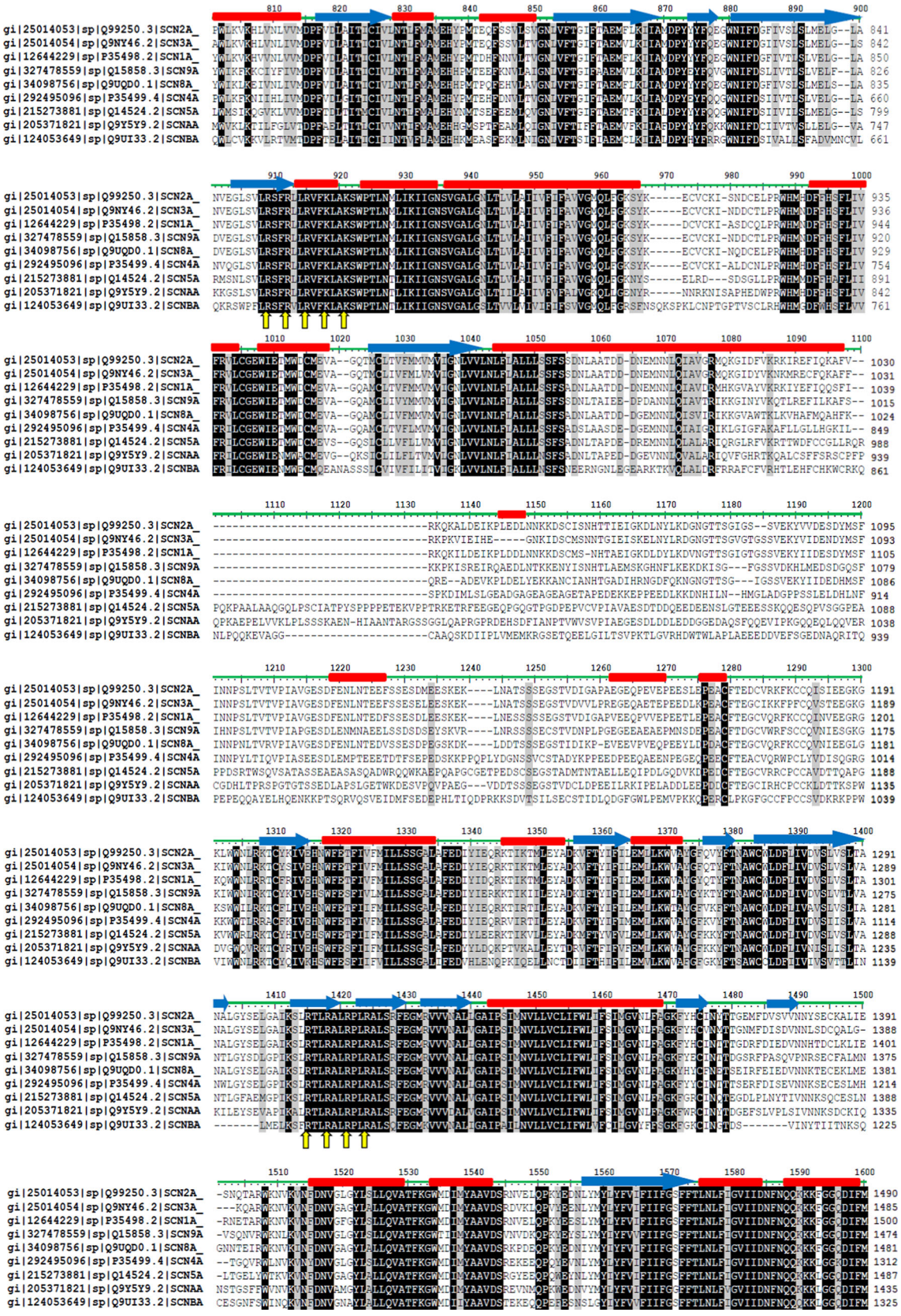


Fig. 1 continued

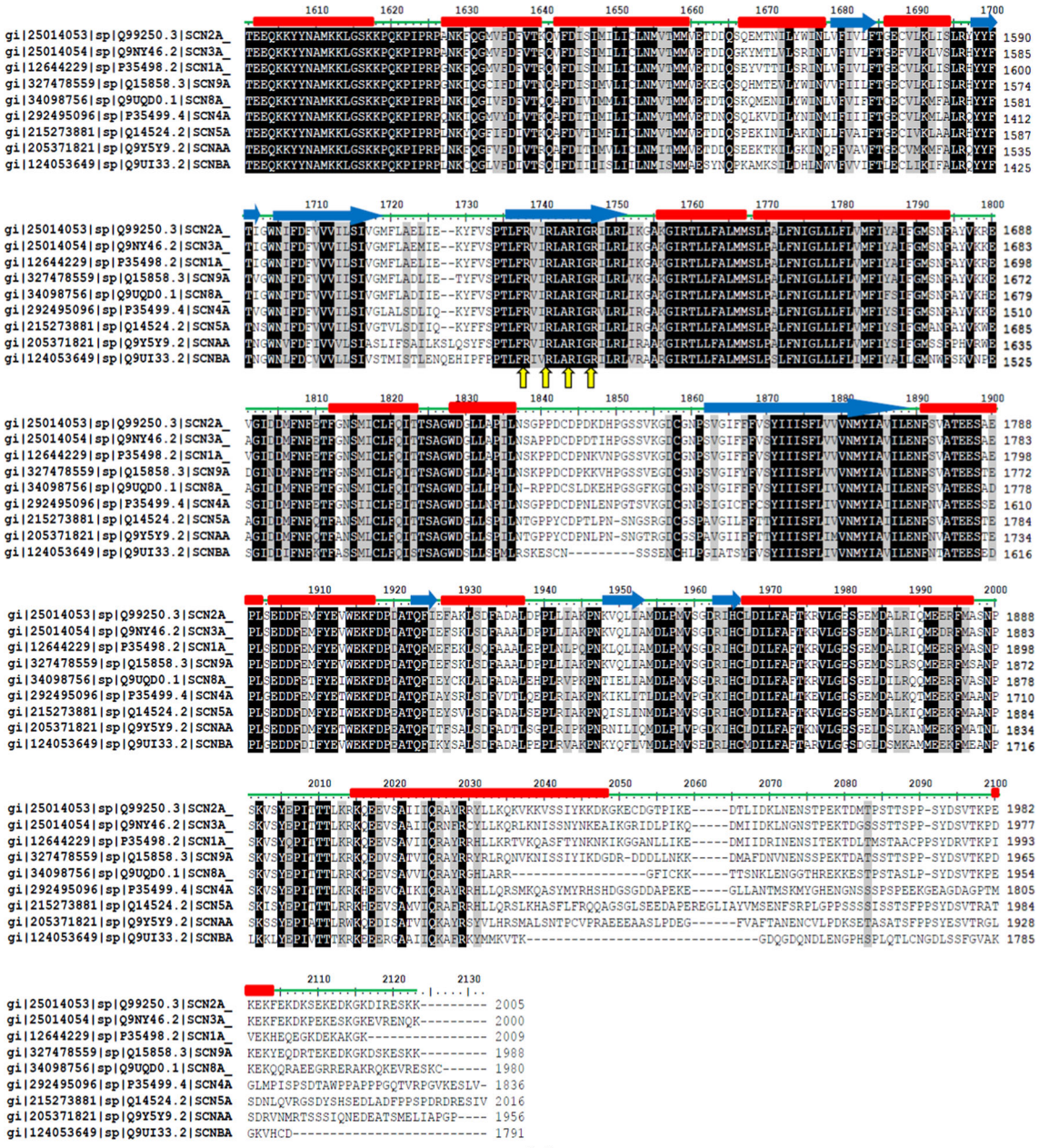


Fig. 1 continued

Table 2 Potassium ion channel subtypes in association with various diseases

Channel name	Subtypes	Genes encoding subtypes	Tissue specificity	Sub cellular location	Structure	Physiological role	Involvement in disease	References
Potassium (Kv) Channel	$K_v1.1$	KCNA1	Unmyelinated Axons, Cell Somas, Axon Terminals, Dendrites	Membrane, Transmembrane	K_v shaker member 1, α-subunit consist of six helical segments (S1–S6)	Circadian Rhythms, Neuronal Firing	Episodic Ataxia Type 1, Myokymia, Periodic Ataxia	Orazio et al. (2012), Brew et al. (2003), Shook et al. (2008)
	$K_v1.2$	KCNA2	Hippocampal Neuron Neocortex, Main olfactory bulb (MOB), and Cerebellum	Membrane, Multi-pass membrane protein	K_v shaker member 2, α-subunit consist of six helical segments (S1–S6)	Regulation of state Transitions and Repetitive activity in Striatal Medium Spiny Neurons	Cerebellar Ataxia, myokymia, and neuromyotonia	Pruss et al. (2009), Lorincz and Nusser (2008)
	$K_v1.3$	KCNA3	Effector memory T-cells	Membrane, Multi-pass membrane protein	K_v shaker member 3, α-subunit consist of six helical segments (S1–S6)	Regulate several physiological functions of Lymphocytes, Cell Proliferation	Down syndrome Neural Progenitors	Wulff et al. (2003), Cidad et al. (2012)
	$K_v1.4$	KCNA4	Heart, Cerebellum	Membrane, Multi-pass membrane protein	K_v shaker member 4, α-subunit consist of six helical segments (S1–S6)	Modulating Electrophysiological Behavior	Chronic Pancreatitis, Hyperalgesia	Chandy et al. (2004), Freedman et al. (1992), Leonard et al. (1992)
	$K_v1.5$	KCNA5	Heart, Brain	Cell membrane, Multi-pass membrane protein	K_v shaker member 5, α-subunit consist of six helical segments (S1–S6)	Physiological processes in Brain and Muscle	Ischemia Affects	Fedida et al. (2003), Gobrit et al. (2007), Vicente et al. (2006), Archer et al. (2001), Stapels et al. (2010)
	$K_v1.6$	KCNA6	Ganglion Cell	Membrane, Multi-pass membrane protein	K_v shaker member 6, α-subunit consist of six helical segments (S1–S6)	Mediates the voltage-dependent potassium ion permeability of excitable membranes	Myokymia and Neuromyotonia	van Poucke et al. (2012)
	$K_v1.7$	KCNA7	Heart, Kidney, Skeletal Muscle	Membrane, Multi-pass membrane protein	K_v shaker member 7, α-subunit consist of six helical segments (S1–S6)	Important Role in the Repolarization of Cell Membranes	Acute myeloid Leukemia	Finol-Urdaneta et al. (2006), Kashuba et al. (2001)
	$K_v2.1$	KCNB1	CNS	Pyramidal Neurons in Cortex	K_v shab member 1, α-subunit consist of six helical segments (S1–S6)	Regulates Neuronal Excitability, Action Potential Duration, and Tonic Spiking	Hyperalgesia	Misonou et al. (2005)
	$K_v2.2$	KCNB2	Trapezoid body neurons	Trapezoid body neurons	K_v shab member 2, α-subunit consist of six helical segments (S1–S6)	Regulate Action Potential Firing	Cardiovascular disease risk	Johnston et al. (2008), Kihira et al. (2010)

Table 2 continued

Channel name	Subtypes	Genes encoding subtypes	Tissue specificity	Sub cellular location	Structure	Physiological role	Involvement in disease	References
	$K_v3.1$	KCNC1	Cortex, Cerebellum, Hippocampus Neurons in the Globus Pallidus, CNS	Hippocampus Neurons in the Globus Pallidus	K_v shaw member 1, α-subunit consist of six helical segments (S1–S6)	Involved in Motor Control	Ataxia with prominent Hypermetria, Constitutive Hyperactivity, Sleep Loss, Impaired Motor performance, Tremor, and Myoclonus	Lewis et al. (2004), Espinosa et al. (2008)
	$K_v3.2$	KCNC2	Cortical GABAergic Interneurons, Hippocampus Somatic, Proximal Dendritic Membrane Axons	Proximal Dendritic Membrane Axons, Cortical GABAergic Interneurons	K_v shaw member 2, Homo- or hetero tetramer, α-subunit consist of six helical segments (S1–S6)	Neurodevelopmental delay Cerebellar Ataxia	Susceptibility to Seizures	Chow et al. (1999), Lau et al. (2000)
	$K_v3.3$	KCNC3	Cortex, Basal Ganglia, and Cerebellum	Membrane, Multi-pass membrane protein	K_v shaw member 3, Homo- or, α-subunit consist of six helical segments (S1–S6)	Involved in Motor Control	Constitutive Hyperactivity, Sleep Loss, Impaired Motor Performance, Ataxia, Tremor, and Myoclonus	Espinosa et al. (2008)
	$K_v4.1$	KCND1	Epithelial Cells, Alveolar and Mammary Epithelial Cells, Adipose Tissue-Derived Stem Cells	Multi-pass membrane protein, Alveolar Mammary Epithelial Cells Adipose Tissue-Derived Stem Cells	K_v shal member 1, Homo tetramer, α-subunit consist of six helical segments (S1–S6)	Contribute to cell Migration and Wound Healing	Gastric Cancer NOS, Malignant Neoplasm of Breast	Sandhiya and Dkhar (2008)
	$K_v4.2$	KCND2	Brain	Localized in the Dendrites near Postsynaptic Regions	K_v shal member 2,, α-subunit consist of six helical segments (S1–S6)	Regulate Synaptic Plasticity	Cardiovascular disease	Jo et al. (2010)
	$K_v4.3$	KCND3	Rat Adult Brain and Heart Tissues	Molecular layer Interneurons	K_v shal member 3,, α-subunit consist of six helical segments (S1–S6)	Internalized in response to Glutamatergic stimulation in Purkinje Cells, Neuronal Somato-dendritic Interactions	Spin cerebellar Ataxia Type 1, Cerebellar Ataxia	Hourez et al. (2011)
	$K_v7.2$	KCNQ2	Peripheral Nerve System	Membrane, Multi-pass membrane protein	K_v KQT like Subfamily member 2, Heteromultimer, α-subunit consist of six helical segments (S1–S6)	Regulate Neurotransmitter Release, Heart Rate, Insulin Secretion Neuronal Excitability, Epithelial electrolyte Transport, Smooth Muscle contraction	Myokymia and Neuromyotonia	van Poucke et al. (2012)

Table 2 continued

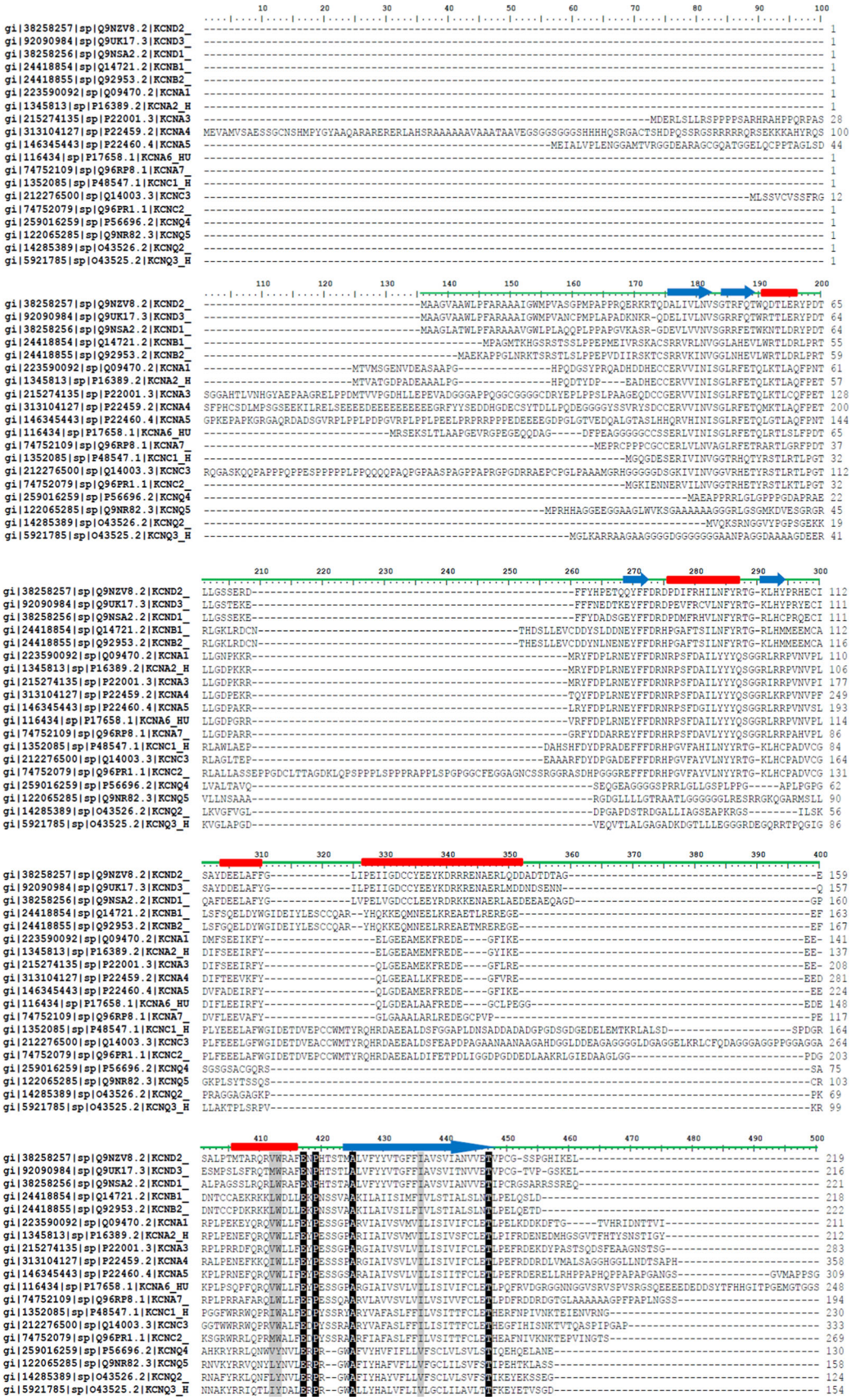
Channel name	Subtypes	Genes encoding subtypes	Tissue specificity	Sub cellular location	Structure	Physiological role	Involvement in disease	References
	$K_v7.3$	KCNQ3	Distributed Broadly in Brain	Membrane, Multi-pass membrane protein	K_v KQT like Subfamily member 3, Heteromultimer, α-subunit consist of six helical segments (S1–S6)	Electrical Hyper excitability in BFNC	Familial Neonatal Convulsions (BFNC), Autosomal Dominant Epilepsy of Infancy, Myokymia	Schroeder et al. (1998), Chung et al. (2006)
	$K_v7.4$	KCNQ4	Almost All Brain Regions	Discrete Nuclei Of Brainstem, Including the Mid- Brain	K_v KQT like Subfamily member 4, Homo/ Hetero tetramer, α-subunit consist of six helical segments (S1-S6)	Participate in both pre- and Post-synaptic Modulation of basal and stimulated excitatory Neurotransmission	Chinese Non-Syndromic Hearing Loss Pedigree	Kharkovets et al. (2000)
	$K_v7.5$	KCNQ5	Neocortex and the Hippocampal	Apical and Lateral Membranes	K_v KQT like Subfamily member 5, Heteromul-timer, α-subunit consist of six helical segments (S1–S6)	Controlling Basal Anion Secretion	Epilepsy	Yus-Najera et al. (2003)

Fig. 2 **a** Multiple sequence alignment of potassium channel subtypes: Highly and less conserved residues have been highlighted in *black* and *light gray* color, respectively, where three highly conserved Arginine residues present in segment 4 impart voltage sensitivity to the channel that has been marked with *yellow arrow*. Moreover, 'GYG' signature sequence has marked with *purple arrow* that provides potassium ion selectivity to the channel. Secondary structure elements of KCND2 (predicted by YASPIN) have shown on the *top* of amino acid sequences that are loop residues (*green line*), α-helices (*rectangles* (*red*)), and β-strands (*filled arrows* (*blue*)). **b** Phylogenetic tree obtained by UPGMA method using clustalW: There are three major clusters where six pairs of subtypes are found to be closely related, which are KCND2–KCND3, KCNB1–KCNB2, KCNA1–KCNA2, KCNA4–KCNA7, KCNC1–KCNC3, and KCNQ4–KCNQ5 (Color figure online)

prolonged muscle contraction begins in infant, while episodes of weakness start at adolescence stage. This disease is also known as Eulenberg disease and comes under rare congenital autosomal dominant neuromuscular disorder (Haass et al. 1981). It is highly cold sensitive and exacerbated due to exercise and cold temperature which affect upper bodily parts, for instance, bulbar, facial, neck, and hand muscles more than the lower limbs (Magee 1966). Prolonged cry in such patients often leads to blepharospasm. Not always but frequently PMC patients are found to be accompanied by Hyperkalemic periodic paralysis with increased level of serum creatine kinase. Voltage-gated sodium channel α-subunit-encoding SCN4A genetic mutation is responsible for PMC (Kim et al. 2002, Pereon et al. 2003), where the cytoplasmic loop region between segment III and IV in sodium channel is hotspot for the mutation (McClatchey et al. 1992; Ptacek et al. 1992; Lerche et al. 1993; Ptacek et al. 1993; Sasaki et al. 1999; Okuda et al. 2001). It has also been studied that R1448H mutation causes cold-induced myotonia that leads to PMC and is responsible for slowed inactivation and faster recovery from inactivation as compared to non-mutant channels (Mohammadi et al. 2003). The problem of myotonia in PAM patients can be relieved by administering mexiletine as a first-line agent, while episodic weakness can be treated with daranide or dianox.

Hyperkalemic Periodic Paralysis (HYKPP)

Hyperkalemic periodic paralysis is a congenital autosomal dominant genetic disorder (Ptacek et al. 1991) with elevated potassium level in blood that causes episodes of muscle weakness (Venance et al. 2006), where intake of potassium-rich foods and rest after exercise are the most prominent factors for triggering of HYKPP. The attack lasts for few hours to a day, where its severity is specified via membrane inexcitability and muscle weakness which affect shoulder, hips more often than hands and legs (Weber et al. 2006; Webb and Cannon 2008). Underlying SCN4A gene mutations affect inner core of transmembrane


gi|38258257|sp|Q9NZV8.2|KCND2_
gi|92090984|sp|Q9UK17.3|KCND3_
gi|38258256|sp|Q9NSA2.2|KCND1_
gi|24418854|sp|Q14721.2|KCNB1_
gi|24418855|sp|Q92953.2|KCNB2_
gi|223590092|sp|Q09470.2|KCNA1
gi|1345813|sp|P16389.2|KCNA2_H
gi|215274135|sp|P22001.3|KCNA3
gi|313104127|sp|P22459.2|KCNA4
gi|146345443|sp|P22460.4|KCNA5
gi|116434|sp|P17658.1|KCNA6_HU
gi|74752109|sp|Q96RP8.1|KCNA7_
gi|1352085|sp|P48547.1|KCNC1_H
gi|212276500|sp|Q14003.3|KCNC3
gi|74752079|sp|Q96PR1.1|KCNC2_
gi|259016259|sp|P56696.2|KCNQ4
gi|122065285|sp|Q9NR82.3|KCNQ5
gi|14285389|sp|O43526.2|KCNQ2_
gi|5921785|sp|O43525.2|KCNQ3_H

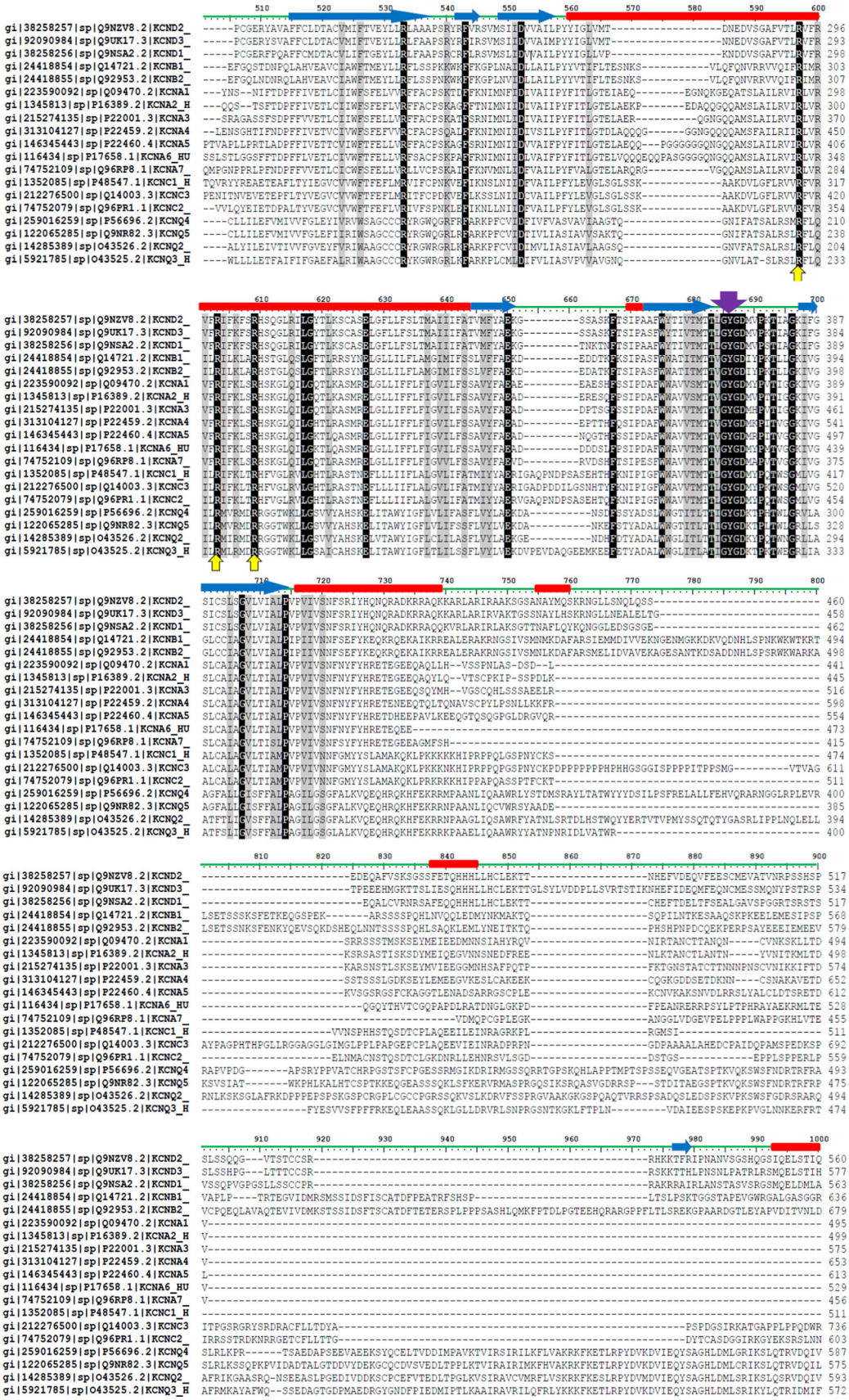


Fig. 2 continued



Fig. 2 continued

Table 3 Calcium ion channel subtypes in association with various diseases

Channel name	Subtypes	Genes encoding subtypes	Tissue specificity	Sub cellular location	Subunit structure	Physiological role	Involvement in disease	References
Calcium (Ca_V) Channel	$Ca_v1.1$	CACNA1S	Skeletal Muscle	Located in Muscle Cells triad junctions	Ca_v L-type, α-1S-subunit, Each α_1-subunit consists of 6 helical transmembrane segments (S1–S6)	Functions as a Voltage Sensor in Skeletal Muscle Excitation–Contraction Coupling	Hypokalemic Periodic Paralysis, Thyrotoxic Periodic paralysis, and Malignant Hyperthermia Susceptibility	Kung et al. (2004), Kim et al. (2001)
	$Ca_v1.2$	CACNA1C	Brain, Heart, Ovary Neurons	Membrane, Multi-pass membrane protein	Ca_v L-type, α-1C-subunit, Each α_1-subunit consists of 6 helical transmembrane segments (S1–S6)	Release of Hormones and Neurotransmitters	Vision, Hearing,, and Gene Expression	Kameda et al. (2006), Reuter (1983)
	$Ca_v1.3$	CACNA1D	Auditory Brainstem, Center Auditory Sensory hair Cells, Neuronal Cells, and Some Epithelial Cells	Somato-dendritic Compartment of many Types of Neurones	Ca_v L-type, α-1D-subunit, Each α_1-subunit consists of 6 helical transmembrane segments (S1–S6)	Regulate Intracellular Processes such as Contraction, Secretion, Neurotransmission, and Gene Expression	Deafness	Roberts et al. (1990), Satheesh et al. (2012)
	$Ca_v1.4$	CACNA1F	Retina	Expressed in the Retina and Localizes at Ribbon Synapses in Cone and Rod photoreceptors	Ca_v L-type, α-1F-subunit, Each α_1-subunit consists of 6 helical transmembrane segments (S1–S6)	Synaptic Transmission and Cellular organization in Retina	Congenital Stationary Night Blindness, Syndromic Autism, Schizophrenia	McRory et al. (2004), Klassen et al. (2011), Wei and Hemmings (2006)
	$Ca_v2.1$ (P/Q)	CACNA1A	Presynaptic Terminals Cerebellar Purkinje Cells Granule Cells, Cortex	Somato-Dendritic membranes throughout the brain	Ca_v P/Q-type, α-1A-subunit, Each α_1-subunit consists of 6 helical transmembrane segments (S1–S6)	Mediating Neurotransmitter release in the Nervous System, Postsynaptic Integration, Neuroplasticity, Neural Excitability, and Gene Transcription	Spin cerebellar Ataxia Type 6	Llinas et al. (1992), Mintz et al. (1992), Chen and Piedras-Rentería (2007)
	$Ca_v2.2$ (N)	CACNA1B	Neuron, Retinal Ganglion cell	Multi-pass membrane protein	Ca_v N-type, α-1B-subunit, Each α_1-subunit consists of 6 helical transmembrane segments (S1–S6)	Controls Neurotransmitter Release from Neurons	Episodic Ataxia Type 2, Schizophrenia, and Bipolar Disorder	Yasuda et al. (2004), Zhang et al. (2008)

Table 3 continued

Channel name	Subtypes	Genes encoding subtypes	Tissue specificity	Sub cellular location	Subunit structure	Physiological role	Involvement in disease	References
	Ca_v 2.3 (R)	CACNA1E	Neuronal Tissues (Kidney)	Multi-Pass membrane Protein	Ca_v R-type, α-1E-subunit, Each α_1-subunit consists of 6 helical transmembrane segments (S1–S6)	Modulation of firing patterns of neurons, Muscle Contraction, Hormone or neurotransmitter release, Cell Motility, Cell Division, and Cell Death	Juvenile Myoclinic Epilepsy	Schneider et al. (1994), Williams et al. (1994), Suzuki et al. (2004)
	Ca_v3.1	CACNA1G	Neurons and Cardiac tissue	Multi-pass membrane protein	Ca_v T-type, α-1G-subunit, Each α_1-subunit consists of 6 helical transmembrane segments (S1–S6)	Neuronal Firing Activity, Cardiac Pacemaker Activity	Epilepsy, Cardiac Hypertrophy	Hagiwara et al. (1988), Huguenard (1996), Tsakiridou et al. (1995)
	Ca_v3.2	CACNA1H	Kidney, Liver, Heart, Brain	Multi-pass membrane protein	Ca_v T-type, α-1H-subunit, Each α_1-subunit consists of 6 helical transmembrane segments (S1–S6)	Secretion of Neuroendocrine Prostate Cancer Cells, Contraction, Secretion Neurotransmission, and gene Expression.	Epilepsy, Idiopathic generalized Type 6, Epilepsy, childhood absence 6 (ECA6)	Splawski et al. (2006)
	Ca_v3.3	CACNA1I	Brain Specific	Somato-dendritic Compartment of many Types of Neurones	Ca_v T-type α- 1I-subunit, Each α_1-subunit consists of 6 helical transmembrane segments (S1–S6)	Electrical and Signaling, generate burst firing, and Pacemaker Activity	Hyperalgesia	Talley et al. (1999), Carbone and Lux (1984), Kim et al. (2003)
	Ca_v β_1	CACNB1	Brain, Heart, Spleen, Central Nervous System & Neuro-blastoma Cell	Sarcolemma, Peripheral membrane protein	Ca_v L-type, β-1 (auxiliary)subunit	Modulating G protein inhibition and controlling the alpha-1 subunit membrane targeting	Malignant Hyperthermia susceptibility (Autosomal Dominant Disorder of Skeletal Muscle)	Gregg et al. (1996)
	Ca_v β_2	CACNB2	Heart, Retina	Membrane of smooth Muscle	Ca_v L-type, β-2(auxiliary)-subunit	Hyperpolarizing Shifts	Lambert-Eaton Myasthenic Syndrome, Brugada Syndrome	Perez-Reyes et al. (1992), Pichler et al. (1997), Ball et al. (2002), Reimer et al. (2000), Singer et al. (1991)
Ca_v β_4	CACNB4	Brain, predominantly in the Cerebellum, Kidney	Vestibular, Cerebellar Neuronal membrane	Cav L-type, β-4(auxiliary)-subunit	Shifting the Voltage dependencies of activation and inactivation, Modulating G protein inhibition	Idiopathic generalized Epilepsy, Juvenile Myoclonic Epilepsy	Xu et al. (2011), Ohmori et al. (2008)	

Table 3 continued

Channel name	Subtypes	Genes encoding subtypes	Tissue specificity	Sub cellular location	Subunit structure	Physiological role	Involvement in disease	References
	$Ca_v\ \Upsilon_2$	CACNG2	Brain	Multi-pass membrane protein	$Ca_v\ \Upsilon$-2 (auxiliary)subunit	Regulates the trafficking and gating properties of AMPA-selective glutamate receptors	Mental Retardation	Hamdan et al. (2011), Shi et al. (2010), Black and Lennon (1999)
	$Ca_v\ \Upsilon_5$	CACNG5	Epithelia	Cell Junction, Postsynaptic Cell Membrane	$Ca_v\ \Upsilon$-5 (auxiliary)subunit	Modulates gating properties	Schizophrenia and Bipolar Disorder	Chen et al. (2007), Curtis et al. (2011), Chu et al. (2001)

segments or intracellular protein loops which inturn impair the anchoring site of fast inactivation particle thereby leading to persistent Na^+ current through unclosed sodium channel (Bendahhou et al. 2002). The persistent sodium current across non-inactivated channel causes depolarization of cell thereby inactivating other normal sodium channels due to inability of action potential generation (Cannon et al. 1991; Lehmann-Horn et al. 2002). Patients suffering from this disease report abnormal muscle biopsy with high level of creatine kinase in the serum and permanent muscle weakness with aging. The treatment focuses on relieving symptoms and preventing further attacks which could be accomplished with the help of low potassium-high carbohydrate meal and medication of acetazolamide and hydrochlorothiazide drugs which are effective with minimal risks (McArdle 1956; Han and Kim 2011).

Primary Erythro-Melalgia (PEM)

Primary erythromelalgia is an autosomal dominant, peripheral nerve pain disorder which can be characterized by severe burning and bilateral pain with swelling in extremities of the body especially in hands and feet (Dib-Hajj et al. 2005; Waxman and Dib-Hajj 2005a, b). Due to micro-vascular arteriovenous shunting in PEM patients, vasomotor changes such as erythema and oedema take place, resulting in the pain sensation around affected area (Mork et al. 2000). The episodic attacks are found to be triggered or aggravated by increased body temperature, spicy food, and exercise, while cold environment relieves the pain (Michiels et al. 2005). Mutations in SCN9A gene are responsible for pathogenesis of PEM that causes alteration in $Na_v1.7$ α-subunit and lead to increased action potential (Cummins et al. 2004) thereby causing prolonged transmission of pain signals (Yang et al. 2004; Dib-Hajj et al. 2005; Drenth et al. 2005; Dib-Hajj et al. 2007). The patch clamp analysis of mutated sodium channel revealed that there is a hyperpolarization shift toward activation of the channel and slowed inactivation kinetics that makes opening of channel easier and prolonged (Cummins et al. 2004). Various treatment modalities have been tried viz. aspirin, cyclosporine, beta blockers, calcium channel antagonists, but patient should take preventive measures along with medication which include sodium channel blocker like ranolazine and mexiletine with highly promising results (Iqbal et al. 2009).

Paroxysmal Extreme Pain Disorder (PEPD)

PEPD is an autosomal dominant peripheral neuropathy that was earlier known as familial rectal pain and is characterized by excruciating pain and flushing in the submandibular, ocular, and rectal region (Fertleman and Ferrie

2006). Recurrent pain and skin flushing begin in childhood, and pain progresses to ocular and mandibular region with age. Although PEPD is a lifelong disorder, the frequency of attack generally decreases with age. Moreover, it has been observed that attacks are provoked by physical trigger like crying, eating, and defecation (Pett et al. 2013). PEPD is caused due to functional gain mutation in SCN9A gene (Choi et al. 2011; Estacion et al. 2011; Fischer and Waxman 2010) that means mutated channel results in sustained flow of sodium ion and hence maintaining action potential which prolongs transmission of pain signals. It has been reported that mutated channel lowers the threshold for single action potential in dorsal root ganglion neurons that results into increased number of action potential in response to a supra-threshold stimuli which leads to elevated pain signal transmission (Dib-Hajj et al. 2008). To relieve the pain, it is important to take preventive measure from triggering factor like managing constipation and use of anticonvulsants, for instance, carbamazepine has been found to be very effective in many patients (Theile and Cummins 2011).

Congenital Insensitivity to Pain (CIP)

CIP is an autosomal recessive peripheral sensory neuropathy characterized by complete loss of pain sensation in response to injuries (Danziger and Willer 2009) and also known as congenital analgia or congenital analgesia, congenital asymbolia, and congenital indifference to pain (Dyck et al. 1983). Congenital insensitivity to pain has been classified to the family of Hereditary Sensory and Autonomic Neuropathies (HSAN) and it has two common occurring forms that are congenital insensitivity to pain (CIP) and congenital insensitivity to pain with anhidrosis (CIPA) which have been classified as HSAN-V and HSAN-IV, respectively. CIP has been observed to be prevalent in children born to consanguineous marriages, and they generally suffer from accumulated wounds due to repeated injuries as a consequence of imperceptions of pain sensation (Protheroe 1991). Earlier, it was reported that CIP patients possess only nonsense mutations in the SCN9A gene (Dabby 2012; Cox et al. 2006) which were responsible for truncated α-subunit of sodium channel ($Na_v1.7$), but recently missense mutation (R896Q), frame shift deletion mutation (ΔR1370-L1374), and splicing mutation (IVS8-2A > G) have also been observed (Cox et al. 2010; Klein et al. 2013). Recent mutation was reported to be associated with pore regions thereby causing defect in the ion conduction through $Na_v1.7$ channel present on nociceptors that lead to complete loss of pain signal transmission from site of injury to brain (Fischer and Waxman 2010; Lampert et al. 2010, Goldberg et al. 2007). CIP patients not only exhibit loss of pain sensation but also sometimes smell sensation as well because $Na_v1.7$ channel is also present on olfactory receptor neurons that can lead to anosmia (Weiss et al. 2011). Convincing treatment for this disease is remain unclear, but case reports showed promising result with the use of naloxone and naltrexone in reversing the effect of analgesia (Protheroe 1991).

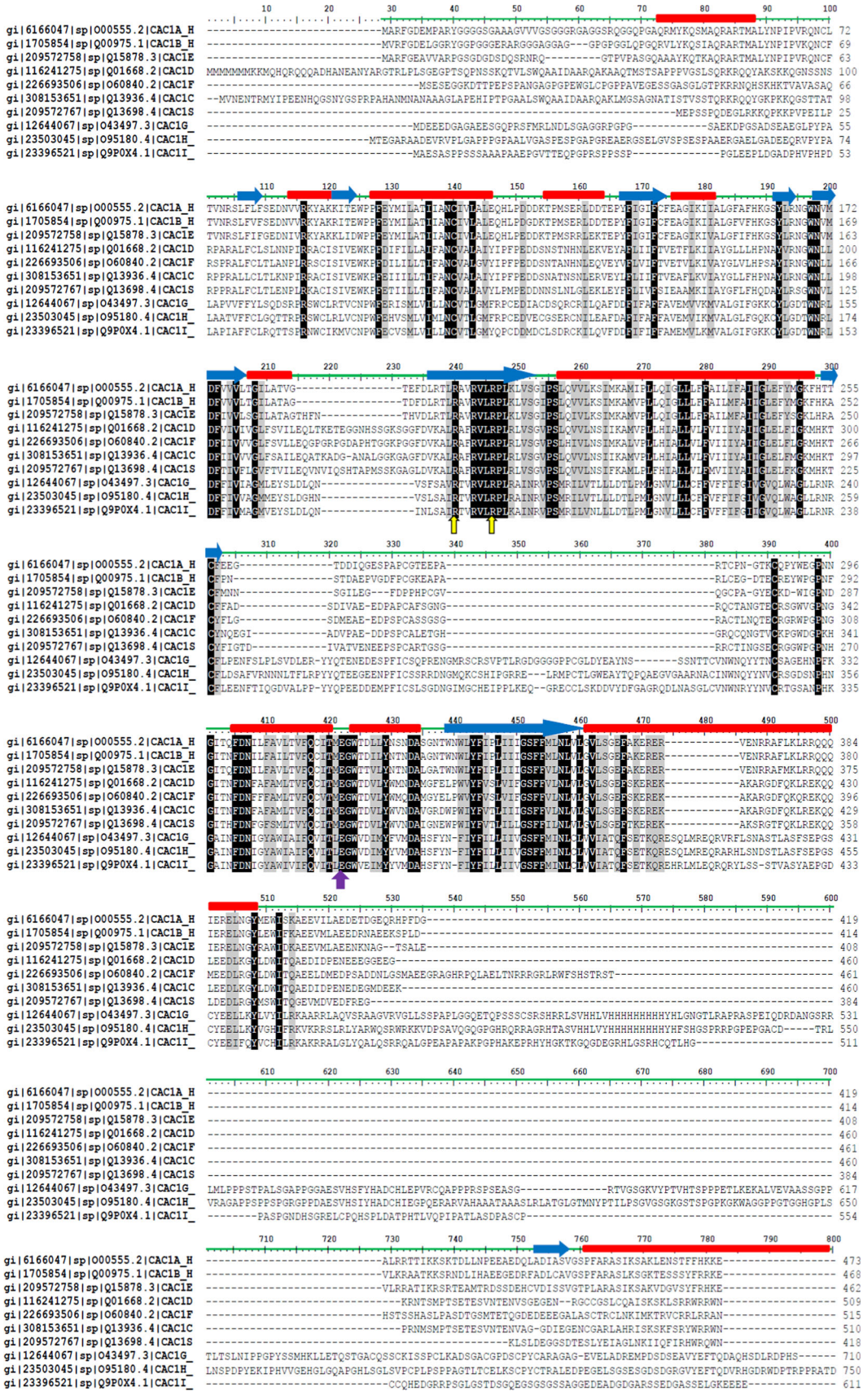
Generalized Epilepsy with Febrile Seizures (GEFS)

Epilepsy is a chronic neurological disorder that can be characterized with the recurrent episodes of convulsions and sensory disturbances due to abnormal electrical signals in the brain. Generalized epilepsy with febrile seizures (GEFS) is a recently described autosomal dominant epileptic syndrome, where convulsions are associated with the elevated temperature of the body (Chang and Lowenstein 2003). It begins in childhood (1 month to 1 year) and may last up to the age of 6 years or sometimes continues till the onset of puberty. GEFS patients exhibit a variety of clinical phenotypes that are typical febrile seizures and other seizure types such as tonic–clonic, myoclonic, myoclonic-astatic, absences, or atonic seizures (Scheffer and Berkovic 1997). Simple febrile seizure generally lasts for 15 min, while complex febrile seizure exhibits episodes that last more than 15 min, and it has also been observed that epilepsies become more prominent in aged people (Brodie et al. 2009). In most of the cases, majorly mutations were found in SCN1A, SCN1B gene, and γ2-subunit of $GABA_A$ receptors (Meisler et al. 2010; Wallace et al. 1998; Wallace et al. 2002; Audenaert et al. 2003; Meisler and Kearney 2005; Fujiwara 2006; Kang et al. 2006), where few mutations in $Na_v1.1$ cause mild epilepsies but several mutations in $Na_v1.1$ channel lead to severe epilepsies (Catterall et al. 2010).The resulting seizures are found to be familial in few cases and sporadic in other cases that imply environmental factors like elevated temperature also play a contributing role. Hyperthermia itself is capable of generating seizures, while resulting mutations are known to aggravate the susceptibility of developing a seizure with fever (Dube et al. 2009). Generally, regular medicines are not prescribed for such patients but for severe cases epileptic medicines like sodium valproate, ethosuximide, clobazam, carbamazepine, and phenytoin drugs are helpful in controlling epilepsies (Tate et al. 2005, 2006; Scheffer et al. 2007; Groot et al. 2012).

Potassium Ion Channelopathies with Molecular Mechanism

Paroxysmal Dyskinesia

Paroxysmal dyskinesia is an autosomal dominant rare episodic movement disorder that exhibits abnormal


gi|6166047|sp|O00555.2|CAC1A_H
gi|1705854|sp|Q00975.1|CAC1B_H
gi|209572758|sp|Q15878.3|CAC1E
gi|116241275|sp|Q01668.2|CAC1D
gi|226693506|sp|O60840.2|CAC1F
gi|308153651|sp|Q13936.4|CAC1C
gi|209572767|sp|Q13698.4|CAC1S
gi|12644067|sp|O43497.3|CAC1G_
gi|23503045|sp|O95180.4|CAC1H_
gi|23396521|sp|Q9P0X4.1|CAC1I_

◀ **Fig. 3** **a** Multiple sequence alignment of calcium channel subtypes: Highly and less conserved residues are highlighted in *black* and *light gray* color, respectively, where 12 highly conserved Arginine residues of segment 4 have been marked with *yellow arrow*, which provide voltage sensitivity to the channel. Moreover, Glutamate residues in loop region between segment 4 and 5 offer ion selectivity that is marked with *purple arrow*. Secondary structure elements of CACNA1A (predicted by YASPIN) are shown on the top of amino acid sequences that are loop residues (*green line*), α-helices (*red rectangle*), and β-strands (*blue arrows*). **b** Phylogenetic tree obtained by UPGMA method using clustalW: There are two major clusters having four pairs of closely related channel subtypes: CAC1A–CAC1B, CAC1D–CAC1F, CAC1C–CAC1S, and CAC1G–CAC1H (Color figure online)

involuntary movements including chorea, dystonia only during attacks (Demirkiran and Jankovic 1995). It has been classified into four different types on the basis of triggering factors responsible for the episodes that are (i) Paroxysmal kinesigenic dyskinesias (PKD) which is known to be triggered by sudden voluntary movements and unexpected stimulus, (ii) Paroxysmal non-kinesigenic dyskinesias (PNKD) that can be triggered by factors other than movement like stress, fatigue, and alcohol consumption, (iii) Paroxysmal exercise(exertion)-induced dyskinesias (PED) which could be triggered by prolonged exercise, and lastly (iv) Paroxysmal hypnogenic dyskinesias (PHD) in which attack can be triggered during Non-rapid eye movement sleep (Unterberger and Trinka 2008). Increased studies revealed that familial PKD can be caused by channel mutations and it has been identified that coexistence of generalized epilepsy and paroxysmal dyskinesiais caused by mutations in KCNMA1 gene. The resulting mutation in this gene promotes excitability of neurons by inducing rapid repolarization of action potential which allows neurons to conduct at a faster rate thereby causing recurrent attacks (Du et al. 2005). Moreover, recent studies identified that PKD is linked to pericentromeric region of chromosome 16 in a number of families and PNKD is caused due to mutation in myofibrillogenesis regulator 1 gene (MR-1) on Chromosome 2, while PED is caused due to mutation in glucose transporter gene (GLUT1, Mehta et al. 2009).There is no cure for paroxysmal dyskinesia, but symptoms can be relieved to some extent inconsistently with the help of anticonvulsants drugs like acetazolamide, anticholinergics, levodopa, and tetrabenazine along with avoiding the precipitating events like prolonged exercise(Mehta et al. 2009; van Rootselaar et al. 2009).

Benign Familial Neonatal Seizure (BFNS)

BFNS is an autosomal dominant inherited form of epilepsy which has been characterized by recurrent seizures in new born babies that cause muscle stiffness, convulsions, and loss of consciousness (Biervert et al. 1998). In majority of the suffering neonates, seizures began within the first week of life and disappeared spontaneously within a few months, but some patients showed dysfunctional channel even in adulthood (Tomlinson et al. 2012). Multiple mutations have been reported in KCNQ2 and KCNQ3 gene in the patients suffering with BFNS thereby generating altered M-current (Singh et al. 1998; Castaldo et al. 2002; Singh et al. 2003). However, normal M-current generated by $K_v7.2$ and K_v 7.3 potassium channel repolarizes the cell and hence ensures the inactivation of neurons, while mutated channel generates reduced or altered M-current that causes over-activation of neurons which leads to the seizure development in brain (Wang et al. 1998; Soldovieri et al. 2007; Volkers et al. 2009). Anticonvulsant therapy has been widely used where phenobarbital is effective in majority of individuals, while some individual may require other epileptic drug like carbamazepine, phenytoin, valproic acid, clonazepam, midazolam, or vigabatrin, but treatment has not had a consistent effect on the duration of seizures (Soldovieri et al. 2007).

Andersen Tawil Syndrome (ATS)

ATS is an autosomal dominant genetic disorder that has been characterized by periodic paralysis, ventricular arrhythmias, and developmental abnormalities typically affect head, face, and limbs (Tawil et al. 1994). Based on the genetic causes, ATS has been classified into two types where mutated KCNJ2 gene (Inward rectifier potassium channel $K_{ir}2.1$) was responsible for ATS type 1, while genetic cause for ATS type-2 is still unknown (Plaster et al. 2001). Its onset generally takes place around 20 years and 70 % of KCNJ2 mutations exhibit prolonged QT interval thereby also classified as Long QT syndrome 7 (Tristani-Firouzi et al. 2002) but a distinctive electrocardiogram has been observed in ATS1 patients with prolonged terminal T wave and prominent enlarged U waves (Zhang et al. 2005). Altered $K_{ir}2.1$ inward rectifier potassium channel disrupts PIP2 (phosphatidylinositol-4,5-bisphosphate) binding which has been responsible for inactivating channel thereby leading to sustained action potential and hence causes periodic paralysis and arrhythmias in skeletal and cardiac muscles (Lopes et al. 2002; Seebohm et al. 2012). Treatment of ATS patients requires closely co-ordinated expertise between a neuromuscular specialist and a cardiologist. However, it has been observed that drugs may have beneficial effect on one tissue while detrimental on other, but amiodarone and acetazolamide are effective in many cases (Junker et al. 2002).

SeSAME and EAST Syndrome

SeSAME/EAST is an autosomal recessive disorder whose nomenclature is based on the characteristic symptoms they

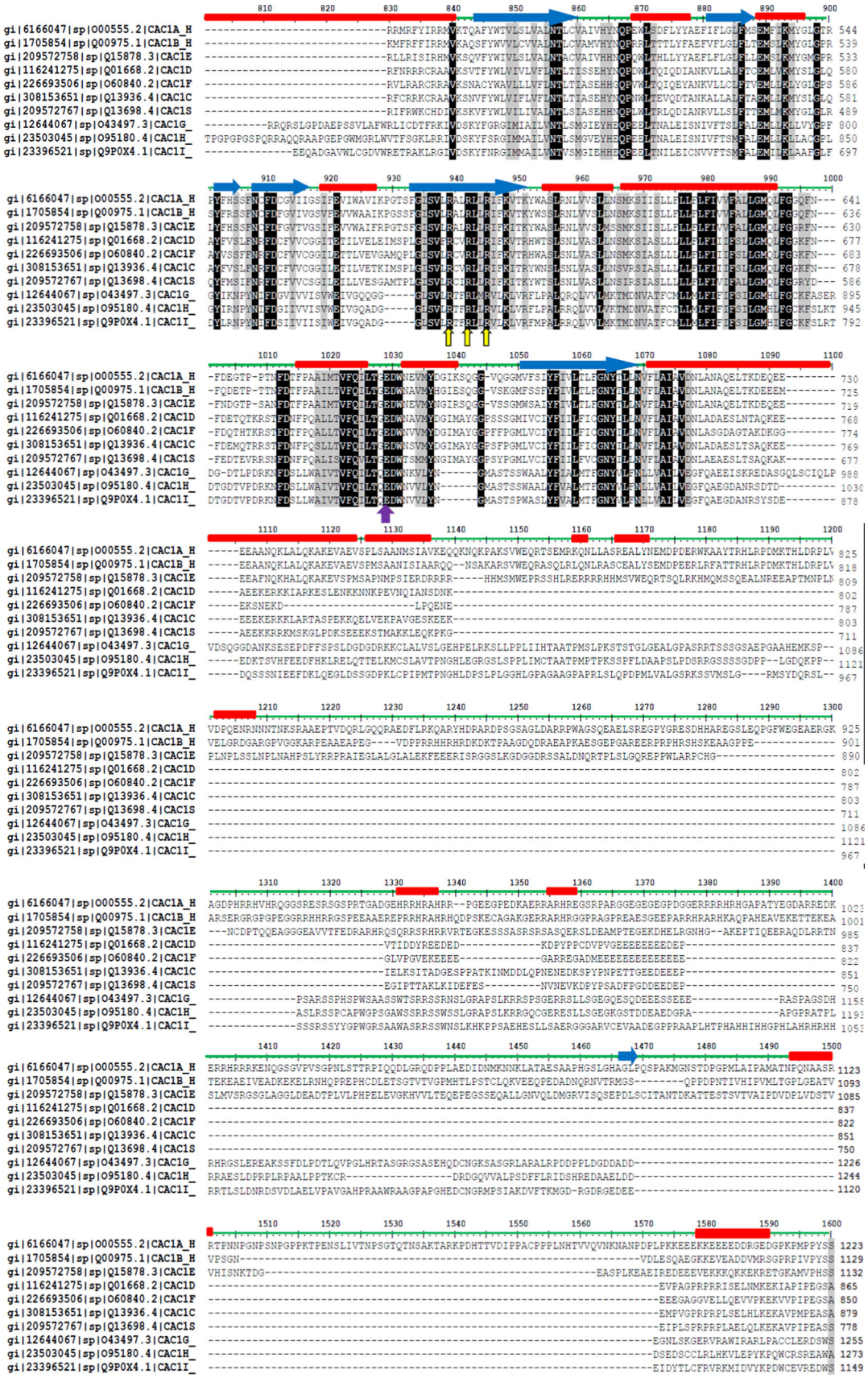


Fig. 3 continued

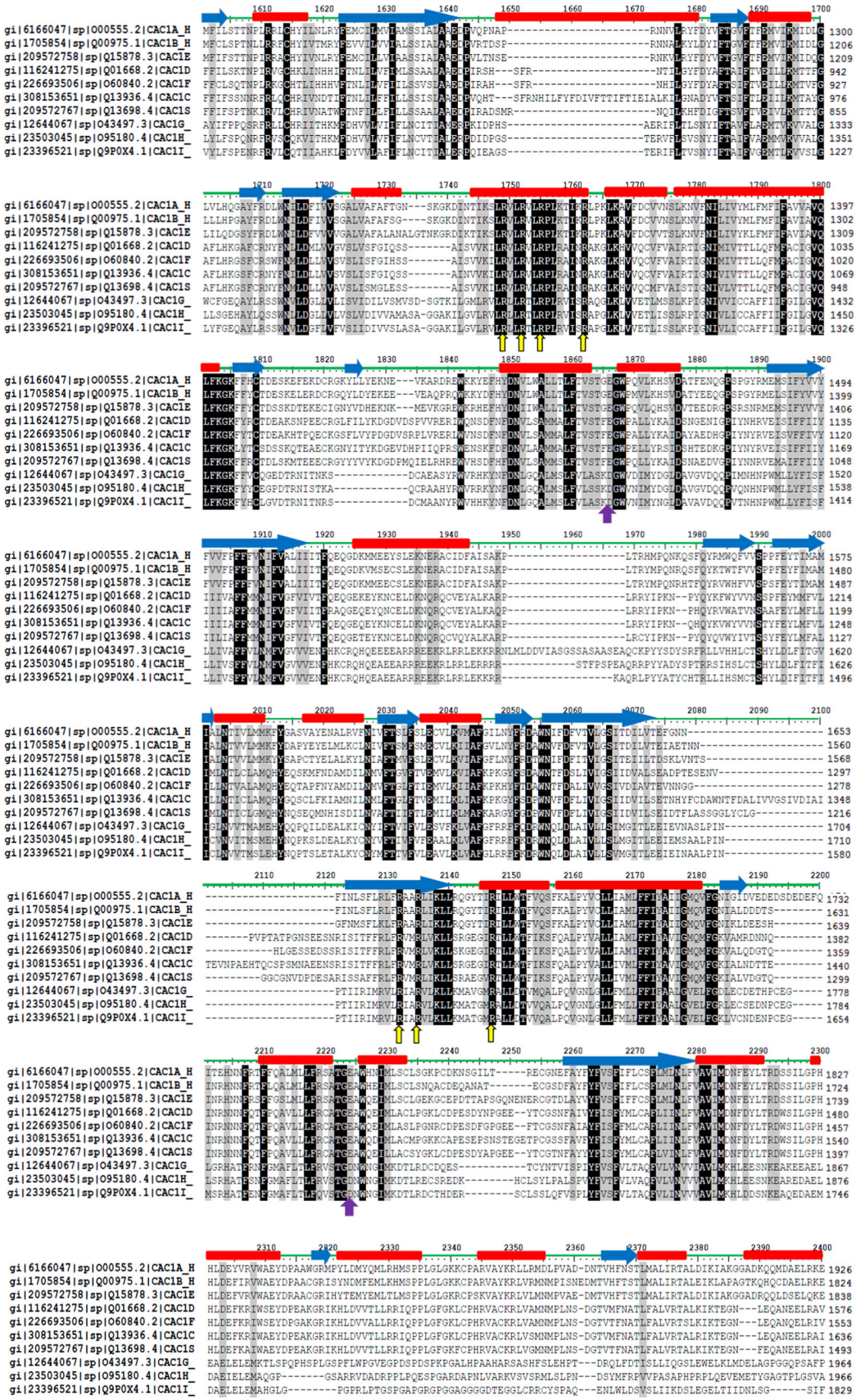


Fig. 3 continued



Fig. 3 continued

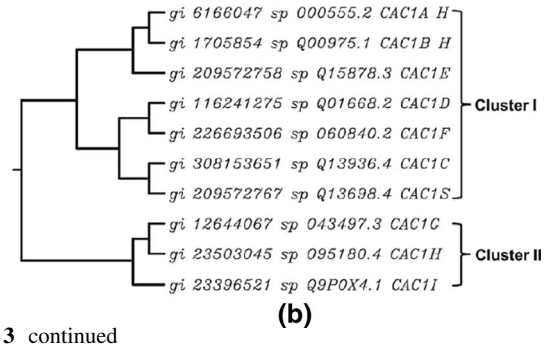


Fig. 3 continued

exhibit, for instance, SeSAME patients are affected with seizures, sensorineural deafness, ataxia, mental retardation, and electrolytic imbalance (hypokalemia, metabolic alkalosis, and hypomagnesaemia, Scholl et al. 2009), whereas EAST patients possess typical symptoms that are epilepsy, ataxia, sensorineural deafness, and tubulopathy (Bockenhauer et al. 2009). Both of them are known to be caused due to mutations in KCNJ10 gene that codes for ATP-sensitive inward rectifier potassium channel 10 (K_{ir} 4.1 channel, Freudenthal et al. 2011). It has been reported that K_{ir} 4.1 channel is expressed in the brain, inner ear, retina, and kidney thereby imparting the functional loss in these organs with mutations. In brain, it contributes potassium buffering for glial cells, controls neuronal excitability, and maintains systemic potassium ion homeostasis, while in kidney it maintains electrolytic balance across distal convoluted tubule (Williams et al. 2010). Multiple mutations in KCNJ10 gene have been reported, which alter inactivation of Kir 4.1 channel via loosing affinity toward channel modulator like PIP2 that results in reduced channel activity with prominent symptoms (Sala-Rabanal et al. 2010). They are lifelong disorders and there is no current treatment that can cure the condition but we can use anti-epileptic medicines to relieve symptoms under the guidance of a nephrologist.

Jervell and Lange-Nielson Syndrome (J-LN)

J-LN is an autosomal recessive most severe variant of long QT syndrome that has been characterized by congenital sensorineural hearing loss and cardiac arrhythmia. It begins in childhood and patient suffers with deafness, recurrent fainting, ventricular arrhythmia and sometimes sudden death (Schwartz et al. 2006). Genetic mutations were reported in KCNQ1 and KCNE1 genes that codes for voltage gated delayed rectifier potassium channel's α and β subunit respectively in J-LN patients which is responsible for potassium ion imbalance in the cochlear hair cells and cardiomyocytes (Chen et al. 1999; Tyson et al. 2000). For normal hearing, a continuous flow of endolymph is required into the cochlear hair cells that are known to maintain the voltage gradient for nerve signal transmission (Lasak et al. 2014), thus mutated channel disrupts the voltage gradient required for transmitting signal through auditory nerves thereby causing deafness. On the other hand, mutated channels in cardiomyocytes exhibit delayed repolarization thereby causing prolonged QT wave responsible for cardiac arrhythmia (Lehnart et al. 2007). There is no cure for J-LN but as a relieving therapy beta blockers are being used to keep heartbeat under control with a limited efficacy. Moreover, automatic defibrillator and cochlear implantation techniques are also being used for treating cardiac arrhythmia and hearing loss, respectively, in case medication fails but patients are highly prone to sudden death (Rocha et al. 2013; Broomfield et al. 2012).

Cardiac Arrhythmia

Cardiac arrhythmia is an abnormal heartbeat-related disorder that can be characterized by dizziness, palpitations, syncope, breathlessness, and *angina*. Arrhythmias can be classified on the basis of two factors that are their origin (atria or ventricle) and heart rate where heartbeat might be very slow (bradycardia), very fast (tachycardia), quite early (premature contraction), and quite irregular (fibrillation, Fenton et al. 2008). Voltage-gated ion channels are responsible for the electrical conductivity in the heart and it has been reported that defects in expression and function of ion channels are responsible for certain types of arrhythmias (Kirsch 1999). In most of the studies, KCNE1, KCNE2, KCNH2, KCNQ1, KCNJ2, and SCN5A genetic mutations were identified in the patients suffering from various kinds of cardiac arrhythmia (Schott et al. 1999; Tsuboi and Antzelevitch 2006; Moss et al. 2007; Tsai et al. 2008). These genetic mutations are responsible for altering the inward rectifying voltage-gated potassium channel and voltage-gated sodium channel, respectively, that leads to various phenotypic consequences of these mutations like Brugada syndrome (BrS, a form of idiopathic ventricular fibrillation), Lev-Lenegre syndrome (familial progressive conduction disease), Long QT syndrome (LQTS), Short QT syndrome (SQTS), and Familial atrial fibrillation (AF) (Campuzano et al. 2010). There are three mechanisms that have been proposed by different research groups for explaining the pathogenesis of cardiac arrhythmias (Gaztanaga et al. 2012) that are (i) Automaticity, where enhanced or suppressed firing of impulse takes place by cardiac muscle cells (Weller and Noone 1989), (ii) triggered activity, which involves impulse initiation due to the membrane potential oscillations occurring just after an action potential that results in abnormal transmission of electrical impulse in the heart cell thereby causing aberrant cardiac rhythm. This mechanism has been widely accepted

Table 4 Chloride ion channel subtypes in association with various diseases

Channel name	Subtypes	Genes encoding subtypes	Tissue specificity	Sub cellular location	Subunit structure	Physiological role	Involvement in disease	References
Chloride (Cl_v) Channel	Cl_vC1	CLCN1	Predominantly expressed in Skeletal Muscles	Multi-pass membrane protein	ClvC Type -1. Homodimer. Each monomer consist of 18 helical segments,	Membrane potential stabilization, Signal Transduction and Transepithelial Transport	Autosomal Recessive Myotonia Congenita	Koch et al. (1992), George et al. (1993), Lorenz et al. (1994)
	Cl_vC2	CLCN2	Skeletal Muscle	Multi-pass membrane protein	ClvC Type -2. Homodimer. Each monomer consist of 18 helical segments,	Homeostasis in various Cells	Susceptibility to Epilepsy, Idiopathic generalized, Myoclonic Jerks	Saint-Martin et al. (2009), Lamb et al. (1999), Jeworutzki et al. (2012)
	Cl_vC3	CLCN3	Coronary Vascular Smooth Muscle Cells and Expressed at a Low level in Aortic Endothelial Cells	Multi-pass membrane protein	ClvC Type -3, Homo- or heterodimer. Each monomer consist of 18 helical segments,	Neuronal cells to establish short-term Memory, Myoclonic Jerks	Juvenile absence Epilepsy Type 2, Idiopathic generalized Epilepsy	Cid et al. (1995), Lamb et al. (1999)
	Cl_vC6	CLCN6	Testis, Ovary, Small intestine, Brain, and Skeletal Muscle.	Endosome membrane	–	Antiporter and Contributes to the Acidification of the Lysosome Lumen	Lysosomal storage disease	Ota et al. (2004), Brandt and Jentsch (1995), Eggermont et al. (1997) Lamb et al. (1999), Ignoul et al. (2007), Poet et al. (2006)
	Cl_vC7	CLCN7	Brain, Testis, Muscle, and Kidney.	Lysosome membrane, Multi-pass membrane protein	ClvC Type -7. Heteromers of α-(CLCN7) and β-(OSTM1)subunits.	Antiporter and Contributes to the Acidification of the Lysosome Lumen	Infantile Malignant, Osteopetrosis Type 2, Albers-Schonberg, Disease or Marble Disease	Schroeder et al. (2007), Graves et al. (2008), Leisle et al. (2011) Kornak et al. (2001)
	$Cl_{Ca}1$	CLCA1	Small Intestine, Colon, Goblet Cells Testis, and Kidney	Localized to Microvilli, Basal Crypt Epithelia, Peripheral membrane protein, Extracellular side	–	Goblet cell, Metaplasia, Mucus Hyper secretion, Cystic Fibrosis, and AHR	Biomarker in Chronic Asthma., Chronic Obstructive Pulmonary Disease	Gruber et al. (1998), Bustin et al. (2001), Hoshino et al. (2002), Toda et al. (2002), Lee et al. (2005), Gibson et al. (2005)
	$Cl_{Ca}2$	CLCA2	Epithelium including Cornea, Esophagus, Larynx,	Single-pass type I membrane protein. Basal cell membrane, Single-pass type I membrane protein	–	May act as a Tumor suppressor in Breast and Colorectal Cancer, Cell Adhesion	Leukemia, Breast Tumor Suppressor Gene	Gruber et al. (1999), Bustin et al. (2001), Abdel-Ghany et al. (2001), Connon et al. (2005), Connon et al. (2006)

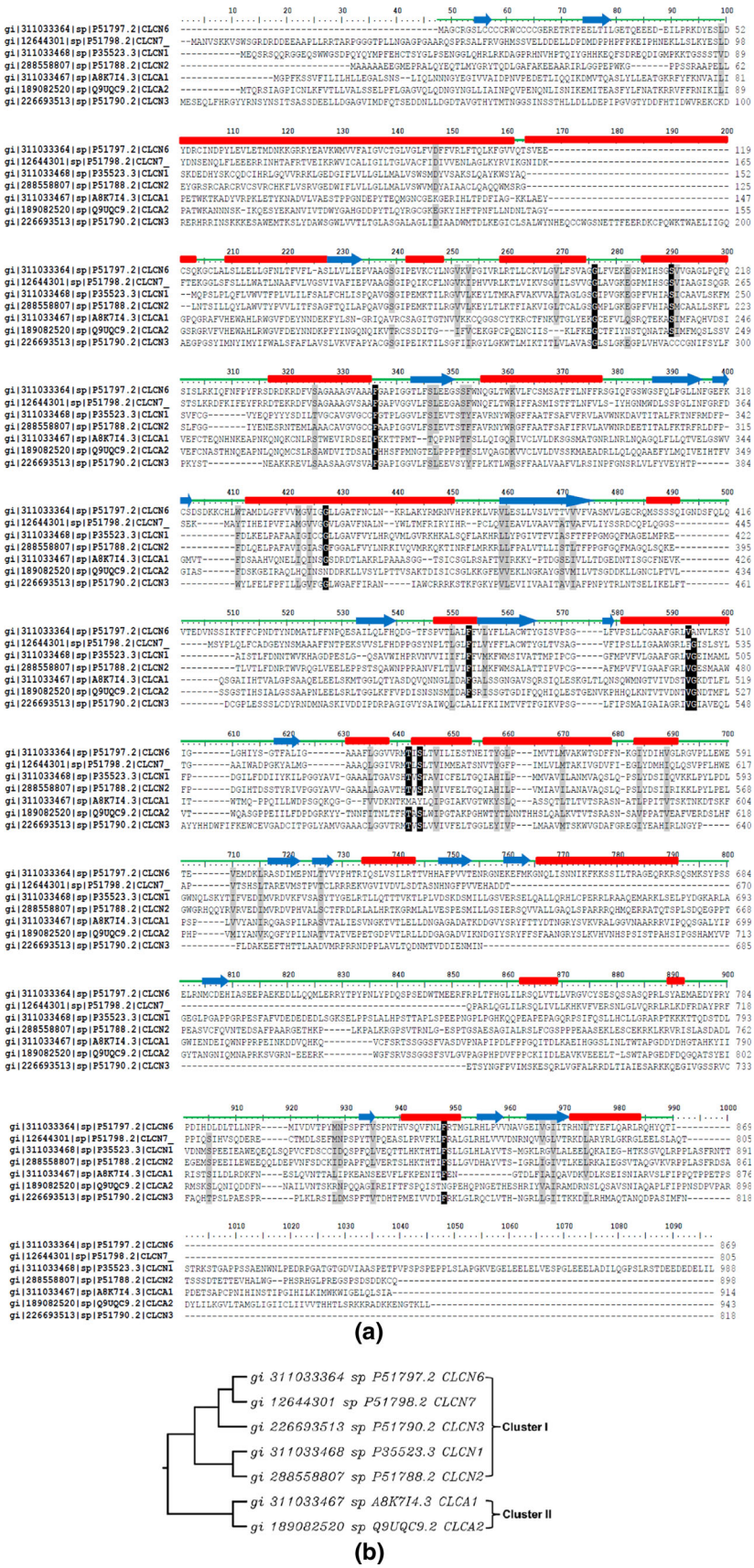
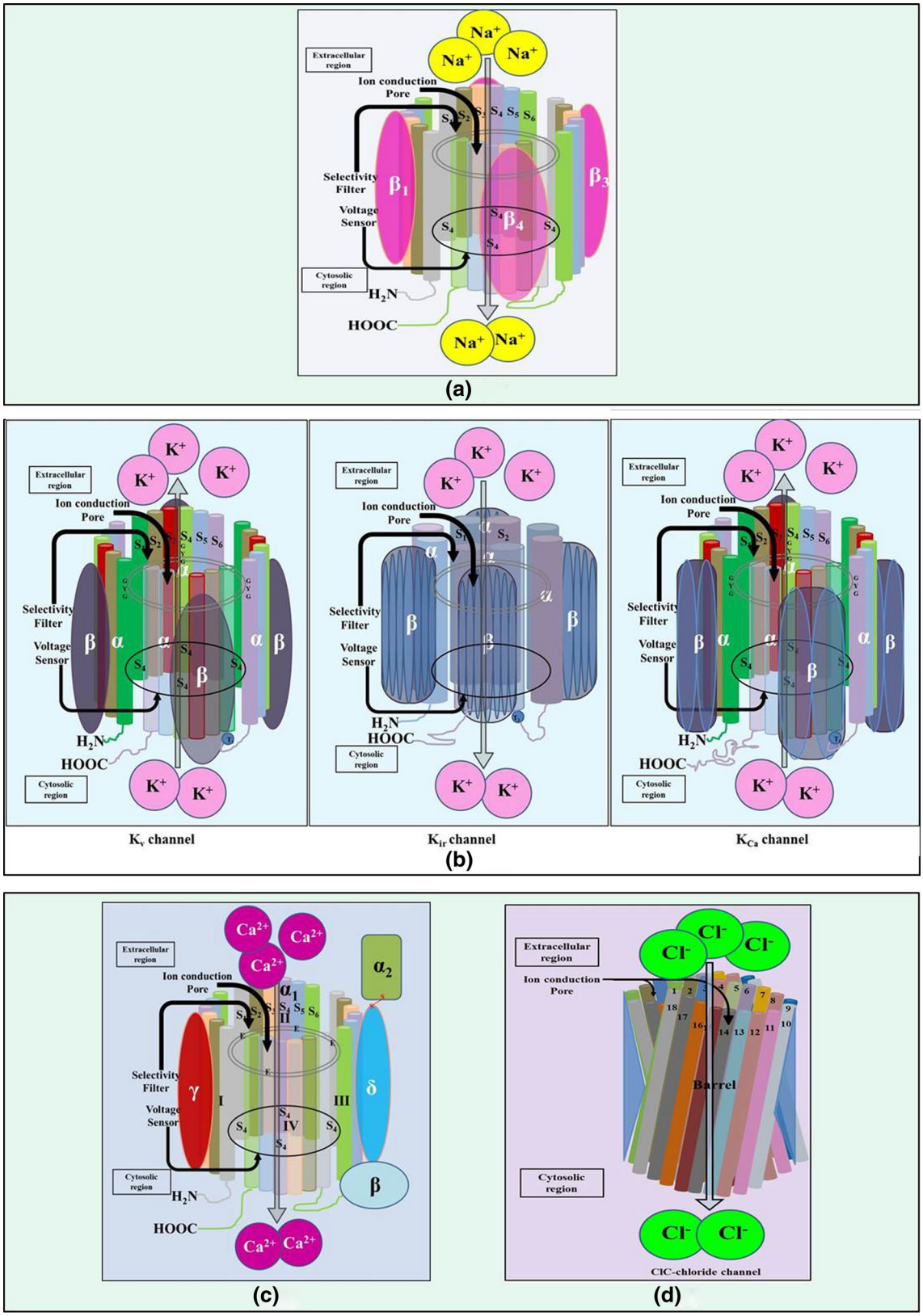


Fig. 4 **a** Multiple sequence alignment of chloride channel subtypes: Highly conserved residues are highlighted in *black,* whereas less conserved residues are highlighted in *light gray* color. Moreover, secondary structure elements of CLCN6 (predicted by YASPIN) are shown on the top of amino acid sequences that are loop residues (*green line*), α-helices (*red rectangle*), and β-strands (*blue arrow*). **b** Phylogenetic tree obtained by UPGMA method using clustalW: There are two major clusters having three pair of subtypes that are closely related, CLCN6–CLCN7, CLCN1–CLCN2, and CLCA1–CLCA2 (Color figure online)


Extracellular region
Ion conduction Pore
Selectivity Filter
Voltage Sensor
Cytosolic region
Na^+
H_2N
HOOC
β_1
β_3
β_4
(a)
K^+
K_v channel
K_{ir} channel
K_{Ca} channel
(b)
Ca^{2+}
α_1
α_2
γ
δ
β
(c)
Cl^-
Barrel
ClC-chloride channel
(d)

◀**Fig. 5** **a** Sodium channel structure: α-subunit of voltage-gated sodium channel comprised tetradomain, where each domain consists of internally repeated transmembrane helical segments (S1–S6) that is associated with four auxiliary β-subunits. **b** Potassium channel structure: α-subunit comprised transmembrane helical segments that is arranged in a tetramer manner and associated with auxiliary β-subunit. **c** Calcium channel structure: In a voltage-gated calcium channel, α1-subunit arranges itself in a tetradomain manner, where each domain consists of six helical transmembrane segments that is associated with other auxiliary subunits α2-δ (disulfide linkage), β, and γ. **d** Chloride channel structure: Voltage-gated chloride channel has double-barrel anti-parallel structure, where each barrel comprised 18 helical transmembrane segments (Color figure online)

to be related with the ion channel mutations (Charpentier et al. 1991), and (iii) Re-entry, it takes place when isolated fibers have not been activated during initial wave of depolarization but get excited before dying of previous impulse which in turn can re-excite those areas which have already recovered from initial depolarization (Zipes 2003). Beta blockers can relieve the symptoms to some extent depending on the severity of arrhythmia.

Calcium Ion Channelopathies with Molecular Mechanism

Spino-Cerebellar Ataxia Type-6 (SCA6)

There are more than 25 types of spino-cerebellar ataxias that are known to affect cerebellum, brainstem, and other parts of central nervous system but among them SCA6 is one of the most common occurring that affects only cerebellum. SCA6 is an autosomal dominant progressively degenerative pure cerebellar ataxia that is characterized by poor coordination of hands, speech, eye movements, and progressive loss of physical control (Paulson 2009). CACNA1A genetic mutation has been reported (Rajakulendran et al. 2010) where expansion of CAG repeats was found at the 3′ region that generates polyglutamine tract thereby producing abnormally extended α_1-subunit of calcium channel (Ishiguro et al. 2010). These polyglutamine residues have been responsible for abnormal aggregation of calcium channel protein thereby affecting calcium ion transport which imparts toxicity to the neurons, for instance, altered release of neurotransmitters in the brain eventually leads to the neuronal death (Purkinje cells, Kordasiewicz and Gomez 2007). However, very limited clinical trials have been done for disease prevention but a recent study showed the beneficial effect of lithium in treating SCA1 (Watase et al. 2007). Apart from that, acetazolamine can be used to eliminate episodes of ataxia, and RNA antisense approach can also be tried to decrease the expression of mutant gene product (Xia et al. 2004).

Hypokalemic Periodic Paralysis (HypoPP)

Hypokalemic periodic paralysis is an autosomal dominant paralytic disorder that can be characterized by recurrent attacks of extreme muscle weakness associated with low potassium levels in serum. In general, the attacks last for several hours but sometimes it lasts for several days that can be precipitated by a variety of factors, for instance, sodium-rich food, carbohydrate load, cold temperature, infection, stress, anesthesia, and rest after exercise (Sternberg et al. 2002). Major impact (up to 60 %) in the pathogenesis of Hypo PP is contributed by CACNA1S genetic mutations that can be followed by mutations in SCN4A and KCNE3 gene (Jurkat-Rott et al. 1994; Abbott et al. 2001; Sternberg et al. 2001; Matthews et al. 2009). Most of the underlying mutations in sodium channel were reported to nullify the outermost positively charged arginine or lysine residues of a voltage sensor, for instance, multiple mutations in $Na_v1.4$ channel were present in the voltage sensor region (S4) of domain I, II, and III (Jurkat-Rott et al. 2000).The homologous location of S4 missense mutations in $Ca_v1.1$ channel associated with HypoPP has led to the conclusion that abnormal gating pore current is the common underlying mechanism of mutated sodium and calcium channel for the progression of HypoPP (Wu et al. 2012). However, the known mutations affect the voltage sensing capability of these channels which are responsible for the deregulated flow of Ca^{2+} and Na^{+} ions into the muscles that cause reduced contractibility of muscles and ultimately muscle weakness (Sokolov et al. 2007). However, it is quite difficult to treat HypoPP but we can prevent the attacks by regulating sodium and potassium intake. Moreover, acetazolamide has been found to be very effective in preventing paralytic attacks among 50 % of the cases (Matthews et al. 2011).

Episodic Ataxia (EA)

Episodic ataxia is a group of related autosomal dominant disorders that have been characterized by episodes of impaired, uncoordinated bodily movements that can eventually cause muscle stiffness and cramps (Jen et al. 2007). These symptoms generally begin in adolescence and period of attacks usually last from hours to days depending on its severity. EA has been classified into seven types i.e., EA-1 to EA-7 based on their various characteristics which include sign, symptoms, attacking period, and onset age, moreover, out of these seven types only episodic ataxia type 2 and 5 are known to be associated with calcium channel mutations. It has been reported that KCNA1, CACNA1A, CACNB4, and SLC1A3 genetic mutations are responsible for the occurrence of episodic ataxia type 1, 2, 5, and 6, respectively, while genetic cause for EA-3,4, and

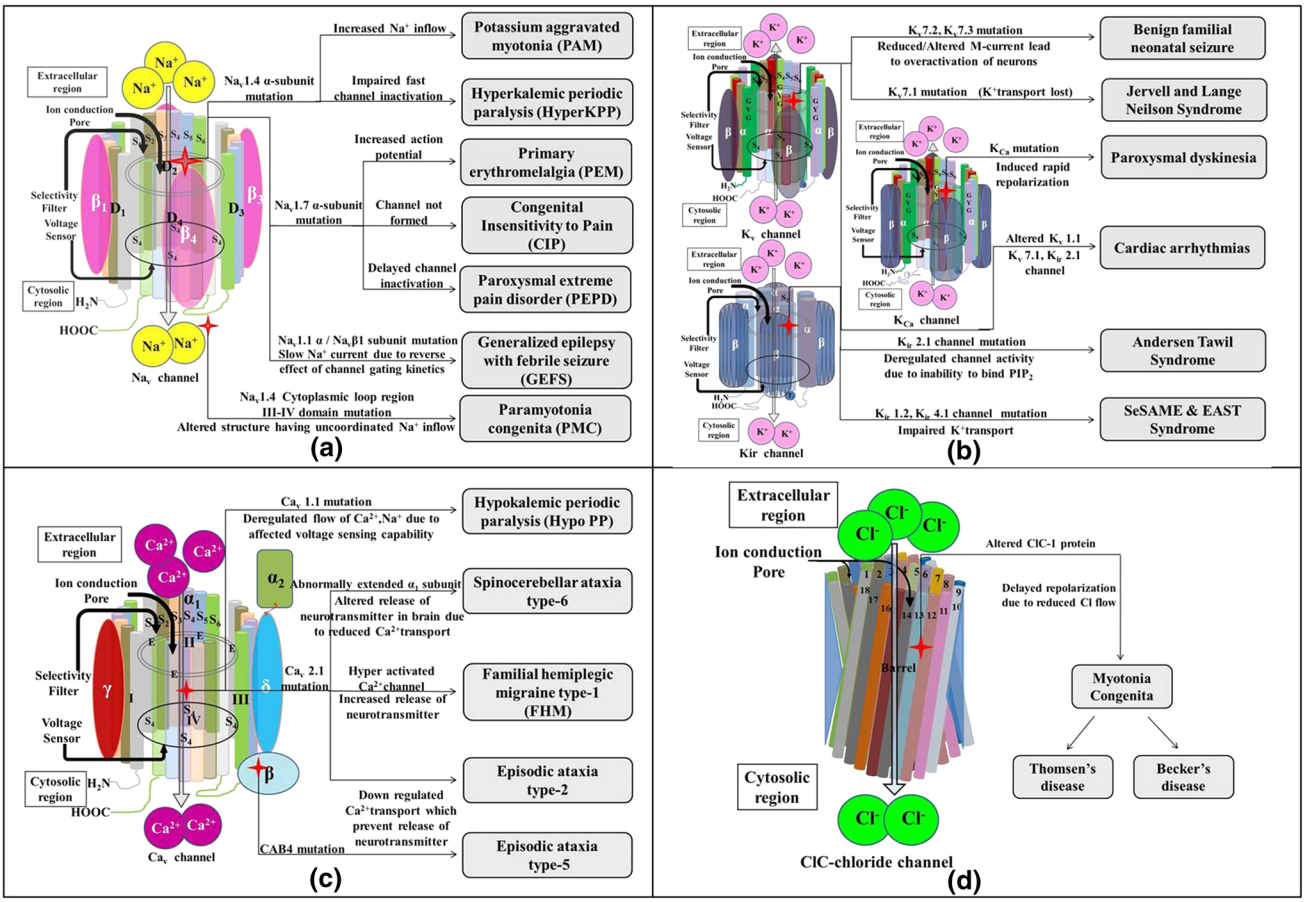


Fig. 6 **a** Sodium ion channelopathies: Mutated $Na_v1.4$ alpha subunit has lead to Potassium-aggravated myotonia (PAM) and Hyperkalemic periodic paralysis, while mutations in $Na_v1.7$ alpha subunit have caused Primary erythromelalgia (PEM), congenital insensitivity to pain (CIP), and Paroxysmal extreme pain disorder (PEPD). Moreover, $Na_v1.1$ alpha and Na_v beta subunit mutations known to cause Generalized epilepsy with febrile seizure, whereas $Na_v1.4$ cytoplasmic loop mutations between domain III and IV have caused Paramyotonia congenita (PMC). **b** Potassium ion channelopathies: Mutated $K_v7.2$ and 7.3 channels resulted in benign familial neonatal seizure, and mutated K_v 7.1 channel leads to Jervell and Lange Nielsen syndrome. Moreover, K_{ca} channel mutation is responsible for Paroxysmal dyskinesia and altered K_v 1.1, K_v 7.1 and K_{ir} 2.1 channel cause Cardiac arrhythmias. Apart from this K_{ir} 2.1 channel mutation leads to Andersen tawil syndrome, while K_{ir} 1.2 and K_{ir} 4.1 channel mutations lead to SeSAME and EAST syndrome. **c** Calcium ion channelopathies: Mutated $Ca_v1.1$ channel is known to cause Hypokalemic periodic paralysis (Hypo PP) and $Ca_v2.1$ channel mutations lead to Spino-cerebellar ataxia type-6, Familial hemiplegic migraine type-1 (FHM-1), and episodic ataxia type-2, while Calcium channel beta subunit CAB4 mutations caused Episodic ataxia type-5. **d** Chloride ion channelopathies: Mutated CLC-1 channel causes Myotonia congenita that can be categorized into Thomsen's and Becker's disease based on symptoms (Color figure online)

7 are still unknown(Adelman et al. 1995; Escayg et al. 2000; Imbrici et al. 2005; Jen et al. 2005). The underlying CACNA1A and CACNB4 genetic mutations have been responsible for down-regulating the Ca^{2+} transport that prevents the release of neurotransmitters into the brain thereby disrupting the signals (Wan et al. 2005). Similarly, decreased transport of K^+ ions due to KCNA1 genetic mutations adds over excitability to the neurons (Maylie et al. 2002), while SLC1A3 genetic mutant glutamate transporter loses its ability to remove glutamate from synaptic region which further provides excitation to the neurons. Thus, altered channels disrupt the normal signaling that triggers episodes of ataxia. The frequency and severity of attacks can be relieved by using anti-epileptic drugs, and carbonic anhydrase inhibitors, for instance, carbamazepine, valproic acid, and acetazolamide, are found to be effective in episodic ataxia type-1 (Eunson et al. 2000; Klein et al. 2004).

Familial Hemiplegic Migraine (FHM)

Familial hemiplegic migraine is an autosomal dominant familial migraine that usually occurs in a particular part of the head preceded by neurological symptoms like double vision, blind spot, or flashing lights (Jen 2001). FHM has been classified into three forms on the basis of clinical or descriptive criteria and can be triggered by emotional stress, certain foods, and minor head injury. It has been

Table 5 Channelopathies associated with various ion channels and their physiology

Tissue affected	Ion channels	Gene	Channel subunit	Disease caused	Symptoms	Mechanism	References
Skeletal muscle	Cl Channel	ClCN1	ClC-1 (chloride channel protein 1)	Myotonia congenita	Muscle stiffness, inability to relax after contraction	Mutated channel either become nonfunctional or open at a more depolarized potential thus losses chloride conductance thereby increasing the time taken for repolarization due to which muscle hyper excitability takes place thus causing myotonia	Lee et al. (2013), Duran et al. (2010), Lossin and George (2008), Koch et al. (1992)
				Thomsen's disease	Proximal muscle weakness, myalgia, and muscular hypertrophy	Mutated channels results in moderate decrease in chloride conduction and following the above-mentioned molecular mechanism it causes mild symptoms	Wu et al. (2002), Kubisch et al. (1998), Koch et al. (1992)
				Becker's disease	Muscle hypertrophy and distal muscle weakness	Mutated channel proteins have not get expressed to the optimum level thereby causing great reduction in chloride conduction and thus causing myotonia by following the above-mentioned mechanism	Graves and Hanna (2005), Wu et al. (2002), (Kubisch et al. (1998)
	Na_v Channel	SCN4A	$Na_v1.4$ (Sodium channel protein type 4 subunit alpha)	Potassium-aggravated myotonia (PAM)	Sustained muscle tension and inability to relax muscle	The altered channels up-regulate the sodium ion influx into the skeletal muscles thereby triggering prolonged muscle contractions due to one or more of the following reasons, for instance, reduced fast channel inactivation, enhanced recovery rate from fast inactivation, slowed deactivation or hyperpolarizing shift in steady-state activation	Orrell et al. (1998) (Cummins and Bendahhou (2009), (Vicart et al. 2005)
				Para-myotonia congenita (PMC)	Cold sensitive myotonia and episodic muscular weakness	Mutated sodium channels exhibit slowed inactivation and faster recovery from inactivation thus causing hyper excitability of muscles (myotonia) and sometimes inexcitability that causes episodic weakness in muscles	Heine et al. (1993), McClatchey et al. (1992), Ptacek et al. (1992), Tamaoka (2003), Vicart et al. 2005)
				Hyper-kalemic periodic paralysis (hyperKPP)	Extreme muscle weakness and increased level of potassium during attacks	Due to altered anchoring site of fast inactivation particle in mutated channel, persistent sodium current takes place that causes depolarization of the cell thereby inactivating other normal sodium channels due to the absence of action potential	(Bendahhou et al. 2002) (Ptacek et al. 1991) (Rojas et al. 1991)
	Na_v & Ca_v Channel	SCN4A and CACNA1S	$Na_V1.4$ (Sodium channel protein type 4 subunit alpha) CaV1.1 (Voltage-dependent L-type calcium channel subunit alpha-1S)	Hypo-kalemic periodic paralysis (hypoKPP)	Extreme muscle weakness associated with low potassium level in serum	Mutated sodium and calcium channels are responsible for abnormal gating pore currents i.e., shift in the resting membrane potential to a more depolarized second stable state (paradoxical depolarization). Moreover, due to their affected voltage sensing capability deregulated flow of Ca^{2+} and Na^{+} ions into the muscles take place thereby causing reduced contractibility of muscles and ultimately muscle weakness	(Sokolov et al. 2010) (Jurkat-Rott et al. 2009) (Sokolov et al. 2007) (Bulman et al. 1999) (Jurkat-Rott et al. 1994) (Ptacek et al. 1994)

Table 5 continued

Tissue affected	Ion channels	Gene	Channel subunit	Disease caused	Symptoms	Mechanism	References
Peripheral Nerve	Na_v Channel	SCN9A	$Na_v1.7$ (Sodium channel protein type 9 subunit alpha)	Primary erythro-melalgia	Burning pain, flushing, and swelling of the feet, hands, and sometimes other areas	Mutated sodium channels exhibit hyperpolarizing shift toward activation and slowed inactivation kinetics that makes opening of channel easier and prolonged. Thus increased inflow of sodium ions enhances transmission of pain signals, leading to the signs and symptoms of erythro-melalgia	(Dib-Hajj et al. 2005) (Waxman et al. 2005a & b) (Estacion et al. 2011)
				Paroxysmal extreme pain disorder (PEPD)	Burning pain and flushing in the submandibular, ocular, and rectal areas	Mutated sodium channels that expressed in nociceptive dorsal root ganglion and sympathetic ganglion neurons cannot be able to close as quickly as usual leading to prolonged transmission of pain signals. Moreover, we can say that gain of function mutations result in increased action potential duration and therefore more synaptic transmission thus causing heightened pain perception	(Fertleman et al. 2007) (Lampert et al. 2010)
				Congenital insensitivity to pain (CIP)	Complete loss of pain sensation	Mutated channel exhibit complete functional loss that leads to an inability to form action potentials and therefore loss of pain sensation	(Cox et al. 2006) (Goldberg et al. 2007)
Central Nervous System	K_v, Ca_v, Channel, and Glutamate transporter	KCNA1, CACNA1A CACNB4 SLC1A3	$K_v1.1$ (Potassium channel subfamily A member 1) Cav2.1 (Calcium channel Subunit alpha), Sodium-dependent glutamate/ aspartate transporter1	Episodic ataxias	Problems with movements, poor coordination and balance	These genes alter the transport of ions and glutamate into the brain that causes certain neurons to become overexcited and disrupts normal communication between these cells. Moreover, it also results in decreased current often due to protein instability. Furthermore, potassium channels are vital in down stroke of action potential and its mutation cause prolonged action potential and altered excitability of different neuronal population	(Jen et al. 2007) (Wan et al. 2005) (Browne et al. 1994) (Zerr et al. 1998)
	K_v Channel	KCNMA1	K_{ca} (Potassium large conductance calcium-activated channel, subfamily M, alpha member 1)	Paroxysmal dyskinesias	Sudden, unpredictable disabling attacks of involuntary movements	Mutated channels formed due to altered KCNMA1 gene promotes excitability of neurons by inducing rapid repolarization of action potential that allows neurons to conduct at a faster rate thereby causing recurrent attacks	(Lee and Cui 2009) (Du et al. 2005)
		KCNQ2 KCNQ3	$K_v7.2$ & $K_v7.3$ (Potassium voltage-gated channel subfamily KQT member 2 & 3)	Benign familial neonatal seizures (BFNS)	Recurrent seizures in newborn babies, muscle rigidity, convulsions, and loss of consciousness	Channels coded by KCNQ2 and KCNQ3 genes transmit M-currents that ensure normal shutting of active neuron, while mutated genes result in reduced or altered M-current which cause excessive excitability of neurons that results in the development of seizures in brain	(Biervert et al,1998) (Singh et al. 1998) (Charlier et al. 1998) (Castaldo et al. 2002)
	Na_v Channel	SCN1A SCN1B	$Na_V1.1$ (Sodium channel type 1 subunit alpha)	Generalized epilepsy with febrile seizures (GEFS)	It is characterized by a long term recurring seizures.	However, it arises from many causes that include metabolic brain disorders, abnormalities of cortical development, brain trauma or structural lesions of the brain (brain tumors), while mutated channel is also one of the prominent factor that causes over excitation of neurons and ultimately epilepsy with seizures	(Catterall et al. 2010) (Tan et al. 2012) (Xu et al. 2012)

Table 5 continued

Tissue affected	Ion channels	Gene	Channel subunit	Disease caused	Symptoms	Mechanism	References
	Ca_v & Na_v Channels	CACNA1A ATP1A2 SCN1A	Ca_v2.1 (Calcium channel Subunit alpha) ATP1A2 (ATPase subunit alpha-2) Na_V1.1 (Sodium channel type 1 subunit alpha)	Familial hemiplegic migraine (FHM)	Intense, throbbing pain in one area of the head, often accompanied by nausea, vomiting, and extreme sensitivity to light and sound.	Altered channels formed by these mutated genes disrupt the normal release and re-uptake of certain neurotransmitters in brain that result in the alteration of signaling between neurons thereby causing hemiplegic migraine. Moreover, these mutated genes cause three different types of Familial hemiplegic migraine that are CACNA1A mutations cause FHM1, ATP1A2 mutations cause FHM2 and SCN1A mutations cause FHM3	(Pietrobon 2010), (Cestele et al. 2008) (Gritz and Radcliffe 2013) (Pelzer et al. 2013) (Ducros et al. 2001)
	Ca_v Channel	CACNA1A	Ca_v2.1 (Calcium channel Subunit alpha)	Spino-cerebellar ataxia type-6 (SCA6)	Progressive pure cerebellar ataxia, poor coordination of hands, speech, and eye movements, Impaired speech, Patient progressively lose physical control	Expansion of CAG repeats were found at the 3′ region that generates polyglutamine tract thereby producing abnormally extended α1-subunit of calcium channel that abnormally aggregate calcium channel protein thereby affecting neurotransmitter's release in the brain eventually causing death of neurons	(Graves and Hanna, 2005) (Denier et al. 1999) (Rajakulendran et al. 2010) (Zhuchenko et al. 1997)
Heart	K_v and Na_v Channels	KCNE1 KCNE2 KCNH2 KCNQ1 KCNJ2 SCN5A	K_v (Voltage-gated potassium channel subfamily E member 1 &2, subfamily H member 2, subfamily Q member 1, subfamily J member 2), Na_v (Sodium channel protein type 5 subunit alpha)	Cardiac arrhythmia	Dizziness, palpitations, syncope, deficits in executive function and abstract reasoning, even cause death	Irregularities in heart rhythm via mutated channel is reported due to triggered activity, which involves impulse initiation due to the membrane potential oscillations occurring just after an action potential that results in abnormal transmission of electrical impulse in the heart cell thereby causing aberrant cardiac rhythm	(Schimpf et al. 2013) (Campuzano et al. 2010)
	Inward Rectifier Potassium (Kir) Channel	KCNJ2	Kir2.1 (Inwardly rectifying potassium channel subfamily J member 2)	Andersen-Tawil syndrome (ATS)	Muscle weakness (periodic paralysis), changes in heart rhythm (arrhythmia), and developmental abnormalities like widespread eyes, cleft palate, and syndactyly of the toes.	Mutations in the KCNJ2 gene alter the usual structure and function of potassium channels that prevent the channels from being inserted correctly into the cell membrane. Moreover, it also prevent binding of PIP2 that disrupt the flow of potassium ions in skeletal and cardiac muscles thus leading to periodic paralysis and irregular heart rhythm	(Plaster et al. 2001) (Tristani-Firouzi et al. 2010) (Donaldson et al. 2004) (Tristani-Firouzi et al. 2002)
		KCNJ10	Kir4.1 (ATP dependent inwardly rectifying potassium channel Kir4.1)	SeSAME syndrome and EAST syndrome	Characterized by generalized seizures with onset in infancy, delayed psychomotor development, ataxia, sensorineural hearing loss, hypokalemia, metabolic alkalosis, and hypomagnesaemia.	Mutated inward rectifier potassium channel disrupts the potassium buffering action of glial cells in the brain and disturbs the homeostasis of potassium ions in various organs like inner ear, retina, and kidney thus exhibiting the symptoms of SeSAME	Bockenhauer et al. 2009) (Scholl et al. 2009)
	K_v Channel	KCNE1 & KCNQ1	K_v (Potassium voltage-gated channel subfamily E member 1,subfamily Q member1)	Jervell and Lange-Nielson syndrome (J-LN)	Cardiac arrhythmia concomitant with deafness	Mutated genes affect potassium channel structure and function thereby preventing the assembly of normal channels. These changes disrupt the flow of potassium ions in the inner ear and in cardiac muscle, leading to hearing loss and an irregular heart rhythm	Schulze-Bahr et al. (1997), Schwartz et al. (2006,) (Wang et al. 2002)

reported that mutations in CACNA1A, ATP1A2, and SCN1A genes are the prevalent causes for FHM type-1, FHM type-2, and FHM type-3, respectively (Ophoff et al. 1996; De Fusco et al. 2003; Dichgans et al. 2005a). Mutated CNCNA1A gene that encodes $Ca_v2.1$ channel gets activated more easily than usual thereby leading to more influx of Ca^{2+} ions which in turn promotes excessive release of neurotransmitters which impart strong signals for severe headache and lead to FHM type-1 (Dichgans et al. 2005b). While in case of FHM type-2, mutated ATP1A2 gene forms either altered or truncated Na^+/K^+ ATPase protein that prevents the flow of K^+ ions out of the neurons thereby causing sustained release of neurotransmitters at the neuronal junction and thus prolongs excitation of pain signals (De Fusco et al. 2003). Moreover, altered $Na_v1.1$ channel encoded by mutated SCN1A gene has also reported to exacerbate headache in a similar fashion as was in case of mutated calcium channel. Thus, resulted mutations in these genes cause FHM due to increased release of neurotransmitters in response to imbalanced ion flow (Pietrobon 2007). Treatment of hemiplegic migraine is quite challenging but apart from anecdotal, verapamil and acetazolamide have shown significant effect in treating FHM (Black 2006).

Chloride Ion Channelopathies with Molecular Mechanism

Myotonia Congenita

Myotonia congenita is a congenital myopathy that can be characterized by muscle stiffness and their inability to relax after contraction which affects the bodily movements. The myotonic attacks may last from seconds to minutes depending on the severity of disease that could range from slightly uncomfortable to complete disability. Cold, sudden pitched sound can trigger the attacks and can affect various body parts, for instance, hands, legs, shoulders, hips, face, feet, tongue, and eyelids (Colding-Jorgensen 2005). Myotonia congenita can be classified into two forms of congenital myopathy based on the inheritance pattern and severity of symptoms, for instance, Thomsen's diseases and Becker's disease have been inherited in an autosomal dominant and autosomal recessive pattern, respectively. It has been reported that mutations in the same ClCN1 gene have been responsible for the occurrence of both Thomsen's and Becker's disease (Zhang et al. 1996; Sun et al. 2001; Pusch 2002). Mutated ClCN1 gene disrupts ClC-1 chloride channel thereby interrupting the normal process of repolarization. Electrophysiological studies in a recessive CLCN1 patient suggested that prolonged repolarization takes place due to reduced inflow of chloride ions into the skeletal muscles thereby causing prolonged muscle contraction in the myotonial patients (Lucchiari et al. 2013). No perfect cure has been reported till now but patients usually learn to adopt preventive measures and can use medicines, for instance, mexiletine, quinine, procanimide, tegretol, and phenytoin to relieve the symptoms (Fazio 1988; Trip et al. 2006).

Thomsen's Disease

It is an autosomal dominant muscle disorder characterized by muscle stiffness and relaxation inability after contraction (Sun et al. 2001). It was first identified by Thomsen in his own family and he himself was also suffering from the same thus named as Thomsen's disease. It exhibits the above-mentioned symptoms but with less severity than Becker's disease with carbamazepine as a potential drug used for relieving against Thomsen's disease (Lyons et al. 2010; Savitha et al. 2006).

Becker's Disease

It is a more common and severe form of myotonia congenita with autosomal recessive pattern of inheritance (Harper and Johnston 1972) that follow the above-mentioned molecular mechanism. Along with the later onset, most of the affected persons feel transient muscle weakness during muscle exertion or after rest and have been encountered by the muscular hypertrophy especially in the region of legs and buttocks, while symptoms can be relieved with the use of sodium channel blocker (Kuhn 1993).

The above-discussed diseases have been defined at either molecular or genetic levels (Fig. 6) that include mutations in the ion channel present in the tissues such as skeletal muscle, brain, and heart (Koopmann et al. 2009) that have been summarized in Table 5. However, disease phenotypes are directly related to the extent of functional deficit in ion channels.

Conclusions

Neurological channelopathies are responsible for a variety of disorders which are threatening to the patient's healthy life. They exhibit three common characteristics that are (i) paroxysmal (i.e., Episodes of impaired neurological function separated by periods of normality), (ii) Triggered by environmental factors, and (iii) tend to share common natural history. Channelopathies must have both a specific molecular lesion (mutation) and inter-current triggering

factor(s) to manifest symptoms. Targeting of these mutated channel protein with drugs became a modern therapeutic approach, and acetazolamide is one of the potential candidate which has been used for treating a variety of channelopathies with promising effects. Scientists have also observed that even synonymous mutations in non-coding regions may lead to dys-functioning of ion channels via altering the process of transcription, splicing, mRNA transport, and translation which is responsible for the occurrence of disease (Goymer 2007). These ion channels differ majorly in their structural and functional aspects. The most diverse type of ion channel is Potassium ion channel (Voltage gated, Inward rectifier, and Calcium mediated) ranging from K_v1–K_v12 gene family. The most complex type of ion channel is Calcium ion channel which consists of α_1-, α_2-δ-, β-, Υ-subunits, whereas least studied ion channel is Chloride ion channel. Apart from their diversity, it has been found that these channels possess highly conserved arginine residues which are responsible for providing voltage sensitivity to the channel, another interesting point is there conserved selectivity filter through diverse subtypes. Sodium channel remained most conserved during evolution in comparison to other channels while due to least study on chloride channel it is difficult to find conserved regions. Mutations in these channels are responsible for various diseases like sodium channelopathies range from muscular disorders to pain disorder (PAM, PEM, Hyper-KPP, CIP, PEPD, GEFS, and PMC), whereas potassium channelopathies range from movement, muscular to heart disorders (Cardiac arrhythmia, ATS, SeSAME & EAST, Paroxysmal dyskinesias, and BFNS). Moreover, calcium channelopathies ranges from muscular disorder to migraine (Hypo-PP, SCA6, FHM1, and EA-2, 5), and chloride channel is likely to cause muscular disorder (Myotonia congenita). Chloride channel is least prone to molecular lesions due to its double-barrel structure. Nowadays molecular lesions are identified with the help of disease loci positional cloning approach. There are still gaps between channelopathies and its cure due to limited knowledge about their mechanisms. Some areas still need to be unraveled for identification and classification of neurological disorders into channelopathies, because there might be possible correlation between ion channel and diseases like Alzheimer's disease, Amyotrophic lateral sclerosis with Calcium channel, Inward rectifier potassium and sodium channel, Huntington's disease with Sodium, Potassium and Chloride ion channel while Parkinson's disease with Calcium, Sodium, and Potassium channel.

Acknowledgments We would like to thanks the senior management of Delhi Technological University for constant support and encouragement. There is no conflict or competing interest declared by authors.

References

Abbott GW, Butler MH, Bendahhou S, Dalakas MC, Ptacek LJ, Goldstein SA (2001) MiRP2 forms potassium channels in skeletal muscle with Kv3.4 and is associated with periodic paralysis. Cell 104(2):217–231

Abdel-Ghany M, Cheng HC, Elble RC, Pauli BU (2001) The breast cancer beta 4 integrin and endothelial human CLCA2 mediate lung metastasis. J Biol Chem 276(27):25438–25446

Adelman JP, Bond CT, Pessia M, Mayliet J (1995) Episodic ataxia results from voltage-dependent potassium channels with altered functions. Neuron 15(6):1449–1454

Anyukhovsky EP, Sosunov EA, Kryukova YN, Prestia K, Ozgen N, Rivaud M, Cohen IS, Robinson RB, Rosen MR (2011) Expression of skeletal muscle sodium channel ($Na_v1.4$) or connexin32 prevents reperfusion arrhythmias in murine heart. Cardiovasc Res 89:41–50

Archer SL, London B, Hampl V, Wu X, Nsair A, Puttagunta L, Hashimoto K, Waite RE, Michelakis ED (2001) Impairment of hypoxic pulmonary vasoconstriction in mice lacking the voltage-gated potassium channel Kv1.5. FASEB J 15(10):1801–1803

Arikkath J, Campbell KP (2003) Auxiliary subunits: essential components of the voltage-gated calcium channel complex. Curr Opin Neurobiol 13(3):298–307

Armstrong CM, Hille B (1998) Voltage-gated ion channels and electrical excitability. Neuron 20(3):371–380

Audenaert D, Claes L, Ceulemans B, Löfgren A, Van Broeckhoven C, De Jonghe P (2003) A deletion in SCN1B is associated with febrile seizures and early-onset absence epilepsy. Neurology 61(6):854–856

Ball SL, Powers PA, Shin HS, Morgans CW, Peachey NS, Gregg RG (2002) Role of the beta(2) subunit of voltage-dependent calcium channels in the retinal outer plexiform layer. Invest Ophthalmol Vis Sci 43:1595–1603

Benatar M (2000) Neurological potassium channelopathies. QJM 93:787–797

Bendahhou S, Cummins TR, Kula RW, Fu YH, Ptácek LJ (2002) Impairment of slow inactivation as a common mechanism for periodic paralysis in DIIS4-S5. Neurology 58(8):1266–1272

Bergsman JB, Wheeler DB, Tsien RW (2000) Classification and function of voltage-gated calcium channels. Pharmacol Ionic Channel Funct Act Inhib 147:55–85

Biervert C, Schroeder BC, Kubisch C, Berkovic SF, Propping P, Jentsch TJ, Steinlein OK (1998) A potassium channel mutation in neonatal human epilepsy. Science 279(5349):403–406

Black DF (2006) Sporadic and familial hemiplegic migraine: diagnosis and treatment. Semin Neurol 26(2):208–216

Black JL, Lennon VA (1999) Identification and cloning of putative human neuronal voltage-gated calcium channel gamma-2 and gamma-3 subunits: neurologic implications. Mayo Clin Proc 74:357–361

Bockenhauer D, Feather S, Stanescu HC, Bandulik S, Zdebik AA, Reichold M, Tobin J, Lieberer E, Sterner C, Landoure G, Arora R, Sirimanna T, Thompson D, Cross JH, van't Hoff W, Al Masri O, Tullus K, Yeung S, Anikster Y, Klootwijk E, Hubank M, Dillon MJ, Heitzmann D, Arcos-Burgos M, Knepper MA, Dobbie A, Gahl WA, Warth R, Sheridan E, Kleta R (2009) Epilepsy, ataxia, sensorineural deafness, tubulopathy, and KCNJ10 mutations. N Engl J Med 360(19):1960–1970

Bocksteins E, Labro AJ, Mayeur E, Bruynsm T, Timmermans JP, Adriaensen D, Snyders DJ (2009) Conserved negative charges in the N-terminal tetramerization domain mediate efficient assembly of Kv2.1 and Kv2.1/Kv6.4 channels. J Biol Chem 284(46):31625–31634

Brandt S, Jentsch TJ (1995) ClC-6 and ClC-7 are two novel broadly expressed members of the CLC chloride channel family. FEBS Lett 377:15–20

Brew HM, Hallows JL, Tempel BL (2003) Hyperexcitability and reduced low threshold potassium currents in auditory neurons of mice lacking the channel subunit Kv1.1. J Physiol 548:1–20

Brodie MJ, Elder AT, Kwan P (2009) Epilepsy in later life. Lancet Neurol 8(11):1019–1030

Broomfield SJ, Bruce IA, Henderson L, Ramsden RT, Green KM (2012) Cochlear implantation in children with Jervell and Lange-Nielsen syndrome—a cautionary tale. Cochlear Implants Int 13(3):168–172

Browne DL, Gancher ST, Nutt JG, Brunt ER, Smith EA, Kramer P, Litt M (1994) Episodic ataxia/myokymia syndrome is associated with point mutations in the human potassium channel gene, KCNA1. Nat Genet 8(2):136–140

Bulman DE, Scoggan KA, van Oene MD, Nicolle MW, Hahn AF, Tollar LL, Ebers GC (1999) A novel sodium channel mutation in a family with hypokalemic periodic paralysis. Neurology 53(9):1932–1936

Bustin SA, Li SR, Dorudi S (2001) Expression of the Ca^{2+}-activated chloride channel genes CLCA1 and CLCA2 is downregulated in human colorectal cancer. DNA Cell Biol 20:331–338

Campbell KP, Leung AT, Sharp AH (1988) The biochemistry and molecular biology of the dihydropyridine-sensitive calcium channel. Trends Neurosci 11(10):425–430

Campuzano O, Beltrán-Alvarez P, Iglesias A, Scornik F, Pérez G, Brugada R (2010) Genetics and cardiac channelopathies. Genet Med 12(5):260–267

Cannon SC, Brown RH, Jr, Corey DP (1991) A sodium channel defect in hyperkalemic periodic paralysis: potassium-induced failure of inactivation. Neuron 6:619–626

Carbone E, Lux HD (1984) A low voltage-activated, fully inactivating Ca channel in vertebrate sensory neurones. Nature 310(5977):501–502

Carmen RV, Argelia MD, Bin Y, Win-Kuang S, Timothy JA, Michael JA, Jonathan CM (2010) Loss-of-function mutation of the SCN3B-encoded sodium channel b3 subunit associated with a case of idiopathic ventricular fibrillation. Cardiovasc Res 86:392–400

Casadei JM, Gordon RD, Barchi RL (1986) Immunoaffinity isolation of Na^+ channels from rat skeletal muscle. Analysis of subunits. J Biol Chem 261:4318–4323

Castaldo P, del Giudice EM, Coppola G, Pascotto A, Annunziato L, Taglialatela M (2002) Benign familial neonatal convulsions caused by altered gating of KCNQ2/KCNQ3 potassium channels. J Neurosci 22(2):RC199

Catterall WA (1988) Molecular properties of voltage-sensitive sodium and calcium channels. Braz J Med Biol Res 21(6):1129–1144

Catterall WA, Curtis BM (1987) Molecular properties of voltage-sensitive calcium channels. Soc Gen Physiol Ser 41:201–213

Catterall WA, Dib-Hajj S, Meisler MH, Pietrobon D (2008) Inherited neuronal ion channelopathies: new windows on complex neurological diseases. J Neurosci 28(46):11768–11777

Catterall WA, Kalume F, Oakley JC (2010) $Na_v1.1$ channels and epilepsy. J Physiol 588(Pt 11):1849–1859

Cestele S, Scalmani P, Rusconi R, Terragni B, Franceschetti S, Mantegazza M (2008) Self-limited hyperexcitability: functional effect of a familial hemiplegic migraine mutation of the $Na_v1.1$ (SCN1A) Na^+ channel. J Neurosci 28(29):7273–7283

Chandy KG, Wulff H, Beeton C, Pennington M, Gutman GA, Cahalan MD (2004) K^+ channels as targets for specific immunomodulation. Trends Pharmacol Sci 25(5):280–289

Chang BS, Lowenstein DH (2003) Epilepsy. N Engl J Med 349(13):1257–1266

Charlier C, Singh NA, Ryan SG, Lewis TB, Reus BE, Leach RJ, Leppert M (1998) A pore mutation in a novel KQT-like potassium channel gene in an idiopathic epilepsy family. Nat Genet 18(1):53–55

Charpentier F, Baudet S, Le Marec H (1991) Triggered activity as a possible mechanism for arrhythmias in ventricular hypertrophy. Pacing Clin Electrophysiol 14(11 Pt 2):1735–1741

Chen H, Piedras-Rentería ES (2007) Altered frequency-dependent inactivation and steady-state inactivation of polyglutamine-expanded alpha1A in SCA6. Am J Physiol Cell Physiol 292(3):C1078–C1086

Chen Q, Zhang D, Gingell RL, Moss AJ, Napolitano C, Priori SG, Schwartz PJ, Kehoe E, Robinson JL, Schulze-Bahr E, Wang Q, Towbin JA (1999) Homozygous deletion in KVLQT1 associated with Jervell and Lange-Nielsen syndrome. Circulation 99(10):1344–1347

Chen RS, Deng TC, Garcia T, Sellers ZM, Best PM (2007) Calcium channel gamma subunits: a functionally diverse protein family. Cell Biochem Biophys 47:178–186

Choi JS, Boralevi F, Brissaud O, Sánchez-Martín J, Te Morsche RH, Dib-Hajj SD, Drenth JP, Waxman SG (2011) Paroxysmal extreme pain disorder: a molecular lesion of peripheral neurons. Nat Rev Neurol 7(1):51–55

Chow A, Erisir A, Farb C, Nadal MS, Ozaita A, Lau D, Welker E, Rudy B (1999) K(+) channel expression distinguishes subpopulations of parvalbumin- and somatostatin-containing neocortical interneuron. J Neurosci 19:9332–9345

Chu PJ, Robertson HM, Best PM (2001) Calcium channel gamma subunits provide insights into the evolution of this gene family. Gene 280:37–48

Chung HJ, Jan YN, Jan LY (2006) Polarized axonal surface expression of neuronal KCNQ channels is mediated by multiple signals in the KCNQ2 and KCNQ3 C-terminal domains. Proc Natl Acad Sci 103(23):8870–8875

Cid LP, Montrose-Rafizadeh C, Smith DI, Guggino WB, Cutting GR (1995) Cloning of a putative human voltage-gated chloride channel (ClC-2) cDNA widely expressed in human tissues. Hum Mol Genet 4:407–413

Cidad P, Jiménez-Pérez L, García-Arribas D, Miguel-Velado E, Tajada S, Ruiz-McDavitt C, López-López JR, Pérez-García MT (2012) Kv1.3 channels can modulate cell proliferation during phenotypic switch by an ion-flux independent mechanism. Arterioscler Thromb Vasc Biol 32(5):1299–1307

Colding-Jorgensen E (2005) Phenotypic variability in myotonia congenita. Muscle Nerve 32(1):19–34

Connon CJ, Kawasaki S, Liles M, Koizumi N, Yamasaki K, Nakamura T, Quantock AJ, Kinoshita S (2006) Gene expression and immunolocalisation of a calcium-activated chloride channel during the stratification of cultivated and developing corneal epithelium. Cell Tissue Res 323:177–182

Connon CJ, Kawasaki S, Yamasaki K, Quantock AJ, Kinoshita S (2005) The quantification of hCLCA2 and colocalisation with integrin beta4 in stratified human epithelia. Acta Histochem 106:421–425

Cox JJ, Reimann F, Nicholas AK, Thornton G, Roberts E, Springell K, Karbani G, Jafri H, Mannan J, Raashid Y, Al-Gazali L, Hamamy H, Valente EM, Gorman S, Williams R, McHale DP, Wood JN, Gribble FM, Woods CG (2006) An SCN9A channelopathy causes congenital inability to experience pain. Nature 444(7121):894–898

Cox JJ, Sheynin J, Shorer Z, Reimann F, Nicholas AK, Zubovic L, Baralle M, Wraige E, Manor E, Levy J, Woods CG, Parvari R (2010) Congenital insensitivity to pain: novel SCN9A missense and in-frame deletion mutations. Hum Mutat 31(9):1670–1686

Cregg R, Laguda B, Werdehausen R, Cox JJ, Linley JE, Ramirez JD, Bodi I, Markiewicz M, Howell KJ, Chen YC, Agnew K,

Houlden H, Lunn MP, Bennett DL, Wood JN, Kinali M (2013) Novel mutations mapping to the fourth sodium channel domain of $Na_v1.7$ result in variable clinical manifestations of primary erythromelalgia. Neuromolecular Med 15(2):265–278

Cummins TR, Bendahhou S (2009) Inherited disorders of skeletal muscle caused by voltage-gated sodium channel mutations. In: Duclohier H (ed) Biophysics of ion channels and diseases, pp 153–176

Cummins TR, Dib-Hajj SD, Waxman SG (2004) Electrophysiological properties of mutant $Na_v1.7$ sodium channels in a painful inherited neuropathy. J Neurosci 24(38):8232–8236

Curtis D, Vine AE, McQuillin A, Bass NJ, Pereira A, Kandaswamy R, Lawrence J, Anjorin A, Choudhury K, Datta SR, Puri V, Krasucki R, Pimm J, Thirumalai S, Quested D, Gurling HM (2011) Case-case genome-wide association analysis shows markers differentially associated with schizophrenia and bipolar disorder and implicates calcium channel genes. Psychiatr Genet 21:1–4

Dabby R (2012) Pain disorders and erythromelalgia caused by voltage-gated sodium channel mutations. Curr Neurol Neurosci Rep 12(1):76–83

Danziger N, Willer JC (2009). [Congenital insensitivity to pain]. Rev Neurol (Paris) 165(2):129–136

De Fusco M, Marconi R, Silvestri L, Atorino L, Rampoldi L, Morgante L, Ballabio A, Aridon P, Casari G (2003) Haploinsufficiency of ATP1A2 encoding the Na^+/K^+ pump alpha2 subunit associated with familial hemiplegic migraine type 2. Nat Genet 33(2):192–196

De Jongh KS, Warner C, Catterall WA (1990) Subunits of purified calcium channels. Alpha 2 and delta are encoded by the same gene. J Biol Chem 265(25):14738–14741

Debanne D, Campanac E, Bialowas A, Carlier E, Alcaraz G (2011) Axon physiology. Physiol Rev 91(2):555–602

Demirkiran M, Jankovic J (1995) Paroxysmal dyskinesias: clinical features and classification. Ann Neurol 38(4):571–579

Denier C, Ducros A, Vahedi K, Joutel A, Thierry P, Ritz A, Castelnovo G, Deonna T, Gérard P, Devoize JL, Gayou A, Perrouty B, Soisson T, Autret A, Warter JM, Vighetto A, Van Bogaert P, Alamowitch S, Roullet E, Tournier-Lasserve E (1999) High prevalence of CACNA1A truncations and broader clinical spectrum in episodic ataxia type 2. Neurology 52(9):1816–1821

Dib-Hajj SD, Cummins TR, Black JA, Waxman SG (2007) From genes to pain: Na v 1.7 and human pain disorders. Trends Neurosci 30(11):555–563

Dib-Hajj SD, Estacion M, Jarecki BW, Tyrrell L, Fisher TZ, Lawden M, Cummins TR, Waxman SG (2008) Paroxysmal extreme pain disorder M1627K mutations in human $Na_v1.7$ renders DRG neurons hyperexcitable. Mol Pain 4:37

Dib-Hajj SD, Rush AM, Cummins TR, Hisama FM, Novella S, Tyrrell L, Marshall L, Waxman SG (2005) Gain-of-function mutation in $Na_v1.7$ in familial erythromelalgia induces bursting of sensory neurons. Brain 128(Pt 8):1847–1854

Dichgans M, Freilinger T, Eckstein G, Babini E, Lorenz-Depiereux B, Biskup S, Ferrari MD, Herzog J, van den Maagdenberg AM, Pusch M, Strom TM (2005a) Mutation in the neuronal voltage-gated sodium channel SCN1A in familial hemiplegic migraine. Lancet 366(9483):371–377

Dichgans M, Herzog J, Freilinger T, Wilke M, Auer DP (2005b) 1H-MRS alterations in the cerebellum of patients with familial hemiplegic migraine type 1. Neurology 64(4):608–613

Donaldson MR, Yoon G, Fu YH, Ptacek LJ (2004) Andersen-Tawil syndrome: a model of clinical variability, pleiotropy, and genetic heterogeneity. Ann Med 36(Suppl 1):92–97

Drenth JP, te Morsche RH, Guillet G, Taieb A, Kirby RL, Jansen JB (2005) SCN9A mutations define primary erythermalgia as a neuropathic disorder of voltage gated sodium channels. J Invest Dermatol 124(6):1333–1338

Du W, Bautista JF, Yang H, Diez-Sampedro A, You SA, Wang L, Kotagal P, Lüders HO, Shi J, Cui J, Richerson GB, Wang QK (2005) Calcium-sensitive potassium channelopathy in human epilepsy and paroxysmal movement disorder. Nat Genet 37(7):733–738

Dube CM, Brewster AL, Barama TZ (2009) Febrile seizures: mechanisms and relationship to epilepsy. Brain Dev 31(5):366–371

Ducros A, Denier C, Joutel A, Cecillon M, Lescoat C, Vahedi K, Darcel F, Vicaut E, Bousser MG, Tournier-Lasserve E (2001) The clinical spectrum of familial hemiplegic migraine associated with mutations in a neuronal calcium channel. N Engl J Med 345(1):17–24

Duran C, Thompson CH, Xiao Q, Hartzell C (2010) Chloride channels: often enigmatic, rarely predictable. Annu Rev Physiol 72:95–121

Dutzler R, Campbell EB, Cadene M, Chait BT, MacKinnon R (2002) X-ray structure of a ClC chloride channel at 3.0 A reveals the molecular basis of anion selectivity. Nature 415(6869):287–294

Dyck PJ, Mellinger JF, Reagan TJ, Horowitz SJ, McDonald JW, Litchy WJ, Daube JR, Fealey RD, Go VL, Kao PC, Brimijoin WS, Lambert EH (1983) Not 'indifference to pain' but varieties of hereditary sensory and autonomic neuropathy. Brain 106(Pt 2):373–390

Eberst R, Dai S, Klugbauer N, Hofmann F (1997) Identification and functional characterization of a calcium channel gamma subunit. Pflugers Arch 433(5):633–637

Eggermont J, Buyse G, Voets T, Tytgat J, De Smedt H, Droogmans G, Nilius B (1997) Alternative splicing of ClC-6 (a member of the ClC chloride-channel family) transcripts generates three truncated isoforms one of which, ClC-6c, is kidney-specific. Biochem J 325:269–276

Escayg A, De Waard M, Lee DD, Bichet D, Wolf P, Mayer T, Johnston J, Baloh R, Sander T, Meisler MH (2000) Coding and noncoding variation of the human calcium-channel beta4-subunit gene CACNB4 in patients with idiopathic generalized epilepsy and episodic ataxia. Am J Hum Genet 66(5):1531–1539

Espinosa F, Torres-Vega MA, Marks GA, Joho RH (2008) Ablation of Kv3.1 and Kv3.3 potassium channels disrupts thalamocortical oscillations in vitro and in vivo. J Neurosci 28(21):5570–5581

Estacion M, Gasser A, Dib-Hajj SD, Waxman SG (2010) A sodium channel mutation linked to epilepsy increases ramp and persistent current of $Na_v1.3$ and induces hyperexcitability in hippocampal neurons. Exp Neurol 224(2):362–368

Estacion M, Han C, Choi JS, Hoeijmakers JG, Lauria G, Drenth JP, Gerrits MM, Dib-Hajj SD, Faber CG, Merkies IS, Waxman SG (2011) Intra- and interfamily phenotypic diversity in pain syndromes associated with a gain-of-function variant of $Na_v1.7$. Mol Pain 7:92

Eunson LH, Rea R, Zuberi SM, Youroukos S, Panayiotopoulos CP, Liguori R, Avoni P, McWilliam RC, Stephenson JB, Hanna MG, Kullmann DM, Spauschus A (2000) Clinical, genetic, and expression studies of mutations in the potassium channel gene KCNA1 reveal new phenotypic variability. Ann Neurol 48(4):647–656

Faber CG, Lauria G, Merkies IS, Cheng X, Han C, Ahn HS, Persson AK, Hoeijmakers JG, Gerrits MM, Pierro T, Lombardi R, Kapetis D, Dib-Hajj SD, Waxman SG (2012) Gain-of-function $Na_v1.8$ mutations in painful neuropathy. Proc Natl Acad Sci USA 109(47):19444–19449

Fazio B (1988) Steinert's myotonic dystrophy. Attempts at therapy. Minerva Med 79(2):137–140

Fedida D, Eldstrom J, Hesketh JC, Lamorgese M, Castel L, Steele DF, van Wagoner DR (2003) Kv1.5 is an important component of

repolarizing K^+ current in canine atrial myocytes. Circ Res 93(8):744–751

Fenton FH, Cherry EM, Glass L (2008) Cardiac arrhythmia. Scholarpedia 3(7):1665

Fertleman CR, Ferrie CD (2006) What's in a name—familial rectal pain syndrome becomes paroxysmal extreme pain disorder. J Neurol Neurosurg Psychiatry 77(11):1294–1295

Fertleman CR, Ferrie CD, Aicardi J, Bednarek NA, Eeg-Olofsson O, Elmslie FV, Griesemer DA, Goutières F, Kirkpatrick M, Malmros IN, Pollitzer M, Rossiter M, Roulet-Perez E, Schubert R, Smith VV, Testard H, Wong V, Stephenson JB (2007) Paroxysmal extreme pain disorder (previously familial rectal pain syndrome). Neurology 69(6):586–595

Finol-Urdaneta RK, Strüver N, Terlau H (2006) Molecular and functional differences between heart mKv1.7 channel isoforms. J Gen Physiol 128(1):133–145

Fischer TZ, Waxman SG (2010) Familial pain syndromes from mutations of the $Na_v1.7$ sodium channel. Ann N Y Acad Sci 1184:196–207

Fontaine B, Khurana TS, Hoffman EP, Bruns GA, Haines JL, Trofatter JA, Hanson MP, Rich J, McFarlane H, Yasek DM et al (1990) Hyperkalemic periodic paralysis and the adult muscle sodium channel alpha-subunit gene. Science 250(4983):1000–1002

Freedman BD, Price MA, Deutsch CJ (1992) Evidence for voltage modulation of IL-2 production in mitogen-stimulated human peripheral blood lymphocytes. J Immunol 149(12):3784–3794

Freudenthal B, Kulaveerasingam D, Lingappa L, Shah MA, Brueton L, Wassmer E, Ognjanovic M, Dorison N, Reichold M, Bockenhauer D, Kleta R, Zdebik AA (2011) KCNJ10 mutations disrupt function in patients with EAST syndrome. Nephron Physiol 119(3):40–48

Fujiwara T (2006) Clinical spectrum of mutations in SCN1A gene: severe myoclonic epilepsy in infancy and related epilepsies. Epilepsy Res 70(Suppl 1):S223–S230

Gaztanaga L, Marchlinskia FE, Betensky BP (2012) Mechanisms of cardiac arrhythmias. Rev Esp Cardiol 65(2):174–185

George AL, Crackower MA, Abdalla JA, Hudson AJ, Ebers GC (1993) Molecular basis of Thomsen's disease (autosomal dominant myotoniacongenita). Nat Genet 3:305–310

Gibson A, Lewis AP, Affleck K, Aitken AJ, Meldrum E, Thompson N (2005) hCLCA1 and mCLCA3 are secreted non-integral membrane proteins and therefore are not ion channels. J Biol Chem 280:27205–27212

Gobrit N, Le Bouter S, Szuts V, Varro A, Escande D, Nattel S, Demolombe S (2007) Regional and tissue specific transcript signatures of ion channel genes in the non-diseased human heart. J Physiol 582(Pt 2):675–693

Goldberg YP, MacFarlane J, MacDonald ML, Thompson J, Dube MP, Mattice M, Fraser R, Young C, Hossain S, Pape T, Payne B, Radomski C, Donaldson G, Ives E, Cox J, Younghusband HB, Green R, Duff A, Boltshauser E, Grinspan GA, Dimon JH, Sibley BG, Andria G, Toscano E, Kerdraon J, Bowsher D, Pimstone SN, Samuels ME, Sherrington R, Hayden MR (2007) Loss-of-function mutations in the $Na_v1.7$ gene underlie congenital indifference to pain in multiple human populations. Clin Genet 71(4):311–319

Goymer P (2007) Synonymous mutations break their silence. Nat Rev Genet 8:92

Graves AR, Curran PK, Smith CL, Mindell JA (2008) The Cl^-/H^+ antiporter ClC-7 is the primary chloride permeation pathway in lysosomes. Nature 453:788–792

Graves TD, Hanna MG (2005) Neurological channelopathies. Postgrad Med J 81(951):20–32

Gregg RG, Messing A, Strube C, Beurg M, Moss R, Behan M, Sukhareva M, Haynes S, Powell JA, Coronado R, Powers PA (1996) Absence of the beta subunit (cchb1) of the skeletal muscle dihydropyridine receptor alters expression of the alpha 1 subunit and eliminates excitation-contraction coupling. Proc Natl Acad Sci 93:13961–13966

Gritz SM, Radcliffe RA (2013) Genetic effects of ATP1A2 in familial hemiplegic migraine type II and animal models. Hum Genom 7:8

Groot MD, Reijneveld JC, Aronica E, Heimans JJ (2012) Epilepsy in patients with a brain tumour: focalepilepsy requires focused treatment. Brain 135:1002–1016

Gruber AD, Elble RC, Ji HL, Schreur KD, Fuller CM, Pauli BU (1998) Genomic cloning, molecular characterization, and functional analysis of human CLCA1, the first human member of the family of Ca^{2+}-activated Cl^- channel proteins. Genomics 54:200–214

Gruber AD, Schreur KD, Ji HL, Fuller CM, Pauli BU (1999) Molecular cloning and transmembrane structure of hCLCA2 from human lung, trachea, and mammary gland. Am J Physiol 276:C1261–C1270

Gulbis JM, Mann S, MacKinnon R (1999) Structure of a voltage-dependent K^+ channel beta subunit. Cell 97(7):943–952

Haass A, Ricker K, Rüdel R, Lehmann-Horn F, Böhlen R, Dengler R, Mertens HG (1981) Clinical study of paramyotonia congenita with and without myotonia in a warm environment. Muscle Nerve 4(5):388–395

Hagiwara N, Irisawa H, Kameyama M (1988) Contribution of two types of calcium currents to the pacemaker potentials of rabbit sino-atrial node cells. J Physiol 395:233–253

Hamdan FF, Gauthier J, Araki Y, Lin DT, Yoshizawa Y, Higashi K, Park AR, Spiegelman D, Dobrzeniecka S, Piton A, Tomitori H, Daoud H, Massicotte C, Henrion E, Diallo O, Shekarabi M, Marineau C, Shevell M, Michaud JL (2011) Excess of de novo deleterious mutations in genes associated with glutamatergic systems in nonsyndromic intellectual disability. Am J Hum Genet 88:306–316

Han JY, Kim JB (2011) Familial hyperkalemic periodic paralysis caused by a de novo mutation in the sodium channel gene SCN4A.Korean. J Pediatr 54(11):470–472

Harper PS, Johnston DM (1972) Recessively inherited myotonia congenita. J Med Genet 9(2):213–215

Heine R, Pika U, Lehmann-Horn F (1993) A novel SCN4A mutation causing myotonia aggravated by cold and potassium. Hum Mol Genet 2(9):1349–1353

Hoshino M, Morita S, Iwashita H, Sagiya Y, Nagi T, Nakanishi A, Ashida Y, Nishimura O, Fujisawa Y, Fujino M (2002) Increased expression of the human Ca^{2+}-activated Cl-channel 1 (CaCC1) gene in the asthmatic airway. Am J Respir Crit Care Med 165:1132–1136

Hourez R, Servais L, Orduz D, Gall D, Millard I, de Kerchove d'Exaerde A, Cheron G, Orr HT, Pandolfo M, Schiffmann SN (2011) Aminopyridines correct early dysfunction and delay neurodegeneration in a mouse model of spinocerebellar ataxia type 1. J Neurosci 31(33):11795–11807

Hu D, Barajas-Martinez H, Burashnikov E, Springer M, Wu Varro A, Pfeiffer R, Koopmann TT, Cordeiro JM, Guerchicoff A, Pollevick GD, Antzelevitch C (2009) A mutation in the beta 3 subunit of the cardiac sodium channel associated with Brugada ECG phenotype. Circ Cardiovasc Genet 2(3):270–278

Hu D, Barajas-Martinez H, Nesterenko VV, Pfeiffer R, Guerchicoff A, Cordeiro JM, Curtis AB, Pollevick GD, Wu Y, Burashnikov E, Antzelevitch C (2010) Dual variation in SCN5A and CACNB2b underlies the development of cardiac conduction disease without Brugada syndrome. Pacing Clin Electrophysiol 33(3):274–285

Huguenard JR (1996) Low-threshold calcium currents in central nervous system neurons. Annu Rev Physiol 58:329–348

Hyde SC, Emsley P, Hartshorn MJ, Mimmack MM, Gileadi U, Pearce SR, Gallagher MP, Gill DR, Hubbard RE, Higgins CF (1990) Structural model of ATP-binding proteins associated with cystic fibrosis, multidrug resistance and bacterial transport. Nature 346(6282):362–365

Ignoul S, Simaels J, Hermans D, Annaert W (2007) Human ClC-6 is a late endosomal glycoprotein that associates with detergent-resistant lipid domains. J PLoS ONE 2:e474

Imbrici P, Eunson LH, Graves TD, Bhatia KP, Wadia NH, Kullmann DM, Hanna MG (2005) Late-onset episodic ataxia type 2 due to an in-frame insertion in CACNA1A. Neurology 65(6):944–946

Iqbal J, Bhat MI, Charoo BA, Syed WA, Sheikh MA, Bhat I (2009) Experience with oral mexiletine in primary erythromelalgia in children. AnnSaudiMed 29(4):316–318

Ishiguro T, Ishikawa K, Takahashi M, Obayashi M, Amino T, Sato N, Sakamoto M, Fujigasaki H, Tsuruta F, Dolmetsch R, Arai T, Sasaki H, Nagashima K, Kato T, Yamada M, Takahashi H, Hashizume Y, Mizusawa H (2010) The carboxy-terminal fragment of alpha(1A) calcium channel preferentially aggregates in the cytoplasm of human spinocerebellar ataxia type 6 Purkinje cells. Acta Neuropathol 119(4):447–464

Jen JC (2001) Familial Hemiplegic Migraine. Jul 17 [Updated 2009 Sep 8]. In: Pagon RA, Adam MP, Bird TD et al (eds) GeneReviews^{TM} [Internet]. University of Washington, Seattle, Seattle (WA), 1993–2013. Available from: http://www.ncbi.nlm.nih.gov/books/NBK1388/

Jen JC, Graves TD, Hess EJ, Hanna MG, Griggs RC, Baloh RW (2007) Primary episodic ataxias: diagnosis, pathogenesis and treatment. Brain 130(Pt 10):2484–2493

Jen JC, Wan J, Palos TP, Howard BD, Baloh RW (2005) Mutation in the glutamate transporter EAAT1 causes episodic ataxia, hemiplegia, and seizures. Neurology 65(4):529–534

Jentsch TJ, Günther W, Pusch M, Schwappach B (1995) Properties of voltage-gated chloride channels of the ClC gene family. J Physiol 482:19S–25S

Jentsch TJ, Stein V, Weinreich F, Zdebik AA (2002) Molecular structure and physiological function of chloride channels. Physiol Rev 82(2):503–568

Jeworutzki E, López-Hernández T, Capdevila-Nortes X, Sirisi S, Bengtsson L, Montolio M, Zifarelli G, Arnedo T, Müller CS, Schulte U, Nunes V, Martínez A, Jentsch TJ, Gasull X, Pusch M, Estévez R (2012) GlialCAM, a protein defective in a leukodystrophy, serves as a ClC-2 Cl(−) channel auxiliary subunit. Neuron 73(5):951–961

Jo A, Nam YJ, Oh JY, Cheon HS, Jeromin A, Lee JA, Kim HK (2010) Dendritic localization and a cis-acting dendritic targeting element of Kv4.2 Mrna. BMB Rep 43(10):677–682

Johnston J, Griffin SJ, Baker C, Skrzypiec A, Chernova T, Forsythe ID (2008) Initial segment Kv2.2 channels mediate a slow delayed rectifier and maintain high frequency action potential firing in medial nucleus of the trapezoid body neurons. J Physiol 586(14):3493–3509

Jurkat-Rott K, Lehmann-Horn F, Elbaz A, Heine R, Gregg RG, Hogan K, Powers PA, Lapie P, Vale-Santos JE, Weissenbach J et al (1994) A calcium channel mutation causing hypokalemic periodic paralysis. Hum Mol Genet 3(8):1415–1419

Jurkat-Rott K, Mitrovic N, Hang C, Kouzmekine A, Iaizzo P, Herzog J, Lerche H, Nicole S, Vale-Santos J, Chauveau D, Fontaine B, Lehmann-Horn F (2000) Voltage-sensor sodium channel mutations cause hypokalemic periodic paralysis type 2 by enhanced inactivation and reduced current. Proc Natl Acad Sci USA 97(17):9549–9554

Jurkat-Rott K, Weber MA, Fauler M, Guo XH, Holzherr BD, Paczulla A, Nordsborg N, Joechle W, Lehmann-Horn F (2009) K^+-dependent paradoxical membrane depolarization and Na^+ overload, major and reversible contributors to weakness by ion channel leaks. Proc Natl Acad Sci USA 106(10):4036–4041

Junker J, Haverkamp W, Schulze-Bahr E, Eckardt L, Paulus W, Kiefer R (2002) Amiodarone and acetazolamide for the treatment of genetically confirmed severe Andersen syndrome. Neurology 59(3):466

Kaczorowski GJ, McManus OB, Priest BT, Garcia ML (2008) Ion channels as drug targets: the next GPCRs. J Gen Physiol 131(5):399–405

Kalume F, Yu FH, Westenbroek RE, Scheuer T, Catterall WA (2007) Reduced sodium current in Purkinje neurons from $Na_v1.1$ mutant mice: implications for ataxia in severe myoclonic epilepsy in infancy. J Neurosci 27(41):11065–11074

Kameda K, Fukao M, Kobayashi T, Tsutsuura M, Nagashima M, Yamada Y, Yamashita TT (2006) NCSN5/Jab1 inhibits cardiac L-type Ca^{2+} channel activity through protein–protein interactions. J Mol Cell Cardiol 40:562–569

Kang JQ, Shen W, Macdonald RL (2006) Why does fever trigger febrile seizures? GABAA receptor γ2 subunit mutations associated with idiopathic generalized epilepsies have temperature-dependent trafficking deficiencies. J Neurosci 26(9):2590–2597

Kariev AM, Green ME (2012) Voltage gated ion channel function: gating, conduction, and the role of water and protons. Int J Mol Sci 13(2):1680–1709

Kashuba VI, Kashuba KSM, Protopopov AI, Gizatullin RZ, Rynditch AV, Wahlestedt C, Wasserman WW, Zabarovsky ER (2001) Initial isolation and analysis of the human Kv1.7 (KCNA7) gene, a member of the voltage-gated potassium channel gene family. Gene 268(1–2):115–122

Kearney JA, Plummer NW, Smith MR, Kapur J, Cummins TR, Waxman SG, Goldin AL, Meisler MH (2001) A gain-of-function mutation in the sodium channel gene Scn2a results in seizures and behavioral abnormalities. Neuroscience 102(2):307–317

Kharkovets T, Hardelin JP, Safieddine S, Schweizer M, El-Amraoui A, Petit C, Jentsch TJ (2000) KCNQ4, a K^+ channel mutated in a form of dominant deafness, is expressed in the inner ear and the central auditory pathway. 97(8):4333–4338

Kihira H, Hermanstyne TO, Misonou H (2010) Formation of heteromeric Kv2 channels in mammalian brain neurons. J Biol 285:15048–15055

Kim D, Park D, Choi S, Lee S, Sun M, Kim C, Shin HS (2003) Thalamic control of visceral nociception mediated by T-type Ca^{2+} channels. Science 302(5642):117–119

Kim DS, Kim EJ, Jung DS, Park KH, Kim IJ, Kwak KY, Kim CM, Ko HY (2002) A Korean family with Arg1448Cys mutation of SCN4A channel causing paramyotonia congenita: electrophysiologic, histopathologic, and molecular genetic studies. J Korean Med Sci 17(6):856–860

Kim SH, Kim UK, Chae JJ, Kim DJ, Oh HY, Kim BJ, Lee CC (2001) Identification of mutations including de novo mutations in Korean patients with hypokalaemic periodic paralysis. Nephrol Dial Transpl 16:939–944

Kirsch GE (1999) Ion channel defects in cardiac arrhythmia. J Membr Biol 170(3):181–190

Klassen T, Davis C, Goldman A, Burgess D, Chen T, Wheeler D, McPherson J, Bourquin T, Lewis L, Villasana D, Morgan M, Muzny D, Gibbs R, Noebels J (2011) Exome sequencing of ion channel genes reveals complex profiles confounding personal risk assessment in epilepsy. Cell 145(7):1036–1048

Klein A, Boltshauser E, Jen J, Baloh RW (2004) Episodic ataxia type 1 with distal weakness: a novel manifestation of a potassium channelopathy. Neuropediatrics 35(02):147–149

Klein CJ, Wu Y, Kilfoyle DH, Sandroni P, Davis MD, Gavrilova RH, Low PA, Dyck PJ (2013) Infrequent SCN9A mutations in congenital insensitivity to pain and erythromelalgia. J Neurol Neurosurg Psychiatry 84(4):386–391

Klugbauer N, Lacinová L, Marais E, Hobom M, Hofmann F (1999) Molecular diversity of the calcium channel alpha2delta subunit. J Neurosci 19(2):684–691

Koch MC, Steinmeyer K, Lorenz C, Ricker K, Wolf F, Otto M, Zoll B, Lehmann-Horn F, Grzeschik KH, Jentsch TJ (1992) The skeletal muscle chloride channel in dominant and recessive human myotonia. Science 257(5071):797–800

Koopmann TT, Postema PG, Bezzina CR, Wilde AAM (2009) Introduction, based on: Ion channels involved in cardiac arrhythmias. Biophys Ion Channels Dis 7:113–138

Kordasiewicz HB, Gomez CM (2007) Molecular pathogenesis of spinocerebellar ataxia type 6. Neurotherapeutics 4(2):285–294

Kornak U, Kasper D, Boesl MR, Kaiser E, Schweizer M, Schulz A, Friedrich W, Delling G, Jentsch TJ (2001) Loss of the ClC-7 chloride channel leads to osteopetrosis in mice and man. Cell 104(2):205–215

Kubisch C, Schmidt-Rose T, Fontaine B, Bretag AH, Jentsch TJ (1998) ClC-1 chloride channel mutations in myotonia congenita: variable penetrance of mutations shifting the voltage dependence. Hum Mol Genet 7(11):1753–1760

Kuhn E (1993) Myotonia congenital (Thomsen) and recessive generalized myotonia (Becker). Nervenarzt 64(12):766–769

Kullmann DM, Hanna MG (2002) Neurological disorders caused by inherited ion-channel mutations. Lancet Neurol 1(3):157–166

Kullmann DM, Waxman SG (2010) Neurological channelopathies: new insights into disease mechanisms and ion channel function. J Physiol 588(Pt 11):1823–1827

Kung AW, Lau KS, Fong GC, Chan V (2004) Association of novel single nucleotide polymorphisms in the calcium channel alpha 1 subunit gene (Ca(v)1.1) and thyrotoxic periodic paralysis. J Clin Endocrinol Metab 89:1340–1345

Lamb FS, Clayton GH, Liu BX, Smith RL, Barna TJ, Schutte BCJ (1999) Expression of CLCN voltage-gated chloride channel genes in human blood vessels. Mol Cell Cardiol 31:657–666

Lampert A, O'Reilly AO, Reeh P, Leffler A (2010) Sodium channelopathies and pain. Pflugers Arch 460(2):249–263

Lasak JM, Allen P, McVay T, Lewis D (2014) Hearing loss: diagnosis and management. Prim Care 41(1):19–31

Lau D, Vega-Saenz de Miera EC, Contreras D, Ozaita, A, Harvey M, Chow A, Noebel JL, Paylor R, Morgan JI, Leonard CS, Rudy B (2000) Impaired fast-spiking, suppressed cortical inhibition, and increased susceptibility to seizures in mice lacking Kv3.2 K^+ channel proteins. J Neurosci 20:9071–9085

Lee SH, Park JH, Jung HH, Lee SH, Oh JW, Lee HM, Jun HS, Cho WJ, Lee JY (2005) Expression and distribution of ion transport mRNAs in human nasal mucosa and nasal polyps. Acta Oto-Laryngol 125:745–752

Lee TT, Zhang XD, Chuang CC, Chen JJ, Chen YA, Chen SC, Chen TY, Tang CY (2013) Myotonia congenita mutation enhances the degradation of human CLC-1 chloride channels. PLoS ONE 8(2):e55930

Lee US, Cui J (2009) {beta} subunit-specific modulations of BK channel function by a mutation associated with epilepsy and dyskinesia. J Physiol 587(Pt 7):1481–1498

Lehmann-Horn F, Jurkat-Rott K, Rüdel R (2002) Periodic paralysis: understanding channelopathies. Curr Neurol Neurosci Rep 2(1):61–69

Lehnart SE, Ackerman MJ, Benson DW Jr, Brugada R, Clancy CE, Donahue JK, George AL Jr, Grant AO, Groft SC, January CT, Lathrop DA, Lederer WJ, Makielski JC, Mohler PJ, Moss A, Nerbonne JM, Olson TM, Przywara DA, Towbin JA, Wang LH, Marks AR (2007) Inherited arrhythmias: a National Heart, Lung, and Blood Institute and Office of Rare Diseases workshop consensus report about the diagnosis, phenotyping, molecular mechanisms, and therapeutic approaches for primary cardiomyopathies of gene mutations affecting ion channel function. Circulation 116(20):2325–2345

Leisle L, Ludwig CF, Wagner FA, Jentsch TJ, Stauber T (2011) ClC-7 is a slowly voltage-gated 2Cl(−)/1H(+)-exchanger and requires Ostm1 for transport activity. EMBO J 30:2140–2152

Leonard RJ, Garcia ML, Slaughter RS, Reuben JP (1992) Selective blockers of voltage-gated K^+ channels depolarize human T lymphocytes: mechanism of the antiproliferative effect of charybdotoxin. Proc Natl Acad Sci 89(21):10094–10098

Lerche H, Heine R, Pika U, George AL, Mitrovic N, Browatzki M, Weiss T, Rivet-Bastide M, Franke C, Lomonaco M (1993) Human sodium channel myotonia: slowed channel inactivation due to substitutions for a glycine within the III-IV linker. J Physiol 470:13–22

Letts VA, Felix R, Biddlecome GH, Arikkath J, Mahaffey CL, Valenzuela A, Bartlett FS, Mori Y, Campbell KP, Frankel WN (1998) The mouse stargazer gene encodes a neuronal Ca^{2+}-channel gamma subunit. Nat Genet 19(4):340–347

Lewis A, McCrossan ZA, Abbott GW (2004) MinK, MiRP1, and MiRP2 diversify Kv3.1 and Kv3.2 potassium channel gating.J. Biol. Chem. 279:7884–7892

Lindstrom J, Anand R, Peng X, Gerzanich V, Wang F, Li Y (1995) Neuronal nicotinic receptor subtypes. Ann N Y Acad Sci 757:100–116

Lion-Francois L, Mignot C, Vicart S, Manel V, Sternberg D, Landrieu P, Lesca G, Broussolle E, Billette de Villemeur T, Napuri S, des Portes V, Fontaine B (2010) Severe neonatal episodic laryngospasm due to de novo SCN4A mutations: a new treatable disorder. Neurology 75:641–645

Llinas R, Sugimori M, Hillman DE, Cherksey B (1992) Distribution and functional significance of the P-type, voltage-dependent Ca^{2+} channels in the mammalian central nervous system. Trends Neurosci 15(9):351–355

Lolignier S, Amsalem M, Maingret F, Padilla F, Gabriac M, Chapuy E, Eschalier A, Delmas P, Busserolles J (2011) $Na_v1.9$ channel contributes to mechanical and heat pain hypersensitivity induced by subacute and chronic inflammation. PLoS ONE 6(8):e23083

Lopes CM, Zhang H, Rohacs T, Jin T, Yang J, Logothetis DE (2002) Alterations in conserved Kir channel-PIP2 interactions underlie channelopathies. Neuron 34(6):933–944

Lorenz C, Meyer-Kleine C, Steinmeyer K, Koch MC, Jentsch TJ (1994) Genomic organization of the human muscle chloride channel ClC-1 and analysis of novel mutations leading to Becker-type myotonia. Hum Mol Genet 3:941–946

Lorincz A, Nusser Z (2008) Cell-type-dependent molecular composition of the axon initial segment. J Neurosci 28(53): 14329–14340

Lossin C, George AL Jr (2008) Myotonia congenita. Adv Genet 63:25–55

Lucchiari S, Ulzi G, Magri F, Bucchia M, Corbetta F, Servida M, Moggio M, Comi GP, Lecchi M (2013) Clinical evaluation and cellular electrophysiology of a recessive CLCN1 patient. J Physiol Pharmacol 64(5):669–678

Lyons MJ, Duron R, Molinero I, Sangiuolo F, Holden KR (2010) Novel CLCN1 mutation in carbamazepine-responsive myotonia congenita. Pediatr Neurol 42(5):365–368

MacKinnon R (2003) Potassium channels. FEBS Lett 555(1):62–65

Magee KR (1966) Paramyotonia congenita. Association with cutaneous cold sensitivity and description of peculiar sustained postures after muscle contraction. Arch Neurol 14(6):590–594

Maricq AV, Peterson AS, Brake AJ, Myers RM, Julius D (1991) Primary structure and functional expression of the 5HT3 receptor, a serotonin-gated ion channel. Science 254(5030):432–437

Matthews E, Labrum R, Sweeney MG, Sud R, Haworth A, Chinnery PF, Meola G, Schorge S, Kullmann DM, Davis MB, Hanna MG

(2009) Voltage sensor charge loss accounts for most cases of hypokalemic periodic paralysis. Neurology. 72(18):1544–1547

Matthews E, Portaro S, Ke Q, Sud R, Haworth A, Davis MB, Griggs RC, Hanna MG (2011) Acetazolamide efficacy in hypokalemic periodic paralysis and the predictive role of genotype. Neurology 77(22):1960–1964

Maylie B, Bissonnette E, Virk M, Adelman JP, Maylie JG (2002) Episodic ataxia type 1 mutations in the human Kv1.1 potassium channel alter hKvbeta 1-induced N-type inactivation. J Neurosci 22(12):4786–4793

McArdle B (1956) Familial periodic paralysis. Br Med Bull 12(3):226–229

McClatchey AI, Van den Bergh P, Pericak-Vance MA, Raskind W, Verellen C, McKenna-Yasek D, Rao K, Haines JL, Bird T, Brown RH Jr et al (1992) Temperature-sensitive mutations in the III–IV cytoplasmic loop region of the skeletal muscle sodium channel gene in paramyotonia congenita Cell 68(4):769–774

McRory JE, Hamid J, Doering CJ, Garcia E, Parker R, Hamming K, Chen L, Hildebrand M, Beedle AM, Feldcamp L, Zamponi GW, Snutch TP (2004) The CACNA1F gene encodes at L-type calcium channel with unique biophysical properties and tissue distribution. J Neurosci 24(7):1707–1718

Medeiros-Domingo A, Kaku T, Tester DJ, Iturralde-Torres P, Itty A, Ye B, Valdivia C, Ueda K, Canizales-Quinteros S, Tusié-Luna MT, Makielski JC, Ackerman MJ (2007) SCN4B-encoded sodium channel beta4 subunit in congenital long-QT syndrome. Circulation 116(2):134–142

Mehta SH, Morgan JC, Sethi KD (2009) Paroxysmal dyskinesias. Curr Treat Options Neurol 11(3):170–178

Meisler MH, Kearney JA (2005) Sodium channel mutations in epilepsy and other neurological disorders. J Clin Invest 115(8):2010–2017

Meisler MH, O'Brien JE, Sharkey LM (2010) Sodium channel gene family: epilepsy mutations, gene interactions and modifier effects. J Physiol 588(Pt 11):1841–1848

Michiels JJ, te Morsche RH, Jansen JB, Drenth JP (2005) Autosomal dominant erythermalgia associated with a novel mutation in the voltage-gated sodium channel alpha subunit $Na_v1.7$. Arch Neurol 62(10):1587–1590

Miller C, White MM (1984) Dimeric structure of single chloride channels from Torpedo electroplax. Proc Natl Acad Sci USA 81(9):2772–2775

Mintz IM, Adams ME, Bean BP (1992) P-type calcium channels in rat central and peripheral neurons. Neuron 9(1):85–95

Misonou H, Mohapatra DP, Trimmer JS (2005) Kv2.1: a voltage-gated k^+ channel critical to dynamic control of neuronal excitability. Neurotoxicology 26(5):743–752

Mohammadi B, Mitrovic N, Lehmann-Horn F, Dengler R, Bufler J (2003) Mechanisms of cold sensitivity of paramyotonia congenita mutation R1448H and overlap syndrome mutation M1360 V. J Physiol 547(Pt 3):691–698

Morgan JI, Curran T (1989) Stimulus-transcription coupling in neurons: role of cellular immediate-early genes. Trends Neurosci 12(11):459–462

Mork C, Asker CL, Salerud EG, Kvernebo K (2000) Microvascular arteriovenous shunting is a probable pathogenetic mechanism in erythromelalgia. J Invest Dermatol 114:643–646

Moss AJ, Shimizu W, Wilde AA, Towbin JA, Zareba W, Robinson JL, Qi M, Vincent GM, Ackerman MJ, Kaufman ES, Hofman N, Seth R, Kamakura S, Miyamoto Y, Goldenberg I, Andrews ML, McNitt S (2007) Clinical aspects of type-1 long-QT syndrome by location, coding type, and biophysical function of mutations involving the KCNQ1 gene. Circulation 115(19), 2481-2489.

Noda M, Shimizu S, Tanabe T, Takai T, Kayano T, Ikeda T et al (1984) Primary structure of Electrophorus electricus sodium-channel deduced from cDNA sequence. Nature 312:121–127

Ohmori I, Ouchida M, Miki T, Mimaki N, Kiyonaka S, Nishiki T, Tomizawa K, Mori Y, Matsui H (2008) A CACNB4 mutation shows that altered Ca(v)2.1 function may be a genetic modifier of severe myoclonic epilepsy in infancy. Neurobiol Dis 32:349–354

Okuda S, Kanda F, Nishimoto K, Sasaki R, Chihara K (2001) Hyperkalemic periodic paralysis and paramyotonia congenita—a novel sodium channel mutation. J Neurol 248(11):1003–1004

Ophoff RA, Terwindt GM, Vergouwe MN, van Eijk R, Oefner PJ, Hoffman SM, Lamerdin JE, Mohrenweiser HW, Bulman DE, Ferrari M, Haan J, Lindhout D, van Ommen GJ, Hofker MH, Ferrari MD, Frants RR (1996) Familial hemiplegic migraine and episodic ataxia type-2 are caused by mutations in the Ca^{2+} channel gene CACNL1A4. Cell 87(3):543–552

Orazio B, Paola I, Mauro P (2012) Kv1.1 knock-in ataxic mice exhibit spontaneous myokymic activity exacerbated by fatigue, ischemia and low temperature. Nerobiol Dis 47(3):310–321

Orrell RW, Jurkat-Rott K, Lehmann-Horn F, Lane RJ (1998) Familial cramp due to potassium-aggravated myotonia. J Neurol Neurosurg Psychiatry 65(4):569–572

Osorio N, Alcara G, Padilla F, Couraud F, Delmas P, Crest M (2005) Differential targeting and functional specialization of sodium channels in cultured cerebellar granule cells. J Physiol 569(Pt 3):801–816

Ota T, Suzuki Y, Nishikawa T, Otsuki T, Sugiyama T, Irie R, Wakamatsu A, Hayashi K, Sato H, Nagai K, Kimura K, Makita H, Sekine M, Obayashi M, Nishi T, Shibahara T, Tanaka T, Ishii S, Sugano S (2004) Complete sequencing and characterization of 21,243 full-length human cDNAs. Nat Genet 36:40–45

Pak WL, Pinto LH (1976) Genetic approach to the study of the nervous system. Annu Rev Biophys Bioeng 5:397–448

Patino GA, Brackenbury WJ, Bao Y, Lopez-Santiago LF, O'Malley HA, Chen C, Calhoun JD, Lafrenière RG, Cossette P, Rouleau GA, Isom LL (2011) Voltage-gated Na^+ channel β1B: a secreted cell adhesion molecule involved in human epilepsy. J Neurosci 31(41):14577–14591

Paulson HL (2009) The spinocerebellar ataxias. J Neuroophthalmol 29(3):227–237

Pelzer N, Stam AH, Haan J, Ferrari MD, Terwindt GM (2013) Familial and sporadic hemiplegic migraine: diagnosis and treatment. Curr Treat Options Neurol 15(1):13–27

Pereon Y, Lande G, Demolombe S, Nguyen The Tich S, Sternberg D, Le Marec, David A (2003). Paramyotonia congenita with an SCN4A mutation affecting cardiac repolarization. Neurology 60(2):340–342

Perez-Reyes E, Castellano A, Kim HS, Bertrand P, Baggstrom E, Lacerda AE, Wei XY, Birnbaumer L (1992) Cloning and expression of a cardiac/brain beta subunit of the L-type calcium channel. J Biol Chem 267:1792–1797

Pett MA, Beck SL, Guo JW, Towsley GL, Brant JM, Smith EML, Berry PH, Donaldson GW (2013) Confirmatory factor analysis of the Pain Care Quality Surveys (PainCQ©) Health Services Res 48(3):1018–1038

Pichler M, Cassidy TN, Reimer D, Haase H, Kraus R, Ostler D, Striessnig J (1997) Beta subunit heterogeneity in neuronal L-type Ca^{2+} channels. J Biol Chem 272:13877–13882

Pietrobon D (2007) Familial hemiplegic migraine. Neurotherapeutics 4(2):274–284

Pietrobon D (2010) $Ca_v2.1$ channelopathies. Pflugers Arch 460(2):375–393

Plaster NM, Tawil R, Tristani-Firouzi M, Canún S, Bendahhou S, Tsunoda A, Donaldson MR, Iannaccone ST, Brunt E, Barohn R, Clark J, Deymeer F, George AL Jr, Fish FA, Hahn A, Nitu A, Ozdemir C, Serdaroglu P, Subramony SH, Wolfe G, Fu YH, Ptácek LJ (2001) Mutations in Kir2.1 cause the developmental

and episodic electrical phenotypes of Andersen's syndrome. Cell 105(4):511–519

Poet M, Kornak U, Schweizer M, Zdebik AA, Scheel O et al (2006) Lysosomal storage disease upon disruption of the neuronal chloride transport protein ClC-6. Proc Natl Acad Sci USA 103:13854–13859

Protheroe SM (1991) Congenital insensitivity to pain. J R Soc Med 84:558–559

Pruss H, Grosse G, Brunk I, Veh RW, Ahnert-Hilger G (2009) Age-dependent axonal expression of potassium channel proteins during development in mouse hippocampus. Histochem Cell Biol 133(3):301–312

Ptacek LJ, George AL Jr, Barchi RL, Griggs RC, Riggs JE, Robertson M, Leppert MF (1992) Mutations in an S4 segment of the adult skeletal muscle sodium channel cause paramyotonia congenita. Neuron 8(5):891–897

Ptacek LJ, Gouw L, Kwieciński H, McManis P, Mendell JR, Barohn RJ, George AL Jr, Barchi RL, Robertson M, Leppert MF (1993) Sodium channel mutations in paramyotonia congenita and hyperkalemic periodic paralysis. Ann Neurol 33(3):300–307

Ptacek LJ, Tawil R, Griggs RC, Meola G, McManis P, Barohn RJ, Mendell JR, Harris C, Spitzer R, Santiago F (1994) Sodium channel mutations in acetazolamide-responsive myotonia congenita, paramyotonia congenita, and hyperkalemic periodic paralysis. Neurology 44(8):1500–1503

Ptacek LJ, Tyler F, Trimmer JS, Agnew WS, Leppert M (1991) Analysis in a large hyperkalemic periodic paralysis pedigree supports tight linkage to a sodium channel locus. Am J Hum Genet 49(2):378–382

Pusch M (2002) Myotonia caused by mutations in the muscle chloride channel gene CLCN1. Hum Mutat 19(4):423–434

Raike RS, Weisz C, Hoebeek FE, Terzi MC, De Zeeuw CL, van den Maagdenberg AM, Jinnah HA, Hess EJ (2013) Stress, caffeine and ethanol trigger transient neurological dysfunction through shared mechanisms in a mouse calcium channelopathy. Neurobiol Dis 50C:151–159

Rajakulendran S, Schorge S, Kullmann DM, Hanna MG (2010) Dysfunction of the Ca(V)2.1 calcium channel in cerebellar ataxias. F1000 Biol Rep. 2, pii:4

Reimer D, Huber IG, Garcia ML, Haase H, Striessnig J (2000) Beta subunit heterogeneity of L-type $Ca(^{2+})$ channels in smooth muscle tissues. FEBS Lett 467:65–69

Reuter H (1983) Calcium channel modulation by neurotransmitters, enzymes and drugs. Nature 301:569–574

Riuro H, Beltran-Alvarez P, Tarradas A, Selga E, Campuzano O, Vergés M, Pagans S, Iglesias A, Brugada J, Brugada P, Vázquez FM, Pérez GJ, Scornik FS, Brugada R (2013) A missense mutation in the sodium channel β2 subunit reveals SCN2B as a new candidate gene for Brugada syndrome. Hum Mutat 34(7):961–966

Roberts WM, Jacobs RA, Hudseth AJ (1990) Co-localization of ion channels involved in frequency selectivity and synaptic transmission at presynaptic active zones of hair cells. J Neurosci 10:3664–3684

Rocha EA, Pereira FT, Monteiro Mde P, Rocha Neto AC, Rodrigues Sobrinho CR, Scanavacca M (2013) Defibrillators in Jervell-Lange Nielsen syndrome. Arq Bras Cardiol 100(2):e25–e26

Rojas CV, Wang JZ, Schwartz LS, Hoffman EP, Powell BR, Brown RH Jr (1991) A Met-to-Val mutation in the skeletal muscle Na^+ channel alpha-subunit in hyperkalaemic periodic paralysis. Nature 354(6352):387–389

Saint-Martin C, Gauvain G, Teodorescu G, Gourfinkel-An I, Fedirko E, Weber YG, Maljevic S, Ernst JP, Garcia-Olivares J, Fahlke C, Nabbout R, LeGuern E, Lerche H, Christophe Poncer J, Depienne C (2009) Two novel CLCN2 mutations accelerating chloride channel deactivation are associated with idiopathic generalized epilepsy. Hum Mutat 30:397–405

Sala-Rabanal M, Kucheryavykh LY, Skatchkov SN, Eaton MJ, Nichols CG (2010) Molecular mechanisms of EAST/SeSAME syndrome mutations in Kir4.1 (KCNJ10). J Biol Chem 285:36040–36048

Sandhiya S, Dkhar SA (2009) Potassium channels in health, disease & development of channel modulators. Indian J Med Res 129:223–232

Sasaki R, Takano H, Kamakura K, Kaida K, Hirata A, Saito M, Tanaka H, Kuzuhara S, Tsuji S (1999) A novel mutation in the gene for the adult skeletal muscle sodium channel alpha-subunit (SCN4A) that causes paramyotonia congenita of von Eulenburg. Arch Neurol 56(6):692–696

Satheesh SV, Kunert K, Rüttiger L, Zuccotti A, Schönig K, Friauf E, Knipper M, Bartsch D, Nothwang HG (2012) Retrocochlear function of the peripheral deafness gene Cacna1d. Human Mol Genet 21(17):3896–3909

Savitha MR, Krishnamurthy B, Hyderi A, Ramachandra NB (2006) Myotonia congenita—a successful response to carbamazepine. Indian J Pediatr 73(5):431–433

Scheffer IE, Berkovic SF (1997) Generalized epilepsy with febrile seizures plus. A genetic disorder with heterogeneous clinical phenotypes. Brain 120(Pt 3):479–490

Scheffer IE, Harkin LA, Grinton BE, Dibbens LM, Turner SJ, Zielinski MA, Xu R, Jackson G, Adams J, Connellan M, Petrou S, Wellard RM, Briellmann RS, Wallace RH, Mulley JC, Berkovic SF (2007) Temporal lobe epilepsy and GEFS+ phenotypes associated with SCN1B mutations. Brain 130:100–109

Schimpf R, Rudic B, Tülümen E, Papavassiliu T, Dösch C, Borggrefe M (2013) Cardiac ion channelopathies: a potential link between cardiomyopathies and cardiac arrhythmias. Dtsch Med Wochenschr 138(12):591–597

Schneider T, Wei X, Olcese R, Costantin JL, Neely A, Palade P, Perez-Reyes E, Qin N, Zhou J, Crawford GD, Smith RG, Appel SH, Stefani E, Birnbaumer M (1994) Molecular analysis and functional expression of the human type E neuronal Ca^{2+} channel alpha 1 subunit. Recept Channels 2:255–270

Scholl UI, Choi M, Liu T, Ramaekers VT, Häusler MG, Grimmer J, Tobe SW, Farhi A, Nelson-Williams C, Lifton RP (2009) Seizures, sensorineural deafness, ataxia, mental retardation, and electrolyte imbalance (SeSAME syndrome) caused by mutations in KCNJ10. Proc Natl Acad Sci USA 106(14):5842–5847

Schott JJ, Alshinawi C, Kyndt F, Probst V, Hoorntje TM, Hulsbeek M, Wilde AA, Escande D, Mannens MM, Le Marec H (1999) Cardiac conduction defects associate with mutations in SCN5A. Nat Genet 23(1):20–21

Schroeder B, Wrocklage C, Pan C, Jaeger R, Koesters B, Schaefer H, Elsaesser HP, Mann M, Hasilik A (2007) Integral and associated lysosomal membrane proteins. Traffic 8:1676–1686

Schroeder BC, Kubisch C, Stein V, Jentsch TJ (1998) Moderate loss of function of cyclic-AMP-modulated KCNQ2/KCNQ3 K^+ channels causes epilepsy. Nature 396(6712):687–690

Schulze-Bahr E, Wang Q, Wedekind H, Haverkamp W, Chen Q, Sun Y, Rubie C, Hördt M, Towbin JA, Borggrefe M, Assmann G, Qu X, Somberg JC, Breithardt G, Oberti C, Funke H (1997) KCNE1 mutations cause jervell and Lange-Nielsen syndrome. Nat Genet 17(3):267–268

Schwartz PJ, Spazzolini C, Crotti L, Bathen J, Amlie JP, Timothy K, Shkolnikova M, Berul CI, Bitner-Glindzicz M, Toivonen L, Horie M, Schulze-Bahr E, Denjoy I (2006) The Jervell and Lange-Nielsen syndrome: natural history, molecular basis, and clinical outcome. Circulation 113(6):783–790

Seebohm G, Strutz-Seebohm N, Ursu ON, Preisig-Müller R, Zuzarte M, Hill EV, Kienitz MC, Bendahhou S, Fauler M, Tapken D, Decher N, Collins A, Jurkat-Rott K, Steinmeyer K, Lehmann-

Horn F, Daut J, Tavaré JM, Pott L, Bloch W, Lang F (2012) Altered stress stimulation of inward rectifier potassium channels in Andersen-Tawil syndrome. FASEB J 26(2):513–522

Sheppard DN, Welsh MJ (1999) Structure and function of the CFTR chloride channel. Physiol Rev 79(1 Suppl):S23–S45

Shi X, Yasumoto S, Kurahashi H, Nakagawa E, Fukasawa T, Uchiya S, Hirose S (2012) Clinical spectrum of SCN2A mutations. Brain Dev 34(7):541–545

Shi Y, Suh YH, Milstein AD, Isozaki K, Schmid SM, Roche KW, Nicoll RA (2010) Functional comparison of the effects of TARPs and cornichons on AMPA receptor trafficking and gating. Proc Natl Acad Sci USA 107:16315–16319

Shook SJ, Mamsa H, Jen JC, Baloh RW, Zhou L (2008) Novel mutation in KCNA1 causes episodic ataxia with paroxysmal dyspnea. Muscle Nerve 37(3):399–402

Simkin D, Léna I, Landrieu P, Lion-Francois L, Sternberg D, Fontaine B, Bendahhou S (2011) Mechanisms underlying a life-threatening skeletal muscle Na^+ channel disorder. J Physiol 589:3115–3124

Singer D, Biel M, Lotan I, Flockerzi V, Hofmann F, Dascal N (1991) The roles of the subunits in the function of the calcium channel. Science 253:1553–1557

Singh NA, Charlier C, Stauffer D, DuPont BR, Leach RJ, Melis R, Ronen GM, Bjerre I, Quattlebaum T, Murphy JV, McHarg ML, Gagnon D, Rosales TO, Peiffer A, Anderson VE, Leppert M (1998) A novel potassium channel gene, KCNQ2, is mutated in an inherited epilepsy of newborns. Nat Genet 18(1):25–29

Singh NA, Westenskow P, Charlier C, Pappas C, Leslie J, Dillon J, Anderson VE, Sanguinetti MC, Leppert MF (2003) KCNQ2 and KCNQ3 potassium channel genes in benign familial neonatal convulsions: expansion of the functional and mutation spectrum. Brain 126(12):2726–2737

Sokolov S, Scheuer T, Catterall WA (2007) Gating pore current in an inherited ion channelopathy. Nature 446(7131):76–78

Sokolov S, Scheuer T, Catterall WA (2010) Ion permeation and block of the gating pore in the voltage sensor of $Na_v1.4$ channels with hypokalemic periodic paralysis mutations. J Gen Physiol 136(2):225–236

Soldovieri MV, Miceli F, Bellini G, Coppola G, Pascotto A, Taglialatela M (2007) Correlating the clinical and genetic features of benign familial neonatal seizures (BFNS) with the functional consequences of underlying mutations. Channels (Austin) 1(4):228–233

Spampanato J, Escayg A, Meisler MH, Goldin AL (2003) Generalized epilepsy with febrile seizures plus type 2 mutation W1204R alters voltage-dependent gating of Na(v)1.1 sodium channels. Neuroscience 116(1):37–48

Splawski I, Yoo DS, Stotz SC, Cherry A, Clapham DE, Keating MT (2006) CACNA1H mutations in autism spectrum disorders. J Biol Chem 281(31):22085–22091

Stapels M, Piper C, Yang T, Li M, Stowell C, Xiong ZG, Saugstad J, Simon RP, Geromanos S, Langridge J, Lan JQ, Zhou A (2010) Polycomb group proteins as epigenetic mediators of neuroprotection in ischemic tolerance. Sci Signal 2, 3(111)

Sternberg D, Maisonobe T, Jurkat-Rott K, Nicole S, Launay E, Chauveau D, Tabti N, Lehmann-Horn F, Hainque B, Fontaine B (2001) Hypokalaemic periodic paralysis type 2 caused by mutations at codon 672 in the muscle sodium channel gene SCN4A. Brain 124(Pt 6):1091–1099

Sternberg D, Tabti N, Hainque B, Fontaine B (2002) Hypokalemic periodic paralysis (2002) [Updated 2009 Apr 28]. In: Pagon RA, Adam MP, Bird TD et al (eds) GeneReviews™ [Internet]. University of Washington, Seattle, 1993–2013. Available from: http://www.ncbi.nlm.nih.gov/books/NBK1338/

Striggow F, Ehrlich BE (1996) Ligand-gated calcium channels inside and out. Curr Opin Cell Biol 8(4):490–495

Sun C, Tranebjaerg L, Torbergsen T, Holmgren G, Van Ghelue M (2001) Spectrum of CLCN1 mutations in patients with myotonia congenita in Northern Scandinavia. Eur J Hum Genet 9(12):903–909

Suzuki M, Morita T, Iwamoto T (2006) Diversity of Cl(−) channels. Cell Mol Life Sci 63(1):12–24

Suzuki T, Delgado-Escueta AV, Aguan K, Alonso ME, Shi J, Hara Y, Nishida M, Numata T, Medina MT, Takeuchi T, Morita R, Bai D, Ganesh S, Sugimoto Y, Inazawa J, Bailey JN, Ochoa A, Jara-Prado A, Yamakawa K (2004) Mutations in EFHC1 cause juvenile myoclonic epilepsy. Nat Genet 36:842–849

Takahashi M, Seagar MJ, Jones JF, Reber BF, Catterall WA (1987) Subunit structure of dihydropyridine-sensitive calcium channels from skeletal muscle. Proc Natl Acad Sci USA 84(15):5478–5482

Talley EM, Cribbs LL, Lee JH, Daud A, Perez-Reyes E, Bayliss DA (1999) Differential distribution of three members of a gene family encoding low voltage-activated (T-type) calcium channels. J Neurosci 19(6):1895–1911

Tamaoka A (2003) Paramyotonia congenita and skeletal sodium channelopathy. Intern Med 42(9):769–770

Tan BH, Iturralde-Torres P, Medeiros-Domingo A, Nava S, Tester DJ, Valdivia CR, Tusié-Luna T, Ackerman MJ, Makielski JC (2007) A novel C-terminal truncation SCN5A mutation from a patient with sick sinus syndrome, conduction disorder and ventricular tachycardia. Cardiovasc Res 76(3):409–417

Tan EH, Yusoff AA, Abdullah JM, Razak SA (2012) Generalized epilepsy with febrile seizure plus (GEFS+) spectrum: Novel de novo mutation of SCN1A detected in a Malaysian patient. J Pediatr Neurosci 7(2):123–125

Tate SK, Depondt C, Sisodiya SM, Cavalleri GL, Schorge S, Soranzo N, Thom M, Sen A, Shorvon SD, Sander JW, Wood NW, Goldstein DB (2005) Genetic predictors of the maximum doses patients receive during clinical use of the anti-epileptic drugs carbamazepine and phenytoin. Proc Natl Acad Sci USA 102(15):5507–5512

Tate SK, Singh R, Hung CC, Tai JJ, Depondt C, Cavalleri GL, Sisodiya SM, Goldstein DB, Liou HH (2006) A common polymorphism in the SCN1A gene associates with phenytoin serum levels at maintenance dose. Pharmacogenet Genomics 16(10):721–726

Tawil R, Ptacek LJ, Pavlakis SG, DeVivo DC, Penn AS, Ozdemir C, Griggs RC (1994) Andersen's syndrome: potassium-sensitive periodic paralysis, ventricular ectopy, and dysmorphic features. Ann Neurol. 35(3):326–330

Theile JW, Cummins TR (2011) Recent developments regarding voltage-gated sodium channel blockers for the treatment of inherited and acquired neuropathic pain syndromes. Front Pharmacol 2:54

Toda M, Tulic MK, Levitt RC, Hamid Q (2002) A calcium-activated chloride channel (HCLCA1) is strongly related to IL-9 expression and mucus production in bronchial epithelium of patients with asthma. J Allergy Clin Immunol 109:246–250

Tomlinson SE, Bostock H, Grinton B, Hanna MG, Kullmann DM, Kiernan MC, Scheffer IE, Berkovic SF, Burke D (2012) In vivo loss of slow potassium channel activity in individuals with benign familial neonatal epilepsy in remission. Brain 135(10):3144–3152

Trip J, Drost GG, van Engelen BGM, Faber CG (2006) Drug treatment for myotonia. Cochrane Database Syst Rev. Issue 1. Art. No.: CD004762

Tristani-Firouzi M, Etheridge SP (2010) Kir 2.1 channelopathies: the Andersen-Tawil syndrome. Pflugers Arch 460(2):289–294

Tristani-Firouzi M, Jensen JL, Donaldson MR, Sansone V, Meola G, Hahn A, Bendahhou S, Kwiecinski H, Fidzianska A, Plaster N, Fu YH, Ptacek LJ, Tawil R (2002) Functional and clinical

characterization of KCNJ2 mutations associated with LQT7 (Andersen syndrome). J Clin Invest 110(3):381–388

Trudeau MM, Dalton JC, Day JW, Ranum LP, Meisler MH (2006) Heterozygosity for a protein truncation mutation of sodium channel SCN8A in a patient with cerebellar atrophy, ataxia, and mental retardation. J Med Genet 43(6):527–530

Tsai CT, Lai LP, Hwang JJ, Lin JL, Chiang FT (2008) Molecular genetics of atrial fibrillation. J Am Coll Cardiol 52(4):241–250

Tsakiridou E, Bertollini L, de Curtis M, Avanzini G, Pape HC (1995) Selective increase in T-type calcium conductance of reticular thalamic neurons in a rat model of absence epilepsy. J Neurosci 15(4):3110–3117

Tsien RW, Fox AP, Hess P, McCleskey EW, Nilius B, Nowycky MC, Rosenberg RL (1987) Multiple types of calcium channel in excitable cells. Soc Gen Physiol Ser 41:167–187

Tsuboi M, Antzelevitch C (2006) Cellular basis for electrocardiographic and arrhythmic manifestations of Andersen-Tawil syndrome (LQT7). Heart Rhythm 3(3):328–335

Tyson J, Tranebjaerg L, McEntagart M, Larsen LA, Christiansen M, Whiteford ML, Bathen J, Aslaksen B, Sørland SJ, Lund O, Pembrey ME, Malcolm S, Bitner-Glindzicz M (2000) Mutational spectrum in the cardioauditory syndrome of Jervell and Lange-Nielsen. Hum Genet 107(5):499–503

Unterberger I, Trinka E (2008) Diagnosis and treatment of paroxysmal dyskinesias revisited. Ther Adv Neurol Disord 1(2):4–11

Van Poucke M, Vanhaesebrouck AE, Peelman LJ, Van Ham L (2012) Experimental validation of in silico predicted KCNA1, KCNA2, KCNA6 and KCNQ2 genes for association studies of peripheral nerve hyperexcitability syndrome in Jack Russell Terriers. Neuromuscul Disord 22(6):558–565

van Rootselaar AF, van Schade Westrum s, Velis DN, Tijssen MA (2009) The paroxysmal dyskinesias. Pract Neurol 9(2):102–109

Vannier C, Triller A (1997) Biology of the postsynaptic glycine receptor. Int Rev Cytol 176:201–244

Venance SL, Cannon SC, Fialho D, Fontaine B, Hanna MG, Ptacek LJ, Tristani-Firouzi M, Tawil R, Griggs RC, CINCH investigators (2006) The primary periodic paralyses: diagnosis, pathogenesis and treatment. Brain 129(Pt 1):8–17

Vicente R, Escalada A, Villalonga N, Texidó L, Roura-Ferrer M, Martín-Satué M, López-Iglesias C, Soler C, Solsona C, Tamkun MM, Felipe A (2006) Association of Kv1.5 and Kv1.3 contributes to the major voltage-dependent K^+ channel in macrophages. J Biol Chem 281(49):37675–37685

Volkers L, Rook MB, Das JH, Verbeek NE, Groenewegen WA, van Kempen MJ, Lindhout D, Koeleman BP (2009) Functional analysis of novel KCNQ2 mutations found in patients with Benign Familial Neonatal Convulsions. Neurosci Lett 462(1):24–29

Wallace RH, Scheffer IE, Parasivam G, Barnett S, Wallace GB, Sutherland GR, Berkovic SF, Mulley JC (2002) Generalized epilepsy with febrile seizures plus: mutation of the sodium channel subunit SCN1B. Neurology 58(9):1426–1429

Wallace RH, Wang DW, Singh R, Scheffer IE, George AL Jr, Phillips HA, Saar K, Reis A, Johnson EW, Sutherland GR, Berkovic SF, Mulley JC (1998) Febrile seizures and generalized epilepsy associated with a mutation in the Na^+-channel beta1 subunit gene SCN1B. Nat Genet 19(4):366–370

Wan J, Khanna R, Sandusky M, Papazian DM, Jen JC, Baloh RW (2005) CACNA1A mutations causing episodic and progressive ataxia alter channel trafficking and kinetics. Neurology 64(12):2090–2097

Wang HS, Pan Z, Shi W, Brown BS, Wymore RS, Cohen IS, Dixon JE, McKinnon D (1998) KCNQ2 and KCNQ3 potassium channel subunits: molecular correlates of the M-channel. Science 282(5395):1890–1893

Wang Z, Li H, Moss AJ, Robinson J, Zareba W, Knilans T, Bowles NE, Towbin JA (2002) Compound heterozygous mutations in KvLQT1 cause Jervell and Lange-Nielsen syndrome. Mol Genet Metab 75(4):308–316

Watase K, Gatchel JR, Sun Y, Emamian E, Atkinson R, Richman R, Mizusawa H, Orr HT, Shaw C, Zoghbi HY (2007) Lithium therapy improves neurological function and hippocampal dendritic arborization in a spinocerebellar ataxia type 1 mouse model. PLoS Med. 4(5):e182

Waxman SG, Dib-Hajj SD (2005a) Erythromelalgia: a hereditary pain syndrome enters the molecular era. Ann Neurol 57(6):785–788

Waxman SG, Dib-Hajj S (2005b) Erythermalgia: molecular basis for an inherited pain syndrome. Trends Mol Med 11(12):555–562

Webb J, Cannon SC (2008) Cold-induced defects of sodium channel gating in atypical periodic paralysis plus myotonia. Neurology 70(10):755–761

Weber MA, Nielles-Vallespin S, Essig M, Jurkat-Rott K, Kauczor HU, Lehmann-Horn F (2006) Muscle Na^+ channelopathies: MRI detects intracellular 23Na accumulation during episodic weakness. Neurology 67(7):1151–1158

Wei J, Hemmings GP (2006) A further study of a possible locus for schizophrenia on the X chromosome. Biochem Biophys Res Commun 344(4):1241–1245

Weiss J, Pyrski M, Jacobi E, Bufe B, Willnecker V, Schick B, Zizzari P, Gossage SJ, Greer CA, Leinders-Zufall T, Woods CG, Wood JN, Zufall F (2011) Loss-of-function mutations in sodium channel $Na_v1.7$ cause anosmia. Nature 472(7342):186–190

Weller DM, Noone J (1989) Mechanisms of arrhythmias: enhanced automaticity and reentry. Crit Care Nurse 9(5):42–67

Westenbroek RE, Ahlijanian MK, Catterall WA (1990) Clustering of L-type Ca^{2+} channels at the base of major dendrites in hippocampal pyramidal neurons. Nature 347(6290):281–284

Williams DM, Lopes CMB, Dantsker AR, Connelly HL, Matavel A, Uchi JO, McBeath E, Gray DA (2010) Molecular basis of decreased Kir4.1 function in SeSAME/EAST syndrome. J Am Soc Nephrol 21(12):2117–2129

Williams ME, Marubio LM, Deal CR, Hans M, Brust PF, Philipson LH, Miller RJ, Johnson EC, Harpold MM, Ellis SB (1994) Structure and functional characterization of neuronal alpha 1E calcium channel subtypes. J Biol Chem 269:22347–22357

Wu F, Mi W, Hernández-Ochoa EO, Burns DK, Fu Y, Gray HF, Struyk AF, Schneider MF, Cannon SC (2012) A calcium channel mutant mouse model of hypokalemic periodic paralysis. J Clin Invest. 122(12):4580–4591

Wu FF, Ryan A, Devaney J, Warnstedt M, Korade-Mirnics Z, Poser Escriva MJ, Pegoraro E, Yee AS, Felice KJ, Giuliani MJ, Mayer RF, Mongini T, Palmucci L, Marino M, Rüdel R, Hoffman EP, Fahlke C (2002) Novel CLCN1 mutations with unique clinical and electrophysiological consequences. Brain 125(Pt 11):2392–2407

Wulff H, Calabresi PA, Allie R, Yun S, Pennington M, Beeton C, Chandy KG (2003) The voltage-gated Kv1.3 $K(^+)$ channel in effector memory T cells as new target for MS. J Clin Invest 111(11):1703–1713

Xia H, Mao Q, Eliason SL, Harper SQ, Martins IH, Orr HT, Paulson HL, Yang L, Kotin RM, Davidson BL (2004) RNAi suppresses polyglutamine-induced neurodegeneration in a model of spinocerebellar ataxia. Nat Med 10(8):816–820

Xu X, Lee YJ, Holm JB, Terry MD, Oswald RE, Horne WA (2011) The Ca^{2+} channel beta4c subunit interacts with heterochromatin protein 1 via a PXVXL binding motif. J Biol Chem 286:9677–9687

Xu XJ, Zhang YH, Sun HH, Liu XY, Wu HS, Wu XR (2012) Phenotype and SCN1A gene mutation screening in 39 families with generalized epilepsy with febrile seizures plus. Zhonghua Er Ke Za Zhi. 50(8):580–586

Yang Y, Wang Y, Li S, Xu Z, Li H, Ma L, Fan J, Bu D, Liu B, Fan Z, Wu G, Jin J, Ding B, Zhu X, Shen Y (2004) Mutations in SCN9A, encoding a sodium channel alpha subunit, in patients with primary erythermalgia. J Med Genet 41(3):171–174

Yasuda T, Lewis RJ, Adams DJ (2004) Overexpressed Ca(v)beta3 inhibits N-type ($Ca_v2.2$) calcium channel currents through a hyperpolarizing shift of ultra-slow and closed-state inactivation. J Gen Physiol 123(4):401–416

Yost CS (1999) Potassium channels: basic aspects, functional roles, and medical significance. Anesthesiology 90(4):1186–1203

Yus-Najera E, Muñoz A, Salvador N, Jensen BS, Rasmussen HB, Defelipe J, Villarroel A (2003) Localization of KCNQ5 in the normal and epileptic human temporal neocortex and hippocampal formation. Neuroscience 120(2):353–364

Zerangue N, Jan YN, Jan LY (2000) An artificial tetramerization domain restores efficient assembly of functional Shaker channels lacking T1. Proc Natl Acad Sci USA 97(7):3591–3595

Zerr P, Adelman JP, Maylie J (1998) Characterization of three episodic ataxia mutations in the human Kv1.1 potassium channel. FEBS Lett 431(3):461–464

Zhang J, George AL Jr, Griggs RC, Fouad GT, Roberts J, Kwieciński H, Connolly AM, Ptácek LJ (1996) Mutations in the human skeletal muscle chloride channel gene (CLCN1) associated with dominant and recessive myotonia congenita. Neurology 47(4):993–998

Zhang L, Benson DW, Tristani-Firouzi M, Ptacek LJ, Tawil R, Schwartz PJ, George AL, Horie M, Andelfinger G, Snow GL, Fu YH, Ackerman MJ, Vincent GM (2005) Electrocardiographic features in Andersen-Tawil syndrome patients with KCNJ2 mutations: characteristic T-U-wave patterns predict the KCNJ2 genotype. Circulation 111(21):2720–2726

Zhang SH, Blech-Hermoni Y, Faravelli L, Seltzer Z (2008) Ralfinamide administered orally before hindpaw neurectomy or post-operatively provided long-lasting suppression of spontaneous neuropathic pain-related behavior in the rat. Pain 139(2):293–305

Zipes DP (2003) Mechanisms of clinical arrhythmias. J Cardiovasc Electrophysiol 14:902–912

Zhou T, Ko EA, Gu W, Lim I, Bang H, Ko JH (2012) Non-silent story on synonymous sites in voltage-gated ion channel genes. PLoS ONE 7(10):e48541

Zhuchenko O, Bailey J, Bonnen P, Ashizawa T, Stockton DW, Amos C, Dobyns WB, Subramony SH, Zoghbi HY, Lee CC (1997) Autosomal dominant cerebellar ataxia (SCA6) associated with small polyglutamine expansions in the alpha 1A-voltage-dependent calcium channel. Nat Genet 15(1):62–69

NFC Based Secure Mobile Healthcare System

Divyashikha Sethia[1], Daya Gupta[1],
Tanuj Mittal, Ujjwal Arora
Department of Computer Engineering
Delhi Technological University
New Delhi, India
[1] (divyashikha@dce.edu, dgupta@dce.ac.in)

Huzur Saran[2]
Department of Computer Engineering
Indian Institute of Technology
New Delhi, India
[2](saran@iitd.cse.ac.in)

***Abstract*— With the recent increase in usage of mobile devices especially in developing countries, they can be used for an efficient healthcare management. In this work, we have proposed a novel architecture for improving healthcare system with the help of Android based mobile devices with NFC [1] and Bluetooth interfaces, smartcard technology on tamper resistant secure element (SE) for storing credentials and secure data, and a HealthSecure service on a hybrid cloud for security and health record management. The main contribution of this paper is proposal of applications for i) Secure Medical Tags for reducing medical errors and ii) Secure Healthcard for storing Electronic Health Record (EHR) based on Secure NFC Tags, mobile device using NFC P2P Mode or Card Emulation Mode. We have also briefly mentioned a basic security framework requirement for the applications. Since NFC NDEF format is prone to security attacks [2], we have utilized low level APIs on Android based mobile devices, to securely access NFC tags such as MIFARE Classic tags with NFC-A (ISO 1443-3A) properties. Simple touch of NFC enabled mobile devices can benefit both the patient as well as the medical doctors by providing a robust and secure health flow. It can also provide portability of devices and usability for health management in emergency situation, overpopulated hospitals and remote locations.**

Keywords— mobile based secure healthcare; NFC in healthcare; e-Health card; medical object identifier; RFID; MIFARE Classic; java card; secure element; patient health record

I. INTRODUCTION

Robust healthcare is a requirement for both developed countries, where the cost of healthcare is high and security and privacy are critical issues and developing countries like India, where there is a mass population to handle in hospitals and robust healthcare procedures are required. An efficient, reliable, robust and secure health flow is important to manage patients, their health records smoothly and for the right care to reach to the patient at the right time.

Identification of objects for secure medical procedures is very essential for a secure workflow. For example, secure identifiers on the medicines can help healthcare professional to administer correct medication to a patient to reduce errors.

Along with this issue the Patient Health Record management is important both for patients as well as hospital management. In developing countries like India, there is no centralized management of health records and records are mostly retained by patients in a paper format OPD (Out Patient Department) card, which is both cumbersome to maintain along with the paper based reports and also unreliable. Work is still being done for a secure, electronic patient record management as a Healthcard on a Smartcard in developing countries like India [3] and other nations [4]. Most of the public healthcare services issue a Healthcard on a Smartcard, which retains just the primary information of the patient. All other records are stored on a centralized medical storage server. In developing countries like India, there are challenges like costly infrastructure, connectivity problem for accessing centralized medical records and acceptability of the Healthcard uniformly across different hospitals.

With the recent advancements in mobile devices involving secure credential storage, larger storage capability, wireless communication interfaces and computational power, they can be used in healthcare for not only gathering vital health parameters, as in the Body Area Networks, but also for healthcare management. Privacy and security is a very important aspect of healthcare [5].We propose that the patient should retain all or major patient's EHR electronically, on a Healthcard that is either on a external Smartcard accessible by a mobile device or on the mobile device retained by a patient. A Healthcard retained on a mobile device can retain the entire EHR including reports and tests. Permitted portion can be accessed securely by an authorized medical provider by a simple tap of mobile device. Due to the computational capabilities the records can be summarized and organized for a quicker action to be taken.

Healthcard on a mobile device can be helpful in developed countries also, where healthcare cost is high and privacy and security are critical. The patient can retain all records and can manage the privacy concerns of which portion of the records are to be accessible. The records can occasionally be synced to the central server for backup or storing past history. EHR on Healthcards retained by people can also help in providing the right care in an emergency situation when the patient is unconscious. It can also help determine location of the patient in case of emergency through location service on recent mobile devices. The business logic of using Healthcard on mobile devices can be beneficial to a medical professional since it can securely identify patients using simple portable mobile devices and also get a concise health report. A simple tap of NFC enabled mobile device, will not only improve the workflow of medical professionals but also prove to be beneficial in emergency and chaotic conditions like mass populated

978-1-4799-3635-9/14/$31.00 ©2014 IEEE

hospitals. Simplified workflows will result in faster and more efficient patient-doctor interaction.

The main contribution of this paper is proposal of a robust secure healthcare architecture using Android based mobile device with Near Field Communication (NFC) [1] and Bluetooth interfaces and smartcard technology on Secure Element (SE) for retaining security credentials and EHR. NFC is already being used for applications related to financial payments and ticketing. We propose a novel usage of NFC enabled mobile devices to access secure external medical tags for identifying medical objects like medicines and patient Healthcards. The Healthcard could be on an external tag or retained on the patient mobile device using NFC P2P or card emulation modes. This can provide greater control of sharing personal records with any authorized doctor by a simple tap of mobile devices. Bluetooth can be used along with NFC to provide faster access of bulky data from mobile device.

There is a strong cryptographic framework required for healthcare data. We have briefly mentioned the security requirement in section VII. However the detailed design, threat analysis, implementation and testing of the framework is still in progress and is beyond the scope of this paper.

The mobile devices and Healthcards can be authorized by a HealthSecure service on a hybrid cloud, to provide services for enhanced security and extended storage for health records. We plan to work on the architecture of the Healthsecure service in the future.

The paper is broadly divided into seven sections. Section II provides an overview of technologies for NFC, NFC tags, SE and Java Card. In section III we discuss about the proposed architecture. Section IV illustrates the implementation part followed by a brief overview of the security framework requirement in section V. In section VI we discuss briefly about some related work, followed by section VII which presents the conclusion and future work.

II. TECHNOLOGY

NFC [1] is an upcoming wireless technology which provides simple interfaces for device to device communication as well as access to NFC, RFID and smartcard tags [6]. NFC enabled mobile device can operate in three modes: i) Reader mode: in which device can read and write to NFC based passive tags. ii) Peer to Peer (P2P) mode in which NFC devices can interact and exchange information with each other iii) Card emulation mode: in which NFC device can operate as a contactless card.

NFC tags are of different types and use NDEF (NFC Data Exchange Format) [6] for storing and sending data. NFC tags must have a secure read and write access for critical applications such as those related to healthcare. NDEF provides no protection against data manipulation, overwrite protections and digital signature records cannot avoid malicious modification of tags [2]. Hence we utilize MIFARE Classic 1 K tags [7], which employ a proprietary protocol compliant to parts of ISO/IEC 14443-3 Type A, and write raw data using NFC-A (ISO 14443-3A) [8] properties for improved security. The MIFARE Classic 1K tag offers 1024 bytes of data storage, split into 16 sectors. Each sector is protected by two different keys, called key A and key B for secure access.

NFC enabled mobile devices have a secure element (SE) which is a secure microprocessor (a smart card chip) that includes a cryptographic processor to facilitate transaction with authentication and security, and provides secure memory for storing applications and credentials. It comes in different form factors such as embedded, microSD card or a UICC (SIM) card [9]. Due to simplicity of accessibility we have used SWP enabled microSD card (by GO-Trust [10]) as a SE to manage cryptographic keys as well as patient medical records. SWP is a contact based protocol between Contactless frontend (CLF) and UICC. It is Java Card 2.2.2 compliant.

Java Card [11] is a technology which enables Java based applets to run on smartcards with very limited memory and processing capabilities and provides data encapsulation, firewall and cryptography. The smart card specification standards [12], ISO/IEC 7816 for contact and ISO/IEC 14443 for contactless, specify that communication between a host application and a smart card is done through Application Protocol Data Units (APDUs).

III. PROPOSED APPLICATION MODELS

We have proposed an architecture for NFC based secure healthcare as illustrated in Fig. 1 for i) secure medical identifiers as in flow steps 1.1 to 1.5 and ii) Healthcard retaining EHR using Android mobile devices as in flow steps 2.1 to 2.5. We have proposed a secure healthcare service like HealthSecure on a hybrid cloud to which all hospitals can subscribe. The HealthSecure hybrid cloud provides service for maintaining Cryptographic servers for secure framework and Storage server to provide backup as well as space for extended EHR. $Mobile_{ADMIN}$ is a mobile device of an authorized medical admin. $Mobile_{PAT}$ is the patient's mobile device with the Healthcard and $Mobile_{DOC}$ is the doctor's mobile device. Since a larger screen would be better suited to view and update the health records, $Mobile_{DOC}$ could either be an NFC enabled tablet, for portability, or a laptop with external smartcard reader. K_A and K_B are the read and write access keys respectively for a secure tag based on MIFARE Classic. For NFC P2P based and card emulation based Healthcards, we use patient's and doctor's set of public and private keys, which are K_{PUBPAT}, K_{PRIPAT} and K_{PUBDOC},K_{PRIDOC} respectively. A symmetrical shared key K_{SH} is used for encrypting data.

Hospital administration has an application for securely reading/writing with a mobile device, $Mobile_{ADMIN}$, to manage smartcard based tags and patient Healthcards. $Mobile_{ADMIN}$ can register with the proposed HealthSecure cloud service on a hybrid cloud, which can issue security keys for our architecture. The mobiles use SE and simple interfaces of NFC and Bluetooth for credential storage and communication. We discuss the architecture of the applications briefly in the following subsections and give the details of the implementation in section IV and security framework requirement in section V.

A. Secure Medical Object Identification using NFC Tags

Reliable medical object identifiers are important for reducing errors in the hospital workflow, like giving correct

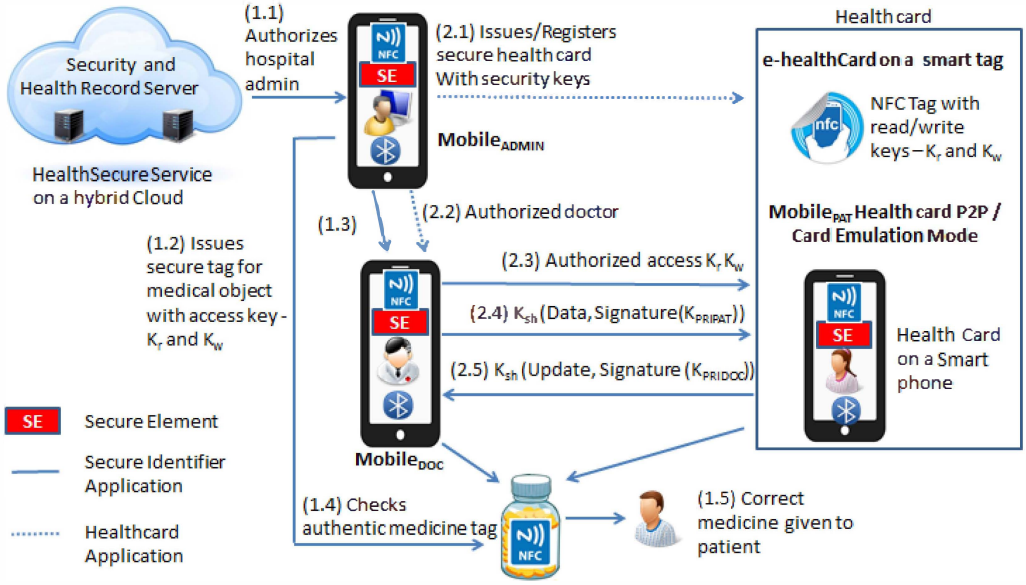


Fig. 1. NFC Based Secure Healthcare Architecture

medicine to a patient [13]. We propose architecture of an application for issuing secure identifiers to reduce the error and also to prevent security attacks like modification, repudiation and masquerading. The secure NFC passive tags have been used for identifiers, specifically MIFARE Classic. Bluetooth Low Energy (BTLE) stickers [14] have lately been used to identify objects. But since they require a dedicated battery to operate, NFC passive tags are cheaper for identifiers to be used in healthcare. As discussed in section II, NFC tags with NDEF format are prone to security flaws [2]. Hence basic NFC-A interface can be used to access smartcards from a mobile device. A valid mobile reader must have security key K_R for read access and a valid writer must have security key K_W for update access. The tag is issued by a healthcare admin mobile device, $Mobile_{ADMIN}$, which has registered to a HealthSecure service. It retains security keys in its SE for issuing tags. To enhance security, the access keys of the tag could be updated on a periodic basis for retaining secure IDs on the medical objects. Fig. 1, steps 1.1 to 1.5, shows the workflow of secure tag identifiers in bold. Along with medical identification records, information related to timestamp can also be updated.

B. e-Health Card using NFC Tags

The secure tags used for application in III-A, are used for a different application for storing EHR on Healthcard of a patient. This is similar to a smartcard based Healthcard. But here we suggest smartcards that can be securely and easily be accessed using mobile devices. The tag could retain patient identification information along with emergency information, insurance information and health records. The tag could be organized into different sections, each administered separately by different set of security access keys. Similar to the secure tag application, this card can be issued and updated by an authorized health admin mobile device $Mobile_{ADMIN}$. A patient can register at the $Mobile_{ADMIN}$ and then later show to an authorized doctor with $Mobile_{DOC}$ in an OPD which would have the required access keys K_R and K_W for reading and updating the health records respectively. All NFC information can be retained with a timestamp. Due to limitation of space on the card, it can only retain recent health records. Detailed health records can be retained on a storage server of the HealthSecure service on hybrid cloud. At the end of the visit the patient can present the tag back to the administrator to tap and store his visit detail on the hybrid cloud. At any point of time if patient's past records are required, they can be retrieved over secure wireless interface (like HTTPS) from the hybrid cloud, using the patient ID on the tag. This application will help the patient to retain the recent health records on a cheap yet secure tag equivalent to a smartcard.

C. e-Health Card based on P2P NFC mode

This application architecture is based on retaining a Healthcard on a mobile device using NFC P2P mode. The EHR is retained on the mobile device in a secure region instead of NFC tag as in III-B. The patient can tap his mobile device onto the doctor's mobile device to exchange his records using NFC NDEF format. The doctor can read and update the records and tap them back onto the patient's mobile device. Both patient and doctor register for the OPD session with the health admin, $Mobile_{ADMIN}$, to get secure keys. The patient's public and private keys K_{PUBPAT}, K_{PRIPAT} and doctor's public and private keys K_{PUBDOC}, K_{PRIDOC} get stored on the SE of their respective mobile devices for the OPD session.

This Healthcard offers more storage space as compared to what a smartcard based tag can provide as in application III-B. It also ensures that only the permitted records of the patient are accessed by an authorized doctor, thus retaining security and privacy of the patient. NFC P2P mode can be utilized for information exchange. But very large health records exchanged over NFC can be slow due to the low data rate of NFC. Bluetooth can be used along with NFC for exchange of larger

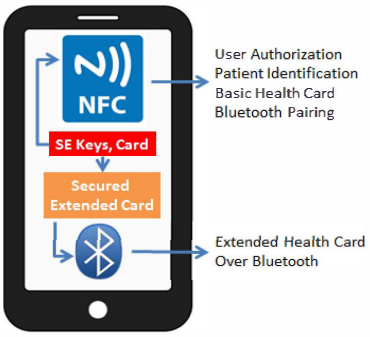


Fig. 2. Proposed Card emulation architecture

health record data. A basic security framework requirement is discussed in section V.

D. e-Health Card based on NFC card emulation

In this application architecture, Healthcard is retained on a mobile device using card emulation and Java card applets installed on the SE. We propose usage of a SE in the form of an SWP enabled microSD card as provided by GoTrust [10], which can be issued to the patient by HealthSecure service. Java Card applet can be used to authenticate and authorize the reader to access and update the health records using NFC SWP protocol. Since the SE has limited space, it can only retain part of the health records. The remaining health records can be retained outside the SE region on the SD card in a secure manner. The Card on the $Mobile_{PAT}$ can be accessed externally by a PC/SC reader that is attached to $Mobile_{DOC}$. Since the SE has limited space, an extended card consisting of past records and other health information, like images and reports, can be stored in encrypted format on an insecure region. Hence this Healthcard is different from a standard plastic smartcard used for Healthcard in the previous scenario. Since NFC has lower data rate, Bluetooth can be used to access the extended card. The Java card applet can be used to initiate Bluetooth pairing between mobile devices. This Healthcard is most secure and can also be used to retain larger information on the mobile device and is similar in idea to the Wireless Medical Card [17]. Fig. 2 shows the proposed card emulation architecture. A basic security framework requirement is discussed in section V.

IV. IMPLEMENTATION

We have developed applications for both Android devices, using Android APIs, and administrative server, using PHP and MySQL, for secure, reliable and robust healthcare system. Mobile applications have been tested on Google Nexus 7 and Samsung Galaxy S3 devices. We have used MIFARE Classic 1K tags for reading and writing data using APIs in Android framework (Android 2.3.3 and above). The Android framework provides android.nfc.tech package, which contains necessary classes and methods to enable interaction with tags. We have used a SWP Secure microSD card (by GO-Trust), which provides a microSD based Java Card 2.2.2 solution. The card supports running Java Card applets on a hardware-backed SE. It also provides a contactless interface (ISO 14443) via SWP which can be used to interact with compliant PC/SC readers. We have tested it using a Samsung Galaxy S3 (i9300, by Samsung) mobile device with Android 4.1.2. The card can be accessed from an authorized Android application developed using Go-Trust library. Since the card supports Global Platform 2.1.1 [15], the installation can be done using custom Global Platform APDUs. Java card applets have been developed to store credentials for security framework and for card emulation mode.

Implementation of Security framework and hybrid cloud service is in progress and will be tested and deployed in the field in our future work.

V. SECURITY FRAMEWORK REQUIREMENT

There is a strong security framework required for the healthcare management. It is different from the financial data security which is small in size and is handled by a set of trained professionals with standardized models [16]. The healthcare data can be large in size as in a Healthcard with entire HER in section III.D. Also the health card could be accessed by various persons: patient, medical professional, emergency person and insurance. The patient should be able to securely manage the access control of the EHR. We provide a brief overview of a basic security framework requirement for the application of Health card on a patient mobile device using NFC P2P or Card Emulation mode as in Figure 3. There is a requirement of confidentiality, integrity, mutual authentication, access control of EHR, privacy threats leading to identity thefts and insurance security breach [5].

The security framework involves various entities. A cryptographic server is used to generate, verify and store security keys. An administrator is present to issue Healthcards / tags and register patients/doctors. Mobile devices used by doctors are equipped with a Doctor App and a secure element (Doctor SE). Healthcard used by patients is called Patient card which in this case is using a NFC P2P or card emulation mode. The SEs involved, like Doctor SE, run a Java Card applet to manage cryptographic keys as well as patient medical records. Since the health card could be accessed by various persons: patient, medical professional and emergency person, they could use the concept of shared key based on Attribute Based Encryption [18]. The patient could access the card using combination of Patient key in the form of a PIN and Biometrics. There could be a separate Doctor PIN for doctor and a super key for emergency team when patient is unconscious. In case of loss of mobile devices the keys which are maintained by the HealthSecure service can be invalidated.

We have suggested usage of Public Key Infrastructure (PKI) for the security framework. The security flow consists of 1. Healthcard personalization 2. Mutual Authentication between the patient and the medical doctor to assure the correct patient is appearing before an authorized doctor and there is no relay attack 3. Access control for data viewable by the doctor 4. Secure healthcard retrieval and updation.

There is an initial phase of personalization in which the Patient Card and the Doctor SE get a unique identification ID (UID_{PAT} and UID_{DOC}) and a set of public and private keys (K_{PUBPAT}, K_{PRIPAT} and K_{PUBDOC}, K_{PRIDOC}) from the security server based on the respective card ID and/or secure element ID. This phase ensures that both the Patient Card and the

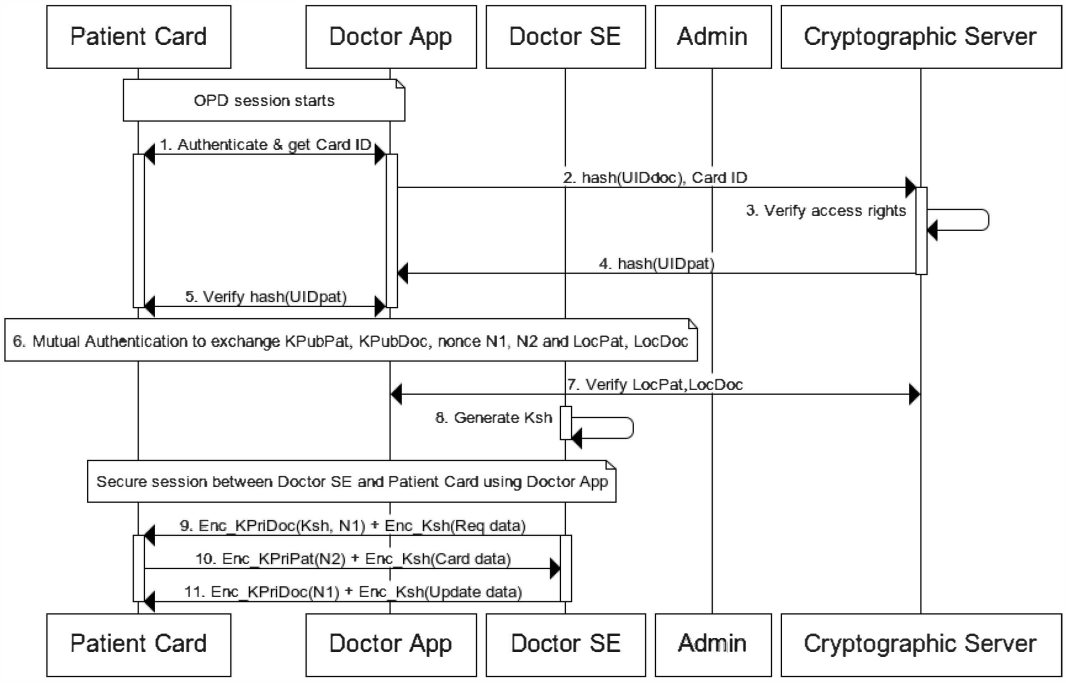


Fig. 3. Sequence diagram of basic security framework

Doctor SE have their respective UIDs and keys securely stored locally.

Now the OPD session can start between the patient and the doctor as detailed under Fig. 3. The Doctor App authenticates the Patient Card and retrieves the card ID. The card ID along with hash (UID_{DOC}) is sent to the server to verify access rights of doctor. Once verified, the server returns hash (UID_{PAT}), which is used to verify the authenticity of doctor by the patient. Now, as given in step 6, the patient and doctor mutually authenticate to exchange respective public keys, K_{PUBPAT}, K_{PUBDOC} and randomly generated nonce, N1 and N2 by patient and doctor SE respectively using algorithm suggested in [19], to prevent man in the middle attack. The location of patient is also shared with doctor, and with the help of server, validation is done to make sure both are same to avoid relay attacks. Loc_{PAT} and Loc_{DOC} could be GPS location or a related parameter in the ambience gathered from audio or light sensors on the mobile devices [20]. Now a symmetric key K_{SH} is generated by the Doctor SE for efficient encryption of health data and secure communication is held (steps 9 to 11). The doctor sends K_{SH} along with its request securely and receives the data. Similarly, an update, like a prescription, can be sent back securely to the Patient Card. A encrypted and signed data communications ensures confidentiality and integrity. This a basic framework requirement and we are working on designing a stronger framework as mentioned in section VII.

VI. Related Work

Emergency NFC tags [21] retain patient medical emergency information. But the work does not consider write protection and reusable NFC tags. NFC mobile devices have been used for storing credentials to be used for billing and identity [22]. We propose using it for healthcare applications with credentials and a much stronger security requirement since it is accessed by number of people and the quantity of data could be large. Smart poster [23] proposes using secure NFC tags since "NFC tags are vulnerable to spoofing as well as cloning", with a web server to securely retain the details of the poster. An application using NFC to track patients with pneumonia has been deployed in Karachi [24]. NFC based tags have also been used to tag medicines to reduce medical errors [13]. None of this work takes care of NFC tag security. We have suggested a novel manner of secure tags based on NFC-A protocol for our applications based on secure NFC tags. In our previous work [25] we have used NFC tags for reliable patient records and automating the health flow with Body Sensors. We have further expanded the work for new applications of NFC enabled devices for health flow data management with medical identifiers and Healthcards. The applications suggested in this paper for the improved workflow management with NFC enable mobile devices are unique to the best of our knowledge. Secure records can be stored on a mobile device for emergency purpose [18] using concept of shared keys. But they do not use any hardware tamper resistant device. Work has been done [17] for a wireless medical card with NFC and high speed interface with bulk memory card. Our work is different since we have proposed a similar larger card as in section III.D using a hardware tamper resistant SE based on a microSD card on a mobile device with NFC and Bluetooth interface.

VII. Conclusion and Future Work

In this work, we have proposed applications based on NFC enabled Android mobile devices for improving healthcare process for secure medical object identification and patient

Healthcard on an external tag or mobile device itself. The applications are simple to use with a simple touch of NFC for secure communication. This will improve the health flow in crowded hospitals of developing countries like India as well as of developed nations. The business model will benefit the patients as well as medical professional since they can use the commonly retained mobile devices conveniently. The cost of the architecture can be reduced by using microSD cards or UICC cards with inbuilt NFC antenna. These forms of SEs can be issued as Healthcards on mass scale to reduce the cost and to be operational on non NFC mobile devices. The proposed architecture can be used for applications other than healthcare with secure identifiers and secure transfer of large data between devices.

Although MIFARE Classic security algorithm Crypto1 has been broken [26], any other secure smartcard based tags like MIFARE DESIRE could be used in future based on the availability of the APIs. We have suggested a basic security framework requirement in this paper. A detailed design, implementation, testing and field deployment of the he security framework is in progress and will be addressed in our future work. We also plan to enhance the security framework using identity encryption using zero knowledge proofs and attribute based encryption for shared key management, access control of health data, and delegation of rights by patient to other trusted person for collection of health data. The current security framework is based on Public Key Infrastructure. Identity based Encryption and Attribute Based Encryption techniques can also be compared in future. We need to work on the security issues of NFC and Bluetooth for accessing secure Healthcard in future for security threats of theft, cloning, man in the middle and relay attacks and loss of a mobile device.

We plan to design architecture of the HealthSecure service on a hybrid cloud in the future with replicated Kerberos cryptographic servers and a Hospital Information System for backup of EHR. We also need to compare NFC and BTLE for card emulation. NFC has higher energy requirement, compared to BTLE, when it is in a reader mode to activate the passive tag. But NFC has an advantage of smoother interfaces and getting initiated by a simple tap, while BTLE requires pairing.

REFERENCES

[1] Vedat Coskun, Busra Ozdenizci and Kerem Ok, "A Survey on Near Field Communication (NFC) Technology", J. Wireless Personal Communications: An International Journal, vol. 71, pp. 2259-2294, 2013.

[2] M. Roland and J. Langer, "Digital Signature Records for the NFC Data Exchange Format", IEEE Proceedings of the Second International Workshop on Near Field Communication (NFC), pp, 71-76, 2010.

[3] Rashtriya Bima Yojana, http://en.wikipedia.org/wiki/Rashtriya_Swasthya_Bima_Yojan

[4] Smart Card Technology in U.S. Healthcare: Frequently Asked Questions, http://www.smartcardalliance.org/resources/pdf/Smart_Card_Technology_in_Healthcare_FAQ_FINAL_096012.pdf, 2012

[5] Sasikanth Avancha, Amit Baxi, and David Kotz, "Privacy in mobile technology for personal healthcare", ACM Computing Surveys (CSUR), vol. 45 Issue 1, article 3, 2012.

[6] NFC Forum Tedchnical Specifications, http://www.nfc-forum.org/specs/spec_list/ndefts

[7] MIFARE Classic 1K specification document, http://www.nxp.com/documents/data_sheet/MF1S50YYX.pdf

[8] NFCA on Android, http://developer.android.com/reference/android/nfc/tech/NfcA.html

[9] Mobile/NFC Security Fundamentals Secure Elements 101, http://www.smartcardalliance.org/resources/webinars/Secure_Elements_101_FINAL3_032813.pdf, 2013

[10] GO-Trust® Secure microSD Java, http://www.go-trust.com/products/microsd-java/

[11] Java Card™ Platform Security, http://www.oracle.com/technetwork/java/javacard/documentation/javacardsecuritywhitepaper-149957.pdf

[12] Smart Card Standards for contact and contactless interfaces, http://www.smartcardalliance.org/pages/smart-cards-intro-standards

[13] Lahtela, A., Hassinen, M.and Jylha, V., "RFID and NFC in healthcare: Safety of hospitals medication care", IEEE proceedings on Pervasive Computing Technologies for Healthcare, pp. 241—244, 2008.

[14] Saroj Kumar Panigrahy, Sanjay Kumar Jena, and Ashok Kumar Turuk, "Security in Bluetooth, RFID and wireless sensor networks", ACM Proceedings on 2011 International Conference on Communication, Computing & Security, pp. 628-633, 2011.

[15] Global Platform Specifications, http://www.globalplatform.org/specificationscard.asp

[16] Why healthcare IT security is harder than the rest, http://www.csoonline.com/article/print/693941

[17] Stefan Krone, Bjoern Almeroth, Falko Guderian and Gerhard Fettweis, "Towards A Wireless Medical Smart Card", IEEE Design, Automation & Test in Europe Conference & Exhibition,pp 1483 – 1488, 2012

[18] Ryan W. Gardner, Sujata Garera, Matthew W. Pagano, Matthew Green, and Aviel D. Rubin, "Securing medical records on smart phones", Proceedings of the first ACM workshop on Security and privacy in medical and home-care systems, pp. 31-40, 2009.

[19] Yun-Seok Lee, Eun Kim, and Min-Soo Jung, "A NFC based Authentication method for defense of the Man in the Middle Attack", 3 rd International Conference on Computer Science and Information Technology (ICCSIT'2013) January 4-5, 2013 Bali, Indonesia

[20] Tzipora Halevi, Di Ma, Nitesh Saxena, and Tuo Xiang, "Secure Proximity Detection for NFC Devices Based on Ambient Sensor Data", Computer Security – ESORICS 2012. Lecture Notes in Computer Science, vol 7459, pp 379-396, 2012.

[21] Sebastian Dunnebeil, Felix Kobler, Philip Koene, Jan Marco Leimeister, and Helmut Krcmar, "Encrypted NFC Emergency Tags Based on the German Telematics Infrastructure", IEEE proceedings on Near Field Communication (NFC), 2011 3rd International Workshop, pp. 50-55.IEEE Press, 2011.

[22] Gergely Alp´ar, Lejla Batina, and Roel Verdult, "Using NFC phones for proving credentials", 16th Measurement, Modelling, and Evaluation of Computing Systems and Dependability and Fault Tolerance. LNCS, vol. 7201, pp. 317-330. Springer Verlag, 2012.

[23] Jason Wu, Lin Qi, Ram Shankar Siva Kumar, Nishant Kumar, and Patrick Tague, "S-SPAN: Secure Smart Posters in Android using NFC", IEEE International Symposium on World of Wireless, Mobile and Multimedia Networks, pp. 1-3, IEEE Press, 2012

[24] Adam Marcus_, Guido Davidzony, Denise Law, Namrata Verma, Rich Fletcher, Aamir Khanz and Luis Sarnenta, "Using NFC-enabled Mobile Phones for Public Health in Developing Countries", IEEE Proceedings on First International Workshop on Near Field Communication, pp. 30-35. 2009.

[25] Divyashikha Sethia, Shantanu Jain and Himadri Kakkar, "Automated NFC enabled Rural Healthcare for reliable patient record maintenance", Proceedings of Global Telehealth Conference, vol. 182, pp. 104-113, 2012.

[26] Gerhard de Koning Gans, Jaap-Henk Hoepman, and Flavio D. Garcia, " A Practical Attack on the MIFARE Classic", Smart Card Research and Advanced Applications. LNCS, vol. 5189, pp. 267—282, 2008.

International Journal of Advanced Science, Engineering and Technology.
ISSN 2319-5924
Vol 3, Issue3, 2014, pp38-43
http://www.bipublication.com

Non-Blind Audio Watermarking Scheme Based on Empirical Mode Decomposition

Jeebananda Panda[1], Karan Raj Gera [2], and Asok Bhattacharyya [3]

[1,3] Deptt of Electronics and Communication Engineering
Delhi Technological University. Delhi, India
[2] Deptt of Electronics and Communication Engineering
S.V National Institute of Technology. Surat, India
[1]jpanda@dce.ac.in, [2]u10ec017@eced.svnit.ac.in, [3]asok_bhattacharyya@yahoo.com
[*]Corresponding author: Email: jpanda@dce.ac.in, Tel: +91 9868417813;

[Received-03/06/2014, Published-21/07/2014]

ABSTRACT:

In this paper, an audio watermarking scheme based on Empirical Mode Decomposition (EMD) is proposed. The audio signal is separated into segments, which, by EMD, are decomposed adaptively to produce intrinsic mode functions (IMFs) that can be fully described by their extrema. These points of the last IMF are then encoded with the watermarking and synchronization bits through Quantization Index Modulation (QIM) embedding technique. Though, watermarking is done on the last IMF, the extraction process is non-blind and can be carried out on the lower order IMFs. The percentage similarity between the extracted watermark and the original watermark decreases as we extract from increasing order of IMFs. This gives an added advantage of extraction of watermark from multiple IMFs in case of masking of a particular IMF. Through rigorous simulations, the algorithm is proven to be robust against various attacks like additive noise, MP3 compression, high pass filtering, low pass filtering, and cropping.

Keywords: Empirical Mode Decomposition, Intrinsic Mode Function, Non-blind Extraction, Quantization Index Modulation, Digital Audio, Binary Watermark.

[I] INTRODUCTION

With the proliferation of the development of Internet and wireless networks, multimedia security and Digital Rights Management (DRM) have received a great deal of attention. Conventional cryptographic techniques do provide security against unauthorized access of the media but once the media has been decrypted, there is no way to track back its reproduction. Thus, Digital watermarking has been viewed as a plausible compliment to the cryptographic methods, for

security against unauthorized duplication and redistribution of these multimedia data [1].

The digital audio watermark must be imperceptible, robust against attacks and should have enough data capacity. Imperceptibility and robustness are the most important of them all, but they are also incompatible. A good scheme must compromise on each other, for which, many watermarking schemes have been proposed. As, the watermark embedding process requires the lowest frequency possible in the audio signal, different methods to separate the frequencies have been considered. In [2], the watermarking bits are embedded into the peaks of the frames on which Discrete Fourier Transform (DFT) has been performed. The use of Fourier transformation, though being the most valuable tool in spectral data analysis, is refrained, as it is limited only to linear systems and stationary data series. Wavelet transform has also been considered for the same. In [3], Discrete Wavelet Transform (DWT) is used to decompose the host audio signal into several multi-resolution sub-bands. The highest resolution sub-band is chosen to embed the watermarking bits. This scheme proves to be promising considering the limitations of the fourier transform, but yet poses a limitation: the basic functions of wavelet transformation are fixed and do not necessarily match the shape of the data series in every instant in time. To overcome this barrier, Empirical Mode Decomposition (EMD) has been introduced that observes non-stationary signal that may or may not be derived from linear systems [4]-[6]. The basic concept of the EMD method is to expand any oscillatory signal into a set of functions, called the Intrinsic Mode Functions (IMF), defined by the signal itself. This process is called the sifting process. According to EMD, any signal can be expanded as:

$$x(t) = \sum_{j=1}^{C} IMF_j(t) + r_C(t)$$

considered

$r_c(t)$

Where C is the number of IMFs and denotes the final residual. The IMFs bear some specific properties; the first being that the number of zero crossings and extrema points are either equal or differ by unity, and the second being that the envelopes defined by the local maxima and minima, respectively, are locally symmetric around the envelope mean. Low frequency components, such as higher order IMFs are signal dominated [7] which makes them good locations for watermark placement as their alteration can cause substantial degradation of the signal. On the other hand, watermarks embedded into lower order IMFs are most vulnerable to attacks such as additive noise, MP3 compression, filtering, cropping etc making the watermark extraction difficult.

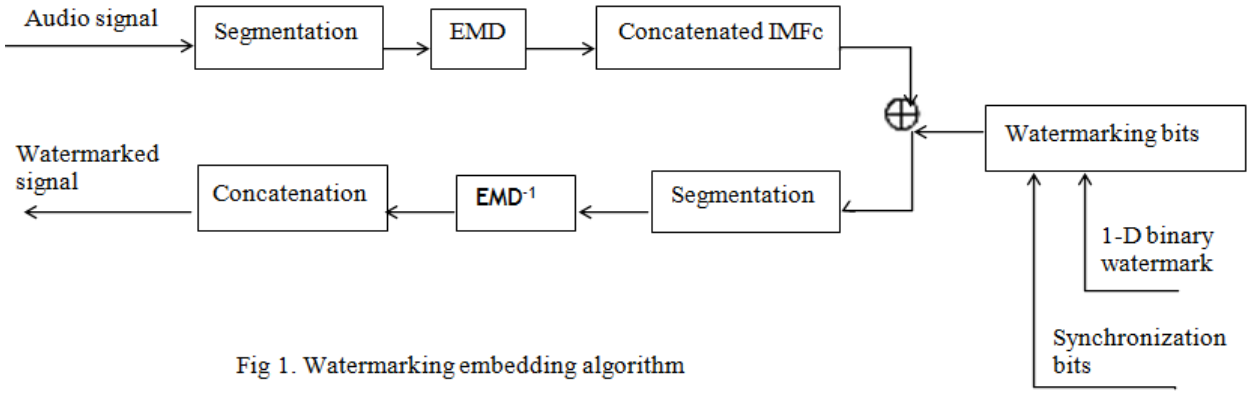


Fig 1. Watermarking embedding algorithm

The usage of a binary watermark is based on the fact that there are only two values to resort to with respect to a decided threshold value. This threshold value can be adaptive as in [11]. In our work, adaptive threshold is used which changes with respect to the IMF order.

In [8], the EMD process is carried out on the frames of the host audio signal. The embedding

and the extraction process are performed on the higher order IMFs with a blind watermarking scheme. Whereas, during the EMD process, as the frequency selection is dependent on the standard deviation, there is a relation established between the magnitude and frequency of a signal. Hence, during the extraction process, the watermark spikes are shifted to the lower order IMFs, with their strength decreasing with the increase in the order of the IMF. Thus, in this paper, the extraction process is performed on the lower order IMFs in a non-blind fashion to yield satisfactory results in case of attacks.

[II] THE WATERMARK EMBEDDING ALGORITHM

The basic concept in embedding, as stated in [8], is that the watermark image is first converted to the binary form so that it can be represented by a matrix $M \in \{0,1\}$. It is then converted into a 1-D array $M' \in \{0,1\}$, which is combined with the synchronization bits to form the watermark array $A \in \{0,1\}$. The synchronization code is a stream of bits $\in \{0,1\}$ chosen, to differentiate between two consecutive message bits. The basic steps to embed the watermark, as shown in fig. 1, are explained as follows:

1. Divide the original audio signal (samples) into segments by considering specific number of samples for each segment. In this case, a total of 88200 samples of the audio signal have been divided into 200 segments of 441 samples each.
2. Perform the Empirical Mode decomposition separately on all the segments separately.
3. Embed P times the binary array A into the extrema points of the last IMF (IMFc) of all the segments concatenated together, by QIM [9]:

$$e_i^* = \begin{Bmatrix} \lfloor e_i / S \rfloor .S + \text{sgn}(3S/4) \rightarrow m_i = 1 \\ \lfloor e_i / S \rfloor .S + \text{sgn}(S/4) \rightarrow m_i = 0 \end{Bmatrix}$$

e_i denotes the extrema of the host audio signal and e_i^*, that of the watermarked signal. sgn function denotes '+' if e_i is a maxima, else it represents a '-' operation. $\lfloor \ \rfloor$ is the floor function used when e_i is a maxima, else the ceil function, is used. S is an optimum embedding strength [10].

4. Separate the concatenated watermarked IMFc into its respective segments.
5. Reconstruct segments by EMD^{-1} using the modified last IMFs of each segment and concatenate them to retrieve the watermarked signal.

[III] PROPOSED NON BLIND WATERMARK EXTRACTION ALGORITHM

The proposed extraction process is based on non-blind method, and is carried out on the lower order IMFs. As stated earlier, the dependency on standard deviation causes the magnitude of the watermarked spikes to move up to the higher frequencies from where it can be successfully extracted. As the deviation reduces as the IMF order increases, the strength of the watermark also

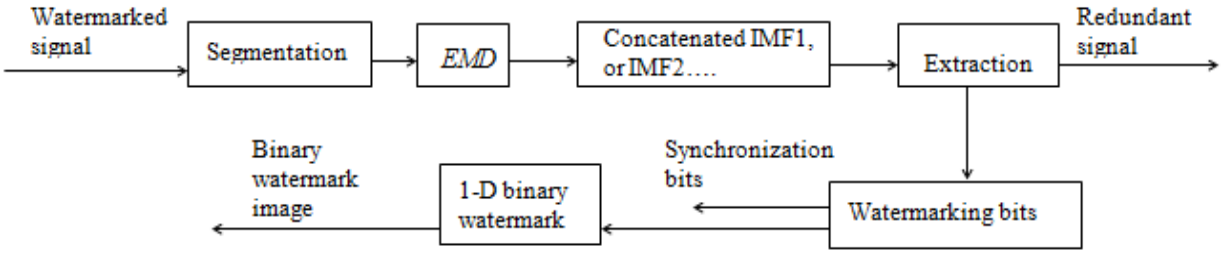


Fig 2. Watermark extraction algorithm

reduces. The basic steps involved in the extraction process, as shown in fig. 2, are explained as follows:

1. Divide the watermarked signal into segments as discussed previously.
2. Perform EMD on each segment to obtain the IMFs.
3. Concatenate the IMF order from which the watermark is to be extracted, of all the segments, from which extrema points $\{e_i^*\}$ is to be extracted.
4. Collect the extrema points of the corresponding IMF order of all the segments from the original audio signal as $\{e_i\}$.
5. Obtain $\{m_i^*\}$ from $\{e_i^*\}$ by the following equation,

$$m_i^* = \begin{cases} 1 & if\ e_i^* - e_i \geq \text{sgn}\dfrac{S}{2^{j+1}} \\ 0 & if\ e_i^* - e_i < \text{sgn}\dfrac{S}{2^{j+1}} \end{cases}$$

S is again the embedding strength and j denotes the IMF order with the sgn function having its usual meaning as stated earlier. The value of $j = 2$ for IMF 1 as an exception.

6. Obtain different sets of the image bits recovered from the extracted bits $\{m_i^*\}$ after deleting the synchronization codes from it.
7. Calculate the percentage similarity of each set with the original embedded 1-D array $M' \in \{0,1\}$.
8. Use the set with the highest percentage to recreate the 2-D watermark image.

[IV] EXPERIMENTAL ANALYSIS

We have formulated our scheme over a 2 sec wav audio signal sampled at 44.1 khz which gives us 88200 samples to embed the image. As discussed previously, the audio signal has been divided into 200 segments of 441 samples each. The binary image to be watermarked is taken as of $M \times N = 10 \times 20 = 200$ bits (fig. 4). This 2-D image is converted into a 1-D array in order to embed it into the audio signal. The synchronization code is chosen to be [0 1 1 1 1 1 1 0] based on the concept of byte-stuffing in synchronous transmissions in serial medium.

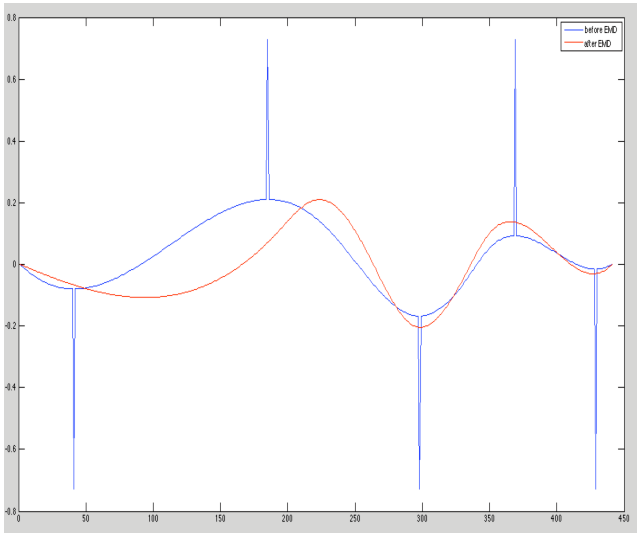


Fig. 3 Last IMF of the watermarked signal before and after EMD

According to [8], if we attempt to extract the watermark from the last IMFs of all the segments, there would, as it is be a need to consult the original host audio signal due to the shift in the extrema after watermarking as shown in fig. 3. Also, the changes in magnitude of the extrema were marginal which led us to believe that the change in magnitude due to embedding has shifted to the higher frequencies.

The embedded bits can be observed across IMF 1, IMF 2, IMF 3 clearly as shown in figs. 5, 6 and 7. However, the strength of these bits could not be observed adequately across IMF 4.

[V] RESULTS

Keeping a balance of both, the imperceptibility as well as the robustness, the value of the embedding strength has been taken as 0.97, which provides us with 98.18%, match of the extracted watermark

with the embedded one. The rest of the statistics have been shown in table no. 1.

IMF order from which the watermark has been extracted	Percentage similarity of the extracted watermark	Extracted watermark
IMF 1	98.18	
IMF 2	86.64	
IMF 3	72.37	

[Table-1]

To add to the robustness of the scheme, different attacks have been performed:

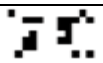
1) **Noise** – White Gaussian Noise (WGN) is added to the signal to make the Signal to Noise Ratio (SNR) as 20 dB.
2) **Filtering** – The signal is filtered through the low pass as well as a high pass filter.
3) **Cropping** – Segments of 441 samples are removes at about 13 locations and are replaced with those segments contaminated with WGN.
4) **Compression** – The watermarked signal compressed and eventually decompressed using MP3 compression at 320 kbps.

Attack type	**Percentage similarity**	**Extracted watermark**
No attack	98.18	
AWGN (20 dB)	64.93	
Cropping	81.79	
MP3 (320 kbps)	79.85	
Low pass filter	84.59	

[Table-2]

Table no. 2 shows the results of the attacks on the watermarked signal. All the attacks deter the binary watermark by less than 50%. Even with adding WGN, detection over 50% is possible. However, the detection, incase of attacks is only possible from IMF 1; IMF 2 and IMF 3 fail to respond to attacks other than the filtering attack.

Detection through multiple IMFs gives us the advantage over filtering attack. If a particular frequency corresponding to an IMF is masked, the watermarked can be successfully extracted from the other frequencies bearing the magnitude change as shown in table no. 3.

IMF order	Percentage similarity	Extracted watermark
IMF 2	74.23	
IMF 3	66.05	

[Table-3]

Moreover, an observation about the embedding strength was made. The embedding strength was expected to give linear results as compared to the percentage similarity of the extracted watermark, which it did for when no attack is performed on the watermarked signal. But, in case of an attack, the embedding strength produces a Gaussian curve with respect to the similarity of the extracted watermark.

[VI] CONCLUSION

In this paper, a new scheme of non-blind extraction of the watermark has been presented. This scheme is found to be as robust as compared to blind watermark extraction technique presented in [8] with an added property of the adaptive nature of the threshold value while detecting the watermark. Further, the extraction process has got an advantage over the filtering attack. It allows the extraction of the watermark from a different IMF if a filter masks the frequency of a particular IMF. As the watermark bits are associated with the synchronization codes, they also tend to resist a

change by cropping attacks, which has been demonstrated in the simulation result of this scheme. Simulation results prove that the extracted watermark has a similarity percentage over 50% in all cases of attacks. In this scheme, the embedding strength S is kept constant at all times as it has given the optimum result in terms of robustness. To improve the inaudibility feature of watermarked audio by this algorithm, the value of embedding strength S can be made adaptive. This would allow better SNR and robustness against attacks. This can be achieved through application of power spectrum compliant technique in our future research work.

REFERENCES

[1] I. J. Cox and M. L. Miller, “The first 50 years of electronic water- marking,” J. Appl. Signal Process., vol. 2, pp. 126–132, 2002.

[2] Dhar, Pranab Kumar, Mohammad Ibrahim Khan, and Jong-Myon Kim. "A new audio watermarking system using discrete fourier transform for copyright protection." *IJCSNS* 10.6 (2010): 35-40.

[3] Al-Haj, A., L. Bata, and A. Mohammad. "Audio watermarking

[4] using wavelets." *Networked Digital Technologies, 2009. NDT'09. First International Conference on*. IEEE, 2009.

[5] Khaldi, Kais, et al. "Audio encoding using Huang and Hilbert transforms." *Communications, Control and Signal Processing (ISCCSP), 2010 4th International Symposium on*. IEEE, 2010.

[6] Schlurmann, T. "The empirical mode decomposition and the Hilbert Spectra to analyse embedded characteristic oscillations of extreme waves." *Actes de Colloques-IFREMER* 32 (2001).

[7] N. E. Huang et al., “The empirical mode decomposition and Hilbert spectrum for nonlinear and non-stationary time series analysis,” Proc. R. Soc., vol. 454, no. 1971, pp. 903–995, 1998.

[8] I. J. Cox, J. Kilian, T. Leighton, and T. Shamoon, “A secure, robust watermark for multimedia,” LNCS, vol. 1174, pp. 185–206, 1996.

[9] Kais Khaldi and Abdel-Ouahab Boudraa, “Audio Watermarking Via EMD,” IEEE Trans. Audio Speech Language Process., vol. 21, no. 3, pp. 675–680, Mar. 2013.

[10] B. Chen and G. W. Wornell, “Quantization index modulation methods for digital watermarking and information embedding of multimedia,” J. VLSI Signal Process. Syst., vol. 27, pp. 7–33, 2001.

[11] Vuckovic, Vesna. "EMBEDDING STRENGTH CRITERIA FOR AWGN WATERMARK, ROBUST AGAINST EXPECTED DISTORTION." *Computing and Informatics* 29 (2010):357-387.

[11] N. K. Zaman, K. M. I. Khalilullah, Md. W. Islam, and Md. K. I.Molla, “A robust digital audio watermarking algorithm using empirical mode decomposition,” in Proc. IEEE CCECE, 2010, pp. 1-4.

Hindawi Publishing Corporation
Advances in Electrical Engineering
Volume 2014, Article ID 392187, 10 pages
http://dx.doi.org/10.1155/2014/392187

Research Article

Performance Analysis of a Shunt Compensator Controlled Using Modified Synchronous Reference Theory

Alka Singh

Department of Electrical Engineering, Delhi Technological University, Bawana Road, Delhi 110042, India

Correspondence should be addressed to Alka Singh; alkasingh.dr@gmail.com

Received 15 April 2014; Revised 2 July 2014; Accepted 2 July 2014; Published 7 August 2014

Academic Editor: José R. C. Piqueira

Copyright © 2014 Alka Singh. This is an open access article distributed under the Creative Commons Attribution License, which permits unrestricted use, distribution, and reproduction in any medium, provided the original work is properly cited.

This paper deals with the control of distribution energy resource (DER) connected to a grid connected system feeding nonlinear loads. The DER is controlled to provide power quality improvement capabilities, namely, power factor correction, harmonic reduction, and load balancing. The developed controller is based on modification of synchronous reference theory. It possesses unique features such as filtration and fundamental voltage extraction from the polluted grid voltages to eliminate harmonics and unbalance. Additionally, the control is implemented over the square of DC link voltage. The distributed generation source is realized as a voltage source converter. Both simulation and experimental results prove the effectiveness of control algorithm with nonlinear loads. The control algorithm works well for power factor correction, harmonic reduction, and operation under unbalanced load condition. The dynamics of the system under load change and load unbalancing are well depicted.

1. Introduction

A number of benefits of renewable energy resources exist, namely, high reliability, modular in nature, and environment friendly operation. These advantages have ensured increased acceptance of distributed resources in the world [1–12]. The renewable energy sources (wind, solar, etc.) are currently being interfaced to the conventional systems using voltage source inverters (VSCs) [2–4]. There are several advantages of distributed resources over conventional sources so a high emphasis is nowadays paid to renewable energy sources (RES) and their interconnection to grid. These sources are connected at the low or medium voltage levels. A primary energy source generally in the form of wind energy, photovoltaic cell, fuel cell, battery, and so forth is connected at the primary of the converter which converts this power and supplies it to the load in islanded mode. A number of such voltage source converters may be connected in parallel and to the utility grid also. Control of such distributed energy sources [5–13] is an important control aspect.

Very recently the concept of multifunctional distributed generators has been introduced which is controlled to provide two equally important tasks of providing power delivery as well as power quality improvement. Active power filters [1, 12, 14] provide reactive power compensation and power quality improvement only. The concept is to flexibly control the distributed generator resource as a source and extract maximum power from it and also provide compensation current from it. Lately, power converters in both voltage and current control mode [7, 8] have been used for utility interface for distributed generation sources. These converters are mainly interfaced with L or higher order LC/LCL filters [9–11]. Repetitive control, hysteresis regulation, and predictive control are frequently used and multiloop feedback control with LC/LCL filters is gaining popularity [4–11]. However, several points of concern relate to LCL filters, namely, the selection of the outer and inner control variables for improving system stability, avoiding resonance condition, and studying the effect on system performance under parameter variation. Figure 1 shows a number of distributed generation sources connected to the utility grid.

2. System Description

The diagram shows the distributed energy source feeding variety of loads (linear/nonlinear) in grid connected mode. A three-leg insulated gate bipolar transistors (IGBTs) based

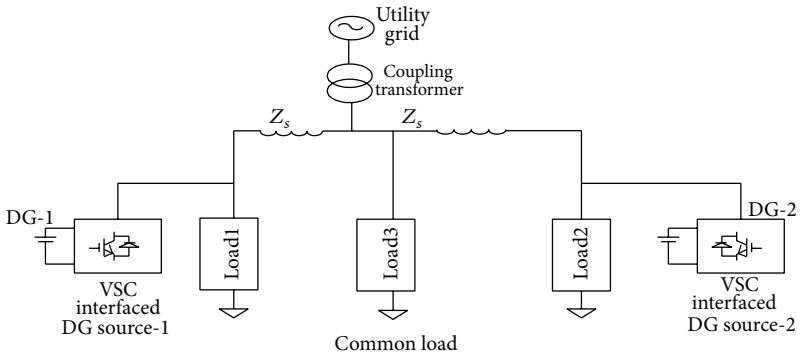


Figure 1: A number of distributed generation sources connected to utility grid.

VSC is used and controlled as DStatcom. It is connected to the point of common coupling (PCC) through a set of interfacing inductors (R, L).

The implemented system requires VSC, interfacing inductors, scaling circuits for sensing the input signals, and driver circuit for output signals. Active power transfer flow can also take place by placing an active source (battery or renewable energy source) at DC link. Three Hall-effect current sensors (LEM LA 25-NP) are used to sense load currents for phases "A," "B," and "C." To sense the source currents for phases "A" and "B," another set of Hall-effect current sensors (LEM LA 25-NP) are used. The third phase source current is estimated by considering that the algebraic sum of three-phase source currents is zero. Two voltage sensors (LV 25-P) are used to sense phases "A" and "B" voltages. The third phase voltage is estimated considering the algebraic sum of three-phase source voltages is zero. The DC link voltage is sensed using the voltage sensor LV 25P/SP5. Scaling circuits are designed to use in between the sensed signals and ADC (analog to digital converter) of DSP to have a zero offset with the sensed signals. The control algorithm is realized in MATLAB environment with real time blocks. Hex codes are loaded in the DSP-dSPACE 1104 to generate six switching signals for IGBTs through PWM (pulse width modulation) pins of a DSP. A Semikron three-phase VSC (model MD B6CI 800/415-35F) with six IGBT based switches is used for experiments. Table 2 lists the parameters of the system used for simulation as well as experiments.

3. Mathematical Model

For the system configuration shown in Figure 2, v_{ta}, v_{tb}, and v_{tc} denote the terminal voltages at the PCC and v_{sa}, v_{sb}, and v_{sc} are the voltages at the three-phase ac source (grid); then the following differential equations can be written:

$$v_{sa} = v_{ta} - R_s i_{sa} - L_s \frac{di_{sa}}{dt},$$
$$v_{sb} = v_{tb} - R_s i_{sb} - L_s \frac{di_{sb}}{dt}, \quad (1)$$
$$v_{sc} = v_{tc} - R_s i_{sc} - L \frac{di_{sc}}{dt}.$$

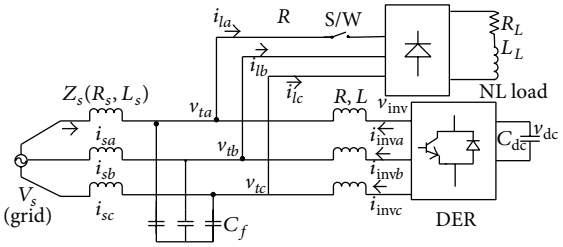


Figure 2: Schematic diagram of utility grid and distributed energy source feeding loads.

The equations relating the inverter voltages with the PCC voltages are written as

$$v_{ta} = v_{inva} - Ri_{inva} - L\frac{di_{inva}}{dt},$$
$$v_{tb} = v_{invb} - Ri_{invb} - L\frac{di_{invb}}{dt}, \quad (2)$$
$$v_{tc} = v_{invc} - Ri_{invc} - L\frac{di_{invc}}{dt},$$

where R, L denote the interfacing resistor and inductor values and i_{inva}, i_{invb}, and i_{invc} and v_{inva}, v_{invb}, and v_{invc} denote the inverter currents and voltages in three phases. At the DC link (3) is valid:

$$\frac{Cdv_{dc}}{dt} = i_{dc}. \quad (3)$$

The equations shown above can be depicted in the form of a single closed loop control for the control of grid current (i_s) as shown in Figure 3.

The PWM inverter is represented as $K_{inv}/(1 + sT_{inv})$; R and L represent the interfacing resistance and inductance, respectively. For further simplification $T_{inv} = 0$.

The current controller is represented in the form of PI controller with transfer function:

$$Gc(s) = K_p + \left(\frac{K_i}{s}\right). \quad (4)$$

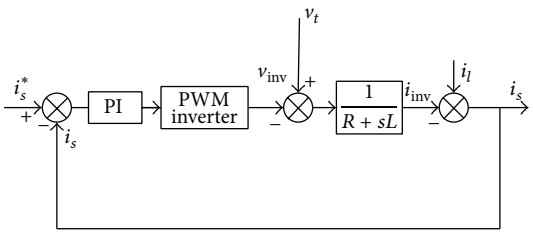


Figure 3: Simplified closed loop analysis of the system.

The closed loop transfer function is derived to be

$$\frac{i_s}{i_s^*} = \frac{K_{\text{inv}}\left(K_p s + K_i\right)}{s^2 L + s\left(R + K_{\text{inv}} K_p\right) + K_{\text{inv}} K_i}. \tag{5}$$

Comparing with the standard closed loop transfer function, we get

$$\frac{i_s}{i_s^*} = \frac{w_n^2}{s^2 + 2s\zeta w_n + w_n^2}. \tag{6}$$

The values of damping ratio ζ and angular frequency w_n are found to be influenced by parameters K_p, K_i, and K_{inv} and parameters R and L. The desired damping ratio is obtained by varying the gain constants.

4. Control Algorithm

The control algorithm used for the control of distributed generation source in this paper is based on modified synchronous reference frame theory. The synchronisation is achieved by deriving unit templates from the supply grid. Since, it is observed that the supply voltages have harmonics and are unbalanced, hence, the use of filters and extraction of fundamental voltage component of the three phases are undertaken as a preliminary step. These filtered supply voltages are used as PCC voltages for the generation of reference current generation as is discussed below. Figure 4 shows the control algorithm developed using synchronous reference frame (SRF) theory. A noticeable difference is that the control is developed over the square of DC link voltage. Although the DC link voltage is sensed, the PI controller is developed over the error between the actual and reference value of square of DC link voltage. The SRF based controller utilizes the *abc-dq* transformation (Park's transformation) to transform the current and voltage waveforms into a reference frame that rotates synchronously with the grid voltage.

Filtered fundamental PCC voltages (v_{saf}, v_{sbf}, and v_{scf}) are obtained by filtering voltages (v_{sa}, v_{sb}, and v_{sc}) through band pass filters, whose cutoff frequency is between 30 Hz and 60 Hz. The symmetrical component method developed by Akagi et al. [1] is used to obtain fundamental voltage components (v_{sa1}, v_{sb1}, and v_{sc1}) from the filtered voltages as below:

$$\begin{aligned} v_{sa1} &= \frac{1}{3}\left(v_{saf} + \lambda v_{sbf} + \lambda^2 v_{scf}\right), \\ v_{sb1} &= \frac{1}{3}\left(v_{sbf} + \lambda a v_{scf} + \lambda^2 v_{saf}\right), \\ v_{sc1} &= \frac{1}{3}\left(v_{scf} + \lambda v_{saf} + \lambda^2 v_{sbf}\right), \end{aligned} \tag{7}$$

where $\lambda = e^{j120} = -0.5 + 0.866j$ and $\lambda^2 = e^{j240} = -0.5 - 0.866j$.

The amplitude of the PCC voltage is now obtained using

$$V_{tm} = \left\{\frac{2}{3}\left({v_{sa1}}^2 + {v_{sb1}}^2 + {v_{sc1}}^2\right)\right\}^{1/2}. \tag{8}$$

The unit in-phase vectors (u_a, u_b, and u_c) are calculated as

$$\begin{aligned} u_a &= \frac{v_{sa1}}{V_{tm}}, \\ u_b &= \frac{v_{sb1}}{V_{tm}}, \\ u_c &= \frac{v_{sc1}}{V_{tm}}. \end{aligned} \tag{9}$$

The quadrature unit current vectors (w_a, w_b, and w_c) are derived from in-phase unit current (u_a, u_b, and u_c) vectors as

$$\begin{aligned} w_a &= \frac{\left(-u_b + u_c\right)}{\left\{(3)^{1/2}\right\}}, \\ w_b &= \frac{\left(u_a(3)^{1/2} + \left(u_b - u_c\right)\right)}{\left\{2(3)^{1/2}\right\}}, \\ w_c &= \frac{\left(-u_a(3)^{1/2} + \left(u_b - u_c\right)\right)}{\left\{2(3)^{1/2}\right\}}. \end{aligned} \tag{10}$$

The basic SRF theory involves the transformation of currents in synchronously rotating *d-q* frame. It uses the PLL block to evaluate θ and transformation angle to convert currents from $\alpha\beta$ to dq frame:

$$\begin{aligned} i_\alpha &= i_{la}\left(\sqrt{\frac{2}{3}}\right)\cos\theta - i_{lb}\left(\sqrt{\frac{1}{6}}\right) - i_{lc}\left(\sqrt{\frac{1}{6}}\right), \\ i_\beta &= i_{lb}\left(\sqrt{\frac{1}{2}}\right) - i_{lc}\left(\sqrt{\frac{1}{2}}\right), \\ i_d &= i_\alpha \cos\theta + i_\beta \sin\theta, \\ i_q &= -i_\alpha \sin\theta + i_\beta \cos\theta. \end{aligned} \tag{11}$$

Instead of the PLL block, the unit templates obtained from filtered PCC voltages are used to estimate i_d, i_q values of load currents. The obtained i_d and i_q currents are now passed over

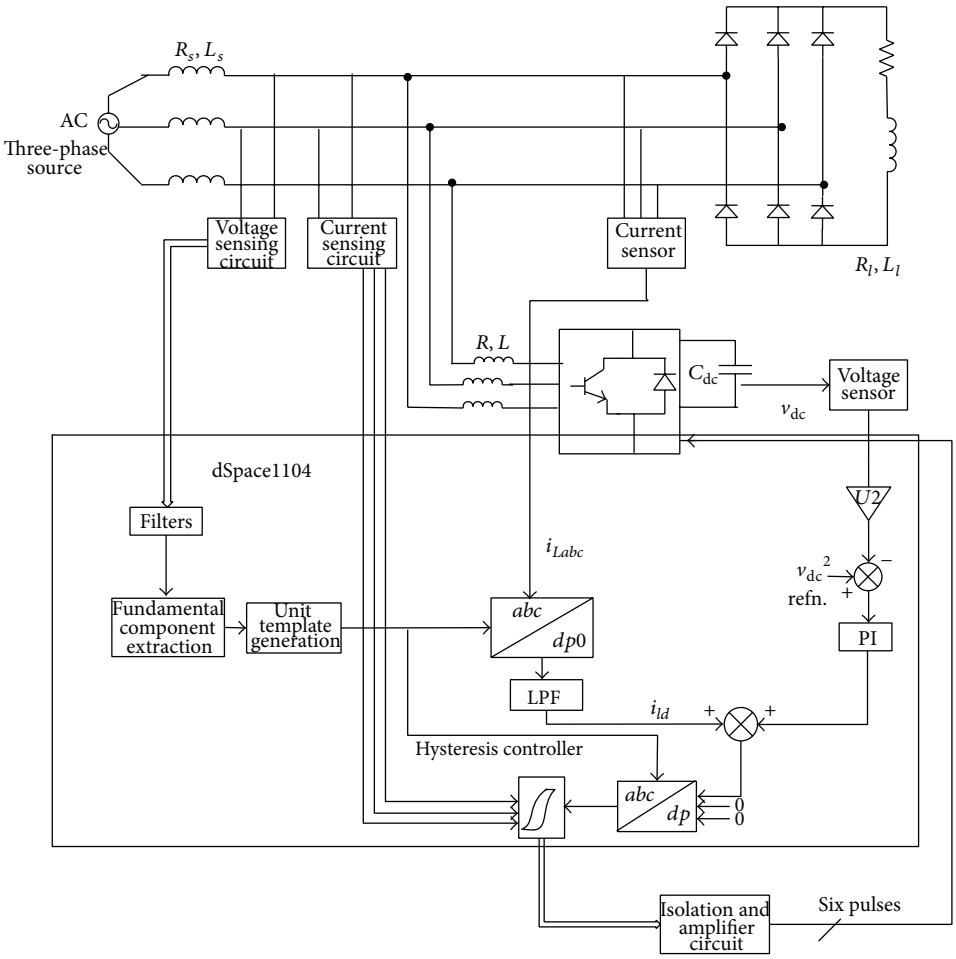


Figure 4: Complete control scheme for the system.

low pass filter (LPF) to extract the dc components $i_{d\mathrm{dc}}$ and $i_{q\mathrm{dc}}$. A PI controller is realised over the square of DC link voltage to regulate it to its reference value:

$$i_{d(n)} = i_{d(n-1)} + K_{pd}\left\{{v_{\mathrm{dc1}}}^2(n) - {v_{\mathrm{dc1}}}^2(n-1)\right\} + K_{id}v_{\mathrm{dc1}}(n), \tag{12}$$

where $v_{\mathrm{dc1}}(n) = {v_{\mathrm{dcref}}}^2(n) - {v_{\mathrm{dc}}}^2(n)$ denotes the error in square of DC link voltage calculated over reference and sensed value obtained from the voltage sensor. K_{pd} and K_{id} are the proportional and integral gains of the PI controller. The output of PI controller accounts for the losses of VSC and this component is added to the $i_{d\mathrm{dc}}$ for power factor correction.

Once the reference d, q components of currents are obtained, the three-phase reference supply currents (i_{sar}, i_{sbr}, and i_{scr}) can be obtained. These reference supply currents are compared with the sensed supply currents (i_{sa}, i_{sb}, and i_{sc}) to estimate the three-phase current error components. The current errors are passed over carrier-less PWM controller to generate gating signals for the six IGBTs (insulated gate bipolar transistors) of VSC. The control scheme is direct and based on supply (grid) currents instead of the inverter currents in the three phases.

5. Performance and Results

A MATLAB based model of distributed energy resource is developed and tested under distorted and unbalanced voltage of ac mains to validate the proposed control algorithm. The performance of modified synchronous detection control algorithm in time domain is simulated and analyzed using a three-leg VSC configuration with nonlinear loads. Simulations as well as experimental results are presented for two cases, namely, power factor correction and load balancing along with power factor correction.

5.1. Power Factor Correction and Load Change. Figure 5 shows the simulated results showing the filtered PCC voltage (v_t), supply currents (i_s), load currents (i_l), currents (i_c) injected by DStatcom, and DC link voltage (v_{dc}). The results are obtained with a nonlinear load of $R_l = 30\,\Omega$ connected at the end of diode rectifier. Load is varied to $R_l = 50\,\Omega$ for time duration from $t = 0.2$ sec to $t = 0.28$ sec. The dynamics of the currents and DC link are evident from Figure 5 and it is observed that the DC link voltage settles down to a reference value of 200 V in less than two cycles. The THD of the supply currents is 4.3% when the load currents have a THD of 28%.

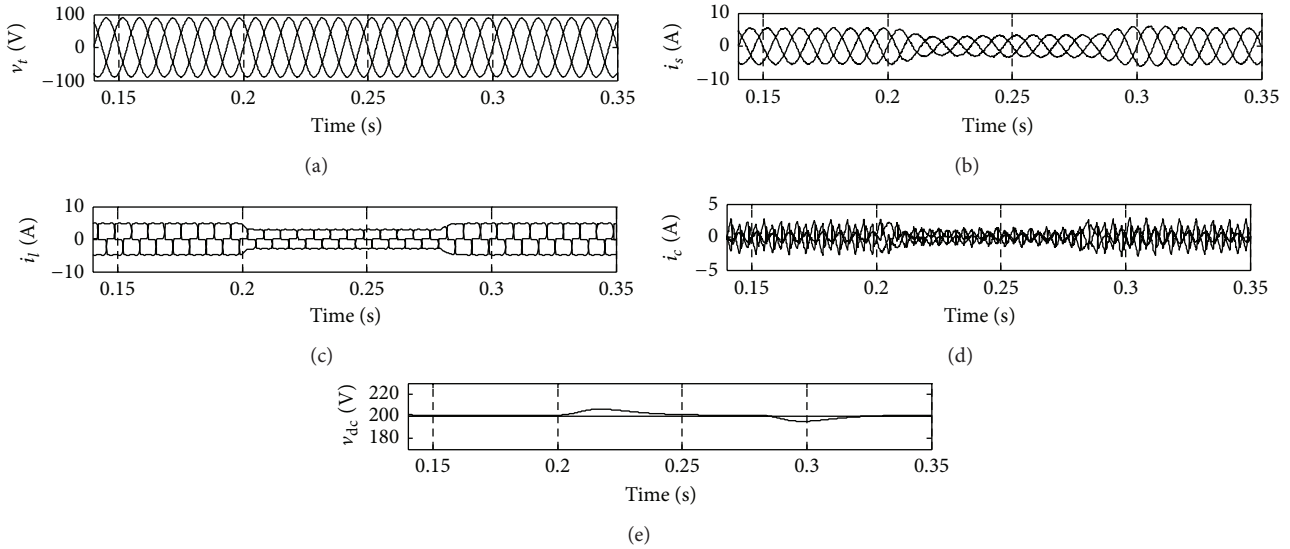


Figure 5: Simulated results for power factor correction in steady state as well as load removal ($t = 0.2$ sec) and addition ($t = 0.28$ sec).

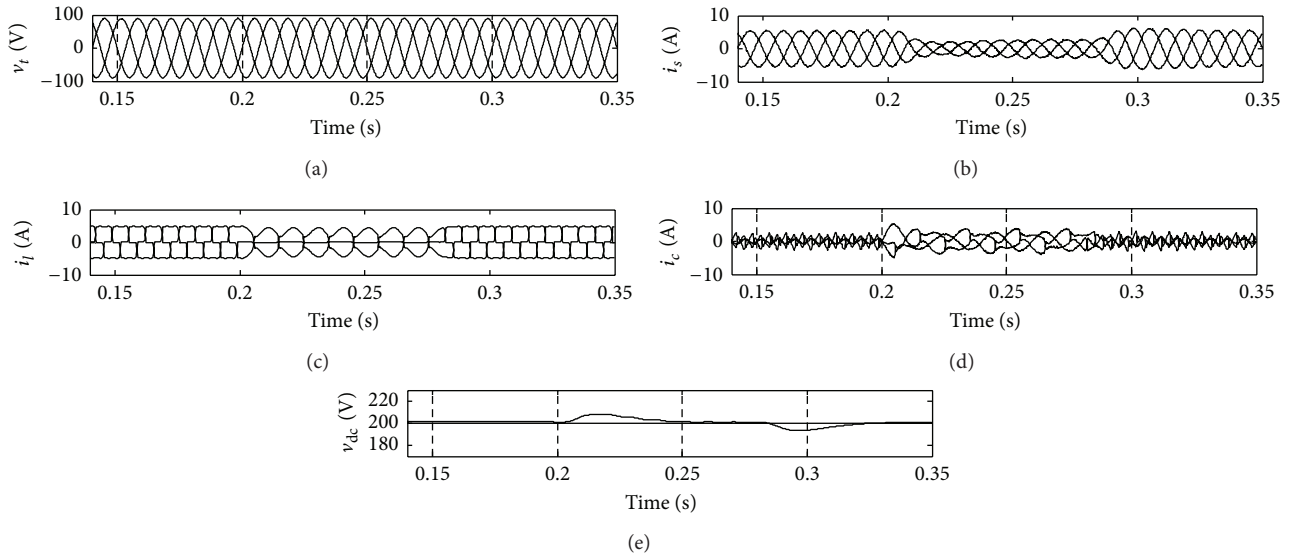


Figure 6: Simulated results for power factor correction and load balancing in steady state as well as one phase load removal ($t = 0.2$ sec) and restoration ($t = 0.28$ sec).

5.2. Power Factor Correction under Unbalanced Load Operation. Figure 6 shows the simulated results for the system under steady state conditions till $t = 0.2$ sec when phase "c" of the load is suddenly disconnected from $t = 0.2$ sec to $t = 0.28$ sec. The simulated results show that the control algorithm not only maintains the DC link voltage but also the grid currents are balanced and sinusoidal during this interval. The distributed energy source works as a shunt compensator and injects compensating currents of higher magnitude now and this can be observed from the simulation results. The normal balanced loads with $R_l = 30\,\Omega$ and $L = 60$ mH are restored at $t = 0.28$ sec. The THD of the supply currents is 4.4% when the load currents have a THD of 29%.

6. Experimental Results for Proposed Scheme

The experimental results for the same system configuration (shown in Table 2) and load are shown in Figures 7 and 8. Figure 7(a) shows the waveforms of phase "a" supply current, load current, compensator current, and Dc link voltage in steady state.

Figures 7(b) and 7(c) show the dynamics of load decrease and load increase, respectively. Figure 8(a) shows the Power Analyser 434 (Fluke) waveforms and THD of the supply current which is 4.4%. The unfiltered PCC voltages are depicted in Figure 8(b) that show a THD of 2.8% and the magnitudes are also slightly different. It is due to this reason only that filtered, positive sequence voltage components

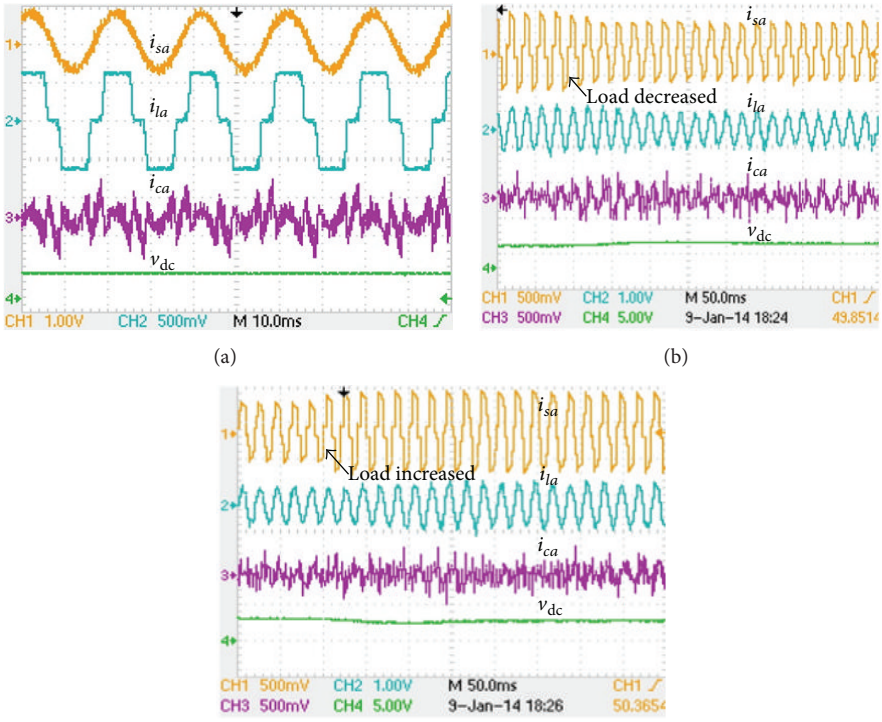


FIGURE 7: (a) Plot of i_{sa}, i_{la}, i_{ca}, V_{dc} (10 A/div, 5 A/div, 5 A/div for the currents). (b) Plot of i_{la}, i_{lb}, i_{lc}, V_{dc} (5 A/div, 5 A/div, 5 A/div for the currents) for load decrease. (c) Plot of i_{la}, i_{lb}, i_{lc}, V_{dc} (5 A/div, 5 A/div, 5 A/div for the currents) for load increase.

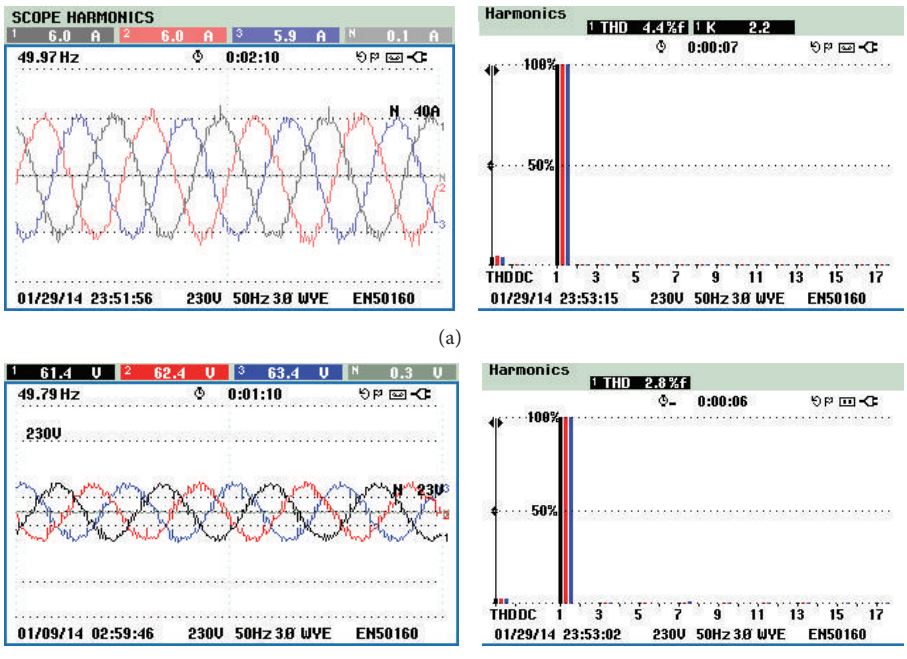


FIGURE 8: (a) Fluke 434 results showing three-phase supply currents (i_{sa}, i_{sb}, i_{sc}) and THD of 4.4%. (b) Supply voltages showing 2.8% THD.

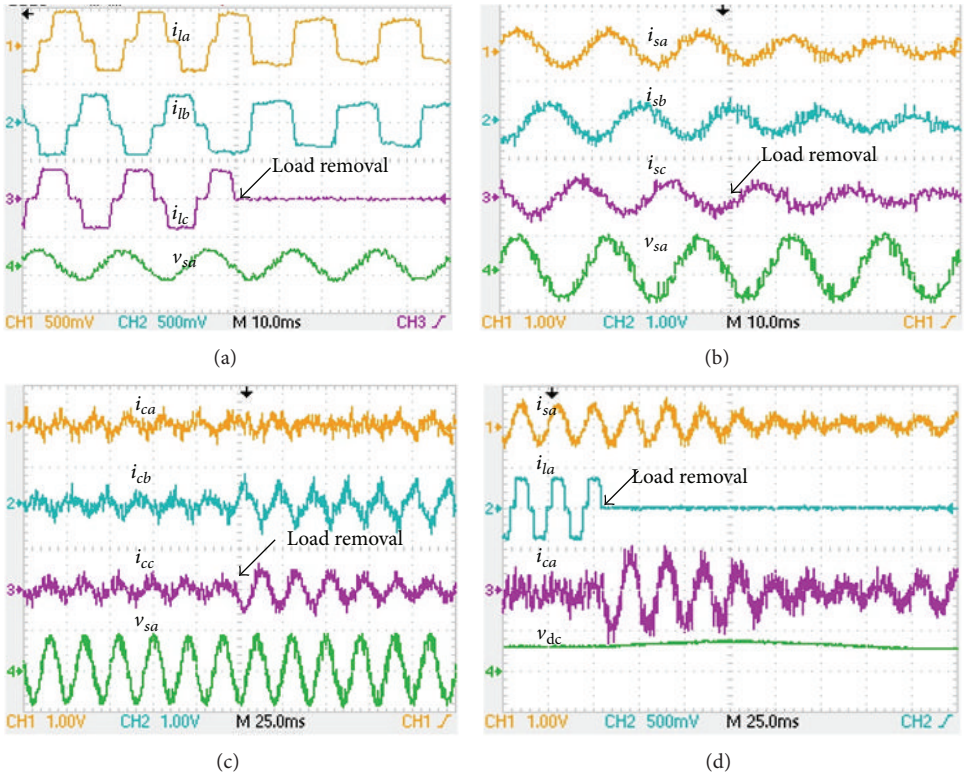


FIGURE 9: (a) Load current s (5 A/div) and v_{sa}. (b) Supply voltages (5 A/div) and v_{sa}. (c) Inverter currents (5 A/div) and v_{sa}. (d) Source, load, inverter currents (5 A/div), and DC link voltage.

are first extracted and then used for further analysis and reference current generation.

Experimental verification for power factor correction and load unbalancing are presented next in Figure 9. The load current in phase "c" is suddenly disconnected and this is evident from the plot Figure 9(b) for ilc. Figure 9(c) shows the variation of grid supply currents in all the three phases before and after the instant of unbalancing.

Figure 9(c) shows the variation of compensator currents in all the three phases before and after load in phase "c" is disconnected for some time. It is observed from Figures 9(a)–9(c) that the distributed source is controlled to provide necessary compensation currents during unbalanced load conditions. The DER acts as a shunt compensator and regulates the grid currents to be equal, balanced, and sinusoidal even when one phase of load is switched off. It provides large compensation currents in all the three phases during the interval. Also, it is observed from Figure 9(d) that the DC link settles down to its reference value of 200 V quite rapidly.

7. Result Comparison

Conventional SRF scheme has a few drawbacks; namely, it cannot be used to obtain optimum results under unbalanced grid supply voltages. The voltage signals are processed by the PLL to generate θ. This transformation angle (θ) is sensitive to voltage harmonics and unbalances. Hence, filtered PCC voltages are used in the modified control algorithm for reference current generation. If the unfiltered voltages are used in control algorithm, the reference supply currents generated would themselves be nonsinusoidal and it would be difficult to achieve three-phase sinusoidal, balanced supply currents. The use of positive, negative, and zero sequence components has been used in this paper, which is simple and effective method for extraction.

The processing of current signals in both the schemes is similar. These are transformed into d-q frame and then filtered. Then, compensating current is transformed back to a-b-c frame and fed to hysteresis current controller for switching pulse generation. The results obtained show that under normal operating conditions, both the control strategies are suitable for compensation, but under the distorted supply conditions and unbalanced operating condition, the performance of the conventional scheme deteriorates. The experimental results for the conventional scheme are shown in Figure 10.

Figure 10 shows the results with conventional SRF scheme. It is evident that the supply voltages have a high THD level of 3.6% (Figure 10(f)). With the controller realised on v_{dc} and the gains optimised, the performance of the shunt compensator is observed. The load current has a high THD content of 23.5%, the controller injects compensating currents to make the supply current sinusoidal. Under the optimised PI gains, the lowest THD observed in supply currents is of the order of 4.8%. This is higher than the THD level of 4.4% observed with the v_{dc}^2 controller and the modified SRF

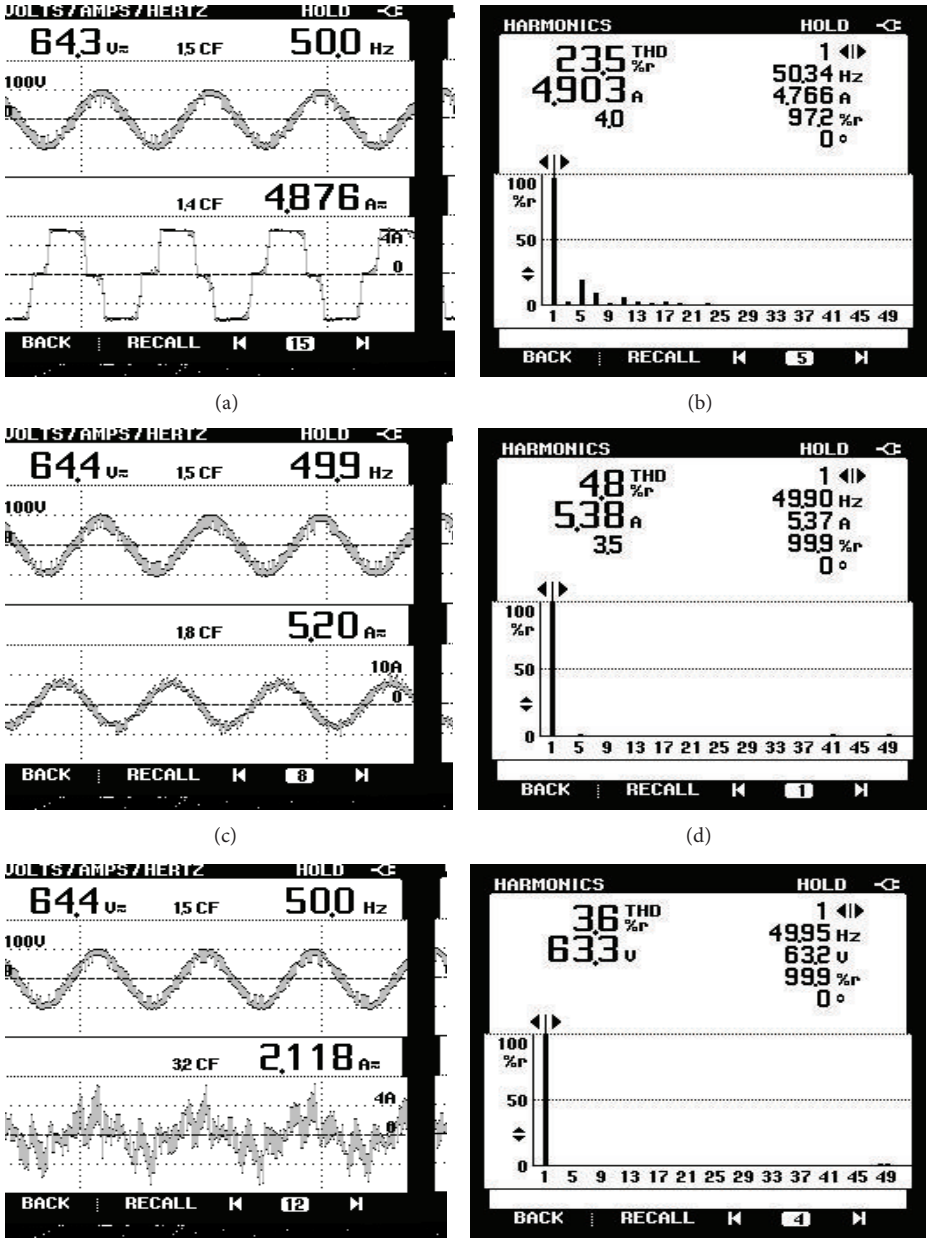


FIGURE 10: (a, b) v_{sa} and load current (i_{la}) (5 A/div) and its THD 23.5%. (c, d) v_{sa} and supply current (i_{sa}) (5 A/div) and its THD 4.8%. (e) v_{sa} and compensator current (i_{ca}) (5 A/div). (f) THD 3.6% in the grid voltage.

theory. Figures 11 and 12 show the waveforms and THD for i_{sa}, i_{la} with modified SRF theory, and conventional SRF theory, respectively. Figures 11 and 12 show the simulation results with both the schemes and Table 1 highlights the comparison between the two schemes.

Comparison results are highlighted in Table 1.

8. Conclusions

This paper discusses and implements a control algorithm based on modification of synchronous reference frame theory for interfacing a distributed energy source to grid. The control algorithm is investigated to inject only reactive power and relieve the grid from supplying it. The control scheme is modified to include fundamental voltage component of the PCC voltage which is having harmonics, and unbalancing of up-to 5%. A single closed loop control for the system is investigated for control of grid currents. The control is developed and experimentally tested on v_{dc}^2 rather than the usual control on v_{dc} alone. Two benefits, namely, lower possible reduction in THD level and lower range of PI controller gain settings, were observed with this control. Simulation

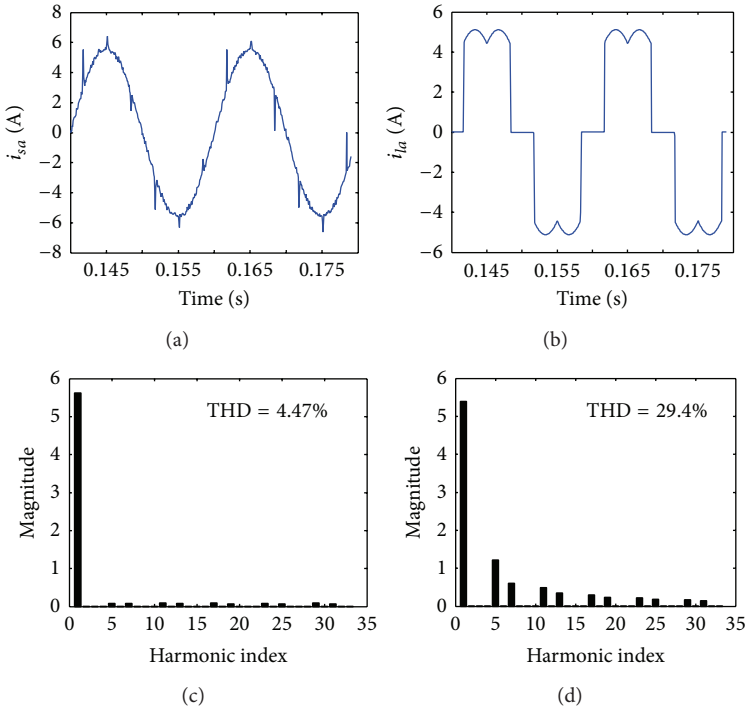


Figure 11: Waveforms and THD for i_{sa} and i_{la} for modified SRF theory.

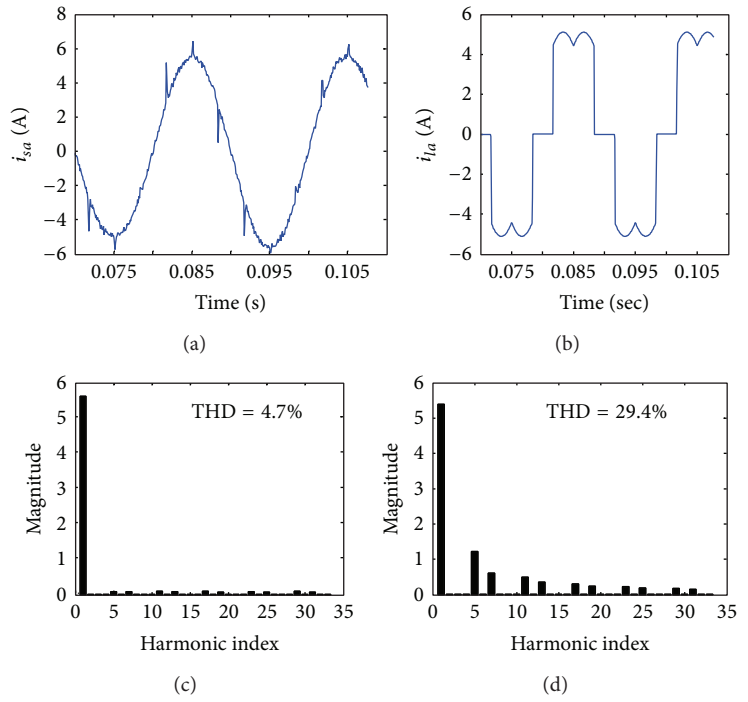


Figure 12: Waveforms and THD for i_{sa} and i_{la} for conventional SRF theory.

Table 1: Comparison of Control schemes.

	Parameters (Kp, Ki)	Overshoot (V)	Undershoot (V)	Settling Time (sec)	THD
Conventional SRF	0.35, 0.1	~3 V	~2 V	<2 cycles	4.9% approx
Modified SRF	0.00028, 0.00034	~4 V	~3 V	<2 cycles	4.5% approx

Table 2: System parameters (Both Simulation and Experimental).

Parameters	Value
Grid voltage E (RMS)	63.5 V
DC-link voltage V_{dc}	200 V
DC link capacitor C_{dc}	1600 μF
Inverter-side filter L	3.5 mH
Filter capacitor C_f	3 μF
Rectifier resistor R_l	30 Ω
Load Inductor L_l	60 mH
Sampling frequency f_s	10 kHz

results and experimental results for the prototype system are obtained for power factor correction, load unbalancing, and reduction of THD in grid currents. The experimental results obtained are very close to the simulation results. The proposed control scheme is able to achieve a THD of 4.4% in grid currents when the load current is 28.7%, thus meeting IEEE 519 standards. The distribution shunt compensator has been utilized to provide reactive power compensation only, though real power injection into the system is also possible with an active source at the DC link.

Conflict of Interests

The author declares that there is no conflict of interests regarding the publication of this paper.

Acknowledgment

The author wishes to thank the Department of Science and Technology, Government of India, for the sponsored Project no. SR/FTP/ETA-20/2010.

References

[1] H. Akagi, E. H. Watanabe, and M. Aredes, *Instantaneous Power Theory and Applications to Power Conditioning*, IEEE Press, Wiley InterScience, 2007.

[2] F. Blaabjerg, Z. Chen, and S. B. Kjaer, "Power electronics as efficient interface in dispersed power generation systems," *IEEE Transactions on Power Electronics*, vol. 19, no. 5, pp. 1184–1194, 2004.

[3] C. K. Duffey and R. P. Stratford, "Update of harmonic standard IEEE-519: IEEE recommended practices and requirements for harmonic control in electric power systems," *IEEE Transactions on Industry Applications*, vol. 25, no. 6, pp. 1025–1034, 1989.

[4] R. Teodorescu, M. Liserre, and P. Rodríguez, *Grid Converters for Photovoltaic and Wind Power Systems*, John Wiley & Sons, New York, NY, USA, 2011.

[5] F. Blaabjerg, R. Teodorescu, M. Liserre, and A. V. Timbus, "Overview of control and grid synchronization for distributed power generation systems," *IEEE Transactions on Industrial Electronics*, vol. 53, no. 5, pp. 1398–1409, 2006.

[6] I. Chung, W. Liu, D. A. Cartes, and E. G. Collins, "Control methods of inverter-interfaced distributed generators in a microgrid system," *IEEE Transactions on Industry Applications*, vol. 46, no. 3, pp. 1078–1088, 2010.

[7] J. He, Y. W. Li, and M. S. Munir, "A flexible harmonic control approach through voltage-controlled DG-grid interfacing converters," *IEEE Transactions on Industrial Electronics*, vol. 59, no. 1, pp. 444–455, 2012.

[8] J. He and Y. W. Li, "Hybrid voltage and current control approach for dg-grid interfacing converters with LCL filters," *IEEE Transactions on Industrial Electronics*, vol. 60, no. 5, pp. 1797–1809, 2013.

[9] P. C. Loh and D. G. Holmes, "Analysis of multiloop control strategies for LC/CL/LCL-filtered voltage-source and current-source inverters," *IEEE Transactions on Industry Applications*, vol. 41, no. 2, pp. 644–654, 2005.

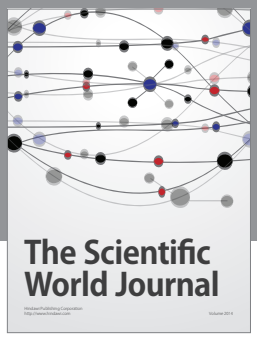
[10] J. He and Y. W. Li, "Generalized closed-loop control schemes with embedded virtual impedances for voltage source converters with LC or LCL filters," *IEEE Transactions on Power Electronics*, vol. 27, no. 4, pp. 1850–1861, 2012.

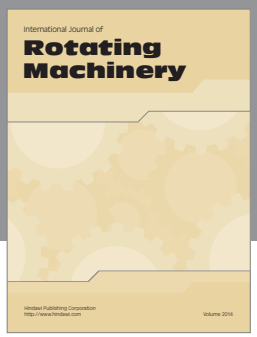
[11] N. He, D. Xu, Y. Zhu et al., "Weighted average current control in a three-phase grid inverter with an LCL filter," *IEEE Transactions on Power Electronics*, vol. 28, no. 6, pp. 2785–2797, 2013.

[12] Y. Li, D. M. Vilathgamuwa, and P. C. Loh, "Microgrid power quality enhancement using a three-phase four-wire grid-interfacing compensator," *IEEE Transactions on Industry Applications*, vol. 41, no. 6, pp. 1707–1719, 2005.

[13] D. N. Zmood and D. G. Holmes, "Stationary frame current regulation of PWM inverters with zero steady-state error," *IEEE Transactions on Power Electronics*, vol. 18, no. 3, pp. 814–822, 2003.

[14] A. Chandra, B. Singh, B. N. Singh, and K. Al-Haddad, "An improved control algorithm of shunt active filter for voltage regulation, harmonic elimination, power-factor correction, and balancing of nonlinear loads," *IEEE Transactions on Power Electronics*, vol. 15, no. 3, pp. 495–507, 2000.



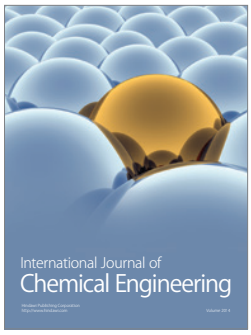


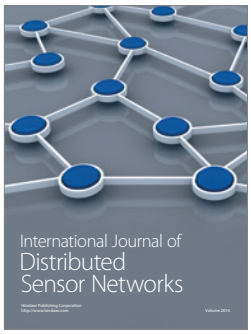


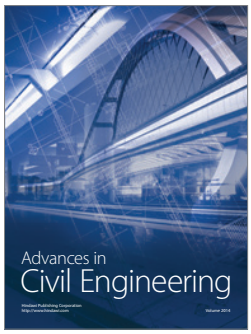


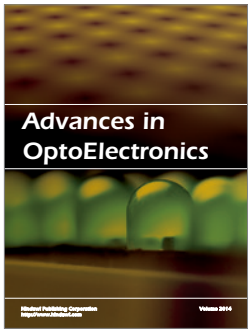






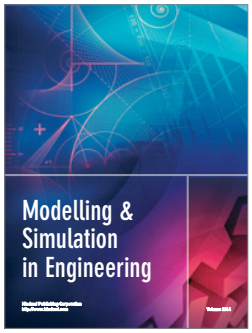


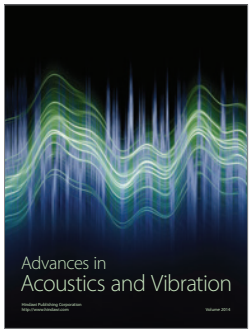




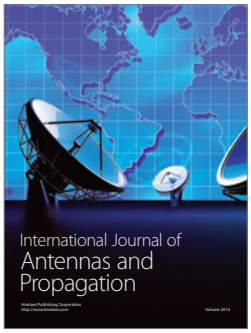


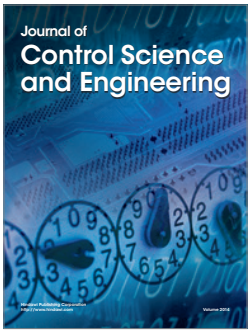


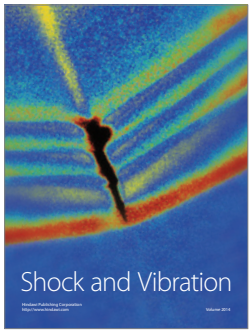














Hindawi

Submit your manuscripts at
http://www.hindawi.com

Energy Technologies, Climate Change and Environmental Sustainability: Innovative Perspective

ISBN: 978-93-83083-87-9

First Impression: 2014

© Krishi Sanskriti
www.krishisanskriti.org

No part of this publication may be reproduced or transmitted in any form by any means, electronic or mechanical, including photocopy, recording, or any information storage and retrieval system, without permission in writing from the copyright owners.

DISCLAIMER

The authors are solely responsible for the contents of the papers compiled in this volume. The publishers or editors do not take any responsibility for the same in any manner. Errors, if any, are purely unintentional and readers are requested to communicate such errors to the editors or publishers to avoid discrepancies in future.

ISBN: 978-93-83083-87-9

Publishing by
EXCELLENT PUBLISHING HOUSE
Kishangarh, Vasant Kunj, New Delhi – 110070
Tel.: 9910948516, 9958167102
E-mail: exlpubservices@gmail.com

Typeset by
Excellent Publishing Services, New Delhi – 110070

Energy Technologies, Climate Change and Environmental Sustainability: Innovative Perspective

Editor:
Prof. (Dr.) Govind Chandra Mishra

Publishing by
EXCELLENT PUBLISHING HOUSE
Kishangarh, Vasant Kunj, New Delhi – 110070
Tel.: 9910948516, 9958167102
E-mail: exlpubservices@gmail.com
Online Link:
www.krishisanskriti.org/books.html

Preface

19th July, 2014

From the Desk of Editor……

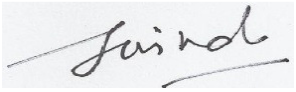
On behalf of organizing committee, I extend my heartiest and warmth welcome to the distinguished delegates and participants of the ***2nd International Conference*** **on** ***Innovative Trends in Applied Physical, Chemical, Mathematical, Statistical Sciences and Emerging Energy Technology for Sustainable Development*****" (APCMSET-2014)** being held at Jawaharlal Nehru University, New Delhi, on 19th and 20th July , 2014, organized by "Social Welfare Foundation" in association with "Krishi Sanskriti". Surely, this Conference will help a lot to increase your knowledge bank. The conference is a source of powerful influence as it draws upon the expertise from various disciplines and also able to bring together leading authorities from academia, industry and R&D Institutions for focusing on new approaches in the field of Energy and Environmental Technology for universal goal of sustainable development. The importance of this conference lies in the fact that during this duration, the feasibility of certain policies for innovations within the frame work of these important subjects which has direct impact in terms of exploring various sources of energy with special emphasis on renewable energy as well as devising techniques to enhance the efficiency of existing energy source, pollution control, environmental management such as sewage treatment, recycling, reuse of materials for various purposes in order to minimize waste generation.

This is the thirteenth publication in the form of edited book of the Society "Krishi Sanskriti". The society is a non-partisan, non-profit making registered voluntary organization of academics, researchers, entrepreneur's, social activists and interested and concerned citizens engaged in the study and understanding of the problems of the general public in India as well as the world. Since its inception in 2003, it has been organizing seminars, workshops, lectures and discussions on issues of current interest for sustainable development of the society.

The present volume of the outcome of a two-day international conference organized by "Social Welfare Foundation" in association with "Krishi Sanskriti" on 19th and 20th July , 2014 titled "**Energy Technologies, Climate Change and Environmental Sustainability: Innovative Perspective**". A number of papers were presented in the international conference and form the core of this volume.

ISBN: 978-93-83083-87-9

This international conference acted as a major forum for the presentation of innovative ideas, approaches, developments and research projects in the area of Environmental Sustainability as well as different streams of energy and environmental technologies by incorporating different Physico-chemical methods in order to full-fill the dreams of sustainable development into reality. The (**APCMSET-2014**) committee invited original Submissions from researchers, faculties, scientists and students that illustrate analytical research results, review works, projects, survey works and industrial experiences describing significant advances in the areas related to the relevant themes and tracks of the conferences. This effort guaranteed submissions from an unparalleled number of recognized top-level researchers. All the submissions underwent a strenuous peer-review process which comprised expert reviewers. Besides the members of the Technical Program Committee, external reviewers were invited on the basis of their specialization and expertise. The papers were reviewed based on their technical content, originality and clarity. The entire process which includes the submission, review and acceptance processes was done electronically. There were a total 115 submissions to the conference and the Technical Program Committee selected 73 full length papers for oral presentation as well as for poster presentations in the conference and Subsequent publication in the International Journal as special issue, as well as edited book with ISBN No. This small introduction would be incomplete without expressing our gratitude and thanks to the General and Program Chairs, members of the Technical Program Committees, and external reviewers for their excellent and diligent work. Thanks to the Jawaharlal Nehru University, New Delhi, for providing venue for this conference. Finally, we thank all the authors who contributed to the success of the conference. We also sincerely wish that all attendees will get benefited academically from the conference and wish them every success in their research Endeavour.



Prof. (Dr.) Govind Chandra Mishra
Editor

Contents

Preface **i**

SECTION- A
ENERGY RESEARCH PAPERS

1. **Design and Analysis of Parameters in Brushless DC Motor with and without Fuzzy Logic Controller** **3**
Akansha Kaushal, Nirbhay Thakur, Rameshwar Singh

2. **Experimental Study on Biogas Production in Pre-fabricated FRP Floating Drum Digester in the month of February** **10**
Anil Kumar, Biswajit Mandal, Prashant Baredar

3. **Production and Comparative Characterization of Castor Biodiesel as Alternative Fuel for Diesel Engines** **18**
Dishika Jagga, S.K. Mahla

4. **Methanol as an Alternative Transportation Fuel** **27**
Gaurav Kumar Verma, Suyash Kumar Sohani, Praveen Nigwal

5. **Reduction of Energy Storage Requirements in Future Smart Grid Using Electric Springs** **35**
Kalyani S. Jadhav, M.R. Roda, B. E. Kushare

6. **Biodiesel Production from Waste Cooking Oil and Performance Analysis by Using Biodiesel and Butanol Blends** **43**
Manu Jindal, S.K. Mahla

7. **Renewable Energy Potential in India and Slackness in RPO Compliance is Affecting the REC Market** **48**
Megha Sharma, Saurabh Chanana

8. **Performance Evaluation of A Diesel Engine with Tamuna Bio Fuel** **56**
S.N. Ch. Dattu V., Gogula Karthik, Mohammad Khasim Mohiddin Shareef

9. **Lignite Resources of Bikaner and Their Utilization** **62**
Pramod Kumar Rajak, Vijay Kumar Singh, and Dharmendra Kumar

10. **Biorefining Crotalaria Juncea (Sunn-hemp): A Promising New Source for the Production of Biodiesel** **69**
Suvra Sadhukhan, Ujjaini Sarkar

ABSTRACTS

1. **Gas Hydrats as Upcoming Source of Energy** **75**
Amit Arora, C.B. Majumder

SECTION B
ENVIRONMENTAL RESEARCH PAPERS

1. Plastic Waste in India- Management and Utilisation **79**
Aakriti Makker, Arushi Gupta, Lovleen Gupta

2. The Econometric Models to Some Aspects of Tourism in Nepal **87**
Dila Ram Bhandari

3. Adsorption Process for Removal Chromium from Electroplating Wastewater by using Coconut Shell **94**
Fazlollah Changani Khorasgani, Sohail Ayub

4. Effect of Factors on Activity of Bioflocculant Produced by Bacterial Strain Isolated from Waste Water Sample **105**
Viraj Krishan Mishra, Geeta Sharma

5. Climate Change – Threat to Endangered Wild Life Species **113**
Hema Kulkarni

6. Impact of Climate Change on Water Resources of India **121**
Prashant Kumar Shrivastava

7. Direct Mineral Carbonation of Coal Fly Ash at Varying Low Pressure Conditions **128**
T. D. Rushendra Revathy, E. Pavithra, K. Palanivelu, A. Ramachandran

8. A Way to Reduce our Environment foot print-Green Constructions **135**
Sujata Sharma

9. Ceramic Supported Facilitated Transport Membranes for the Separation of Carbon Dioxide and Nitrogen **141**
Uma Maheswari, K. Palanivelu

ABSTRACTS

1. Bioenergy Production from the Pre-treatment of Bagasse as raw Material for Paper Making **149**
Sneha Gupta, A.S. Reddy

2. Performance of Carbon Cloth Electrode in Mediator less Microbial Cell Applications using mixed Sewage Culture **150**
Praveena Mishra, Himanshu Dubey

SECTION- A
ENERGY RESEARCH PAPERS

Design and Analysis of Parameters in Brushless DC Motor with and without Fuzzy Logic Controller

Akansha Kaushal[1], Nirbhay Thakur[2], Rameshwar Singh[3]

[1]M.tech, scholar EE deptt. N.I.T.M, Gwalior,M.P
[2]M.tech scholar EE deptt N.I.T.M, Gwalior,M.P
[3]EE deptt. N.I.T.M, Gwalior,M.P

ABSTRACT

The Brushless DC motor does not require commutator and due to its electrical and mechanical characteristics it is more reliable than the DC motor. BLDC motors are available in many different power ratings. Three phase motors are most common of brushless dc motors which will be helpful in solving problems, The BLDC motor drive system consists of a dc power supply switched to the stator phase windings of the motor through an inverter by power switching devices. This paper shows the behavior of back emf in three phase star connected brushless dc motor through the simulink model and analyzing the speed with fuzzy logic controller. Three phases are displaced by 120^0. Thus we observed the behavior of back emf and speed with and without controller.

Keywords - BLDC, Back EMF, Fuzzy Logic Controller.

1. INTRODUCTION

BLDC motor is conventionally defined as a permanent magnet synchronous motor, Here EMF is considered with a trapezoidal waveform shape. As the name implies, BLDC motors do not use brushes for commutation; instead, they are electronically commutated. Recently, high performance BLDC motors are widely used for variable speed drive systems of the industrial applications and electric vehicles. It has all the good advantage of DC drives and eliminating the drawbacks using electronic commutation. So in this motor current and torque, voltage and rpm are related linearly. [1].The optimization of the permanent magnet pole shape is performed for making balance of the back EMF between the outer and inner windings. [2]

In this paper, mathematical modeling of a BLDC motor and its parameters are described by simulink model using fuzzy logic controller and without using any controller. A comparison can also concluded through these parameters by analyzing the different results from simulink models. Thus, simplicity of control and performance makes the BLDC motor the best choice for low-cost and high-efficiency applications. [3]

2. MODEL AND MATHEMATICAL EXPRESSION OF BLDC MOTOR.

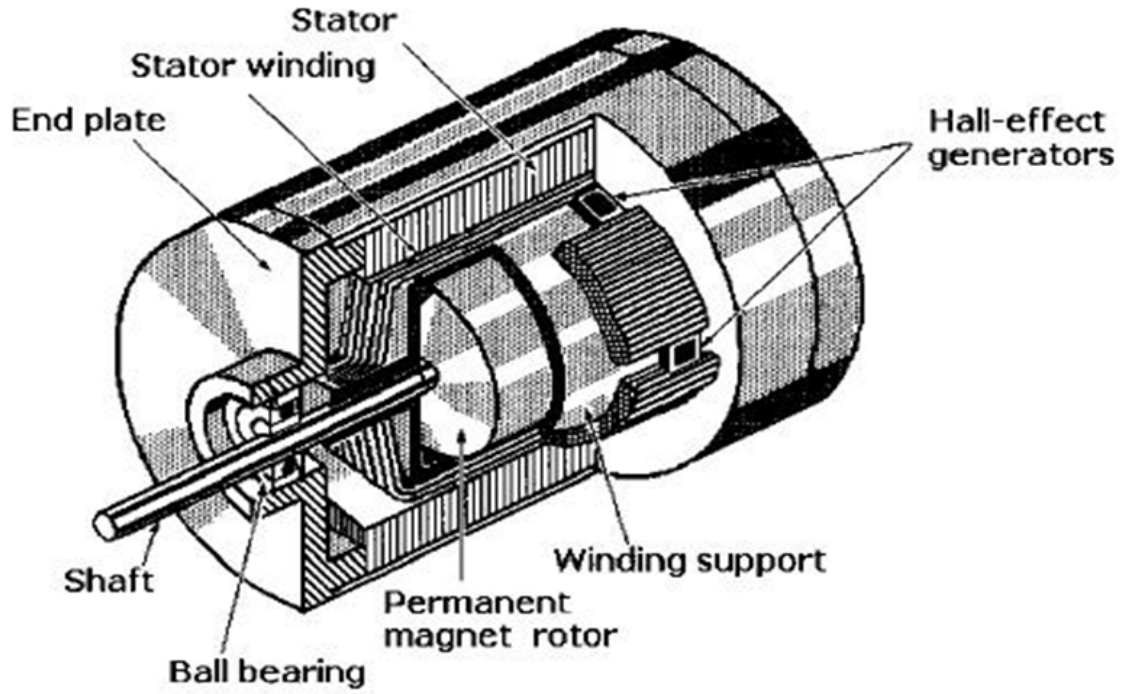


Fig.1: BLDC Motor – schematic diagram

The model of the armature winding for the BLDC motor is expressed as follows

$$V_A = RI_a + L\frac{di_a}{dt} + e_a \quad (1)$$

$$V_B = RI_b + L\frac{di_b}{dt} + e_b \quad (2)$$

$$V_C = RI_c + L\frac{di_c}{dt} + e_c \quad (3)$$

Where,

L is the armature self-inductance.[H]

R is the armature resistance.[Ω]

V is the terminal voltage.[V]

e_a,e_b,e_c is the back EMF.[V]

I_a, I_b, I_c is the input current.[A]

In the 3-phase BLDC motor, the back-EMF is related to a function of rotor position and the back-EMF of each phase has 120o phase angle difference so equation of each phase should be as follows:

$$e_a = B_e f(\theta_e)\omega \quad (4)$$

$$e_b = B_e f(\theta_e - \frac{2\pi}{3})\omega \quad (5)$$

$$e_c = B_e f(\theta_e + \frac{2\pi}{3})\omega \quad (6)$$

Where,
B_e = back EMF constant of one phase[V/rad.s^{-1}]
θ_e = electrical angle
ω = rotor speed [rad.s^{-1}]

3. POWER LOSSES IN BLDC MOTOR

In the BLDC motor, the power losses consist of core losses in the magnetic core, copper losses in the winding and mechanical losses

3.1Copper Losses

The copper losses are I^2R losses. All three-phase windings must be taken into account. Thus, the total armature copper loss (P_{cu}) is equated as follows.

$$P_{cu} = I^2{}_a + I_b{}^2 + I^2{}_c$$

3.2 Core Losses

Core losses are the open circuit losses due to hysteresis property and induced eddy current in the core, which exist as long as the excitation winding energized.

3.3 Mechanical Losses

Mechanical losses are caused by friction and the dynamic drag to oppose the motion of the rotor or so-called the friction and windage losses[4]

Thus to overcome these losses. Certain parameters should be strong enough. The analysis of speed also a part of it. Which result in better outcomes

ISBN: 978-93-83083-87-9

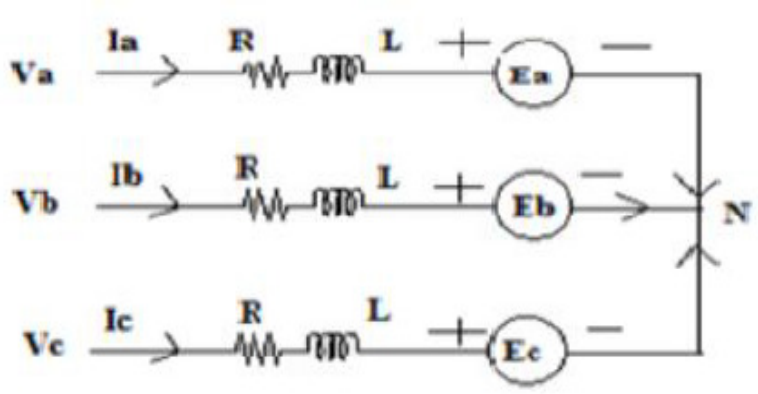


Fig.2: Equivalent circuit diagram of stator winding.

The above diagram shows the arrangement of resistance and inductance in three phase motors by which the EMF get displaced by 120^0.and we get the balanced resultants

4. MODEL OF BLDC MOTOR WITHOUT CONTROLLER.

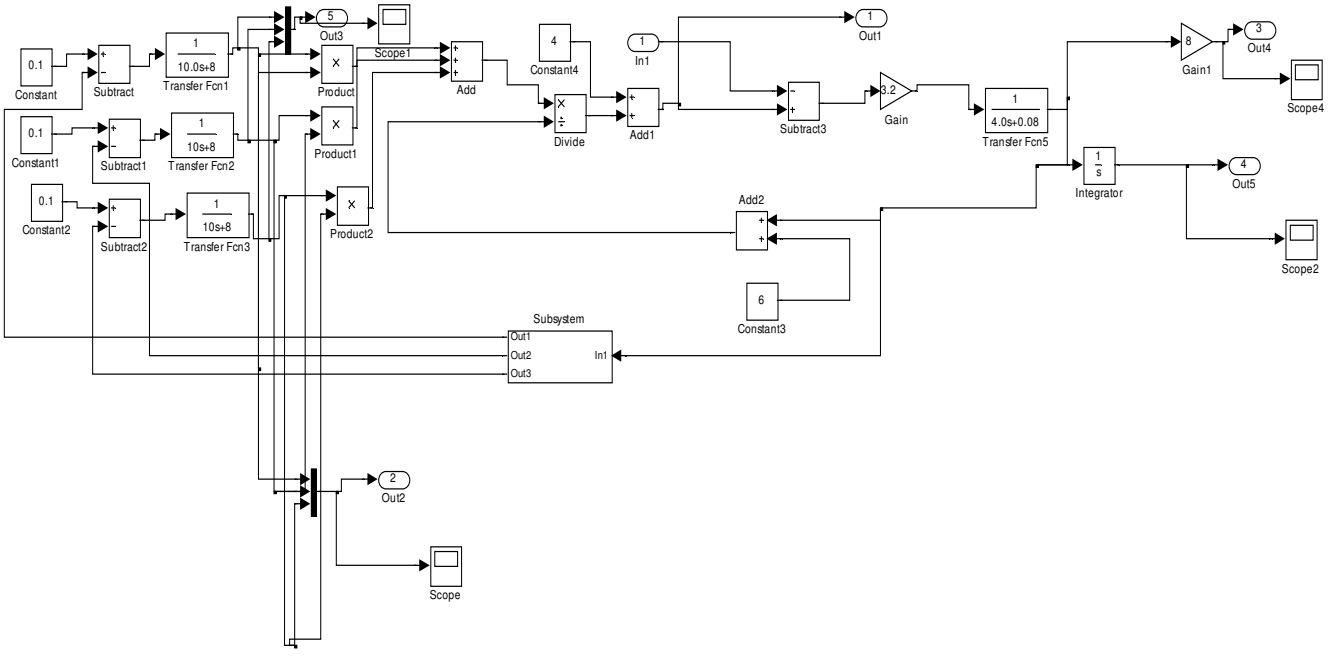


Fig.3: Simulink model of brushless dc motor without controller

In this model, without controller the parameters like current, torque, speed and back EMF can be calculated. For simplicity the analysis of back EMF and speed are calculated for three phase brushless dc motor

ISBN: 978-93-83083-87-9

Results:

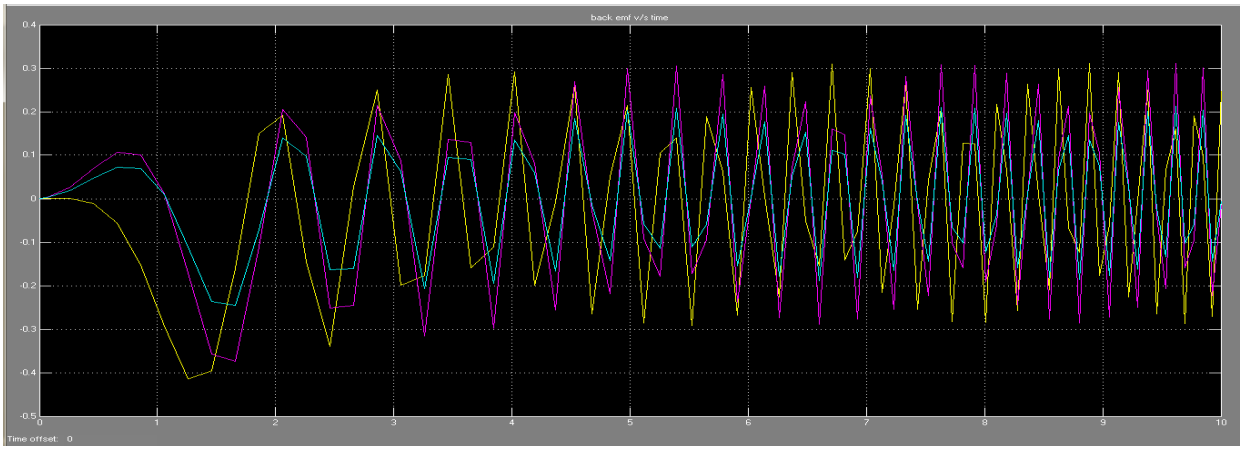


Fig.4: Output waveform for back EMF.

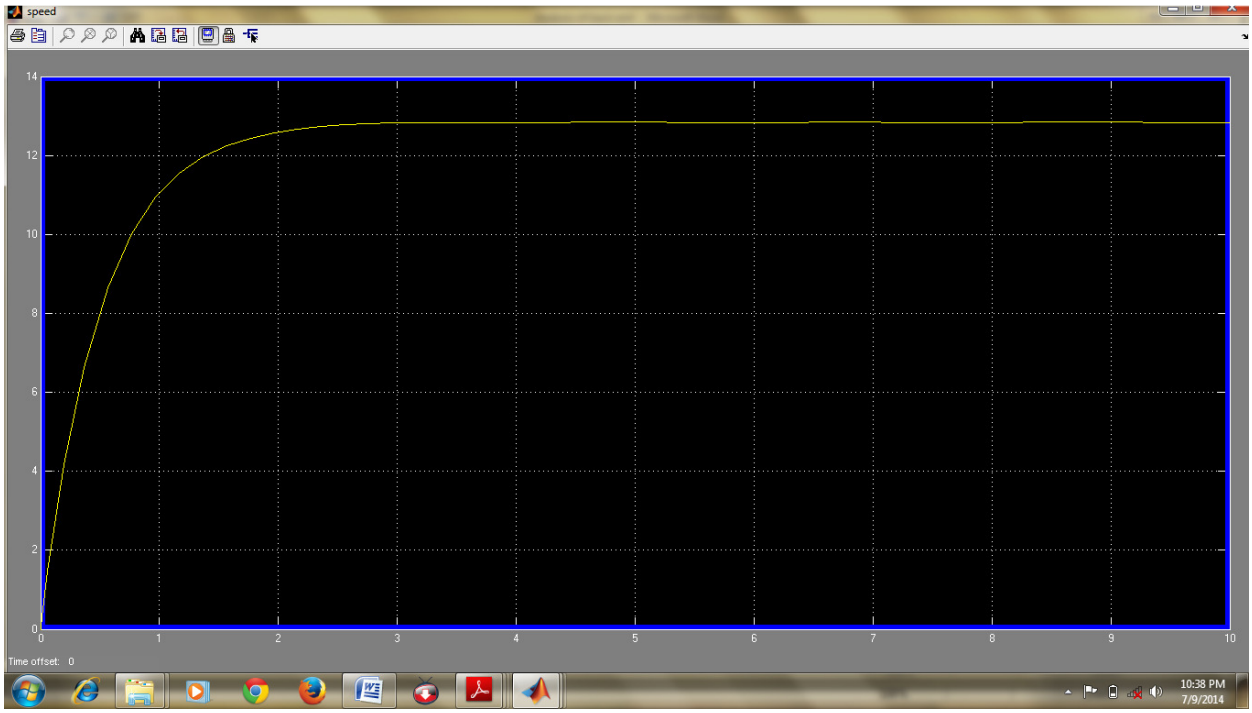


Fig.5: Speed of BLDC motor without controller

5. BLDC MOTOR WITH FUZZY LOGIC CONTROLLER.

Many machine design and control schemes have been developed to improve the performance of BLDC motor drives. The model of motor drive has to be known in order to implement an effective control in simulation. Furthermore, fuzzy logic controllers (FLCs) have been used to analyze BLDC motor drives.

In this paper, a comprehensive simulation model with a fuzzy logic controller is presented. MATLAB/fuzzy logic toolbox is used to design the FLC, which is integrated into simulations with Simulink [5].

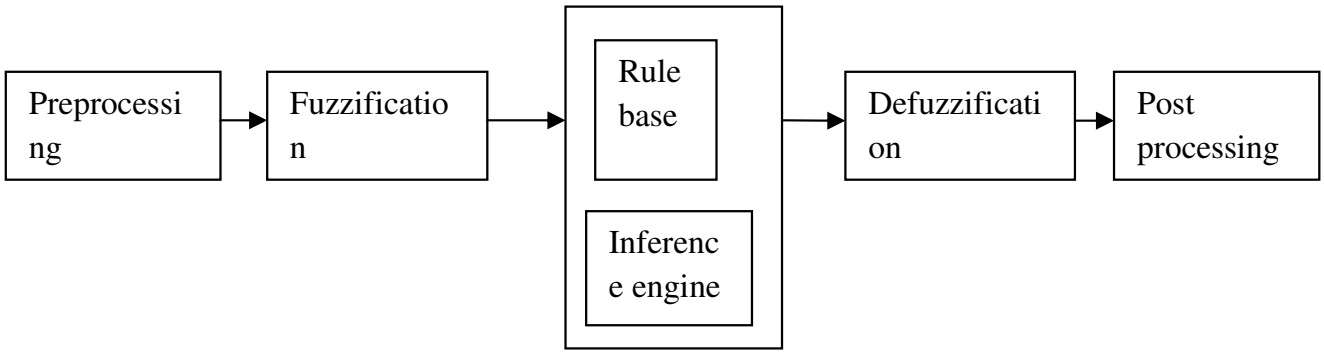


Fig.6: Fuzzy Logic Controller-Schematic Diagram

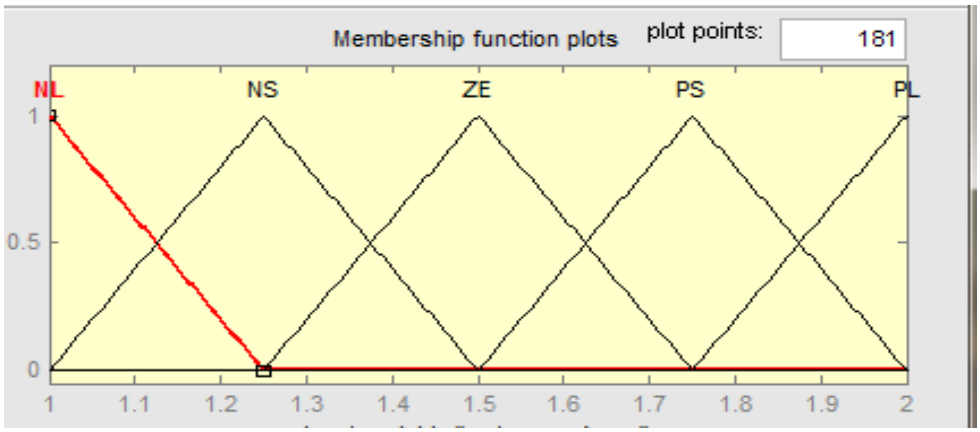


Fig.7: Membership functions of fuzzy logic controller.

5.1 BLDC with FLC

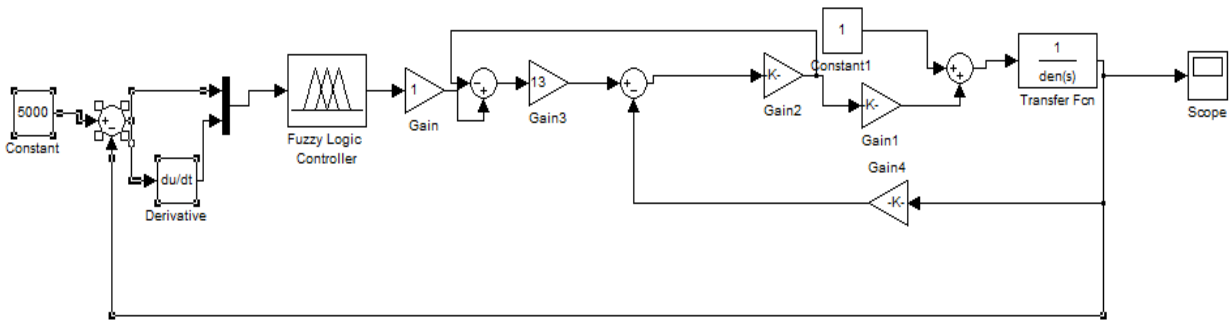


Fig.8: simulation diagram of BLDC motor using fuzzy logic controller.

Result

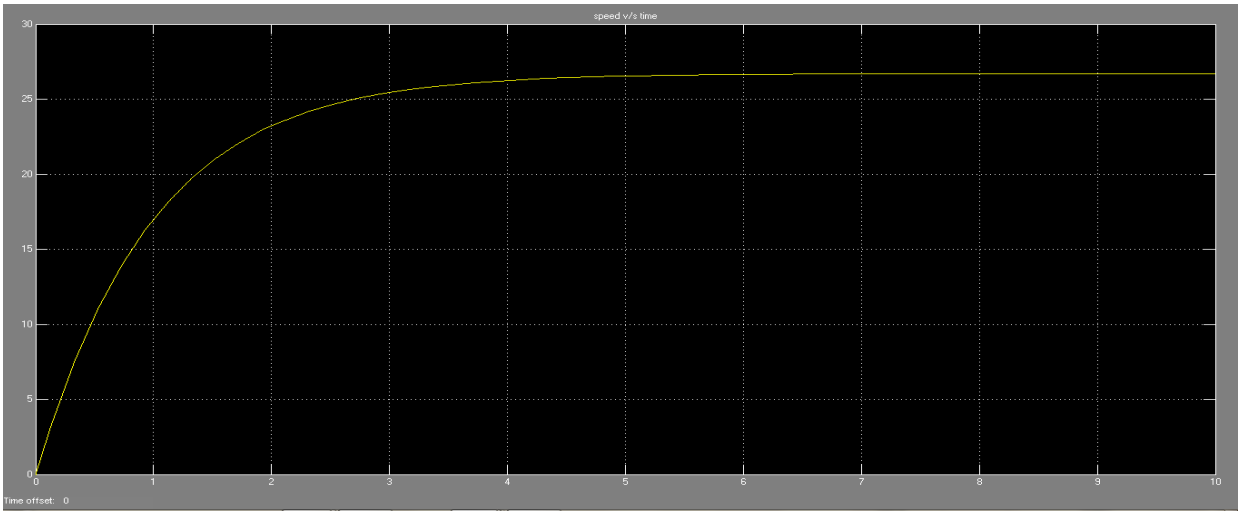


Fig.9: Result of Speed with Fuzzy Logic Controller

6. CONCLUSION

In this paper, speed regulation and back EMF with trapezoidal back-EMF of brushless DC motor is obtainable. the speed result can be determined by fuzzy logic controller or without using controller. But in case of back EMF without controller the result is far better. For further implementation another controllers can be used for best results. Thus, simplicity of control and performance makes the BLDC motor the best choice for low-cost and high-efficiency applications.

REFERENCES

[1] Richa papdeja,P.sankala.Modelling and simulation of Three Phase Brushless DC Motor with using Model Reference Adaptive Controller.IJICSE, ISSN:2348-3539.

[2] Yong Bae Kim,Hong Soon Koh, Chang Seop Shin.A Back EMF Optimizattion of Double Layered Large Scale BLDC Motor using Hybrid Optimization Method., IEEE Transactions VOL.4.

[3] 3-phase BLDC Motor Control with Sensorless Back-EMF ADC Zero Crossing Detection using 56F80x. AN1913 Rev. 3, 11/2005

[4] S.Poonsawat,T.Kulworanichpong.Speed Regulation of Small BLDC Motor using Genetic Based Proportional Control, World Academy of Science, Engineering and Technology.,Vol:2 2008-11-21

[5] Tan Chee Siong, Baharuddin Ismail, Siti Fatimah Siraj, Mohd Fayzul Mohammed.Fuzzy Logic Controller for BLDC Permanent Magnet Motor Drives. IJECS-IJENS Vol: 11 No: 02

[6] http://uniquemachines.blogspot.in/2010/10/servomotors-stepper-motorsand-actuators.html

[7] Akansha kaushal,Nirbhay thakur,Deepak nagaria.Comparison of Speed Control of DC Motor using Fuzzy-PID and PSO-PID Technique

Experimental Study on Biogas Production in Pre-fabricated FRP Floating Drum Digester in the month of February

Anil Kumar[1], Biswajit Mandal[2], Prashant Baredar[3]

[1,2,3]Dept. of Energy Centre, Maulana Azad National Institute of Technology, Bhopal-462 051 (India)

[2]Corresponding author; Email: biswajit.off@gmail.com,

ABSTRACT

Biogas is a value-added product of anaerobic digestion of organic compounds. Production of biogas depends on different factors including: pH, temperature, substrate, loading rate, hydraulic retention time (HRT), C/N ratio, and mixing. Small scale waste digesters are cheap, easy to handle and reduce the amount of waste. Biogas got after anaerobic digestion inside biogas digester could be used for cooking, lighting and electricity. Slurry of cow dung was used for initiating the process. After that 2.0 kg kitchen waste was fed every alternative day. Experiments were conducted in the month of February. Ambient temperature, global radiation and slurry temperature are recorded every hour for different climatic conditions. Based on these data pressure and volume of the biogas are calculated. Experimental investigation was done for bio gas production in prefabricated FRP made floating drum biogas digester. It has been found that ambient parameters such as solar radiation and ambient temperature affect significantly the biogas production.

Keywords: Global radiation, ambient temperature, slurry temperature, pressure, volume.

1. INTRODUCTION

Due to the increasing prices of fossil fuels and taxes on energy sources compelled to find alternative, clean and economical sources of energy. It has now a day's become a major apprehension for nations' economies. In addition, economic prosperity and quality of life, which are linked in most countries to per-capita energy consumption, is a great determinant and indicator of economical development. The demand for energy is a major reason for extensive climate change, resource use and also restricts the living standards of humans. By the time fuel and fertilizer reaches rural areas, the end price is relatively expensive due to high carrying costs, leaving people to find alternative resources other than oil. Wood is used as the conventional source of fuel to produce energy for the household requirements of 4.3 billion people of Asia [1].

Several traditional methods have been used to utilize energy capacity embedded in carbon neutral biomass sources and anaerobic digestion is one of them. Anaerobic digestion (AD) is a natural process whereby bacteria existing in oxygen-free environments decompose organic matter. In anaerobic digestion, organic material is stabilized and gaseous byproducts, primarily methane (CH_4) and carbon dioxide (CO_2) are released. Anaerobic digesters are designed to run in either the mesophilic (20-45°C) or thermophilic (45-60°C) temperature. However, methanogenesis is also probable under low temperature (< 20°C) [2]. Biogas typically refers to a gas produced by the breakdown of organic matter in the absence of oxygen. It is a renewable energy source. Furthermore, biogas can be produced from regionally available raw materials such as recycled waste and is environmentally friendly [3]. A biogas digester, also known as a methane digester, is a piece of equipment which can turn organic waste into usable fuel. In addition to providing a source of renewable fuel, biogas digesters also provide low-cost fuel to people in poverty, and they help to dispose of waste materials which would otherwise be discarded.

The biogas digester relies on bacterial decomposition of biomass, waste material which is biological in origin, ranging from kitchen scraps to cow dung [4]. The main part of a biogas system is a large tank, or digester. Inside this tank, bacteria convert organic waste into methane gas through the process of anaerobic digestion. Each day, the operator of a biogas system feeds the digester with household by-products such as market waste, kitchen waste, and manure from livestock. The methane gas produced inside biogas system may be used for cooking, lighting, and other energy needs. Waste that has been fully digested exits the biogas system in the form of organic fertilizer [5]. New technologies in the field of biogas digesters include bag-type biogas digester plants, Vacvina biogas digester and plastic-drum type biogas digesters. The waste generation rate is increasing in India by 1.33 times per year as per calculated by recent studies. Up to 2047 India will produce around 260 million tones of solid waste and for the disposal of this waste the total land area around 1400 hectare km square is required.

The rate of generation of waste is really impossible to reduce and to supply such a big land area for its disposal. In India for solid waste management approx. Rs.1500 Crore is issued for its overall management [6]. In the present communication, efforts are made toward present status of biogas digester, government policy and market growth in India. Indian government has started a scheme “Biogas based Distributed / Grid Power Generation Programme” from 2005-06 (4th January 2006) with a vision to promote biogas based power generation, particularly in the small capacity range, based on the accessibility of large amount of animal wastes and wastes from forestry, rural based industries (agro / food processing), kitchen wastes, etc.

2. MATERIALS AND METHODS

2.1 Experimental setup

In this experiment a polymer biogas digester has been used which is made up of FRP and HDPE. The biogas digester is of Single Stage Floating Drum Type. Its volume is 1 cubic meter. It was fitted with a feedstock inlet and a gas outlet. The gas outlet was connected to a U-tube manometer via a Y-shaped nozzle. K-type thermocouple was used for the measurement of the interior temperature of the gas holder and the slurry. Various chemicals were used for fixing the U-tube manometer and the K-type thermocouple to the digester. These chemicals were resin, hardener, M-seal, Flex-quick, Araldite and FRP cloth. Initial seeding was done with cow dung. The feedstock provided was mainly kitchen waste. Fig.1 shows the biogas digester drum and Fig.2 shows the Thermocouple setting.



Fig.1: Picture of the biogas digester drums



Fig.2: Thermocouple setting

Fig.3 shows experimental setup biogas digester and Fig.4 shows pressure measurement of biogas digester.



Fig.3: Experimental setup biogas digester



Fig.4: Pressure measurement of biogas digester

ISBN: 978-93-83083-87-9

2.2 Materials to be used

FRP and HDPE drum, cow dung, kitchen waste, hardener, resin, FRP cloth, PVC pipe, U-tube manometer , Y-shaped nozzle, K-type thermocouple, M-seal, Flex-quick, Araldite.

2.3 Instrument used

Solar radiation intensity has been measure by a solar power meter at the tilted surface of the biogas digester. Surface temperature of gas holder and digester measurements have been done with the help of infrared thermometer and temperature indicator. Ambient temperature and humidity has been measure by a thermo-hygro meter. Water column has been measure by a U-tube manometer. K-type thermocouple has been used to measure the inside slurry temperature and gas holder temperature. Spring type weighing machine has been used to measure the weight (like as kitchen waste, cow dung etc.).

2.4 Methodology

For the first time, feedstock provided was 230 kg cow dung and equal amount of hot water. The water temperature was between 44^{o}C. The hot water was used for properly mixing the cow dung. 15 liter of waste water was mixed with 2 kg of kitchen waste. The mixture was left for anaerobic digestion for 15-20 days. After the anaerobic digestion was over the various parameters were measured. The governing parameters such as global radiation, ambient temperature, humidity, inside temperature of gas holder, surface temperature of gas holder, slurry temperature, outside temperature of digester, pressure and volume of the gas chamber was measured from morning to evening. The gas generated could be used for kitchen purposes.

3. RESULTS AND DISCUSSION

This graph shows to the various parameters like, global radiation, ambient temperature, slurry temperature of biogas digester, pressure inside the biogas digester and volume of the biogas digester in the month of February.

Fig.5 shows the variation of ambient temperature, global radiation with respect to time of the day. The ambient temperature depends on the weather of the day. In a clear day, during afternoon the ambient temperature was maximum but during morning and evening ambient temperature was lower. The global radiation was maximum during afternoon. During morning and evening the global radiation was lower. The global radiations depend on the weather of the day. The maximum and minimum ambient temperature and global radiation were found to be 29.7 &17.0^{o}C and 824.48 & 24.22W/m^{2} respectively.

ISBN: 978-93-83083-87-9

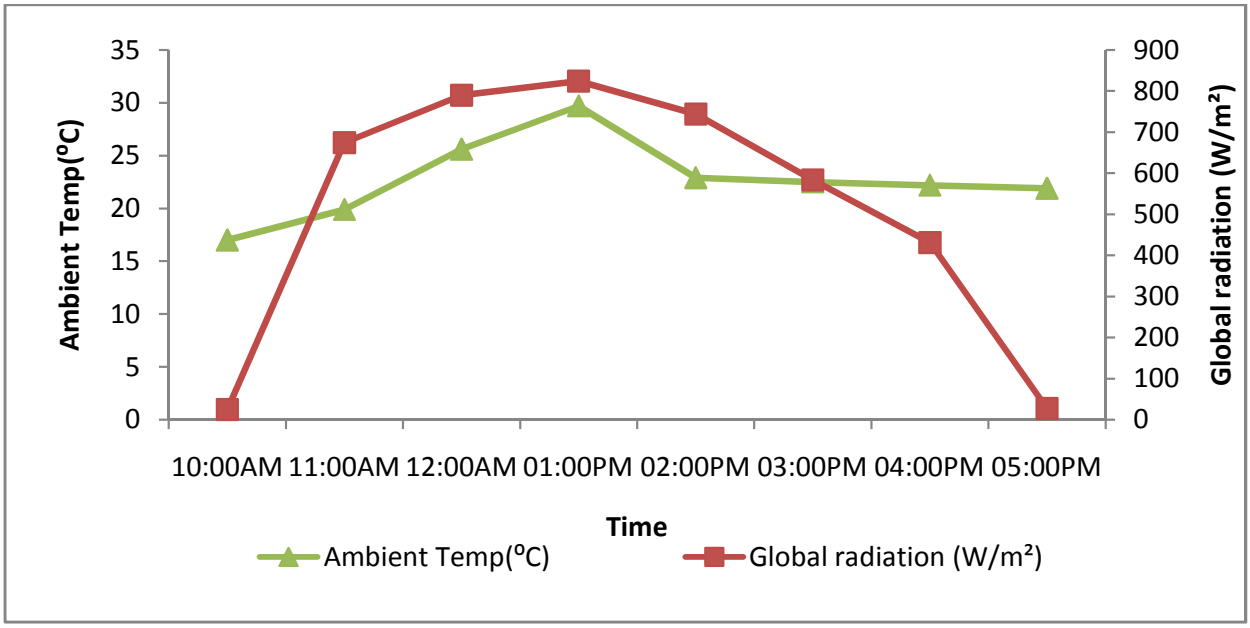


Fig.5: Variation of ambient temperature, global radiation with respect to time

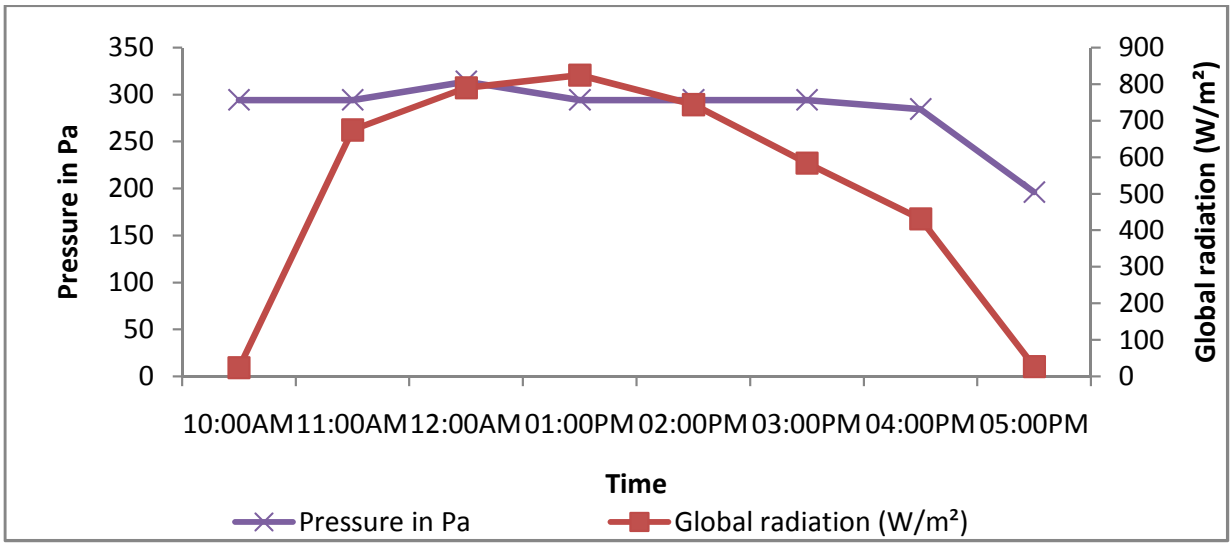


Fig.6: Variation of Pressure, global radiation with respect to time

Fig.6 shows the variation of Pressure, global radiation with respect to time of the day. The pressure of the biogas digester depends on the global radiation on that day and various parameters inside the biogas digester. When global radiation was maximum then the pressure of the biogas digester was also maximum. The global radiation was maximum during afternoon. During morning and evening the global radiation was lower. The global radiations depend on the weather of the day. The

maximum and minimum pressure and global radiation were found to be 313.92 &196.20 in Pa and 824.48 & 24.22 W/m^2 respectively.

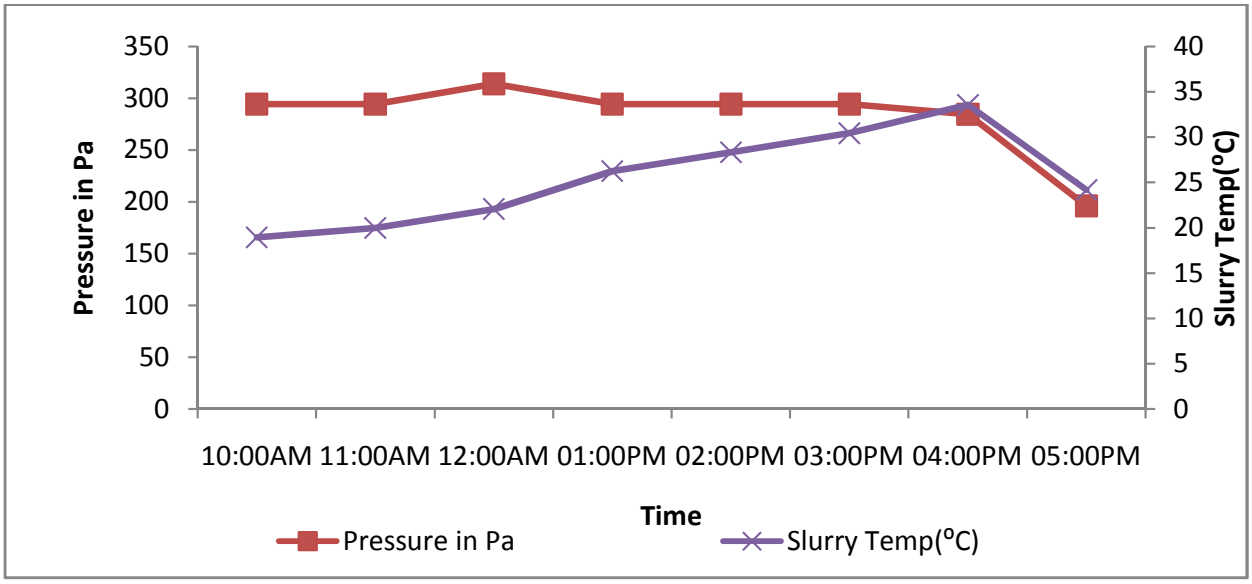


Fig.7: Variation of Pressure, slurry temperature with respect to time

Fig.7 shows the variation of Pressure, slurry temperature with respect to time of the day. The pressure of the biogas digester depends on the global radiation on that day and various parameters inside the biogas digester. When global radiation was maximum then the pressure of the biogas digester was also maximum. The slurry temperature of the biogas digester varies from month to month. During the winter month of February the slurry temperature was lower as compared to that of warmer month of April. During morning and evening the slurry temperature was low and during afternoon time the slurry temperature was high. The slurry temperatures depend on the global radiation of the day. The maximum and minimum pressure and slurry temperature were found to be 313.92 &196.20 in pa and 33.54 & 18.93^{o}C respectively.

Fig.8 shows the variation of volume, global radiation with respect to time of the day. The volume of the biogas also depends on the global radiation. The volume of the gas was maximum when the global radiation was maximum. Usually during morning, the volume of the gas of the biogas was lower and the volume of the biogas continuously increases till afternoon after which it again starts to decrease till evening. The global radiation was maximum during afternoon. During morning and evening the global radiation was lower. The global radiations depend on the weather of the day. The maximum and minimum volume and slurry global radiation were found to be 2512 &1570 in mm^3 and 824.48 & 24.22 W/m^2 respectively.

ISBN: 978-93-83083-87-9

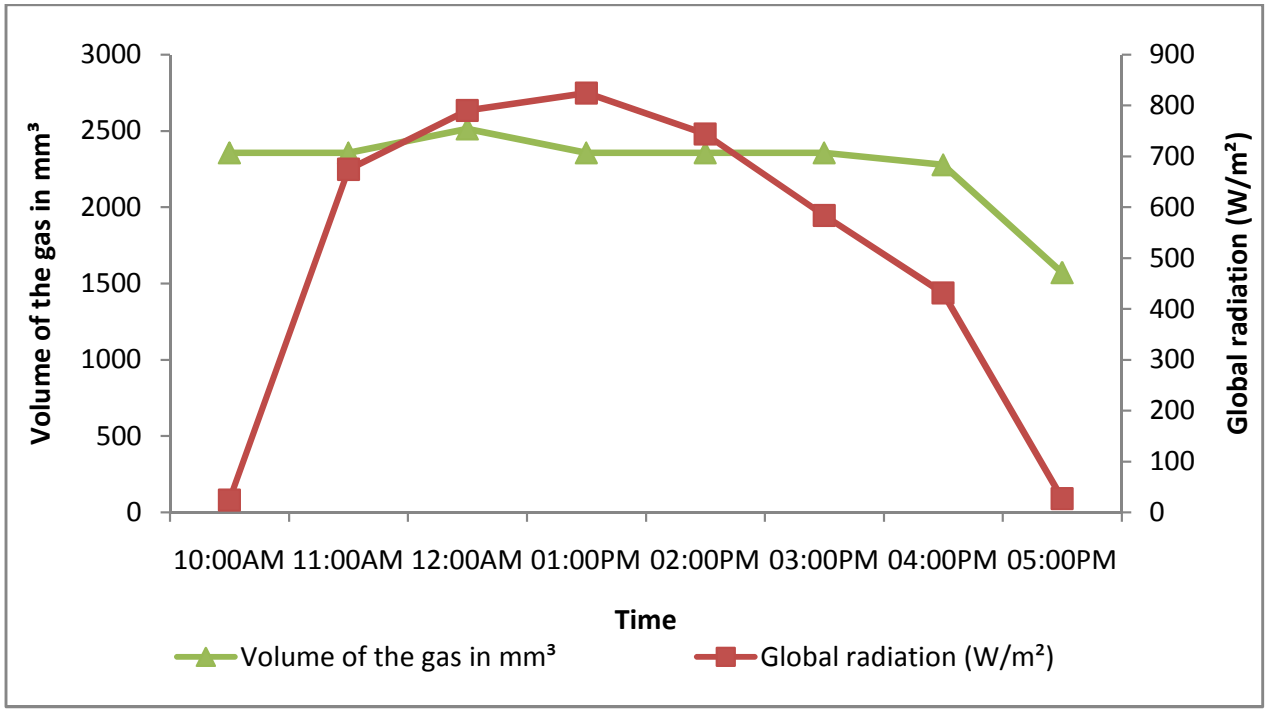


Fig.8: Variation of volume, global radiation with respect to time

4. CONCLUSIONS

The following conclusions were drawn on successful completion of the experimentation on biogas Production in Pre-fabricated FRP Floating Drum Digester:

The slurry temperature inside the digester is very important factor for proper production of biogas as mesophilic and thermophilic bacteria sustain in the range of 30-45^{o}C and 45-52^{o}C respectively. The slurry temperature inside the biogas digester varies from day to day. During morning and evening the slurry temperature were low where as it raised significantly from 10:00 am to 04:00 pm up to 34^{o}C. The global radiation also varies from day to day. During morning and evening the global radiations were low where as it raised significantly from 10:00 am to 01:00 pm to about 824 W/m^{2}. The ambient temperature also varied from day to day. The ambient temperature increased from 10:00 am to a maximum value of 30^{o}C. It was found that the production of biogas is dependent on the global radiation, slurry temperature, ambient temperature and various other parameters. In the month of February, the inside pressure of biogas digester was on an average 299.90pa at 12:00 noon to 01:00 pm and 199.00pa at 05:00 pm. In the month of February, the volume of the biogas was on an average 2399.85mm^{3} at 12:00 noon to 01:00 pm and 1592.78mm^{3} at 05:00pm. The pressure of the biogas and volume showed a direct proportionality with changes in the global radiation, slurry temperature and ambient temperature.

ISBN: 978-93-83083-87-9

REFERENCES

[1] Rajendran Karthik, Aslanzadeh Solmaz and Taherzadeh Mohammad J. Household biogas Digesters. *Energies 2012; 5*(8): 2911-2942.

[2] Vanegas Carlos, artlett John. Anaerobic Digestion of Laminaria digitata: The Effect of Temperature on Biogas Production and Composition. Springer 2012; 3: 305-310.

[3] Information on www.en.wikipedia.org/wiki/Biogas_digester

[4] Information on www.wisegeek.com/what-is-a-biogas-digester.htm

[5] Information on www.simgas.com/advantages-of-biogas/how-does-biogas-work/item46

[6] Bansal Ankur K., Kapoor Shivam, Agrawal Mayank, Kaushlendra. The road to zero waste: Anaerobic digestor. International Journal of Environmental Sciences 2013; 3(5):0976 – 4402.

Production and Comparative Characterization of Castor Biodiesel as Alternative Fuel for Diesel Engines

Dishika Jagga[1], S.K. Mahla[2]
[1]*M.Tech student at Thapar University, Patiala*
[2]*Thapar University, Patiala*

ABSTRACT

Biodiesel being as a clean, environment friendly, biodegradable fuel can deal with the crisis of fossil fuel depletion and environmental pollution. This paper represents the method of production of castor biodiesel by transesterification using methanol and NaOH. The factors that affect transesterification reaction such as alcohol content, temperature, reaction time, free fatty acid content were optimized. The fuel properties of castor biodiesel like kinematic viscosity, density, calorific value, flash and fire point, cloud and pour point were determined and compared with Indian standard biodiesel. It was concluded that after optimization of transesterification reaction, 130 ml of methanol and 2.5 g of NaOH were mixed with 500 ml of castor oil without heating for 1 h gives yield of 94.6% castor biodiesel. The calorific value of castor biodiesel was 4.84% lesser than that of diesel. The flash and fire point of castor biodiesel were higher than that of diesel. This paper revealed that the production of biodiesel from castor oil is a promising alternative fuel for diesel engines.

Keywords: Castor oil, biodiesel, transesterification, fuel properties, Indian standards

1. INTRODUCTION

In the recent years, world is facing the crisis of natural resources depletion and environmental degradation. As fossil fuel reserves are limited and continue to deplete to deal with energy demand increasing day by day. Biodiesel has become an attractive alternative fuel for diesel engine (Cao and Zhao, 2013). Biodiesel is a clean, biodegradable, renewable and promising source of fuel. Biodiesel can be easily blended with diesel in any proportion with no modification to the engine (Agarwal and Das, 2001). The transesterification reaction of castor oil were carried out at optimum conditions of reaction temperature of 59.89˚C, methanol to oil ratio of 8:10:1 and KOH catalyst of 1.22 wt% of oil. The methyl ester content under these optimum conditions was 94.5% w/w of oil and properties met the standards of EN14214 and ASTM D 6751. The viscosity and density of ester was reduced by blending with diesel upto B45 to satisfy within the ASTM 6751 and EN 14214 limits for castor biodiesel (Molla Asmare et al, 2014). The method of production of

ISBN: 978-93-83083-87-9

biodiesel from castor oil (treated with mineral turpentine oil) by transesterification with methanol in the presence of NaOH as catalyst to obtained conversion of 92% at 60˚C. (Babu et al., 2012)

1.1 Castor oil as biodiesel

Concept of using vegetable oils as fuel was introduced when Dr. Rudolf diesel developed first diesel engine to run on vegetable oil in 1885. His predictions come true and lots of countries are taking step towards alternative fuel for diesel engine (Babu et al., 2012). Nation is facing shortage of edible oil with increase in population demand, it would be viable to produce biodiesel from castor oil. Castor oil is non-edible oil which is yellowish in color extracted from castor bean (Shrirame et al., 2011). Castor oil consists of 80-90% ricinoleic acid (Table 1). The high viscosity of castor oil is mainly due to presence of ricinoleic acid (Achaya K, 1971).

Table 1. Composition of castor oil

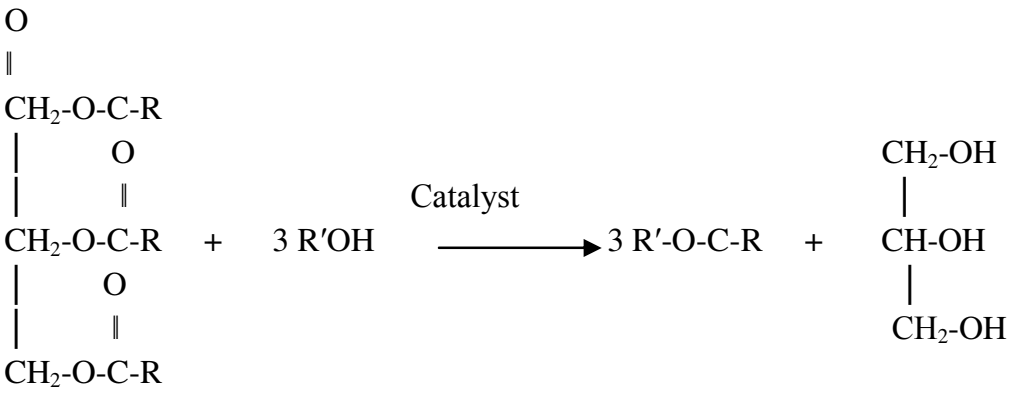
Acid name	Composition (%)
Ricinoleic acid	85-90
Linoleic acid	4-5
Oleic acid	2-4
Stearic acid	1
Palmitic acid	1
Others	0.3-1%

The high viscosity of castor oil creates operational and durability problems in diesel engines if castor oil is directly run on the conventional diesel engine. High viscosity leads to poor atomization which in turn results in poor combustion, ring sticking, injector coking, injector deposits, injector pump failure & lubricating oil dilution. To improve the performance of diesel engine, viscosity has to be reduced. (M.C. Navindgi et al., 2012)

1.2 Need of Transesterification

The performance of castor oil in diesel engine can be improved by reducing viscosity of castor oil using transesterification. Transesterification is a reversible reaction in which castor oil reacts with a short chain alcohol and alkaline catalyst to form fatty acid methyl ester and glycerol as a product (Equation 1). Glycerol has low solubility in the oil so it gets settle down easily. Castor oil is filtered prior to use to remove impurities and also preheated prior to transesterification process. Alcohols that can be used in transesterification process are methanol, ethanol, propanol and butanol.

Methanol is mostly used because of its low cost, polar group, shortest chain alcohol. Basic as well as acidic catalysts are used in transesterification reaction. Basic catalyst are most preferable than acidic catalysts because of higher conversion rate and minimum reaction time. The basic catalysts that used in transesterification are KOH, NaOH, potassium methoxides etc. For base-catalyzed transesterification, factors that affects the reaction are alcohol content, temperature, reaction time, free fatty acid content, moisture content (J.M.Encinar et al., 2010).



Equation 1. Transesterification reaction

2. MATERIALS AND METHOD



Figure 1. Transesterification setup

An experimental setup was used to perform transesterification reaction (Figure 1). Transesterification setup consists of a hot plate with magnetic stirrer and temperature regulator. The conical flask of 1000 ml covered with foil was placed over hot plate. The separating funnel is used to separate out the products such as crude biodiesel and glycerol.

2.1 Transesterification procedure

The transesterification process (Figure 2) was performed at laboratory of Thapar University, Patiala. Castor oil was filtered to remove gums and impurities. The transesterification method proposed by (Yung and Ping Lin, 2011) was optimized the factors to get higher ester recovery and low viscosity. Freshly prepare the mixture of 130 ml of methanol and 2.5 g of sodium hydroxide (NaOH) in the conical flask and stirred it until the flasks of NaOH dissolves in the methanol. At ambient temperature, add this mixture of methanol and NaOH into 500 ml of castor oil and quickly stirred it for 1 hour without heating. The products were allowed to settle overnight in the separating funnel. After that glycerol was removed from bottom of separating funnel. The crude biodiesel was washed with distilled water for about 3-4 times. After washing, crude biodiesel was stirred and heated at 110˚C to remove moisture traces and allow it for cooling at room temperature. The light yellow crystal clear biodiesel was produced and stored for usage.

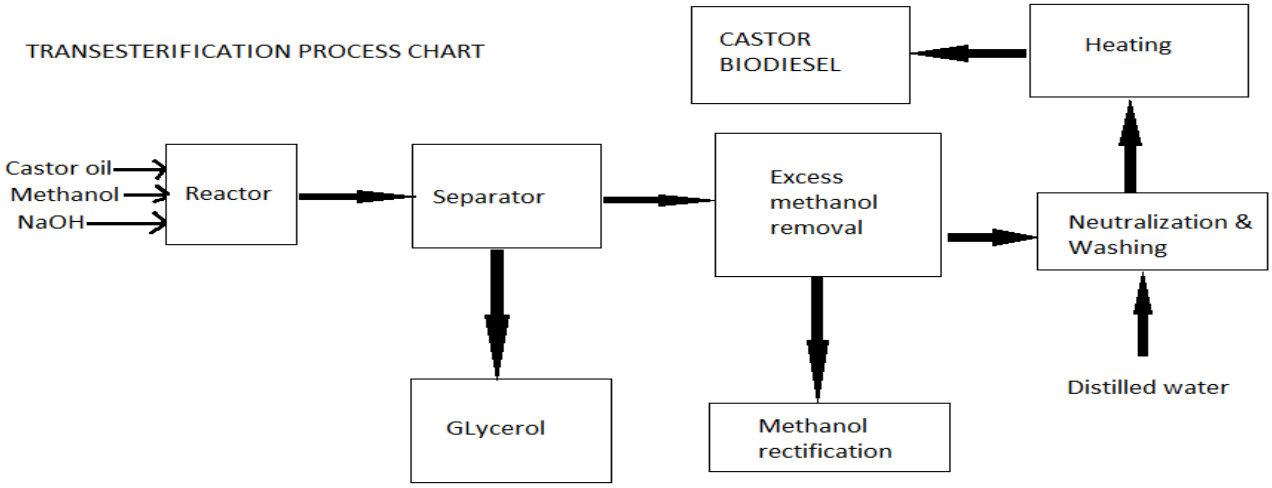


Figure 2. Transesterification process chart

2.2 Determination of fuel properties of castor biodiesel at MERADO, Ludhiana

After transesterification of castor oil, fuel properties of castor biodiesel were measured. The castor biodiesel properties were comparatively analyzed with diesel.

ISBN: 978-93-83083-87-9

2.2.1 Calorific value

It is quantity of heat liberated by completely burning of one unit mass of fuel. Bomb calorimeter was used to measure the calorific value of biodiesel and diesel. A fuel sample of 1 ml was burnt in the bomb calorimeter in the presence of pure oxygen. The sample was ignited electrically. As heat was produced, the rise in temperature was measured. The effective heat capacity was also determined using pure and dry benzoic acid as test fuel. (Van Gerpan et al., 2005)

2.2.2 Kinematic viscosity

It is measure of resistance to flow of a liquid due to internal friction of one part of a fluid moving over another. Redwood viscometer was used for determining the viscosity of oil expressed as a time of flow in seconds through specified hole over a metallic piece. Viscosity is measured in centistokes. Fuels having low viscosity may not provide sufficient lubrication for pumps and plunger results in leakage and abnormal wear. Fuels having high viscosity increase the pumping losses and reduce injection pressure results in poor atomization and insufficient mixing with air ultimately affects the combustion process. (Tate et al., 2006)

2.2.3 Density

It is mass per unit volume. It is calculated by weighing apparatus. Biodiesel was slightly heavier than conventional diesel fuel. This allows use of splash blending by adding biodiesel on the top of diesel for making blends of biodiesel. Biodiesel should be added at top of diesel fuel. If biodiesel was first put at the bottom and then diesel fuel was added, it would not mix. (Van Gerpan et al., 2005)

2.2.4 Flash and Fire point

It is a temperature at which it will ignite when exposed to a flame of light. Pensky–Martens flash and fire point apparatus was used to measure the flash and fire point of the biodiesel and diesel. Flash point can indicate the possible presence of highly volatile and flammable material in a non-volatile material. The fire point was an extension of flash point in a way that it reflects the condition at which vapour burns continuously for five seconds. The fire point was always higher than flash point by 5-8˚C. (Tate et al., 2006).

2.2.5 Cloud point

Cloud point is a temperature at which a haze of crystals appears in the fuel under test conditions. Pour point is a lowest temperature at which diesel will begin to flow. In the determination of the cloud point, sample was cooled under prescribed conditions and was inspected at intervals of 1˚C until a cloud or haze appears.

In determination of pour point, the sample cooled under prescribed conditions and inspected at intervals of 3˚C until it will no longer move when the place of surface was held vertical for 6 seconds, the pour point was then taken as 3˚C above the temperature of cessation of flow. It becomes important for low temperature operations. Both properties may indicate filter plugging and flow problems in the fuel line. (Van Gerpan et al., 2005)

3. RESULTS AND DISCUSSION

3.1 Optimization of transesterification results

The studies were conducted on optimizing the factors that affects the transesterification of castor proposed by Yung and Ping Lin, 2011. The ester recovery and viscosity was affected by the transesterification factors such catalyst quantity, reaction temperature, amount of methanol used (Table 2). The factors that affect the transesterification reaction were standardized to obtain castor biodiesel with lowest kinematic viscosity and highest level of ester recovery.

Table 2. Change in ester recovery and viscosity with respect to methanol quantity

Castor oil (ml)	NaOH Quantity (gm)	Methanol Quantity (ml)	Reaction time (hour)	Settling time (hour)	Ester recovery (gm)	Kinematic viscosity (cst)
500	2.5	110	1	24	95	8.14
500	2.5	130	1	24	94.6	7.37
500	2.5	150	1	24	71.3	6.93
500	2.5	160	1	24	68.7	6.46

It was observed that highest recovery of methyl ester of castor was obtained when 500 ml of castor oil was reacted with 110 ml of methanol and 2.5g of NaOH for 1 hour without heating and settled for 24 hours. After settling in the separating funnel, separate out the glycerol from biodiesel. The crude biodiesel was heated at 110˚C until it gets crystal cleared. Then biodiesel was allowed to cool down and store it for use. As ester recovery was higher at 110 ml of methanol, but at this percentage the value of viscosity was also higher. At methanol quantity of 130 ml, the ester recovery is slightly less but the viscosity was lie in the range (Table 3). Further addition of methanol was decreasing the ester recovery and also decreases the value of viscosity.

ISBN: 978-93-83083-87-9

Table 3. Optimized factors that affect the transesterification

Castor oil (ml)	NaOH Quantity (gm)	Methanol Quantity (ml)	Reaction time (hour)	Settling time (hours)	Ester content (gm)	Kinematic viscosity (cst)
500	2.5	130	1	24	94.6	7.37

3.2 Fuel properties analysis

The fuel properties were determined by various apparatus at (Cmeri, Ludhiana) (Table 4). The results of fuel properties were analyzed with the petrodiesel.

Table 4. Comparative properties of castor biodiesel and diesel

Properties	Method	Limit	Castor Biodiesel	DIESEL
Calorific value (KJ/Kg)	IS:1350	>33000	39967.19	42000
Density (Kg/cm^3)	ASTM D1298	-	900	830
Viscosity (cst)	IS:1448[P: 25] 1976	<5	7.37	3.04
Flash point (˚C)	IS:1448[P:32] 1992	>130	180	68
Fire point (˚C)	IS:1448[P:32] 1992	>53	185	73
Cloud point (˚C)	IS:1448[P:10] 1970	-3 to 12	2	-1
Pour point (˚C)	IS:1448[P:10] 1970	-15 to 10	- 3	-6

The overall studies based on production of castor biodiesel, fuel characterization of castor biodiesel and diesel were carried out. The following results were found out –

- The calorific value of castor biodiesel and diesel were found as 39967.19 KJ/kg, 42000 KJ/kg respectively. The calorific value of castor biodiesel is decreased by 4.84% than that of diesel.
- The kinematic viscosity of castor biodiesel and diesel were found as 7.37, 3.04 centistokes at 40˚C. The results indicated that the castor biodiesel has kinematic viscosity 58.7 percent more than that of diesel.
- The flash point and fire point of castor biodiesel was found to have higher than that of diesel.
- The cloud and pour point of castor biodiesel was found to have higher than those of diesel.

ISBN: 978-93-83083-87-9

- The density of castor biodiesel and diesel were found as 900 kg/cm^3 and 830 kg/cm^3 respectively. The results showed that the castor biodiesel has density more than that those of diesel

4. CONCLUSION

This study concluded that after optimization of transesterification reaction, mixture of 130 ml of methanol and 2.5 g of NaOH were react with 500 ml of castor oil without heating for 1 hour gives yield of 94.6% castor biodiesel. The calorific value of castor biodiesel was 4.84% less than that of diesel. The kinematic viscosity of castor biodiesel was 58.7% higher as compared to diesel. The flash point and fire point of castor biodiesel was higher than that of diesel. The castor biodiesel has more density than that of diesel. The cloud point and pour point of castor biodiesel was more as compared to those of diesel. The properties of castor biodiesel has meets the standards like ASTM, IS at some point except viscosity. The viscosity of castor biodiesel has slightly high above 5cst which was not within limit of Indian Standards. The viscosity further reduced by blending with diesel upto 30% to get within the Indian Standard Limit.

5. ACKNOWLEDGEMENT

The authors would like to acknowledge the financial assistance given by TEQIP, AICTE for carrying out this work.

REFERENCES

[1] Chun-yan Cao and Yong-hua Zhao, “Transesterification of castor oil to biodiesel using KOH/NaY as solid base catalyst”, International Journal of Green Energy, Taylor & Francis, vol. 10: 219-229, 2013.

[2] Agarwal A.K. and L.M. Das, Biodiesel development and characteristics for use as a fuel in compression ignition engines, Journal of Engineering for Gas, Turbines and Power, vol. 123: 440-447, 2001.

[3] Molla Asmare, Nigus Gabbiye, “Synthesis and characterization of biodiesel from castor bean as alternative fuel for diesel engine”, American Journal of Energy Engineering, vol. 2(1): 1-15, 2014.

[4] Penugonda Suresh Babu, Venkata Ramesh Mamilla, “Methanolysis of castor oil for production of biodiesel”, International Journal of Advanced Engineering Technology, vol. 3: 146-148, 2012.

[5] Hemant Y.Shrirame, N.L.Panwar, B.R.Bamniya, “Biodiesel from castor oil – a green energy option”, Scientific research, vol. 2: 1-6, 2011.

[6] Achaya K, “Chemical derivatives of castor oil”, J Am Oil Chem Soc. 1971, vol. 48: 758-763.

[7] M.C.Navindgi, Maheswar Dutta, B. Sudheer Prem kumar, “Performance evaluation, emission characteristics and economic analysis of four non-edible straight vegetable oils on a single cylinder CI engine”, ARPN Journal of Engineering & Applied Sciences, vol. 7: 2, 2012.

[8] J.M.Encinar, J.F.Gonalez, G.Martinez, N.Sanchez, C.G.Gonalez, “Synthesis and characterization of biodiesel from castor oil transesterification”, International Conference on Renewable Energies and Power Quality, 2010.

[9] Yung-Sung Lin, Ha-Ping Lin, "Spray characteristics of emulsified castor biodiesel on engine emissions and deposit formation", Renewable Energy, Elsevier, vol.36: 3507-3516, 2011.

[10] Tate, R.E., Watts, K.C., Allen, C.A.W. and Wilkie, K.I. "The viscosities of three biodiesel fuels at temperatures up to 300˚C", Fuel, vol. 85: 1010-1015, 2006.

[11] Knothe, Van Gerpan and Krahl, "The Biodiesel Handbook", National Centre of Agricultural Utilization Research Agricultural Research Service U.S. Department of Agricultural Peoria, Illinois, U.S.A, Department of Mechanical Engineering Iowa State University Ames, Iowa, U.S.A, University of Applied Sciences Coburg, Germany, 2005.

[12] Test report of characterization of castor biodiesel, www.cmeri.res.in, Central Mechanical Engineering Research Institute (MERADO), Ludhiana.

Methanol as an Alternative Transportation Fuel

Gaurav Kumar Verma[1], Suyash Kumar Sohani[2], Praveen Nigwal[3]
[1,2,3]SPITM Mandleshwer, Mechanical Engineering

ABSTRACT:

This paper is General review of methanol as an alternative transportation fuel, Analysis of conversion pathways from technical, economical and environmental point of view. Concerns with petroleum oil supplies and greenhouse gas emissions have stimulated research into new alternative fuels, including natural gas, ethanol, methanol, bio diesel, electricity and hydrogen. Methanol has been promoted as an alternative transportation fuel from time to time over the past forty years. In spite of significant efforts to realize the vision of methanol as a practical transportation fuel in the US, such as the California methanol fuelling corridor of the 1990s, it did not succeed on a large scale. This white paper covers all important aspects of methanol as a transportation fuel.

Keywords: methanol, transportation, use, production.

1. INTRODUCTION

In the aftermath of the first oil crisis in 1973, the potential of methanol as a liquid fuel to satisfy world transportation demand was highlighted by Reed and Lerner [Reed, W1]. Although methanol was being manufactured from hydrocarbon feedstock (natural gas and coal) through a gasification process at production levels small compared to diesel or gasoline, the process was well established and could be scaled. Any feedstock that could be gasified into synthesis gas could potentially be used in the manufacture of methanol. Soon afterwards, the potential of using renewable resources (biomass) were described. [Hagen] The ultimate approach, the recovery of CO2 from the atmosphere for methanol manufacturing, was discussed in 2005 by Prof. George A. Olah and his colleagues at the University of Southern California. They have coined the phrase "methanol economy," with methanol as a CO2 neutral energy carrier [Olah].

Initial interest in methanol was not in its role as a sustainable fuel, but as an octane booster when lead in gasoline was banned in 1976. The Clean Air Act Amendment in 1990 envisioned the potential of methanol blends as means of reducing reactivity of vehicle exhaust, although in the end, refiners were able to meet the goals with the use of reformulated gasoline and after treatment catalysts [EPA-1]. Interest in alternative fuels, including methanol, was also raised after the first and second oil crisis.

The only role for methanol currently as a transportation fuel in the world is as a component to make bio diesel, where it is used as a reagent to form methyl esters.

2. PRODUCTION PROCESSES AND FEEDSTOCKS

The typical feedstock used in the West in the production of methanol is natural gas, although a substantial fraction of the world's methanol is made from coal. Methanol also can be made from renewable resources such as wood, forest waste, peat, municipal solid wastes, sewage and even from CO2 in the atmosphere. The production of methanol also offers an important market for the use of otherwise flared natural gas.

3. PRODUCTION PROCESSES

The methanol production is carried out in two steps. The first step is to convert the feedstock into a synthesis gas stream consisting of CO, CO2, H2O and hydrogen. For natural gas, this is usually accomplished by the catalytic reforming of feed gas and steam (steam reforming). Partial oxidation is another possible route. The second step is the catalytic synthesis of methanol from the synthesis gas. Each of these steps can be carried out in a number of ways and multiple technologies offer a spectrum of possibilities which may be most suitable for any desired application.

The steam reforming reaction for methane (the principal constituent of natural gas) is:

$$2\ CH_4 + 3\ H_2O \rightarrow CO + CO_2 + 7\ H_2 \text{ (Synthesis Gas)}$$

This process is endothermic and requires externally provided energy of reaction.
In the case of coal, the synthesis gas is manufactured through gasification using both oxygen and steam (including water-shift reaction):

$$C + \tfrac{1}{2}O_2 \leftrightarrow CO \text{ (Partial oxidation)}$$

$$C + H_2O \leftrightarrow CO + H_2 \text{ (Water-gas reaction)}$$

$$CO + H_2O \leftrightarrow CO_2 + H_2 \text{ (Water-gas shift reaction)}$$

$$CO_2 + C \leftrightarrow 2\ CO$$

Biomass is converted into synthesis gas by a process similar to that of coal. In the case of biomass, the synthesis gas needs to be upgraded (through reforming or water-gas shifting) and cleansed to produce a synthesis gas with low methane content and proper H2- to-CO ratio. There are tars (heavy hydrocarbons) as well as ash (that can be removed dry or as a slag) that are produced in the gasification, and they need to be removed upstream from the catalytic reactor Once the synthesis gas of the correct composition is manufactured, methanol is generated over a catalyst; in the case of natural gas,

$$CO + CO2 + 7\ H2 \rightarrow 2\ CH3OH + 2\ H2 + H2$$

There are excellent catalysts that have been developed for the catalytic production of methanol, operating at relatively mild conditions (10's of atmospheres, a few hundred degrees C), with very high conversion and selectivity.

The natural gas process results in a considerable hydrogen surplus. If an external source of CO2 is available, the excess hydrogen can be consumed and converted to additional methanol. The most favorable gasification processes are those in which the surplus hydrogen reacts with CO2 according to the following reaction:

$$CO2 + 3\ H2 \rightarrow CH3OH + H2O$$

Unlike the reforming process with steam, the synthesis of methanol is highly exothermic, taking place over a catalyst bed at moderate temperatures. Most plant designs make use of this extra energy to generate electricity needed in the process. Control/removal of the excess energy can be challenging, and thus several processes use liquid-phase processes for manufacturing of methanol. In particular, Air Products developed the Liquid Phase Methanol Process (LPMEOH) in which a powdered catalyst is suspended in an inert oil. This process also increases the conversion, allowing single pas

TABLE NO. 1: PHYSICAL AND CHEMICAL PROPERTIES OF METHANOL FUEL:

Fuel type		**Gasoline**	**Ethanol E100**	**Methanol M100**	**Methanol with cosolvent 50%methanol**
Chemical formula					
RON					
MON					
(R+M)/2					
Specific gravity	Kg/l	0.75	.794	.796	.789
Stoic air/fuel ratio		14.6	9	6.4	8.8
Net heat of Combustion (LHV)	MJ/l	32	21	16	21
Net heat of Combustion (LHV)	MJ/kg	43	27	20	21

ISBN: 978-93-83083-87-9

Energy density	MJ/L	32	21	16	21
Lower flammability limit	%VOL	1.4	3	6	
Upper flammability limit	%VOL	7.6	19	36	
Autoignition temperature	K	514	638	738	
Flash temperature	K	230	285	280	
Laminar flame speed	MJ/kg	33	41	50	
Vapour pressure	psi	9	2.3	4.6	
Latent heat of vaporization	MJ/kg	.27	.85	1.1	.80
Vaporization energy/LHV	MJ/kg	0.006	0.031	0.058	0.03

Methanol has lower energy density than gasoline, ethanol or diesel (not shown). The engine fuel system needs to deliver larger flow rates of methanol than gasoline, and also the fuel range (miles driven on a tank-full) decrease. These effects depend on the blending level of methanol in the gasoline. For comparable vehicle efficiencies, the range is decreased by 50% when using M100. However the efficiency of operation of the engines in the vehicle demonstrations described in Section I is comparable or slightly better to that when using gasoline, when compensating for the lower heating value of the fuel [Pefley] With a dedicated methanol engine, the vehicle can be as efficient as a diesel, or about 25-30% more efficient than conventional vehicles operating on gasoline. [Brusstar] The range of dedicated high-efficiency methanol vehicles is about 30% lower than conventional gasoline vehicles.

The flame speed of stoichiometric air mixtures with ethanol and methanol at 1 bar, 300K are comparable to that of n-heptane, which is in small amounts present in Primary-Reference-Fuel (PRF) gasoline simulants. The flame speed of iso-octane, which is in high concentration in PRF gasoline, is substantially slower than the flame speed of either alcohol or n-heptane. Faster flame speed is useful for maximizing the performance of spark ignited engines.

Methanol has been used as a diesel fuel, and the heavy-duty engines described in Section I were compression ignited. Various approaches have been used to achieve ignition in methanol engines: electrical ignition (spark plug) or glow plug; ignition-improving additives; very high compression ratios (> 22:1); dehydrating some of the methanol into DME before injection; and pilot ignition with diesel fuel. Although any of these approached work, successful diesel engines used one or more combinations of the first three. [Short, Mueller] Modern interest in use of methanol as a fuel in compression engines has been displaced by DME, a methanol-derivative and an excellent compression ignited fuel. Trucks, refueling stations and DME plants have been completed in

Sweden, in the BioDME project, a combination of Chemrec, Volvo, the paper industry and government, generating the methanol/DME from black liquor [Landaly].

4. RELATIVE PROMISE AS A WIDELY USED TRANSPORTATION FUEL:

VEHICLES PERFORMANCE:

When methanol is used in FFV, the requirement of operation in conventional gasoline prevents substantial modification of the engine characteristics. Performance of methanol FFV's has been comparable or slightly better than conventional gasoline. [Nichols] However, options exist for better performance/efficiency using the excellent combustion properties of methanol. These options are discussed below.

- ***Light Duty Applications with dedicated vehicles***

Work done at EPA's National Vehicle and Fuel Emissions Laboratory with small- displacement, stoichiometric light-duty engines [Brusstar1] demonstrated improved brake thermal efficiencies over the baseline diesel engine and low steady state NOx, HC and CO, along with inherently low PM emissions. The engine is also expected to have significant system cost advantages compared with a diesel engine of comparable torque/power, mainly by virtue of its low-pressure port fuel injection (PFI) system and simpler aftertreatment. While recognizing the considerable challenge associated with cold start, the alcohol-fueled engine nonetheless offers the advantages of being a more efficient, cleaner alternative to gasoline and diesel engines.

An interesting alternative to dedicated methanol vehicles, which are needed to achieve the efficiency advantages described above, is to use two tanks, the main tank filled with gasoline and the second tank filled with methanol. This concept, Direct Injection Alcohol Boosted (DIAB), uses direct injection (DI) of methanol when the engine is prone to knock (usually at conditions of high torque). [Cohn] The charge cooling, which derives from the high latent heat of vaporization of methanol, is primarily responsible for the knock suppression. Due to the charge cooling from the DI process, the effective octane rating [Bromberg1] greatly exceeds the chemical octane rating that these fuels would exhibit using conventional induction methods such as port fuel injection (PFI). In the DIAB concept, DI of the knock suppressing fuel is used only in the amount required to prevent knock and gasoline is supplied to the cylinder by conventional PFI. Since the engine operates at stoichiometry (using a typical oxygen feedback), a very high specific torque output can be produced while emissions can be maintained at low levels through the well-proven and relatively simple three-way catalyst system without the use of EGR as a major diluent. The

technology opens the possibility of a spark-ignited gasoline engine operating at high compression ratio (12 - 14) and high boost ratios of 2.0- 2.5 times ambient pressure, which is sufficient to produce a torque output equivalent to or greater than more highly turbocharged heavy duty diesel engines operating lean with significant EGR. The methanol-boosted DIAB engine can be almost as efficient (as measured by BTE, brake thermal efficiency) as a diesel and have comparable specific CO2 emissions as well. The concept has been demonstrated and proven in systematic dynamometer tests at Ford [Stein]. In addition, Honda has independently investigated the concept [Kamio].

- ***Medium/Heavy Duty Applications with dedicated vehicles***

Following tests with light duty SI methanol engine, the EPA's National Vehicle and Fuel Emissions Laboratory conducted engine tests for medium duty applications in a dedicated alcohol (methanol and ethanol) engine, using high level blends of alcohols. [Brusstar] A 4.5-liter V6 diesel engine was modified for spark ignition (SI) operation and port fuel injection (PFI), for use with M85. The high octane number of alcohol fuel, together with its latent heat of vaporization, makes it well suited to high compression ratio and boosted applications [Bromberg2, Kapus]. Moreover, alcohol's high laminar flame speed relative to gasoline [Marinov] enables greater charge dilution with EGR, reducing the need for throttling at light to moderate loads, while still allowing for stoichiometric operation. Stoichiometric operation eliminates the need for a lean NOx catalyst and instead lower-cost, proven three-way catalysts can be used. This technology approach was developed as part of EPA's Clean Automotive Technology Program. [Brusstar1] Brusstar and Gray concluded that "the engine developed … shows promise with either E85 or M85 fuel, as a clean and efficient alternative to other heavy duty engines." They concluded that the M85 and E85 engines could provide efficiencies comparable or higher than the diesel, in dedicated fuel, high compression ratio turbo charged/downsized engines (allowed because of the high antiknock properties of methanol or ethanol).

5. METHANOL AS TRANSPORTATION FUEL IN THE WORLD:

Methanol has attractive features of use in transportation:

- It is a liquid fuel which can be blended with gasoline and ethanol and can be used with today's vehicle technology at minimal incremental cost. THERE ARE NO TECHNICAL HURDLES.
- It is a high octane and safe fuel, and has combustion characteristics that allow engines to match the best efficiencies of diesels while meeting current pollutant emission regulations, although it has the drawback of reduced energy density.
- There is a very large potential supply of methanol since it can be made from natural gas, coal and biomass feedstocks

- It is currently produced from natural gas and coal at costs that are comparable to or less than gasoline and diesel fuel on an energy basis
- It is an attractive green house gas reduction option in the longer term, if produced from renewables/biomass. A bridging option is to use methanol derived from natural gas, with a CO2 intensity that is no worse than conventional fuels. There is also the possibility of achieving greenhouse gas reduction by CO2 sequestration in the methanol generation process.
- Multiple ways exist for introduction of methanol into the infrastructure (light blends or heavy blends) and into the vehicles (light duty or heavy duty applications). The optimal approaches are different in different countries and in different markets.

6. CONCLUSION

- Methanol is a safe and viable transportation fuel, although it is not as good a fuel as ethanol in terms of energy density and ease of handling. While significant investment needs to be made for large-scale methanol deployment in the transportation sector, there is no technical hurdle both in terms of vehicle application and of distribution infrastructure.
- As a long term strategy to substantially replace petroleum fuel by renewable, methanol offers the following advantage
  - Thermo-chemical production of methanol from biomass is energetically efficient and the technology has been well developed.
  - In comparison, large-scale bio-chemical production of ethanol from cellulose biomass is promising, but currently the technology is not sufficiently developed.
- Methanol from non-renewable could be used as a bridging option towards transition towards renewable methanol. Methanol can readily be made from natural gas or coal (there is plentiful supply of both feedstock's) so that large-scale production, infrastructure, and vehicle use could be developed. The system that is developed can then be applied to renewable methanol. It should be further noted that such system is also amenable to the use of renewable ethanol, should large scale bio-production of cellulose ethanol be realized in the future.
- Non-crop based biomass derived fuels have the potential to supply a major part of the US transportation liquid fuel; this is especially so if substantial decrease of energy use in transportation is achieved. Renewable methanol from thermo-chemical biomass conversion is an attractive and viable future fuel option.

7. ACKNOWLEDGEMENTS

This work was supported by the Department of Mechanical Engineering, Sardar Patel Institute of Technology And Management Mandleshwer. We want to thanks Mr. Sankar Patidar(Director), Mr. P.c. Shethiya(Principal), Mr. Manoj Kushwah(Head Of Dept.).

REFERENCES

[1] http://www.enginemanufacturers.org/admin/content/upload/186.pdf
[2] http://www.swri.org/4org/d03/engres/pwrtrn/hedge/default.htm
[3] http://www.typepad.com/services/trackback/6a00d8341c4fbe53ef0133f2c10caa970b

[4] http://news.frbiz.com/shanxi_chemical_industry_12--‐423379.html
[5] http://en.wikipedia.org/wiki/Title_42_of_the_United_States_Code
[6] http://hdl.loc.gov/loc.uscongress/legislation.110hr6
[7] http://www.methanol.org/fuelcell/special/stationcosts.pdf
[8] http://www.eia.doe.gov/cneaf/alternate/page/datatables/aft1--‐13_03.html
[9] http://www.crcao.com/reports/auto--‐oil/default.htm
[10] http://www.carbonrecycling.is/index.html
http://cnrp.ccnmatthews.com/client/methanex/release.jsp?actionFor=1315818&releaseS
[11] http://ieahia.org/pdfs/cafcp_case_study.pdf
[12] http://www.greencarcongress.com/2009/12/bure--‐saudron--‐20091225.html
[13] http://www.c1energy.com/Common/2793755,0,0,0,2.htm [CFCP]
[14] http://www.bp.com/statisticalreview
[15] http://www.bluefuelenergy.com/
[16] http://www.netl.doe.gov/technologies/coalpower/cctc/cctdp/bibliography/demonstratio
n/pdfs/estmn/VOL_I--‐2.pdf

Reduction of Energy Storage Requirements in Future Smart Grid Using Electric Springs

Kalyani S. Jadhav[1], M.R. Roda[2], B. E. Kushare[3]

[1]*PG Scholar, K.K.Wagh College of Engineeering, Nashik, Maharashtra, India*
[2]*Professor, (PG co-ordinator) K.K.Wagh College of Engineeering, Nashik, Maharashtra, India*
[3]*Professor, HOD(Electrical DEPT.)K.K.Wagh College of Engineeering, Nashik, Maharashtra, India*

ABSTRACT

The electric spring is an emerging technology proven to be effective in i) stabilizing smart grid with substantial penetration ofintermittent renewable energy sources and ii)enabling load demand to follow power generation. The subtle change from output voltage control toinput voltage control of a reactive power controller offers the electric spring new features suitable forfuture smart grid applications. In this project, the effects of such subtle control change are highlighted, and the use of the electric springs in reducing energy storage requirements in power grid is theoretically proven and practically demonstrated. Unliketraditional Statcom and Static Var Compensation technologies, the electric spring offers not only reactive power compensation but also automatic power variation in non-critical loads. Such an advantageous feature enables non- critical loads with embedded electric springs to be adaptive to future power grid. Consequently, the load demand can followpower generation and the energy buffer and thereforeenergy storage requirements can be reduced. Circuitmodels are developed for two bus system with andwithout DVR and the corresponding simulationresults are presented

Keywords: Distributed power systems, energystorage, smart grid, stability.

1. INTRODUCTION

The existing control paradigm of power systems is togenerate power to meet the load demand, i.e., "powergeneration following load demand". With the increasing use of intermittent renewable energy sources, known or unknown to the utility companies, it is impossible todetermine the instantaneous total power generation in real time. In order to achieve balance of power supply anddemand, which is an essential factor for power systemstability, the control paradigm for future smart grid has to be shifted to "load demand following power generation". Various load demand management methods have previously been proposed. Some examples include loadscheduling, use of energy storage as a buffer, electricitypricing, direct control or on-off control of smart loadsetc.However, most of these methods are suitable for loaddemand management i n the time frame of hours andare not suitable for instantaneous energy balance inreal time. Energy storage is

probably the most effectivemeans for instantaneous energy balancing. In order tocope with fast transient, energy storage elements such asbattery banks are installed with parallel connected supercapacitorswhich can absorb current at a faster rate thanchemical batteries. However, energy storage elementssuch as batteries are expensive and disposed batteries aremajor sources of pollutants. Although they areconsidered to be essential elements in future smart grid,it would be preferable to reduce their size for cost andenvironmental reasons.In this project, an investigation is conducted to examinethe use of electric springs in reducing energy storageelements in future smart grid. The electric spring conceptwas recently presented as a new smart grid technologyfor regulating the mains voltage of power grid with substantial intermittent renewable power and forachieving the new control paradigm of load demandfollowing power generation.

Traditional seriesreactive power compensators use output voltagecontrol (Fig. 1); by shifting from the output voltagecontrol to the input voltage control for a reactivepower controller, electric springs demonstratecharacteristics different from traditional devices suchas series reactive power controller. The effects of thissubtle change of control methodology and theinteractions between the electric springs and energystorage in a power grid, which have not been previouslyaddressed, are highlighted with practical tests in thisproject. Unlike Statcom, Static Var Compensation, andUPFC technologies [21]–[26], electric springs offer notonly reactive power compensation, but also automaticload variation in non-critical loads (with electricsprings embedded). This advantageous featureprovides the possibility of reducing energy storagerequirements in future smart grid.

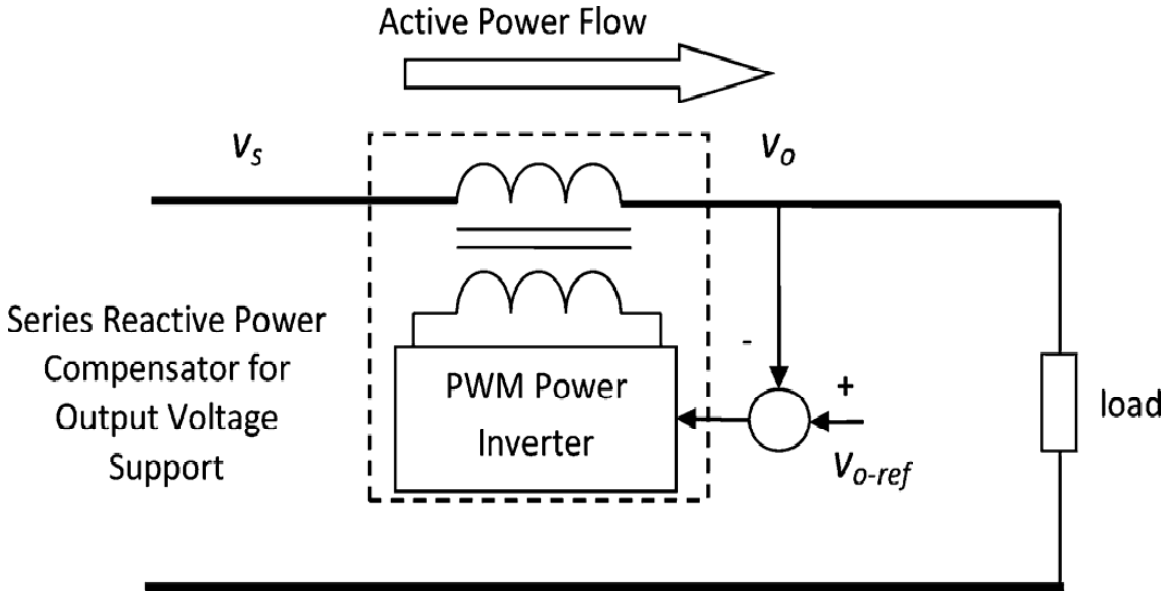


Fig. 1. "Output voltage control" of a series reactive power compensator.

ISBN: 978-93-83083-87-9

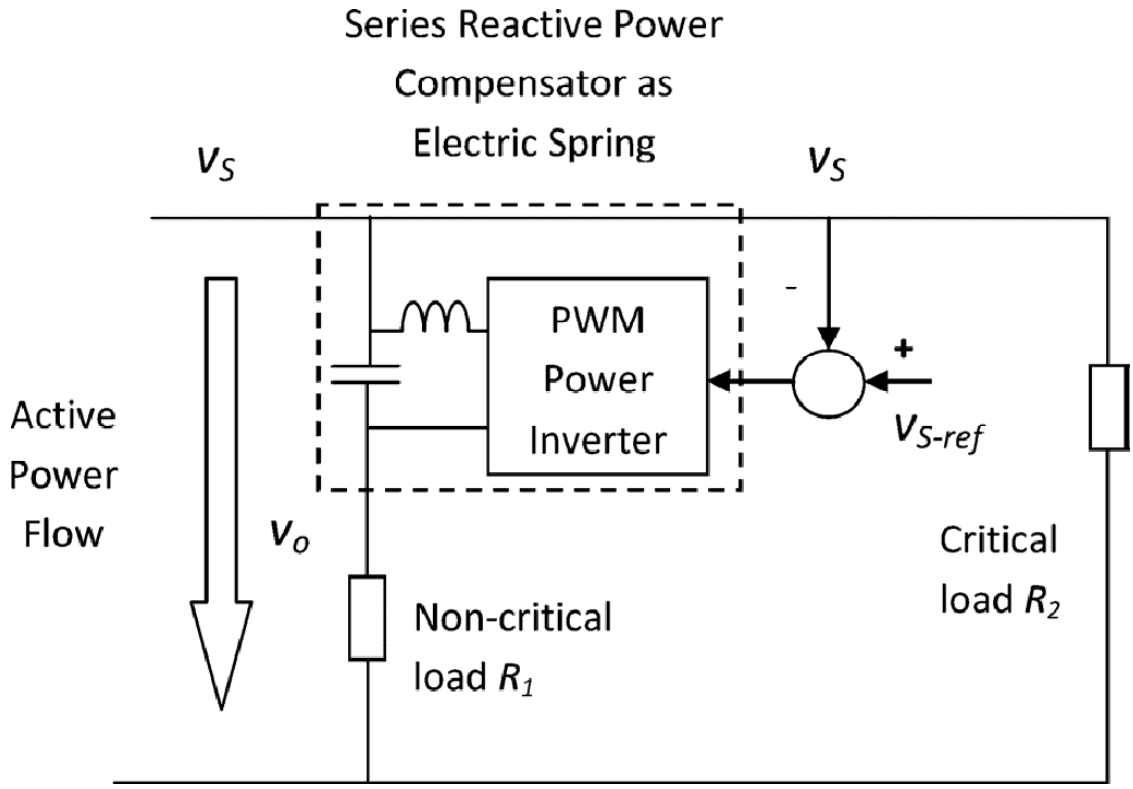


Fig. 2. Arrangement of an electric spring connected in series with a non-critical load anusing the "input voltage control") [18].

2. BASIC PRINCIPLES OF ELECTRIC SPRINGS

Electric springs are reactive power controllers withinput voltage control instead of the traditional outputvoltage control used in series reactive powercompensators. Details of the system operation canbe found in [17]. In this session, the basicprinciples of electric springs are summarized so as to facilitate readers' understanding of the power flowanalysis and the effects of the electric springs onreducing energy storage requirements in smart grid.Fig. 2 shows a typical installation of a single-phaseelectric spring connected in series with a non-criticalload. The electric spring comprises a power inverterwith a dc bulk capacitor on the dc side and inductive-capacitive (LC) filter on the ac side of thepower inverter. The four freewheeling diodes of thepower inverter behave like a diode rectifier whichrectifies the ac voltage into a dc one across the bulkcapacitor. The pulse-width-modulation switchingmethod is adopted in the power inverter to generate acontrollable ac voltage across the filter capacitor. Thiscontrollable ac voltage is the output voltage of theelectric spring. For pure reactive power control, thevector of the electric spring voltage and the currentmust be perpendicular. The input voltage control loopdepicted in Fig. 2 is designed to generate dynamicallywith the purposed of regulating the ac mains voltage toa reference value.

ISBN: 978-93-83083-87-9

3. POWER ANALYSIS OF ELECTRIC SPRINGS FOR REDUCTION OF ENERGY STORAGE

Now consider a general power grid consisting of an ac generator, a renewable power source, energy storage(battery banks), a set of non-critical loads and a set ofcritical loads as shown in Fig. 3. The power flowdiagram is shown in Fig.4 in which the power fromthe energy storage can be positive or negativedepending on whether the storage device is discharging orcharging

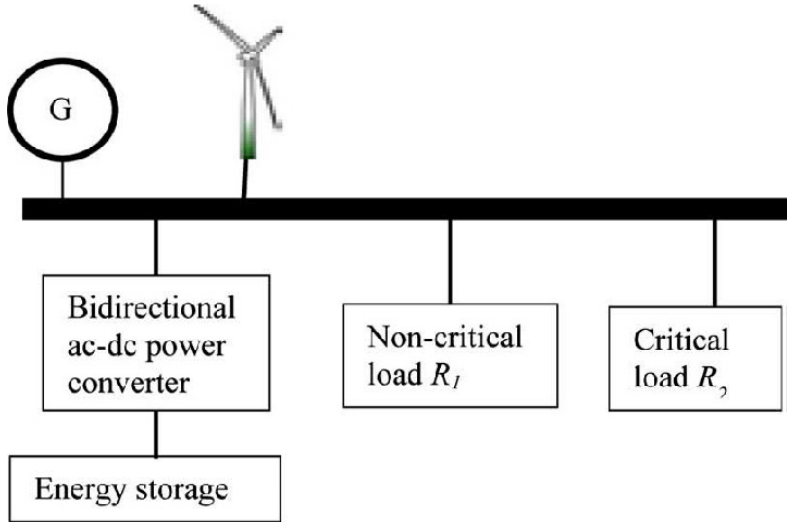


Fig. 3. Schematic of a power grid

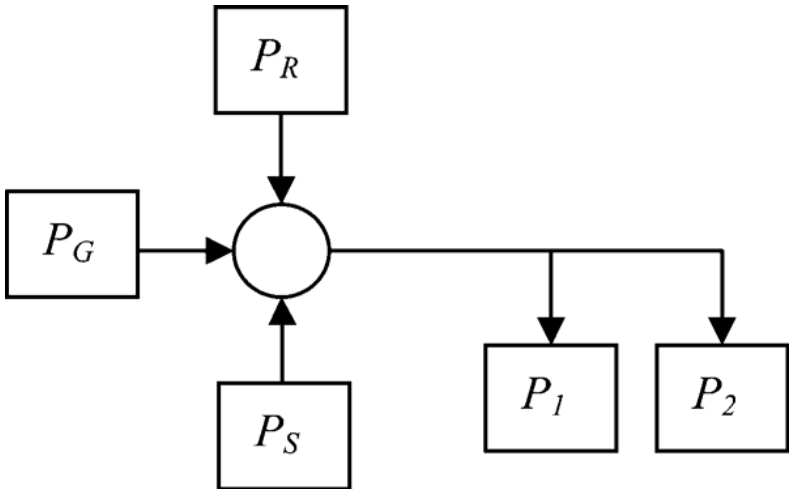


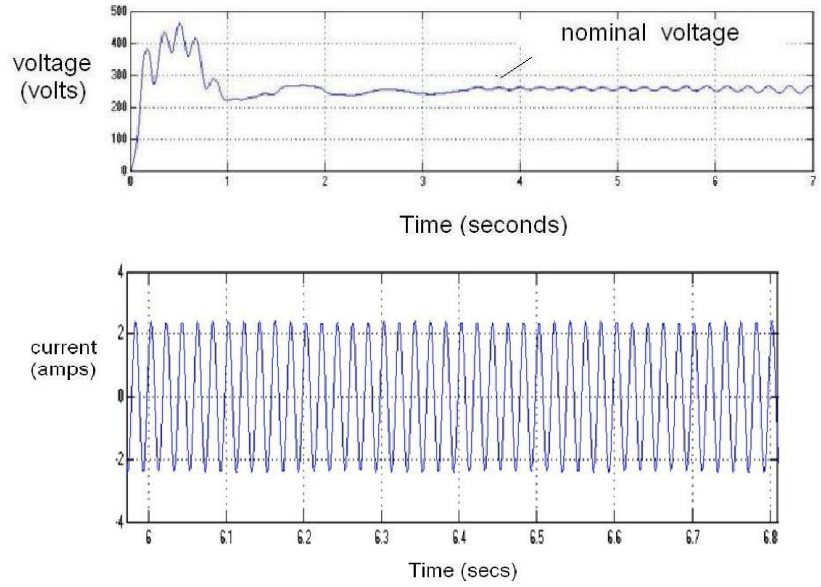
Fig. 4. Power flow diagram.

Where PG is the power generated by the ac generator, PRis the renewable power, and Ps is the power from theenergy st or age . Ps is positive when the battery isdischarging and Negative when it is charging.

4. PRACTICAL EVALUATION

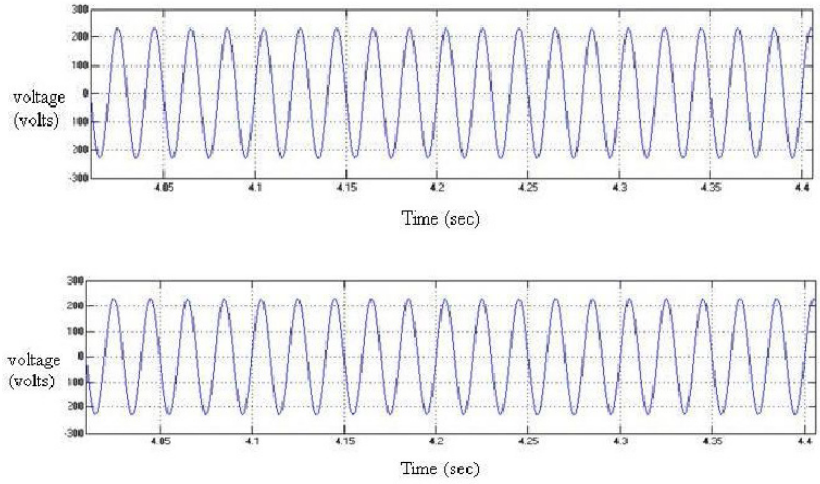
The simulation results are done with the batterysystem,wind system and for the hybrid system.

WIND SYSTEM MODEL



BATTERY SYSTEM MODEL INVERTER

OUTPUT VOLTAGE



OUTPUT VOLTAGE HYBRID SYSTEM

The reactive power profile of the electric spring underinput voltage control follows the charging anddischarging time of the battery.The voltage stays within 1% tolerance of 220v andthe power of the critical load remains essentiallyconstant with tight tolerance

FFT ANALYSIS

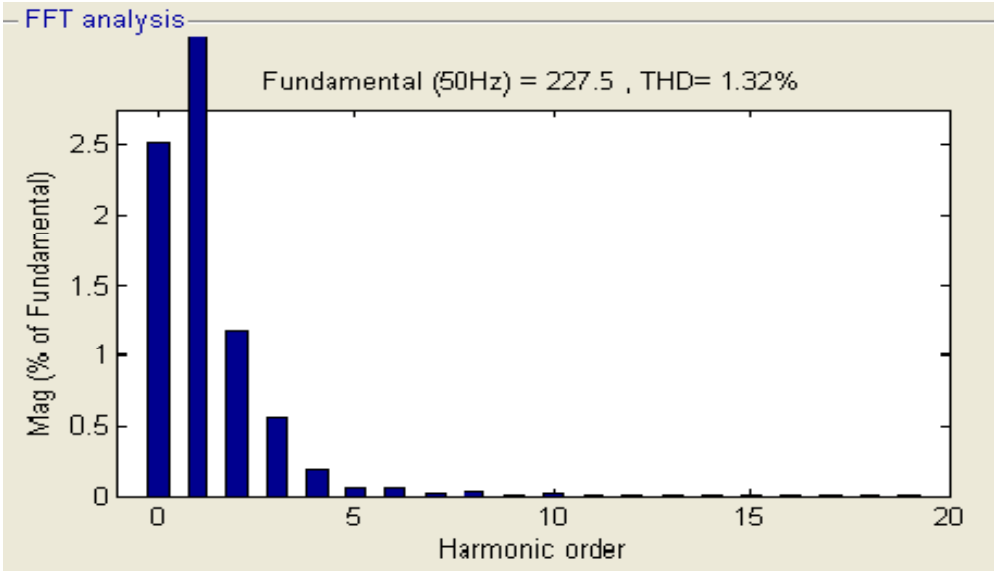


Fig .6 FFT Analysis

$$THD = \frac{\sqrt{(V_2^2 + V_3^2 + V_4^2 + \cdots + V_n^2)}}{V_1} * 100\%$$

TWO BUS SYSTEM WITHOUT DVR

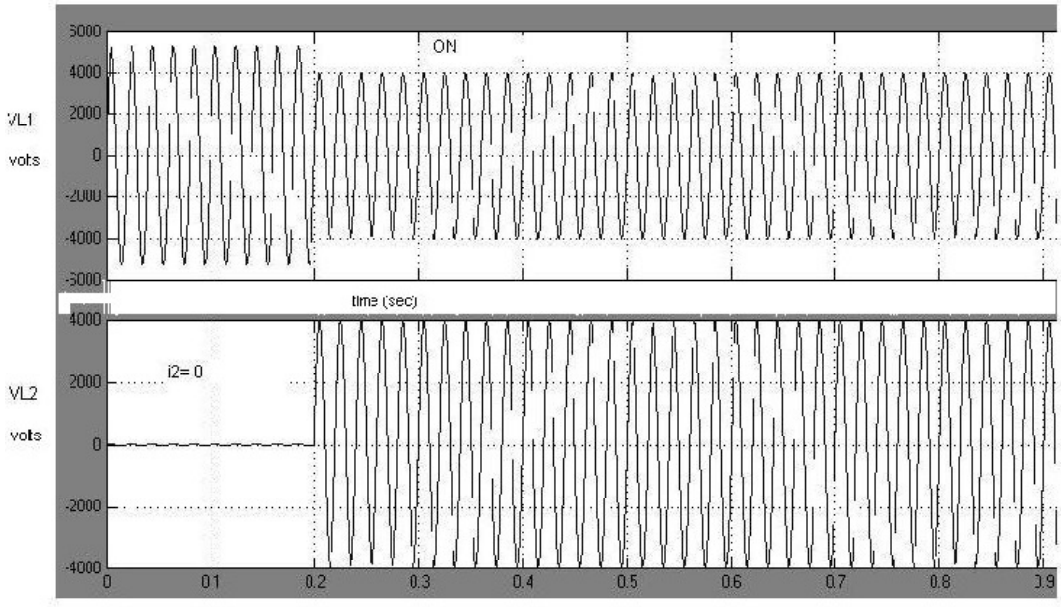


Fig7 Voltage Across Load -1 And Load -2

ISBN: 978-93-83083-87-9

TWO BUS SYSTEM WITH DVR

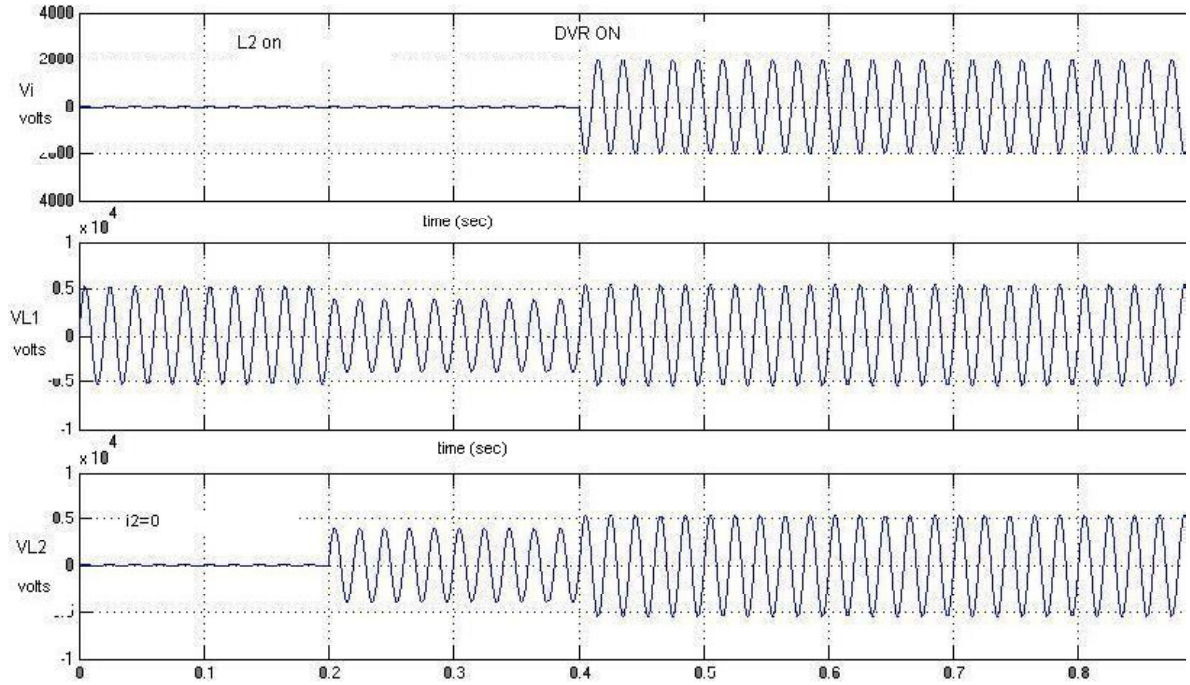


Fig .8 Voltage Across Transformer Primary In External Source and Load1andLoad-2

DVR WITHOUT LC FILTER

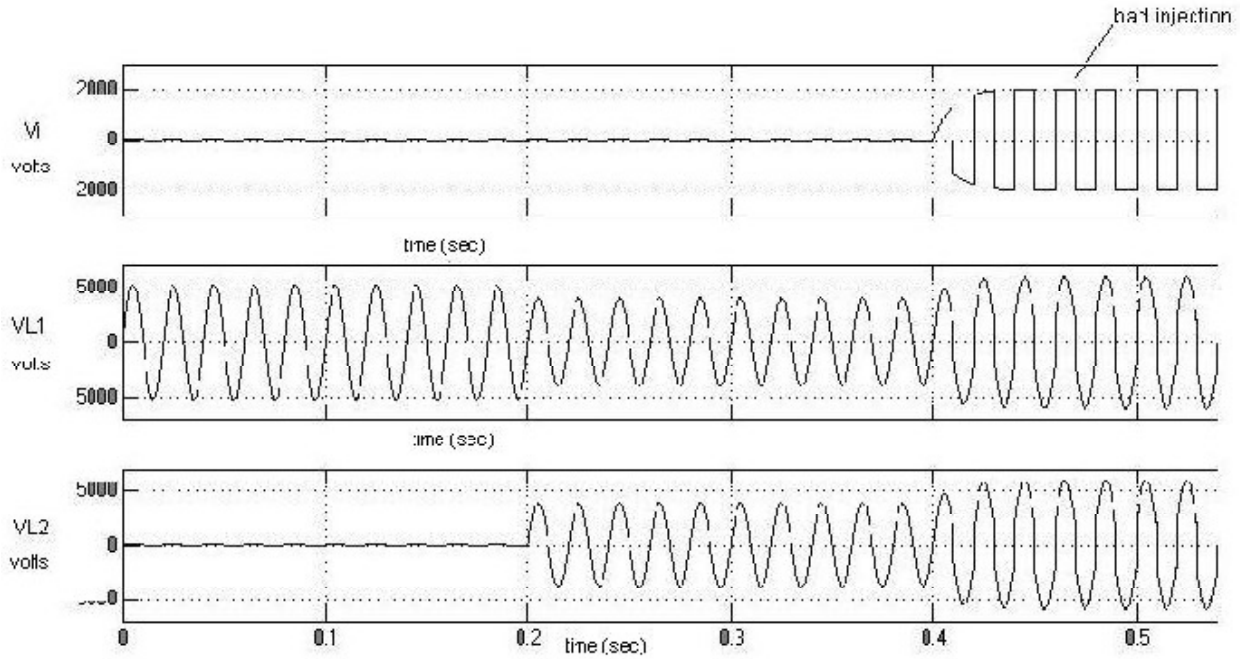


Fig.9 Voltage Across External ,Load1 and Load-2

ISBN: 978-93-83083-87-9

DVR WITH LC FILTER

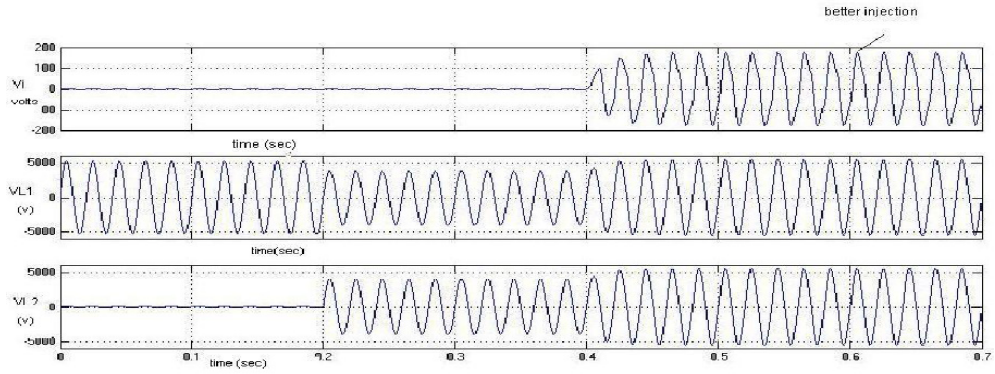


Fig 10 Voltage Across External, Load1 and Load

5. CONCLUSION

This project has presented the Simulation results of"Reduction of Energy Storage Requirements in FutureSmart Grid Using Electric Springs", showing a goodagreement with the theoretical analysis.The wind system, battery system and hybrid system aresuccessfully modeled and simulated. THD is reduced by using LC filter.

REFERENCES

[1] D. Westermann and A. John, "Demand matching wind powergeneration with wide-area measurement and demand-sidemanagement," IEEE Trans. Energy Convers., vol. 22, no. 1 , pp.145–149, 2007.

[2] P. Palensky and D. Dietrich, "Demand side management: Demandresponse,intelligent energy systems, and smart loads," IEEETrans. Ind. Inform., vol. 7 , no. 3 , pp. 381–388, 2011.

[3] P. Varaiya, F. Wu, and J. Bialek, "Smart operation of smart grid:Risk limiting dispatch," Proc. IEEE, vol. 99, no. 1 , pp. 40–57,2011.

[4] Koutsopoulos and L. Tassiulas, "Challenges in demand loadcontrol for the smart grid," IEEE Netw., vol. 25, no. 5 , pp. 16–21,2011.

[5] Mohsenian-Rad, V. W. S. Wong, J. Jatskevich, R. Schober, andA. Leon-Garcia, "Autonomous demand-side management basedon gametheoretic energy consumption scheduling for the futuresmart grid," IEEE Trans. Smart Grid, vol. 1 , no. 3 , pp. 320–331,2011.

[6] S.Y.R. Hui, C.K. Lee and F.F. Wu, "Electric springs – A new smartgrid technology", IEEE Transactions on Smart Grid, Vol.3, No.3,Sept. 2012, pp: 1552-1561.

[7] S.C. Tan, C.K. Lee and S.Y.R. Hui, "General steady-state analysis and control principle of electric springs with active and reactivepower compensations", IEEE Transactions on Power Electronics,Volume: 28 , Issue: 8, Page(s): 3958 – 3969

[8] C.K. Lee, N. Chaudhuri, B. Chaudhuri and S.Y.R. Hui, "DroopControl of Electric Springs for Distributed Stability Support of SmartGrid", IEEE Transactions on Smart Grid (in press)

[9] Institite for Energy Resaerch, "Germany's green energy destabilizing electric grids", posted Jan. 23, 2013[Online].Available:http://www.instituteforenergyresearch.org/2013/01/23/germanysgreen-energy-destabilizing-electric-grids/

Biodiesel Production from Waste Cooking Oil and Performance Analysis by Using Biodiesel and Butanol Blends

Manu Jindal[1], S.K. Mahla[2]

[1& 2]*Thapar University, Patiala, Punjab*

ABSTRACT

Biodiesel is receiving much attention these days as an alternative fuel to diesel which can be used without any modification to diesel engine. It can also work against the increasing environment degredation problems such as global warming and green house effect etc. The use of waste cooking oil (WCO) as biodiesel feedstock solves the problem of waste disposal in developing countries like India as well. It decreases the cost of biodiesel as expenses at biodiesel feedstock are reduced significantly. In this study, biodiesel was produced from waste cooking oil by trans-esterification reaction using molar ratio 6:1 of alcohol: WCO. Methanol was used as alcohol. A constant speed, stationary diesel engine was used to conduct performance analysis. The experiments were performed using 20, 40 and 60% biodiesel and diesel blends and were compared with diesel as basis. BHP inceased upto average 15% with the use of biodiesel. BTE increased upto 13%. Performance was checked also by adding oxygenated fuel butanol and it proved economic. Results indicated that 20% biodiesel blend and 10% butanol blends were optimum to use in diesel engine.

Keywords: Biodiesel, trans-esterification, waste cooking oil, performance.

1. INTRODUCTION

The new process technologies raised during last years made it possible to use used vegetable oil as biodiesel feedstock against edible raw oils with additional advantage of being lower in price. It is good from disposal management point of view as well as the problem of disposal of waste cooking oil is also solved with this. It provides a clean method to dispose used oil and biodiesel produced will cut exhaust emissions as well. There are some other alternative fuels to diesel also but biodiesel is being most attractive among them. Biodiesel consists of mono-alkyl esters of long chain fatty acids derived from vegetable oils and used potentially as alternative fuel to diesel.

There is limitation in biodiesel from some oils of getting freezed in winter season. So oxygentaed fuels program was started in 1990. It was mainly to combat caron mono oxide emissions from

ISBN: 978-93-83083-87-9

vehicles. n- Butanol among oxygenated fuels was used in this study. It has various advantages over other oxygenated fuels like ethanol. It is less hygroscopic and evaporative and can be used as transportation fuel more potentially. Oxygenated fuels contain oxygen component so that it's helpful to reduce PM emissions. There are no PM emissions from diesel engines when the mass of oxygen in the fuels is more than approximately 30% [2].

Blending oils with alcohols improves fuel properties [1]. This study indicates that biodiesel is more efficient as compared to diesel and its efficiency raised by 13% by adding n-butanol.

2. MATERIALS AND METHODOLOGY

Biodiesel was produced from waste cooking oil (WCO) by trans-esterification reaction (as shown in Figure 1) using 6:1 molar ratio. Trans-esterification is a reaction of forming esters by reacting oils and alcohols. Alkali catalyst was used as fatty acid content was lower than 5%. KOH was used at 1% weight. Methanol was prefered due to its less cost. Biodiesel production process is shown in figure 2.

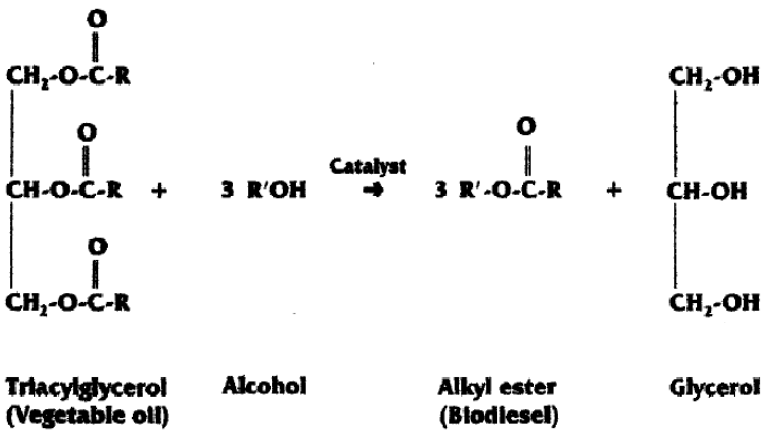
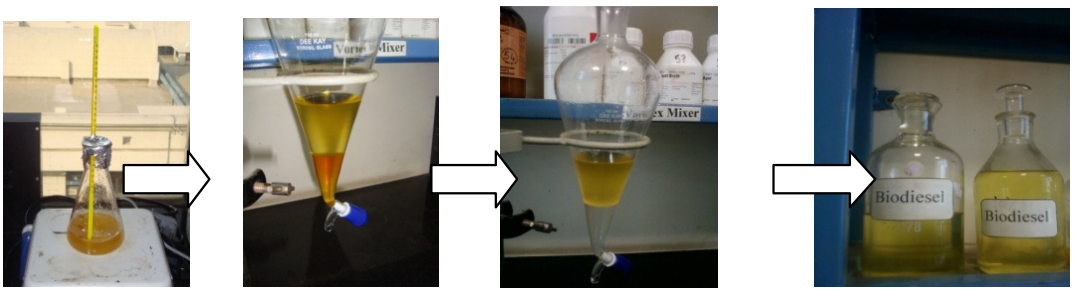


Figure 1 Trans-esterification reaction



Esterification **separation in separatory Funnel** **washing of biodiesel until lower layer gets crystal clear** **Biodiesel produced**

Figure 2 Biodiesel obtained from waste cooking oil

ISBN: 978-93-83083-87-9

3. ENGINE ANALYSIS

An engine of 3.73 kW rated power, one cylindrical, 4-stroke engine at constant speed 1500 rpm was used for engine performance analysis with following specifications as mentioned in Table 1.

Table 1 Engine Specifications

Parameters	Details
Manufacturer	Kirloskar Oil Engines Limited India
Dynamometer	Eddy Current
Bore, mm	80
Stroke, mm	110
Displacement Volume, cc	252.9
Compression Ratio	16.5:1
Cooling System	Air Cooled
Horse Power	6.5
Injection Pressure	200 kg/cm^2
Voltage, V	240
Current, Ampere	17.5

4. ENGINE PERFORMANCE ANALYSIS

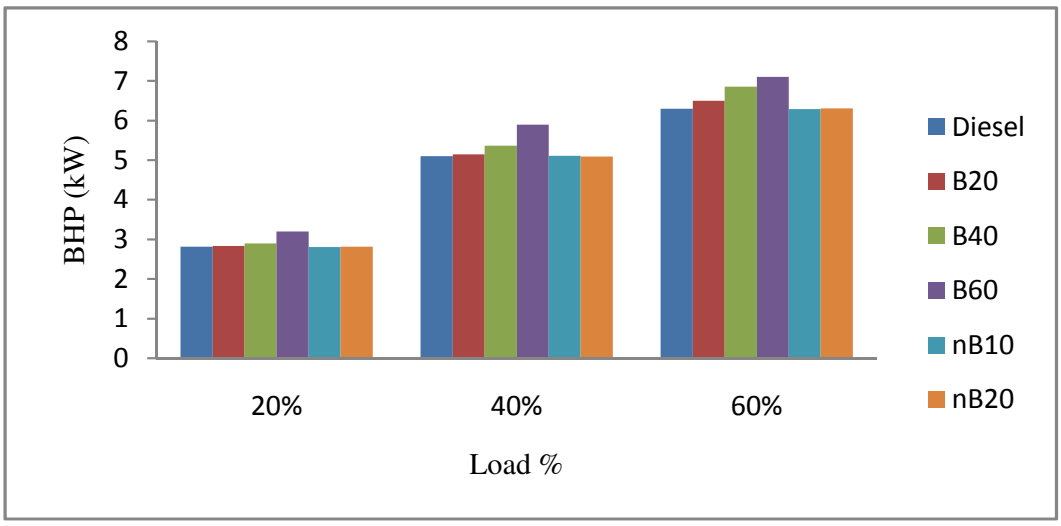


Figure 3 BHP Vs Load

ISBN: 978-93-83083-87-9

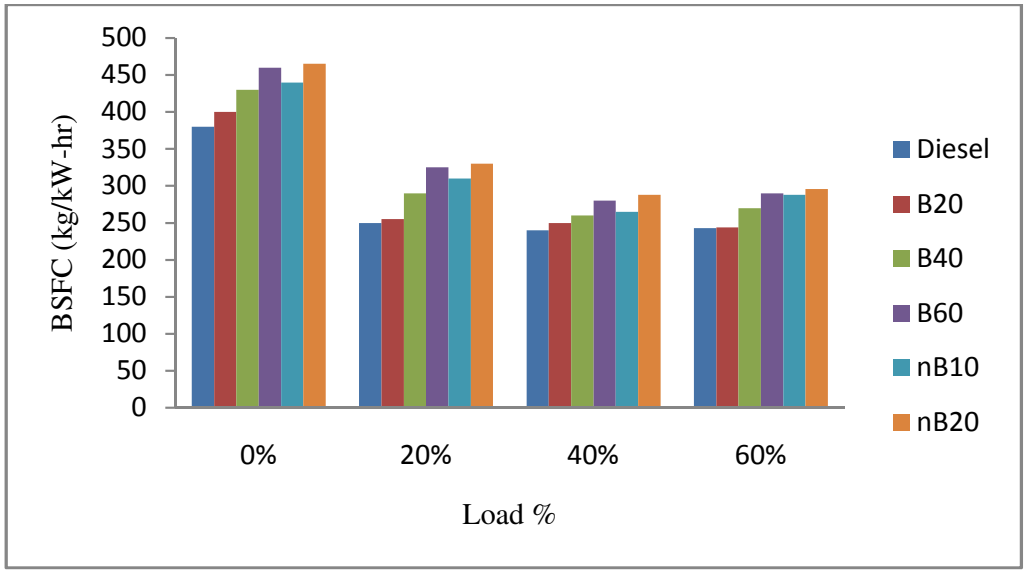


Figure 4 BSFC Vs Load

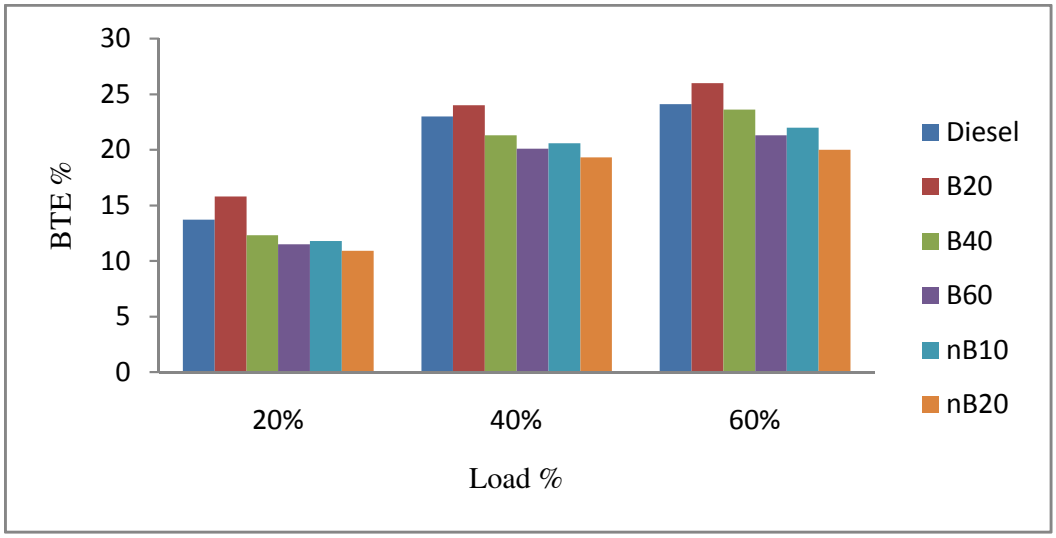


Figure 5 BTE Vs Load

5. OBSERVATIONS

1. Brake Horse Power (BHP) increases with load for every blend (Figure 3). BHP varies with current as voltage is almost constant. At no load, there is no current flow, so BHP is zero for every blend at no load. B60 showed higher increase level (15-20%) as compared to others where as B20 showed 8% increase. n-Butanol also had similar variations as B20.

2. Brake Fuel specific Consumption (BSFC) comes from brake power output and equivalent mass flow rate. It varied inversly to loads (Figure 4). At higher loads, BSFC decrease was

more as compared to lower loads. B20 showed 5% difference at lower loads and of 2% at higher loads. Butanol addition can be of great advantage as the differnce grew more in butanol blends. It was about 25% at lower loads and 15% at higher loads.

3. Brake Thermal Efficiency (BTE) is realted with BHP directly and with mass flow rate & calorific value inversly. B20 showed higher efficiency as compared to diesel and other blends. B20 proved 13.2% more efficient as compared to diesel at lower loads and 7.3% more at higher loads. Other blends were less efficient though this differnce was very little of about 2-7%. So, B20 blend can be suggested as best blend for biodiesel preparation with WCO (Figure 5).

6. CONCLUSION

1. The lower blends of WCO methyl ester can be used in diesel engine without any engine modifications. The fuel filter needs to be changed after some interval of time.

2. Brake thermal efficiency of B20 is superior to diesel at all load conditions.

3. Bio-diesel from n-butanol biodiesel diesel blends resemble very much with the conventional diesel, in properties as well as in the performance on CI engines. The economical analysis suggests good scope for biodiesel in comparison to diesel.

REFERENCES

[1] Boehman AL, Morris D, Szybist J, Esen E. The impact of the bulk modulus of diesel fuels on fuel injection timing. Energy Fuels 2004;18:1877–82.

[2] Miyamoto N, Ogawa H, Nurun NM. Smokeless, Low NOx High Thermal Efficiency and Low Noise Diesel Combustion with Oxygenated Agents as Main Fuel. SAE Technical Paper 980506.

Renewable Energy Potential in India and Slackness in RPO Compliance is Affecting the REC Market

Megha Sharma[1], Saurabh Chanana[2]

[1]*M. Tech Student, School of Renewable Energy and Efficiency, NIT Kurukshetra, Haryana*
[2] *Electrical Department, NIT Kurukshetra, Haryana*

ABSTRACT

India is now recognized as a leading country in the world for the development and utilization of renewable energy, particularly in wind power development. In fact, power generation from wind has emerged as one of the most successful programs in the renewable energy sector, and has started making a meaningful contribution to the overall power requirement in some of the States. The renewable energy potential of different states in India is different. The barrier for RE abundant states to sell their surplus power to the states having lower potential is scheduling of energy and too high long term open access charges. Consequently, lower RE potential states keep their Renewable Purchase Obligation (RPO) target lower. In this paper, we will discuss the renewable energy potential of India, state wise wind power installed capacity of India and the future of REC market is dependent on how effectively SERCs enforces RPO compliance by obligated entities.

Keywords: Renewable Purchase Obligation, Obligated entities, Feed-in-Tariff, Central fiscal incentives.

1. INTRODUCTION

The wind power programme in India was initiated towards the end of sixth plan, in 1983-84. A market–oriented strategy was adopted from inception, which has lead to the successful commercial development of the technology. The broad based National programme includes wind resource assessment activities, research and development support; implementation of demonstration projects to create awareness and opening up of new sites; involvement of utilities and industry; development of infrastructure capability and capacity for manufacture, installation, operation and maintenance of wind electric generators; and policy support. The programme aims at catalyzing the commercialization of wind power generation in the country. The Wind Resources Assessment Programme is being implemented through the State Nodal Agencies, Field Research Unit of Indian Institute of Tropical Meteorology (IITM-FRU) and Center for Wind Energy Technology (C-WET).

Wind in India is influenced by the strong southwest summer monsoon, which starts in May-June, when cool, humid air moves towards the land and the weaker northeast winter monsoon, which starts in October, when cool, dry sir moves towards the ocean. During the period March to August, the winds are uniformly strong over the whole Indian Peninsula, except the eastern peninsular coast. Wind speeds during the period November to march are relatively weak, though higher winds are available during a part of the period on the Tamil Nadu coastline. A notable feature of the Indian programme has been the interest among private investors/developers in setting up of commercial wind power projects. The wind power generation capacity in India is 49,130 MW as per the official estimates in the Indian Wind Atlas (2010) by the Centre for Wind Energy Technology (C-WET). The potential is calculated with respect to 2 per cent land availability at windy locations and pertains to a 50 meter hub height level of the wind turbines.

As on March 31, 2013 a total of about 19,052 MW of commercial projects has been established until. The break-up of projects implemented in prominent wind potential states (as on March 31, 2013) is given in the Table 2.1:

Table 1: State-wise Wind Power Installed Capacity in India (till 31.03.2013) [1].

State	Estimated Potential* (MW)	Installed Capacity (MW)
Tamil Nadu	14,152	7,162
Gujarat	35,071	3,175
Maharashtra	5,961	3,022
Karnataka	13,593	2,135
Rajasthan	5,050	2,685
Madhya Pradesh	2,931	386
Andhra Pradesh	14,497	448
Kerala	837	35
Others	10,696	4
All India	1,02,788	19,052

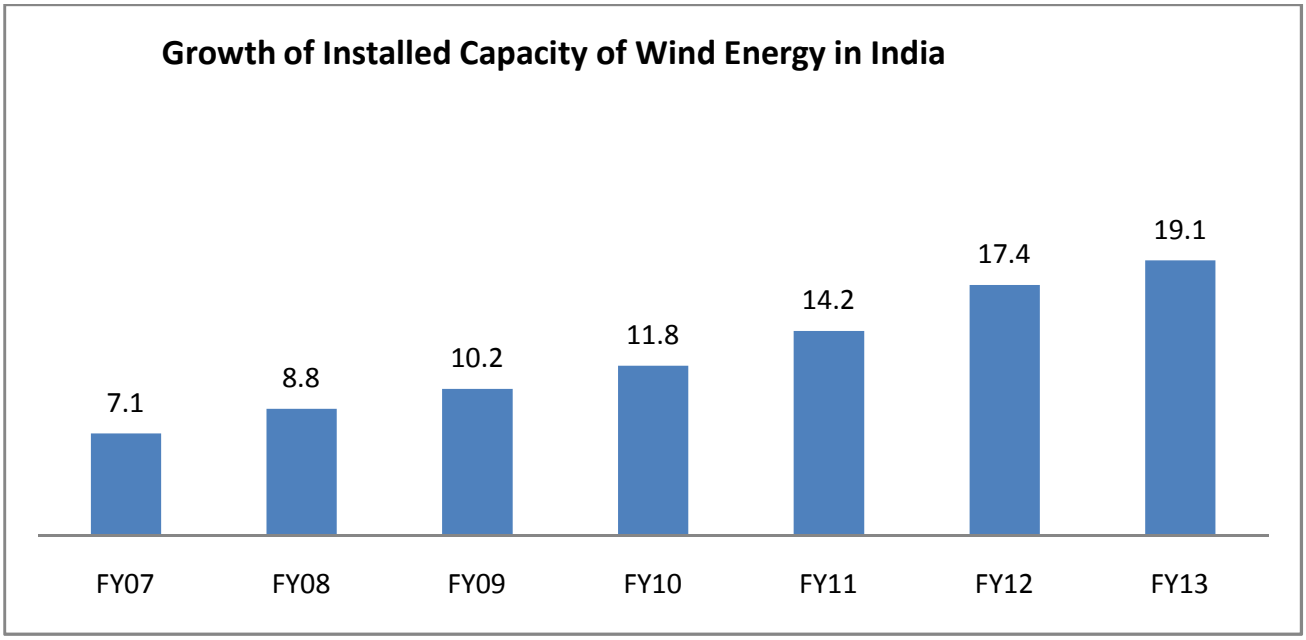


Fig 1: Growth of installed capacity of wind energy in India (GW) [5].

2. BENEFITS & INCENTIVES TO WIND ENERGY PROJECTS IN INDIA

The Government is promoting wind power projects through private sector investment by providing fiscal and promotional incentives such as concessional import duty on certain components of wind electric generators, excise duty exemption to manufacturers. 10 years tax holiday on income generated from wind power projects is also available. Loans for installing windmills are also available from Indian Renewable Energy Development Agency (IREDA) and other financial institutions [2]. Technical support, including wind resource assessment is provided by the Centre for Wind Energy Technology (C-WET), Chennai. This apart, preferential tariff is being provided in potential states. The Government has also announced a Generation Based Incentives (GBI) under which Rs. 0.50/unit generated from wind power projects is being provided for the projects which do not avail the accelerated depreciation benefit. 80% of accelerated depreciation is provided to the investors of wind power projects and it is considered to be the main driver but was stopped as from 1st April 2013.

The central fiscal incentives from Ministry of Finance which the wind energy sector enjoys are:

a) Direct Taxes

- Wind power projects shall have normal depreciation of 15%. In addition, there is a provision of availing 20 % depreciation in the first year.
- Exemption of Income Tax on earnings from the Project u/Sec 80IA for 10 years.

b) Indirect Taxes

- Exemption of Excise Duty on Wind Energy Generator (WEG).
- Concessional Custom Duty on specified WEG components.

Fig 2 shows various incentive based schemes started by Government of India in order to promote renewable energy in India.

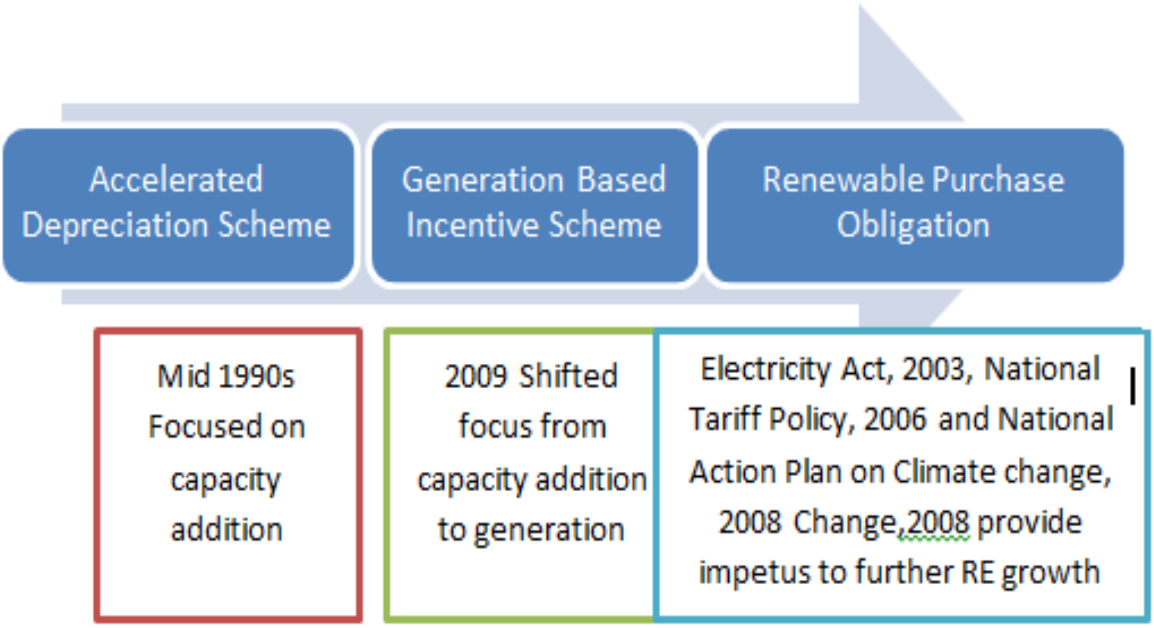


Fig 2: Schemes to promote RE in India [3].

3. RENEWABLE PURCHASE SPECIFICATION

The Electricity Act 2003 proposed mandatory Renewable Purchase Specification (RPS) for all states. To date, 26 states have specified targets for the uptakes of renewable electricity. With the introduction of the new Renewable Energy Certificate scheme, states are looking at fulfilling the RPS set by the Electricity Act through this provision.

4. STATE FEED-IN TARIFF

At present thirteen SERCs have declared preferential feed-in tariffs for the purchase of electricity generated from the wind power project established in respective states. All the SERCs have adopted a 'cost plus' methodology to fix the feed-in tariff, which varies across the states depending upon the state resources, project cost and other tariff computing parameters as considered by the respective SERCs.

5. RENEWABLE ENERGY CERTIFICATES

In order for distribution utilities or licensees to meet the RPS, renewable energy needs to be available. To ensure this, a mechanism to create tradable Renewable Energy Certificates (RECs) is put into place by the CERC in 2010. All the renewable energy projects commissioned after 01.04.2010 are eligible to register under the REC framework. Status of Renewable Purchase Specification (RPS) and Renewable Energy Certificate (REC) regulations of State Electricity Regulatory Commissions (SERCs) is shown in the Table 2:

Table 2: State wise comparisons of Feed-in-Tariff policy for wind power [4].

States	Current Tariff rates per kWh	Details of available tariff rates	RPS Targets (% for wind)
Andhra Pradesh	INR 4.70	Constant for 25 years for the PPAs to be signed by 31-03-2015	5% for all RE (2012-2013)
Gujarat	INR 4.23	No escalation for 25 years of project life	5.5% for wind (2012-2013)
Haryana	Wind Zone I– INR 6.14	Tariff is for FY 2012-13	3% for all RE (2012-2013)
	Wind Zone II– INR 4.91		
	Wind Zone III– INR 4.09		
	Wind Zone IV–INR 3.84		
Karnataka	INR 3.70	No escalation for 10 years	7-10% (2011/12) for all Non-Solar
Kerala	INR 3.64	No escalation for 20 years of project life	3.3% (2011-2012) & 3.63% (2012-2013) for all RE
Madhya Pradesh	INR 4.35	No escalation for 25 years of project life	4% for wind (2012-2013)
Maharashtra	Wind Zone I– INR 5.67	No escalation for 13	8% for all RE (2012-

	Wind Zone II- INR 4.93	years	2013)
	Wind Zone III– INR 4.20		
	Wind Zone IV– INR 3.78		
Orissa	INR 5.31	No escalation for 13 years	5.5% for all RE (2012-2013)
Punjab	INR 5.07 (for zone I)	No escalation for 10 years	2.9% for all RE (2012-2013)
Rajasthan	INR 4.46 & 4.69 (for FY 2011-12)	No escalation over project life of 25 years	7.5% for wind (2011-2012)
		INR 4.46/kWh for Jaisalmer, Jodhpur & Barmer districts while INR 4.69/kWh for other districts	
Tamil Nadu	INR 3.51	No escalation for 20 years of project life	9% for all RE (2011/12)
Uttarakhand	Wind Zone I– INR 5.15	INR 5.65 for the first 10 years & INR 3.45 11th year onwards	5.05% for all RE (2012/13)
	Wind Zone II– INR 4.35	INR 4.75 for 1st 10 year & INR 3.00 for 11th year onward	
	Wind Zone III– INR 3.65	INR 3.95 for 1st 10 year & INR 2.55 for 11th year onward	
	Wind Zone IV– INR 3.20	INR 3.45 for 1st 10 year & Rs.2.30 for 11th year onward	
West Bengal	INR 4.87	No escalation for 10 years	4% for all RE (2012/13)

6. RPO REGULATIONS

Renewable Purchase Obligation (RPOs) requires distribution licensees, captive power consumers and open access consumers to purchase or generate a certain percentage of their total electricity requirement from appropriate renewable source. States with low renewable energy potential can meet their target by buying Renewable Energy Certificate (RECs). SERCs have specified progressive, and in many cases, renewable specific RPO targets. Non-compliance with RPOs would result in penalties on obligated entities [5].

While RPO regulations are in place, the absence of strict enforcement has lead to obligated entities not complying with targets. Most of the states are not in a position to enforce these regulations on distribution licensees and captive generators. The sale ability of REC is also an issue. RPO guidelines specifies that if an obligated entities fails to comply with targets, it has to purchase RECs as penalty at a forbearance price decided by CERC.

Although the RPO regulation clearly specifies that state agencies will need to submit a quarterly status report of their RPO compliance, none of the state agencies are adhering to this requirement. States that outperformed their 2012 target are Meghalaya, Nagaland, Uttarakhand, Himachal Pradesh and the southern coastal states of Tamil Nadu and Karnataka. While Meghalaya set an RPO target of 0.75% and achieved 4.10%, Tamil Nadu achieves 19.14% against 9%.

On the other hand Delhi, Maharashtra, Panjab, Andhra Pradesh and Madhya Pradesh are among the states that missed their targets. In a recent order in August, the Maharashtra Electricity Regulatory Commission (MERC), the power regulator in Maharashtra, have directed all distribution companies to fulfill their RPO targets for both solar and non-solar for four years, i.e., financial year 2010-11, 2011-12, 2012-13, 2013-14, cumulatively, before 31st March 2014. Non-compliance will result in strict penalties. The decision is expected to give some push to the struggling REC market in the country.

7. CONCLUSION

Hence we can conclude that India is the 3rd largest annual wind power market in the world, and provides great business opportunities for both domestic and foreign investors. The Indian wind power sector experienced record annual growth in 2011 with the addition of more than 3 GW of new installations. Diverse incentives supported by a long-term policy and regulatory framework at the central and state levels have played a crucial role in achieving this goal. Wind power is now increasingly accepted as a major complementary energy source for securing a sustainable and clean energy future for India.

REFERENCES

[1] Information at www.cwet.tn.nic.in

[2] GWEC, WISE and IWTMA,"Indian Wind Energy Outlook 2012", Available: http://www.gwec.net/fileadmin/image/India/IWEO_2012_lowres.pdf

[3] Information at www.iexindia.com

[4] Information at www.mnre.gov.in

[5] Ernst & Young, "Mapping India's Renewable Energy growth potential: Status and outlook 2013", Available: http://www.ey.com/Publication/vwLUAssets/Mapping_Indias_Renewable_Energy_growth_potential/$FILE/EY-Mapping-Indias-Renewable-Energy-growth-potential

Performance Evaluation of A Diesel Engine with Tamuna Bio Fuel

S.N. Ch. Dattu V.[1], Gogula Karthik[2], Mohammad Khasim Mohiddin Shareef[3]

[1]*Department of Mechanical Engineering,*
Pragati Engineering College, Surampalem, Andhra Pradesh, India.
[2]*Under Graduate Student, Department of Mechanical Engineering,*
Pragati Engineering College, Surampalem, Andhra Pradesh, India.
[3]*Under Graduate Student, Department of Mechanical Engineering,*
Pragati Engineering College, Surampalem, Andhra Pradesh, India

ABSTRACT

Alternate fuels can be produced from vegetable oils and also from animal fats these comes under Bio-Diesel category. Alternate fuels are mono-alkyl-ester of long chain fatty acids derived from vegetable oils and waste oils by trans esterification process. The present challenge in automotive engine technology is the improvement of thermal efficiency and hence the fuel economy and lower emission levels. The aim of my work is to evaluate the performance of a fixed compression ratio engine in terms of specific fuel consumption with respect to break thermal efficiency, mechanical efficiency, and volumetric efficiency, with mixtures of different proportions of esterified Tamanu Oil and diesel fuel and comparing the results with 100% diesel fuel.

Keywords: Biofuel, Trans esterification Process, Thermal Efficiency, Emissions.

1. INTRODUCTION

1.1 Introduction to Tamanu Oil

Bio-diesel and also in some cases it is used as skin care oil. Tamanu Oil or Calophyllum Inophyllum has traditionally been used as a unique and significant skin healing agent, environmental pressures for renewable energy has created an ever-growing demand for bio fuel in the form of biodiesel produced from vegetable oils. Tamanu oil is prepared from Tamanu seeds by trans esterification process.

1.2 Production of Tamanu Oil

Single-phase method if the percentage of FFA present in the raw vegetable oil is less than 4%, the trans esterification process by single-phase method has to be chosen. In this method, a measured amount of methanol (CH3OH) and sodium hydroxide (NaOH) has to be mixed thoroughly with a measured amount of vegetable oil. The mixture is heated and maintained at 65°C for 2 h, and then,

it undergoes natural cooling. Glycerol will deposit at the bottom of the flask, and it is separated out using a separating funnel. The remnants in the flask are the esterified vegetable oil. Another commercial name for esterified vegetable oil is biodiesel.

Two-phase method if the percentage of FFA present in the raw vegetable oil is more than 4%, then we have to choose the two-phase method. In this method, the oil has to undergo esterification. Measured quantity of sulphuric acid and methanol has to be taken and mixed thoroughly and added with a measured amount of vegetable oil. The mixture is heated and maintained at 65°C for 2 h. The fatty ester is separated after natural cooling. At second level, the separated oil from the separating funnel has to undergo trans esterification. Methoxide (methanol + sodium hydroxide) is added with the above ester and heated to 65°C. The same temperature is maintained for 2 h with continuous stirring, and then, it undergoes natural cooling for 8 h. Glycerol will deposit at the bottom of the flask, and it is separated out by a separating funnel. The remnants in the flask are the esterified vegetable oil (biodiesel).

1.3 Tamanu Oil Properties

Table No: 1 Properties of Tamanu Oil

Density	896 Kg / m^3	Fire Point	114 ^{0}C
Specific Gravity	0.86	Calorific Value	44000 KJ./Kg -K
Viscosity	9.1 Cst	Carbon content	1.14 %
Flash Point	108 ^{0}C	Hydro Carbons	2450



Fig No: 1 Seeds of Tamanu



Fig No: 2 Samples of Tamanu

ISBN: 978-93-83083-87-9

2. 0 EXPERIMENTATION

2.1 Experimental set up

Table No: 2 Specifications of Engine

Engine Make	Kirloskar
BHP	5HP
RPM	1500
Bore	80 mm
Length	110 mm
Working Cycle	4 Stroke
Method of Cooling	Water
Method of Ignition	Compression Ignition
Compression Ratio	16.5:1
Dynamometry	Mechanical
Capacity	661 cc
Orifice Plate Dia	15 mm
Brake Drum Dia	300 mm
Rope Dia	15mm
Weight of Rope	1 Kg
Weight's	1, 2,4 Kgs



Fig No: 3 Diesel Engine Set up

2.2 Description of Engine

The engine is loaded by the mechanical dynamometry (brake drum). The brake drum is directly coupled to engine flywheel and rope is wounded round the drum. Top end of the rope is connected to spring balance and bottom end of the rope is connected to weight platform. On adding the slotted weights can vary the load on the engine. The suction side of the engine is connected to an air tank, thorough which atmospheric air is drawn into the engine cylinder. Manometers were provided to measure the pressure drop across the engine, orifice is provided in the tank to calculate the volume of the air drawn into the cylinder.

2.3 Results

Table No: 3 Composition vs. Heat Supplied when speed = 1500 RPM

Composition	$Q_{Supplied}$ at 2 Kg load (KJ/ min)	$Q_{Supplied}$ at 4 Kg load (KJ/ min)	$Q_{Supplied}$ at 6 Kg load (KJ/ min)
100% Diesel	309.46	418.73	497.2
95%+5%	380.196	540	603.185
90%+10%	290.87	363.6	565.6
85%+15%	297.69	422.19	596.08

Table No: 4 Composition vs. Heat Equivalent to BP when speed = 1500 RPM

Composition	Heat Equivalent to BP at 2 Kg load (KJ/Min)	Heat equivalent to BP at 4 Kg load (KJ/Min)	Heat equivalent to BP at 6 Kg load (KJ/Min)
100% Diesel	22.08	44.26	88.5
95%+5%	33.198	71.1	135.96
90%+10%	25.296	88.5	151.74
85%+15%	33.198	96.42	167.58

Table No: 5 Composition vs. Heat Loss Due to Exhaust Gases when speed = 1500 RPM

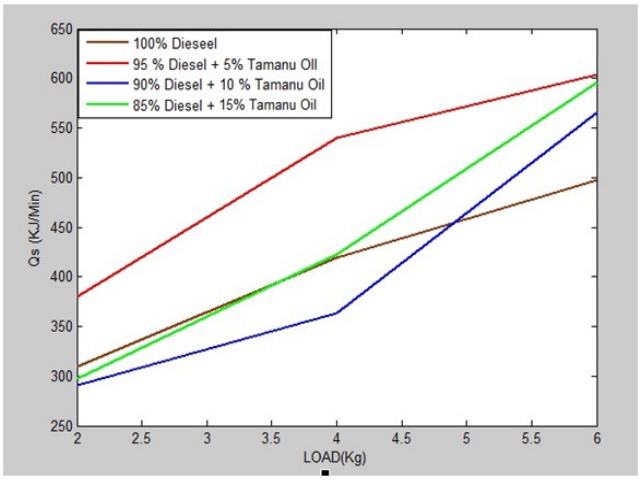
Composition	Heat loss due to Exhaust gases at 2 Kg load (KJ/Min)	Heat loss due to Exhaust gases at 4 Kg load (KJ/Min)	Heat loss due to Exhaust gases at 6 Kg load (KJ/Min)
100% Diesel	158.16	239.8	294.66
95%+5%	192.15	283.89	317.85
90%+10%	143.52	167	263.65
85%+15%	141	197.83	279.3

ISBN: 978-93-83083-87-9

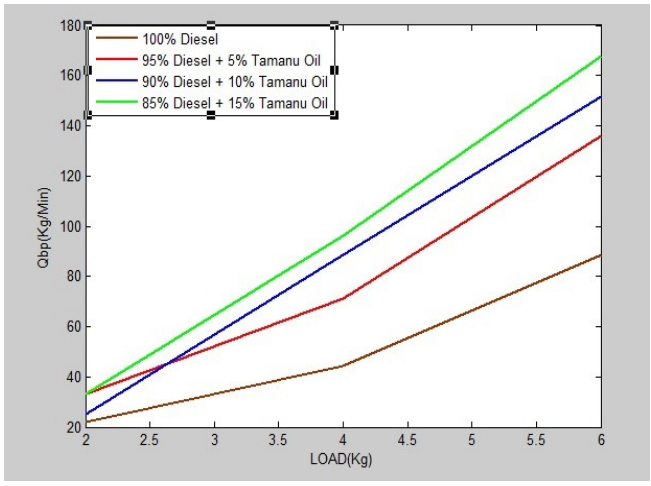
Table No: 6 Composition vs. Heat Loss by Cooling Water when speed = 1500 RPM

Composition	Heat loss due to cooling water at 2 Kg load (KJ/Min)	Heat loss due to cooling water at 4 Kg load (KJ/Min)	Heat loss due to cooling water at 6 Kg load (KJ/Min)
100% Diesel	70.22	90.28	100.32
95%+5%	50.16	60.192	80.256
90%+10%	70.224	70.224	90.288
85%+15%	60.192	80.256	100.32

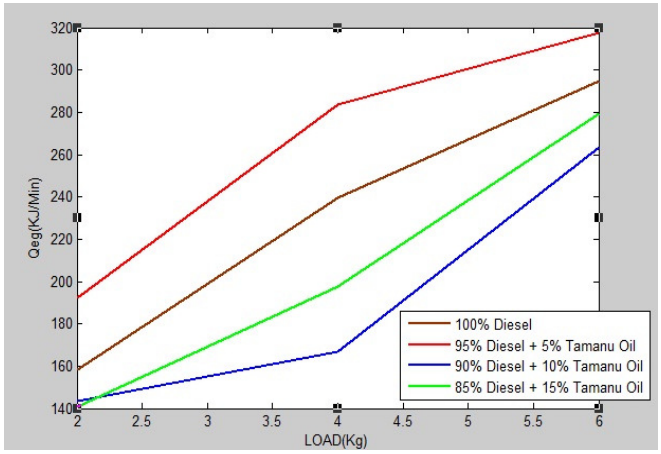
2.4 Graphs



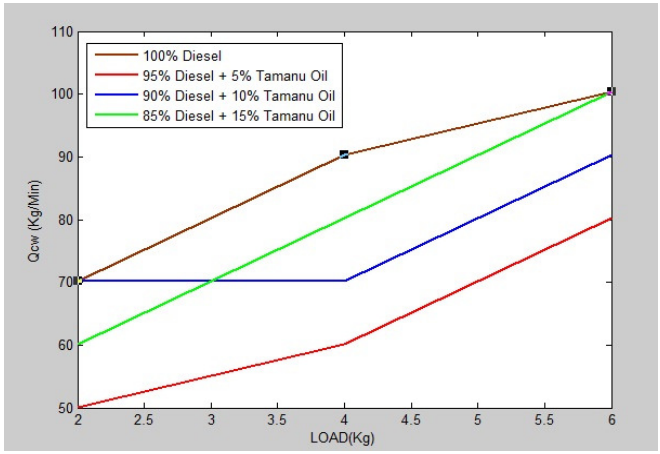
Graph No: 1 Load vs. $Q_{Supplied}$



Graph No: 2 Load vs. Q_{BP}



Graph No: 3 Load vs. $Q_{Exhaust\ gases}$



Graph No: 4 Load vs. $Q_{cooling\ water}$

3. CONCLUSIONS

Tamanu oil mixed with diesel at different compositions is used as alternative fuel in CI engines. There is improvement in break power at different loads when % of Tamanu oil is increased (5% to 15%). The flash point of Tamanu oil is much higher than that of diesel, so they are much safer to store than diesel. Even they may be slighter increase in carbon monoxides (CO) by using mixture of Tamanu oil and diesel, but hydrocarbons (HC) are decreased to greater extent. Since Tamanu oil is a vegetable oil it has good ignition quality, high flash point and cetane number. Thus the combustion quality and temperature increases at higher load conditions, so there by unaccounted losses are reduced considerably. Thus Tamanu oil can also be used as alternative fuel.

REFERENCES

[1] Ganesan V., Internal Combustion Engines. New Delhi, Tata McGraw-Hill, 1999.

[2] Mathur M.L., Sharma R.P., A Course in Internal Combustion Engines. New Delhi, Dhanpat Rai Publications, 2005.

[3] Nag P.K., Heat And Mass Transfer. New Delhi, Tata McGraw-Hill, 2007.

[4] Lu Y.Z., Wang R.Z., Jianzhou S., Xu Y.X. Practical experiments on an adsorption air conditioner powered by exhausted heat from diesel locomotive, Applied Thermal Engineering Sc., 24(2004) 1051-1059.

[5] M. Pons, Ph. Grenier, Experimental data on a solar-powered ice maker using activated carbon and methanol adsorption pair, Solar Energy Engineering 109 (1987) 303–310.

[6] Wong Y.W., Sumathy K. Solar thermal water pumping systems, Renewable and sustainable energy reviews, 3(1999) 185-217.

[7] S. Jiangzhou, R.Z. Wang, Y.Z. Lu, Y.X. Xu, J.Y. Wu, Experimental investigations on adsorption air-conditioner used in internal-combustion locomotive driver-cabin, Applied Thermal Engineering 22 (10) (2002) 1153–1162.

[8] Bhattacharyya TK, Ramachandra S, Goswami AK, Low temperature bellow actuated solar pump, Proceedings of the International Solar Energy Society Congress (1978) 2118-2121.

[9] Rao KR, Shrinivasa U, Srinivasan J. Synthesis of cost-optimal shell-and-tubeheat exchangers. Heat Trans Eng 1991;12(3):47–55.

[10] Kuppan T. Heat exchanger design handbook. New York: Marcel Dekker; 2000.

Lignite Resources of Bikaner and Their Utilization

Pramod Kumar Rajak[1], Vijay Kumar Singh[2], and Dharmendra Kumar[3]

[1,2] Coal & Organic Petrology Laboratory, Department of Geology, B.H.U. Varanasi - 221005.(UP)

[3] Geological Survey of India, Dehradun (Uttarakhand)

ABSTRACT

Coal is the main source of energy and is considered as the backbone of industries as well as Indian economy. In India, about 99% of coal is from Gondwana and rest 1% is from Tertiary period. The major Gondwana coal deposits are located in the eastern and south eastern parts of India and the Tertiary coals are located in Assam and other north eastern states, as well as Tamil Nadu, Gujarat, Rajasthan and Jammu & Kashmir. In Rajasthan lignite producing basins are Jaisalmer basin, Barmer basin and Bikaner-Nagaur basin of Tertiary age. Lignite/Brown coals have very low calorific value, high moisture and high ash content. It is widely used as fuel for thermal power plants for electricity generation. Combustion process converts coal into useful heat energy, but it also pollutes the environment. Combustion of coal at thermal power plants emits mainly carbon dioxide, sulphur oxides, nitrogen oxides; CFCs, other traces gases and airborne inorganic particulates, such as fly ash and suspended particulate matter (SPM). CO_2, NOx and CFCs are green house gases (GHGs). High ash content in Indian coal and inefficient combustion technologies contribute to India's emission of air particulate matter and other trace gases, including gases that are responsible for the green house effects.

1. INTRODUCTION

Coal is the abundantb fossil present in India. It is widely used in thermal plants as thermal energy source for thermal power plants for producing electricity. Power generation in India has increased manifold in recent decades due to the demand of electricity based industries, house holds, etc. Its usage will be increased day by day.

In India, Gondwana and Tertiary coal is present in different geological horizon. The Gondwana coal is of semi-bituminous to bituminous and the tertiary coal is lignite. The geographical distribution of Gondwana coal is in Jharkhand, Orissa, West Bengal, Chhattisgarh, Maharashtra, etc. and the tertiary coal/lignite is in Tamilnadu, Gujarat, Rajasthan, Assam, Jammu & Kashmir, etc. The lignite deposits in India are of Eocene (Jammu & Kashmir, Gujarat and Rajasthan), Miocene (Neyveli, Tamil Nadu) and Plio-Pleistocene (Nichahom, Jammu & Kashmir) ages (Singh, P.K. et. al., 2010.). The Gondwana and Tertiary coals are of poor quality, with very high ash content and low calorific value. The coal supplied to power plants is of the worst quality. Some of

ISBN: 978-93-83083-87-9

the coal mines are owned by private companies, and they do not wish to invest on the quality improvement. Combustion process converts coal into useful heat energy and ash, but it is also a part of the process that produce the greatest environmental and health concerns.

Each segment of the coal system has some kind of environmental problem—from coal extraction, via preparation, to processing and utilization. Coal utilization processes in industry mainly include are greenhouse gases (GHGs) High ash content in Indian coal and inefficient combustion technologies contribute to India's emission of air particulate matter and other trace gases, including gases that are responsible for the greenhouse effect. The present coal consumption in thermal power station in India results in adding fly ash to air and the rest is dumped on land or water. In spite of various research results a consistent utilization is not evident, and it is expected that stock piles of fly ash will continue to grow with the increasing number of super thermal power stations in India. These large quantities of this material will be increasingly brought into contact with the water and soil environment.combustion and gasification for generating electricity, process heat and residential heat as well as carbonization for making metallurgical coke, and chemical materials. Of these, electricity generated by coal combustion is by far the largest consumer.

Combustion of coal at thermal power plants emits mainly carbon dioxide (CO2), sulphur oxides (SOx), nitrogen oxides (NOx); CFCs other trace gases and air borne inorganic particulates, such as fly ash and suspended particulate matter (SPM). CO2, NOx and CFCs

2. GEOLOGY

The Tertiary sediments in Bikaner basin are elongate in shape and occur in two distinctly separate areas in Bikaner districts and is separated by an aranaceous high represented by the Marwar Supergroup. The Tertiary sequence contains sediments of continental and marine origin deposited over the Neoproterozoic Nagaur Group (Marwar Supergroup) of rocks. It is represented by the Palana, Marh and Jogira Formations in ascending order having conformable contacts. It is bound on the north and south by E-W trending faults and marked by basement highs at Dulmera, Suratgarh and adjoining areas. Recent open cast lignite mining in the area exposed new geological sections at Matasukh and Barsingsar.

The Bikaner basin, better known as Palana – Ganganagar shelf, is an E-W trending elongated basin extending for about 200 km with a maximum width of about 50 km in north-south direction. The basin preserves Palana and Ganganagar embayments, closing eastwards, connecting with the Indus basin. The entire area is under alluvial cover. The Palana Shale is recorded subsurface and includes black shales, lignite, fuller's earth and fire clay all thinning towards the west.

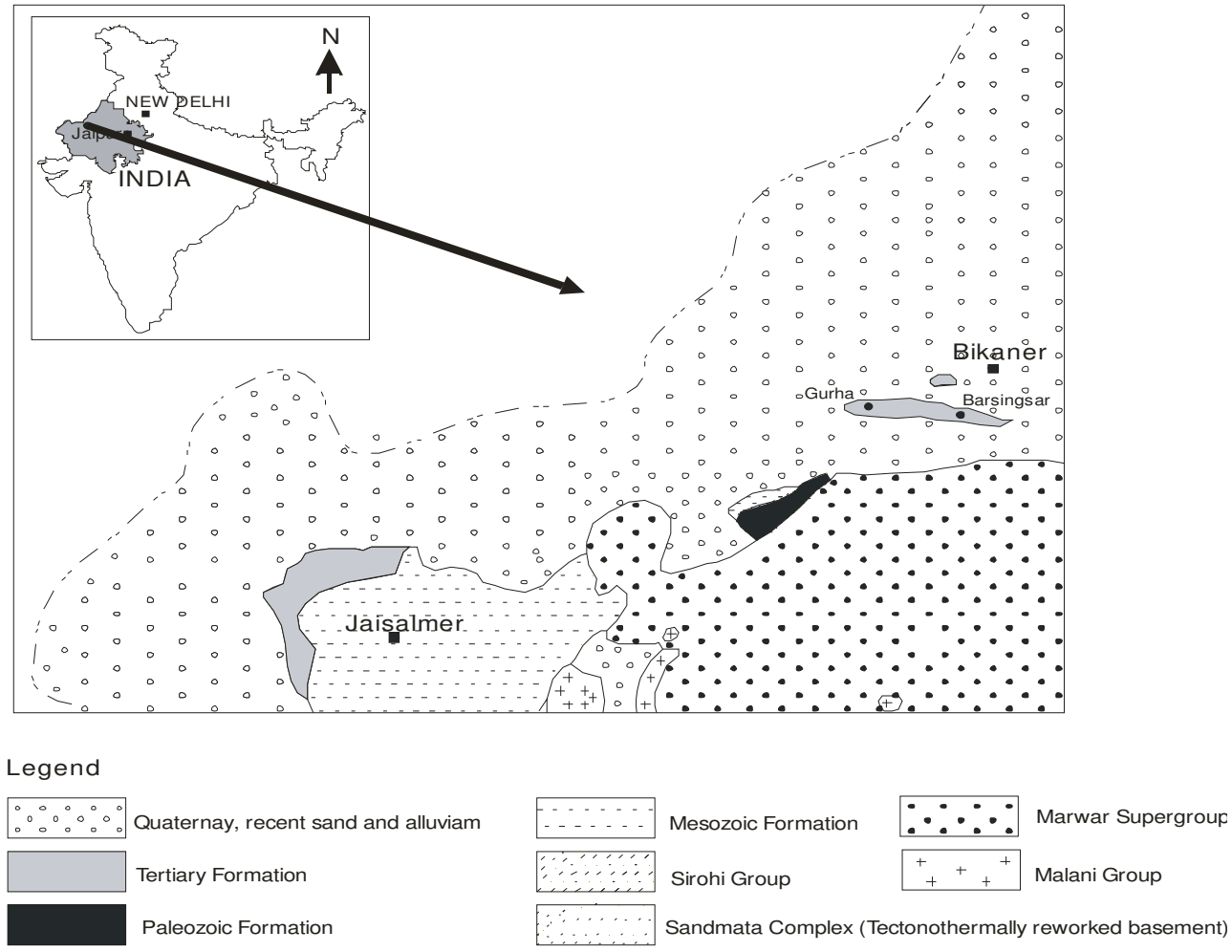


Fig.1 Geology of Bikaner basin, Rajasthan. (after Roy & Jakhar,2002)

3. GENERAL STRATIGRAPHY OF BIKANER BASIN

Age	Formation
Pleistocene to Recent	Kolayat Formation
~~ Unconformity ~~~~~~~	
Early to Middle Eocene	Jogaria Formation(Calcareous facies)
~~ Angular Unconformity ~~~~~~~	
*[2]Late Paleocene (?)	Marh Formation (Arenaceous facies)
~~ (?)Gradational Contact ~~~~~~~	
*[3] Early Paleocene (?)	Palana Formation (Carbonaceous facies)
~~ Base not encountered ~~~~~~~	

Table 1: Tertiary formation of Bikaner-Nagaur basin (After Ghose, 1983a)

**[2]* *The formation has been described to be of Early Eocene (Bhandari, 1999).*

**[3]* *The formation has been described to be of Eocene (La Touche, T. D. 1897; Rao and Vimal, 1952).*

ISBN: 978-93-83083-87-9

4. LIGNITE/COAL OCCURRENCES IN BIKANER BASIN

Bikaner basin is a major repository of Tertiary coals in Rajasthan and is estimated to house substantial deposits of lignitic coal. The Basin has some high potential but lesser-known lignite fields e.g. Barsingasar. The lignite deposits of Eocene (Jammu & Kashmir, Gujarat and Rajasthan), Miocene (Neyveli, Tamil Nadu) and Plio-Pleistocene (Nichahom, Jammu & Kashmir) ages. These lignite mines are also a late comer in the Indian coal-mining scenario. The total lignite bearing area, though difficult to prognosticate owing to lignite occurrences as lensoid bodies, is not less than 3-4 thousand square kilometers. Coal industry over the years has generated limited geological and coal characteristic data for the Palana and Matasukh mines.

The data is specific to coal exploration and is confined predominantly to the working mines in the area. Further, data generated by the coal and power industry is usually confined to depths less than 100m and thus, major part of the coalfield, both in terms of area and depth is unexplored, primarily on account of less demand and discouraging results of initial exploration.

The lignite deposits of Bikaner district of Rajasthan are Palaeocene to Lower Eocene age (Ghose, 1983a) and are known to occur at several places in Bikaner district of Rajasthan. The desert sand of Rajasthan conceals all the outcrops of lignite and the associated formations. Out of all the deposits of lignite in this part of the Basin, the deposits of Palana – Barsingsar is the most important where workable mines exist. Lignite was proven and mined in Palana since 1898 through underground shaft but was stopped in 1967 following auto-combustion and was re-opened in early nineties. Here, a half-saucer shaped lignite seam occurs associated with Nummulitic limestone and Fuller's earth. The lignite body extends over 6 to 8 km's and has a NW-SE trend.

A large part of coal bearing Palana & Marh (?) Formations are devoid of lignite, but wherever so, it appears to have been replaced by carbonaceous shales. Lignite bearing Palana Formation is overlain by sequence of alternation of medium to coarse grained sandstone and clay belonging to Marh Formation with gradational contact. Marh Formation is completely covered by a thick pile of Quaternary sediments and the top part consists of blanket of desert sand. The lithological association of grey to black carbonaceous pyritic shale, fine to medium grained sandstone intercalation and presence of lignite, indicate deposition in reducing parallic / swampy environment.

Only one prominent regionally established unit, of thick lignite in the Palana Formation is identified in the area, wherein a cumulative coal thickness of about 30 - 40 m is expected.

5. METHODOLOGY

Twenty two pillar coal samples (Schopf, J.M., 1960.) were taken from Barsingsar lignite mine in such a way that the entire thickness of the seam was exposed. For the purpose the coal samples were crushed to -18 and -72 mesh size to make coal powder, to determine the constituents viz. Maceral analysis, proximate analysis, traces element analysis, etc.

6. TRACE ELEMENT ANALYSIS

Take 0.5 g (dry weight) of coal to a digestion vessel., Add 10 ml of digestion mixture (10 part conc. HNO_3 and 1 part $HClO_4$) and reflux for further 30 min. Repeat this step over and over until no brown fumes are given off by the sample. Filter through Whatman No. 41 filter paper. Rinse the digestate samples with 1% Conc. HNO_3 and transfer the sample in separate test tube and make the volume up to 20 ml. Digestated samples were analyzed by Atomic Absorption Spectrophotometer (AAS, Model Perkin Elmer Analyst 800).

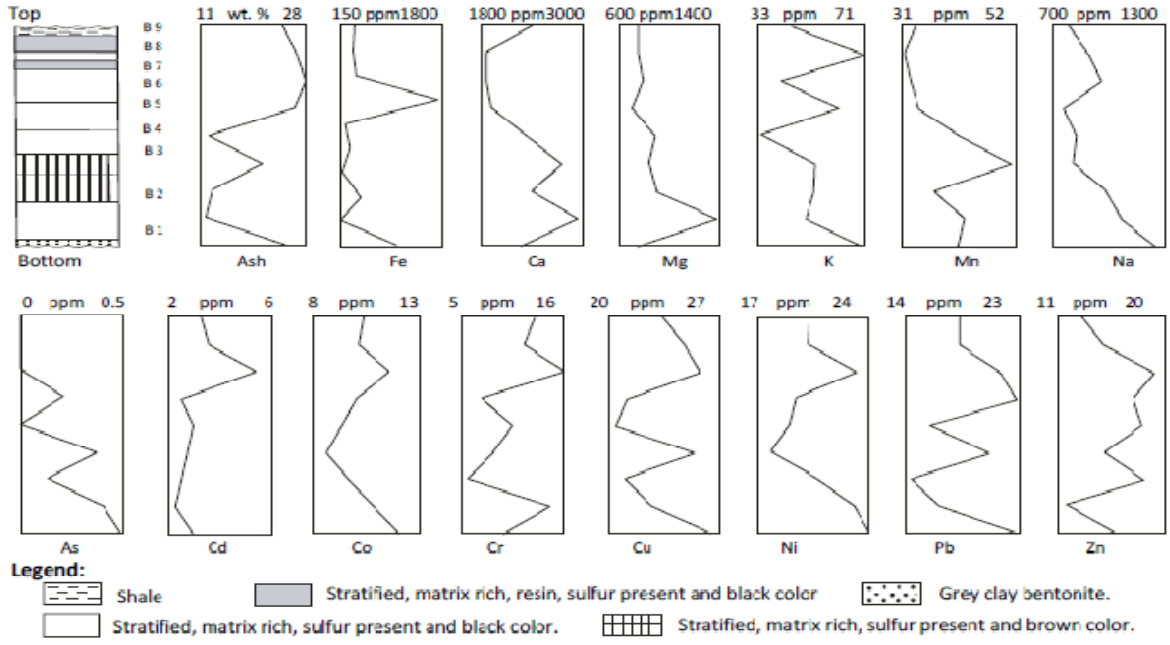


Fig.2a. Vertical variation of Ash and some elements in Barsingsar lignite seam.

7. DISCUSSION AND CONCLUSION

In recent years there has been increasing environmental concern related to the pollutant emissions from coal combustion. Not only are large amounts of pollutants discharged from coal combustion, but there are diverse pollutants produced, covering gaseous, liquid, and solid forms. It has increasingly been recognized that these pollutants pose various adverse impacts to the environment, harming public health and reducing the quality of life.

ISBN: 978-93-83083-87-9

Sulfur:

During coal combustion, sulfur will produce SO_2 and H_2S, which will be emitted into atmosphere in the form of gases and aerosols. In atmosphere, they will react chemically with O_2 and vapor to form vitriol-vapor. Under suitable conditions, acid-rain will be formed and it will affect the atmosphere quality, reduce water quality, depress the function of soil, block the normal growth of plants, and finally influence the life and existing environment of human beings (Patra, J., 2010).

Arsenic:

Arsenic poisoning interferes with cellular longevity by allosteric inhibition of an essential metabolic enzyme pyruvate dehydrogenase (PDH) complex which catalyzes the reaction Pyruvate + CoA-SH + NAD+ PDH Acetyl-Co-A + NADH + CO_2. With the enzyme inhibited, the energy system of the cell is disrupted resulting in an apoptosis episode. Arsenic in cells clearly stimulates the production of hydrogen peroxide (H_2O_2).

When the H_2O_2 reacts with Fenton metals such as iron, it produces a highly reactive hydroxyl radical. Inorganic Arsenic trioxide found in ground water particularly affects Voltage-gated potassium channels , disrupting cellular electrolytic function resulting in neurological disturbances, cardiovascular episodes such as prolonged qt interval, high blood pressure central nervous system dysfunction and death (Patra, J.,2010).

Lead:

Lead poisoning (also known as plumbism, Colica pictonium, saturnism, Devon colic, or painter's colic) is a medical condition caused by increased levels of the heavy metal lead in the body. Lead interferes with a variety of body processes and is toxic to many organs and tissues including the heart, bones, intestines, kidneys and reproductive and nervous systems. It interferes with the development of the nervous system and is therefore particularly toxic to children, causing potentially permanent learning and behavior disorders. Symptoms include abdominal pain, headache, anemia, irritability, and in severe cases seizures, coma, and death (Patra, J., 2010).

Cadmium:

Cadmium is highly toxic and has been implicated in some cases of poisoning through food. Minute quantities of cadmium are suspected of being responsible for adverse changes in arteries of human kidneys. Cadmium also causes generalized cancers in laboratory animals and has been linked epidemiologically with certain human cancers. Cadmium may enter water as a result of industrialized discharges or the deterioration of galvanized pipe (Patra, J., 2010).

Iron:

The excess iron affects organ function, presumably by direct toxic effect. Excessive iron stores exceed the body's capacity to chelate iron, and free iron accumulates. This unbound iron promotes free radical formation in cells, resulting in membrane lipid peroxidation and cellular injury (Patra, J.,2010).

Copper:

Continuous ingestion of copper from food or water supply at intakes is sufficient to induce chronic copper poisoning in man is extremely unlikely; judging by the amounts required for this purpose in other monogastric species. The accumulation sometimes results in chronic copper poisoning, followed by death (Gouch, L.P. et al.).

Magnese:

Underwood (1971, p. 202) reported, "Chronic manganese poisoning occurs in miners working with manganese ores. The manganese enters the lungs as oxide dust from the air and also enters the body via the gastrointestinal tract. The disease is characterized by a severe psychiatric disorder (Gouch, L.P. et al.).

8. ACKNOWLEDGEMENT

I would like to express my special thanks of gratitude to my revered Prof. P.K.Singh, Prof. M.P.Singh and Dr. Asha Lata Singh (Department of Botany), for using AAS facility for her help in analysis of trace metals. Who gave me the golden opportunity to do this wonderful project on the topic " Lignite resources of Bikaner and their utilization" which also helped me in doing a lot of research and I came to know about so many new things. I am immensely thankful to him for his fruitful and invaluable guidance.

REFERENCES

[1] Ghose, K. P., 1983. Generalised structural and metamorphic map around Batia, Udaipur District, Rajasthan; a study. Indian Jour. Eart Sci., 10.

[2] Gouch, L.P., Shacklette, H.D., and Case, A.A., 1979. Element Concentrations Toxic to Plants, Animals, and Man. Gelogical Survey Bulletin, United States Government printing office, Washington.

[3] Patra, J., 2010. Report: Effect of coal based industries on surface water quality, Department of Mining Engineering, NIT, Rourkela.

[4] Roy, A.B.,Jakhar S.R., 2002. Geology of Rajasthan (Northwest India) Precambrian to Recent. Scientific Publishers (India), Jodhpur.

[5] Schopf, J.M., (1960). Field description and sampling of coal beds. U.S. Geological Survey Bulletin 1111(B).

[6] Singh, P.K., Singh, M.P., Singh, A.K., (2010). Petrochemical characterization and evolution of Vastan lignite, Gujarat, Indai. Intrnational Journal of Coal Geology.

Biorefining Crotalaria Juncea (Sunn-hemp): A Promising New Source for the Production of Biodiesel

Suvra Sadhukhan[1], Ujjaini Sarkar[2]

[1,2]Departmentof Chemical Engineering, Jadavpur University, Kolkata-700032, India

ABSTRACT

Nowadays, clean biodiesel can be produced from biomass based agricultural oils. Crotalaria Juncea, or Sunn-hemp, is a member of the pea family (Fabaceae) grown in many countries to be used as a green manure or forage crop. In our research work, biodiesel is produced by trans-esterification of bio-oil obtained from Crotalaria Juncea (Sunn-hemp) seed using methanol and different catalysts. Here standard solvent extraction method, using Soxhlet apparatus is done for oil extraction using crushed Crotalaria Juncea seeds. In order to obtain the maximum yield of bio-oil, two parameters such as extraction time and choice of solvents are optimized. Isopropanol solvent is best for obtaining maximum yield of oil at 3.5 hour time. Trans-esterification reaction is done using three types of catalysts like, KOH, CaO and sea shell with different oil-methanol molar ratio in the range of 1:9-1:13 at different time intervals. Maximum yield of biodiesel is obtained with KOH as catalyst at 4hour time with 1:11 oil-methanol mole ratio. The yield of biodiesel is 91.365%.

Keywords: Biodiesel; Crotalaria Juncea; Soxhlet apparatus; Isopropanol.

1. INTRODUCTION

Global warming presents the gravest threat to life on Earth in all of human history. The worldwide emissions of CO_2 and other harmful gases such as CO, SO_x, NO_x and particulates generated by fossil fuel combustion have led to serious crisis to the environment. Biofuels offer an attractive alternative to fossil fuel [1]. Numerous countries are moving towards the partial and gradual replacement of fossil fuels with biofuels, mainly ethanol and biodiesel. The demand for diesel is five times higher than the demand for petrol in India. While the ethanol industry is mature, the biodiesel industry is still in its infancy [2]. India's current biodiesel technology of choice is the trans-esterification of vegetable oil. Biomass based agricultural oils have a great potential towards production of cleaner biodiesel substitute. These bio oils are better than diesel fuel in terms of sulfur content, flash point, aromatic content and biodegradability [3-4]. Bio oil from Crotalaria Juncea (Sunn-hemp) seed is a promising new source for the production of biofuel.

Crotalaria Juncea, or Sunn-hemp, is a member of the pea family (Fabaceae) grown in many countries as a green manure or forage crop. Sunn-hemp (Crotalaria Juncea, L), a plant of sub-order Paplionaceae of order Leguminoseae is an annual shrub cultivated as multipurpose legume especially for its fine fibre in many countries including India. The crop is grown also for legume or as a fodder. The Sunn-hemp crop is native to India. It is generally considered to have originated in India, where it has been cultivated since prehistoric times. However, this is now widely grown throughout the tropics and subtropics. Sunn-hemp seeds contain moisture (8.6%), crude protein (34.6%), fat (4.3%), starch (41.1%), fibre content (8.1%), ash (3.3%), and oil (12.6%). The endosperm of Sunn-hemp seeds contains thin walled cells, enriched in oil [5]. The oil contains saturated fatty acids (20.3%), Linolenic acid (4.6%), Linoleic acid (46.8%) and Oleic acid (28.3%). The 60 days old crop accumulates about 170 kg N, 20 kg P and 130 kg K/ha.

2. MATERIALS & METHODS

2.1. Materials

2.1.1. Sunn-hemp

In this research work Sunn-hemp seeds (K-12 Yellow) were collected from Central Research Institute for Jute and Allied Fibers (CRIJAF), Kolkata, India. After cleaning, the raw seeds were dried and milled using a domestic kitchen mill (Make: Morphy Richards; Model: Cutie Mixer-Grinder; Power consumption: 500 W; Speed: 21,000 rpm).

2.1.2. Solvents

Four types of organic solvents like Iso-Propanol, Chloroform, Toluene and Hexane [Make: Merck Emparta; Grade: ACS; Purity (GC): P95%] are all purchased from local vendors.

2.1.3. Preparation of Catalysts

Here three types of catalysts were used. Potassium hydroxide and calcium oxide powder were purchased from local vendors. The sea shell (*capiz*) was obtained from local market. It was washed by water to remove dirt and other impurities. Then it was dried overnight at 100 ^{0}C. The shell was then crushed by mortar and pestle and calcined at 900°C for 2 h in a muffle furnace to convert $CaCO_3$ to CaO. After that the catalyst was removed from the furnace and kept in a desiccator to prevent any kind of contact with air.

2.2. Experimental methods

2.2.1. Bio-oil production

Oil extraction was done using Soxhlet Extractor with a round-bottom flask of capacity 1lt. The cylindrical Soxhlet extractor was placed onto the round-bottom flask containing the extraction

solvent. A bulb-condenser, operated on cooling water was fitted onto the top of the Soxhlet. The solvent was heated to reflux and then the vapour moved up a distillation arm and flooded into the chamber housing the thimble packed with crushed seeds. The solvent vapour was cooled, dripped back into the chamber and then emptied automatically. At that time the solvent was siphoned through a special side arm into the flask. This cycle was repeated many times in order to ensure completion of extraction.

2.2.2. Biodiesel production

All experiments were carried out in a 500 ml 3-necked round-bottom flask, equipped with a mechanical stirrer and a water-cooled condenser. The trans-esterification reaction was performed with 20g of oil at a temperature of 60°C and a stirring speed of 400 rpm. The reaction was carried out with different oil-methanol molar ratio in the range of 1:9 - 1:13 at different time intervals in the range of 2-6 hrs for three types of catalysts. The oil was charged into the flask and heated to the desired temperature. Then methanol and catalyst were added into the reactor. After the reaction was complete, the mixture was allowed to cool down and then transferred to a separating funnel for separating the phases. The upper methyl ester layer was taken and analyzed.

3. RESULTS AND DISCUSSION

3.1. Effect of use of different solvents on oil extraction

Table 1 describes the oil yield using four extraction solvents. Isopropanol gives highest yield (11.24%). From this result, it is shown that polar solvents like isopropanol and chloroform give better oil yield as compared to some of the non-polar solvents like hexane and toluene. Chloroform gives second best oil yield. After getting the best solvent, oil extraction time is optimized in order to get maximum yield. Fig. 1 predicts the maximum yield at 3.5 hours.

3.2. Effect of various process variables on the yield of biodiesel

In trans-esterification, the nucleophilic alkoxide from the alcohol attacks the electrophilic part of the carbonyl group of the triglycerides [6]. The polarization effect causes the carbon atom to be positively polarized and electrophilic. Triglyceride can break into three steps. First, an intermediate tetrahedral is generated from the attack of electrophilic carbon atom by nucleophilic alkoxide and then the breakdown of unstable intermediate tetrahedral to diglyceride ion and fatty acid ester would occur. Finally the catalyst is recovered by proton transfer.

The trans-esterification of Sunn-hemp oil was done using various parameters like choice of catalyst, reaction time and oil to methanol molar ratio. Table 2 describes the yield of biodiesel obtained for different catalysts (KOH, CaO and sea shell) at different oil to methanol molar ratio

1:9-1:13. Fig. 2 shows that the yield is maximum at 4h reaction time. With further increase of reaction time, it decreases. Here KOH catalyst gives best result as compared to other heterogeneous catalysts. The maximum yield of biodiesel obtained in this study was 91.365% at the operation condition: catalyst used 2% (w/w) KOH, oil to methanol ratio 1:11, reaction time 4hrs.

4. CONCLUSIONS

In this study, a bio oil was produced from Sunn-hemp seeds by solvent extraction method using a Soxhlet extractor. Since oil content is low (<20%), solvent extraction technique offers the only viable solution for the extraction of oil from the Sunn-hemp seeds. Biodiesel was produced using three types of catalysts. By using KOH catalyst maximum yield is obtained.

REFERENCES

[1] Leung D. Y.C, Wu X, Leung M.K.H. A review on biodiesel production using catalyzed trans-esterification. Applied Energy 2010; 87:1083–1095.

[2] Wang Y, Wang X, Liu Y, Ou S, Tan Y, Tang S. Refining of biodiesel by ceramic membrane separation. Fuel Processing Technology 2009; 90: 422-427.

[3] Helwani Z, Othman M.R, Aziz N, Fernando W.J.N, Kim J. Technologies for production of biodiesel focusing on green catalytic techniques: A review. Fuel Processing Technology 2009; 90: 1502–1514.

[4] Sharma Y.C, Singh B, Upadhyay S.N. Advancements in development and characterization of biodiesel: A review. Fuel 2008; 87: 2355–2373.

[5] Chaudhury J, Singh D.P, Hazra S.K. Sunnhemp (Crotalaria Juncea, L), CRIJAF, ICAR.

[6] Endalew A.K, Kiros Y, Zanzi R. Inorganic heterogeneous catalysts for biodiesel production from vegetable oils. Biomass and Bioenergy 2011; 35: 3787-3809.

Table 1

Variation of the yields (%) of Sunn-hemp seed oil using various extraction solvents (amount of seed taken: 107 g, amount of solvent taken: 500 ml).

Run	Name of solvent	Amount of seed used [gm]	Amount of oil obtained[gm]	Amount of oil [%]
1.	Iso-propanol	107	12.03	11.24
2.	Chloroform	107	10.4	9.72
3.	Toluene	107	7.7	7.2
4.	Hexane	107	2.46	2.3

ISBN: 978-93-83083-87-9

Table 2: The effect of different process variable on the yield of biodiesel

Type of catalyst	Reaction time, h	Oil to methanol ratio	Yield of biodiesel (%)
KOH	4	1:9	78.274
		1:11	91.365
		1:13	65.32
CaO	4	1:9	52.313
		1:11	60.261
		1:13	56.63
Sea shell	4	1:9	43.621
		1:11	50.563
		1:13	35.264

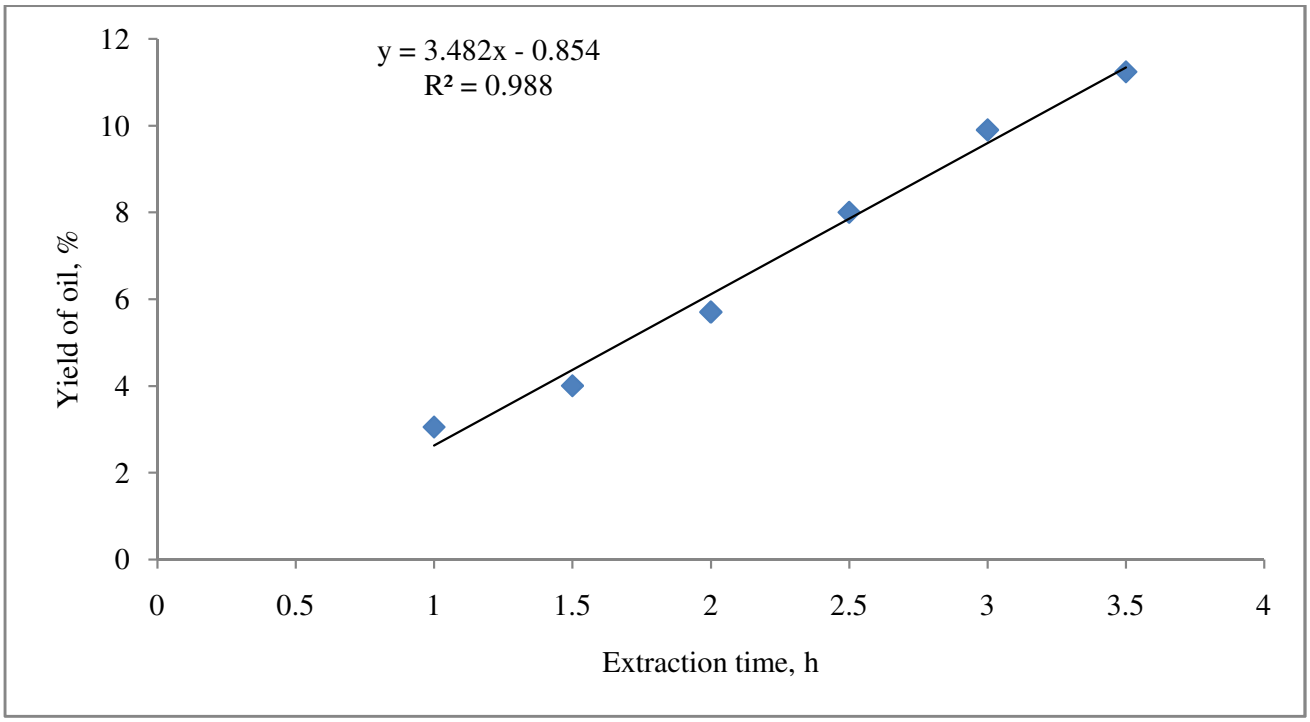


Fig.1. Variation of Sunn Hemp oil recovery with different extraction time for isopropanol solvent.

ISBN: 978-93-83083-87-9

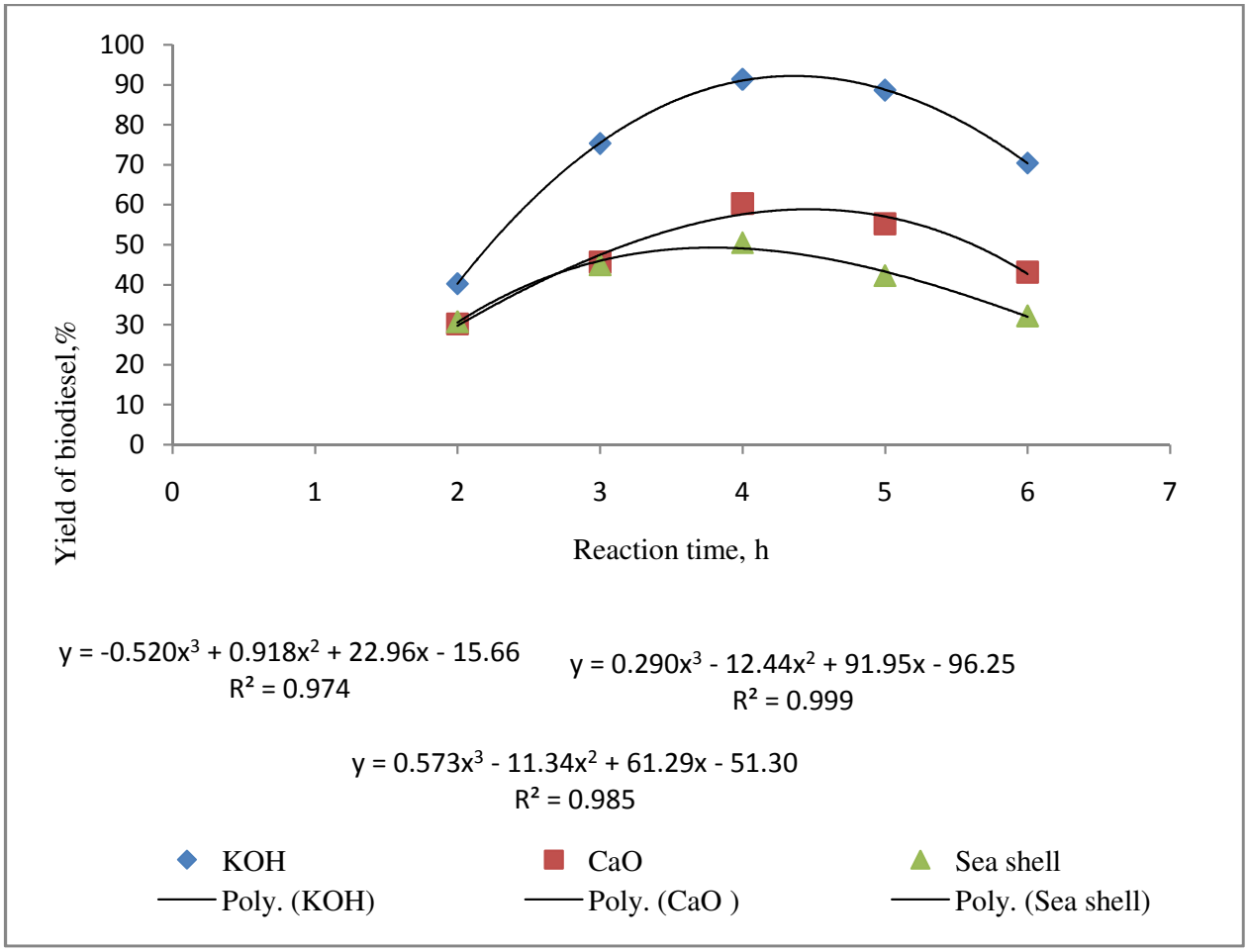


Fig.2. Yield of biodiesel for different catalysts at different time intervals.

Gas Hydrats as Upcoming Source of Energy

Amit Arora[1], C.B. Majumder[2]

[1,2]*Chemical Engineering Department, IIT Roorkee*

ABSTRACT

Gas Hydrates are crystalline form of natural gas present in down sea and In the permafrost region. They are seen as new generation fuels. It is also known as burning ice. These are presents in KG, KK, and Mahanadi, Andaman nicabar regions in India and round the world in country like USA, Canada, and Japan etc. Lots of research is going on to exploit this source of energy. These are seen as substitute of the fossil fuel for future generation.

ISBN: 978-93-83083-87-9

SECTION B
ENVIRONMENTAL RESEARCH PAPERS

Plastic Waste in India- Management and Utilisation

Aakriti Makker[1], Arushi Gupta[2], Lovleen Gupta[3]

[1, 2, 3]Department of Environmental Engineering, Delhi Technological University (Formerly Delhi College of Engineering), Shahbad Daulatpur, Main Bawana Road, Delhi -110042

ABSTRACT

India being a developing country, consumption of plastic products and hence the generation of waste is increasing at an alarming rate. Around 60% of the plastic waste is recycled, mainly by the informal sector, under serious constraints due to the lack of fiscal incentives. Financial limitations are a constraint to the technical improvements needed to satisfy market demand. Non-recyclable plastic wastes are of major concern as they lead to serious environmental and health issues. They are either subjected to landfilling or incineration emitting toxic fumes of dioxins, furans, methane, carbon monoxide, chlorine, hydrochloric acid etc. The aim of the study is to provide an overview of the plastic waste management scenario in India and improving the same taking the aid of newer technologies. The study is divided into two parts: the first part comprises of general outlook towards the present status of plastic waste management and a brief interaction with few of the people dealing in the recycling process. This helped to gather information on the use of recycled products and their hub of recycling. The second part includes the examination of a South Korean model which can be replicated in India. It effectively converts plastic waste into fuel by the process of pelletization and can be used as a substitute for coal by the use of a waste plastic burner. Waste will prove to be a resource rather than a burden. In addition, this paper suggests certain strategies which when adapted can improve the plastic waste management process in India.

Keywords: lastic waste, recycling, pelletisation, incineration

1. INTRODUCTION

Almost all the major cities in India have experienced unprecedented population and industrial growth over the last few years. Continuous migration of the people from rural to urban centers in search of better employment opportunities has put a lot of pressure on the limited natural resources in the urban cities. Human activities and the rate of utilization of resources always generate waste, large concentration of which constitutes plastic waste.

Plastics are inherently unsustainable, derived from non-renewable petroleum sources. From cradle to grave, plastics are implicated in a variety of problems, including environmental pollution and

worker health hazards during manufacture, processing and disposal; toxic exposure to consumers during use; cattle and wildlife deaths due to ingestion of plastic wastes. Despite of this, plastics have become an integral part of our lives because of their low cost, high durability and low weight. They can be classified as given in Table 1.

India is a developing country with a present population of approx. 1020 million [1]. Plastic consumption has increased from 61,000 tonnes in 1996 to 135, 00,000 tonnes in 2011[1]. Per Capita Generation of plastic waste is 6 kg per annum and hence the Plastic Waste Generation comes out to be approx. 16,500 tonnes per day [1]. There are more than 20,000 plastic processing units that generate an average output of Rs 85,000 Crore per annum. Around 7,500 recycling units are responsible for the recycling of 60% of the plastic waste generated in the country[1]. The plastic industry as a whole also provides gainful employment to about 3.3 million people.[1] Hence, plastic industry is not just any other chemical industry in this country but it is one of the most promising and prominent source of income and livelihood for millions of people.

Table 1: Categorization of plastics [2]

Symbol	Short Name	Scientific Name	Uses
	PET	Polyethylene Terphthalate (PET)	Water bottles, PET Bottles, etc.
	HDPE	High Density Polythylene (HDPE)	Milk/detergent bags, Carry bags, containers
	PVC	Poly Vinyl Chloride (PVC)	Cable, pipes, Flooring
	LDPE	Low Density Polyethylene (LDPE)	Carry bags, films
	PP	Polypropylene (PP)	Medicines bottles, Packaging films, cereal Liners
	PS	Polystyrene (PS)	Foam packaging, Tea Cups, ice cream cups
	O	Others	Thermoset plastics, Multilayer and laminated Plastics, PUF, nylon etc.

ISBN: 978-93-83083-87-9

2. CURRENT SCENARIO OF PLASTIC WASTE MANAGEMENT (PWM) IN INDIA

Due to enormous amount of plastic waste generated per day, a series of steps are being implemented involving a chain of people comprising of the **Ragpickers** (Form the backbone of plastic waste management in India and clean about 12-15% of municipal solid waste generated), the **Khabariwala** (move house to house to collect the waste whereas **Raddiwala** remain stationery at their shop and carry out their business), the **Scrap dealer** (get their waste from mobile khabariwala and stationery raddiwala) and the **Bulk Buyer**s (traders that collect material until it is sufficient to be sent to the recycling plant . The current scenario of PWM in India is presented in Figure 1 in the flow chart form Generally, the major operations involved in waste management process includes the collection of plastic waste followed by their disposal in landfills or incineration to reduce their volume and obtain energy[3]. The negatives of plastic waste disposal in landfills and incineration of plastic waste are presented in the following paragraphs.[3]

Disposal of plastic waste in landfill: Disposal of plastic in landfills leads to slow degradation which reduces the quality of the material. Land filling plastic waste decreases the density of the wastes and thus a lot of area is taken up. Moreover, plastics interfere with the degradation of other organic wastes. If plastic cover other biodegradable wastes, air supply ceases and anaerobic decomposition produces methane that is a potent green house gas that contributes to climate change. It also leads to water pollution and contaminates the land.

Incineration of plastic wastes: The heat content of plastic waste can be recovered by incineration. Plastic wastes are a good source of fuel in addition to reduction in the volume of garbage by about 90-95%. [4]Through incineration, plastic proves to be an alternate source of energy but it leads to a lot of resistance by the public due to the emission of toxic gases like Carbon Monoxide, Chlorine, Hydrochloric Acid, Dioxins, Furans, Amines, Nitrides, Styrene, Benzene, 1,3- butadiene, CCl_4 and Acetaldehyde . [4] These can pose a serious threat to human health by causing damage to the reproductive system, immune system and cancer.[4]

A brief interaction was also carried out with few of the persons involved in recycling of plastic waste. Results obtained of the same are presented in Table 2.

3. PROPOSED TECHNOLOGIES FOR PWM IN INDIA

Waste Plastic has been a burden to mankind and is known for exhausting the resources on the planet earth. However, tremendous advancement in science and technology has led to the miraculous transformation of the non-hazardous and combustible plastic waste into potential energy generating fuel.[6] The vital factors which are solemnly responsible for the quality of the

plastic fuel are the smooth feeding to conversion equipment, effective conversion into fuel products, well-controlled combustion and clean flue gas in fuel user facilities[6]. Two of these technologies that can be implemented in India are presented in the following paragraphs:

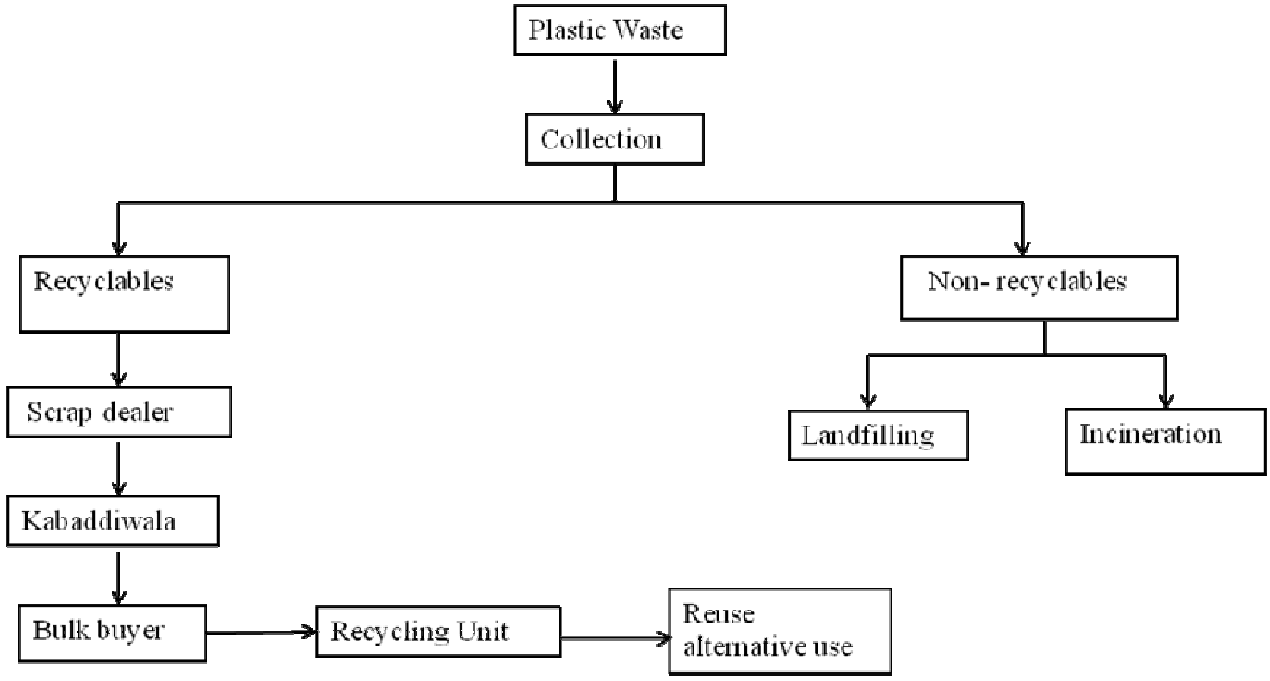


Figure 1: Current scenario of Plastic Waste Management in India

Table 2: Results of the survey

Plastic Waste	Hub of plastic recycling	Use of the recycled product
Plastic pet bottles (juice, cold drinks, liquor bottles)	Surat	Variety use of material
Vegetable bags thrown in drains and on roads	Jaipur	High strength underground wiring for telephone and electricity purpose in West Bengal.
Used tyres of vehicles	Punjab	Rubber gives a)Furnace oil - a substitute for diesel b)Carbon -in the form of black powder can be sold

ISBN: 978-93-83083-87-9

		c)Iron -can be recycled again
Side waste of polyester films (10mm from each side)	Bhavnagar, Gujarat	Ropes that serve as a substitute for jute and have high strength, durability, long life and are cheap. These are used in villages as well as in developed areas
Waste from polyester films/ X-ray films	Surat	It is washed and the silver water obtained is cleared which is used to make collar bone and fibre
Milk bags	Delhi, Punjab	Vegetable bags
Plastic Bags	Surat, parts of Punjab	PVC chappals, paper on plastic bottles and local suitcases

1. Pelletisation and Eco-Clean Burner [5,6]

Pelletising is the process of compressing or moulding a material into the shape of a pellet. For the pellets to be formed, pretreatment is required to be given to the waste plastic. Pre-treatment includes fine and coarse shredding and removal of non-combustible materials. Here vegetables, cartons and papers are disintegrated into fine particles of size 4-5 mm which serve as a binder to form pellets or briquettes by melting and adhering to other non-melting substances such as paper, wood and thermosetting plastics. Lime is then added to prevent continuing decay of organic matter. The mixture is then fed to the horizontal rotary dryer at 300°C which serves the purpose of proper mixing of fine and coarse garbage and ensures its homogeneity with lime. Secondly, it leads to the reduction in moisture of waste to 12% as it is a pre-requisite for pelletization. The mixture is then transferred to the pelletizing machine through the conveyor belt. The machine effectively works at a pressure of 1200 psi, with a capacity of 4 tonnes per hour and moisture content of 10-12%. This results in the production of compressed pellets. The pelletization of the waste plastic produces pellets of three forms:

a) Solid Fuel Pellet: Solid fuel is prepared from both municipal and industrial non-hazardous waste. Solid waste plastic pellet overtakes coal and their derived fuels as well as solid bio fuels like firewood and dried manure. They are further classified into two categories:

   - A. Refuse Derived Fuel = Waste Plastics are generally containing moisture and obtained from kitchen and other municipal wastes and require heating as pretreatment process.

ISBN: 978-93-83083-87-9

- B. Refuse-derived Paper and Plastic Densified Fuel = Waste Plastics are prepared from used paper and other dry feedstock and are widely used.

Output

i. Pellets of dimension between 6 to 60 mm in diameter and 10 to 100 mm in length.

ii. Pellets having calorific value of 18,000-20,000 kJ/kg. Every 1 tonne of pellets can produce 1MW power in the gasification plant.

iii. Plastic burns cleanly giving high energy levels and less dioxin emissions.

b) Liquid Fuel Pellet: They are plastic derived liquid hydrocarbons at normal temperature and pressure. Poly Styrene (PS), Poly Ethylene (PE), Poly propylene (PP), Acrylonitile butadiene styrene (ABS) etc are widely used and they are likely subjected to the contamination by amines, alcohols, waxy hydrocarbons, some inorganic substances, nitrogen, sulphur and halogens gives flu gas pollution. They generally require certain fuel like Gasoline and kerosene for the advanced process. However, they are likely to have more moisture.

c) Gas Fuel Pellet: They are heavily subjected to the polluted contaminants and have not met their utilization on the large scale.

Once the pellets are formed, they are burned in a burner commonly called **Eco Clean Burner** which derives energy out of the plastic pellets. This waste plastic burner is the mechanical and electrical framework which is responsible for the conversion of the waste plastic pellet into the energy. They use the pellet type of Polyethylene, Polypropylene, ABS Pellets and have an efficiency of 75% which could reach to 89% at 150 F of water but produces dioxin emission of 0.119 ng-TEQ/sm^3 at 12 % of O_2. The fuel from this burner has a variety of applications in greenhouses, agricultural structures, commercial applications and light industrial applications.

4. CONSTRUCTION AND WORKING OF ECO CLEAN BURNER

The present invention relates generally to burners that use solid fuels, especially waste plastic fuels. Burner size is minimized by having multiple combustion chambers arranged concentrically around a rotating screw conveyor. Heat efficiency is improved by having an air chamber disposed around the combustion chambers, because the air for the combustion is preheated prior to being delivered to the combustion chambers, while the air chamber at the same time thermally insulates the combustion chambers against the environment. Waste plastic is transported from a fuel hopper to

the combustion chambers by a rotating screw conveyor having spiral auger blades. Speed of the screw conveyor rotation controls the consumption of waste plastic and, hence, the amount of thermal energy generated in the burner. Parts of the combustion chambers can also rotate to auger waste plastic for better oxidation, therefore enhancing the combustion process.

1.5 litres of kerosene is preheated for 20 minutes and then it is mixed thoroughly with the pellet and the mixture is fed in the chamber.

Output:

The output is 100,000 kcal/hr with use of 11,500 kcal/kg of Plastic fuel pellets with boiling water heat of 1 ton water requiring 45 heating minutes and power needed is 4KW @ 110 – 208 Vac of vacuum fuel supply with operating temperature in the chamber of 900-1100 C.Average fuel Gas Temperature is 151 degree Celsius and average fuel gas flow rate is 5.1 m/s. Boiling heat Time is 5 hours where 2 hours for heating and 5 hours for Circulation.

There are several models yet getting proposed in order to reduce waste plastic and result into a better living environment.

2. Incineration

An eco-friendly incineration unit should be designed which can capture all the unwanted toxic gaseous emissions mainly dioxins and furans so that they cannot directly pollute the atmosphere. These trapped gases can be used in a productive way and at the same time the volume of the garbage can be reduced up to 90%. Bottom ash produced from incineration as a result of combustion process and is the largest residue from incineration. It consists mainly of aggregate (80%), organics (5%), and other trace amounts can be used in infrastructure processes or as road fillers.[7]

5. CONCLUSION

Source separation of solid waste is one option that can be effectively carried out by involving the waste generating agents and integrating the formal and informal authorities. It is necessary to bring a change in attitudes, which views waste management as a responsibility of the municipal body and treats waste picking as an illegal activity. Therefore, it is worth considering the integration of the informal practices with the existing formal system and look into options of decentralizing waste management with the involvement of the waste pickers. The recycling industry has to be promoted as it presents a source of livelihood to millions of people in the country. Technology as mentioned above will help people to see value of plastic waste. Our Government should encourage

government companies to adopt such technologies. The newer technologies and efforts of every individual will go a long way in making the Earth a better place to live in.

REFERENCES

[1] Report on Plastic by Shriram Lab- Work carried out by RITES, Ltd. sponsor from CPCB. Assessment of Plastics Waste and its Management at Airports and Railway Stations in Delhi.. Published by CPCB & MoEF; February 2010.

[2] Indicative Guideline for Plastic Waste Management (PWM)- Annual Report (2011-2012) by Central Pollution Control Board.

[3] S.P. Agrawal, K.L. Samdhani, B.S. Singhvi, R.S. Shekhawat and R.P. Arora- Plastic Waste Management- An Indian Perspective- February 8, 2012.

[4] TERI Project Report No. 2002EE62 – Plastic Waste Management for Delhi of 2003.

[5] http://www.wasteplastictechnology.blogspot.in/

[6] http://www.unep.or.jp/Ietc/Publications/spc/WastePlasticsEST_Compendium.pdf

[7] S.M. Al-Salem, S. Evangelisti, P. Lettieri - Life cycle assessment of alternative technologies for municipal solid waste and plastic solid waste management in the Greater London area

The Econometric Models to Some Aspects of Tourism in Nepal

Dila Ram Bhandari
PhD Scholar, Nepal Commerce Campus
Tribhuvan University, Kathmandu, Nepal

ABSTRACT

Tourism is very important sector of the world economy and of Nepal's economy too. Tourism is the largest industry in Nepal and the largest Source of foreign exchange and revenue. Possessing 8 of the 10 highest mountains in the world, Nepal is a hotspot destination for mountaineers, rock climbers and people seeking adventures. Nepal is the country where Mount Everest, the highest mountain peak in the world, is located. Mountaineering and other types of adventure tourism and ecotourism are important attractions for visitors. Tourism forecasting plays an important role in providing awareness and support for future development of the Nepal's tourism industry. International tourists from many countries such as India, China, USA, Japan, Sri Lanka, Canada, and South Korea in Nepal. This one tries to use econometric models and econometric methods to answer some questions about tourism in Nepal during 20 years. This study identifies some new research directions, which include improving the forecasting accuracy through forecast combination; integrating both qualitative and quantitative forecasting approaches, tourism cycles and seasonality analysis, events' impact assessment and risk forecasting.

Keywords: tourism demand; modeling; forecasting, International tourists, ecotourism.

1. INTRODUCTION

Nepal is landlocked country lies between two huge countries China and India. **Nepal** Surrounded by the lofty heights of the Himalayas and is a land of eternal beauty and attraction. It's a land of colorful cultures, ancient history and people, picturesque scenery and some of the best walking on earth. It is popularly known for the highest mountain peak of the world, **Mt. Everest** which stands tall at 8848 meters. Nepal tourism informs about places to visit in Nepal, famous for the birthplace of Gautam Buddha who laid the foundation of Buddhism in the country. Come and explore Nepal having rich traditions of art, culture and heritage. Kathmandu, the capital city of Nepal is a treasure house of ancient art and culture. The number of tourists had increased by 21.4 percent in 2011 and 9.8% 2012, which was Nepal Tourism Year (NTY). According to statistics from Nepal Tourism

Board (NTB), a total of 598,204 foreign tourists entered the country via aerial route in 2012. Tourism is one of the largest industries in the global economy and has been both a key driver and a beneficiary of the prolonged period of economic growth seen in recent years. It also has significant social and cultural benefits because of its potential to promote understanding and international relationships. These socioeconomic dimensions make tourism a vital component of globalization.

1.2 Literature Review

There is a vast literature examining the relation-ship between particular projects and local economic growth. These studies primarily have examined how particular infrastructure projects or policies influence local economic growth. The information, econometric model and other data collected from different websites.

1.3 Objectives of Study

The natural resources and environment are the fundamental fabric upon which the tourism of Nepal is based. Today tourism industry hosts employment to the largest number of people of the nation and relatively helps to bring large number of tourist to the nation.

- To find the societal effects (both positive and negative) caused due to the tourism.
- To find how tourism is directly involved in the country's economic condition, per capita income of the people and the employment of the destination.
- Finding the management of the environment and tourist satisfaction.
- To find the implication on sustainable tourism development, environmental impact assessment and carrying capacity.
- Compute econometric model for sustainable tourism demand and others.

1.4 Research Methodology

To cover the problems faced by the visitors as well as the local people and the tourism entrepreneur different types of research methodology were carried out. The purpose of this work is to model the international tourism demand for Nepal. The principal objective is to know the main determinants affecting tourism to Nepal. Given the importance of the sector in the regional economy, the model will be a very useful tool to forecast the possible arrivals of tourism by origin country.

1.4.1 Variables specification

For the elaboration of any model, the first decision is the selection of the dependent variable. Tourism demand can be measured using tourist arrivals to a destination, overnight stays of tourists, and tourism expenditure. Among the most important independent variables, the own price of tourism has been found to have an important role to play in determining the demand for

international tourism. Prices associated with demand are the cost related to the consumption of tourism goods and services at a given destination and the cost of international transport.

1.4.2 Nature and Sources of data

There are two sources of data .i.e. Primary and Secondary. Primary data are collected by observing the scenario and interviewing the tourism entrepreneurs, local households who are engaged to the tourism and also to those who are not. The visitors are also interviewed and the data are collected. Secondary data are collected from the relevant books, previously published data and articles, different websites, Nepal Tourism Board and others.

1.4.3 Data analysis method

The Primary and the Secondary data collected are classified under the appropriate heading and analyzed. These data are analyzed as frequency of visiting, age factor of visitors, tourism effects, pollution and many more. The outcomes of the analysis are presented by using various modes such as tabular formats, bar graphs, line graphs, pie charts, etc. The field of Econometrics is a part of Economics and deals with mathematical and statistical data. It contributes to economic models development, problem solving, and testing theories and data analysis. Econometrics is based on quantitative analysis of various economic phenomena. Statistical theory contributes to development of econometric models and methods that help to solve economic questions. Dummy variables used in economics to express qualitative or quantitative characteristics. By dummy variables we can take into account the effect of qualitative factors in econometric models. These variables take 1 or 0 values.

$$Z_t = \begin{cases} 1 \; if \; characteristic \; is \; present \\ 0 \; if \; characteristic \; is \; absent \end{cases} \quad \ldots\ldots\ldots\ldots\ldots\ldots \quad (1)$$

Consider the simple linear econometric model:

$$Y_t = c_1 + c_2 X_t + e_t \quad \ldots\ldots\ldots\ldots\ldots\ldots \quad (2)$$

Dummy variable with new parameter c_3, we get,

$$Y_t = c_1 + c_2 X_t + c_3 Z_t + e_t \quad \ldots\ldots\ldots\ldots\ldots \quad (3)$$

If characteristic is present $Z_t=1$, and the intercept of the econometric model and, vice versa if, characterize it is not present and the intercept of the econometric model.

Consider the variables formed by multiplying $\geq two$ explanatory variables together which are called interaction variables. From model 2 with parameter c_3,

$Y_t = c_1+c_2X_t+c_3(X_tZ_t)+e_t$…… (4)

Where X_tZ_t is known a slope dummy variable. If characteristic is present i.e. Z_t=1 slope of model 4 is c_2+c_3 and characteristic absent i.e Z_t=0, slope is c_2 . By including both intercept and the slope, we get:

$Y_t=c_1+c_2X_t+c_3Z_t+c_4(X_tZt)+e_t$ …….. (5)

In this model, if characteristic is absent, the intercept is c_1 and slope c_2. The variables: Y_t= bed-nights in Nepal (millions), X_t=time. Then,

$$Zt = \begin{cases} 1\ if\ pease\ time \\ 0\ if\ conflict-\ time \end{cases}$$

The number of tourists from 1988-2012

Year No. Tourists	**1988**	**1989**	**1990**	**1991**	**1992**	**1993**	**1994**	**1995**
	265,943	239,945	254,885	292,995	334,353	293,567	326,531	363,395
1996	**1997**	**1998**	**1999**	**2000**	**2001**	**2002**	**2003**	**2004**
393,613	421,857	463,684	491,504	463,646	361,237	275,468	338,132	385,297
2005	**2006**	**2007**	**2008**	**2009**	**20010**	**2011**	**2012**	
375,398	383,926	526,705	500,277	509,956	602,867	736,215	803,092	

Therefore,

$X_t = \in \{1,2,3, \ldots \ldots,25\}$……5.1 (Exhibit-1)
The Maoist conflict against Nepal was waged from 1995 -2012. It follows.

$Z_t = 1, t \in \{1,2, \ldots.7\} \cup \{`18,19\ldots,25\}$ and $Z_t = 0$, t $\in \{8,9,10 \ldots\ldots17\}$. Ordinary least square estimates of the relationships 2,3,4 and 5 were computed by E Views. E views regression output is presented in Exhibit 2:

	Model-2	Model-3	Model-4	Model-5
R-squared	0.42315	0.74523	0.56783	0.74562
Adj. R- squared	0.34765	0.65784	0.43567	0.73241
F-statistic	9.7243	28.3456	26.3245	16.3462
d.f	23	22	22	21

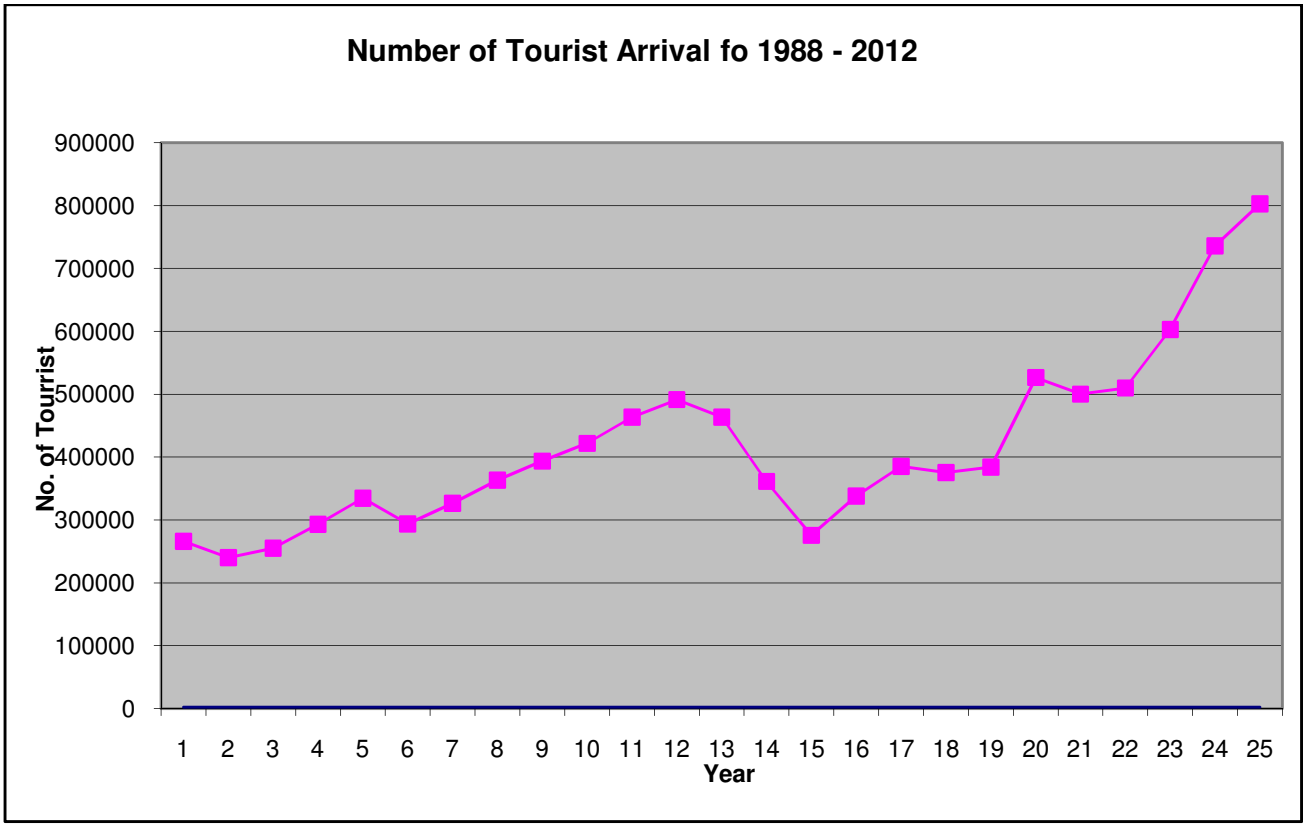
The H_0 to models 2, 3, 4, 5 are respectively. (Exhibit-2)

H_0: $c_1=c_2=0$…… ..6.1 H_0: $c_1=c_2=c_3=0$……6.2 H_0: $c_1=c_2=c_3=0$…….6.3 H_0: $c_1=c_2=c_3=c_4=0$……6.4	If they are false and we accept the alternatives H_1: at least one of the c_1 is nonzero……7.1 H_1: at least one of the c_1, c_2 is nonzero……7.2 H_1: at least one of the c_1, c_2, c_3 nonzero……7.3 H_1: at least one of the c_1, c_2, c_3 and c_4 nonzero….7.4

Towards criteria of the coefficient of determination i.e. a measure how well the explanatory variables explain the response variable, we select the model 5. But let us observe the other part of E Views regression output:

Model-5	coefficient	Std. Error	T-statistic	Probability
C1	-92541	60774.12	-0.894	0.842
C2	1347	3578.42	0.346	0.567
C3	74380	60058.34	1.244	0.321
C4	-2612.47	3228.12	-0.624	0.428

Express low absolute values of T-statistic joined to parameter estimates.



$Y_t=c_1+c_2X_t+c_3X_t^2+c_4X_t^3+ c_5Z_t+e_t$ …….. (8)

(Exhibit 4)

From calculation, R^2=0.87347, F= 39.675 with d.f 20. The H_0 and H_1 are:

H0: $c_1=c_2=c_3=c_4=c_5=0$ vs H_1: at least one of nonzero. H_2 will be accepted at 99% level. Now the next one:

Model-8	Coefficient	Std. Error	T-Statistic	Probability
C_1	-612.768	6794.42	-0.0842	0.9456
C_2	9823.456	2534.02	3.562	0.0043
C_3	915.452	228.364	-3.904	0.0004
C_4	29.235	6.345	3.4456	0.006
C_5	28763.45	4832.563	6.045	0.0000

T-statistic jointed to the intercept and H_0 for single coefficient c_1:

H_0:c_1=0 is true with high level of significance. R^2 = 0.8456 , F = 54.8654 with d.f.=21.

ISBN: 978-93-83083-87-9

Model-9	Coefficient	Std. Error	T-statistic	Probability
C_1	10534.56	1986.465	5.3425	0.0003
C_2	-973.567	197.534	-4.4986	0.0002
C_3	20.4357	5.3467	3.6754	0.0016
C_4	25745.86	4164.56	6.3425	0.0006

Exhibit -6. The best econometric model estimate is:

$Y_t = 10324.6X_t - 9037X_t^2 + 20.12X_t^3 + 28915.96Z_t$ (Exhibit-6) …… (9)

2. CONCLUSIONS

The purpose of the model illustrated above is to estimate the impacts of tourism on local government revenues and costs, through statistical analysis of general economic and tourism data for tourism. The model is designed to overcome the drawbacks of applying a multiplier to a single causal factor such as employment growth, because the regression analysis is based on actual fiscal changes observed tourism arrivals.

Among numerous model findings, the statistical analysis of the effects of tourism growth on municipal revenues suggested that tourism growth in this case reduced the cost of government per capita below what it would have been otherwise. These and other model findings provide a data-driven basis from which to draw conclusions regarding the net impacts of tourism growth on fiscal revenues and expenditures, and to assess competing claims regarding the impacts of casino tourism in Connecticut.

REFERENCES

[1] A county studies. URL: “http://countrystudies.us/”. 2008.
[2] Ancot, J.p: Analyzing the structure of Econometric Models, Martinus Nijhoff publishers, The Hauge, 1984.
[3] Central Bureau of Statistics. Survey of Hotels and Lodges. 2010.
[4] Fletcher, John E., (1989). "Input-Output Analysis and Tourism Impact Studies." *Annals of Tourism Research*, Vol. 16, pp. 514-529.
[5] Government of Nepal, Ministry of finance. URL: “http://mof.gov.np/”. 2012.
[6] Jamaica Tourist Board. “Tourism in Jamaica: An Economic Analysis of 1997.” Jamaica Tourist Board Library
[7] Nepal Rastra Bank. Report for 2004.
[8] Nepal Rastra Bank. URL: http://www.nrb.org.np/. 2010.
[9] Nepal Tourism Board . Nepal Departing Visitors Survey. 2010.
[10] The Impact of Travel and Tourism on Jobs and the Economy. World Travel and Tourism Council (WTTC). 2004.
[11] Weber, S: Tourism, Special Issue: Tourism and Voilence, Crisis and Recovery,, Zagreb, Crotia, 1999

Adsorption Process for Removal Chromium from Electroplating Wastewater by using Coconut Shell

Fazlollah Changani Khorasgani[1], Sohail Ayub[2]

[1]*Department of Environmental Health Engineering, School of Public Health, Tehran University of Medical Sciences, Tehran, IRAN*

[2]*Department Civil Engineering Z.H. College Faculty of Engineering & Technology. A.M.U., Aligarh. India*

[1]*Research Scholar, Department of Civil Engineering, A.M.U., Aligarh. India*

ABSTRACT

The electroplating wastewater industry is one of the major industries which generate a large portion of wastewater containing heavy metals. Electroplating units mostly scattered in urban areas. Adsorption of heavy metal on the solid surfaces is an important technique to remove them from the industrial wastewaters. The purpose of the present study is to evaluate the ability of agro-waste material coconut shell to remove Cr (VI) from electroplating wastewater. The extant of removal was found to be dependent on pH, contact time, adsorbent dose, and concentration of metal and particle size. The adsorption follows a first order kinetics. The adsorption process is endothermic with a maximum adsorption of 83 percent at 30^o C for an initial concentration of 50 mg/l at pH 1.5.Thermodynamics parameters indicates the feasibility of the process. Column studies have been carried out to compare these with batch capacities. The adsorption data obtained is found to fit well the Freundlich.

Keyword: adsorption, electroplating wastewater, Cr concentration,Cr(VI), coconut shell

1. INTRODUCTION

In recent years the use of adsorption technique for the removal of heavy metals has received global attention [1]. Several researchers have been working on the heavy metals removal. However, most of them have used commercially available activated carbon in their studies. The high cost of activated carbon and its loss during the regeneration restricts its application. Thus there is need to undertake studies to substitute the costlier commercial activated carbon with the unconventional, low cost and locally available agricultural waste adsorbents [2]. India is an agricultural country and generates considerable amount of agricultural wastes such as sugar cane bagassess, coconut jute, nut shell, rice straw, rice husk, waste tea leaves, ground nut husk, crop wastes, peanut hulls, fertilizer wastes etc. Successful studies on these materials could be beneficial to the developing countries and could be easily incorporated in development of appropriate technologies. The

successful utilization of agricultural waste in the treatment of wastewater would be quite economical due to its high adsorption capacity ([3,4].

The stability of the various chromium species is dependent upon the various reduction, oxidation and pH conditions. The stable domains for various chromium species in aqueous system as affected by the oxidation potential (E_h) and pH (Landrigan 1975). Under the pH (< 3), temperature (20-30^oC) and reducing - oxidizing conditions commonly found in industrial wastewaters, the predominant species are bicarbonate, $HCrO^-_4$, dichromate $Cr_2O_7^{-2}$ and $Cr^{+3.}$ It is interesting to note that the divalent chromium ions, Cr^{+2}, may be found in extremely reducing environment. The concentration distribution between $HCrO^-_4$ and $Cr_2O_7^{-2}$ is largely governed by the total Cr (VI) present. The fraction of $Cr_2O_7^{-2}$ only becomes significant at high concentration of total Cr (VI) (Stumm, 1970). The distribution of Cr (VI) species as function of pH for total Cr (VI) covering from 10^{-4} M to 6×10^{-3} M (or 5.2 to 312 ppm as Cr), an average concentration range which generally occurs in most industrial wastewaters .It is obvious that treatment of electroplating wastewaters prior to municipal discharge is necessary to alleviate this problem. However, the current methods of treatment are both expensive and inconsistent in operation due to poor selectivity. Ion exchange is unpredictable and in efficient due to many interfering agents present in the system. Recently a few researchers have explored the possibility of using agricultural waste adsorbent for the Cr (VI) removal [5].

2. MATERIAL AND METHODS

Collection of Samples

Aligarh is a medium sized semi industrialized town located in northern India 135 Km South – East of New Delhi. The samples of electroplating effluents were also collected from the discharge points of the factory / surroundings and ground water samples in its nearby and stored as per standard methods before analyzing the physico-chemical parameters. All the samples were tested for detection of pH, chloride, alkalinity, suspended solids, fluoride, total dissolved solids and heavy metal (chromium) contamination. The study reveals that most of the places the ground water is safe for drinking purpose, except a few places where the ground water was observed to be hard and contained chromium (VI) contamination. However the chromium contamination in the surface water was found above the prescribed safe limit. In order to have waste of uniform characteristics and to avoid interference with other impurities the laboratory wastewater was prepared by dissolving a known amount of potassium dichromate in a known volume of distilled water. For 1000 mg/l-hexavelent-chromium concentration 2.282 g $K_2Cr_2O_7$ (AR Grade) is dissolved in 1.0 L of distilled water.

Adsorbent

The coconut shell was first dried at a temperature of 150 °C for 5 hours. After grinding it was sieved to obtain particle size of 600 micron, 300 micron, 150 micron and 75 micron (Indian.Standard Sieve). It was then washed several times with distilled water to remove dust and other impurities. Finally it was dry again in an oven at 150 °C for 6 hours. The adsorbent was then stored in dissector for the final studies.

Batch Studies

In order to understand the adsorption behavior a number of batch studies have been conducted to investigate the effect of adsorbent dose and contact time, pH, concentration of metal, and particle sizes. For these studies, wastewater of various concentrations of Cr (VI) was prepared from the stock solution and kept separately in glass stoppered conical flasks. Then suitable doses of adsorbent were added to the wastewater. The system is equilibrated by shaking the contents of the flasks at room temperature so that adequate time of contact between adsorbent and the metal ion is maintained. The suspension is filtered through Whatman No. 1 filter paper and the filtrate is analyzed to evaluate the concentration of Cr (VI) metal in the treated wastewater by using atomic absorption spectrophotometer. All the analyses have been carried out according to the Standard Methods.

Column Studies

Column studies were conducted using a glass column (Internal diameter =1.0 cm). Adsorbent was suspended in distilled water for 15 minutes by shaking in a beaker at the speed of 150 rpm, and then transferred in to the glass column. The glass wool was kept at the bottom and top ends in order to avoid its loss with the liquid flow or floating. The flow rate was maintained at 1.0 l / d.

3. RESULTS AND DISCUSSION

The results obtained from the above studies have been discussed with plausible explanations as follows:

4. EFFECTS OF ADSORBENT DOSE AND PARTICLE SIZE ON FRACTION ADSORBED

The response of adsorbent dose and contact time on the removal of Cr (VI) is presented through Figure 1. The observation reveal that an increase in the fraction adsorbed of Cr (VI) occurs with corresponding increase in the dose of coconut shell up to certain level, beyond which the fraction adsorbed remains constant. It is evident that a dose of 10g/l is sufficient to remove 53.3 - 84.1% Cr (VI) for 75 um particle size. The increase in the removal efficiency with simultaneous increase in

adsorbent dose and particle size is due to the increase surface area and hence more active sites are available for the adsorption of Cr (VI).

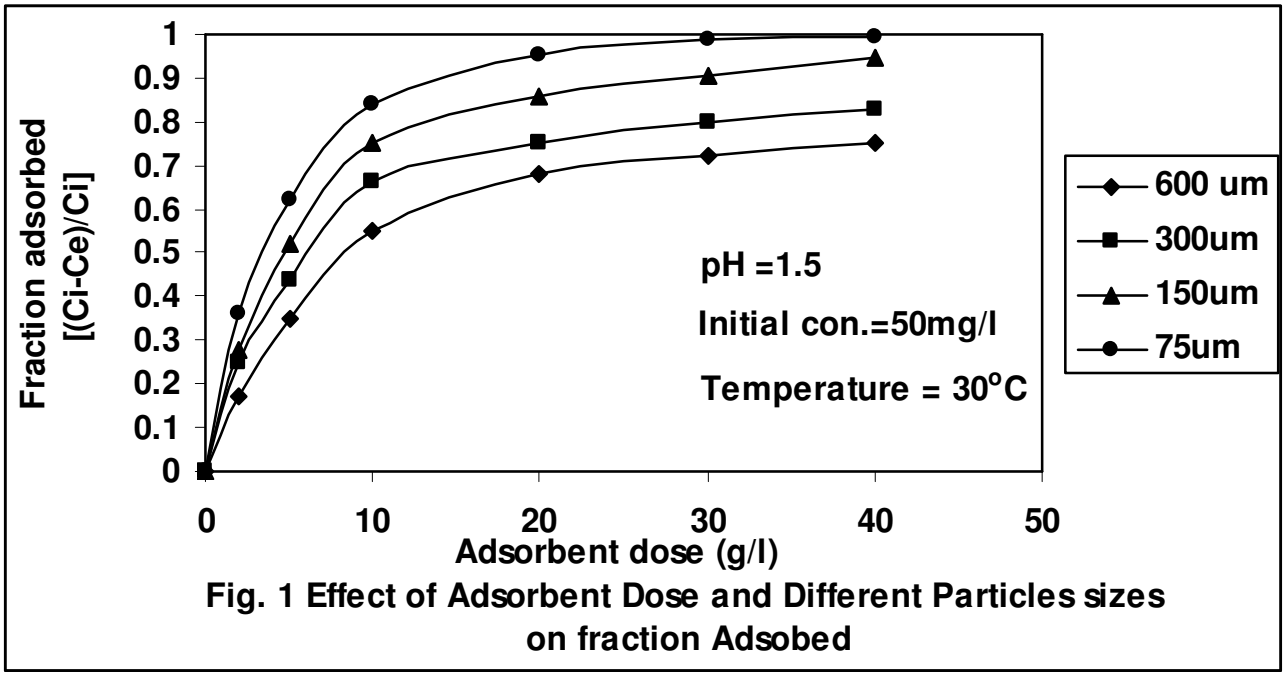


Fig. 1 Effect of Adsorbent Dose and Different Particles sizes on fraction Adsobed

Influence of pH and particle size on Fraction Adsorbed

Influence of pH and particle size on fraction adsorbed is shows in Figure 2. The results show the maximum removal efficiency is observed at pH 1.5 for 75 um size particle. While on increasing the pH value it decreases. About 36 % removal efficiency is recorded at neutral pH 7. One if the reasons for the better adsorption capacity observed at low pH values may be attributed to the large number of H^+ ions present at these pH values, which in term neutralize the negatively charged hydroxyl group (-OH) on adsorbed surface thereby reducing hindrance to the diffusion of dichromate ions. At higher pH, the reduction in adsorption may be possible due to abundance of OH^- ions causing increased hindrance to diffusion of positively charged dichromate ions. It is the common observation that the surface adsorbs anions favorably in low pH range due the presence of H^+ ions [6].

The effects of initial Cr (VI) concentrations on fraction adsorbed (Figure 3) were studied over the wide range of chromium concentration (5-100 mg/l). It may be observed that the chromium uptake is rapid during the initial period of adsorption and the maximum removal (86- 100%) is achieved at 5-20 mg/l concentration for 75 um size particle. The removal efficiency of chromium decreases when chromium concentration is increased. However the removal efficiency is recorded as 87.3 %

at a concentration of 50 mg/l. In a similar study [7] obtained 90% removal efficiency at a Cr (VI) concentration of 10 mg/l in a dose of 1.0 g/100 ml at a contact time of 1.5 hr when the pH of the solution was 2.0.

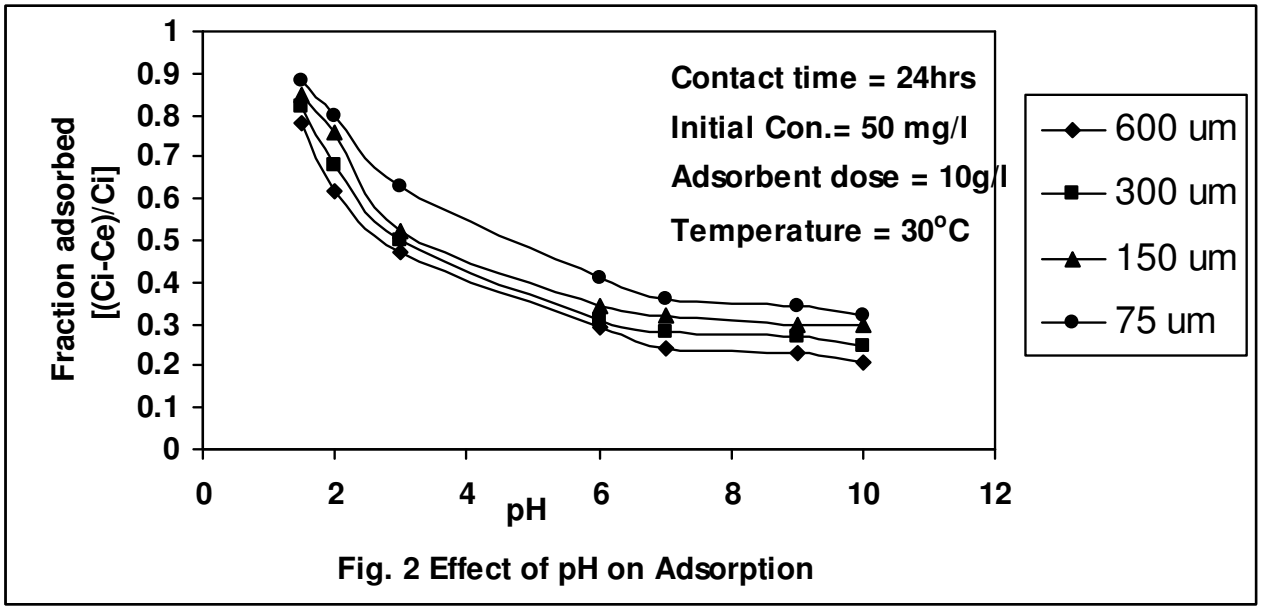


Fig. 2 Effect of pH on Adsorption

Effects of various Initial Cr (VI) Concentrations and particle size on Fraction Adsorbed.

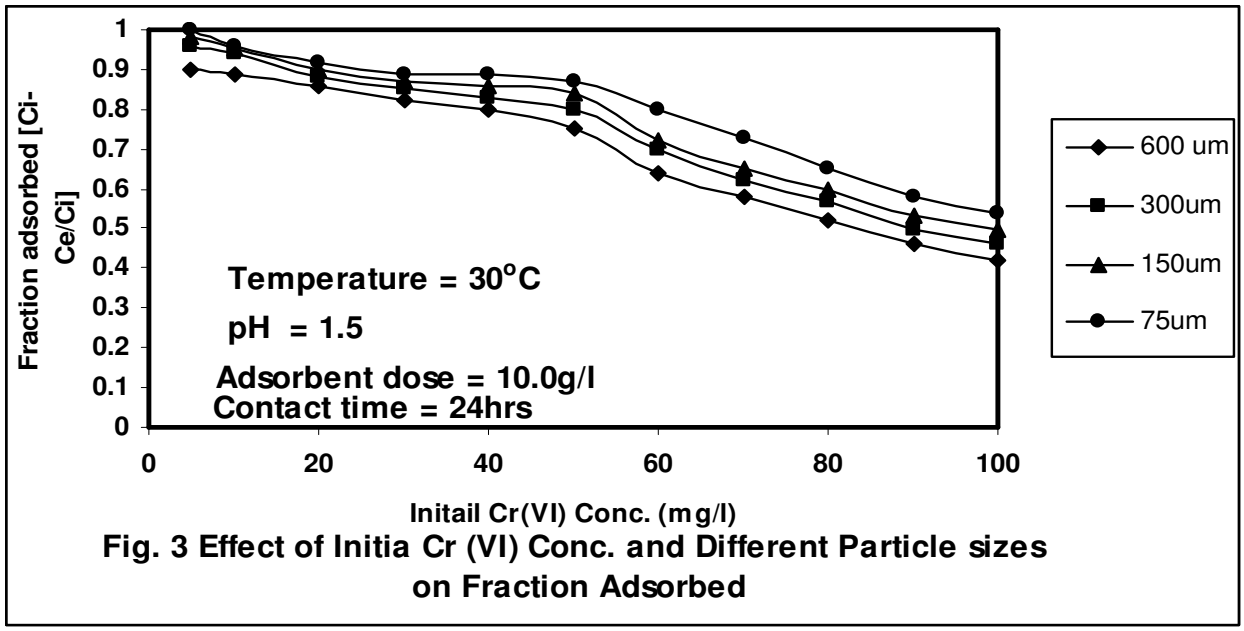


Fig. 3 Effect of Initia Cr (VI) Conc. and Different Particle sizes on Fraction Adsorbed

Effect of variation of Contact Time and different Particles sizes on Fraction Adsorbed

The adsorbent particle size has significant influence on the adsorption time and kinetics of adsorption. The influence of particle size furnishes important information for achieving optimum utilization of adsorbent and on the nature of breakthrough curves for designing packed bed absorbers. Three particle sizes 75 micron,150 micron 300 micron and 600 micron sieve (Indian standard Sieves) under optimal conditions of adsorbent dose, pH and contact time with an initial adsorbate concentration of 50mg/l were studied. A plot fraction adsorbed against contact time shown in Figure 4 indicates that, with an increase in adsorbent particle size, fraction decreases. This may be explained on the basis of the active surface area available for the adsorption, which is greater for small particle sizes .Finer adsorption material offers a significantly lesser mass transfer diffusion resistance in microspores.

Adsorption Isotherms

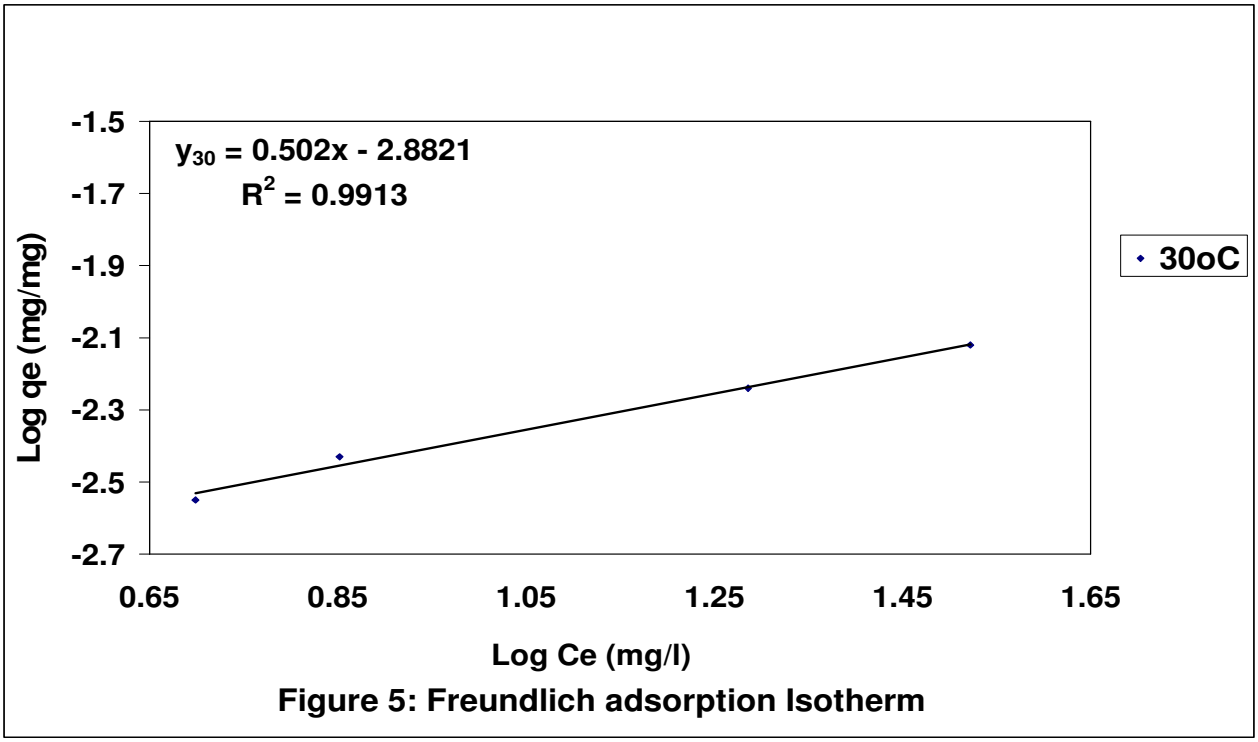


Figure 5: Freundlich adsorption Isotherm

Freundlich adsorption isotherm model applied to equilibrium data is expressed as,

$$qe = \frac{x}{m} = KCe^{1/n} \qquad IV$$

The above equation is also referred as Van - Bemmelen equation. Fitting into the logarithmic form (Mahesh et al., 1999).

$$\log\frac{x}{m} = \log K + \frac{1}{n}\log Ce \qquad V$$

$$\log\left[\frac{(Ci-Ce)}{Ci}\right] = \log K + \frac{1}{n}\log Ce \qquad VI$$

where, x/m is the amount of Cr (VI) adsorbed per unit mass of adsorbent (mg/mg) and Ce is the equilibrium concentration of aqueous solution. K is a constant, which is measure of adsorption capacity, and 1/n is a measure of adsorption intensity (Figure 6). Langmuir and Freundlich adsorption isotherm constants are shown in Table 1.

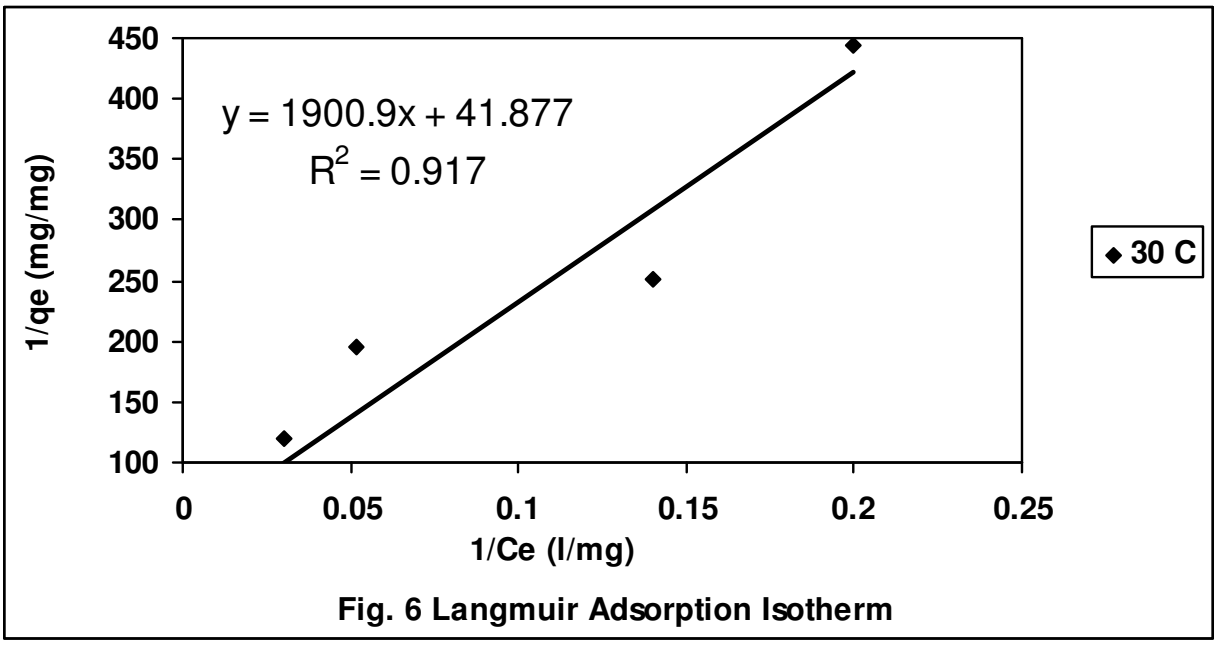


Fig. 6 Langmuir Adsorption Isotherm

Table 1: Values of Langmuir and Freundlich Isotherms Constants

Temperature	Langmuir Constants				Freundlich Constants			Recommended Isotherms
	a	b	Cc	R_l	K	1/n	Cc	
30^0 C	1900.9	0.0220	0.917	0.476	.0013	0.502	0.991	$0.00131Ce^{0.502}$

5. KINETICS OF ADSORPTION

$$\log(qe - q) = \log qe - \left(K_{ad}/2.303\right)t \qquad \text{VII}$$

The kinetic modeling for the removal of chromium (VI) by coconut shell has been carried out using the following first order rate expression

Which is nothing but a Lagergren equation. Where q and qe are the amount adsorbed at equilibrium and any time t respectively. The straight line plots of log (qe-q) V_s t for the adsorption show the validity of lagergren equation and suggest the first order kinetics (Figure 7). The rate constant K_{ad} is 0.2194 .

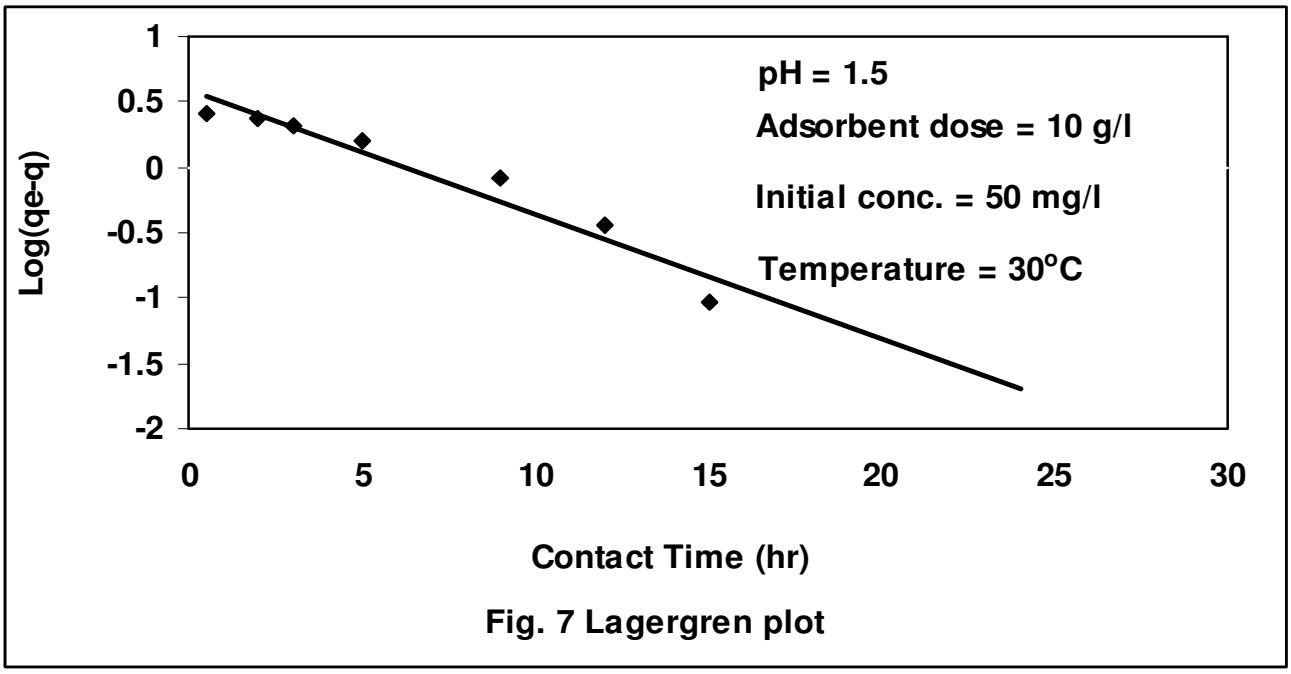


Fig. 7 Lagergren plot

Thermodynamic Parameters

$$\ln b = \ln b_o - \frac{\Delta H}{RT} \qquad \text{VIII}$$

The apparent heat change (ΔH) related to Langmuir constant b, and should follow the Van't Hoff equation

The enthalpy changes of sorption as calculated from the slope of ln b Vs 1/T (Figure 8) is found 14.23 Kj/mole. The positive ΔH values confirm the endothermic nature of the sorption process and suggest the possibility of strong binding between sorbate and sorbent.

The change in free energy (ΔG) and (ΔS) are calculated using the following relationships.

$$\Delta S = -RT \ln\left(1/b\right) \qquad \text{IX}$$

$$\Delta S = \frac{\Delta H - \Delta G}{T} \qquad \text{X}$$

The negative values of ΔG indicates the process to be feasible and spontaneous (Singh et al.1982) and positive values of entropy reflected the affinity of the adsorbent material. The values of ΔG and ΔS are listed in Table 2.

Table 2: Thermodynamic Parameters at Different Temperatures.

Temperature (^{o}K)	- ΔG Kj/mole	ΔS j/mole
303	9.614	78.693

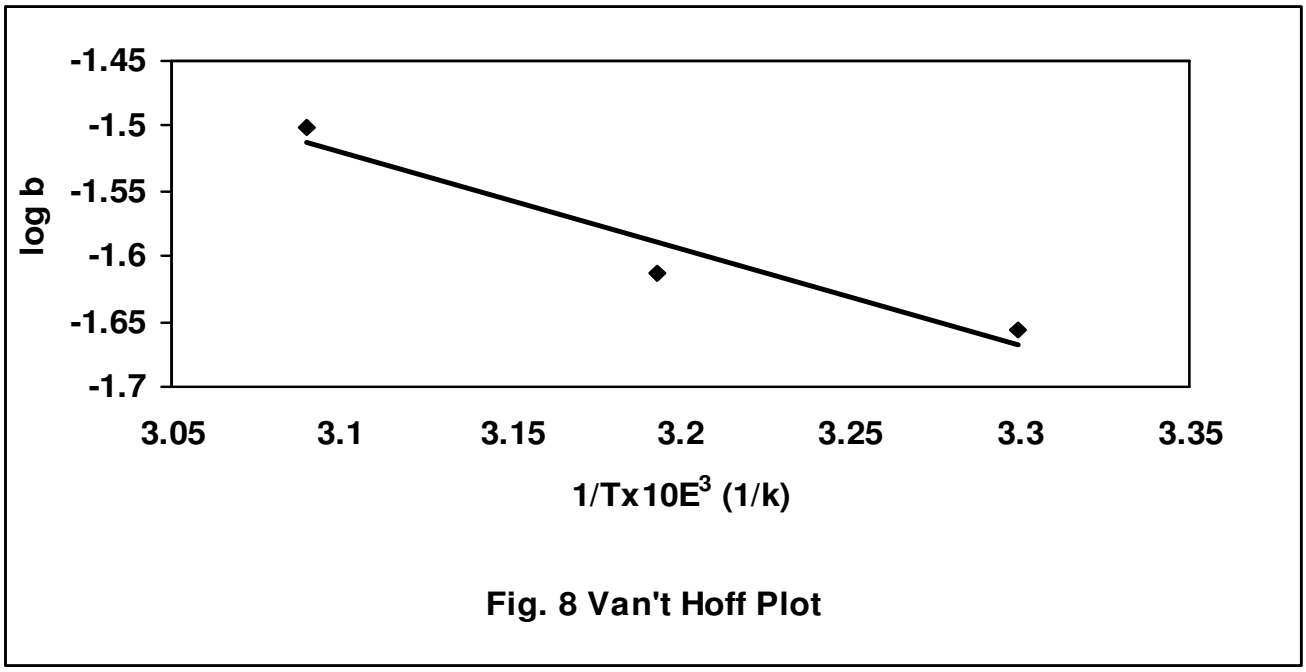


Fig. 8 Van't Hoff Plot

6. INTERPARTICLE DIFFUSION RATE

Plot of amount adsorbed per unit mass of adsorbent versus square root of time is shown in Figure 9. It is seen from this plot that there are two distinct linear sections, the initial steep linear portion and the final relatively flat linear part. The initial linear part indicates that the interparticle diffusion, the letter, less steeper linear, part suggested that adsorption is being controlled by the microspores.

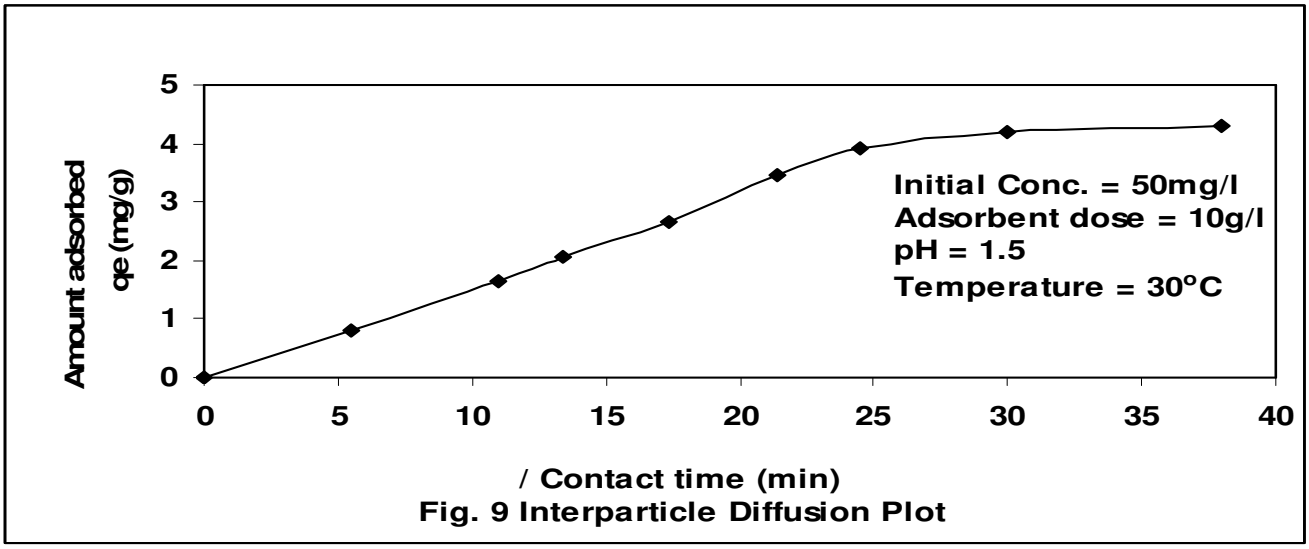


Fig. 9 Interparticle Diffusion Plot

7. COLUMN STUDY

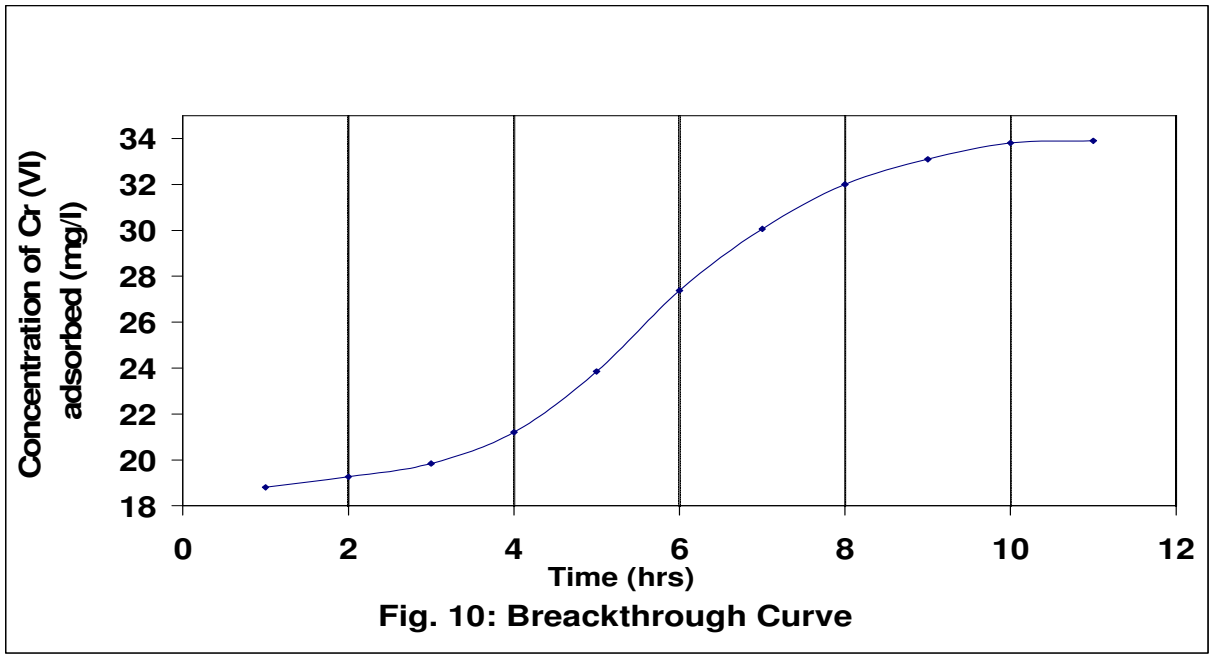


Fig. 10: Breackthrough Curve

ISBN: 978-93-83083-87-9

The breakthrough curve plotted in Figure 10. The column was run till the coconut shell in the adsorption column gets exhausted and the treated effluent was analyzed at different time intervals. Column capacities were found greater than the batch capacities due to continuously large concentration at the interface of the sorption zone as the sorbate solution passes through the column while the concentration gradient decreases with time in a batch process .

8. DESORPTION TEST

Desorption test was conducted for coconut shell after their use in the equilibrium adsorption studies. About 10 g of saturated adsorbent was placed in an 300 ml capacity stoppered BOD bottle with double distilled water and was shaken at room temperature for over two hours. After this the adsorbent was filtered and the suspension was analyzed for the chromium content. No chromium was detected in the water. Thus it indicate that adsorbed chromium was not being desorbed.

9. CONCLUSIONS

In conclusion, it has been shown that the use of coconut shell, waste appears to be technically feasible, eco-friendly with high efficiency in the removal of cadmium from wastewaters. Besides it is composed entirely of agricultural waste and this help in the reduction of waste generation. They adsorbed comparatively like the expensive traditional activated carbon.

REFERENCES

[1] Raji, C and Anirudhan T.S,(1998), Sorptive behavior of chromium (VI) on saw dust carbon in aqueous media. Ecol. Env. Cons. 04 (1-2), 33

[2] Baily, S.E; Olin, T.J; Bricka R.M and Adrian D.D,(1999). A review of potentially low- cost sorbents for heavy metals, Water research 33 (1), pp.2469-2479.

[3] Drake, D.O; S.Lin, G.D Rayson; Jackson P.J,(1996) Chemical modification and metal binding studies of datura innoxia, Env. Sc. & Tech. 30 (1),pp 110-114.

[4] Ayub, S., Ali, S. I., and Khan, N. A). (2001)“ Efficiency Evaluation of Neem bark (Azadirachta indica) bark in the treatment of industrial wastewater ”. *Environmental Pollution Cont. Journal*, vol.4 (4), 34-38..

[5] Gang, D; Banerji, S.K and clevenger, T.E,(1999) Chromium (VI) removal by modified PVP coated silica gel, Proceeding of Hazardous waste research conference **.**

[6] Gebehard H and Coleman N.T,(1974) Soil. Sci. Soc., Amer. Proc., 38,255.

[7] Chand S; Aggarwal, V.K; Kumar, P, (1994) Removal of Hexavelent Chromium from the Wastewater by Adsorption Indian J. Environ.Hlth 36,3,pp. 151-158

Effect of Factors on Activity of Bioflocculant Produced by Bacterial Strain Isolated from Waste Water Sample

Viraj Krishan Mishra[1], Geeta Sharma[2]

[1,2]*Ambala College of Engineering and Applied Research, Kurukshetra University, Haryana*

ABSTRACT

Industrial waste water, sludge and soil samples were screened for bacterial isolates capable of producing flocculants. The aim of this study is to identify the best flocculating strain. P3, S2 and W3 were the three best bioflocculant producing strains isolated out of 24 bacterial strains. The flocculating activity of strain P3, S2and W3 was assayed using kaolin clay. Strain P3 showed the best flocculating activity (96%). Optimized conditions were observed for best flocculating activity. Effect of different carbon and nitrogen sources were assayed to obtain the best suitable carbon and nitrogen sources. The best carbon source, nitrogen source preferred was ethanol and yeast +$NaNO_3$ respectively. The effect of different pH and temperature was also determined. The best flocculating activity occurred at pH7 at temperature 35^oC. Ca^+ improved the flocculating activity. The weight of the purified bioflocculant was 0.1gm. The flocculating activity of Consortia SS1 (P3+S2+W3) was 76%.

Keywords: bioflocculant, consortia.

1. INTRODUCTION

In wastewater treatment for removing suspended solids and metal ions flocculation is a common and effective technique (Deng *et al.,* 2003). Flocculants are special natural organic macromolecule substances that can flocculate cells, suspended solids, colloidal solids, etc (Zhang, 2005). They are the chemicals used in various industrial processes, like food, fermentation, waste water treatment and downstream processing etc, these all are the material separation processes so flocculants are used here. Flocculants are of three types (1) inorganic flocculants (chemical flocculants) (2) organic flocculants (chemical flocculant) (3) natural occurring flocculants (Zhang *et al*., 2007). Inorganic flocculants are aluminum sulfate and poly aluminum chloride, organic flocculants are polyacrylamide derivatives and polyethylene imine and naturaly occuring flocculants are chitosan, sodium alginate and bioflocculants.

Chemical flocculants have low cost and also have effective flocculating activity but still they are not so good because of their toxicity and nondegrability. Aluminium has found to induce alzhimer

ISBN: 978-93-83083-87-9

disease. Furthermore the acrylamide monomer is toxic as well as carcinogenic and also non-biodegradable in environment. So, bioflocculants replaced the chemical flocculants because of their degrability, non-toxicity and enviornment friendly nature (Abd-El-Haleem *et al*., 2008). Bioflocculants can be produced economically and can be recovered easily from fermentation broth. Instead of someadvantages bioflocculant have one disadvantage like they are cost effective (Zhang *et al.,* 2010). Now a days they have wide applications in many industries like waste water treatment, textiles and food industries (Salehizadeh and Shojaosadati 2001). Bioflocculants have also been used to treat dye solution (Deng, S.B., G. Yu and Y.P. 2005), inorganic solid suspension (Labille *et al.,* 2005). Flocculation is the most widely used process for treating the waste water (Salehizadeh H *et al.,* 2000).

Bioflocculants are produced by microorganisms like Bacteria, fungi and alga (Desouky *et al*., 2008). Bioflocculants are used in bioflocculation process. Bio flocculation is a simple and effective mechanism, under which living cells are used for the precipitation of suspended solids, colloids and debris. Proteins, polysaccharides, glycoprotein's, nucleic acids and some other macromolecular compounds are main constituents of Bioflocculants (Lin J and Harichund C, 2012).

2. MATERIALS AND METHODS

Bacterial strain. Bioflocculant producing strains were isolated from various waste water sources (pharmaceutical, sugar and hoggery waste water). About 24 bacterial colonies were isolated out of those 3 strains were their which produced bioflocculants. Strain P3, S2 and W3 were those bioflocculant producing strains.

Media and cultivation conditions. The medium for bioflocculant production contained (per liter) glucose, 5gm; yeast extract, 1gm; urea, 1gm ;KH_2Po_4, 0.1gm; K_2HPO4, 0.1gm; NaCl, 0.1gm; $MgSO_4.7H_2O$, 0.2gm; agar, 20gm. Slant medium contained (per liter) yeaste extract , 1gm; beef extract, 1gm; tryptone, 2gm; glucose, 10gm; $FeSO_4$, 0.02gm and agar, 20 gm. Fermentation medium contained (per liter) sucrose, 10gm; yeast extract, 1gm; urea, 1gm ;KH_2Po_4, 0.1gm; K_2HPO4, 0.1gm; NaCl, 0.1gm; $MgSO_4.7H_2O$, 0.2gm; agar, 20gm. The composition of culture medium and fermentation medium are same. The initial pH of all media was adjusted to 7.2 to 7.5 with NaOH and HCl. All the media were prepared with distilled water and sterilized at 121^0Cfor 20 min. The cultivation temperature was adjusted to 37^0C.

Isolation of bacteria. Serial dilution was done for the isolation of strains. After that the pure colonies was obtained on agar plates. Three bioflocculant producing strains were obtained. Each colony was inoculated into 250-ml flasks containing 50ml fermentation medium. The strains were

incubated for 48 h at 37^0C with shaking speed 250rpm. The strain with highest flocculating activity (P3) was selected. Identification was done on the basis of morphological identification, biochemical characterization.

Determination of flocculating activity. The flocculating activity was measured using a kaoline clay suspension. 0.5 gm kaoline clay was suspended in 100 ml distilled water, and 1 ml of the liquid bioflocculant was mixed thoroughly with 45 ml of the kaoline suspension. Then, 4.5 ml of 1% $CaCl_2$ solution was added to the mixture. The mixture was stirred with a vortex mixer and left standing for 5 min at room temperature. The optical density (O.D.) of the supernatant and the blank control where distilled water was used instead of the supernatant was measured at 600 nm. The flocculating activity was defined and calculated as follows

Flocculating activity = (A-B)/A* 100.

Where A and B are the optical densities at 600 nm of the control and the sample, respectively

Effect of Different Parameters on Flocculating Activity. Following variables were assayed to check the nutritional and environmental factors affecting bioflocculant production: incubation period (1–5 days), carbon source (glucose, fructose, sucrose, lactose, galactose, mannose, maltose, starch, sodium acetate, citric acid, glycerol and ethanol), nitrogen source (yeast extract, beef extract, peptone, urea, glutamic acid, ammonium sulphate, ammonium nitrate, ammonium chloride and sodium nitrate), initial pH (pH5-12) and incubation temperature (20, 25, 30, 35 and 40°C).

Bioflocculant purification. The purification and characterization of the bioflocculant was performed using the method described by (Chang *et. al*. (1998) and (Chen *et. al*. 2002). Fermentation culture was prepared based on the optimal culture conditions determined earlier. After three days of cultivation, the culture was centrifuged at 6000 rpm for 30 min and at 4^0C to remove cells. One volume of distilled water was added to the supernatant and centrifuged again for 15 min to remove insoluble solutes. Two volumes of cold ethanol were added to the supernatant, and the solution was mixed and left standing at 4ºC for 12 hr. The resultant precipitate was vaccum dried to obtain the crude bioflocculant.

Multiple microorganisms consortia. Strains that have flocculants producing microorganisms were screened in lab. These strains were used to construct multiple microorganism consortia producing bioflocculant of high flocculating activity. Combination of two or three strains were their to construct the multiple microorganism consortia producing bioflocculant.

ISBN: 978-93-83083-87-9

Results and discussion. Waste water, sugar waste water and pharmaceutical waste water was taken and check for their flocculating activity. W3, S2 and P3 were the best flocculating producing strains; out of them the P3 showed excellent flocculating activity. P3 had 75% flocculating activity. P3 showed the best flocculating activity so we considered the pharmaceutical waste water for the study of different factor i.e. temperatures, pH, carbon sources and nitrogen sources on Bioflocculating activity.

3. FACTORS AFFECTING THE BIOFLOCCULANT PRODUCTION

The bioflocculant production is affected by many factors, such as the constituents of the culture medium and environmental conditions (He *et al*., 2004)

The pH of the reaction mixture is a key factor influencing the flocculating activity. The flocculating activity increased gradually when the pH value went up and reached its maximum at pH 7.0.

At low pH the, the absorbance of H^+ ions tend to weaken the bioflocculant- kaolin complex formation process and a similar effects is also observed at high pH value (He *et al.,*2010).The pH stability of biopolymer solution was observed at the pH ranges 3-9 and reached maximum stability at pH 7. It is demonstrated that bioflocculant solution is suitable to be applied in neutral, weakly acid and weakly alkaline circumstances. Gao *et al.* (2006) and He *et al.,(*2010) reported similar optimal pH value (7.0) for the activity of the bioflocculants produced by *Vagococcus sp*. and a mutant *Halomonas sp*., respectively.

The effect of the temperature on kaolin clay mixture was tested. The highest flocculating activity was achieved at 35^0C (96%). Bioflocculants containing sugar as the main flocculation components are heat stable, and their flocculating activity could retain more than 50%.

The main backbone of the bioflocculant is made up of polysaccharide and high temperature may cause degradation of this polysaccharide chain of bioflocculant that reduces its flocculation efficiency. This thermal behaviour of the bioflocculant is supported by other studies (Gong *et al.,* 2008)

The effect of bioflocculant dosage showed flocculation activity over 90% in the range of 1-3mgl^{-1} the maximum flocculating activity of 96% was observed at an optimum bioflocculant dosage of 2$mgl^{-1.}$

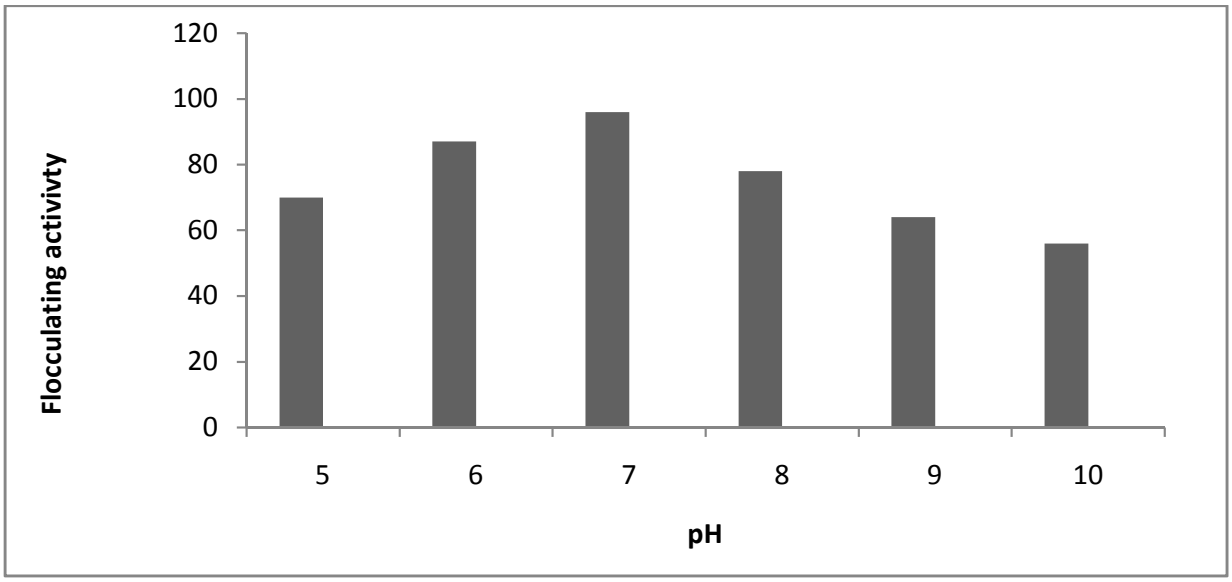
ISBN: 978-93-83083-87-9

The divalent cation (Ca^{2+}) was more effective than others. Ca2+ could destabilize and bridging. However, trivalent cations could change the surface charge of kaolin particle and cover particles and less absorb sites induce the low flocculation activity (Gong *et.al ,2008).* It was studied that bioflocculants produced by *Citrobacter* sp. TKF04 (Fujita *et al.,* 2000) and *Bacillus* sp. F19 w (Zheng *et al*., 2008) were capable of flocculating kaolin clay without metals.

The highest effect of Ca^{2+} is one of the significant characteristics because trivalent cations are difficult to remove and can cause environmental problems.Fe^{3+} form the gelatinous precipitate, which was more difficult to remove. Similarly, Al^{3+} gives rise to an environmental problem; therefore $CaCl_2$ has own coagulant aid. Increase in the positive charge density over the clay particle surface may be giving the same influence of the trivalent cations presence that inhibits the biopolymer efficiency (Gong *et al.,* 2008).

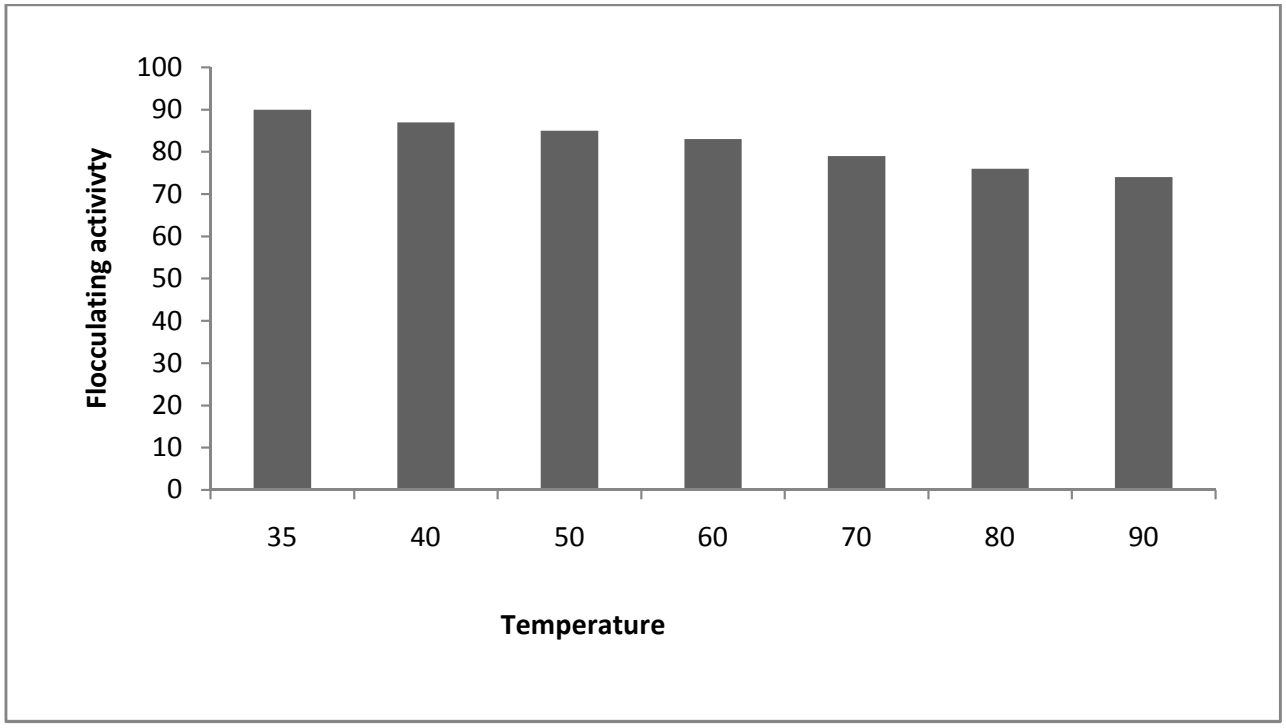
It has been well documented that changing the carbon and nitrogen sources highly influences bacterial growth and bioflocculant production (Sheng *et al.,* 2006).. Ethanol was the favoured carbon source for bioflocculant production in the industrial scale. Multiple nitrogen sources were better than a single nitrogen source. The medium containing yeast extract and $NaNO_3$ was the most favourable for production of bioflocculant as they caused the highest bioflocculant activity.

Effect of pH. The best flocculating activity was shown at pH 7. So, pH 7 was considered as standard for optimization of other factors.

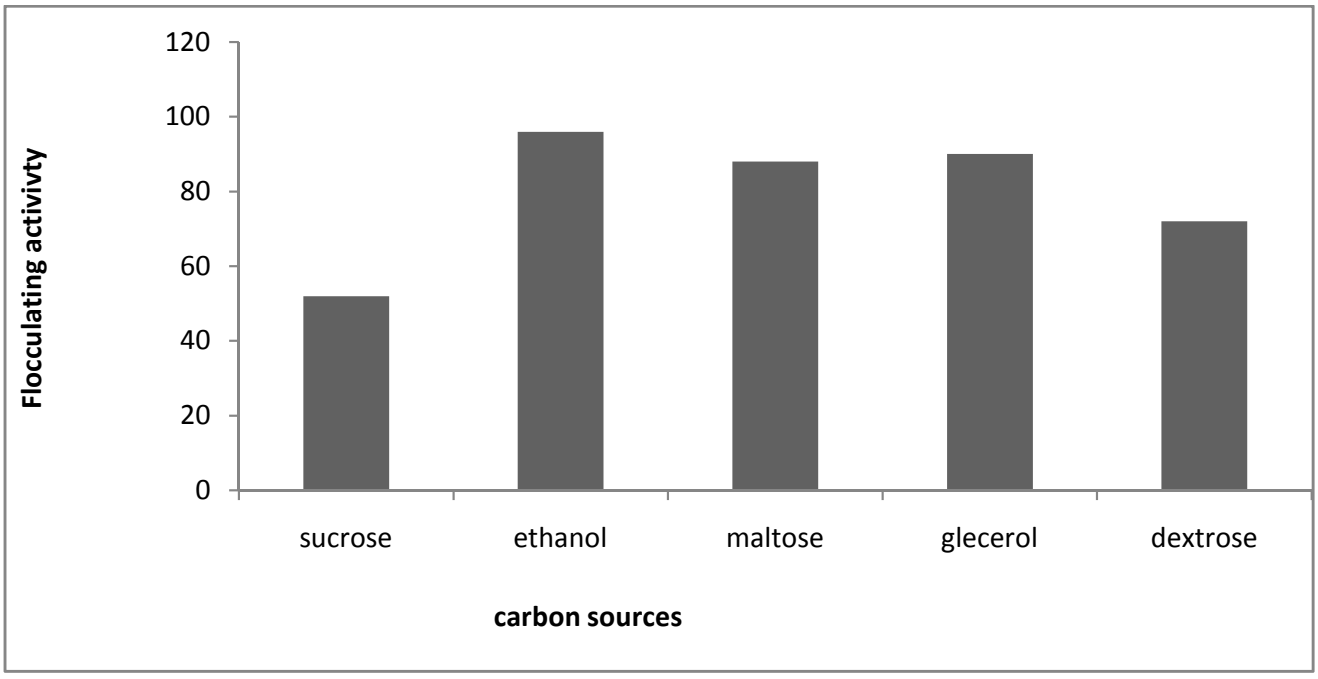


Effect of temperature. The highest flocculating activity of P3 strain was shown at 35^0C.

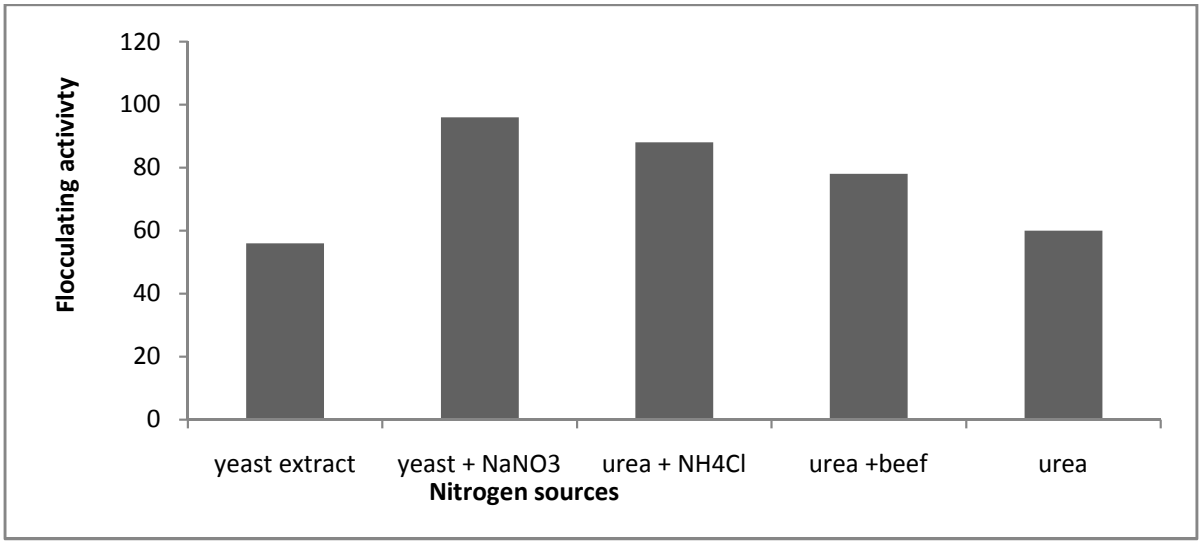
ISBN: 978-93-83083-87-9



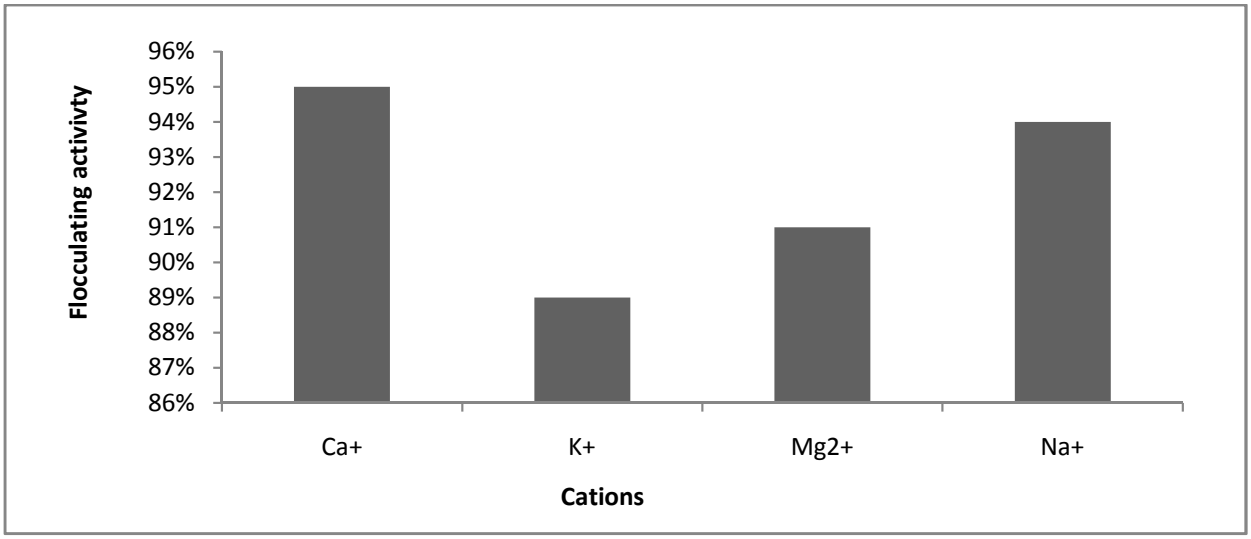
Effect of carbon sources. The best flocculating activity were observed when ethanol was used as carbon source.



Effect of nitrogen sopurces. The best flocculating activity were observed when yeast + $NaNO_3$ was used as nitrogen source.



Effect of cations. The best flocculating activity was shown at Ca^{+}.



Multiple microorganism consortia. Multiple microorganism consortia were constructed in which 3 strains were selected out of 6 best strains and combined cultivation occurred. Now the flocculating activity of their cell-free supernatant was investigated. Strain MM1 (P3+S2+W3) has the flocculating activity 70%.

4. CONCLUSION

The flocculating activity of P3, S2 and W3 were 96%, 78% and 87% respectively.The following suggestions are made to guide prospect for future studies: Development of process conditions for large scale production of the bioflocculants, Identification of bacteria and study of flocculant stability and toxicity.

REFRENCES

[1] Abd-El-Haleem, Dam, Al-Thani, R.; Al-Mokemy, T.; Al Marii, S.; Hassan, F. (2008). Isolation And Characterization Of Extracellular Bioflocculants Produced By Bacteria Isolated From Qatari Ecosystems. *Pol. J. Microbiol.,* 57(3): 231– 239.

[2] Deng S, Yu G, and Ting Y. (2005). Production of a bioflocculant by *Aspergillus parasiticus* and its application in dye removal. *Colloids and Surfaces B: Biointerfaces*, 44: 179-168.

[3] Deng S.B., Bai R.B., HuX. M., Luo Q. (2003). Characteristics of a bioflocculant produced by *Bacillus mucilaginosus* and it susein starch waste water treatment. *Appl. Microbiol. Biotechnol.* 60: 588-593.

[4] Desouky AM Haleem AE, Roda FT, Thourya M, Sidra M and Fatima H. (2008). Isolation and characterization of extracellular bioflocculants produced by bacteria isolated from Qatari Ecosystems. Polish *J. Microbiol.* 57(3): 231-239.

[5] Fujita M., Ike M., Tachibana S., Kitada G., Kim S. M. and Inoue Z. (2000). Characterization of a bioflocculant produced by Citrobacter sp. TKF04 from acetic and propionic acids. *Journal of Bioscience and Bioengineering,* 89(1): 40-46.

[6] Gao. J., BaoH. Y., Xin M. X., Liu Y. X., LiQ., Zhang Y. F. (2006). Characterization of a bioflocculant from an ewly isolated *Vagococcus*sp. W31. *J . Zhejiang Univ .Sci .B*. 7: 186-192.

[7] Gong, Wenxin, Wang, Shuguang, Sun, Xuefei and et al. (2008). Bioflocculant production by culture of Serratia ficaria and its application in wastewater treatment. *Bioresource Technology*. 99: 4668 46.

[8] He J., J. Zou, Z. Shao, J. Zhang, Z. Liu and Z.Yu. (2010). Characteristics and flocculating mechanism of a novel bio!occulant HBF-3 produced by deep-sea bacterium mutant Halomonas sp. World J.!Microbiol. Biotechnol. 26: 1135–1141.

[9] He N, Li Y, Chen J. (2004). Production of a polygalacturonic acid bioflocculant REA-11 by *Corynebacterium glutamicum*. *Bioresour. Technol.* 94: 99-105

[10] Labille, J., F. Thomas, M. Milas and C. Vanhaverbeke. (2005). Flocculation of colloidal clay by bacterial polysaccharides: Effect of macromolecule charge and structure. *J. Colloid Interf. Sci., 284(1), 149-156 Shih, I.L., Y.T. Van, L.C. Yeh, H.G*

[11] Salehizadeh H, Vossoughi M, and Alemzadeh I. (2000) *Biochem. Eng*. 5: 39-44.

[12] Salehizadeh, H., Shojaosadati, S. A. (2001). Extracellular biopolymeric flocculants recent trends and biotechnological importance. *Biotechnol. Adv.* 19: 371-385.

[13] Sheng Y., Q. Zhang, Y. Sheng, C. Li and H. Wang. (2006). Screening and flocculating properties of bioflocculant-producing microorganisms. *Sci. Technol*. 13: 289–292.

[14] Zang, Z., S.Xia, J.Zhaoa and J. Zhang: Caracterization and flocculation mechanism of high efficiency microbial flocculant TJ-F1 from Proteus micrabilis. Coll Surf B: bioinfaces 75: 247-251.

[15] Zhang Z.Q. (2005). Study on microbial flocculants produced by multiple microorganisms. *Nanchang Univeristy Press, Nanchang*.

[16] Zhang Z.Q., B. Lin, S.Q. Xia, X.J. Wang, A.M. Yang. (2007). Production and application of a novel bioflocculant by multiple microorganism consortia using brewery wastewater as carbon source. *J. Environ. Sci.* 19: 667–673.

[17] Zheng Y., Z.L. Ye, X.L. Fang, Y.H. Li, W.M. Cai. (2008). Production and characteristics of a bioflocculant produced Bacillus sp. F19. *Bio- resour. Technol*. 99: 7686–7691.

Climate Change – Threat to Endangered Wild Life Species

Hema Kulkarni
Govt. NCJ College, Dalli Rajhara, District Balod, Chhattisgarh

ABSTRACT

It is nearly impossible the overstate the threat of climate change. Global worming will have catastrophic effects such as accelerating sea level rise, droughts, floods, storms, and heat waves. This will threaten vitally important species, habitats and ecosystems. Animals and plants are suited to cooler climates will need to move pole wards or uphill when the climate becomes even just that little bit warmer. The processes have been observed in many places- in the Alps, in mountainous Queensland in Australia and in the misty forests of Costa Rica. Fish in the North sea have been observed moving northwards too- fish stocks that used to be common around Cornwall have moved as far north as the Shetland and Orkney islands. The impact on species are becoming so significant that their movements can be used as an indicator of a warming world. They are the silent witnesses of the rapid changes being reflected on the earth. Scientists predicted that global warming could contribute to the mass extinction of wild animals in the near future. An overheating world is creating a big change in climatic conditions and this can harm the dedicate ecosystems in which species live. The polar bear could disappear in the wild unless the pace of global warming slows. Experts believe that the Arctic sea ice is melting at a rate of 9% per decade, endangering the polar bears habitat and existence. Similarly, sea turtles in South America lay their eggs on Brazilian beaches, many of which are threatened by rising sea levels. Climate change also threatens the offspring of sea turtles, as nest temperature strongly determines the sex- the coldest sites produce male offspring while the warmer sites produce female offspring. In America, North Atlantic right whale is one of the most endangered species of all large whales. Since warming water contains less plankton for whales to feed on , the availability of food due to climatic fluctuations is also becoming an increasing cause of morality. Experts estimate that there are as few as 3200 tigers left in the wild, due to poaching, the loss of their habitat. The largest remaining areas where tiger occur are the mangroves forests of India. The projected rise in the sea levels could cause these living spaces of the tiger to vanish altogether.

1. INTRODUCTION

The earth's climate varies naturally, but scientists now have strong evidence that the relatively big, long-lasting changes in climate we are experiencing are likely to be the result of human behavior.

Greenhouse gases have a vital role in keeping the planet warm enough to support life. They allow the sun's rays through but stop some of the heat from escaping back into outer space.

However, a lot of greenhouse gases, such as water vapour, carbon dioxide and methane are now produced through human activity. These extra greenhouse gases trap more of the sun's heat and cause the temperature to rise. A rising carbon dioxide (CO2) level is a particular problem because it has a long lifespan. Humans upset the natural carbon cycle by emitting CO_2 through the burning of fossil fuels and the destruction of habitats. The effects of climate change are already apparent and will become more so in future. The average temperature of the earth's surface has already risen by 0.75ºC since 1900, with most of this warming occurring in the last 30 years. This may not sound like much but small changes in temperature can have a massive effect on people and wildlife. Rainfall patterns are changing worldwide. Scientists predict that extreme weather conditions, such as torrential rain, flooding and heat waves could become more common in future. One quarter of CO_2 is absorbed by the world's oceans, making them more acidic. However, they also absorb heat and warmer oceans expand, causing sea levels to rise. Rising temperatures also mean that glaciers are retreating and land ice is shrinking, which again increases sea levels. If this continues, coastal areas and small islands are at risk of flooding and land loss. The way we live is strongly linked to the world's climate. A changing climate will affect our water supplies, agriculture, power and transport systems and our health and safety.

Living things face a constant barrage of external stresses or threats that challenge their ability to survive and reproduce. If a species is unable to successfully cope with these threats through adaptation, they may face extinction. A constantly changing physical environment requires organisms to adapt to new temperatures, climates, and atmospheric conditions. Living things must also deal with unexpected events such as volcanic eruptions, earthquakes, meteor strikes, fires, and hurricanes.

In nature, pathogens can be transmitted directly between animals or indirectly through intermediate "hosts," such as infected prey or biting insects. Indirect transmission cycles are often affected by environmental conditions such as temperature and rainfall. Higher temperatures associated with climate change may contribute to an increase in pathogens within intermediate hosts and vectors, or increased survival of animals that harbor disease. For example, warmer summer temperatures in the Arctic now allow the lung nematode larvae often found in muskoxen to develop to the infectious stage within the intermediate host, the marsh slug, at a rate that has reduced the parasite's life cycle from 2 years to 1 year (Kutz and others, 2005).

2. PREVENTABLE MAN MADE THREATS TO ENDANGERED SPECIES

Since man is indeed part of nature, man-made threats are merely a subset of natural threats. But unlike other natural threats, man-made threats are threats that we can prevent by changing our behavior.

As humans, we have a unique ability to understand the consequences of our actions, both present and past. We are capable of learning more about the effects our actions have on the world around us and how changes in those actions could help to alter future events. By examining how human activities have adversely impacted life on earth, we can take steps to reverse past damages and prevent future damage. Man-made threats can be classified into the following general categories:

- **Habitat Destruction & Fragmentation** - The destruction or splitting up of once continuous habitat to enable humans to use the land for agriculture, development of towns and cities, construction of dams, or other purposes.
- **Climate Change** - Human activities such as the burning of fossil fuels, have altered the Earth's atmosphere and have resulted in global climate changes.
- **Introduction of Exotic Species** - Accidental and intentional introduction of non-native species into regions never before occupied by the species have resulted in the extinction of numerous endemic species.
- **Pollution** - Pollutants (pesticides, herbicides, etc.) released into the environment are ingested by a wide variety of organisms.
- **Over-Exploitation of Resources** - Exploitation of wild populations for food has resulted in population crashes (over-fishing, for example).
- **Hunting, Poaching, Illegal Trade of Endangered Species** - Some endangered species are targeted for their value on illegal markets.
- **Accidental Deaths** - Car hits, window collisions (birds), collisions with ships (whales).

Sea levels are rising and oceans are becoming warmer. Longer, more intense droughts threaten crops, wildlife and freshwater supplies. From polar bears in the Arctic to marine turtles off the coast of Africa, our planet’s diversity of life is at risk from the changing climate. Climate change poses a fundamental threat to the places, species and people’s livelihoods WWF works to protect. To adequately address this crisis we must urgently reduce carbon pollution and prepare for the consequences of global warming,

Greenhouses gases, such as carbon dioxide, trap heat in the atmosphere and regulate our climate. These gases exist naturally, but humans add more carbon dioxide by burning fossil fuels for energy (coal, oil, and natural gas) and by clearing forests. Greenhouse gases act like a blanket. The thicker the blanket, the warmer our planet becomes. At the same time, the Earth’s oceans are also

absorbing some of this extra carbon dioxide, making them more acidic and less hospitable for sea life.

The increase in global temperature is significantly altering our planet's climate, resulting in more extreme and unpredictable weather. For instance, heat waves are becoming more frequent and many places are experiencing record droughts followed by intense rainfalls

3. DEFORESTATION

Forests help protect the planet by absorbing massive amounts of carbon dioxide (CO2), the most abundant type of pollution that causes climate change. Unfortunately, forests are currently being destroyed or damaged at an alarming rate. Logging and clearing land for agriculture or livestock release huge amounts of carbon dioxide and other harmful greenhouse gases into the atmosphere. It also diminishes those regions' ability to absorb carbon pollution.

4. FOSSIL FUELS

Burning fossil fuels, such as coal, oil and natural gas, to generate energy has the greatest impact on the atmosphere than any other single human activity. Globally, power generation is responsible for about 23 billion tonnes of CO2 emissions per year – in excess of 700 tonnes every second. Coal is especially damaging to our atmosphere, releasing 70% more carbon dioxide than natural gas for every unit of energy produced.(Burchmore 1990)

Humans and wild animals face new challenges for survival because of climate change. More frequent and intense drought, storms, heat waves, rising sea levels, melting glaciers and warming oceans can directly harm animals, destroy the places they live, and wreak havoc on people's livelihoods and communities.

5. ENDANGERED ILD LIFE SPECIES

We all hear about how polar bears are decreasing at an unruly rate due to the climate change all around the world. But did you know there are many more animals with the same fate? With pollutants in the air, land and sea, it has become hard to live a safe life for anyone. Climate change not only is hitting the arctic with the Polar Bears, Emperor Penguin and seals, it's also hitting those in the warmer climate areas as well.

The impacts of climate change are much faster melting of ice in the Arctic, an effect much faster than anywhere else in the world; it threatens the ecosystem of the species native to this region of the planet. Ocean acidification caused by increased uptake of carbon dioxide is occurring more

rapidly in the Arctic than in warmer waters. Marine creatures like sea butterfly are particularly vulnerable to acidification. (Tynan, Cynthia1994)

On land, the Arctic fox, found in the southern edges of the Arctic tundra, is facing "multiple threats of climate change, including the shrinking sea ice and tundra, the decline of prey for food and increasing competition from larger and dominant species. The Arctic is ground zero for climate change and we are pushing many species to extinction. The key to preventing their loss is the reduction of emissions of greenhouse gases. Specifically carbon dioxide, a level of 350 ppm or less is the ideal level at which leading scientists believe they can restore the Arctic sea ice. Other animals listed as most endanger from climate change is a wide range from land to sea are as follows-

Leather back sea turtles. Unfortunately, these gentle giants are threatened by dual environmental forces. Over-hunting and becoming entangled in fishermen's nets kill thousands of sea turtles each year. Global warming plays an equally destructive role with beaches eroding away due to severe storms, and the sands in which the turtles lay their eggs literally becoming too warm for healthy development of baby turtles.

Stag horn Coral. Coral bleaching occurs when conditions lead to the decline of the corals' symbiotic algae, which results in a pale, dying reef. Stag horn Coral is currently one of the most threatened species of coral.

Coral Reefs: Corals are affected by the warming of surface waters, which causes bleaching to occur. Coral bleaching is whitening caused by the death or expulsion of symbiotic, algae-like protozoa, from the coral, which is a result of stress to the coral .There are key temperature thresholds for mass bleaching to occur. It is projected that annual or bi-annual exceedance of bleaching thresholds will occur at the majority of reefs worldwide by 2030 to 2050 In 1998 the largest bleaching event to date occurred, killing 16% of the worlds corals, and leading to shifts in reef fish species composition . (Hoegh-Guldberg, 1999) Corals are also affected by increased atmospheric CO^2 concentrations, which results in declining calcification Corals are also physically damaged through wave action and light attenuation by storms, such as hurricanes, tropical storms, and tsunamis. Climate change is increasing the intensity and frequency of storm, posing further threat to reefs. Corals could become rare on tropical and subtropical reefs by 2050 due to the combined effects of increasing CO2 and increasing frequency of bleaching events. Coral reefs are habitat for about a quarter of marine species and are the most diverse marine ecosystems . (Hennessy etal 2007)

Clown fish. With the decline of coral reefs (some estimate that more than half of the world's coral reefs will vanish in the next 20 years), the fish that depend on their cover could be left homeless. The Clownfish – famously depicted in Disney's "Finding Nemo" is one flagship species under watch by the IUCN (International Union for Conservation of Nature)

Emperor Penguins. Penguins are at risk as the Antarctic Peninsula is warming faster than anywhere else in the Southern Hemisphere. The loss of sea ice in harming Emperor Penguins who rear their chicks on land locked sea ice. When the sea ice breaks up before the chicks have matured and grown their waterproof feathers, chicks are likely to be swept into the ocean and drown. Loss of sea ice also leads to lower food availability, which raises mortality rates . Along with the Arctic Fox, Emperor Penguins are literally feeling the heat from shrinking ice and snow cover, on the opposite pole. The Antarctic, like the Arctic region, is affected by melting ice and snow, which threatens the penguins' habitat. Emperor penguins breed almost exclusively on pack ice, with only a very small number that have ever breed on land. In addition, icebergs and ice cliffs form protective barriers for the breeding colonies. Without them, the chances of survival diminish.

Beluga Whale. The Beluga Whale has been in severe decline in waters off the coast of Alaska, and has been listed as an endangered species under the U.S. Endangered Species Act. Sadly, the listing has done little to help its numbers. A number of factors have contributed to the Belugas' decline, from hunting to noise pollution and strikes by shipping vessels. Changes in the temperature of Arctic waters affect not only the whales' habitat, but its food supply.

Koalas. The icon of Australia, Koalas are among the animals most affected by global warming. With rising CO2 levels in the atmosphere, eucalyptus plants produce fewer leaves, which are lower in protein and also filled with poor-tasting tannins. Because Koalas live exclusively on eucalyptus leaves, their survival is directly connected to the health of the plants. In recent years, the marsupials have had to consume greater amounts of eucalyptus to prevent starving to death. They have also been found getting diseases such as AIDS as well as urban encroachment.

Salmon. The reason why the scientists chose Salmon as a flagship species is because its home streams have been experiencing changes in flow rate due to earlier snow melt. We'll be able to witness the impact of a rise in a few degrees in temperature relatively quickly when it comes to these spawning fish.

6. STEPS TO BE TAKEN FOR MINIMIZING EFFECTS OF CLIMATE CHANGE

To avoid the worst consequences of climate change, we need to dramatically reduce the world's carbon emissions. But we must also prepare for the significant changes in weather that the world is

presently experiencing because of the pollution already in the atmosphere. Around the globe. (Kutz, etal 2005)WWF works with local communities, governments and others to help nature and people successfully adapt to a changing climate. WWF prepares communities around the globe for climate change. To do this WWF -

- Help communities in the Eastern Himalayas adapt to increasing water scarcity by collecting rainwater and promoting drought-resistant crops
- Restore mangrove forests in Coastal East Africa to buffer shorelines from storm erosion
- Protect coral reefs in the Coral Triangle to build their resilience against bleaching events
- Identify areas where polar bears can live on solid Arctic sea ice for decades to come
- Help farmers protect their crops from severe rainfall and droughts .

7. PROTECTING FORESTS

Forests are home to many of the world's most endangered wildlife. They also protect the planet by absorbing carbon dioxide (CO2), a major source of pollution that causes climate change. WWF fights climate change by saving forests. To do this WWF :

- Ensure that global climate change agreements reduce forest destruction and degradation and protect wildlife
- Work directly with countries, especially developing ones, to protect forests and benefit the livelihoods of local communities
- Use satellite images and aerial mapping technologies to track illegal logging
- Study the vulnerability of forests to climate change and explore ways to help them adapt

8. POLICY IMPLEMENTATION WITH PROPER INFLUENCE

Government must play a central role to tackle the climate crisis. Govt. must have work to implement advance policies that reduce carbon pollution, support clean energy technologies, prepare for the effects of climate change, and curb deforestation. At international negotiations, WWF encourages to play a constructive role in developing global climate agreements that:

- Substantially reduce carbon pollution to avoid the worst consequences of climate change
- Provide financial support to developing countries so people and nature can successfully adapt
- Combat forest destruction and protect wildlife that live there
- Help transition developing countries to clean energy sources like wind and solar .

The issues facing the animal kingdom are broad and complex. The link between climate change and observed impacts on species can be difficult to substantiate given all the contributing factors

that can possibly affect changes in animal behavior, distribution, and health. While more evidence is needed, there is a strong correlation between the observed physical changes to the environment and responses from animals. The countless studies and observations of animal species across the globe show us how animals are being affected, and expert predictions for the future are grim without a halt to the current climatic trends. (Freeman etal.1994)

9. ACKNOWLEDGEMENT

The author is grateful to Principal, Govt. N.C.Jain College, Dallirajhara, District Balod, Chhattisgarh for providing all necessary facilities.

REFERENCES

[1] Burchmore, J.J.. Implications of the Greenhouse effect for native freshwater fishes in New South Wales. *Wetlands 1990,* **10:** 30-32.

[2] Freeman, C., Gresswell, R., Guasch, H., Hudson, J., Lock, M., Reynolds, B., Sabater, F. and Sabater, S. The Role of Drought in the Impact of Climatic-Change on the Microbiota of Peatland Streams. *Freshwater Biology*(1994). **32(1):** 223-230.

[3] Hennessy, K., Fitzharris, B., Bates, B.C., Harvey, N., Howden, S.M., Hughes, L., Salinger J. and Warrick, R. Australia and New Zealand. *Climate Change 2007: Impacts, Adaptation and Vulnerability. Contribution of Working Group II to the Fourth Assessment Report of the Intergovernmental Panel on Climate Change,* M.L. Parry, O.F. Canziani, J.P. Palutikof, P.J. van der Linden and C.E. Hanson, (Eds), Cambridge University Press, Cambridge, UK, 2007 pp507-540.

[4] Hoegh-Guldberg, O. Coral bleaching, climate change and the future of the world's coral reefs: A review. *Marine and Freshwater Research*(1999) **50:** 839-866

[5] Kutz, S.J.; Hoberg, E.P.; Polley, L.; and Jenkins, E.J Global warming is changing the dynamics of Arctic host-parasite systems: Proceedings of the Royal Society B, 2005 v. 272, no. 1581, p. 2571–2576.

[6] Tynan, Cynthia T. and Douglas P. DeMaster,.*Observations and Predictions of Arctic Climate Change: Potential Effects on Marine Mammals.* Arctic. 1997Vol. 50: 308-322.

Impact of Climate Change on Water Resources of India

Prashant Kumar Shrivastava
Department of Geology, Govt. V.Y. T. P. G. Autonomous College, Durg, C.G India

ABSTRACT

Climate change is not only a major global environmental problem but also an issue of great concern to a developing country like India. Studies have been carried out earlier to analyze the trends of temperature varieties over India/ Indian subcontinent and results have been compared with the global trend. An analysis done by NIH Roorkee of temperature data of 125 stations distributed all over India shows an increase of 0.42^0 C, 0.92^0C and 0.09^0Cin annual mean temperature, mean maximum temperature and mean minimum temperature respectively over the 100 years. However trends are varying on regional basis. It has been observed that the changes in temperature in India, Indian subcontinent over last century are broadly consistent with global trends of increase in temperature.

Temperature drives the hydrological cycle, influencing hydrological processes in a direct or indirect way. A warmer climate may lead to intensification of the hydrological cycle, resulting in higher rates of evaporation and increase of liquid precipitation. These processes in association with a shifting pattern of precipitation may affect the spatial and temporal distribution of runoff, soil moisture, ground water resources etc and may increase the frequency of drought and floods. Extreme conditions exist in India – these are flood followed by drought. It has been estimated that 40mha of area is flood prone which constitute 12% of total geographical area of the country and it has been found that 51mha area is drought prone which constitute 16% of total geographical area.

Keywords: global, hydrological, evaporation, precipitation, drought

1. INTRODUCTION

In order to minimize the adverse impacts of climate change on water resources and attaining its sustainable development and management, there is a need for developing rational adaptation strategies. Three prominent visible signals of climate change are: (i) increase in global average temperature, (ii) change in regional precipitation patterns, and (iii) rise in sea level.

In India the distribution of rainfall is highly non-uniform both in terms of time and space. As a result water is required to be stored and utilized for meeting the demands of different sectors

throughout the year. Efficient water management requires sustainable development of the available surface and ground water resources and their optimal utilizations. To understand the regional implications of climate change on water policy and infrastructure, it is necessary to first obtain regional projections on temperature, precipitation, stream flow, and other relevant variables. Although specific regional effects in this regard are still uncertain, climate change is expected to lead to an intensification of the global hydrological cycle and can have major impacts on regional water resources, affecting both ground and surface water supply. Circulation patterns that affect precipitation in terms

Of impacts affecting normal human life, the biggest impact will be on water—with respect to both water availability and extremes of floods and droughts.

In its Fourth Assessment Report, the IPCC suggests that average temperatures will climb 1.56 to 5.44°C in south Asia by 2099. Dry season rainfall will drop by 6 to 16 per cent, while wet season rains will increase by 10 to 31 per cent. Such shifts in temperature and precipitation patterns could carry major repercussions for India\'s freshwater resources and food production. Rising surface temperatures appear to be contributing to melting of snow and ice pack in the Himalaya, thus threatening the water supplies on which hundreds of millions of people depend. As per IPCC analysis India could suffer from outright water stress – annual availability of less than 1,000 cubic meters per capita – by 2025, and gross water availability could fall as much as 37 percent by mid-century. In addition to the implications for drinking water and sanitation, this could considerably diminish crop yields in the region. Temperature increase of as little as 0.5 to 1.5°C might trim yield potentials for Indian wheat and maize by 2 to 5 per cent. For greater warming, above 2.5 degrees centigrade, the losses in non-irrigated wheat and rice yields in south Asia could cut net farm level revenues by 9 to 25 per cent.

Where some parts of India will face shrinking water supplies, others will face rising seas. Average global sea levels are projected to rise at a rate of 2 to 3 mm per year over the coming 100 years. Low end scenarios estimate sea levels in Asia will be a minimum, 40 cm higher by the end of the 21st century. The IPCC calculates that this would expose from 13 million to 94 million people to flooding, with about 60 per cent of this total in South Asia. In India, sea level rise of 100 cm would inundate 5,763 km3 of the country\'s landmass. Because of their high population density, susceptibility to coastal flooding and saltwater intrusion from sea level rise, and exposure to storm surges, the IPCC has specifically designated several of India\'s low-lying coastal river deltas-the Ganges (shared with Bangladesh), the Godavari, the Krishna, and the Mahanadi- as particular "hotspots" of climate change vulnerability.

2. CLIMATE CHANGE AND WATER RESOURCES

Temperature drives the hydrological cycle, influencing hydrological processes in a direct or indirect way. A warmer climate may lead to intensification of the hydrological cycle, resulting in higher rates of evaporation and increase of liquid precipitation. These processes, in association with a shifting pattern of precipitation, may affect the spatial and temporal Distribution of runoff, soil moisture, groundwater reserves etc. and may increase the frequency of droughts and floods. The future climatic change, though, will have its impact globally but likely to be felt severely in developing countries with agrarian economies, such as India. Surging population, increasing industrialization and associated demands for freshwater, food and energy would be areas of concern in the changing climate scenarios. Increase in extreme climatic events will be of great consequence owing to the high vulnerability of the region to these changes.

The utilizable water potential of the country has been variously estimated in the past. The Central Water Commission estimated the utilizable surface water in each river basin considering the suitable sites/locations of diversion and storage, as 690 BCM. The National Commission for Integrated Water Resources Development Plan (NCIWARDP 1999) as well as the Standing Sub-Committee for \'Assessment of Availability and Requirement of Water for Diverse Uses in the Country\' constituted by the Ministry of Water Resources (August, 2000) have adopted this value.

The annual replenish able ground water resource for the country was estimated at 433 billion cubic maters (bcm) as on March 2004. The sources of replenishment include rainfall (67%) and other sources like canal seepage, return flow from irrigation, seepage from water bodies and artificial recharge due to water conservation structures (33%).

3. STUDY OF ASSESSMENT AND MAJOR THREATS DUE TO CLIMATE CHANGE

- With unmitigated emissions, by the 2080s, large changes are predicted in the availability of water from rivers, with substantial decreases in Australia, India, Southern Africa, most of South America and Europe, and the Middle East and increases across North America, central Asia and central eastern Africa.
- Any climate change impact assessment on water resources study requires the down-scaling of the precipitation and other variables such as temperature, relative humidity, solar radiation, wind direction and wind speed from the global scale to the regional scale.
- 3 -5 degrees annual rise in mean surface temperature by the end of century, and 2.5 to 4° C, with warming more pronounced in the northern part of India.
- A 20% rise in all India summer monsoon rainfall over all states, except Punjab, Rajasthan and Tamil Nadu, which show a slight decrease. Increase in extremes in maximum and minimum temperatures and precipitation, particularly over the western coast and west central India.

However, studies by the Central Water Commission have predicted that per capita availability of water will go down drastically by 2050, even without considering climate change, due to population growth.(Raje and Majumdar 2010)

4. IMPACT OF CLIMATE CHANGE

The projections indicate that the warming would vary from region to region, accompanied by increases and decreases in precipitation. In addition, there would be changes in the variability of climate, and changes in the frequency and intensity of some extreme climatic phenomenon. Flood magnitude and frequency are likely to increase in most regions, and low flows are likely to decrease in many regions. However, there have been very few studies addressing the issue directly, largely due to difficulties in defining credible scenarios for changes in flood producing climatic events.

Water resources will come under increasing pressure in the Indian subcontinent due to the changing climate. An attempt has been made here to give a brief account of the possible impacts of climate change on India's water resources, change in India's water needs, climate of India, river basins of the country, present water resources and future demand and supply, impacts of projected climate change and variability, and associated hydrological events and vulnerability of regional water resources to climate change.

Extreme conditions exist in the country – there are floods followed by droughts. Due to excess rainwater, floods occur in certain parts. It has been estimated by RBA that 40 mha of area is flood-prone which constitute 12% of total geographical area of the country. Droughts are also experienced due to deficient rainfall. It has been found that 51 mha area is drought prone which constitute 16% of total geographical area.

Climate change presents a significant challenge to the urban water management agencies. The urban water infrastructure, consisting of water supply systems and sewage networks ,storm water drainage systems, pumping systems, detention tanks, groundwater pumping, and recycling of wastewater, is vulnerable to stresses caused by climate change. Most cities in India depend on surface water sources for municipal water supply.

The first level of impact of climate change on urban water supply is through the depletion of surface and groundwater sources, because of reduction in stream flows and reduction in recharge due to rainfall. An indirect effect of climate change is an increase in water demand, because of rise in temperatures, for the same given population. Increasing intensities of rainfall along with

unplanned development of cities exacerbate the already critical problem of urban flooding .It is essential that the water administrators as well as companies in charge of municipal and industrial water supply and storm water drainage account for climate change impacts in planning for infrastructure investments.

The population of the country has increased from 361 million in 1951 to 1201 million in March 2011. Accordingly, the per capita availability of water for the country as a whole has decreased from 5177 m3/year in 1951 to 1519 m3/year in 2011. Due to spatial variation rainfall, the per capita water availability also varies from basin to basin. The stage of groundwater development in the country is 58%. The status of groundwater development is comparatively high in the states of Delhi, Haryana, Punjab and Rajasthan and UTs of Daman & Diu and Pondicherry, where the Stage of Groundwater Development is more than 100%, which implies that in the these states, the average annual groundwater consumption is more than average annual groundwater recharge. In the states of Gujarat Karnataka, Tamil Nadu and Uttar Pradesh, the average stage of ground development is 70% and above. In rest of the states/UTs the stage of groundwater development is below 70%.Growing demand of water in agriculture, industrial and domestic sectors, has brought problems of over-exploitation of the groundwater resource, continuously declining groundwater levels, sea water ingress in coastal areas, and groundwater pollution in different parts of the country. The falling groundwater levels in various parts of the country have threatened the sustainability of the ground-water resource, as water levels have gone deep beyond the economic lifts of pumping. With rapid expansion in groundwater extraction, development-related problems have started emerging. Substantial decline of groundwater levels occurs even in blocks with sufficient groundwater resources due to climatic vicissitudes and localized development. (NDMA 2010)

The following specific adaptation options are relevant in the water sector, to combat the adverse effects of climate change: (i) demand management to suit the supply, by choosing appropriate cropping patterns and technologies to reduce water consumption in industry;(ii) increasing efficiency of water usage, particularly in the irrigation sector where the current efficiencies are very low; (iii) structural measures of increasing reservoir storage; (iv) non-structural measures of developing and operational izing adaptive reservoir operating rule curves, taking into account the likely mismatch between supply and demand; (v) out-of-the-box solutions to use the flood waters as a resource, say through diverting flood waters to potential groundwater recharge zones;(vi) large scale recycling of wastewater; and (vii)desalination of sea water to meet the municipal needs.

India, China and Bangladesh are especially susceptible to increasing salinity of their groundwater as well as surface water resources, especially along the coast, due to increases in sea level as a direct impact of global warming For two small, flat coral islands off the coast of India, the thickness of the freshwater lens was computed to decrease from 25 m to 10 m and from 36 m to 28 m for a sea-level rise of only 0.1 m (Kelkar etal 2008). It is expected that climate change will alter the frequency of occurrence of extreme rainfall events and we are likely to experience more frequent high intensity rainfall in cities.

5. FUTURE ISSUES AND ACTIONS

Rapid urbanization will continue for the next three to four decades. Many towns and cities will Struggle to meet water demands even for domestic purposes unless specific c policy and administrative mechanisms are put in place. Climate change is only likely to increase such stresses. In this context, wastewater recycling and desalination technologies gain importance. Diversion of flood waters for groundwater recharge must also be practiced by the municipal corporations. Legal regulation of groundwater use will soon be a necessity.

Unlike in most developed countries, agriculture in India (and other similar countries) is characterized by small farmers (farmers with small land holdings, typically less than 2 hectares) .Most of whom depends on rainfall for agriculture. For food security and long-term sustainability of Agriculture—and ensuring enhanced quality of rural life—irrigated agriculture needs to be given Importance, with technologies and non-structural measures put in place to increase efficiency of water use. Alternatively, decentralized irrigation systems including watershed development, rainwater harvesting, development of village tanks and water bodies, need to be encouraged as an insurance against the uncertainties due to climate change.

For each degree Celsius warming, global average precipitation is projected to increase by 2- 4%, but at the regional scale both increases and decreases are projected. Global climate modeling studies suggest that the precipitation may increase or decrease by as much as 15% under the assumption of a doubling of atmospheric CO2. Increases in the amount of precipitation are very likely in high latitudes, while decreases are likely in most subtropical land regions. It is predicted that increasing atmospheric concentrations of GHG would result in changes in frequency, intensity, and duration of the extreme events, such as more hot days, heat waves, heavy precipitation events, and fewer cold days. The impact of climate change is projected to have different effects within and between countries. Clearly, variations in key climatic parameters such as precipitation and temperature will produce significant changes in the hydrological regime (rainfall-runoff, snow and glacier melt runoff, evaporation, stream flow etc.) of a basin/country. The resulting changes in

regional weather patterns will vary widely but there is widespread agreement that in many parts of the world the frequency and severity of both floods and droughts will increase.

It is quite clear that even if countries do undertake immediate and rapid action to reduce their emissions, some degree of climate change is inevitable. Abilities to deal with weather extremes in the present day are considered to be very limited, the situation may get worse in the future. Therefore, the need is to significantly improve ability to plan and adapt to extreme events such as floods, droughts, cyclones and other meteorological hazards. Any robustness that we build into the system in this regard will always stand us in good stead, no matter what climate change actually transpires. In spite of the uncertainties about the precise magnitude of climate change and its possible impacts particularly on water resources at regional or basins scales, measures must be taken to anticipate, prevent or minimize the causes of climate change to mitigate its adverse effects.

6. ACKNOWLEDGEMENT

Author is grateful to Principal, Govt.V.Y.T.P.G. Autonomous College, Durg, Chhattisgarh for providing all necessary facilities.

REFERENCES

[1] Intergovernmental Panel on Climate Change 'Climate Change 2007—Th e Physical Science Basis', Contribution of Working Group I to the Fourth Assessment Report of the Intergovernmental Panel on Climate Change, S. Solomon et al. (eds), Cambridge University Press, Cambridge, UK (2007), available at http:// www.ipcc.ch/publications_and_data/ar4/wg1/en/ contents.html

[2] Kelkar, U., K.K. Narula, V.P. Sharma, and U. Chandna 'Vulnerability and Adaptation to Climate

[3] Variability and Water Stress in Uttarakhand State, India', *Global Environmental Change*, (2008), Vol. 18, pp.

[4] 564–74.

[5] Majumdar P.P. Implication of Climate Change for water Resource Management, India infrastructure Report (2011), pp 18-28

[6] National Disaster Management Authority [NDMA] *National Disaster Management Guidelines—Management of Urban Flooding*, National Disaster Management Authority, Government of India, (2010) September available at http://ndma.gov.in/ndma/guidelines.htm

[7] Raje, D. and P.P. Mujumdar 'Reservoir Performance under Uncertainty in Hydrologic Impacts of Climate Change', *Advances in Water Resources*, (2010), Vol. 33, No. 3,pp. 312–26.

Direct Mineral Carbonation of Coal Fly Ash at Varying Low Pressure Conditions

T. D. Rushendra Revathy[1], E. Pavithra[2], K. Palanivelu[1,2], A. Ramachandran[1]

[1]*Centre for Climate Change and Adaptation Research, Anna University, Chennai, Tamilnadu-600 025*
[2]*Centre for Environmental Studies, Anna University, Chennai, Tamilnadu-600 025*

ABSTRACT

Climate change and its associated impacts have stirred global attention towards the rising carbon dioxide emissions. In this regard, carbon capture and storage technology is viewed as a promising option towards climate change mitigation. Among the various approaches available in this technology, direct mineral carbonation of industrial alkaline solid residue is an attractive tool for large scale industrial applications. In this work, coal fly ash one of the major solid wastes produced from the power sector of the country was considered for carbon capture. Direct mineral (dry and wet) carbonation of coal fly ash has been studied at room temperature and at varying initial CO_2 partial pressure conditions (1-10 bar). The carbonation experiments were conducted in a batch reactor with 99.99% pure CO_2 gas for a time period of 1 h .On completion of the experiment, the net carbon increase of the waste was analyzed using total organic carbon analyzer. The maximum net carbon increase that was realized at the initial CO_2 partial pressure of 10 bar (maximum value used) is 7.18 g/ kg through dry carbonation. In case of wet carbonation the maximum achieved is 11.18 g/kg at 6 bar. Of the two routes considered, better results (55.3%) were obtained for the later one in terms of carbonation efficiency which emphasis the significance of water in the reaction process. The results suggest that for the specified reaction time the carbonation process in both the routes (wet and dry) is pressure dependent.

Keywords- Carbon dioxide; Climate change; Mineral carbonation; Coal fly ash

1. INTRODUCTION

The emission of greenhouse gases (GHGs) particularly CO_2 into the atmosphere is the reason behind global warming which subsequently induces changes in global climate. Even if the emission of the CO_2 gas is stopped at current levels, the impacts of climate change are likely to persist for years to come. Thus reduction of CO_2 emissions and thereby climate change mitigation is of utmost global importance [1]. In this context, carbon capture and storage (CCS) technology is viewed as a potential tool with many promising routes to tackle climate change and lead the energy sector towards sustainability [2]. India being an emerging economic power, its energy demand is projected

to increase drastically [3]. The country is in need of technologies such as CCS in order to cope up with climate change and minimize its CO_2 emissions [4].

Mineral carbonation is a promising approach unlike other storage options under the CCS technology owing to the fact that the CO_2 stored will not be released to the atmosphere [5]. In direct mineral carbonation, the alkaline metal oxides present in the minerals are made to react with CO_2 in dry or wet route [6]. Yet the major drawback in this technology is the consequences associated with the mining of the minerals and the disposal of the end products formed in the process [5]. Thus the need for an alternative material to capture CO_2 emerged out and industrial alkaline solid residues came into the limelight as an attractive resource whose disposal is difficult otherwise. These residues are alkaline, easily accessible and also available in abundant quantities near the point source of the CO_2 emissions. Alkaline wastes such as steelmaking slags, cement klin dust, red mud, coal fly ash (CFA), paper mill waste etc has been subjected to direct mineral carbonation and the majority of these studies are in laboratory scale concerning process optimization [6]. In addition to the fact that the process promises permanent storage of CO_2, it also renders the alkaline waste eco-friendly [7].

CFA is one of the major industrial wastes generated in the country whose per annum production is 112 million tons and is supposed to increase in future. Of the total CFA produced, only 38% is being utilized in the construction sector whereas the remaining is land filled [8]. It is the by-product obtained from power plants which are the major point source emitters of CO_2 in the country. Though its major composition is silica and aluminium, it also consists of calcium and magnesium oxides that could be used for storing carbon [9]. Attempts have been made to optimize the different process parameters in aqueous carbonation of CFA with water [10, 11] and in brine solution [12] in order to realize the most efficient system and its parameters. A pilot scale testing using CFA with direct flue gas through accelerated mineral carbonation has also been demonstrated in a power plant after successful lab scale study [13]. Thus there exists a scope to study mineral carbonation of CFA which is generated in abundant quantities in the country and optimize the process parameters. The current study is to perform direct mineral carbonation of CFA at room temperature with 99.99% CO_2 gas. The objective of the work was to evaluate the carbonation potential of CFA and to determine the effect of initial CO_2 partial pressure on carbonation process.

2. MATERIALS AND METHODS

2.1 Materials

CFA was collected from a power plant situated in Tamilnadu, India. The waste thus obtained was dried to constant weight and then stored in air tight containers. The CO_2 gas used in the study was

100% pure gas purchased from Indogas, Chennai. X-ray flouresence (XRF) analysis was performed in Bruker-S4 Pioneer WD-XRF instrument to determine the composition of CFA.

2.2 Carbonation experiments

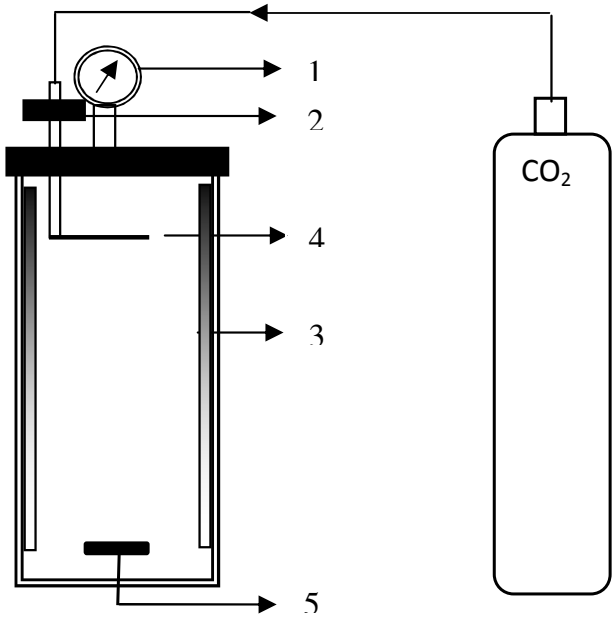


Fig. 1 Schematic diagram of the experimental set up used for carbonation studies
1- pressure gauge; 2- gas inlet valve; 3- baffle; 4- gas inlet port; and 5- magnetic pellet

Experiments were conducted in a batch reactor made up of stainless steel with the maximum operating volume of 1 L as shown in figure 1. The reactor consists of four baffles to provide mixing and a pressure gauge to monitor pressure inside the reactor. Known quantity of the CFA was taken in the reactor and then filled with the CO_2 gas from the cylinder fitted with the regulator. Each run was carried out at specific initial CO_2 partial pressure at room temperature for a time period of 1 h. In the case of wet capture studies, the CFA water slurry (L/S ratio-15) was stirred at 500 rpm using magnetic pellet and placing the reactor on magnetic stirrer. On completion of each run, the slurry was filtered and the solid product was separated, oven dried and then analyzed. In the case of dry carbonation, the solid product was directly taken for analysis. All the experiments were conducted in triplicates and after each run the carbonated product was analyzed for carbon.

2.3 Material Characterization

About five representative samples were analyzed for carbon content taken from the solid product obtained from each run of the experiment. The carbon content was determined using Analytikjena make multi N/C® 2100 S BUTOC Analyzer and solid module HT 1300, Germany.

3. RESULTS AND DISCUSSION

3.1 Carbonation of CFA

Carbonation of CFA in dry and wet conditions was performed for the fixed reaction time of 1 h at room temperature. After the completion of the experiment, the pressure reading inside the reactor dropped which may be due to the carbonation process. The carbonation process is dependent on the partial pressure as indicated in Figure 1 at a specified temperature in accord to Henry's law (Eq. 1).

$$P \alpha C \quad (1)$$

The amount of CO_2 gas molecules in collision with the waste/waste slurry is directly proportional to the partial pressure of the gas above it. This may be the reason behind the observed getter results at high initial CO_2 partial pressure values [11]. Here P is the partial pressure of the gas above the solution and C is the concentration of the dissolved gas. Figure 2 shows the comparison in net carbon increase observed through both routes in the carbonated samples at varying initial CO_2 partial pressure. As seen in the figure, the net carbon increase was maximized in wet route than in the dry route for the specified reaction time. In the case of dry carbonation route the net carbon increase in CFA was found to be increasing with increasing pressure value and reaching its maximum value of 7.18 + 0.27 g/kg at 10 bar. In wet carbonation approach, the carbon content in the CFA increased up to certain level of pressure after which it gets saturated as indicated by the curve. The maximum value of net carbon increase reached was 11.18 + 0.37 g/kg at 6 bar.

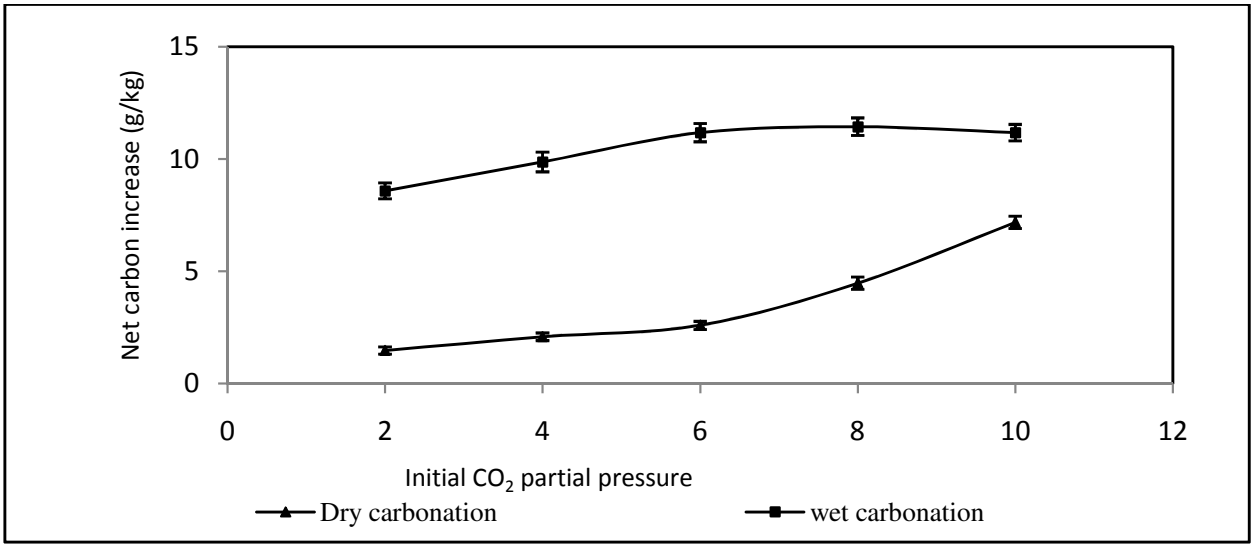


Figure 2: Net carbon increase in CFA at varying initial CO_2 partial pressure (Reaction time - 1 h, Room temperature and L/S ratio-15 for wet carbonation)

ISBN: 978-93-83083-87-9

In dry carbonation, the alkaline oxides directly react with CO_2 gas to form carbonates under the controlled atmosphere as shown in Eq. 2 and 3 which is the mechanism by which the process takes place [6].

$$CaO + CO_2 \longrightarrow CaCO_3 \quad (2)$$

$$MgO + CO_2 \longrightarrow MgCO_3 \quad (3)$$

With regard to wet carbonation, CO_2 dissolution takes place due to the presence of water in the system as indicated in Eq. 4 [6]. This may be the reason behind the enhanced level of carbonation achieved in this route.

$$CO_2 + H_2O \longrightarrow H_2CO_3 \longrightarrow H^+ + HCO_3^- \quad (4)$$

These results suggest a simple mechanism for aqueous carbonation involving hydration of CaO and its conversion into carbonates (Eq. 5 and 6) [10].

$$CaO + H_2O \longrightarrow Ca(OH)_2 \quad (5)$$

$$Ca(OH)_2 + CO_2 \longrightarrow CaCO_3 \quad (6)$$

3.2 Carbonation Efficiency

The theoretical sequestration capacity was found using the chemical composition of CFA and applying Stenoir's formula (Eq. 7) [12].

$$CO_2\ (\%) = 0.785\ (\%\ CaO - 0.7\%\ SO_3) + 1.09\%\ MgO + 0.71\%\ Na_2O + 0.468\%\ K_2O \quad (7)$$

$$\text{Carbonation Efficiency} = (\text{Actual} / \text{Theoretical}) \times 100 \quad (8)$$

XRF analysis revealed that the CFA particles consists of 6.74% of CaO, 2.22% of MgO, 3.29 % of SO_3, 1.38% of Na_2O and 1.13% of K_2O. Assuming that all the alkaline oxides that are available in CFA will undergo complete carbonation, the theoretical sequestration capacity of CFA comes to the value of 74.11 g of CO_2/ kg i.e 1 kg of CFA could sequester 74.11 g of CO_2. For calculations, actual sequestration capacity of CFA at their maximum values i.e 26.33 g of CO_2/kg (at 10 bar) for dry route and 41.0 g of CO_2/kg (at 6 bar) for wet route was taken. These values were obtained from the net carbon increase achieved in that particular run. The carbonation efficiency achieved in CFA was calculated using Eq. 8.

ISBN: 978-93-83083-87-9

The carbonation efficiency achieved in both the routes is presented in Figure 3. About 55.32% of efficiency was achieved through slurry phase aqueous carbonation and 35.52% in gas-solid carbonation. These results confirm that direct mineral carbonation of CFA at low pressure conditions (1-10 bar) and at room temperature is an realizable process with significant carbonation efficiency. This is in agreement with the pilot scale study reported with CFA, in which it was subjected to gas-solid carbonation at 1.151 bar with real flue gas wherein carbonation was achieved at room temperature and low pressure conditions [13].

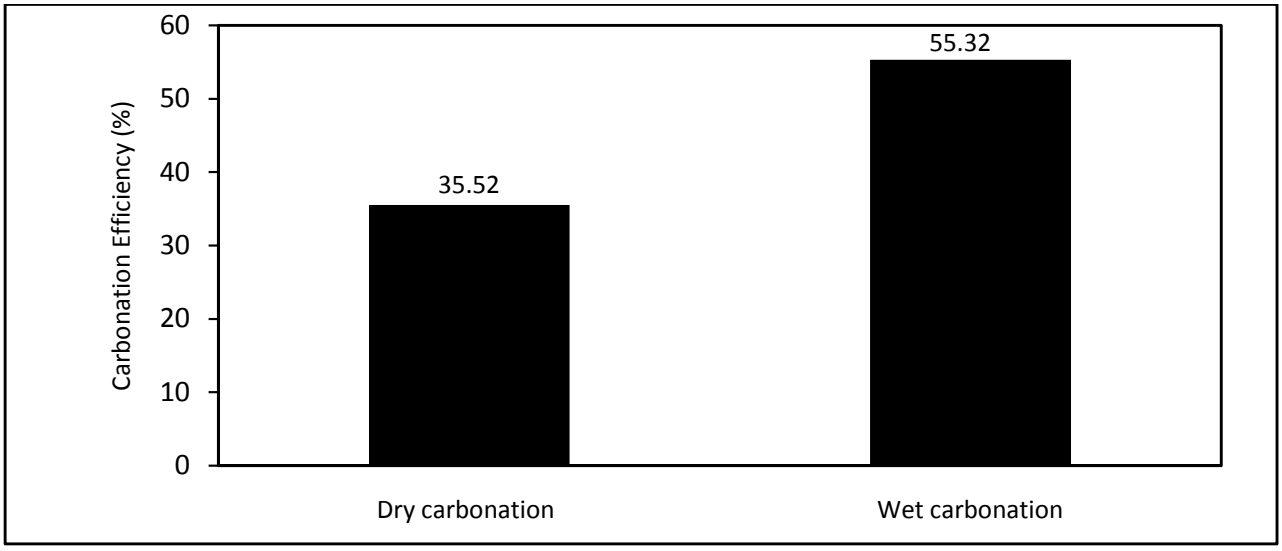


Figure 3: Maximum carbonation efficiency achieved in both the carbonation routes

4. CONCLUSION

This study provided an insight into the direct mineral carbonation of CFA at varying pressure conditions and at room temperature. The carbonation process was observed to be dependent on initial CO_2 partial pressure for a fixed reaction time whether it is wet or dry route. The optimum initial CO_2 partial pressure for both the routes has been determined at room temperature and for the reaction time of 1 h. The maximum carbonation efficiency of CFA achieved is 55.3% with the sequestration capacity of 41 g of CO_2/kg. When applied to the net annual production of CFA (112 million tons) in the country, the amount of CO_2 that could be sequestered is 61.94 million tons/ annum.

5. ACKNOWLEDGEMENT

The authors are thankful to "Department of Science and Technology" (DST), New Delhi, India for financial support. (Ref N0. Ref N0.DST/IS-STAC/CO2-SR-56/09).

REFERENCES

[1] Working Group I Contribution to the IPCC Fifth Assessment Report Climate Change 2013: The Physical Science Basis. 2013.

[2] Praetorius B, Schumacher K. Greenhouse gas mitigation in a carbon constrained world: The role of carbon capture and storage. Energy Policy 2009; 37:5081–5093.

[3] IEA. World Energy Outlook 2013 (WEO 2013). OECD publishing. On line at: http://www.iea.org/Textbase/npsum/WEO2013SUM.pdf.

[4] Dunnett A, Faist M, Foster S, Jennings M, Munuera L, Tong D. An assessment of india's 2020 carbon intensity target. Grantham Institute for Climate Change, Report GR4, April 2012.

[5] Mazzotti M, Abanades JC, Allam R, Lackner KS, Meunier F, Rubin E, et al. Mineral carbonation and industrial uses of carbon dioxide. In: IPCC special report on carbon dioxide capture and storage. Cambridge, UK: Cambridge University Press; 2005.

[6] Bobicki ER, Liu Q, Xu Z, Zeng H. Carbon capture and storage using alkaline industrial wastes. Prog Energy Combust Sci 2012; 38:302-20.

[7] Zevenhoven R, Teir S, Elonev S. Heat optimisation of a staged gas–solid mineral carbonation process for long-term CO_2 storage. Energy 2008; 33: 362-70.

[8] Lokeshappa B, Dikshit AK. Disposal and Management of Flyash. International Conference on Life Science and Technology IPCBEE vol.3 (2011); IACSIT Press, Singapore, 11-14.

[9] Siddique R, Iqbal Khan M. Fly Ash. Supplementary Cementing Materials, Engineering Materials 2011;1-16.

[10] Montes-Hernandez G, Perez-Lopez R, Renard F, Nietob JM, Charlet L, Mineral sequestration of CO_2 by aqueous carbonation of coal combustion fly-ash. J Hazard Mater (2009); 161: 1347-54.

[11] Ukwattage NL, Ranjith PG, Wang SH. Investigation of the potential of coal combustion fly ash for mineral sequestration of CO_2 by accelerated carbonation. Energy 2013; 52:230-236.

[12] Nyambura MG, Mugera GW, Felicia PL, Gathura NP. Carbonation of brine impacted fractionated coal fly ash: Implications for CO_2 sequestration. J. Environ. Manage 2011; 92:655-664.

[13] Reddy KJ, John S, Weber H, Argyle MD, Bhattacharyya P, Taylor DT, Christensen M, Foulkec T, Fahlsing P. Simultaneous capture and mineralization of coal combustion, flue gas carbon dioxide (CO_2). Energy Procedia 2011; 4:1574–83.

A Way to Reduce our Environment foot print-Green Constructions

Sujata Sharma
Department of biology, SHCS, Jagadhri, Haryana

ABSTRACT

The built environment has a vast impact on the natural environment, human health, and the economy. At least one third of all energy related CO_2 emissions are from construction sector. Green construction is the practice of creating structures and using processes that are environmentally responsible and resource-efficient throughout a building's life-cycle from siting to design, construction, operation, maintenance, renovation and deconstruction.

Faced with an increasing scarcity of resources, the construction subsector which directly impinged on the viability of the sector, there was an increasing focus on "Green Building as a solution. As a result, India has emerged as one of the world's top destination for green buildings and has implemented a number of home rating scheme and building codes, which open a wide range of opportunity in construction, architecture and engineering design, building materials and equipment manufacture. By adopting green building strategies, we can maximize both economic and environmental performance. However, the most significant benefits can be obtained if the design and construction team takes an integrated approach from the earliest stages of a building project. This practice expands and complements the classical building design concerns of economy, utility, durability, and comfort. Green building is also known as a sustainable or high performance building. Green Homes are healthier, more comfortable, more durable and more energy efficient and have a much smaller environmental footprint then the conventional homes. Green buildings improve productivity and trade energy. It presents exciting new challenges for environmental stewardship. Green building can help electricity utilities by reducing peak demand. It inspire not only innovation but also raises the quality and standards of building generally.

Keywords: Green Building, Energy efficiency, Environmental Footprint, Better Productivity

1. INTRODUCTION

Our daily and routine activities have a vast impact on surroundings. A person who washes his car daily waste a lot of water every day. Going from home to office everyday by car emits plenty of

CO^2 . Cooking,bathing, generation of waste, use of various appliances for comfort future increase burden on nature. These are some very common examples. If we think of industrial level the pressure exceeds much more. Construction sector is one such sector. Buildings are one of the heaviest consumers of natural resources and account for a significant portion of the greenhouse gas emissions that affect climate change. In the U.S., buildings account for 38% of all CO2 emissions, 73% of electricity consumption. In short constructing a home for could be relaxing and a happy moment for a human but not for nature. It means that building sector accounts for major increase in environment footprint. So what is the solution? Solution is 'go green' in every aspect. 'GREEN CONSTRUTIONS" offers vast opportunities to reduce burden on nature and also to lessen cur environment footprint. As per U.S.G.B.C.record, by 2015, an estimated 40-48%of new non residential constructions by value will be green, equating to a$120-145billion opportunity. More than 2.8 billion space are LEED- certified(as of January 1,2014) in U.S. and 41% of all residential building starts in 2012 were green, as compared to 2% of all non residential buildings starts in 2005. India is also emerging as one of the top destinations of green constructions India has significant opportunity to go the green way and concerted efforts by all the stakeholders is the need of the hour, vice-chairman of Indian Green Building council (IGBC), Bharat Kamat says. One survey reveals that built space in India will increase 5-fold from 20,000 million sq ft in 2005 to over 100,000 million sq ft in 2030.This growth will put enormous pressure on various resources such as energy, water, minerals and will have a discernible impact on the environment. Hence by adopting green construction stategy ,we can contribute a lot for conservation as wellas for sustainability.

2. NEEDS FOR GREEN CONSTRUCTIONS

The green building boom is well in progress, with around ten percent of new homes expected to be green houses by the year 2015. This rise in green building is not just thanks to increased environmental awareness, and also to increased perception of the benefits of green building, including serious cost benefits. Here are the most important reasons the green construction boom is only going to get larger. A green home consumes less energy, reduced upkeep cost , reduced water usage, reduced heating cost and more. Normally a green house owner consumes 50% less energy and 50% less water than a normal non green home. Green homes also provide better health benefits and hold their prices over a long run than conventionally built houses in their neighbourhood.

3. ISSUES RELATED TO GREEN CONSTRUCTIONS

3.1 Market impact in India

Today, constructing green buildings is technically feasible and economically viable, says Syed Beary, Chairman, the Indian Green Building Council-Bangalore. IGBC has recently crossed 2

ISBN: 978-93-83083-87-9

billion square foot in india. That by 2022 (India @75), IGBC aspires to cross over 10 billion sq. ft of green building footprint and in the process consolidate its global leadership position in green buildings is something that speaks of a huge responsibility. But with over 2,400 green building projects in the country, the dream has turned a reality a year earlier, ranking India as the country with the largest green footprint in the world after the U.S. (Green Building Council). (Source- THE HINDU)

3.2 An overview at international level

Green constructions are increasing internationally. At the end of year 2013 , 42% of all square footage per suing LEED certification exist outside U.S. In 2015,project expectation in four countries are

a) Brazil - 83% of firms planning new green commercial projects
b) Singapore - 69% of firms planning green renovation projects
c) United Arab Emirates - 73% of firms planning green institutional projects
d) United Kingdom - 65% of firms planning green renovation projects

3.3 Energy consumptions in building sector

Energy consumptions is the major impact on the sustainability of the environment. TERRI accounts for energy consumption in various sectors like agriculture, transport, building sector etc. It has been found the energy consumption in building sector (residential and commercial sectors) is consistently rising at a rate of 8% annually and hence increases from a low of 14% to nearly 33% in 2004-2005. (Source-BEE)

Table 1: Final energy consumption in India in building sector (residential and commercial) in MTOE (million tonns of oil equivalent)

YEAR	ENERGY CONSUMPTION
1980-81	5.6
1986-86	8.9
1990-91	12.6
1995-96	15.3
2000-01	24.1
2005-06	32.6
2010-11	43.43

Source: MoC2011, MoPNG 2010,TERI (variousyears)

Green constructions consume less energy. Compared to average commercial building the LEED certified buildings consume lesser energy (25%), emits lesser green house gases (34%), consumes lesser water(11%) and also have lower maintenance costs(19%).

3 .4 Water consumption

Buildings use 13.6% of all potable water, or 15 trillion gallons per year. A water efficient construction decreases energy use by 10-11%, save 11-12% 0f operating cost and reduce water use by 15%. Use of water efficient fixtures not only increase water efficiency of a building but also reduces greenhouse gas emissions. Retrofitting 1 out of 100 american homes with water efficient fixtures could avoid approximately 80,000tons of GHG emissions,the equivalent of removing 15,000 cars from the road for one year.[18]

3.5Materials used

Buildings use 40% of raw materials globally (3 billion tons annually)[2]The EPA estimates that 170 Million tons of building-related construction and demolition (C&D) debris was generated in the U.S. in 2003, with 61% coming from non-residential and 39% from residential sources[3]. They also estimated that 250 million tons of municipal solid waste was generated in the U.S. in a single year[21].

Green buildings consume less energy and fewer resources and hence accounts for lesser solid waste generation.

3.6 Rating for green constructions

Green constructions movement is gaining momentum in country under LEED rating system the most widely accepted benchmark for green building over the world. In the words of U.S.G.B.C. LEED is national, consensus based, market driven building rating system designed to accelerate the development and implementation of green building practices. In short, it is the leading edge system for designing, certifying and constructing the world's greenest and best buildings. The rating system has been developed based on materials and technologies that are presently available. The objective of LEED rating system for New Buildings is to facilitate the creation of water efficiency, handling of waste, energy efficiency, and environmentally friendly buildings

Confederation of Indian industry (CII) formed IGBC in year 2001.IGBC has licensed the LEED green building standard from USGBC. Till date the following green building rating systems are available under IGBC:

- LEED India for new construction (LEED India NC)

- LEED India for core and shell(LEED India CS)
- IGBC green homes
- IGBC Green Factory building
- IGBC Green SEZ(Special economy zone)

IGBC-LEED prepared a check list for various particulars such as site selection and planning, water efficiency ,energy efficiency, materials and resources ,innovation and design, indoor environmental quality etc. For each type particular mandatory requirements and credit points are assigned. Based upon the points earned by a green construction, certifications like gold, silver, platinum is awarded to it. The table 2 showing the above said features is shown asfollows:

CHECKLIST FOR IGBC GREEN CONSTUCTIONS				
PARTICULARS	**GREEN SEZ**		**GREEN HOME**	
	M	**C**	**M**	**C**
SITE PRESERVATION AND RESTORATION	Local Regulations Soil Erosion control	16	---------	-------
SITE PLANNIG AND DESIGN	TobaccoSmoke Control	25	Local Regulations Soil Erosion control	8
WATER EFFICIENCY	Rainwater Harvesting, 25% Waste Water Treatment, 100%	15	Rainwater Harvesting, 50% Water efficient fixtures	20
ENERGY EFFICIENCY	Minimum Energy Efficiency	30	CFC free Equipment Minimum energy performance	22
MATERIALS AND RESOURCES	Segregation of Waste	10	Separation of waste	13
INNOVATION AND DESIGN PROCESS	--------	04	-------	04
INDOOR ENVIRONMENTAL QUALITY	---------	--------	Tobacco smoke control	13
TOTAL POINTS		100		80

Source---IGBC check list(Abbereviations-M-mandatory,C-credit points) IGBC green home data is for the projects with interiors.

ISBN: 978-93-83083-87-9

3.7 Barriers for green constructions

- Lack of awareness about green buildings.
- Limited availability of local materials and equipments.
- Combating the cost of higher cost of green buildings which new cost is Only around 2% higher of conventional buildings.
- Performance evaluation tools to measure and verify the needs of green buildings under occupation.

3.8 Conclusions

Green constructions provide the best opportunity to create low carbon and sustainably built environment. Green buildings save 30-40% of energy consumptions, reduce operation cost and also enhance good health. This technology not only benefits mankind , society and country but also shows global environment concerns on large scale.

REFRENCES

[1] McGraw Hill Construction (2010). Green Outlook 2011: Green Trends Driving Growth.

[2] Lenssen and Roodman (1995). Worldwatch Paper 124: A Building Revolution: How Ecology and Health Concerns are Transforming Construction. Worldwatch Institute

[3] Energy Information Administration (2008). Assumptions to the Annual Energy Outlook.

[4] Department of Energy (2011). Buildings Energy Data Book. Buildings Share of Electricity Consumption/Sales. Accessed October 26, 2011

[5] U.S. Environmental Protection Agency (2009). Estimating 2003 Building-Related Construction and Demolition Materials Amounts.

[6] U.S. Environmental Protection Agency (2009). Estimating 2003 Building-Related Construction and Demolition Materials Amounts.

[7] IGBC Green SEZ Reference guide

[8] IGBC Green Home Reference guide

[9] Information available at http// www.igbc.ac.in

[10] McGraw-Hill Construction (2012). World Green Buildings Study. Accessed Nov. 29, 2012.

[11] McGraw Hill Construction (2010). Smart Market Reports. Green BIM – How Building Information Modeling is Contributing to Green Design and Construction.

[12] U.S. Green Building Council (2012) New analysis-LEED buildings are in top 11th percentile for energy performance in the nation. Accessed December 14, 2012.

[13] McGraw Hill Construction (2010). Green Outlook 2011: Green Trends Driving Growth.

[14] McGraw Hill Construction (2010). Green Outlook 2011: Green Trends Driving Growth

Ceramic Supported Facilitated Transport Membranes for the Separation of Carbon Dioxide and Nitrogen

Uma Maheswari[1], K. Palanivelu[2]

[1]Centre for Environmental Studies, Anna University, Chennai-600 025, India,
[2]Centre for Climate Change and Adaptation Research, Anna University, Chennai-600 025, India,
2Presenting Author: uma.maheswari992@gmail.com

ABSTRACT

In this study, Selective removal of CO_2 gas from N_2 gas stream was studied by the composite membranes, in which cross linked polyvinyl alcohol (PVA/Acetaldehyde) with triethyelenetetramine (TETA 10 wt %) acts as a active layer and ceramic filter acts as a support layer. The prepared membrane was characterised by Scanning Electron Microscope (SEM). The gas transport properties of the membranes, including gas permeance, flux and selectivity were investigated by using pure CO_2 and N_2 and by varying the parameters such as cross linking agent and membrane thickness. The permeance of both CO_2 and N_2 gas decreases with increase in cross linking agent and membrane thickness, whereas the selectivity was found to be increased. Under optimized conditions the maximum permeability of 69 GPU and selectivity of 50 was obtained. The membrane was found to be stable for 120 hours.

Keywords: Carbon Dioxide, Facilitated transport membranes, TETA, PVA

1. INTRODUCTION

Concern for the changing climate and emission of greenhouse gases, especially CO_2, has resulted in the acceleration of innovative solutions for CO_2 capture and sequestration [1]. IPCC claims [2] that burning of fossil fuel is the primary source of this increased atmospheric concentration of CO_2. According to their report the global surface temperature is likely to increase by 1.1 to 6.4°C between 1990 and 2100. Hence, it is very important from both the environmental and the economical point of views to find an efficient way for separating carbon dioxide from flue gas to minimize its emission into atmosphere. Among various solutions, membranes for CO_2 capture is a low cost, energy saving and environmental friendly process compared to other conventional process [3, 4]. Membranes may be prepared from various types of materials, but currently only polymeric membranes are commercially available for gas separation [5]. Despite, they are stable in nature, the permeability of CO_2 gas through polymeric membranes is less. This could be enhanced by Facilitated Transport Membranes (FTM) [6]. FTMs are the membranes, in which the carrier

ISBN: 978-93-83083-87-9

containing special affinity towards CO_2 gas has been incorporating into the polymeric membrane which gives high permeability and selectivity.PVA is a polyhydroxy and water soluble polymer. It is used for many practical applications due to their ease of its preparation as well as its excellent physical properties and film forming ability, good compatibility with amine, hydrophilic nature. In this study, the facilitated transport of CO_2 through the TETA incorporated polymeric membrane, supported by ceramic filter was studied. The morphology of the composite membrane was observed by Scanning Electron Microscope (SEM). The effect of cross linking agent and membrane thickness on the permselectivity was also examined.

2. EXPERIMENTAL

2.1. Materials

The amine (TETA) was purchased from the Merck Company with 96-98% purity. Poly (vinyl alcohol) (PVA) (99%+ hydrolyzed; Mw = 1, 25,000) was purchased from fisher scientific company, India. The chemicals were used without further purification. Commercially available ceramic water filter is used as a membrane support (height=18.5 cm, radius=2.5 cm). Research grade carbon dioxide (99 % pure) and nitrogen (99 %pure) gases were purchased from Supreme Engineering Services. India.

2.2. Membrane preparation

PVA solution (10 wt.%) was prepared by dissolving pre-weighed dry PVA in water followed by heating at 90^{o}C for six hours with vigorous stirring on a tightly capped glass container [7,8]. Then the solution was allowed to cool down to 70^{o}C. Then a certain amount of acetaldehyde was added into the polymer to obtain PVA cross-linked solution. The PVA/ acetaldehyde solution was heated at about 80ºC for 6 hrs under stirring. Afterwards, TETA (10 %) was added into the polymer solution to achieve desired amine concentration. Thereupon, the amine-PVA blend was stirred continuously followed by heating at 60ºC for 12 hrs. The solution was then cooled to room temperature for at least three hours, and then allowed to stand for at least one day before casting. The ceramic filter was boiled in a hot water and dried at 100^{0}C in an oven for one hour and kept at atmosphere for 24 hours for drying. Then, the PVA-amine blend solution is coated on the ceramic filter. The membrane was further dried at room temperature for at least 24 hours before being used for permeation test.

2.3. Gas permeation measurement

The set-up of the gas permeation experiments using the facilitated transport membranes is shown in Fig.1. The apparatus consisted of a cylindrical-type stainless steel membrane cell with permeation area of 942 cm^2, a gas flow system (canister) that delivered CO_2 and N_2 gas and pressure gauges.

The feed pressure was152 kPa (P_0), while the downstream/permeate was vented to the atmosphere (P_L). The permeate flow rates were measured by volume displacement using a volume flow gas analyzer. All experiments were performed at room temperature (296-298 K). Each experiment was repeated at least twice. Steady-state permeation was determined by permeate flow rate (V/t) measurements made at 30-minute intervals. Steady state was assumed to have reached when the flow rate no longer changed with time.

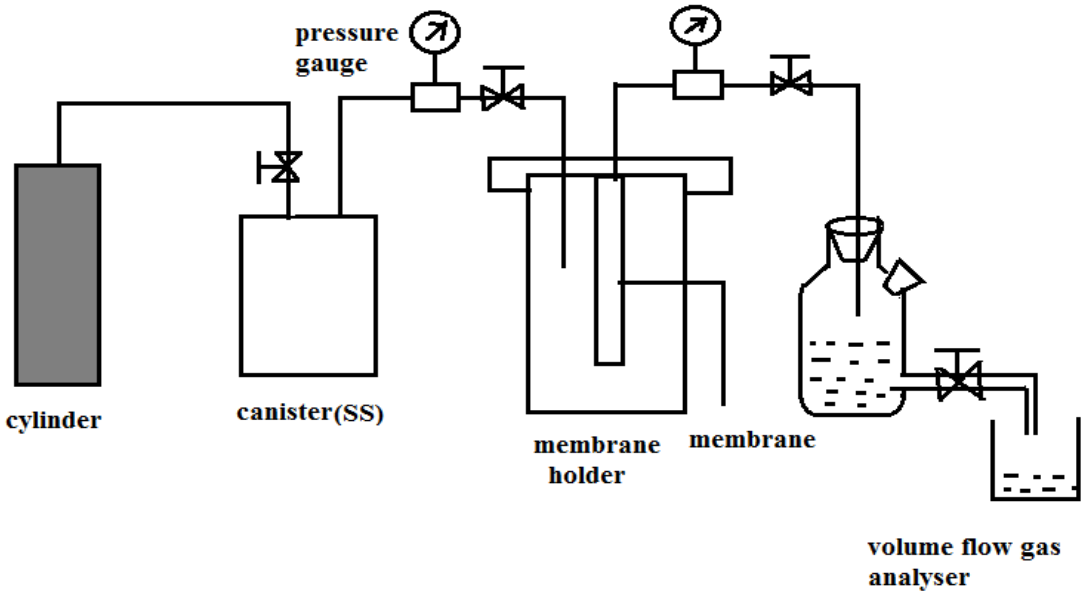


Fig.1. Schematic diagram of the experimental set up

The experimental steady-state permeance through the membrane is calculated as follows [9, 10].

$$J = \frac{273.15}{T} \frac{V}{t} \frac{1}{A} \frac{1}{P_0 - P_L} \longrightarrow (1)$$

The selectivity of carbon dioxide over nitrogen is calculated as the ratio of carbon dioxide permeance to nitrogen permeance.

$$\alpha = \frac{J_{CO_2}}{J_{N_2}} \longrightarrow (2)$$

ISBN: 978-93-83083-87-9

3. RESULTS AND DISCUSSION

3.1. Morphology analysis by SEM:

Figure 2 (a) depicts the surface of ceramic filter before coating. Figure 2(b) illustrates the front surface of PVA-amine blend coated ceramic filter. As can be observed, no macrovoids exist and the homogeneous pattern is created. Furthermore, the ceramic filter pores were totally filled with the PVA-amine blend. Consequently, a nonporous structure was created due to the penetration of PVA-amine blend into the pores of support. Figure 2(c) shows the cross section of the membrane. A thin layer of PVA blended with amine was formed on the top surface of ceramic filter support.

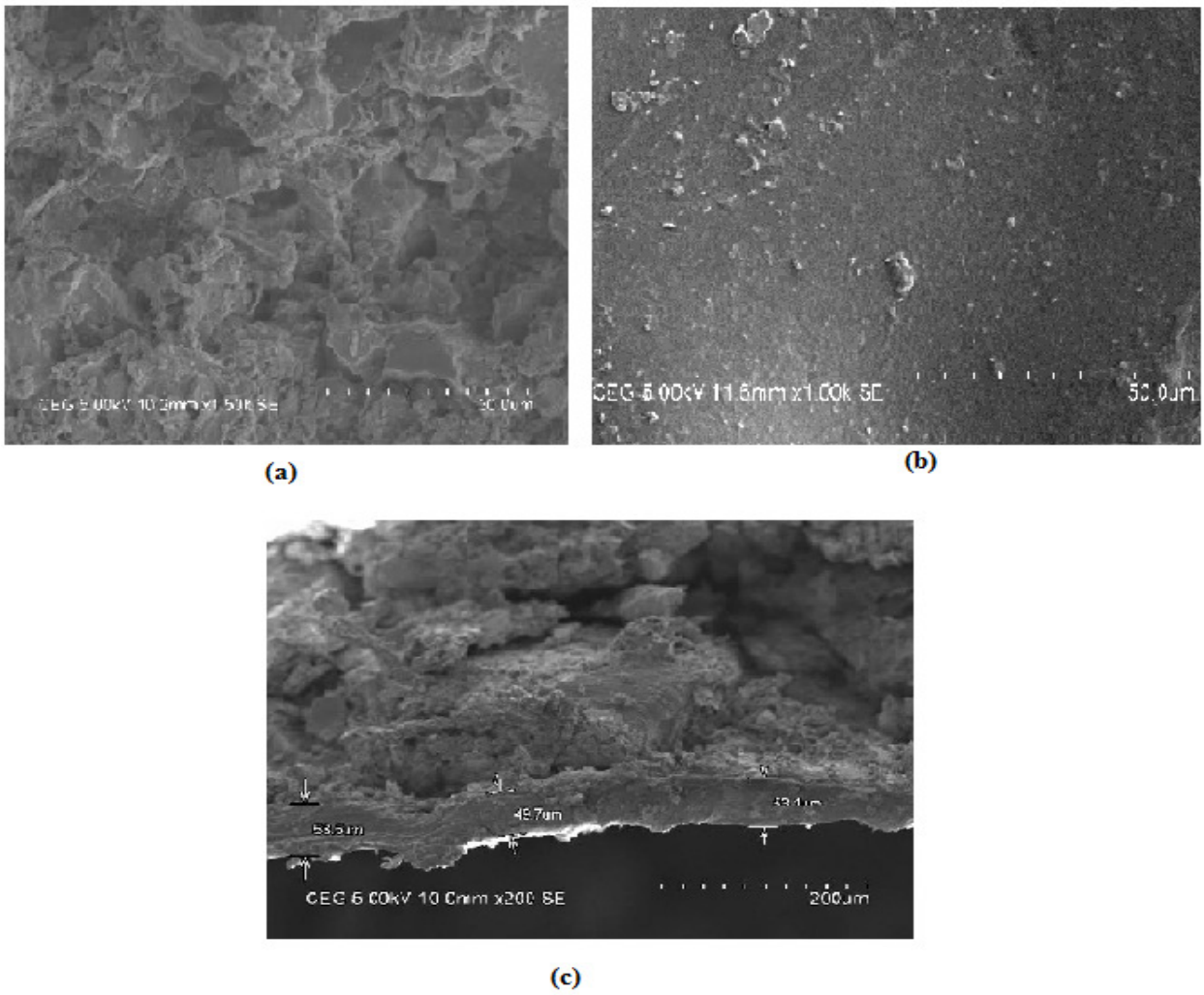


Fig.2.SEM pictures of the top and cross-section of the membranes. (a) Ceramic filter support without coating (b) after coating PVA-TETA (10 wt %) (c) Cross section of PVA-TETA (10 wt %) coated ceramic filter support

3.2. Effect of cross linking agent

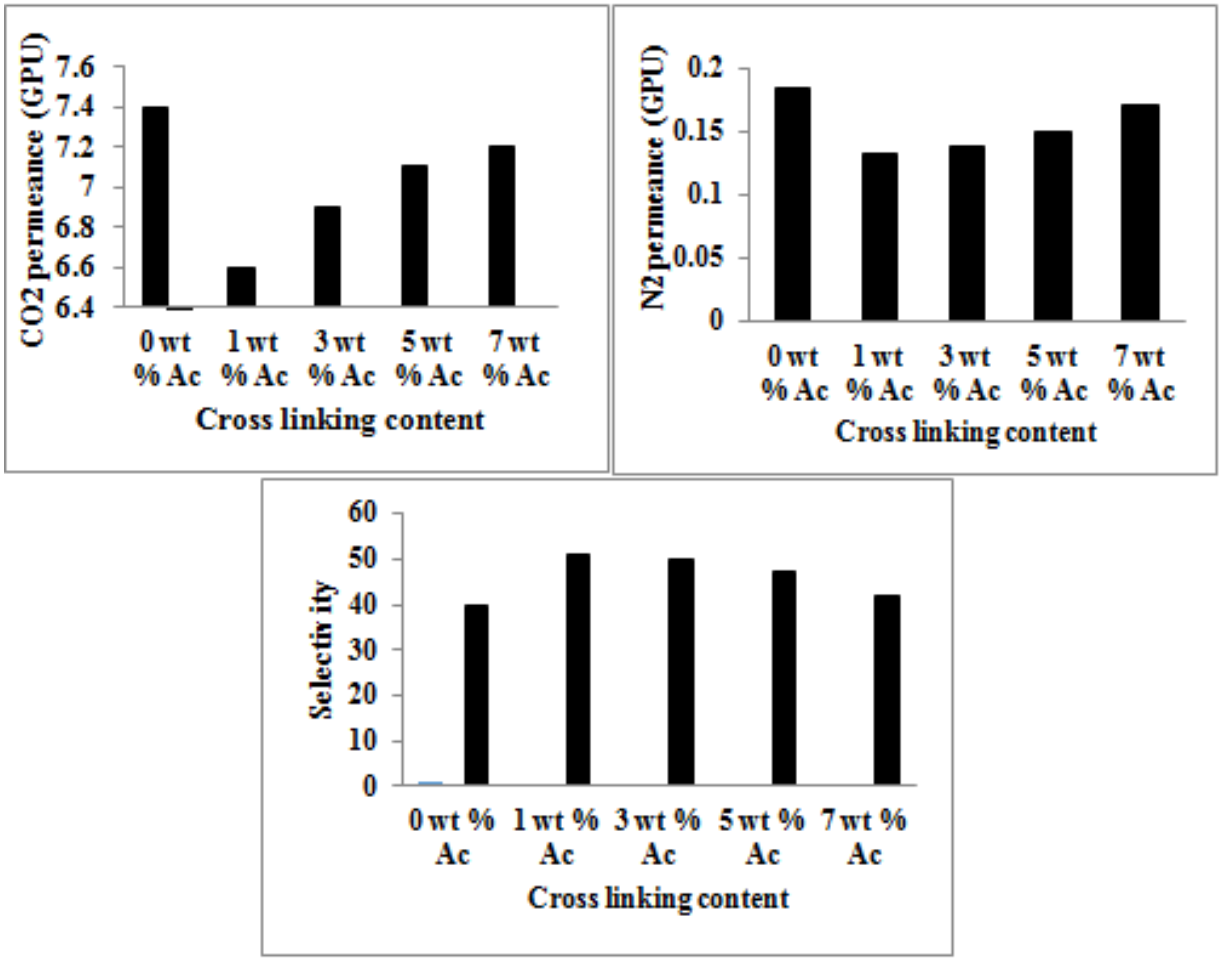


Fig.3. Effect of cross linking agent on the permeability and selectivity of CO_2 gas

The effect of cross linking agent on the permeance of CO_2 and N_2 and selectivity is illustrated in Fig.3. The PVA/Acetaldehyde ratio was varied from 1 wt % to 7 wt %. In general, with increasing PVA/Acetaldehyde mass ratio, CO_2 and N_2 permeances were decreased in comparison with uncross-linked membranes. However, the permeance increased significantly with the increase in cross linking content but the selectivity decreased beyond the cross linking concentration of 3 wt %This trend indicates that low Acetaldehyde content has led to probable higher cross-linking densities. [11, 12]

3.3. Effect of Membrane thickness:

Membrane thickness is likely to have an effect on CO_2 transport across the membrane. To investigate this concept, four membranes were prepared with effective thickness of about 36, 42, 55

ISBN: 978-93-83083-87-9

and 64 µm respectively and it is presented in Fig. 4. Variations in thickness were achieved by repeatedly casting the polymer solution into the substrate. Both CO_2 and N_2 permeance decreases with an increase in the membrane thickness because the diffusion rate in the membrane is inversely proportional to the membrane thickness [13, 14]. The membrane thickness is likely to have an impact on the selectivity between CO_2 and N_2. For thicker membranes (i.e. 55 and 62 µm), the residence time of CO_2 was longer so that it consumes more TETA to react with. The effect was greater facilitation leading to an increase in selectivity.

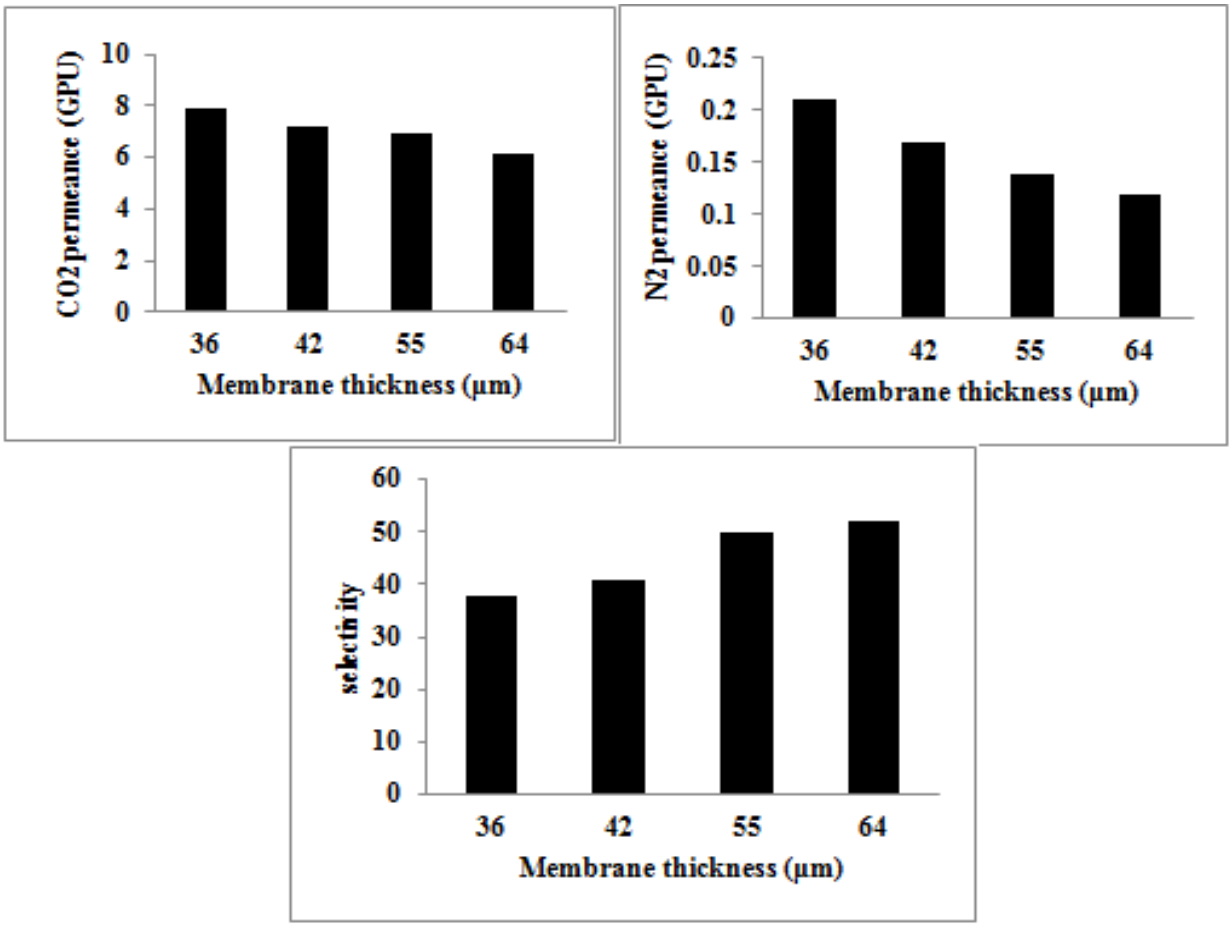


Fig. 4. Effect of Membrane thickness on the permeability and selectivity of CO_2 gas

3.4. Stability of Membrane:

In evaluating the practicality of these facilitated transport membranes for CO_2 separation, one parameter of paramount importance is the membrane lifetime. As shown in Fig 5. the membrane showed roughly constant permeance up to 120 hours. Beyond that the permeance decreased due to

the membrane drying. This decrease in membrane performance could be regenerated by introducing certain amount of water into the permeation unit.

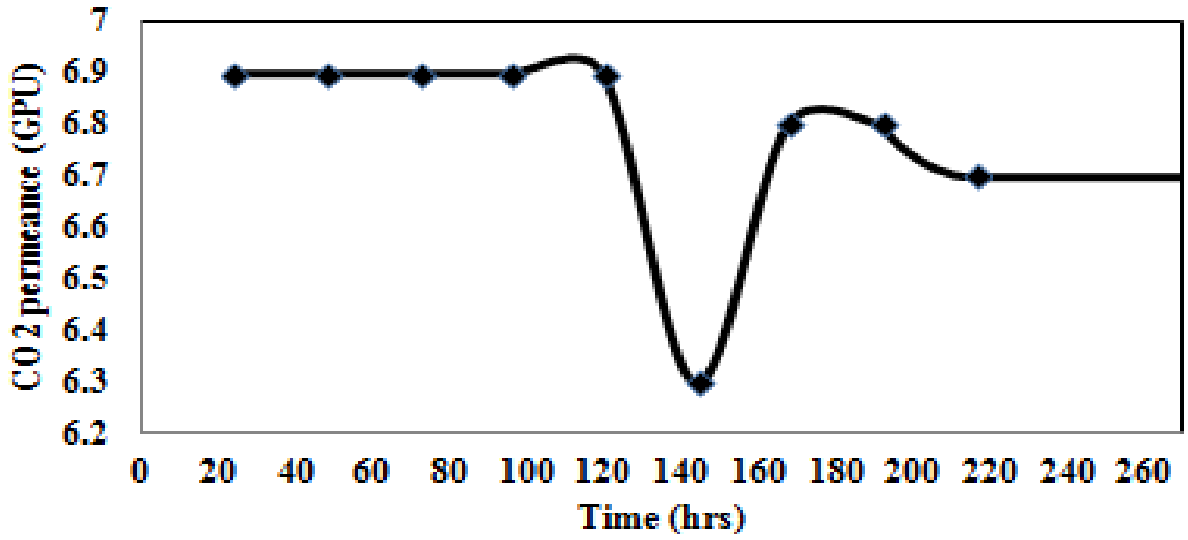


Fig. 5. Permeance of CO_2 as a function of time

4. CONCLUSION

Selective removal of CO_2 gas from N_2 of both CO_2 and N_2 gas decreases with increase in cross linking agent and membrane thickness, whereas the gas stream was studied by the composite membranes, in which cross linked polyvinyl alcohol (PVA/Acetaldehyde) with triethyelenetetramine (TETA 10 wt %) acts as a active layer and ceramic filter acts as a support layer. The parameters such as cross linking agent content and the membrane thickness have been optimized. The PVA/Acetaldehyde ratio of 3 wt % and the membrane thickness of 55 μm were found to give the maximum permeability. Under optimized conditions the maximum permeability of 69 GPU and selectivity of 50 was obtained. The membrane was found to be stable for 120 hours.

5. ACKNOWLEDGEMENT

One of the authors (AUM) would like to acknowledge the financial support provided by the **DST-INSPIRE (IF 10580),** New Delhi, India for this research work.

REFERENCES

[1] C.E. Powell, G.G. Qiao. Polymeric CO_2/N_2 gas separation membranes for the capture of carbon dioxide from power plant flue gases. J.Membr.Sci. 2006; 279:1–49.

[2] IPCC 2011, Summary for Policymakers, in IPCC Special Report on Renewable Energy Sources and Climate Change Mitigation, O. Edenhofer, Pichs- Madruga R., Sokona, Y., Seyboth, K., Matschoss,

P., Kadner, S., Zwickel, T., Eickemeier, P., Hansen, G., Schlömer, S., von Stechow, C., Editor, Cambridge, United Kingdom and New York, NY, USA: Cambridge University Press.

[3] T. Yamaguchi, L.M. Boetje, C.A. Koval, R.D. Noble, C.N. Brown. Transport properties of carbon dioxide through amine functionalized carrier membranes. Ind. Eng. Chem. Res. 1995; 34:4071–4077.

[4] H. Matsuyama, M. Teramoto, H. Sakakura. Selective permeation of CO_2 through poly {2-(N,N-dimethyl) aminoethyl methacrylate} membrane pre- pared by plasma-graft polymerization technique. J.Membr. Sci. 1996; 114:193–200.

[5] R. Quinn, D.V. Laciak, G.P. Pez. Polyelectrolyte-salt blend membranes for acid gas separations. J. Membr. Sci. 1997; 131: 61–69.

[6] H. Matsuyama, A. Terada, T. Nakagawara, Y. Kitamura, M. Teramoto. Facilitated transport of CO_2 through polyethylenimine/poly (vinyl alcohol) blend membrane. J. Membr. Sci. 1999; 163:221–227.

[7] J.H. Meldon, P. Stroeve, C. Gregoire. Facilitated transport of carbon dioxide: a review. Chem. Eng. Commun. 1982;16:263–300.

[8] A. Aroonwilas, A. Veawab. Characterization and comparison of the CO_2 absorption performance into single and blended alkanolamines in packed column. Ind. Eng. Chem. Res., 2004; 43:2228–2237.

[9] M. Teramoto, Q. Huang, T. Watari, Y. Tokunaga, R. Nakatani, T. Maeda, H. Matsuyama. Facilitated transport of CO_2 through supported liquid membranes of various amine solutions-effects of rate and equilibrium of reaction between CO_2 and amine. J. Chem. Eng. Jpn. 1997; 30:328– 335.

[10] T. Yamaguchi, C.A. Koval, R.D. Noble, C.N. Bowman. Transport mechanism of carbon dioxide through perfluorosulfonate ionomer membranes containing an amine carrier. Chem. Eng. Sci. 1996; 51: 4781– 4789.

[11] Z. Wang, C. Yi, Y. Zhang, J. Wang, S. Wang. CO_2-facilitated transport through poly(N-vinyl-sodium amino butyrate-co-sodium acrylate)/polysulfone composite membranes. J. Appl. Polym. Sci. 2006; 100:275–282.

[12] B.C. Tripp, K. Smith, J.G. Ferry. Carbonic anhydrase: new insights for an ancient enzyme. J. Biol. Chem. 2001;276:615–618.

[13] A.L. Crumblis, K.L. McLachlan, J.P. O'Daly, R.W. Henkens. Preparation and activity of carbonic anhydrase immobilized on porous silica beads and graphite rods. Biotech. Bioeng. 1988; 31:796–801.

[14] L.H. Bao, M.C. Trachtenberg. Modeling CO_2 facilitated transport across a diethanolamine liquid membrane. Chem. Eng. Sci. 2005; 60:6868–6875.

Bioenergy Production from the Pre-treatment of Bagasse as raw Material for Paper Making

Sneha Gupta, A.S. Reddy

School of Energy and Environment, Thapar University, Patiala 147004 (INDIA)

ABSTRACT

Bagasse is fibrous waste generated in sugar industry from sugar cane crushing. It is widely used as raw material in pulp and paper industry. Seasonal availability, limited storability and relatively higher pulping chemical consumption make bagasse a less favoured raw material for paper making. Residual sugar, extractables and high pith content in bagasse are responsible for this. Because of this reason, bagasse is mostly burnt as fuel in the cogeneration units of sugar mills. Reduction of residual sugar, extractables and pith content at source (within the sugar mills), can enhance quality and storability of bagasse and pulp chemical consumption can also be reduced.

Controlled dry digestion of fresh bagasse is believed to remove, specially, residual sugars and other extractables from bagasse, improve its storability and reduce pulping chemical requirement. Leachate generated from the dry digestion can be treated for the biogas generation. The biogas can be brunt as fuel in the cogeneration units of the sugar mills and the treated leachate can be reused in the bagasse dry digestion. In the present study, dry digestion of bagasse has been attempted and its impacts on bagasse as raw material for paper making have been studied. Further, a two stage anaerobic baffled reactor has been tried for the treatment of the leachate generated and biogas generation potential has been attempted. Material loss from the dry digestion, improvement in quality in terms of residual sugars, extractables, cellulose, hemicellulose, lignin, and biogas generation rates observed are discussed in this paper.

Anaerobic digestion of bagasse has resulted in reduction of cellulose, hemicellulose, lignin, residual sugars content upto 30.1%, 7.5%, 3.2%, 0.5% respectively.

Keywords: Bagasse, leachate, biogas, anaerobic baffled reactor.

Performance of Carbon Cloth Electrode in Mediator less Microbial Cell Applications using mixed Sewage Culture

Praveena Mishra, Himanshu Dubey

Schools of studies in Chemistry, Jiwaji University, Gwalior (M.P.) INDIA

ABSTRACT

A mediator less two chambered microbial fuel cell (MFC) setup has been prepared using carbon cloth as anode and cathode. Mixed sewage culture was used as inoculum in anodic compartment for the treatment of waste water generated from different industries of Gwalior region i.e. sewage waste water, food industry waste water, oil mil waste water, pharmaceutical company waste water and waste water generated from a hostel mess. All the waste water samples were respectively monitored for generation of energy in the form of electricity as well as for chemical oxygen demand (COD) removal efficiency. All waste water samples generate electricity out of which best results are observed for Sewage waste waster which shoes 91% COD removal efficiency while producing 1.42 mA current and 1168.5 mW Power at 7th day of inoculation. The electrochemical activity and stability of carbon cloth (CC) anode is evaluated in the light of bio-film formation, bio-fouling and biocompatibility testing. The results obtained, suggests good promises and feasibility of carbon cloth anode and our developed MFC setup for the generation of electricity while treating waste water.

Keywords: Microbial Fuel Cells, Mixed sewage culture, Carbon Cloth electrode

INTERNATIONAL JOURNAL OF CIVIL ENGINEERING AND TECHNOLOGY (IJCIET)

ISSN 0976 – 6308 (Print)
ISSN 0976 – 6316(Online)
Volume 5, Issue 7, July (2014), pp. 107-112
© IAEME: www.iaeme.com/ijciet.asp
Journal Impact Factor (2014): 7.9290 (Calculated by GISI)
www.jifactor.com

IJCIET

©IAEME

STRENGTH & DENSITY OF AN AUTOCLAVED AERATED CONCRETE USING VARIOUS AIR ENTRAINING AGENTS

Shashank Gupta[1], Shiva Garg[2]

[1, 2]Civil Engineering Department, Delhi Technological University, Delhi, India

ABSTRACT

The purpose of the present paper is to study the changes in the strength characteristics of autoclaved aerated concrete (AAC) and also the density when different expansion agents are used. The expansion agent so used releases air in the concrete thereby making it lighter by reducing its density. It also increases the workability of the concrete. The various air entraining agents used for this study are hydrogen peroxide, oleic acid and olive oil. The addition of these agents causes the concrete to rise like cake but it reduces the strength of concrete due to the formation of air voids. The amount of agents chosen for concrete production are 0.5%, 1%, 1.5% by weight of cement.

Key Words: AAC, Olive Oil, Hydrogen Peroxide, Oleic Acid, Steam Curing.

1. INTRODUCTION

In year 1923, ACC was first developed in Europe. AAC is not only best for its structural insulation property available today but also for its easy & fast installation as the material which can be cut to the desired size on the construction site. AAC is a well known environment friendly construction material. The production process of AAC does not emit any pollutants and emanates no harmful waste products. All waste products can be reused, produced during the manufacturing process.

Recently, AAC has been used as a substitute for normal concrete in various structural applications related with construction cost because of its light weight, considerably reducing the dead weight of structures and its eco-friendly nature. The density of lightweight aerated concrete plays a more important role than its strength. Lightweight aerated concrete with almost same strength reduces its self-weight as a result of decreased density [1]. Lightweight aerated concrete can easily be produced by utilizing waste material as well as natural lightweight aggregate [2]. Aerated concrete has been widely used for many years. A slurry is formed by mixing the ingredients of AAC, which are then poured into the metal moulds. The reaction between the air entraining agents and other components present in the mix results in expansion (rise) in the mould & formation of "cake". After stripping out

the mould carefully, they are then put into an autoclave, in which it is steamed cured under pressure) Then, AAC prepared can be shipped to the desired site and immediately used after autoclaving.

1.1 Research Significance

The use of air entraining agent increases workability and its resistance to abrasion, lower permeability and satisfactory chemical resistance. Structures made out of AAC are less susceptible to freezing and thawing. Also, AAC can be used to build structures in areas with high seismicity as it can absorb the shock waves and lower their amplitude. It can also be used to manufacture structures which are likely to be exposed to moderate to severe exposure conditions such as sewer structures. Addition of olive oil which is a fatty acid results in reduction in both flexural as well as compressive strength of concrete. Addition of oleic acid results in better workability at lower water cement ratios. It lubricates the cement particles and forms a mono-molecular film around it. Addition of oleic acid also reduces the absorption capacity of hardened concrete. Since, in the preparation of concrete no coarse aggregates have been used, so in order to increase the compressive strength, some amount of gypsum is added to it. Calcium carbonate is the chief component responsible for the binding of various constituents together. So to ensure that it is present in adequate amount, lime is added into the mixture. Lime also provides the necessary heat that is required for the setting of mixture into the mould. It helps in reduction of setting time of the mixture due to this additional heat liberated.

2. MATERIALS

1. Cement: OPC 43 cement was used confirming to IS :12269. The initial setting time of the cement was 35 minutes and final setting time was 360 minutes.

2. Fine-Aggregate: Locally available silica sand was taken and sieved through 300 microns and is used constantly for every experiment throughout the casting.

3. Lime: Locally available lime was taken and added 100% by weight of cement.

4. Gypsum: Locally available gypsum was taken and added 20% by weight of cement.

5. Oleic acid: It was used in 0.5% to 1.5% by weight of cement.

6. Olive acid: It was used in 0.5% to 1.5% by weight of cement.

7. Hydroden Peroxide: It was used in 0.5% to 1.5% by weight of cement.

3. EXPERIMENTAL PROCEDURE

3.1 Preparation of test specimen

All the Test specimens were cubes of size 150 x 150 x 150mm cast in moulds made of steel (Figure 1). The cubes formed were kept for a time period of 15 to 18 minutes under normal room temperature conditions and moulds were removed. They were then subjected to steam curing and then drying.

3.2 Steam curing process

The process of autoclaving is done in a steam curing chamber. After the concrete in the mould solidifies, it is put in the autoclaving chamber for 8-10 hours at a temperature of about 200ºC and 9-10 bars of pressure. At such a high temperature and pressure, the sand reacts with calcium hydroxide and produces calcium silica hydrate which gives the concrete its desired properties

International Journal of Civil Engineering and Technology (IJCIET), ISSN 0976 – 6308 (Print), ISSN 0976 – 6316(Online), Volume 5, Issue 7, July (2014), pp. 107-112 © IAEME

3.3 Process

Raw materials stated in section 2 are mixed in the desired proportion to achieve the best possible mix design as explained further. A sample of 150mm x150mm x 150mm is prepared by mixing 1 kg of cement,1 kg of lime, 200gm of gypsum and 3000gm of water. Then the mixture proportions remains constant and the air entraining agents are added to it in the proportions 0.5%,1% and 1.5% respectively. After mixing all the constituents in the desired proportion, the mould is filled up to 75 percent of the height of the mould.



Fig.1: AAC cube being made at lab using H_2O_2

With the passage of time, the concrete rises up to the top due to evolution of gas.. This happens because of the liberation of gas in the concrete which causes the concrete to rise up to the top. The fatty acids or hydrogen peroxide reacts with the oxides present in lime and cement to produce gases. As these gases increase the total volume of the concrete mix, it results in rising up of the mass. The Water/Cement ratio is kept constant for preparing each sample.



Fig.2: Porous structure of AAC

4. RESULT AND DISCUSSION

The results summarizes the compressive strength and the dry density of the autoclaved aerated concrete, prepared with the addition of three different admixtures, Hydrogen peroxide, oleic acid and

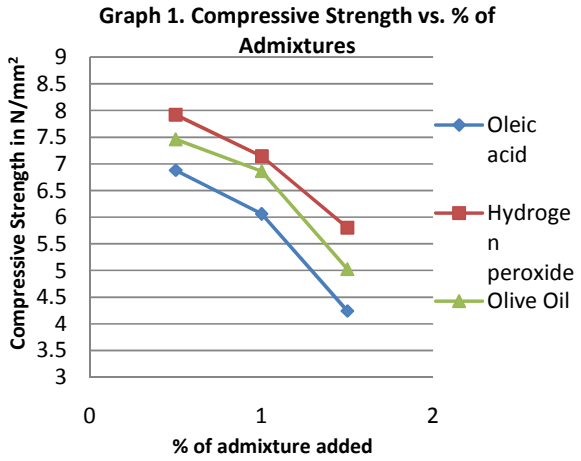
Olive oil with three different percentages as 0.5%, 1.0% and 1.5%. Based on the test result obtained and observing the graphs, the replacement of admixture reduces the dry density of the autoclaved aerated concrete but the corresponding compressive strength of the mix also get reduced. Adding the air entrained agents in the mix reduced the dry density considerably as compared to the conventional concrete. Less segregation and bleeding was also observed in addition to a better homogeneity in the autoclaved aerated concrete. The results are also plotted on the graphs showing dry density of the concrete & compressive strength at different proportions obtained shown in Table 1 & Table 2.

Table 1: Compressive strength of autoclaved aerated concrete

S.no	Type of Admixture used	% of admixture added	Compressive Strength N/mm^2
1	Oleic acid	0.5	6.88
2.	Oleic acid	1	6.06
3.	Oleic acid	1.5	4.24
4.	Hydrogen peroxide	.5	7.92
5.	Hydrogen peroxide	1	7.14
6.	Hydrogen peroxide	1.5	5.80
7.	Olive Oil	0.5	7.46
8.	Olive Oil	1	6.86
9.	Olive Oil	1.5	5.02

4.1. Compressive Strength Test Results

Table 1 summarizes the reduction in compressive strength of autoclaved aerated concrete as the percentage of replacement of the admixture was increased. The decrease of the compressive strength for all autoclaved aerated concrete can been largely after replacing the admixture from 1% to 1.5%. The observed reduction shows similar type of trends that was seen in the some of the previous research work done. The entrapped air within the concrete leading to formation of pores within, which is the reason for decrease of strength of the autoclaved aerated concrete. Based on percentage of air entrained in the concrete, the percentage of decrease of strength was observed. Further from the graph 1, the conclusion was made that hydrogen peroxide gave the maximum compressive strength as compared to the remaining agents, Olive oil and oleic acid.

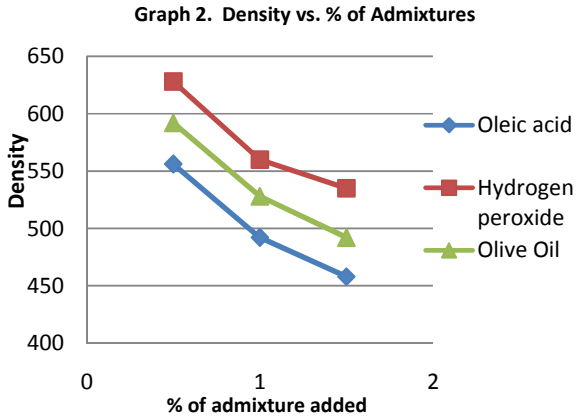


4.2 Density of Autoclaved Entrained Concrete

Table 2 summarizes the reduction in density of autoclaved aerated concrete as the percentage of replacement of admixture is increased. The observed reduction shows similar type of trends that was seen in the research work previously done, that is the reduction of density of concrete as compared to the conventional concrete. The entrapped air within the concrete leading to formation of pores within is the reason for decrease of density of the autoclaved aerated concrete. Based on percentage of entrapped air, the percentage of decrease of density was observed. Further on the table 2 and the graph 2, the conclusion was made that Oleic acid gave the best results in reduction of density as compared to other admixtures.

Table 2: Density of air entrained concrete

S.no	Type of Admixture used	% of admixture added	Dry Density (N/mm^2)
1.	Oleic acid	0.5	556
2.	Oleic acid	1	492
3.	Oleic acid	1.5	458
4.	Hydrogen peroxide	.5	628
5.	Hydrogen peroxide	1	560
6.	Hydrogen peroxide	1.5	535
7.	Olive Oil	0.5	592
8.	Olive Oil	1	528
9	Olive Oil	1.5	492



5. CONCLUSION

1). Autoclaved aerated concrete block has the low density when compared to the conventional concrete Therefore, it's use results in reduced dead weight of structure which results in overall economy.

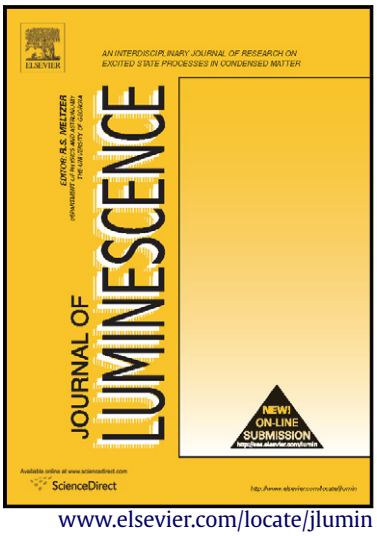
2). It has been inferred from the graph 2, Density v/s % admixture added, that oleic acid results in maximum reduction of density as compared to other air entraining agents, hydrogen peroxide and olive oil.

3). It has been inferred from the graph 1, compressive strength v/s % admixture added, that use of oleic acid results in least compressive strength in comparison to other air entraining agents, hydrogen peroxide which gives maximum compressive strength and olive oil.
4). The dry density and compressive strength of the mix reduces slowly when the admixture proportion is increased from 0% to 0.5% and then to 1%.
5). From the graph 1 & 2, it can be inferred that the dry density and compressive strength of the mix reduces gradually when the admixture proportion is increased from 1% to 1.5%.

6. REFERENCES

[1] Rossignolo, J.A., Agnesini, M.V.C. and Morais, J.A., 2003. Properties of high-performance LWAC for precast structures with Brazilian light weight aggregates. Cement and Concrete Composites 25(1), pp. 77-82.
[2] Babu, D.S., Ganesh Babu, K. and Tiong-Huan, W., 2006. Effect of polystyrene aggregate size on strength and moisture migration characteristics of lightweight concrete. Cement and Concrete Composites, 28(6): p. 520-527.
[3] Mouli, M. and Khelafi, H., 2008. Performance characteristics of lightweight aggregate concrete containing natural pozzolan. Building and Environment 43(1), pp. 31-36.
[4] Huai-Shuai Shang and Ting-Hua Yi, "Freeze-Thaw Durability of Air-Entrained Concrete", The Scientific World Journal (2013).
[5] Khedr, S., Abou-Zeid, M., and Abadir, J. "Response of Air-Entrained Concrete to Severe Chemical Aggression", American Society of Civil Engineers (2012).
[6] Ali Tugrul Albayrak, Muzaffer Yasar, M. Ali Gurkaynak and Ismet Gurgey, "Investigation of the effects of fatty acids on the compressive strength of the concrete and the grind ability of the cement", Journal of Cement and Concrete Research, Vol no 35, Issue no2, Feb 2005, pp 400-404.
[7] S. Laustsen, M.T. Hasholt, O.M. Jensen, "A new technology for air-entrainment of concrete", RILEM publications (2008), pp. 1223 –1230.
[8] Mladenovic, A., Suput, J.S., Ducman, C. and Skapin, A.S. 2004. Alkali-silica reactivity of some frequently used lightweight aggregates. Cement Concrete Research. 34(10), 1809-1816.
[9] H. Justnes, T. A. Østnor and N. Barnils Vila, "VEGETABLE OILS AS WATER REPELLENTS FOR MORTARS" https://www.tekna.no/arkiv/NB/.
[10] A. Gokce, S. Nagatak, T. Saeki and M. Hisada, "Freezing and Thawing resistance of air entrained concrete incorporating recycled aggregate: The role of air content in demolished concrete", Cement and Concrete Research (2004), pp 799 - 806.
[11] TSE,. TS EN 678 Determination of the Density of Autoclaved Aerated Concrete. (1995).
[12] Shell S. Hodgson, "The Effects of water/cement ratio and air entraining on Portland cement concrete freeze/thaw durability, Undergraduates Engineering Review (2000).
[13] Sitiradziah Abdullah, Ahmad Shayan and Riadh Al-Mahaidi, "Assessing the Mechanical Properties of Concrete Due to Alkali Silica Reaction", International Journal of Civil Engineering & Technology (IJCIET), Volume 4, Issue 1, 2013, pp. 190 - 204, ISSN Print: 0976 – 6308, ISSN Online: 0976 – 6316.
[14] Dr. V. Bhaskar Desai, A. Sathyam and S. Rameshreddy, "Some Studies on Mode-Ii Fracture of Artificial Light Weight Silica Fume Pelletized Aggregate Concrete", International Journal of Civil Engineering & Technology (IJCIET), Volume 5, Issue 2, 2014, pp. 33 - 51, ISSN Print: 0976 – 6308, ISSN Online: 0976 – 6316.
[15] Ghassan Subhi Jameel, "Study the Effect of Addition of Waste Plastic on Compressive and Tensile Strengths of Structural Lightweight Concrete Containing Broken Bricks as a coarse Aggregate", International Journal of Civil Engineering & Technology (IJCIET), Volume 4, Issue 2, 2013, pp. 415 - 432, ISSN Print: 0976 – 6308, ISSN Online: 0976 – 6316.

Author's Accepted Manuscript



www.elsevier.com/locate/jlumin

Tb^{3+} doped Zinc Alumino Bismuth Borate Glasses for Green Emitting Luminescent Devices

K. Swapna, Sk. Mahamuda, A. Srinivasa Rao, M. Jayasimhadri, Suman Shakya, G. Vijaya Prakash

PII: S0022-2313(14)00455-4
DOI: http://dx.doi.org/10.1016/j.jlumin.2014.08.019
Reference: LUMIN12832

To appear in: *Journal of Luminescence*

Received date: 19 April 2014
Revised date: 1 July 2014
Accepted date: 5 August 2014

Cite this article as: K. Swapna, Sk. Mahamuda, A. Srinivasa Rao, M. Jayasimhadri, Suman Shakya, G. Vijaya Prakash, Tb^{3+} doped Zinc Alumino Bismuth Borate Glasses for Green Emitting Luminescent Devices, *Journal of Luminescence,* http://dx.doi.org/10.1016/j.jlumin.2014.08.019

This is a PDF file of an unedited manuscript that has been accepted for publication. As a service to our customers we are providing this early version of the manuscript. The manuscript will undergo copyediting, typesetting, and review of the resulting galley proof before it is published in its final citable form. Please note that during the production process errors may be discovered which could affect the content, and all legal disclaimers that apply to the journal pertain.

ACCEPTED MANUSCRIPT

Tb^{3+} doped Zinc Alumino Bismuth Borate Glasses for Green Emitting Luminescent Devices

K. Swapna[1], Sk. Mahamuda[1], A. Srinivasa Rao*[1, 2], M. Jayasimhadri[2], Suman Shakya[3] and G. Vijaya Prakash[3]

[1]Department of Physics, K L University, Green Fields, Vaddeswaram-522 502, Guntur (Dt). A P, India
[2]Department of Applied Physics, Delhi Technological University, Bawana Road, New Delhi-110 042, India
[3]Nanophotonics Laboratory, Department of Physics, Indian Institute of Technology-Delhi, Kauz Khas, New Delhi-110016, India.
Corresponding author, E-mail: drsrallam@gmail.com, Tel: +91 85860 39007, Fax: +91 01127871023.

Abstract

Zinc Alumino Bismuth Borate (ZnAlBiB) glasses doped with Terbium (Tb^{3+}) ions with a chemical composition $20ZnO\text{-}10Al_2O_3\text{-}(10\text{-}x)Bi_2O_3\text{-}60B_2O_3\text{-}xTb_2O_3$ (x=0.1, 0.5, 1.0, 1.5, 2.0,2.5 and 3 mol %) were prepared by conventional melt quenching method and studied their optical absorption, photoluminescence and decay spectral properties. The Judd-Ofelt (J-O) parameters evaluated from the experimental oscillator strengths were used to measure the radiative properties for the prominent luminescent transitions of Tb^{3+} ions such as $^5D_4 \rightarrow {}^7F_6$, $^7F_5$, $^7F_4$ and $^7F_3$. The effect of Tb^{3+} ion concentration on the luminescence process observed in the visible region was discussed in detail. The emission spectra recorded for all the ZnAlBiB glasses doped with Tb^{3+} ions, show an intense peak in green region at 542 nm. The stimulated emission cross-section, branching ratios and quantum efficiency values evaluated for green emission ($^5D_4 \rightarrow {}^7F_5$) suggests the utility of these glasses for green luminescence applications. It was found that, within the concentration range investigated, 2.5 mol% of Tb^{3+} doped ZnAlBiB glass is most suitable for green luminescence applications at 542 nm in principle.

Accepted manuscript

ACCEPTED MANUSCRIPT

1. Introduction:

Recently transition metal (TM) and rare earth (RE) ions doped materials have attracted researchers because of their novel characteristic futures such as memory and photo conducting properties [1-3]. Quite recently RE ions have attracted great deal of attention because of their efficient visible emission transitions observed within the 4f shell, which are insensitive to the effect of surroundings because of the shielding effect of outer 5s, 5p electrons [4-8]. Due to this reason, the RE doped materials have been used as fluorescent materials and have been found to be utilized for lightening devices [9-11]. Quite recently, Light Emitting Diodes (LEDs) are emerging as one the important class of lighting devices, which are capable to replace the ordinary conventional lighting sources like incandescent bulbs and fluorescent lamps [10,12-13] . These luminescent materials possess many attractive characteristics futures such as longer lifetime, lower fabrication cost, higher reliability, lower energy consumption and environmental friendliness over the conventional light sources [14, 15]. In addition to the above, Rare earth doped glasses are promising materials for active displays and attractive as potential lasers, optical fibers and phosphors due to their transparency, easy shaping and cost effective properties. To develop highly efficient luminescent optical devices doped with rare earth ions, a host glass must possesses phonon energies as low as possible. Among various oxides, B_2O_3 besides being a good glass former can form glass alone with superior qualities such as good transparency and chemical durability. Another interesting property of borate glasses is that, it can accommodate the doped rare earth ions even at higher concentrations. But the stretching vibrations of network forming oxides in borate glasses have large phonon energies and they reduce the probabilities of radiative process. Consequently luminescent efficiency of borate glassy systems falls down drastically. In order to reduce the magnitudes of phonon energies possessed by borate glasses, they are added with heavy metal oxides (HMO) such as Bi_2O_3. Similarly, incorporation of Al_2O_3 in borate glasses can modifies the basic structural network units causing a change of co-ordination from BO_3 to BO_4 units [16]. Moreover addition of Al_2O_3 to a borate glass network can increase its chemical durability by increasing its glass transition temperature and decreasing its thermal expansion coefficient [17, 18]. It is also reported in literature that Al^{3+} ions can occupy both tetrahedral and octahedral sites in a glass and improves the optical response of the materials [19- 21]. Addition of ZnO to a borate glass can improve its physical, chemical stability and higher transparency from UV to mid-IR. The

Accepted manuscript

ACCEPTED MANUSCRIPT

detail description of the additive compositions like Bi_2O_3, Al_2O_3 and ZnO to a borate glasses were also explained in detailed in our previous publications [11-12, 22].

Among various rare earth ions, the trivalent terbium (Tb^{3+}) has gained lot of interest due to its strong luminescence originating from $^5D_4 \rightarrow {}^7F_5$ transitions at 542 nm (i.e., green emission), whose emission intensity purely depends on doping ion concentration, composition of the host material and on the excitation wavelength [23]. Moreover, as human eye is more sensitive to green color, a signal in green region would be better detected. The luminescence property of Tb^{3+} ions in a material is quite useful in determining the energy level structure and in characterizing the transitions involved in the material. Hence, Tb^{3+} doped glasses have been used in the development of electromagnetic transmission window of sea water, efficient green emitting phosphors, solid state lasers, white LEDs, neutron detection and medical devices [24-27]. Tb^{3+} ions will have blue and green emission in which green luminescence dominates the other one. Pondering on all the aforementioned applications and considering the scientific patronages offered by the chemical constituents such as B_2O_3, Bi_2O_3, Al_2O_3 and ZnO, we prepared a germane glassy system namely Zinc Alumino Bismuth Borate (ZnAlBiB) glass doped with Tb^{3+} ions at different concentrations. The aim of the present work is to study the green emission of ZnAlBiB glasses as a function of Tb^{3+} ion concentration for better luminescence performance.

2. Experimental methods:

ZnAlBiB glasses doped with Tb^{3+} ions with chemical composition $20ZnO\text{-}10Al_2O_3\text{-}(10\text{-}x)$ $Bi_2O_3\text{-}60$ $B_2O_3\text{-}xTb_2O_3$ (where x=0.1, 0.5, 1.0, 1.5, 2.0, 2.5 and 3 mol %) were prepared by using melt quenching method. Depending on Tb^{3+} dopant ion concentration from 0.1 to 3 mol% these glasses are designated as ZnAlBiBTb0.1, ZnAlBiBTb0.5, ZnAlBiBTb1.0, ZnAlBiBTb1.5, ZnAlBiBTb2.0, ZnAlBiBTb2.5 and ZnAlBiBTb3 respectively. About 10 g batches of the analytical grade samples measured as per the above chemical composition were weighed and mixed thoroughly in an agate motor, until smooth powders are obtained. Such powders were then placed in an aluminum crucible and melted at 1200^0C for 40 min. When the melting process was completed, then the liquid was air quenched in between two brass plates. The glasses so prepared were annealed at 400^0C for one hour in order to make them free from thermal strains produced inside the glasses during the quenching process. Finally, the annealed glass samples were cut and polished before taking spectral measurements. The density of the glass samples were measured by using the Archimedes' principle with distilled water as an immersion liquid. Refractive indices for the prepared

Accepted manuscript

ACCEPTED MANUSCRIPT

glasses were measured with the help of He-Ne laser (λ= 650 nm) using Brewster's method with an accuracy ± 0.01. The optical absorption spectra for the prepared glasses were recorded using JASCO V-670 UV-vis-NIR spectrophotometer in the range 400-2400 nm. Shimadzu RF-5301 PC spectrofluorophotometer is used to record the excitation and emission spectra. The steady-state and time-resolved photoluminescence (PL) measurements were carried out using home-built setups with 337 nm (N2 gas) laser as the excitation sources. The emission was dispersed into a monochromator (Acton) coupled to a photo multiplier tube (PMT) through the appropriate lenses and filters. For time-resolved photoluminescence, a function generator (12 Hz), lock-in amplifier and digital storage oscilloscope were employed. All the aforementioned measurements were performed at room temperature.

3. Result and Discussion

3.1 Physical properties of the ZnAlBiB Glasses:

Measurements of physical properties of glassy materials are important as they can play a major role in deciding the optical properties. Density gives information such as degree of structural compactness, geometrical configuration modification, coordination and the dimension of interstitial space in the glass network. Density and refractive index for the present glasses were measured using the standard procedure as outlined in the previous section are given in Table 1. Based on density, refractive index and Tb^{3+} ion concentration present in ZnAlBiB glasses, various other physical properties were calculated using the expressions given in our earlier paper [28] and are given in Table 1. Fig. 1(a) shows the variation of density and average molecular weight of the titled glasses with Tb^{3+} ion concentration. From Fig.1 (a), it can be observed that the density and average molecular weight of the titled glasses are decreasing with increasing the Tb^{3+} ions concentration. This may be due to decrease in the heavy metal oxide (Bi_2O_3) content in the glass network. Decrease in density of the titled glasses indicates the increase in the compactness of the glass by increasing the number of bridging oxygen. This leads to increase in the rigidity of the prepared glasses. Fig. 1(b) shows the variation of interionic distance and field strength with increase in the concentration of Tb^{3+} ions in the titled glasses. From Fig. 1(b), it can be observed that the interionic distance decreases with increase in Tb^{3+} ion concentration. This may be due to the enhanced compactness with increase in Tb^{3+} ion concentration and decrease in the distance between rare earth ion and oxygen. As a result of this, the bond strength between rare earth ion and oxygen increases, producing more field strengths around

Accepted manuscript

ACCEPTED MANUSCRIPT

the rare earth ion with concentration as seen from Fig.1 (b). The optical basicity values for the present glasses are increasing with increase in the concentration of Tb^{3+} ions indicates the increasing the negative charge on the oxygen atom and thus increasing covalency of the cation in the oxygen atom bonding. The understanding of the optical basicity would be useful for the design of novel optical functional materials with higher optical performance.

3.2 Analysis of Absorption spectral data and J-O parameters

The absorption spectrum of ZnAlBiB glass doped with 2.5 mol % Tb^{3+} ions recorded at room temperature is shown in Fig 2. All the absorption transitions shown in Fig. 2 are observed from $^7F_6$ ground state of Tb^{3+} ions. Four absorption bands were observed in the spectrum, representing manifolds of $^5D_4$, $^7F_1$, $^7F_2$ and $^7F_3$ corresponding to 485, 1894, 1953 and 2210 nm respectively. All the absorption transitions observed are from the induced electric dipole interactions originated according to the selection rules $\Delta S=0$, $|\Delta L| \leq 6$, $|\Delta J| \leq 6$ [7]. From Fig. 2 it can be observed that, Tb^{3+} ion in ZnAlBiB glasses show weak absorption in UV/ blue region because of the forbidden nature of 4f-4f transitions [29]. From the spectral futures of the absorption spectra, the band intensities expressed in terms of oscillator strength (f_{exp}) are calculated using the expression given in our previous paper [11]. By applying the Judd-Ofelt (J-O) theory [6, 7] to the measured oscillator strengths, the J-O parameters were evaluated using the least square fitting procedure and are given in Table 2. Host invariant square reduced matrix elements necessary for the fitting were collected from literature [30]. The J-O intensity parameters (Ω_λ) are important to know the effect of host glass on the emission characteristics of doped rare earth ions because; it consists of crystal field parameters, interconfigurational radial integrals and interaction of central metal ions with the surrounding environment [31]. As shown in Table 2, the J-O parameters follows the same trend ($\Omega_4 > \Omega_2 > \Omega_6$) in all the ZnAlBiB glasses. In general, the Ω_2 J-O parameter is used to find the structural changes produced in the vicinity of Tb^{3+} ions and the covalency existing between rare earth ions and oxygen atoms. Relatively lower values observed for Ω_2 J-O parameter indicates weak field strength around the RE ions and larger distance between RE and oxygen [32]. Lesser the value of Ω_2, the more Centro symmetrical the ion site and the more ionic its chemical bond with the ligands [33]. The extreme small value of Ω_2 might be due to the lower ligand polarizability [34]. The J-O parameters Ω_4 and Ω_6 are useful to know the information related to the long range effects and bulk properties such as viscosity and rigidity of the medium [35, 36]. The J-O parameters of Tb^{3+} ions activated in different hosts are also listed in Table 2. From Table 2, it is clear that the Ω_4 parameter varies significantly

Accepted manuscript

ACCEPTED MANUSCRIPT

in different hosts while Ω_2 and Ω_6 values changes within a reasonable range in different hosts [37-39].

3.3 Analysis of Excitation, Emission spectra and Radiative properties

Fig. 3 shows the excitation spectra of Tb^{3+} ions doped ZnAlBiB glasses recorded by fixing the emission wavelength (λ_{em}) at 542 nm. As shown in Fig.3, the excitation spectra of all the ZnAlBiB glasses show bands at 351, 368, 377 and 485 nm corresponding to the transitions $^7F_6 \rightarrow {}^5L_9$, $^5L_{10}$, $^5G_6$ and $^5D_4$ respectively. From the excitation spectra, it can be observed that, the transition $^7F_6 \rightarrow {}^5G_6$ at 377 nm is highly intense than the other transitions. Its intensity is increasing along with the concentration of Tb^{3+} ions up to 2.5 mol% of Tb^{3+} and then decreasing in the titled glasses. Fig. 4 shows the emission spectra recorded for all the titled glasses fixing the excitation wavelength at 377 nm. Normally, Tb^{3+} ions doped materials exhibit strong luminescence bands in blue ($^5D_3 \rightarrow {}^7F_4$) and green ($^5D_4 \rightarrow {}^7F_5$) spectral regions. In Tb^{3+} ions doped glass hosts, the emission below 480 nm originate from $^5D_3$ level and the emission above 480 nm originate from $^5D_4$ levels. Small energy gap existing between $^5D_4$ and $^5D_3$ (5618 cm^{-1}) emission levels causes a non-radiative decay and increases the population of $^5D_4$ level at higher concentration of Tb^{3+} ions resulting increasing intensity of that level. From Fig.4, it can be observed that, the emissions from $^5D_3$ excited state are less in intensity in all the titled glasses. Such less intensity observed for $^5D_3$ emission transition, indicates pronounced energy transfer through non-radiative relaxation to the lowest $^5D_4$ excited levels. Under non-radiative relaxation process, two mechanisms namely cross-relaxation and multi phonon relaxation may be responsible for the increase in the population of $^5D_4$ level [40, 41]. As shown in Fig.4, the emission spectra in all the ZnAlBiB glasses, gives four luminescence bands centered at 488, 542, 584 and 622 nm corresponding to the transitions $^5D_4 \rightarrow {}^7F_J$ (J=6, 5, 4, 3) in weak blue, strong green, weak yellow and red regions respectively. The weak blue emission at 488 nm corresponding to the transitions $^5D_4 \rightarrow {}^7F_6$ obeys the magnetic dipole transition selection rule of $\Delta J = \pm 1$ [42, 43]. Laporte-forbidden transition $^5D_4 \rightarrow {}^7F_5$ observed at 542 nm gives very intense green emission [44]. The green emission band ($^5D_4 \rightarrow {}^7F_5$) splits into two peaks indicating the glassy network has distortion effect on Tb^{3+} leading to the stark split of energy level.

On the other hand, with increase in Tb^{3+} ion concentration, in the titled glasses the intensity of both $^5D_4$ and $^5D_3$ emission transitions increases continuously up to 2.5 mol% of Tb^{3+} and beyond decreases. Fig.5 shows the partial energy level diagram of 2.5 mol% of Tb^{3+} ions in

Accepted manuscript

ACCEPTED MANUSCRIPT

ZnAlBiB glasses. From Fig. 5, it can be observed that the energy gaps existing between $^7F_0$ to $^7F_6$ and $^5D_3$ to $^5D_4$ match well with each other. Similarly the energy gaps between $^5D_3$ to $^7F_0$ and $^7F_6$ to $^5D_4$ match well with each other. Excitation from $^7F_6$ to $^7F_0$ level can promote a non-radiative energy transfer from $^5D_3$ to $^5D_4$ level and on the other hand, an emission transition from $^5D_3$ to $^7F_0$ level can induce a non-radiative energy transfer from $^7F_6$ to $^5D_4$. Because of these two non-radiative cross-relaxations channels shown in Fig. 5, the population of $^5D_4$ levels of Tb^{3+} ion increases continuously and hence the intensity of green emission predominates over blue emission. The probability for the above mentioned cross relaxation process to happen strongly dependent on the distance of separation between the Tb^{3+} ions. An increase in Tb^{3+} ion concentration in the present glasses reduces the distance of separation between the Tb^{3+} ions and this gradually enhances the population of $^5D_4$ level increasing the green emission than blue [45]. From the emission spectra shown in Fig.4, it can also be observed that, the intensity of all peaks originated from $^5D_4$ emission state increases with increase up to 2.5 mol% of Tb^{3+} ion concentration and then decreasing beyond showing concentration quenching. In general for Tb^{3+} green emission, concentration quenching is observed at rarely higher concentration of the dopant ion under intense excitation due to cooperative up conversion mechanism [46, 47]. Fig. 6(a) shows variation of blue ($^5D_3 \rightarrow {}^7F_4$) and green ($^5D_4 \rightarrow {}^7F_5$) emission intensities with Tb^{3+} ion concentration in the titled glasses. Fig. 6(b) shows the relative intensity variation of green to blue emission (I_G/I_B) with Tb^{3+} ions concentration in ZnAlBiB glasses. In both the figures, the increase in intensity is slow in the beginning followed by a rapid increase and again exhibiting a slow increase at higher concentration of Tb^{3+} ions. This trend at higher concentration of the doped rare earth ion shows that the green and blue emissions have reached to the quenching stage at 2.5 mol% and beyond decreases. Therefore 2.5 mol% of Tb^{3+} ions is the optimum concentration for both blue and green emissions in these ZnAlBiB glasses.

The radiative parameters such as transition probability (A_R), total transition probability ($A_{T,}$), radiative lifetime (τ_R), radiative and experimental Branching ratios (β_R, β_{exp}), stimulated emission cross-sections (σ_{se}) have been evaluated by coupling J-O parameters with the emission spectral data. These values are given in Tables 3-5. The necessary equations to calculate the above said properties were collected from our previous paper [12]. From Table 3, it is observed that, A_R, A_T, β_R and β_{exp} values increases with the increase in Tb^{3+} ion concentration and found to be maximum for ZnAlBiBTb2.5 glass. For this glass, the experimental and radiative branching ratios are (β_{exp} & β_R) $\geq$ 0.50 for $^5D_4 \rightarrow {}^7F_5$ transition

Accepted manuscript

speaks about the lasing potentiality of that transition. Branching ratio is another important parameter considered by the laser designers as it decides the potential of stimulated emission [37]. From the data presented in Table 3, it is suggested that ZnAlBiBTb2.5 glass can be suggested to act as a good visible green laser. The stimulated emission cross-section (σ_{se}), gain band width ($\sigma_{se} \times \Delta\lambda_P$), optical gain parameters ($\sigma_{se} \times \tau_R$) were evaluated in order to estimate the intensity of probable laser transitions and are given in Table 4. From the Table 4, it is observed that, among all the transitions, $^5D_4 \rightarrow {}^7F_5$ transition possesses maximum stimulated emission cross-section (σ_{se}), gain band width (σ_{se} X $\Delta\lambda_P$) and optical gain parameters (σ_{se} X τ_R) values for ZnAlBiBTb2.5 glass. Hence ZnAlBiBTb2.5 glasses can be suggested as a suitable host to produce efficient green luminescence at 542 nm. Among the seven glasses studies here, the ZnAlBiBTb2.5 glass with its intense green emission at 542 nm can also be efficiently used as a fluorescence probe in the study of biological systems.

3.4 Fluorescence Decay Analysis

It is well know that the decay curves give information pertaining to measured lifetimes of an excited state of an active RE ion in any host material. Especially for Tb^{3+} doped materials, such decay measurements are highly useful to get a comprehensive idea regarding the energy transfer mechanisms involved in the emission process. The decay profiles recorded for the prominent green emission transition $^5D_4 \rightarrow {}^7F_5$ (at 542 nm) of Tb^{3+} ions in ZnAlBiB glasses under 337 nm excitation are shown in Fig. 7 (a). From Fig.7 (a), it is observed that, the decay curves for all ZnAlBiB glasses are single exponential in nature. From such decay curves, the measured lifetimes can be evaluated using the equation $I(t) = I_0 \exp(-\tau_m/\tau_0)$, Where I_0 is constant, I(t) is emission intensity, τ_m is the measured lifetime and τ_0 is the intrinsic donor lifetime [48]. Table 5 gives the measured lifetimes values obtained for all the ZnAlBiB glasses along with radiative decay times (τ_R). From Table 5, it can be observed that, the measured lifetimes for the present glasses are decreasing with increase in concentration of Tb^{3+} ions. This decrease in the measured lifetimes with increasing Tb^{3+} ion concentration can be attributed to resonance energy transfer through cross-relaxation mechanism as shown in the energy level diagram (Fig. 5). Quantum efficiency (η) is another important characteristic parameter for lasers to predict efficiency of a laser media [49]. It is usually defined as the ratio of the number of photons emitted to the number of photons absorbed. Such quantum efficiency values measured for all the ZnAlBiB glasses are also given in Table 5. As shown in Table 5, the quantum efficiency values observed for Tb^{3+} doped ZnAlBiB glasses are comparable to the other reported values [37, 50-52]. The variation of measured lifetime and quantum efficiency with Tb^{3+} ion concentration in the titled glasses are shown in Fig.7 (b).

Accepted manuscript

ACCEPTED MANUSCRIPT

Especially, at higher concentration of Tb^{3+} ions, the efficiency is more as evidenced from Table 5 and Fig. 7(b). Relatively higher quantum efficiency (89 %) value observed for the $^5D_4 \rightarrow {}^7F_5$ laser transition of ZnAlBiBTb2.5 glass indicates its suitability for green luminescence applications at 542 nm.

3.5 CIE chromaticity coordinates:

The visible luminescence properties of the glasses can also be evaluated by the International Commission on Illumination (CIE) chromaticity diagrams drawn from the emission spectral futures. The CIE coordinates calculated for all the ZnAlBiB glasses under investigation falls in green region. Among all the ZnAlBiB glasses, the color emitted by ZnAlBiBTb2.5 glass exactly falls in bright green region. Fig.8 shows the chromaticity coordinates calculated for ZnAlBiB2.5 glass. Therefore with in the concentration range studies, ZnAlBiBTb2.5 glass is more suitable to emit bright green luminescence at 542 nm.

4. **Conclusion**

In the present investigation we have successfully prepared Zinc Alumino Bismuth Borate (ZnAlBiB) glasses doped Tb^{3+} ions at different concentrations by using conventional melt quenching technique. The J-O parameters evaluated from the oscillator strengths of the absorption spectral futures are following the same trend ($\Omega_4 > \Omega_2 > \Omega_6$) in all the glasses and are used to calculate the radiative properties such as transition probability, total transition probability, branching ratio, radiative lifetimes and stimulated emission cross-sections. The photoluminescence spectra recorded for all the ZnAlBiB glasses have shown blue and green emissions from $^5D_3$ and $^5D_4$ states respectively. The intensities of both blue and green emissions increase continuously up to 2.5 mol% of Tb^{3+} ion concentration and beyond decreases. The continuous increase in intensity of green emission up to 2.5 mol% of Tb^{3+} ions has been attributed to the non-radiative cross-relaxation process. The decrease in the measured lifetimes with increasing Tb^{3+} ion concentration is attributed to resonance energy transfer through cross-relaxation mechanism. Based on the emission spectra, stimulated emission cross-section, branching ratios and quantum efficiency values evaluated for the green emission ($^5D_4 \rightarrow {}^7F_5$) for all the glasses suggests the feasibility of using these materials for green luminescence. The CIE chromaticity coordinates evaluated from the emission spectra also confirms the same thing. Within the concentration range studies, ZnAlBiBTb2.5 glass is found to have the highest values of branching ratio, stimulated emission cross-section

Accepted manuscript

ACCEPTED MANUSCRIPT

and quantum efficiency for the $^5D_4 \rightarrow {}^7F_5$ green emission transition. Hence this glass is found to be a potential candidate for green luminescence applications at 542 nm in principle.

Acknowledgements

Two of the authors, **Swapna Koneru (**File No: SR/WOS-A/PS-35/2011) and **Mahamuda Shaik** (File No: SR/WOS-A/PS-53/2011) are highly grateful to the Department of Science and Technology (DST), Govt. of India, New Delhi, for providing financial assistance in the form of women scientist scheme(WOS-A) to carry out their research work. This work is also partly supported by High-impact Research initiative of IIT-Delhi, UK-India Education Research Initiative (UKIERI) and DST, Govt. of India, New Delhi.

References:

[1] R. Rama Kumar, A. S. Rao, B. C. Venkata Reddy, Opt. Mater 4(6) (1995)723.

[2] A. Srinivasa Rao, J. Lakshmana Rao, R. Ramakrishna Reddy, T.V. Ramakrishna Rao, Opt.Mater.4(6),(1995) 717.

[3] M.Srinivasulu, A.S.Rao, J.Mater.Sci.Lett. 20(2001)737.

[4] Sk.Mahamuda, K.Swapna, M.Venkateswarlu, A.Srinivasa Rao, Suman Shakya, G.Vijaya Prakash, J.Lumin. 154(2014) 410.

[5] Sk.Mahamuda, K.Swapna, P.Packiyaraj, A.Srinivasa Rao, G.Vijaya Prakash, Opt.Mater. 36(2013) 362.

[6] B. R. Judd, Phys. Rev. 127 (1962) 750.

[7] G. S. Ofelt, J. Chem. Phys. 37 (1962) 511.

[8] Sk.Mahamuda, K.Swapna, A.Srinivasa Rao, M.Jayasimhadri, T.Sasikala, K.Pavani, L.Rama Moorthy, J.Phys.Chem. Solids 74 (2013) 1308.

[9] S.A. Saleem, B.C. Jamalaiah, M. Jayasimhadri, A. Srinivasa Rao, Kiwan Jang, L. Rama Moorthy, J. Quant. Spect. Radiat. Trans. 112 (2011)78.

[10] Sk. Mahamuda, K. Swapna, P. Packiyaraj, A. Srinivasa Rao, G. Vijaya Prakash,. J. Lumin.153 (2014) 382

[11] Sk. Mahamuda, K. Swapna, A. Srinvasa Rao, T. Sasi Kala, L. Rama Moorthy, Physica B 428 (2013) 36.

[12] K. Swapna, Sk. Mahamuda, A. Srinivasa Rao, M. Jayasimhadri, T. Sasikala, L. Rama Moorthy, J. Lumin 139 (2013) 119.

[13] K. Swapna, Sk. Mahamuda, A. Srinivasa Rao, , T. Sasikala, L. Rama Moorthy,.

Accepted manuscript

ACCEPTED MANUSCRIPT

J. Lumin. 146 (2014) 288

[14] Y. Q. Li, J. E. J. Van steen, J. W. H. Van kervel, G. Botty, A. C. A. Delsing, F.J. DiSalvo, G. de With, H.T. Hintzen , J. Alloys. Compd. 417 (2006) 273.

[15] X. Y. Sun, J. H. Zhang, X. Zhang, Y. S. Luo, X. J. Wang, J. Rare Earths 26 (2008) 421.

[16] C. Hirayama, J. Am. Ceram. Soc. 45 (1962) 288.

[17] A.B. Corradi, V. Cannillo, M. Montorsi, C. Siligardi, J. Mater. Sci. 41 (2006) 2811.

[18] M. Srinivasa Reddy, G. Naga Raju, G. Nagarjuna, N. Veeraiah, J. Alloys. Comp. 438 (2007) 41.

[19] S. R. Elliott section 3, Essex 1984 p. 53.

[20] K. Arai, H. Namikawa, K. Kumata, T. Honda, Y. Ishii, T. Handa, J. Appl. Mat. 59 (1986) 3430.

[21] S. Tanabe, J. Non. Cryst. Solids 259 (199) 1.

[22] K. Swapna ,Sk. Mahamuda, A. Srinivasa rao, S. Shakya, T. Sasikala, D. Haranath, G. Vijaya Prakash, Spectrochim Acta Part A 25 (2014) 53.

[23] Chengkui Zu, Yanhang Wang, Jiang Chen, Bin Han, Haizheng Tao, J.Non. Cryst. Solids 357 (2011) 2435.

[24] T. Welker, J. Lumin 48- 49 (1991) 49.

[25] A. Vedda, M. Martini, M. Nikl, E. Mihokona, E. Nitsch, N. Solovieva, J. Phys. Condens. Mater 14 (2002) 7417.

[26] Goldberg DJ, Dermatol Surg 25 (1999) 463.

[27] S. Baccaro, R. Dall'Igna, P. Fabeni, M. Martini, J.A. Mares, F. Meinardi, M. Nikl, K. Nitsch, G.P. Pazzi, P. Polato, C. Susini, A. Vedda, G. Zanella, R. Zannoni, J. Lumin. 87- 89, (2000) 673.

[28] A. S. Rao, Y. N. Ahammed, R. R. Reddy , T. V. R. Rao, Opt. Mater 10 (1998) 245.

[29] Jiajia Zhou, Yu Teng, Song Ye, Yixi Zhuang, Jianrong Qiu, chemical physics letters, 486 (2010) 116.

[30] W.T. Carnall , H. Crosswhite, H.M Crosswhite, Report Argonne National Laboratory, 1997.

[31] Dhira K. Sardar, Kelly L Nash, Raylon M, Yow , Johm B. Gruber, Uygun V. Vallev, Edvard P. Kokanyan, J. Appl. Phys 100, 083108 (2006).

[32] S.V.G.V.A Prasad, M. Srinivasa Reddy, V. Ravi Kumar, N. Veeraiah, J. Lumin.127 (2007) 637.

[33] S. Shanmuga sundari, K. Marimuthu, M. Sivraman, S. Surendra Babu, J. Lumin. 130

Accepted manuscript

ACCEPTED MANUSCRIPT

(2010) 1313.

[34] H. Ebendorff-Heideprien, D. Ehrt, J. Non-Cryt . Solids 248(1999) 247.

[35] R. D. Peacock, Struct. Bond 22 (1975) 83.

[36] W. F. Krupke, Phys. Rev. 145 (1966) 325.

[37] D. Umamaheswari, B.C. Jamalaiah, T. Sasikala, T. Chengaiah, Il-Gon Kim, L. Rama Moorthy, J. Lumin. 132 (2012) 1166.

[38] V. Aruna. S. Buddhudu, Spectral properties of Tb^{3+}: B_2O_3–P_2O_5–R_2SO_4 glasses, Mater. Lett. 36 (1998) 24.

[39] M.J. Weber*,* T.E. Varitimos*,* and B.H. Matsinger*,* Phys. Rev. B. 8, (1973) 47

[40] S. Chang, H.J. Liu, Y.C. Li, Y.L. Chai, Y.Y. Tsai, Journal of Solid. State Chem.180 (2007) 3076.

[41] F.S. Kao, Teng-Ming Chen, J. Lumin. 96 (2002) 261.

[42] Hjk V. Aruna, S. Buddhudu, Mater. Lett. 36 (1998) 24.

[43] H. X. Zhang, S. Buddhudu, C. H. Kam, Y. Zhou, Y.L. Lam, K. S. Wong, B.S. Ooi, S. L. Ng, W.X. Que, Mater-chem. Phys. 68 (2001) 31.

[44] C. H. Kam, S. Buddhu, Phys. B 344 (2004) 182.

[45] Choafeng Zhu, Yiaoluan Liang, Yunxa Yang, Guorong chan , J. Lumin 130 (2010)74.

[46] M. Yamane, Y. Ashara, Cambridge University press 2000.

[47] Y.Y. Choi, K.S. Sohn, H.D. Park, S.Y. Choi, J. Mater. Res. 16 (2001) 881.

[48] L. Huang, X. Wang, H. Lin, X. Liu, J. Alloys. Comp 316 (2001) 256.

[49] Vineet Kumar Rai, S. B. Rai, J. Solid State. Commun 132 (2004) 647.

[50] A. D. Sontakke, K. Biswar, K. Annapurna, J. Lumin. 129 (2009) 1347.

[51] B. C. Jamalaiah, M. V. V. Kumar, K. R. Gopal, Physica B 406 (2011) 2871.

[52] L. Zhang, M. Peng, G. Dong, J. Qiu, Opt. Mater 34 (2012) 1202.

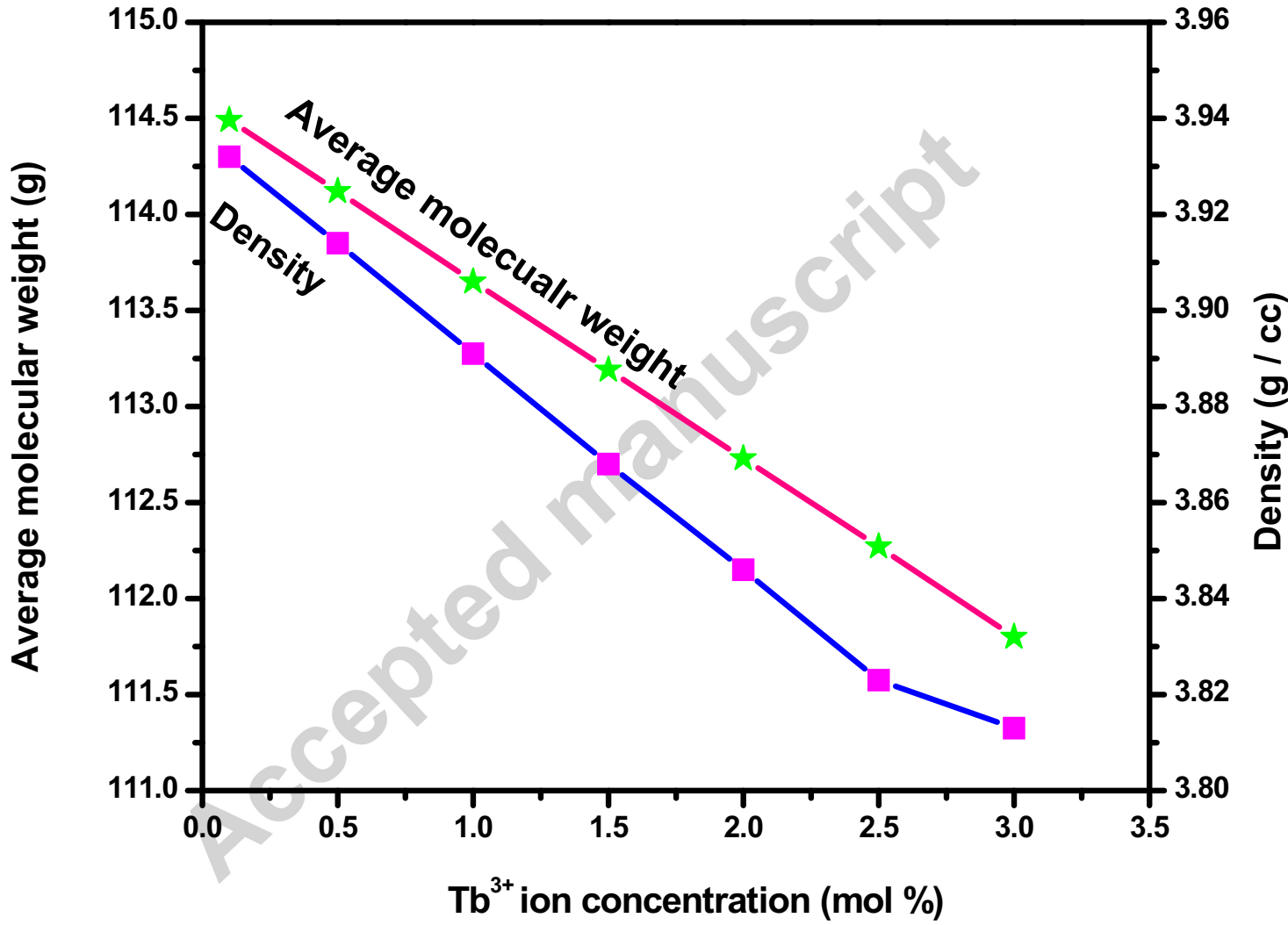
Accepted manuscript

High lights

- ZnAlBiB glasses doped with Tb^{3+} ions were prepared by conventional melt quenching technique.
- Judd- Ofelt and Radiative properties are measured from the Emission spectra.

ACCEPTED MANUSCRIPT

- Quantum efficiency of the ZnAlBiB glasses is measured by using radiative and measured lifetimes.
- CIE Chromaticity co-ordinates are evaluated from emission spectra.



Accepted manuscript

Fig. 1 (a): Variation of Density and Average molecular weight as a function of Tb^{3+} ion concentration in ZnAlBiB glasses.

ACCEPTED MANUSCRIPT

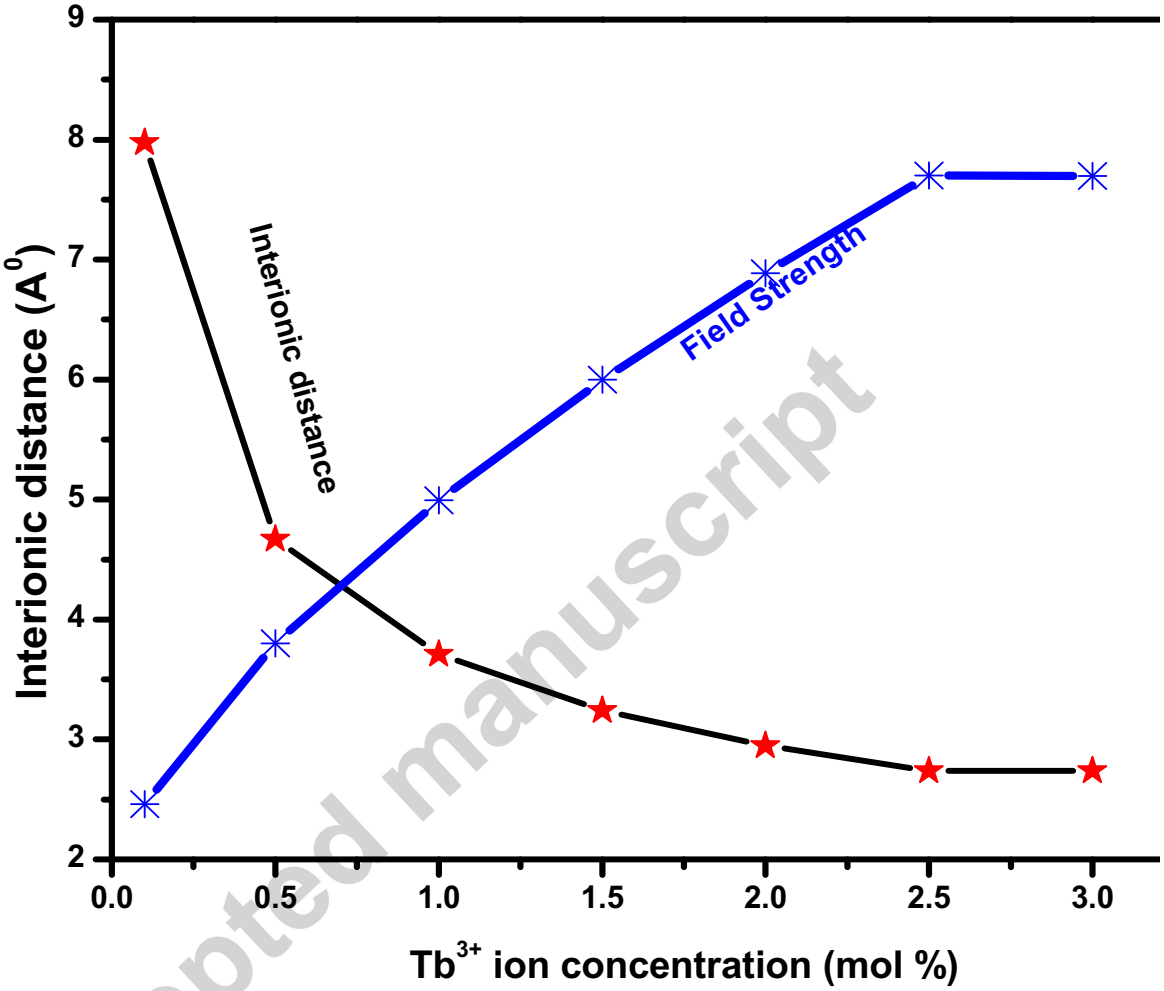


Fig. 1(b): Variation of Interionic distance and filed strength as a function of Tb^{3+} ion concentration in ZnAlBiB glasses

Accepted manuscript

ACCEPTED MANUSCRIPT

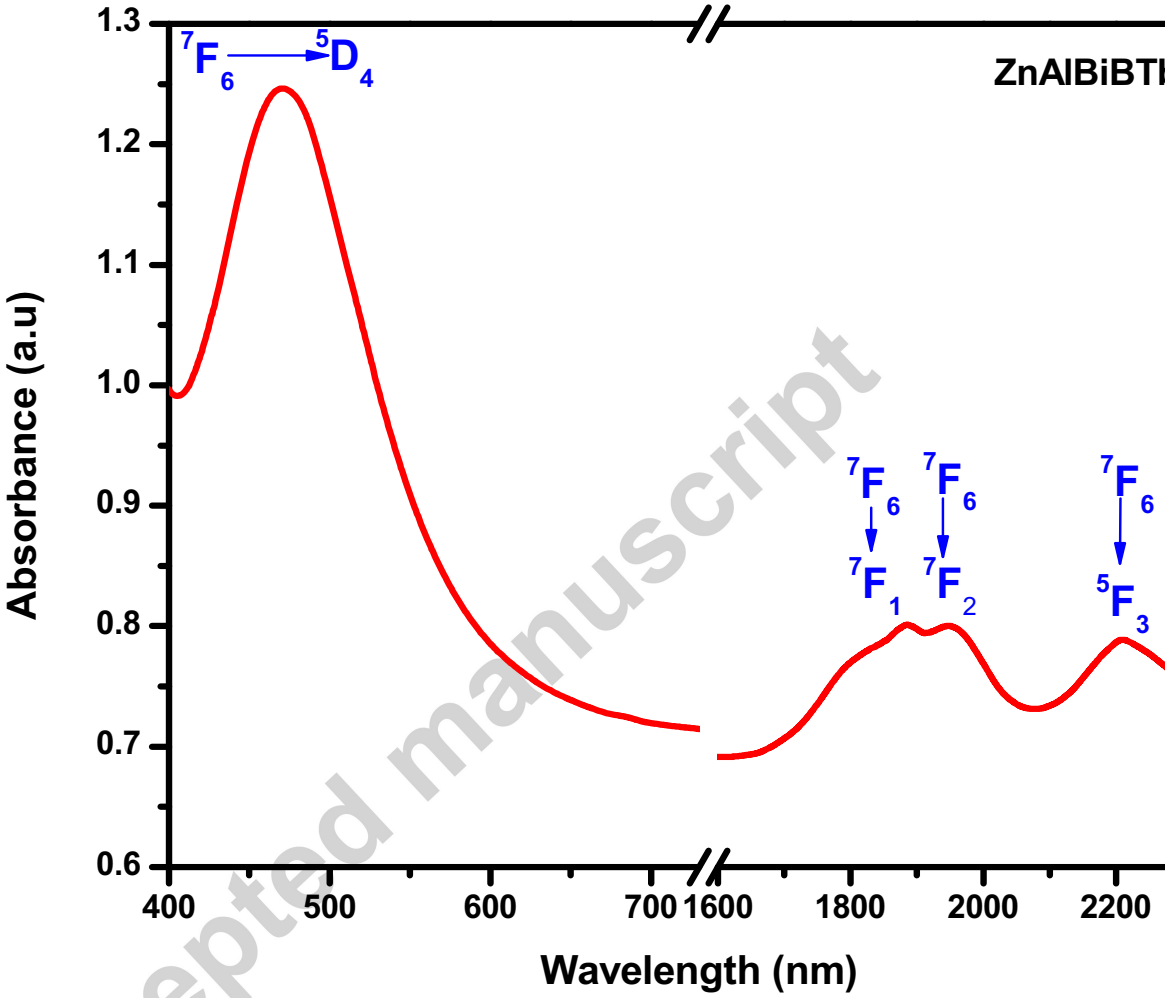
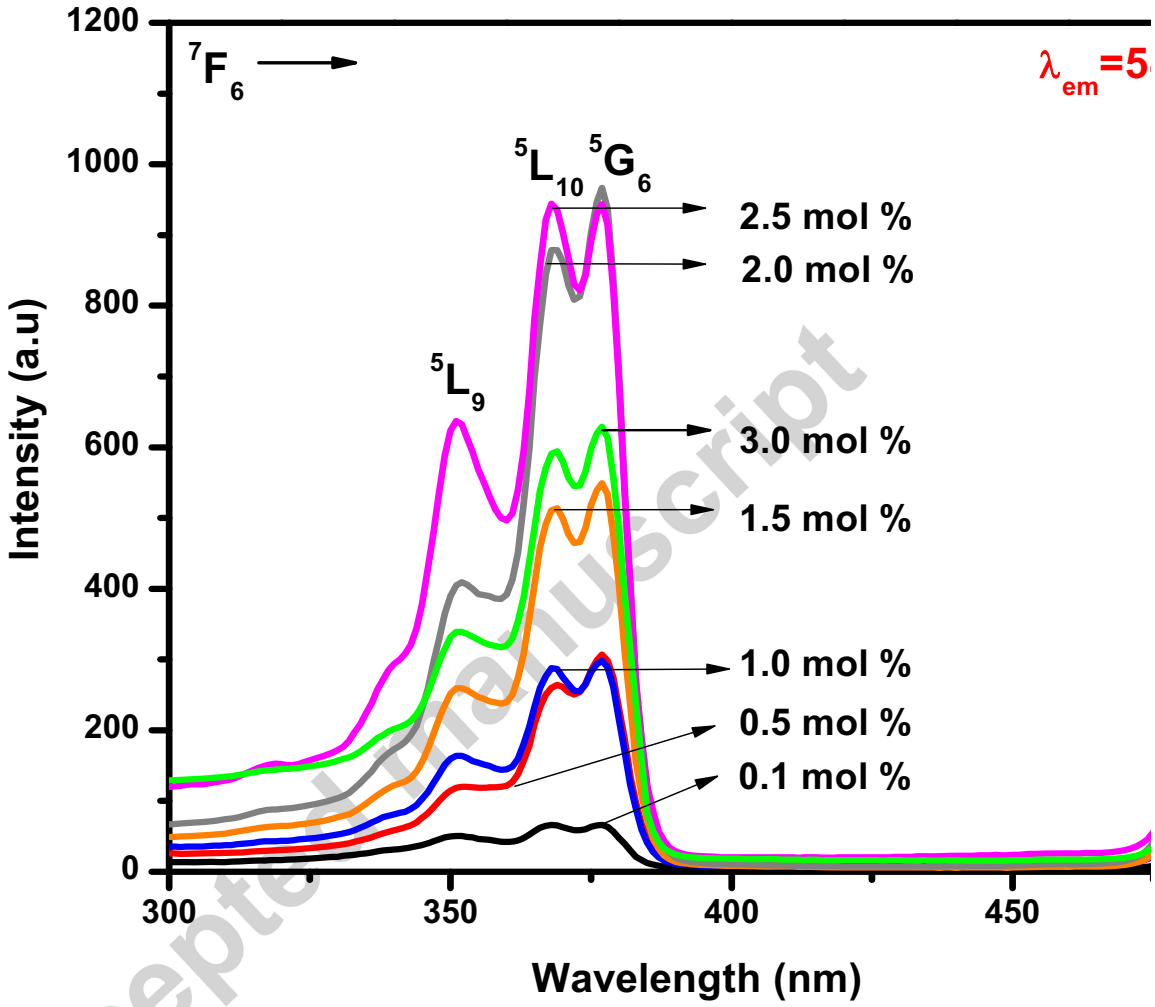


Fig. 2: Absorption spectrum of 2.5 mol % of Tb^{3+} ions in ZnAlBiB glass

Accepted manuscript

ACCEPTED MANUSCRIPT



Accepted Manuscript

Fig. 3: Excitation spectra of the Tb^{3+} ions in ZnAlBiB Glasses.

ACCEPTED MANUSCRIPT

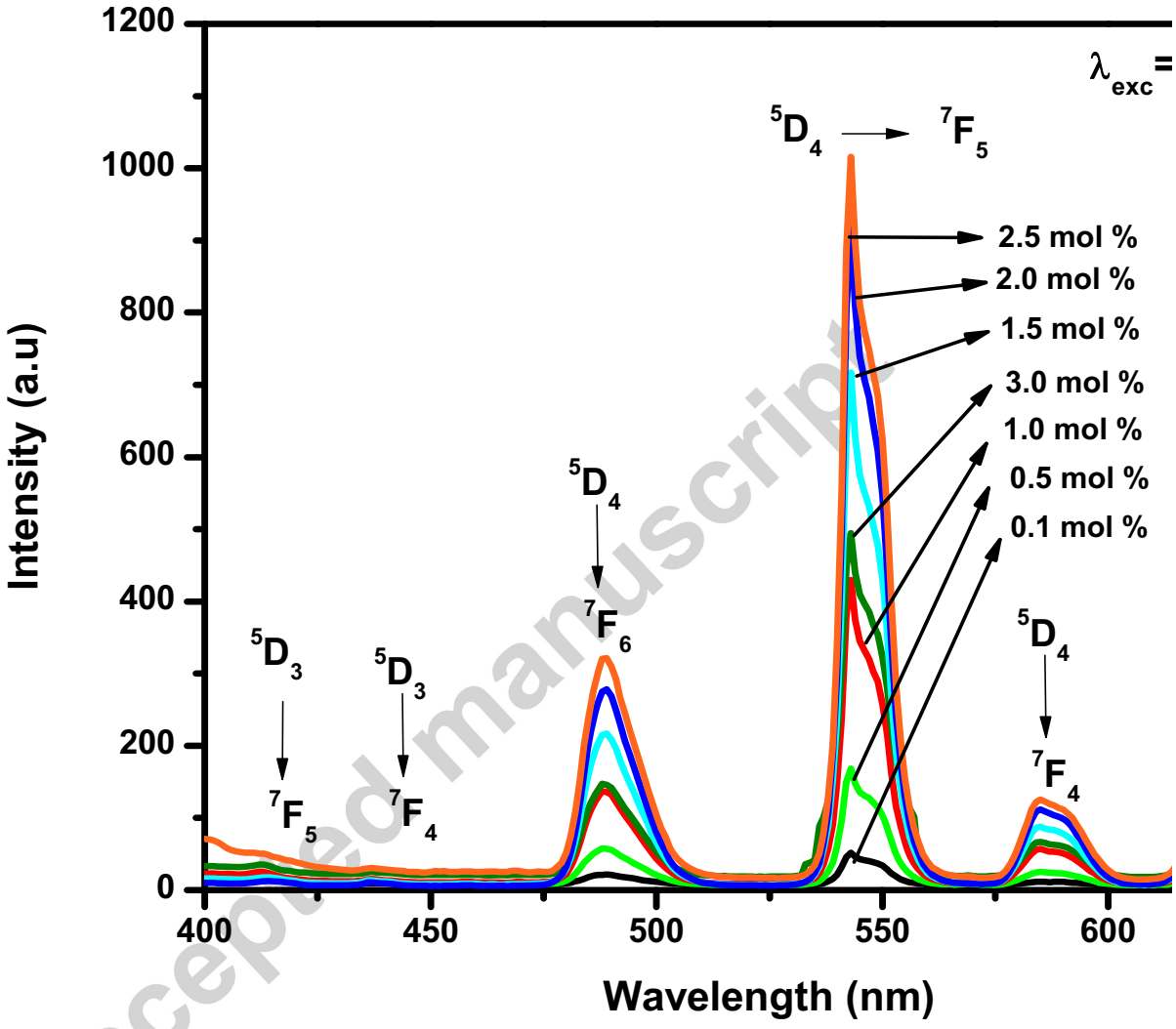


Fig. 4. Emission spectra of Tb^{3+} ions in ZnAlBiB glasses recorded at an excitation wavelength 377 nm.

Accepted manuscript

ACCEPTED MANUSCRIPT

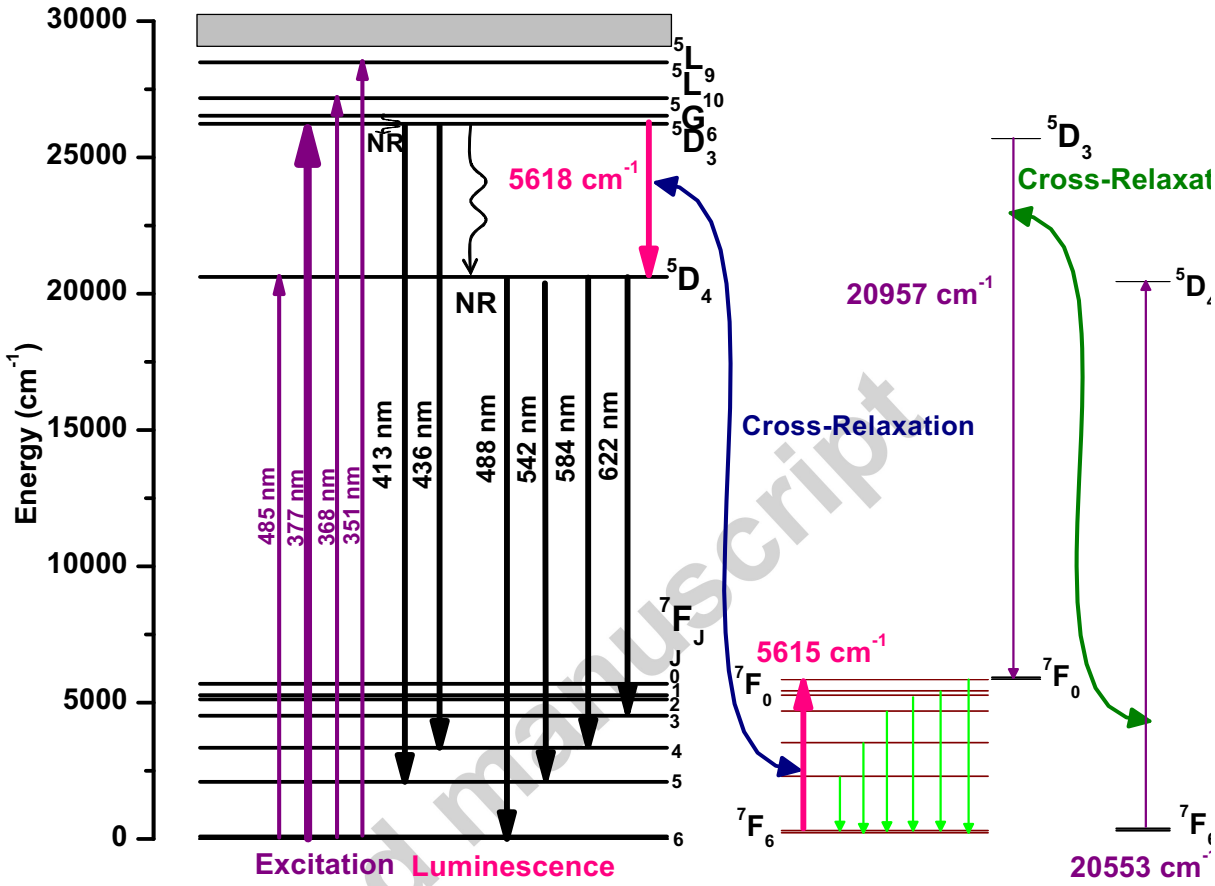
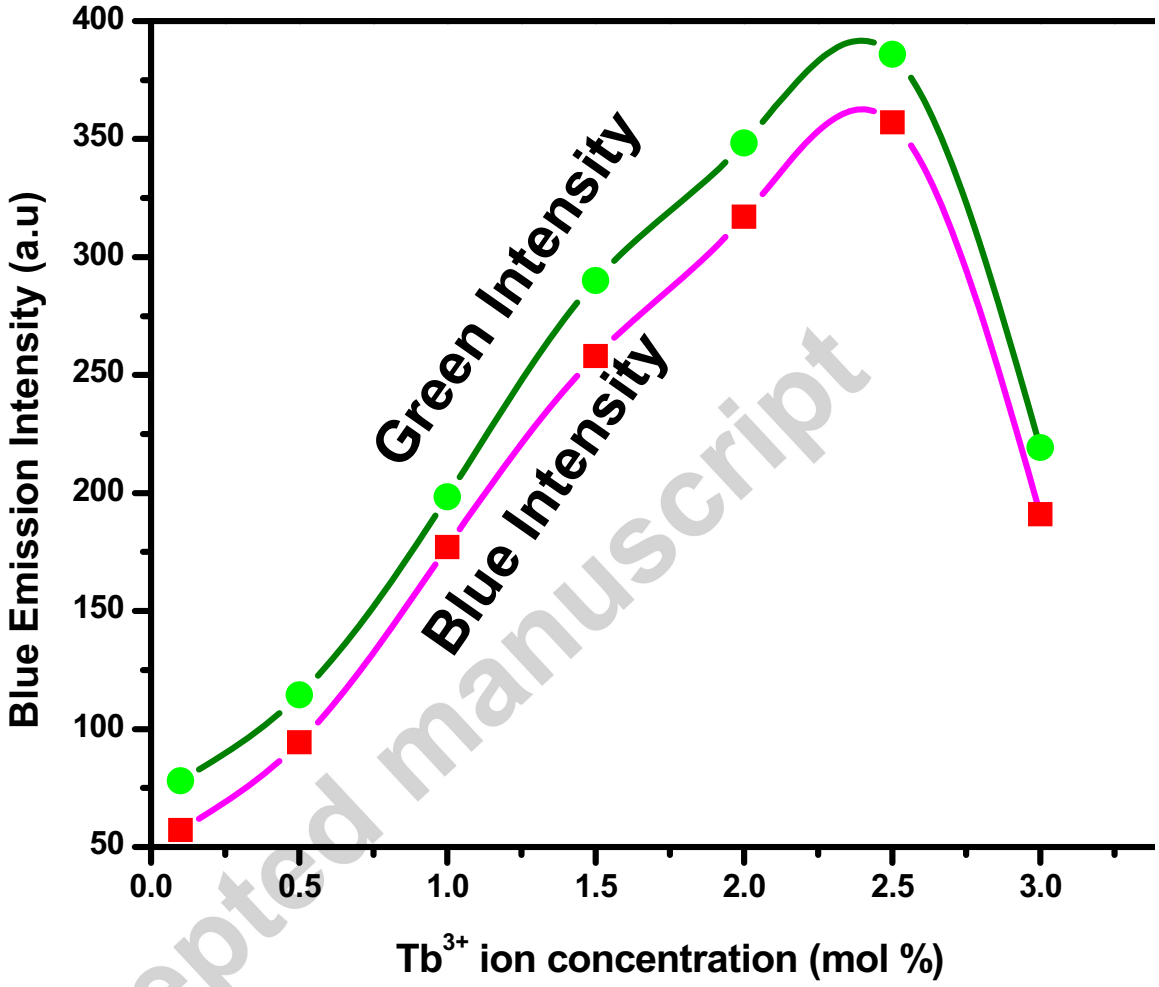


Fig. 5: Partial Energy level diagram of 2.5 mol% of Terbium ions in ZnAlBiB Glass.

Accepted manuscript

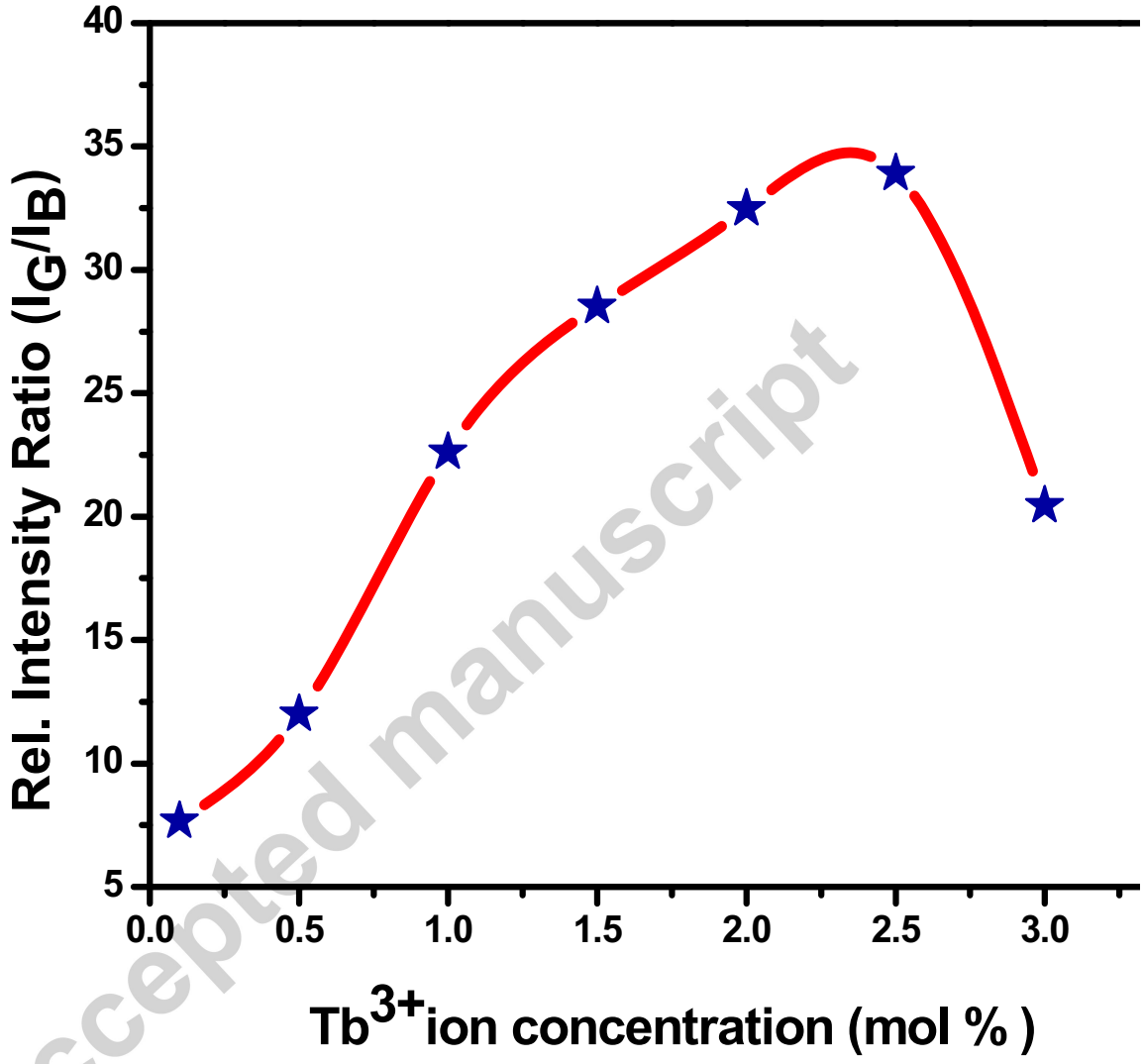
ACCEPTED MANUSCRIPT



Accepted manuscript

Fig. 6(a): Variation of Blue ($^5D_3 \rightarrow {}^7F_4$) and Green ($^5D_4 \rightarrow {}^7F_5$) luminescent intensity as a function of Tb^{3+} ion concentration in ZnAlBiB glasses.

ACCEPTED MANUSCRIPT



Accepted manuscript

Fig 6 (b). Variation of relative luminescence intensity ratio (I_G/I_B) as a function of Tb^{3+} ion concentration in ZnAlBiB glasses

ACCEPTED MANUSCRIPT

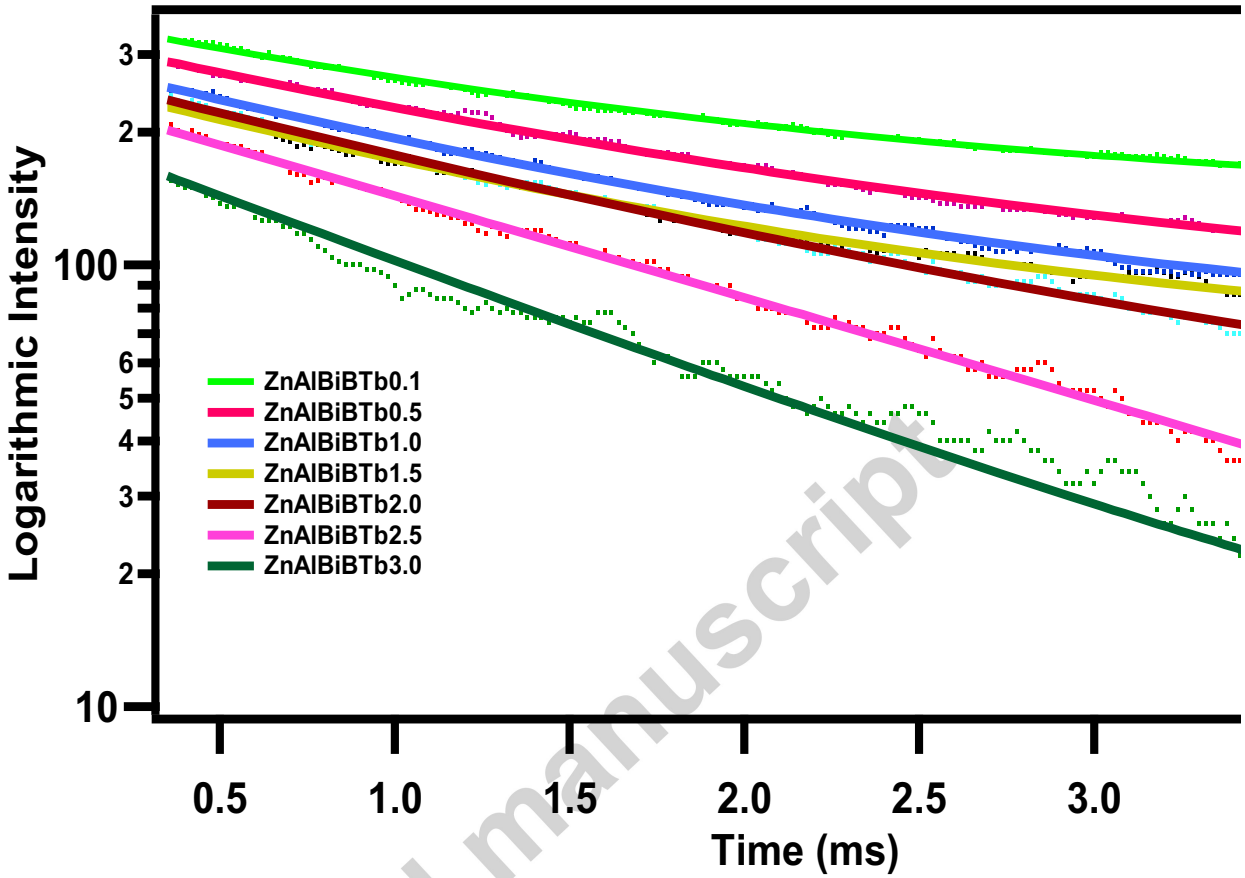


Fig.7 (a): Decay curves for the luminescent transition ($^5D_4 \rightarrow {}^7F_5$) of Tb^{3+} ions doped ZnAlBiB glasses at 337 nm excitation.

Accepted manuscript

ACCEPTED MANUSCRIPT

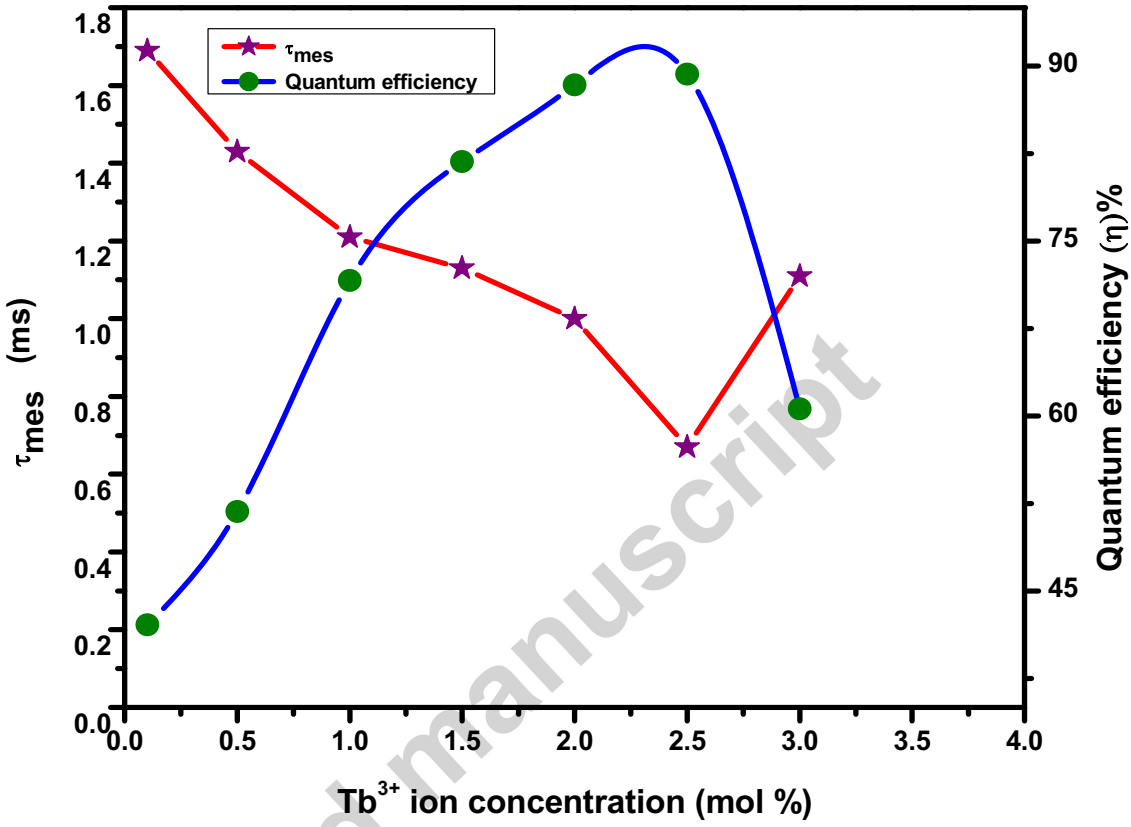


Fig. 7 (b): Variation of decay time (τ_{mes}) and quantum efficiency (η) % of $^5D_4$ excited level as a function of Tb^{3+} ion concentration in ZnAlBiB glasses.

Accepted manuscript

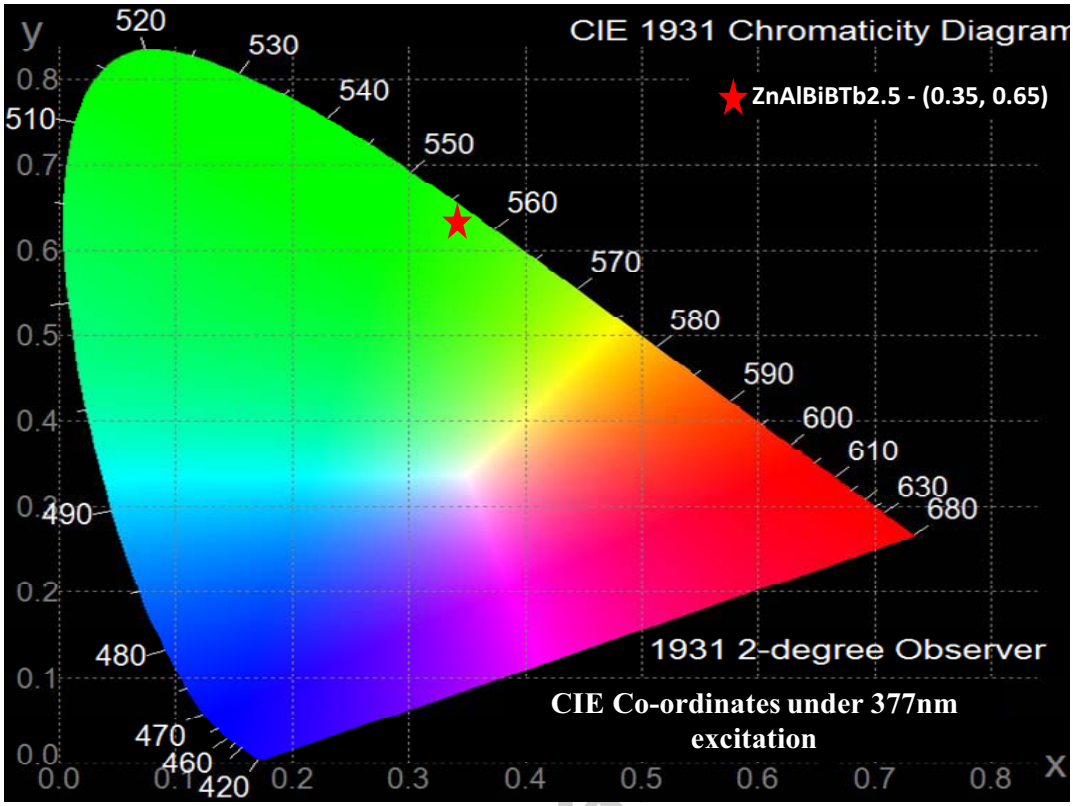


Fig. 8: CIE co-ordinates of ZnAlBiBTb2.5 Glass.

Accepted ma

Table 1:

Physical properties of terbium ions doped ZnAlBiB Glasses.

Physical properties	ZnAlBiBTb0.1	ZnAlBiBTb0.5	ZnAlBiBTb1.0	ZnAlBiBTb1.5	ZnAlBiBTb2.0	ZnAlBiBTb2.5	ZnAlBiBTb3.0
Refractive index (n_d)	1.799	1.797	1.795	1.793	1.791	1.699	1.697
Density (d) (g/cc)	3.932	3.914	3.891	3.868	3.846	3.823	3.813
Average molecular weight ($\bar{M}$)(g)	114.49	114.12	113.65	113.19	112.73	112.27	111.8
Tb^{3+} ion concentration (x10^{22} ions/cm^3)	0.207	1.0327	2.060	3.087	4.109	5.127	5.13
Mean atomic Volume (g/cm^3/atom)	6.616	6.626	6.637	6.649	6.661	6.673	6.663
Dielectric Constant (ϵ)	3.236	3.229	3.222	3.214	3.207	2.886	2.879
Optical Dielectric constant ($p\,\partial t/\partial p$)	2.236	2.229	2.222	2.214	2.207	1.886	1.879
Reflection losses (R %)	8.148	8.119	8.090	8.061	8.032	6.707	6.678
Molar Refraction (R_m)(cm^{-3})	12.434	12.428	12.427	12.426	12.426	11.337	11.295
Polaron radius (r_p) (Å)	3.215	1.882	1.500	1.307	1.188	1.103	1.1
Interionic distance (r_i) (Å)	7.977	4.670	3.710	3.243	2.948	2.739	2.74
Molar electronic polarizability α (x$10^{-23}$$cm^3$)	4.931	0.985	0.493	0.328	0.2464	0.188	0.179
Field Strength (x $10^{15}$$cm^{-2}$)	2.902	8.468	13.4	17.56	21.243	24.617	24.6

Accepted manuscript

ACCEPTED MANUSCRIPT

Optical basicity ($_{th}$)	0.438	0.4403	0.443	0.4456	0.4482	0.4509	0.4535

Table 2:

Comparison of Judd-Ofelt Parameters ($\Omega_{\lambda=2,4,6}$ X10^{-20}cm^2) of terbium ions doped ZnAlBiB Glasses with other reported values.

Name of the Sample	Ω_2	Ω_4	Ω_6	Trend	References
ZnAlBiBTb0.1	2.29	9.89	1.29	$\Omega_4 > \Omega_2 > \Omega_6$	Present
ZnAlBiBTb0.5	3.07	15.8	1.65	$\Omega_4 > \Omega_2 > \Omega_6$	Present
ZnAlBiBTb1.0	7.60	16.7	2.69	$\Omega_4 > \Omega_2 > \Omega_6$	Present
ZnAlBiBTb1.5	9.67	18.5	3.09	$\Omega_4 > \Omega_2 > \Omega_6$	Present
ZnAlBiBTb2.0	12.5	20.2	3.72	$\Omega_4 > \Omega_2 > \Omega_6$	Present
ZnAlBiBTb2.5	26.9	28.7	5.36	$\Omega_4 > \Omega_2 > \Omega_6$	Present
ZnAlBiBTb3.0	8.22	20.6	1.94	$\Omega_4 > \Omega_2 > \Omega_6$	Present
SFB Glasses	0.45	5.53	1.39	$\Omega_4 > \Omega_6 > \Omega_2$	[37]
B_2O_3+ P_2O_5+ Li_2SO_4	13.7	146.5	1.60	$\Omega_4 > \Omega_2 > \Omega_6$	[38]
B_2O_3+ P_2O_5+ K_2SO_4	8.47	119.5	0.88	$\Omega_4 > \Omega_2 > \Omega_6$	[38]

Accepted manuscript

ACCEPTED MANUSCRIPT

B_2O_3+ P_2O_5+ Na_2SO_4	2.92	70.1	0.71	$\Omega_4 > \Omega_2 > \Omega_6$	[38]
YAlO3 Crystal	3.25	7.13	2.00	$\Omega_4 > \Omega_2 > \Omega_6$	[39]

Table 3:

Transition	Energy	ZnAlBiBTb0.1			ZnAlBiBTb0.5			ZnAlBiBTb1.0			ZnAlBiBTb1.5			ZnAlBiBTb2.0			ZnAlBiBTb2.5			ZnAlBiBTb3.0		
	(cm^{-1})	A_R	β_R	β_{exp}	A_R	β_R	β_{exp}	A_R	β_R	β_{exp}	A_R	β_R	β_{exp}	A_R	β_R	β_{exp}	A_R	β_R	β_{exp}	A_R	β_R	β_{exp}
$^5D_4 \rightarrow {}^7F_6$	20419	19.7	0.08	0.20	28.5	0.08	0.10	48.5	0.08	0.10	58.6	0.08	0.16	72.0	0.08	0.09	109	0.08	0.09	44	0.08	0.10
$^5D_4 \rightarrow {}^7F_5$	18450	52.3	0.21	0.21	81.7	0.23	0.18	90.9	0.15	0.13	101	0.14	0.13	112	0.13	0.13	104	0.05	0.14	89	0.16	0.17
$^5D_4 \rightarrow {}^7F_4$	17035	133	0.54	0.35	186	0.51	0.47	364	0.62	0.51	460	0.64	0.56	580	0.66	0.57	960	0.73	0.59	330	0.61	0.50

Accepted manuscript

ACCEPTED MANUSCRIPT

$^5D_4 \rightarrow {}^7F_3$	16077	43.7	0.18	0.25	65.5	0.18	0.24	88.1	0.15	0.08	102	0.14	0.21	119	0.14	0.20	147	0.11	0.17	81	0.15	0.12
A_T			249			363			592			723			884			1322			546	

Radiative transition Probability (A_R) (s^{-1}), total transition probability (A_T) (s^{-1}), radiative and experimental branching ratios (β_R & β_{exp}), of terbium ions doped ZnAlBiB Glasses.

Table 4:

Emission peak wavelength (λ_P) (nm), effective band widths ($\Delta\lambda_P$) (nm), stimulated emission cross-section (σ_{se}) ($\times 10^{22}$) (cm^2), gain band width ($\sigma_{se} \times \Delta\lambda_P$) ($\times 10^{28}$) ($cm^3$) and optical gain ($\sigma_{se} \times \tau_R$) ($\times 10^{25}$) ($cm^2$ s) for the emission transitions of terbium ions doped ZnAlBiB Glasses.

Transitions	Parameters	ZnAlBiBTb0.1	ZnAlBiBTb0.5	ZnAlBiBTb1.0	ZnAlBiBTb1.5	ZnAlBiBTb2.0	ZnAlBiBTb2.5	ZnAlBiBTb3.0
$^5D_4 \rightarrow {}^7F_6$	λ	488	488	488	488	488	488	488
	$\Delta\lambda_P$	12.0	14.1	13.0	13.0	13.0	13.0	12.5
	σ_{se}	0.38	0.47	0.87	1.05	1.30	2.20	0.92
	σ_{se} x $\Delta\lambda_P$	0.46	0.66	1.13	1.37	1.69	2.86	1.15

Accepted manuscript

ACCEPTED MANUSCRIPT

	σ_{se} x τ_R	1.53	1.30	1.47	1.46	1.47	16.6	1.68
$^5D_4 \rightarrow {}^7F_5$	λ	542	542	542	542	542	542	542
	$\Delta\lambda_P$	10.9	10.9	10.9	10.9	10.9	10.9	10.7
	σ_{se}	17.0	26.7	30.0	33.2	36.8	38.2	33.1
	σ_{se} x $\Delta\lambda_P$	1.85	2.90	3.23	3.61	4.00	4.15	3.54
	σ_{se} x τ_R	68.2	73.6	50.2	46.0	41.6	289	60.5
$^5D_4 \rightarrow {}^7F_4$	λ	584	584	584	584	584	584	584
	$\Delta\lambda_P$	16.3	15.2	14.1	12.0	14.1	14.1	14.2
	σ_{se}	3.91	5.86	12.3	18.5	19.8	36.3	12.5
	σ_{se} x $\Delta\lambda_P$	6.38	8.92	17.4	22.1	27.9	51.3	17.7
	σ_{se} x τ_R	15.6	16.2	20.9	25.6	22.4	275	22.8
$^5D_4 \rightarrow {}^7F_3$	λ	622	622	622	622	622	622	622
	$\Delta\lambda_P$	14.1	14.4	11.9	9.78	10.9	10.9	10.7
	σ_{se}	1.90	2.80	5.00	6.46	6.80	9.34	5.22
	σ_{se} x $\Delta\lambda_P$	2.68	4.03	5.43	6.32	7.39	10.2	5.59
	σ_{se} x τ_R	7.60	7.73	8.45	8.93	7.70	70.6	9.55

Table 5:

Measured, radiative lifetimes (τ_{mes} & τ_R) (ms) and quantum efficiency (η) % of terbium ions doped ZnAlBiB glasses for the luminescent emission transition $^5D_4 \rightarrow {}^7F_5$.

Name of the Glass Samples	τ_R	τ_{mes}	Quantum efficiency (η) %	References
ZnAlBiBTb0.1	4.01	1.69	42.1	Present system

Accepted manuscript

ACCEPTED MANUSCRIPT

ZnAlBiBTb0.5	2.76	1.43	51.8	Present system
ZnAlBiBTb1.0	1.69	1.21	71.6	Present system
ZnAlBiBTb1.5	1.38	1.13	81.8	Present system
ZnAlBiBTb2.0	1.13	1.00	88.4	Present system
ZnAlBiBTb2.5	0.75	0.67	89.3	Present system
ZnAlBiBTb3.0	0.69	0.53	76.8	Present system
SFB glass	-	-	36.0	[37]
4.0 wt % Tb^{3+}: Calcium AluminoSilicate glass	-	-	31.3	[50]
0.1 mol % Tb^{3+} :Lead telluroborate	-	-	28 .0	[51]
10 mol % Tb^{3+}: Phospahate glasses	-	-	78 .0	[52]

Accepted manuscript

ACCEPTED MANUSCRIPT

ACCEPTED MANUSCRIPT

Tb^{3+} doped Zinc Alumino Bismuth Borate Glasses for Green Emitting Luminescent Devices

K. Swapna[1], Sk. Mahamuda[1], A. Srinivasa Rao*[1, 2], M.Jayasimhadri[2], Suman Latha Shakya[3] and G. Vijaya Prakash[3]

[1]Department of Physics, K L University, Green Fields, Vaddeswaram-522 502, Guntur (Dt). A P, India
[2]Department of Applied Physics, Delhi Technological University, Bawana Road, New Delhi-110 042, India
[3]Nanophotonics Laboratory, Department of Physics, Indian Institute of Technology-Delhi, Kauz Khas, New Delhi-110016, India.
Corresponding author, E-mail: drsrallam@gmail.com, Tel: +91 85860 39007, Fax: +91 01127871023.

Abstract

Zinc Alumino Bismuth Borate (ZnAlBiB) glasses doped with Terbium (Tb^{3+}) ions with a chemical composition $20ZnO\text{-}10Al_2O_3\text{-}(10\text{-}x)\ Bi_2O_3\text{-}60B_2O_3\text{-}xTb_2O_3$ (x=0.1, 0.5, 1.0, 1.5, 2.0 and 2.5 mol %) were prepared by conventional melt quenching method and studied their optical absorption, photoluminescence and decay spectral properties. The Judd-Ofelt (J-O) parameters evaluated from the experimental oscillator strengths were used to measure the radiative properties for the prominent luminescent transitions of Tb^{3+} ions such as $^5D_4 \rightarrow {}^7F_6$, $^7F_5$, $^7F_4$ and $^7F_3$. The effect of Tb^{3+} ion concentration on the luminescence process observed in the visible region was discussed in detail. The emission spectra recorded for all the ZnAlBiB glasses doped with Tb^{3+} ions, show an intense peak in green region at 542 nm. The confocal PL images recorded under 410 nm CW laser excitation for all these glasses confirms the green emission in principle, which is also further confirmed by the CIE color chromaticity diagram. The stimulated emission cross-section, branching ratios and quantum efficiency values evaluated for green emission ($^5D_4 \rightarrow {}^7F_5$) suggests the utility of these glasses for green luminescence applications. It was found that, within the concentration range investigated, 2.5 mol% of Tb^{3+} doped ZnAlBiB glass is most suitable for green luminescence applications at 542 nm in principle.

Keywords: Borate Glasses, Optical Properties, Stimulated emission cross section, Lifetime.

Accepted manuscript

This article has been accepted for publication in a future issue of this journal, but has not been fully edited. Content may change prior to final publication. Citation information: DOI 10.1109/TVT.2014.2323699, IEEE Transactions on Vehicular Technology

Time-Domain Solution for Transmitted Field through Low-loss Dielectric Obstacles in a Microcellular and Indoor Scenario for UWB Signals

P. Tewari, S. Soni, and B. Bansal

***Abstract*—An analytical time-domain (TD) solution based on an established FD transmission model is presented for transmission of Ultra wideband (UWB) signals through low-loss dielectric obstacles, in a microcellular and indoor propagation environment. The proposed work provides an in-depth analysis of the FD transmission model and presents a computationally more efficient direct TD transmission solution. Various obstacles considered in the work include dielectric-wedge and rectangular-building with homogenous, isotropic, low-loss dielectric characteristics. Novel, TD transmission coefficients, for transmission through an interface between air and a low-loss dielectric medium, are proposed for both hard and soft polarizations. The proposed TD solution is validated against the numerical inverse fast Fourier transform of the exact FD (IFFT-FD) solution and the results are found to be in very good agreement with each other. The computational efficiency achieved through the proposed TD solution is demonstrated by comparing its computation time with that of the exact IFFT-FD solution.**

***Index Terms*—Building-transmission, Physical-optics (PO), Radio propagation, Ray-Tracing, Ultra wideband (UWB), Uniform theory of diffraction (UTD).**

I. Introduction

THE exciting features of Ultra wideband (UWB) communication such as large bandwidth and high data rates promise major advances in the field of high speed wireless communication and thus UWB has become the prime focus of the research community. UWB communication systems employ very short duration pulses, which are usually 1 ns wide, for both transmission and reception [1]-[6]. Its salient features are [1]-[7] (i) possibility of extremely high data rates (ii) immunity to Intersymbol Interference(ISI) (iii) accurate position location and ranging (iv) covert communication due to low transmission power operation. The main areas of application of UWB communication systems are (i) radar applications in military (ii) precision asset location system (iii) high data-rate wireless personal area networks (HDR-WPAN) (iv)Wireless Ethernet interface link (WEIL) (v) intelligent wireless area network (IWAN). The UWB signals suffer pulse distortion due to the frequency selectivity of the propagation path-loss, hence it is more efficient to study UWB propagation directly in the time-domain (TD) where all the frequencies are treated simultaneously [6], [8]. Also all the necessary parameters of a UWB system such as the number of multipaths, the delay, the power, and the distortion of every path can be easily obtained from the TD analysis [6]. Besides, it seems to be more efficient to work directly in the TD than applying the numerical inverse fast Fourier transform on each frequency separately [20]. In TD, the channel's impulse response is calculated in closed form for each possible propagation path and then convolved with the input signal to obtain the received field. The main propagation mechanisms considered in radio propagation are specular reflections, diffuse reflections, diffraction and transmission through the obstacles [6], [42]. An overview on UWB propagation channels, their theory, measurement & modeling of UWB channels was presented in [2]. For the analysis of diffraction phenomena uniform theory of diffraction (UTD) [9] is the most popular theory. The TD-UTD theory was first given by [10], and its applications to various scenarios involving single, double and multiple diffractions were discussed in [11]-[16]. A new approach TD-UTD-PO was proposed in [18]-[21] to calculate the received field after double and multiple diffractions with much less computation time than that of the TD-UTD approach for multiple diffractions including slope diffraction terms discussed in [6].

Results in [22], [23] and [42] proved that along with the diffracted field components, transmitted field components are also very significant for accurate prediction of the total field at the receiver in urban microcellular and indoor wireless

Manuscript received May 11, 2012; revised November 30, 2012, April 14, 2013, August 21, 2013, November 27, 2013, and March 02, 2014, accepted March 20, 2014.

Copyright (c) 2013 IEEE. Personal use of this material is permitted. However, permission to use this material for any other purposes must be obtained from the IEEE by sending a request to pubs-permissions@ieee.org.

P. Tewari is with the Department of Electrical Engineering, Indian Institute of Technology, Delhi, India (e-mail: piyushtewari@gmail.com).

S. Soni is with the Department of Electronics and Communication Engineering, Delhi Technological University, Delhi, India (e-mail: sanjoo.ksoni@gmail.com).

B. Bansal is with the Department of Electronics and Communication Engineering, Delhi Technological University, Delhi, India (e-mail: bajrangbnsl@gmail.com).

0018-9545 (c) 2013 IEEE. Personal use is permitted, but republication/redistribution requires IEEE permission. See http://www.ieee.org/publications_standards/publications/rights/index.html for more information.

This article has been accepted for publication in a future issue of this journal, but has not been fully edited. Content may change prior to final publication. Citation information: DOI 10.1109/TVT.2014.2323699, IEEE Transactions on Vehicular Technology

communication. Especially in the case of non-line of sight (NLOS) communication in deep shadow regions, where the reflected and diffracted field components are weak, the transmitted component is more significant and thus needs to be taken into account [22],[23]. So a propagation model considering the effect of transmitted field component for UWB communication in microcellular scenario becomes important.

The propagation of UWB signals through a dielectric slab of a fixed thickness was presented in [24], [25]. Here multiple reflections inside the slabs were ignored due to their weak contribution. Another solution for transmission through a dielectric slab, considering up to three internal reflections within the slab, was presented in [26]. The measurements depicting the characterization of different materials within UWB range along with the discussion about dispersion suffered by UWB signals due to penetration through the walls were presented in [27],[28] and [32]. According to them in certain cases the multiple reflections inside the slab decay rapidly so for such cases the single pass and multiple pass techniques provide the same results. Another work in [29] discussed UWB pulse reflections and transmissions through complex wall structures, found in indoor propagation environments, through numerical FDTD simulations. A new simplified TD model over that of [24]-[25]was presented in [30]-[31] for the calculation of refraction coefficients and propagation loss expressions for a UWB signal transmitting through a dielectric slab. A generalized solution, accounting the effect of multiple internal reflections, for the transmission of field through a low-loss dielectric-slab was presented in [17].

Despite all these propagation models for UWB microcellular and indoor propagation environments, a TD solution for received field calculation after penetration through walls and across canonical shaped obstacles has not yet been presented for UWB communication.

In this work, we propose an approximate TD solution for the field transmitted through low-loss dielectric obstacles, such as dielectric-wedges or flat-roofed rectangular-buildings, in a microcellular propagation environment, for UWB signals. The proposed TD solution is based on the established FD transmission model of [23], [34] and [40], upon which suitable approximations are applied to obtain a simpler and computationally more efficient TD solution. The UWB frequency range, focused in this work, lies from 3.1 GHz to 10.6 GHz [1]. Novel, analytical TD transmission and reflection coefficients, for transmission through an interface between free-space and a low-loss dielectric medium considering oblique incidence, are proposed for both soft and hard polarizations for the UWB signals. Through these TD formulations, expressions for TD transmission and reflection coefficients are obtained for both the faces of a dielectric-wedge and dielectric-slab. Here we have ignored the effect of weak multiple internally reflected signals following the approach in [23]-[25], [30]-[31]. The result shown in ([17], Fig. 5) shows that even in the case of low-loss dielectric slab, the transmitted pulses after multiple-internal-reflections are almost negligible in comparison to the field component transmitted without any internal-reflection. The TD results of the proposed work are validated against the IFFT [37], [38] of the corresponding exact FD solution results. At last a comparison between the TD transmitted field and the diffracted field obtained through TD-UTD-PO [21] analysis is done for two specific profiles to emphasize the significance of transmitted field in indoor and microcellular scenarios. The proposed TD solution has the potential benefit of having very high computational efficiency as opposed to conventional frequency domain method and, thus, it can be integrated with the existing ray tracing tool achieving higher speed without compromising accuracy.

The paper is organized as follows: In Section II, the propagation environment is discussed. Section III discusses the proposed TD transmission and reflection coefficients along with the TD analysis for calculation of transmitted field component, for the single-obstacle profiles using inverse Laplace transformation of already established FD results [6], [39]. In Section IV, the aforementioned numerical TD results are calculated and compared against the numerical IFFT of the corresponding exact FD results and finally Section V concludes the work.

II. Propagation Environment

The propagation environments are shown in Fig. 1(a) and Fig. 1(b), where a single dielectric-wedge profile and a single rectangular-building profile is considered. As shown in Fig. 1(a), the parameters r_1, r_2 and r_3 are the distances traversed by the transmitted field through the obstacles from the source up to the receiver. Angles θ_1, ψ_3 are the incidence angles, and ψ_2, ψ_4 are the angles of refraction at points 'P' and 'Q', respectively. The parameters h_t, h_r are the heights of the transmitter (Tx) and the receiver (Rx), h_w is the height of the wedge, Tx is at a distance d_1 from the wedge and Rx is at a distance d_2 from the wedge. In Fig. 1(b), a rectangular-building profile is considered with its walls modeled as fixed width, homogenous and isotropic dielectric-slabs. In Fig. 1(b)

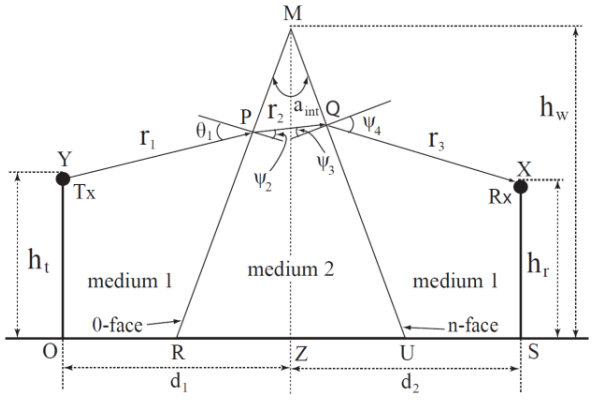


Fig. 1(a).Propagation environment for the transmitted field through a double dielectric-wedge profile.

0018-9545 (c) 2013 IEEE. Personal use is permitted, but republication/redistribution requires IEEE permission. See http://www.ieee.org/publications_standards/publications/rights/index.html for more information.

This article has been accepted for publication in a future issue of this journal, but has not been fully edited. Content may change prior to final publication. Citation information: DOI 10.1109/TVT.2014.2323699, IEEE Transactions on Vehicular Technology

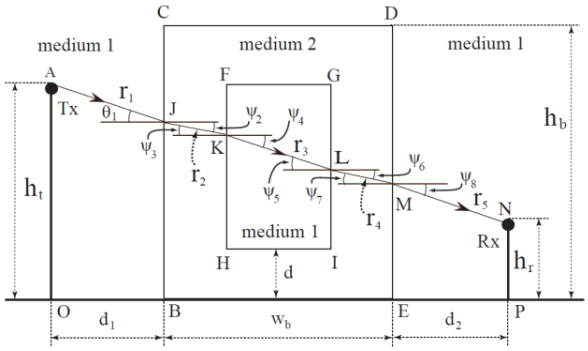


Fig. 1(b).Transmission through a rectangular-building, with walls modeled as homogenous and isotropic dielectric slabs of constant thickness.

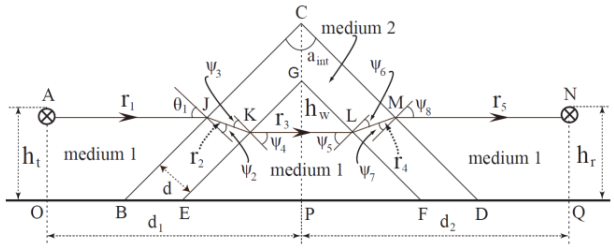


Fig. 1(c).Transmission through a right-angled corner of a single rectangular-building profile, with walls modeled as constant thickness, homogenous and isotropic dielectric slabs.

Tx is at a distance d_1 from the first wall of the building and Rx is at a distance d_2 from the second wall of the building. Angles θ_1, ψ_3, ψ_5 and ψ_7 are the incidence angles and ψ_2, ψ_4, ψ_6 and ψ_8 are the angles of refraction at points 'J', 'K', 'L' and 'M', respectively. Height of the building is h_b, width of the building is w_b and the width of each wall is d. Another possible propagation profile in an indoor propagation scenario, representing two-dimensional top-view of a right-angled corner of single rectangular-building profile, is shown in Fig. 1(c).

III. Proposed Transmission Model

A. The FD Model

The general expression for the received field at Rx after transmission through the obstacles, for any polarization, is given by [23], [34], and [40].

$$E_{RX}(\omega)=\left(\frac{E_i}{r_{total}}\right)T_{total,s,h}(\omega)L_{total,s,h}(\omega) \tag{1}$$

Here, E_i is the relative amplitude of the spherical source in Fig. 1([21], Equation (2)), r_{total} represents the total distance traversed by the transmitted field from Tx to Rx, $T_{total,s,h}(\omega)$ represents the total FD transmission coefficient, which is equal to the product of all the FD transmission coefficients occurring along a given transmission path between Tx and Rx in a given scenario and the 's' and 'h' subscripts refer to the soft and hard polarizations. Here $L_{total,s,h}(\omega)$ [30], [31] represents the total propagation path-loss suffered by the transmitted field during propagation between Tx to Rx. The total path-loss term of (1) includes all the losses during transmission between Tx and Rx, including the free-space propagation loss and the loss that depends on the internal architecture of the considered obstacle.

In general, the transmission coefficients for hard and soft polarizations are given as [23], [40]

$$T_h(\omega)=1+R_h(\omega)=\frac{2\eta\cos\theta_i}{\eta\cos\theta_i+\eta_0\cos\theta_t} \tag{2}$$

$$T_s(\omega)=\left(\frac{\cos\theta_i}{\cos\theta_t}\right)\{1+R_s(\omega)\}=\frac{2\eta\cos\theta_i}{\eta\cos\theta_t+\eta_0\cos\theta_i} \tag{3}$$

where θ_i is the angle of incidence, θ_t is the refracted angle both considered with respect to the normal to the surface of incidence, $R_h(\omega)$ and $R_s(\omega)$ are the Fresnel reflection coefficients for hard and soft polarizations. The parameters $\eta_0=\sqrt{\mu_0/\varepsilon_0}$ and $\eta=\sqrt{\mu/\tilde{\varepsilon}}$ are the characteristic impedances of free space and dielectric medium respectively, where μ and $\tilde{\varepsilon}=\varepsilon+(\sigma/j\omega)$ are the permeability and complex permittivity of the dielectric medium. The term σ represents the conductivity of the dielectric medium in S/m and the permeability of the dielectric medium is given by $\mu=\mu_o\mu_r$ with μ_0 as the free space permeability. The real part of the complex dielectric permittivity is $\varepsilon=\varepsilon_o\varepsilon_r$ with ε_0 and ε_r as the free space permittivity and the relative dielectric permittivity of the dielectric medium. The amount of attenuation and distortion suffered by the transmitted signal within the dielectric medium depends on the distance travelled within the dielectric and its dielectric properties (conductivity, dielectric permeability and dielectric permittivity).

The general expression for the propagation constant is given by $\gamma(\omega)=\alpha(\omega)+j\beta(\omega)$ [40] where $\alpha(\omega)$ is the attenuation constant and $\beta(\omega)$ is the phase constant for the given medium and are given by

$$\alpha(\omega)=\omega\sqrt{\left(\frac{\mu\varepsilon}{2}\right)\left(\sqrt{1+\frac{\sigma^2}{\omega^2\varepsilon^2}}-1\right)} \tag{4}$$

$$\beta(\omega)=\omega\sqrt{\left(\frac{\mu\varepsilon}{2}\right)\left(\sqrt{1+\frac{\sigma^2}{\omega^2\varepsilon^2}}+1\right)} \tag{5}$$

In a general case, when medium 2 is a lossy material (nonzero conductivity which, from (4), implies $\alpha(\omega)\neq 0$, the refracted angle $\theta_t(\omega)$ is a frequency dependent complex number and the true, real refraction angle $\psi_t(\omega)$ can be calculated with the help of Snell's law of refraction as [40], [43]:

$$\gamma_1(\omega)\sin\theta_i=\gamma_2(\omega)\sin\{\theta_t(\omega)\} \tag{6}$$

0018-9545 (c) 2013 IEEE. Personal use is permitted, but republication/redistribution requires IEEE permission. See http://www.ieee.org/publications_standards/publications/rights/index.html for more information.

This article has been accepted for publication in a future issue of this journal, but has not been fully edited. Content may change prior to final publication. Citation information: DOI 10.1109/TVT.2014.2323699, IEEE Transactions on Vehicular Technology

$$\cos\{\theta_t(\omega)\} = \sqrt{1-\sin^2\{\theta_t(\omega)\}} = \sqrt{1-\sin^2\theta_i[\gamma_1(\omega)/\gamma_2(\omega)]^2} \quad (7)$$
$$= s(\omega)\exp[j\zeta(\omega)] = s(\omega)[\cos\zeta(\omega) + j\sin\zeta(\omega)]$$

where $\gamma_1(\omega) = j\beta_1(\omega)$ and $\gamma_2(\omega) = \alpha_2(\omega) + j\beta_2(\omega)$. Thus the true refracted angle is given as

$$\psi_t(\omega) = \tan^{-1}\{u(\omega)/q(\omega)\} \quad (8)$$

with $u(\omega) = \beta_1(\omega)\sin\theta_i$ and $q(\omega) = s(\omega)[\alpha_2(\omega)\sin\zeta(\omega) + \beta_2(\omega)\cos\zeta(\omega)]$.

From (8) it is clear that the true refraction angle is also frequency dependent in nature, which means that for different frequency components of the UWB signal the true, real angles of refraction are different. Thus, a single UWB ray incident on a lossy dielectric material actually splits into a beam of rays after refraction, corresponding to all the frequency components comprising the bandwidth of the signal (See Fig. 2). It implies that the different frequency components of the transmitted signal follow different paths after refraction up to Rx (See Fig. 2). However, we show later that for low-loss dielectric obstacles, for UWB signals, the different complex refracted angles and the true refracted angles, respectively, become identical and reduce to a constant, frequency independent real value. So during the TD analysis for the low-loss cases we assume the refracted angle to be a constant value to simplify the development of the TD formulations and to obtain the effective single path travelled by the TD transmitted field as shown in the propagation profiles of section II. The validity of such an assumption is established through the comparison between the obtained TD transmitted field and the IFFT of the actual FD transmitted field.

B. The TD Model

We employ inverse Laplace transform, like [39], to the FD formulation for transmitted field obtained after applying the low-loss approximation to the original FD solution discussed in the previous section, to obtain the simplified TD formulation for the transmitted field. In [39], an approximate TD expression corresponding to the FD Fresnel reflection coefficient is presented. The work in [39] is accurate only for large values of ε_r and for non-grazing incident rays for a lossy half plane. Our work is also approximate as it is only defined for low-loss dielectric obstacles, but the approximation employed in our work is different from that of [39]. Our work is valid only for low-loss dielectric obstacles of a microcellular and indoor scenario where the value of the loss tangent is necessary to be much less than unity rather than the requirement of any limitation over the individual value of the relative permittivity of the obstacle and the incidence angle. This implies that our solution holds for any incidence angle and even for low values of relative permittivity as long as the loss tangent is maintained very less than unity. The most important outcome of our approximation is the constant and frequency independent value of the refracted angle that results in dispersion less and distortion less transmission of the incident signal through the obstacle, which ultimately results in the development of a simplified TD solution. In TD, the transmitted field at Rx is given by

$$e_{RX}(t) = \left[e_i(t)/r_{total}\right] * \Gamma_{total,s,h}(t) * l_{total,s,h}(t) \quad (9)$$

with ' * 'representing the convolution operator, $\Gamma_{total,s,h}(t)$ is the TD counterpart of the term $T_{total,s,h}(\omega)$ of (1) $l_{total,s,h}(t)$, [30], [31] is the TD counterpart of the term $L_{total,s,h}(\omega)$.

C. Proposed TD Transmission and Reflection Coefficients

Here we derive the TD transmission coefficients corresponding to (2) and (3) for two cases that occur during propagation through low-loss dielectric obstacles, for both soft and hard polarizations. The first case refers to the condition when the wave travels from air to the low-loss dielectric medium, as in the case of refraction through the 0-face of the dielectric-wedge at point 'P' (See Fig. 1a), and the second case is the propagation of the signal from the low-loss dielectric medium to free space as at point 'Q' in Fig. 1a. In the following derivations, the '*ad*' and '*da*' subscripts refer to the propagation of wave from air to dielectric medium and vice-versa. For a non-magnetic medium, like dry-wall, concrete, wooden-door etc., $\mu_r \approx 1$, thus in such cases $\mu \approx \mu_0$. The dielectric obstacles considered in this work have low-loss characteristics i.e. their loss-tangent value $(\sigma/\omega\varepsilon)$ is very much less than unity, within the UWB frequency range. Due to the assumed low-loss condition we neglect the term $(\sigma^2/\omega^2\varepsilon^2)$ in comparison to unity from (4)-(8) and obtain $\alpha_2(\omega) \approx 0$, $\gamma_2(\omega) \approx j\omega\sqrt{\mu\varepsilon}$, $\cos(\theta_t) \approx s$, $\zeta \approx 0$, $q(\omega) \approx s\beta_2(\omega)$, and hence we get the following real, frequency independent expression

$$\psi_t \simeq \theta_t \simeq \sin^{-1}(\sin\theta_i/\sqrt{\varepsilon_r}). \quad (10)$$

Thus in this section we treat the real refracted angle ψ_t as constant and frequency independent, to obtain the approximate analytical TD transmission coefficients. Starting with the hard polarization case, for the wave entering a low-loss dielectric medium from air or free space, from (2), (10), ([40], example 5-8) and from the definitions of the characteristic impedances of the two mediums involved we obtain

$$T_{ad,h}(\omega) \simeq \frac{2\cos\theta_i}{\cos\theta_i + \left(\sqrt{\frac{\varepsilon_0\varepsilon_r + \sigma/j\omega}{\varepsilon_0}}\right)\cos\psi_t} \quad (11)$$

After further manipulation and doing the replacement $s \to j\omega$ in (11), we obtain

$$T_{ad,h}(s) \simeq 1 - \left\{\frac{\sqrt{s+\tau} - k_{ad,h}\sqrt{s}}{\sqrt{s+\tau} + k_{ad,h}\sqrt{s}}\right\} \quad (12)$$

where $\tau = (\sigma/\varepsilon)$ and $k_{ad,h} = (\cos\theta_i/\cos\psi_t)(1/\sqrt{\varepsilon_r})$.

Now using the inverse Laplace technique we get

$$\gamma_{ad,h}(t) = L^{-1}\left[T_{ad,h}(s)\right] \simeq L^{-1}\left[1 - \left\{\frac{\sqrt{s+\tau} - k_{ad,h}\sqrt{s}}{\sqrt{s+\tau} + k_{ad,h}\sqrt{s}}\right\}\right] \quad (13)$$

Finally the TD transmission coefficient for this case is given by

0018-9545 (c) 2013 IEEE. Personal use is permitted, but republication/redistribution requires IEEE permission. See http://www.ieee.org/publications_standards/publications/rights/index.html for more information.

This article has been accepted for publication in a future issue of this journal, but has not been fully edited. Content may change prior to final publication. Citation information: DOI 10.1109/TVT.2014.2323699, IEEE Transactions on Vehicular Technology

$$\gamma_{ad,h}(t) \simeq \delta(t) - r_{ad,h}(t) \tag{14}$$

where $r_{ad,h}(t)$ is of the form, [35]-[36], (equation 14-18 and equation 25, [39]) and [45]

$$r_{ad,h}(t) = \left[K_{ad,h}\delta(t)\right] + \frac{4k_{ad,h}}{\left(1-k_{ad,h}{}^2\right)} e^{-pt} \left[\frac{K_{ad,h}}{2} X_{ad,h} + \frac{\left(1-X_{ad,h}\right)}{2K_{ad,h}} - \frac{(pt)X_{ad,h}}{4}\right] \tag{15}$$

with $X_{ad,h} = e^{-\left(\frac{K_{ad,h}pt}{2}\right)}$, $K_{ad,h} = \left(\frac{1-k_{ad,h}}{1+k_{ad,h}}\right)$ and $p = \frac{\sigma}{2\varepsilon} = \frac{\tau}{2}$.

Now the TD transmission coefficient for hard polarization for the field entering from a dielectric medium into airis obtained from (2) as

$$T_{da,h}(\omega) \simeq \frac{2\eta_0 \cos\theta_i}{\eta_0 \cos\theta_i + \eta \cos\psi_t} \tag{16}$$

$$T_{da,h}(s) \simeq \frac{2cos\theta_i \left(\sqrt{1+\frac{\sigma}{s\varepsilon}}\right)\sqrt{\varepsilon_r}}{\cos\theta_i \sqrt{\varepsilon_r}\left(\sqrt{1+\left(\frac{\sigma}{s\varepsilon}\right)}\right) + \cos\psi_t} \tag{17}$$

Similar to (11)-(12), after manipulating (17) we get

$$T_{da,h}(s) = 1 + \left\{\frac{\sqrt{s+\tau} - k_{da,h}\sqrt{s}}{\sqrt{s+\tau} + k_{da,h}\sqrt{s}}\right\} \tag{18}$$

Thus we obtain

$$\gamma_{da,h}(t) = L^{-1}\left[T_{da,h}(s)\right] \simeq L^{-1}\left[1 + \left\{\frac{\sqrt{s+\tau} - k_{da,h}\sqrt{s}}{\sqrt{s+\tau} + k_{da,h}\sqrt{s}}\right\}\right] \tag{19}$$

where $k_{da,h} = (\cos\psi_t / \cos\theta_i)\left(1/\sqrt{\varepsilon_r}\right)$ and the expression for the TD transmission coefficient is given as

$$\gamma_{da,h}(t) \simeq \delta(t) + r_{da,h}(t) \tag{20}$$

$$r_{da,h}(t) \simeq \left[K_{da,h}\delta(t)\right] + \frac{4k_{da,h}}{\left(1-k_{da,h}{}^2\right)} e^{-pt} \left\{\frac{K_{da,h}}{2} X_{da,h} + \frac{\left(1-X_{da,h}\right)}{2K_{da,h}} - \left(\frac{pt}{4}\right) X_{da,h}\right\} \tag{21}$$

with $X_{da,h} = e^{-\left(K_{da,h}pt/2\right)}$, $K_{da,h} = \left(\frac{1-k_{da,h}}{1+k_{da,h}}\right)$.

The TD counterpart for equation (2), for constant incidence and refracted angles, during transmission through air to dielectric or dielectric to air, is obtained as

$$\gamma_h(t) = \left[\delta(t) + r_h(t)\right] \tag{22}$$

On comparing (22) with (2) we see that $\gamma_h(t)$ is the TD counterpart for $T_h(\omega)$, $\delta(t)$ is the TD counterpart for '1' and $r_h(t)$ is the TD counterpart for $R_h(\omega)$. From (2), (14) and (22) we get $-r_{ad,h}(t)$ and $r_{da,h}(t)$ as the TD reflection coefficients for hard polarization, corresponding to the two cases of propagation discussed above. After this we look forward to obtain the TD transmission coefficient expression for a soft polarized wave propagating from air to low-loss dielectric medium, thus similar to the hard polarization case, from (3) and (10) we get

$$T_{ad,s}(\omega) \simeq \frac{2\eta \cos\theta_i}{\eta \cos\psi_t + \eta_0 \cos\theta_i} \tag{23}$$

Similar to (11)-(13), after manipulating (23) we obtain

$$\gamma_{ad,s}(t) \simeq L^{-1}\left[1 - \left\{\frac{\sqrt{s+\tau} - k_{ad,s}\sqrt{s}}{\sqrt{s+\tau} + k_{ad,s}\sqrt{s}}\right\}\right]\left(\frac{\cos\theta_i}{\cos\psi_t}\right) \tag{24}$$

where $k_{ad,s} = \left(\cos\psi_t / \cos\theta_i\right)(1/\sqrt{\varepsilon_r})$. Thus finally we get

$$\gamma_{ad,s}(t) \simeq \left[\delta(t) - r_{ad,s}(t)\right]\left(\frac{\cos\theta_i}{\cos\psi_t}\right) \tag{25}$$

where

$$r_{ad,s}(t) \simeq K_{ad,s}\delta(t) + \frac{4k_{ad,s}}{\left(1-k_{ad,s}{}^2\right)} e^{-pt} \left[\frac{K_{ad,s}}{2} X_{ad,s} + \frac{\left(1-X_{ad,s}\right)}{2K_{ad,s}} - \frac{(pt)X_{ad,s}}{4}\right] \tag{26}$$

with $X_{ad,s} = e^{-\left(\frac{K_{ad,s}pt}{2}\right)}$, $K_{rd,s} = \left(\frac{1-k_{rd,s}}{1+k_{rd,s}}\right)$.

Similarly, the TD transmission coefficient for the soft polarized wave propagating from the dielectric medium to air, is given by

$$\gamma_{da,s}(t) \simeq \left[\delta(t) + r_{da,s}(t)\right]\left(\frac{\cos\theta_i}{\cos\psi_t}\right) \tag{27}$$

with

$$r_{da,s}(t) \simeq K_{da,s}\delta(t) + \frac{4k_{da,s}}{\left(1-k_{da,s}{}^2\right)} e^{-pt} \left[\frac{K_{da,s}}{2} X_{da,s} + \frac{\left(1-X_{da,s}\right)}{2K_{da,s}} - \frac{(pt)X_{da,s}}{4}\right] \tag{28}$$

where $X_{da,s} = e^{-\left(\frac{K_{da,s}pt}{2}\right)}$, $K_{da,s} = \left(\frac{1-k_{da,s}}{1+k_{da,s}}\right)$, and $k_{da,s} = (\cos\theta_i / \cos\psi_t)(1/\sqrt{\varepsilon_r})$.

The TD counterpart for equation (3), for transmission through air to low-loss dielectric medium or low-loss dielectric medium to air, is obtained as

$$\gamma_s(t) = \left[\delta(t) + r_s(t)\right]\left(\frac{\cos\theta_i}{\cos\psi_t}\right) \tag{29}$$

On comparing (3) and (29) we see that $\gamma_s(t)$ is the TD counterpart for $T_s(\omega)$, $\delta(t)$ is the TD counterpart for '*1*' and $r_s(t)$ is the TD counterpart for $R_s(\omega)$. After comparing (25) and (27) with (29) we get '$-r_{ad,s}(t)$' and '$r_{da,s}(t)$' as the

0018-9545 (c) 2013 IEEE. Personal use is permitted, but republication/redistribution requires IEEE permission. See http://www.ieee.org/publications_standards/publications/rights/index.html for more information.

This article has been accepted for publication in a future issue of this journal, but has not been fully edited. Content may change prior to final publication. Citation information: DOI 10.1109/TVT.2014.2323699, IEEE Transactions on Vehicular Technology

TD reflection coefficients for soft polarization, corresponding to the two cases of propagation discussed above.

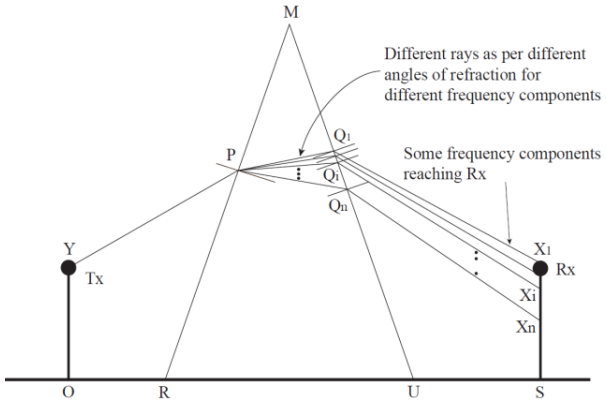


Fig. 2.Splitting of an incident ray into a beam of rays, for UWB signals.

D. *Transmitted Field through a Single Dielectric-Wedge Profile*

According to (1), the FD expression for the transmitted field at Rx (See Fig. 2) through the single dielectric-wedge profile, is given by

$$E_{RX}(\omega)=\left(E_i(\omega)/r_{total}(\omega)\right)\left(\prod_{l=1}^{2}T_{l,s,h}(\omega)\right)\left(\exp(-j\beta_0 r_1)\prod_{m=2}^{3}\exp\left\{-\left(\alpha_{em}(\omega)+j\beta_{em}(\omega)\right)\right\}\right) \quad (30)$$

The above equation is obtained by extending the formulation presented in ([34], [40], Section 5.4.2, equation 5-53 to 5-61), for the case of transmission through a single dielectric-wedge profile. Here it is important to note that (30) is to be calculated for each frequency component of the UWB signal which is contributing to the total transmitted field at Rx. The term β_0 represents the free space phase shift constant [23]. On comparing (1) and (30) we get the following actual FD path loss expression for the single dielectric-wedge profile

$$L(\omega)=\left(\exp(-j\beta_0 r_1)\prod_{m=2}^{3}\exp\left\{-\left(\alpha_{em}(\omega)+j\beta_{em}(\omega)\right)\right\}\right) \quad (31)$$

From (30) and (Section 5.4.2, equation 5-53 to 5-61, [40]), we get

$$\alpha_{e2}(\omega)=A_1(\omega)p_1(\omega) \text{ and } \alpha_{e3}(\omega)= [\alpha_2(\omega)\sin\{\theta_3(\omega)\}A_1(\omega)-s_2(\omega)\sin\{\zeta_2(\omega)\}\beta_1(\omega)A_2(\omega)] \quad (32)$$

The term $\alpha_{e2}(\omega)$ is the total effective attenuation constant during propagation of the refracted wave through the dielectric medium and the term $\alpha_{e3}(\omega)$ refers to the total effective attenuation constant, past the dielectric obstacle.

Further

$$A_1(\omega)=[x_2(\omega)-x_1]\cos(a_{\text{int}}/2)-[y_2(\omega)-y_1]\sin(a_{\text{int}}/2) \quad (33)$$

$$p_1(\omega)=s_1(\omega)[\alpha_2(\omega)\cos\{\zeta_1(\omega)\}-\beta_2(\omega)\sin\{\zeta_1(\omega)\}] \quad (34)$$

Here (x_1, y_1) are the coordinates of the point 'P' in Fig. 2. Moreover, $[x_2(\omega), y_2(\omega)]$ are the coordinates of point 'Q_i' and $[x_3(\omega), y_3(\omega)]$ are the coordinates of point 'X_i', respectively, along different transmission paths followed by the different frequency components of the UWB signal which contribute to the total transmitted field at Rx (See Fig. 2). The point of refraction 'Q_i' and the point 'X_i' (See Fig. 2) correspond to the 'i^{th}' transmission path followed by a frequency component of the transmitted UWB signal which contributes to the total transmitted field at Rx. Following are the expressions for the total effective phase constants during transmission through the dielectric-wedge.

$$\beta_{e2}(\omega)=\beta_{2e}(\omega)[x_2(\omega)-x_1]\cos[\psi_2(\omega)-a_{\text{int}}/2] +[y_2(\omega)-y_1]\sin[\psi_2(\omega)-a_{\text{int}}/2] \quad (35)$$

$$\beta_{e3}(\omega)=\beta_{3e}(\omega)[x_3(\omega)-x_2(\omega)]\cos[\psi_4(\omega)-a_{\text{int}}/2] -[y_3(\omega)-y_2(\omega)]\sin[\psi_4(\omega)-a_{\text{int}}/2] \quad (36)$$

The term $\beta_{e2}(\omega)$ is the total effective phase constant for the dielectric medium within the obstacle and the term $\beta_{e3}(\omega)$ is the total effective phase constant for the region past the obstacle.

The expressions for the effective frequency dependent phase constants $\beta_{2e}(\omega)$ and $\beta_{3e}(\omega)$, as mentioned in (35), (36), for the regions between points 'P', 'Q_i' and 'Q_i', 'X_i', respectively, of Fig. 2, are given by

$$\beta_{2e}(\omega)=\sqrt{u_1^2(\omega)+q_1^2(\omega)} \quad (37)$$

where $u_1(\omega)=\beta_1(\omega)\sin\theta_1$ and

$q_1(\omega)=s_1(\omega)[\alpha_2(\omega)\sin\{\zeta_1(\omega)\}+\beta_2(\omega)\cos\{\zeta_1(\omega)\}]$.

$$\beta_{3e}(\omega)=\sqrt{u_2^2(\omega)+q_2^2(\omega)} \quad (38)$$

where $u_2(\omega)=\beta_2(\omega)\sin\{\theta_3(\omega)\}$ and $q_2(\omega)=s_2(\omega)\beta_1(\omega)\cos\{\zeta_2(\omega)\}$ with

$$\cos\{\theta_2(\omega)\}=\sqrt{1-\sin^2\{\theta_2(\omega)\}} =\sqrt{1-\sin^2\{\theta_1(\omega)\}[\gamma_1(\omega)/\gamma_2(\omega)]}=s_1(\omega)\exp[j\zeta_1(\omega)] \quad (39)$$

$$\cos\{\theta_4(\omega)\}=\sqrt{1-\sin^2\{\theta_4(\omega)\}} =\sqrt{1-\sin^2\{\theta_3(\omega)\}[\gamma_2(\omega)/\gamma_1(\omega)]}=s_2(\omega)\exp[j\zeta_2(\omega)] \quad (40)$$

The true angles of refraction corresponding to the points of refraction 'P' and 'Q_i', as per [40], are given by $\psi_2(\omega)=\tan^{-1}\{u_1(\omega)/q_1(\omega)\}$ and $\psi_4(\omega)=\tan^{-1}\{u_2(\omega)/q_2(\omega)\}$, respectively. Now, these expressions for the true angles of refractions are to be used in place of the complex refracted angles along each transmission path (See Fig. 2), during the calculation of the total transmitted field at Rx.

For loss-tangent much less than unity $\sigma/\omega\varepsilon<<1$, (30) and (31) reduce to the following approximate forms with constant values of angles of refraction as in (10) and along a single effective path for transmission

$$E_{RX}(\omega)\simeq\frac{E_i(\omega)}{r_{total}}T_{1,s,h}(\omega)T_{2,s,h}(\omega)\exp\left[-\sqrt{\frac{\mu}{\varepsilon}}\left(\frac{\sigma}{2}\right)r_2\right] \exp(-j\omega\sqrt{\mu\varepsilon}r_2)\exp\left(-j\beta_0(r_1+r_3)\right) \quad (41)$$

0018-9545 (c) 2013 IEEE. Personal use is permitted, but republication/redistribution requires IEEE permission. See http://www.ieee.org/publications_standards/publications/rights/index.html for more information.

This article has been accepted for publication in a future issue of this journal, but has not been fully edited. Content may change prior to final publication. Citation information: DOI 10.1109/TVT.2014.2323699, IEEE Transactions on Vehicular Technology

$$L(\omega) \simeq \exp\left[-\sqrt{\mu/\varepsilon}\left(\sigma/2\right)r_2\right]\exp(-j\omega\sqrt{\mu\varepsilon}r_2)\exp\left(-j\beta_0(r_1+r_3)\right) \tag{42}$$

with $r_{total} = r_1 + r_2 + r_3$, $T_{1,s,h}(\omega)T_{2,s,h}(\omega) = T_{total,s,h}(\omega)$ where $T_{1,s,h}(\omega)$ and $T_{2,s,h}(\omega)$ are the FD transmission coefficients at points 'P' and 'Q' obtained as per (11), (16) and (23), $r_1 + r_3 = r_o$ is the total distance travelled in free space by the field from point 'Y' to point 'X'(See Fig. 1(a)). The approximated propagation path-loss term in (42) is obtained similar to [23], [30]-[31].

Now the TD expression for the transmitted field at Rx, corresponding to (41), is as follows

$$e_{RX}(t) \simeq \left(\frac{e_i(t)}{r_{total}}\right) * \Gamma_{1,s,h}(t) * \Gamma_{2,s,h}(t) * l_{total,s,h}(t) \tag{43}$$

Here $\Gamma_{1,s,h}$, $\Gamma_{2,s,h}$ are the TD transmission coefficients at points 'P' and 'Q' (See Fig. 1(a)), that are obtained according to (14), (20), (25) and (27). The last term in (43) is the TD propagation path-loss expression, corresponding to the FD path-loss term $L_{total,s,h}(\omega)$ in (42). The TD expression for the propagation path-loss in (43) is obtained as [30-31]:

$$l(t) \simeq \exp\left[-\sqrt{\mu/\varepsilon}\left(\sigma/2\right)r_2\right]\delta\left[t-\left(\sqrt{\mu\varepsilon}r_2\right)\right] * \delta\left(t-\frac{r_1+r_3}{c}\right) \tag{44}$$

E. Transmitted Field through a Single Rectangular-Building Profile

According to (1), the actual transmitted field through the single rectangular-building profile is calculated with the help of the following FD expression:

$$E_{RX}(\omega) = \left(E_i(\omega)/r_{total}(\omega)\right)\left(\prod_{l=1}^{4} T_{l,s,h}(\omega)\right) \left(\exp(-\alpha_b r_3)\exp(-j\beta_0 r_1)\prod_{m=2}^{5}\exp\left\{-\left(\alpha_{em}(\omega)+j\beta_{em}(\omega)\right)\right\}\right) \tag{45}$$

Here α_b, as per [22], [33], is the assumed specific attenuation constant for the interior of the building. The specific attenuation constant is independent of frequency; it depends on the internal architecture of the building considered and on the materials being used in the interior of the building. It can only be calculated through measurement of the site under investigation. As in the case of single dielectric-wedge profile, after applying the low-loss approximation to (45) the approximate transmitted field for the single rectangular-building profile along a single effective path (See Fig. 1(b)), is given by

$$E_{RX}(\omega) \simeq \left(\frac{E_i(\omega)}{r_{total}}\right)\left(T_{1,s,h}(\omega)T_{2,s,h}(\omega)T_{3,s,h}(\omega)T_{4,s,h}(\omega)\right)L_{total,s,h}(\omega) \tag{46}$$

with $r_{total} = r_1 + r_2 + r_3 + r_4 + r_5$ and $T_{1,s,h}(\omega)\ T_{2,s,h}(\omega)\ T_{3,s,h}(\omega)\ T_{4,s,h}(\omega) = T_{total,s,h}(\omega)$, where $T_{1,s,h}(\omega)$, $T_{2,s,h}(\omega)$, $T_{3,s,h}(\omega)$, $T_{4,s,h}(\omega)$ are the FD transmission coefficients with respect to points 'J', 'K', 'L', 'M' (See Fig. 1(b)). From the analysis in [30-31], [23], [40], the approximate FD path-loss term for this case (assuming low-loss assumption) is given as

$$L_{total,s,h}(\omega) \simeq \exp\left[-j\omega d\sqrt{\mu\varepsilon}\left(1+\frac{\sigma}{2j\omega\varepsilon}\right)\left(\sqrt{\frac{\varepsilon_r}{\varepsilon_r-\sin^2\theta_1}}+\sqrt{\frac{\varepsilon_r}{\varepsilon_r-\sin^2\theta_5}}\right)\right] \exp\left(-j\beta_0(r_1+r_3+r_5)\right)\exp(-\alpha_b r_3) \tag{47}$$

Here $r_1 + r_5$ is the total distance travelled by the field in free space from point 'A' to point 'N' and r_3 is the distance travelled by the field in the interior of building.

Equation (46) is translated in TD as

$$e_{RX}(t) \simeq \left(\frac{e_i(t)}{r_{total}}\right) * \Gamma_{1,s,h}(t) * \Gamma_{2,s,h}(t) * \Gamma_{3,s,h}(t) * \Gamma_{4,s,h}(t) * l_{total,s,h}(t) \tag{48}$$

where $\Gamma_{1,s,h}(t) * \Gamma_{2,s,h}(t) * \Gamma_{3,s,h}(t) * \Gamma_{4,s,h}(t) = \Gamma_{total,s,h}(t)$ with $\Gamma_{1,s,h}, \Gamma_{2,s,h}, \Gamma_{3,s,h}, \Gamma_{4,s,h}$ as the TD expressions for the transmission coefficients at points 'J', 'K', 'L' and 'M' in Fig. 1(b) and are obtained as per (10), (14), (20), (25) and (27). The term $l_{total,s,h}(t)$ in (48) is the TD propagation path-loss expression corresponding to the FD term $L_{total,s,h}(\omega)$ in (46) and is given as [30]-[31]:

$$l_{total,s,h}(t) \simeq \exp\left\{\left(-(\sigma d)/2\right)\sqrt{\frac{\mu_2}{\varepsilon_2}}\left(\sqrt{\frac{\varepsilon_r}{\varepsilon_r-\sin^2\theta_1}}+\sqrt{\frac{\varepsilon_r}{\varepsilon_r-\sin^2\theta_5}}\right)\right\} * \delta\left(t-\frac{r_1+r_5}{c}\right) * \delta\left\{t-d\sqrt{\mu_2\varepsilon_2}\left(\sqrt{\frac{\varepsilon_r}{\varepsilon_r-\sin^2\theta_1}}+\sqrt{\frac{\varepsilon_r}{\varepsilon_r-\sin^2\theta_5}}\right)\right\}\exp(-\alpha_b r_3) \tag{49}$$

IV. Results and Discussion

In this section the numerical simulation results, based on the aforementioned TD and FD solutions for the transmitted field are presented. In FD analysis first the frequency components contributing to the total transmitted field at Rx are identified. Following (Table I, [43]), all the transmitted frequency components reaching within an error or proximity of 10^{-6} m with respect to the Rx, are considered as if reaching exactly at Rx. Considering only these frequencies, the FD transmitted field is calculated as per (30) and (45), and then IFFT of this result is computed to obtain the reference transmitted field. In TD analysis, first the single effective path of the transmitted field for the given scenario is traced using a path-tracing algorithm, based on the low-loss approximation [43], and then the transmitted field along that path is calculated in TD through (43) and (48). The TD results are then compared with the reference IFFT-FD transmitted field for validation of the proposed solution. Throughout our work the Gaussian doublet pulse is used as the excitation UWB signal which is expressed in TD as [21]

$$s(t) = \left(\frac{1}{\tau}\right)\left(\sqrt{\frac{\tau}{3\sqrt{\pi/2}}}\right)\left(1-\frac{2t^2}{\tau^2}\right)\exp\left(-\frac{t^2}{\tau^2}\right) \tag{50}$$

where τ is the full width half maximum pulse duration with a value of 0.1 ns. The Fourier transform of (50) is given as

0018-9545 (c) 2013 IEEE. Personal use is permitted, but republication/redistribution requires IEEE permission. See http://www.ieee.org/publications_standards/publications/rights/index.html for more information.

This article has been accepted for publication in a future issue of this journal, but has not been fully edited. Content may change prior to final publication. Citation information: DOI 10.1109/TVT.2014.2323699, IEEE Transactions on Vehicular Technology

$$S(f) = 2 \times \sqrt{\pi} \times \sqrt{\frac{\tau}{3\sqrt{\pi/2}}} \times \left(\pi^2 \tau^2 f^2\right) \times e^{-\pi^2 \tau^2 f^2} \qquad (51)$$

The presented results also show the simulated effective transmission path and the simulated propagation profile in their inset along with the transmitted field. Throughout the paper, obstacles made up of low-loss dielectric materials are considered, with relative magnetic permeability as unity. In all the results the values of relative dielectric permittivity and conductivity are chosen such that the resulting loss-tangent values are in accordance with that of dry-concrete, dry-wall, Styrofoam, door, plaster and dry-brick[30-31], ([27], Figure 6)([41], Table 1), [42], [44] and [46].At last the TD transmitted field is compared against the TD diffracted field obtained through TD-UTD-PO [21], for a single dielectric-wedge profile and single corner of a rectangular building profile.

During UWB signal propagation through single dielectric-wedge profile, it was found that for a ray incident at the n-face with an angle greater than the critical angle given by $\theta_c \simeq \sin^{-1}(1/\sqrt{\varepsilon_r})$, total internal reflection occurs. Thus it was found that up to a maximum internal angle $a_{\text{int(max)}} \simeq 2\sin^{-1}(1/\sqrt{\varepsilon_r})$, of the dielectric-wedge, transmission through the wedge is possible, but for an internal angle greater than this maximum value propagation through the dielectric-wedge would be negligible due to total internal reflection at the n-face. For $\varepsilon_r = 5$ and $\sigma = 0.016$ S/m, this maximum internal angle comes out to be 53.130 degrees.

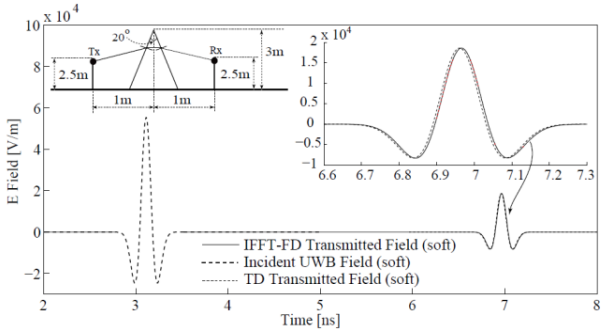


Fig. 3.Distortion less transmission through a low-loss dielectric wedge compared with a reference, received Gaussian Doublet pulse, with $\sigma = 0.016$ S/m and $\varepsilon_r = 2.4$ [27].

First, a case of transmission through a low-loss dielectric-wedge is shown in Fig. 3, where the transmitted field suffers negligible distortion in shape in comparison to the shape of the UWB pulse incident at 0-face; however the amplitude of the transmitted field is attenuated.

Another simple case, consisting of single dry-concrete dielectric-wedge, as the obstacle between Tx and Rx is shown in Fig. 4 with internal angles $a_{\text{int}} = 30^o, 35^o$ and 40^o. The TD results for the transmitted field for both hard and soft polarizations are in excellent agreement with corresponding IFFT-FD results, thus validating the proposed TD solution. The result signifies that for low-loss dielectric obstacles, variation in the refracted angle corresponding to different frequency components is approximately zero, and the beam of rays past refraction can be approximated with a single effective ray as considered in the proposed TD analysis. Also, it can be inferred that the results for soft and hard polarized fields come closer to each other as the distance travelled by the field within the dielectric wedge decreases.

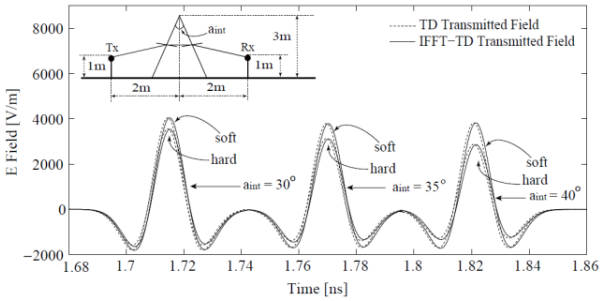


Fig. 4.Transmitted field for single dielectric-wedge profile, with $\sigma = 0.016$ S/m and $\varepsilon_r = 5$ [30-31], [27], for different internal angles with the inset depicting simulated approximate path followed by the transmitted field.

However, for lossy dielectric obstacles the true angles of refraction vary with time and frequency, in a much more prominent way. In such condition the distortion in the transmitted waveform at Rx seems inevitable as shown in Fig. 8. Thus in case of lossy-dielectric obstacles, analysis for the transmitted field is to be looked upon with a greater degree of care and it is a matter of future investigation.

The single rectangular-building profile of a microcellular scenario is analyzed in Fig. 5, where the specific attenuation constant is $\alpha_b = 0.3$ dB/m [22], [33]. The figure shows transmitted field at Rx for both the polarizations for different thickness of the dielectric walls and the TD results match quite closely with the IFFT-FD results.

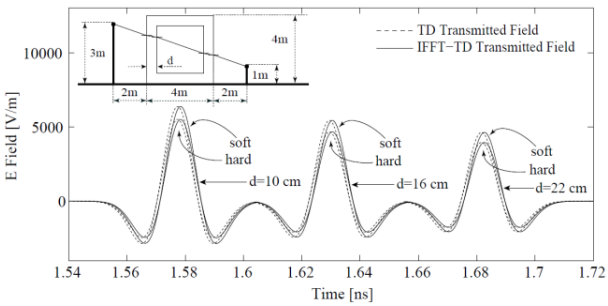


Fig. 5.Transmitted field for different cases of transmission through single rectangular-building profile where $\sigma = 0.016$ S/m, $\varepsilon_r = 5$ [30-31], [27] and $\alpha_b = 0.3$ dB/m, with the inset depicting the simulated approximate path followed by the transmitted field.

In Fig. 6 the transmitted field past the corner of a rectangular-building profile, with specific attenuation constant $\alpha_b = 0.3$ dB/m, is presented. The transmitted fields in all the cases discussed above are undistorted due to very small magnitude of loss-tangent with respect to unity. As expected,

0018-9545 (c) 2013 IEEE. Personal use is permitted, but republication/redistribution requires IEEE permission. See http://www.ieee.org/publications_standards/publications/rights/index.html for more information.

This article has been accepted for publication in a future issue of this journal, but has not been fully edited. Content may change prior to final publication. Citation information: DOI 10.1109/TVT.2014.2323699, IEEE Transactions on Vehicular Technology

the results in Fig. 2-6 show that the soft polarized transmitted field suffers lesser attenuation than the hard polarized transmitted field.

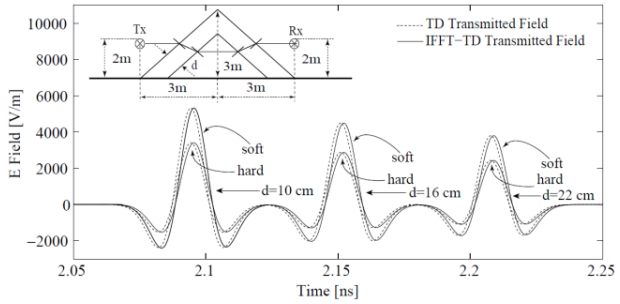


Fig. 6.Transmitted field for different cases of transmission through the profile shown in Fig. 1c. Here $\sigma = 0.016$ S/m, $\varepsilon_r = 5$ [30-31], [27] and $\alpha_b = 0.3$ dB/m with the inset depicting the simulated traced path of the transmitted field.

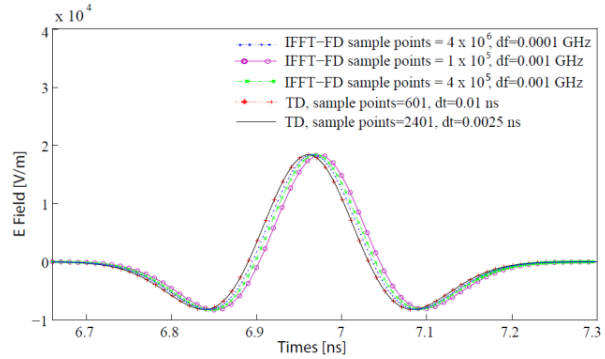


Fig. 7.Comparison between results of TD and IFFT-FD solution for a single dielectric-wedge profile, with different values of dt, df and number of sample points with $\sigma = 0.016$ S/m, $\varepsilon_r = 2.4$ [27].

In all the results produced above, we have chosen the time step *dt* as 0.0025 ns for the TD analysis and in case of IFFT-FD calculations, we used frequency step *df* as 0.0001 GHz. For accurate results we took 4 x10^6 frequency sample points to calculate the IFFT-FD transmitted field (See Fig. 7), [37], [38]. The software tool MATLAB 7.6 was used and all the cases were run on an Intel Core-i5 II-generation 3.10 GHz computer, with 6 GB of RAM. An analysis to provide an idea about the values of parameters that provide accurate transmitted field prediction is presented in Fig. 7. Here, a single dielectric-wedge profile is considered with, h_t=2.5 m=h_r, h_w=3 m, d_1=1 m=d_2 and a_{int}=20^o.

Result shown in Fig. 7 demonstrates that in order to correctly obtain the IFFT-FD result, very large number of frequency sample points and very small value of *df* are required whereas, comparatively, very few number of time sample points are needed to obtain the TD transmitted field properly. As the numbers of sample points are increased and value of *df* is decreased in the IFFT-FD approach, the transmitted field curve shifts in position. This occurs, considerably, till we chose *df* as 0.0001GHz (See Fig. 7). On further reducing *df* there is no change in the obtained IFFT-FD curve. Moreover, as mentioned earlier in Section III-A, the frequency components actually contributing to the total transmitted field were determined first in all the cases presented. From the path tracing algorithm [23], [43] it was found that for the considered profiles, all the frequency components of the UWB signal were received within a proximity of order 10^{-6} m or less, with reference to Rx.

A comparison between the computation times of the IFFT-FD method and the proposed TD solution is presented in Table I. The presented results in Table I establish that the proposed TD analysis is computationally very efficient in comparison to the IFFT-FD solution. The two main reasons for such a significant reduction in the computational time in TD are: (i) the efficient convolution technique (Section 10.1, Figures 10.1-10.2 in [37]), due to which few number of time samples suffice to provide accurate results. (ii) Approximation of the multiple transmission paths in FD by a single effective path for low-loss dielectric case.

The proposed TD solution agrees exceptionally well with the corresponding IFFT-FD solution if the loss-tangent value is of the order of 10^{-2} or less in the considered UWB bandwidth, which is the case presented in Fig. 2-7 and Fig. 9. These values of loss-tangents correspond to the dielectric materials like dry-wall, Styrofoam, dry-brick and plaster etc. [27], [41] and [46]. If we increase the value of loss tangent then the agreement tends to decrease which is evident from Table II. The result in Fig. 8 presents the TD transmitted field past a dielectric obstacle with loss-tangent value in close accordance with that of wall made up of concrete blocks [27].

TABLE I
AVERAGE RATIOS OF THE COMPUTATION TIME OF THE TWO METHODS

Propagation Profile	$T_{IFFT-FD}/T_{TD}$
Single Dielectric-wedge	52.03
Single Rectangular-building	95.69
Single Corner of a Building	97.16

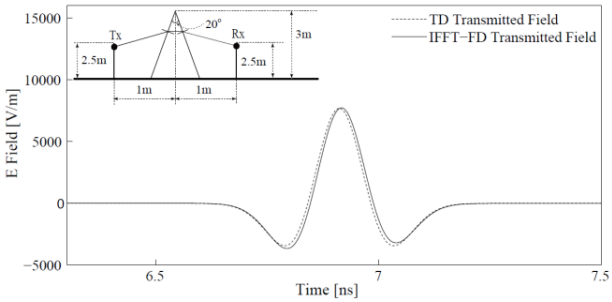


Fig. 8.Transmitted field for the single dielectric-wedge profile, with $\sigma = 0.06$ S/m and $\varepsilon_r = 2.1$ ([27], Fig. 7b), with inset depicting the simulated traced approximate path of the transmitted field.

In Fig. 8, the TD result is in good agreement with IFFT-FD result except for a little distortion in the negative peaks which is quite feeble. Here the distance travelled by the transmitted field inside the dielectric material is approximately equal to 15 cm. Similar results were obtained for transmission through a single dielectric wall with width 15 cm, height of Tx and Rx equal to 2 m and 3 m respectively and with dielectric properties in close accordance with that of concrete blocks [27]. However, the TD results lost their agreement with the

0018-9545 (c) 2013 IEEE. Personal use is permitted, but republication/redistribution requires IEEE permission. See http://www.ieee.org/publications_standards/publications/rights/index.html for more information.

This article has been accepted for publication in a future issue of this journal, but has not been fully edited. Content may change prior to final publication. Citation information: DOI 10.1109/TVT.2014.2323699, IEEE Transactions on Vehicular Technology

TABLE II
NORMALIZED MEAN SQUARE ERROR OF ALL THE THREE CASES

Loss tangent		0	0.01918	0.02452	0.03997	0.08269	0.13114	0.17128	0.18734	0.19983	0.23663	0.25478
Dielectric Wedge (Fig. 4)	Mean Square error	1.92E-4	1.77E-4	3.45E-4	3.33E-4	2.46E-4	3.12E-4	2.71E-4	4.94E-4	5.20E-4	7.34E-4	8.55E-4
Rectangular Building (Fig. 5)	Mean Square error	2E-3	2.03E-3	2.10E-3	2.29E-3	2.17E-3	2.54E-3	3.60E-3	3.68E-3	4.05E-3	6.01E-3	6.69E-3
Corner of Building (Fig. 6)	Mean Square error	2.8E-3	2.92E-3	2.95E-3	3.38E-3	6.95E-3	2.07E-2	4.34E-2	5.44E-2	6.55E-2	9.36E-2	1.04E-1

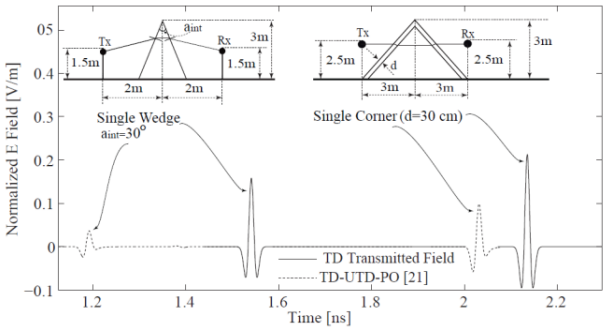


Fig. 9.Comparison between the transmitted field and the diffracted field component obtained through TD-UTD-PO, for the single dielectric-wedge and single corner profile with $\sigma = 0.016$ S/m, $\varepsilon = 2.4$ [27] and $\alpha_b = 0.3$ dB/m.

exact IFFT-FD results when the scenario was changed either to the single rectangular building profile or the corner of a rectangular building profile. Thus, for a single obstacle scenario such as discussed in Fig. 3-4, 7, 8 and a single dielectric wall, it is observed that the proposed method is in close agreement with the IFFT-FD solution until the loss tangent value is 0.17 (corresponding to $\sigma = 0.06$ S/m, and at frequency 3 GHz) in the considered UWB bandwidth (See Table II).

There are two factors responsible for the error between TD and IFFT-FD results. These are (i). the error in MATLAB computations due to numerical rounding (ii). the paths followed by TD and IFFT-FD fields not being exactly the same. Table II presents the normalized mean square error for all three cases considered in the proposed work for different values of loss tangent. It is evident from Table II that for the considered low loss cases (See Fig. 3-8) the error between the TD and IFFT-FD results is predominantly due to the round off error of the MATLAB platform used for simulation. The slight time offset present in Fig. 3-8 was also found to be predominantly due to this round off error. This observation was made by comparing the results of the proposed scenarios with lossless and low-loss dielectric characteristics. In the presented work the maximum time offset is obtained in the case of transmission through rectangular building profile and the corner of a rectangular building profile and it is approximately equal to 0.01 ns, which can be considered as negligible (See Fig. 5-6). The offset observed in case of transmission through a single dielectric wedge profile was found to be 0.001 ns (See Fig. 3-4 and Fig. 8), which is negligible.

Table II also shows that the discrepancy between TD and IFFT-FD results increase with an increase in the value of loss tangent. It shows that with an increase in loss tangent the error due to beam splitting or dispersion (see Fig. 2) dominates.

In Fig. 9 a comparison between the normalized transmitted field obtained by the proposed TD solution and the normalized diffracted field obtained by TD-UTD-PO [21] solution is presented for a single low-loss dielectric-wedge profile and a right-angled corner of a rectangular-building profile. Both the diffracted and transmitted fields presented in Fig. 9 have been normalized against the maximum field obtained at Rx in absence of the obstacles. The comparison in Fig. 9 tells about the dominance of the transmitted field component over the diffracted field component in certain microcellular and indoor propagation scenarios, where the dielectric properties of the obstacles are similar to that of the considered low-loss dry-concrete, dry-wall and dry-brick etc. [30-31], [27], [42]. Thus it is clear that for accurate prediction of the total received field past dielectric obstacles, for UWB signals, transmitted field is necessary to be accounted. The presented work also establishes that the proposed TD solution is computationally more efficient in determination of the transmitted field than the conventional IFFT-FD method.

V. CONCLUSION

An approximate analytical TD solution has been presented for the transmitted field through low-loss dielectric obstacles, with canonical geometry, in an urban microcellular and indoor propagation scenario. Novel, approximate, analytical TD transmission and reflection coefficients were proposed for soft and hard polarizations, for the cases involving transmission through an interface between air and a low-loss dielectric medium and vice-versa. A deeper insight, based on the analytical FD formulations obtained by extension of the established FD formulations from technical literature, is presented to explain the physical propagation mechanism of the transmitted field through the lossy and low-loss dielectric obstacles. The results of the proposed TD solution are validated against the corresponding IFFT-FD results. The proposed TD solution outperforms the IFFT-FD analysis in terms of the computational complexity and efficiency. Finally,

0018-9545 (c) 2013 IEEE. Personal use is permitted, but republication/redistribution requires IEEE permission. See http://www.ieee.org/publications_standards/publications/rights/index.html for more information.

This article has been accepted for publication in a future issue of this journal, but has not been fully edited. Content may change prior to final publication. Citation information: DOI 10.1109/TVT.2014.2323699, IEEE Transactions on Vehicular Technology

a comparison between the TD transmitted field and the TD-UTD-PO diffracted field, for low-loss dielectric obstacles; manifests that the transmitted field component plays a major role in the accurate determination of the total received field for the UWB signals. The proposed TD solution and the in-depth analysis of the underlying physical propagation mechanism during transmission of the UWB signals through dielectric obstacles, are supposed to be vital in the analysis of UWB communication as they provide a fast and better prediction of the total transmitted field in microcellular and indoor propagation scenarios.

ACKNOWLEDGMENT

The authors are indebted to the reviewers for their valuable comments which helped to improve the presentation. The authors also want to thank Mr. Sanjeev Sharma for his continuous support, guidance and valuable suggestions.

REFERENCES

[1] M. Ghavami, L. B. Michael and R. Kohno, *Ultra Wideband Signals and Systems in Communication Engineering*. Chichester, U.K.: Wiley, 2004.

[2] A. F. Molisch, "Ultrawideband propagation channels-theory, measurement, and modeling," *IEEE Trans. Veh. Technol.*, vol. 54, no. 5, pp. 1528-1545, September 2005.

[3] L. Yang and G. B. Giannakis, "Ultra-wideband Communications," *IEEE Signal Process. Mag.*, vol. 21, no. 6, pp. 26-54, November 2004.

[4] W. Hirt, "Ultra-wideband radio technology: overview and future research," *Comput. Commun.*, vol. 26, no. 1, pp. 46–52, 2003.

[5] A. Muqaibel, A. Safaai-Jazi, A. Attiya, B. Woerner and S. Riad, "Path-loss and time dispersion parameters for indoor UWB propagation," *IEEE Trans. Wireless Commun.*, vol. 5, no. 3, pp. 550-559, March 2006.

[6] A. Karousos and C. Tzaras, "Multiple time-domain diffraction for UWB signals," *IEEE Trans. Antennas Propag.*, vol. 56, no. 5, pp. 1420–1427, May 2008.

[7] D. Porcino and W. Hirt, "Ultra-wideband radio technology: potential and challenges ahead," *IEEE Commun. Mag.*, vol. 41, no. 7, pp. 66-74, July 2003.

[8] R. C. Qiu, C. Zhou and Q. Liu, "Physics-based pulse distortion for ultra-wideband signals," *IEEE Trans. Veh. Technol.*, vol. 54, no. 5, pp. 1546-1555, September 2005.

[9] R. G. Kouyoumjian and P. H. Pathak, "A uniform geometrical theory of diffraction for an edge in a perfectly conducting surface," *Proc. IEEE*, vol. 62, no. 11, pp. 1448–1461, November 1974.

[10] T. W. Veruttipong, "Time domain version of the uniform GTD," *IEEE Trans. Antennas Propag*., vol. 38, no. 11, pp. 1757–1764, November 1990.

[11] P. Rousseau and P. Pathak, "Time-domain uniform geometrical theory of diffraction for a curved wedge," *IEEE Trans. Antennas Propag.*, vol. 43, no. 12, pp. 1375–1382, December 1995.

[12] R. C. Qiu and C. Zhou, "Pulse distortion caused by cylinder diffraction and its impact on UWB communications," *IEEE Trans. Veh. Technol.*, vol. 56, no. 4, pp. 2385–2391, July 2007.

[13] F. Capolino and M. Albani, "Time domain double diffraction at a pair of coplanar skew edges," *IEEE Trans. Antennas Propag.*, vol. 53, no.4, pp. 1455–1469, April 2005.

[14] P. Górniak and W. Banduriski, "Direct time domain analysis of an UWB pulse distortion by convex objects with the slope diffraction included," *IEEE Trans. Antennas Propag.*, vol. 56, no. 9, pp. 3036–3044, September 2008.

[15] P. R. Rousseau and P. H. Pathak, "A time domain formulation of the uniform geometrical theory of diffraction for scattering from a smooth convex surface," *IEEE Trans. Antennas Propag.*, vol. 55, no. 6, pp. 1522–1534, June 2007.

[16] A. Karousos and C. Tzaras, "Time-domain diffraction for a double wedge obstruction," *in Proc. IEEE Antennas Propag. Society Int. Symp.*, HI, Honolulu, June 2007, pp. 4581–4584.

[17] A. Karousos, G. Koutitas and C. Tzaras, "Transmission and reflection coefficients in time-domain for a dielectric slab for UWB signals," *in Proc. IEEE VTC-Fall*, Singapore, 2008, pp. 455-458.

[18] P. Liu and Y. Long, "Time domain UTD-PO solution for multiple building diffraction for UWB signals," *IEEE Electron. Lett.*, vol. 45, no. 18, pp. 924-926, August 2009.

[19] T. Han and Y. Long, "Time-domain UTD-PO analysis of a UWB pulse distortion by multiple-building diffraction," *IEEE Antennas Wireless Propag. Lett.*, vol. 9, pp. 795-798, 2010.

[20] P. Liu, J. Guo, J. Liu, J. Wang and Y. Long, "Multiple time-domain diffraction of plane waves by an array of perfectly conducting wedges for UWB signals," *in Proc. IEEE Int. Conf. ICMMT*, 2010, pp. 1173-1176.

[21] P. Liu, J. Tan and Y. Long, "Time domain UTD-PO solution for the multiple diffraction of spherical waves for UWB signals," *IEEE Trans. Antennas Propag.*, vol. 59, no. 4, pp. 1420-1424, April 2011.

[22] Y. L. C. d. Jong, M. H. J. L. Koelen and M. H. A. J. Herben, "A building-transmission model for improved propagation prediction in urban microcells," *IEEE Trans. Veh. Technol.*, vol. 53, no. 2, pp. 490-502, March 2004.

[23] S. Soni and A. Bhattacharya, "An analytical characterization of transmission through a building for deterministic propagation modeling," *Microw. Opt. Technol. Lett.*, vol. 53, no. 8, pp. 1875-1879, August 2011.

[24] Z. Chen, R. Yao and Z. Guo, "The characteristics of UWB signal transmitting through a lossy dielectric slab," *in Proc. 60th IEEE VTC-Fall*, Los Angeles, CA, USA, September 2004, pp. 134–138.

[25] R. Yao, Z. Chen and Z. Guo, "An efficient multipath channel model for UWB home networking," *in Proc. IEEE Radio and Wireless Conference (RAWCON)*, 2004, pp. 511-516.

[26] R. C. Qiu, "A generalized time domain multipath channel and its application in ultra-wideband (UWB) wireless optimal receiver design—part II: physics-based system analysis," *IEEE Trans. Wireless Commun.*, vol. 3, no. 6, pp. 2312-2324, November 2004.

[27] A. Muqaibel, A. Safaai-Jazi, A. Bayram, A.M. Attiya and S.M. Riad, "Ultrawideband through-the-wall propagation," *IEE Proc.-Microw. Antennas Propag.*, vol. 152, no. 6, pp. 581-588, December 2005.

[28] A. Muqaibel and A. Safaai-Jazi, "Characterization of wall dispersive and attenuative effects on UWB radar signals," *J. Franklin Inst.*, vol. 345, no. 6, pp. 640–658, 2008.

[29] Z. Yun and M. F. Iskander, "UWB pulse propagation through complex walls in indoor wireless communications environments," *in Proc. IEEE Int. Conf. Wireless Networks, Commun. Mobile Computing*, 2004, pp. 1358-1361.

[30] W. Yang, Z. Qinyu, Z. Naitong and C. Peipei, "Transmission characteristics of ultra-wide band impulse signals," *in Proc. IEEE Int. Conf. Wireless Commun., Networking Mobile Computing*, Shanghai, 2007, pp. 550-553.

[31] W. Yang, Z. Naitong, Z. Qinyu and Z. Zhongzhao, "Simplified calculation of UWB signal transmitting through a finitely conducting slab," *J. Syst. Eng. Electron.*, vol. 19, no. 6, pp. 1070–1075, December, 2008.

[32] M. Jing, Z. Nai-tong, "Transmission characteristics analysis of IR-UWB signal," *in Proc. IEEE Int. Conf. Wireless Opt. Commun. Networks*, 2009, pp. 1-5.

[33] Y. Miura, Y. Oda and T. Taga, "Outdoor-to-indoor propagation modeling with the identification of path passing through wall openings," *in Proc. IEEE 13th Int. Symp. Pers. Indoor Mobile Radio Commun.*, 2002, pp130-134.

[34] Remcom, Wireless insite, Site-specific radio propagation prediction software user's manual version 2.3, Remcom, 2008.

[35] A. D. Poularikas, Ed., *The Transforms and Applications Handbook*. Boca Raton, FL: CRC Press, 1996.

[36] A. Erdelyi, Ed., *Tables of Integral Transforms*. New York: McGraw-Hill, 1954, Bateman Manuscript Project.

[37] E. O. Brigham, *The Fast Fourier Transform.* Englewood Cliffs, NJ: Prentice-Hall, 1988.

[38] L. Sevgi, "Numerical Fourier transforms: DFT and FFT," IEEE Antennas Propag. Mag., vol. 49, no. 3, pp. 238-243, June 2007.

[39] P. R. Barnes and F. M. Tesche, "On the direct calculation of a transient plane wave reflected from a finitely conducting half space," IEEE Trans. Antennas Propag., vol. 33, no. 2, pp. 90–96, May 1991.

[40] C. A. Balanis, *Advanced Engineering Electromagnetics*. New York: Wiley, 1989.

0018-9545 (c) 2013 IEEE. Personal use is permitted, but republication/redistribution requires IEEE permission. See http://www.ieee.org/publications_standards/publications/rights/index.html for more information.

This article has been accepted for publication in a future issue of this journal, but has not been fully edited. Content may change prior to final publication. Citation information: DOI 10.1109/TVT.2014.2323699, IEEE Transactions on Vehicular Technology

[41] F. Sagnard and G. E. Zein, "Characterization of building materials for propagation modeling: frequency and time responses," *Int. J. Electron. Commun. (AEÜ)*, vol. 59, pp. 337–347, 2005.
[42] A. M. Attiya and A. Safaai-Jazi, "Simulation of ultra-wideband indoor propagation," *Microw. Opt. Technol. Lett.*, vol. 42, no. 2, pp. 103-108, July 2004.
[43] S. Grubisic, W. P. Carpes, Jr., C. B. Lima and P. Kuo-Peng, "Ray-tracing propagation model using image theory with a new accurate approximation for transmitted rays through walls," *IEEE Trans. Magn.*, vol. 42, no. 4, pp. 835-838, April 2006.
[44] A. H. Muqaibel and A. Safaai-Jazi, "A new formulation for characterization of materials based on measured insertion transfer function," *IEEE Trans. Microw. Theory Tech.*, vol. 51, no. 8, pp. 1946-1951, August 2003.
[45] P. Tewari, S. Soni and S. Goswami, "A comparison between transmitted and diffracted field in a microcellular scenario for UWB signals," *in Proc. IEEE Asia-Pacific Conf. Antennas Propag.*, Singapore, August 2012, pp. 221-222.
[46] International Telecommunication Union, ITU-R Recommendation P.1238-7, *Propagation Data and Prediction Methods for the Planning of Indoor Radio communication Systems and Radio Local Area Networks in the Frequency Range 900 MHz to 100 GHz*, February, 2012.



Piyush Tewari was born in Uttarakhand, India, in 1988. He received his B.Tech. degree in Electronics and Communication Engineering in 2010 from DBIT, Dehradun, India, M.Tech degree in Digital Signal Processing in 2012 from G. B. Pant Engineering College, Pauri, India. He is currently working toward the Ph.D. degree in wireless communication from the Indian Institute of Technology, Delhi, India.

From 2013 to 2014, he was with the Department of Electronics Engineering, National Institute of Technology, Uttarakhand, India as an Assistant Professor. His research interest is focused on wireless channel modeling and its applications to new wireless communication systems.



Sanjay Soni was born in Uttar Pradesh, India, in 1975. He received his B.E. degree in Electronics Engineering in 1997 from Madan Mohan Malviya Engineering College, Gorakhpur, India, M.Tech. degree in Communication Engineering in 2004 from the Indian Institute of Technology, Kanpur, India and the Ph.D. degree in Wireless Communication Engineering in 2011 from the Indian Institute of Technology, Kharagpur, India.

From 1998 to 2007, he was with the Department of Electronics and Communication Engineering, G. B. Pant Engineering College, Pauri, India as an Assistant Professor. Currently he is with the Department of Electronics and Communication Engineering, Delhi Technological University, Delhi, India where he is an Associate Professor. His research interest is focused on propagation modeling and characterization of wireless channel, time-domain analysis of propagation channel for UWB signals.



Bajrang Bansal was born in Haryana, India, in 1983. He received his B.E. degree in Electronics and Communication Engineering in 2005 from Institute of Technology and Management, Gurgaon, India, M.Tech. degree in VLSI Design and CAD in 2008 from Thapar University, Punjab, India. He is currently working toward the Ph.D. degree in wireless communication from Delhi Technological University, Delhi, India.

From 2008 to 2009, he was a Software Engineer with HCL Technologies, Noida. From 2009 to 2011, he was with the Department of Electronics and Communication Engineering, Jind Institute of Engineering and Technology, Jind, India and with the Department of Electrical, Electronics and Communication Engineering, Institute of Technology and Management, Gurgaon, India as an Assistant Professor. His research interest is focused on wireless channel modeling and UWB technology.

0018-9545 (c) 2013 IEEE. Personal use is permitted, but republication/redistribution requires IEEE permission. See http://www.ieee.org/publications_standards/publications/rights/index.html for more information.

ISSN 2278-7763

Women Engineers: A Comparative Study between India and Australia

Dr. Seema Singh[1], Er. Susan Lee Fenton[2]

[1]Associate Professor in Economics, Delhi Technological University, Delhi, India
[2]Fenton Partners Pty Ltd, Melbourne, Victoria, Australia
Corresponding Author's email- seemasinghdtu@gmail.com

Abstract

Though India and Australia are quite different from each other on so many economic indicators but women participation in engineering is low at both places. However, after globalization and advent of information technology, participation of women in engineering education has increased manifold in India and it has gone ahead of the participation of women engineer in Australia while in Australia, it is experiencing a plateau. On the basis of twenty four case studies among which fifty-fifty are from India and Australia, the paper tries to study socio-cultural reasons for present status.

Keyword - engineering education, market, discrimination, liberalisation, gender, employment, work-life balance

1. INTRODUCTION

IJOART

Engineering is, generally, considered to be a male bastion and women participation is very low. The paper tries to discuss that it is true for both countries, India and Australia even though socio-economic life of women at both places are quite different from each other. The second section of the paper discusses that participation of women in engineering education is quite low in both the countries which is followed by inquiry of probable reasons on the basis of case studies of women engineers in the third section**.** Concerted efforts made to enhance participation in both Australia and India has been discussed in the fourth section. Some suggestions for improving the situation have been discussed in the fifth section. Last section concludes the discussion.

2. WOMEN STUDENTS IN ENGINEERING IN INDIA AND AUSTRALIA

A comparison between the Development Indicators of India and Australia has been made in the Table-1 which shows the differences in socio-economic life of women exist in both countries. Women's share in Australian population is more than fifty percent while they are only 48.3 percent in India. Again, the per capita GNI in Australlia is 36 times of the per capita GNI of India. There is universal primary and secondary education among women in Australia while in India participation in the primary education was just 73% in 1991 which has

Copyright © 2014 SciResPub.

ISSN 2278-7763

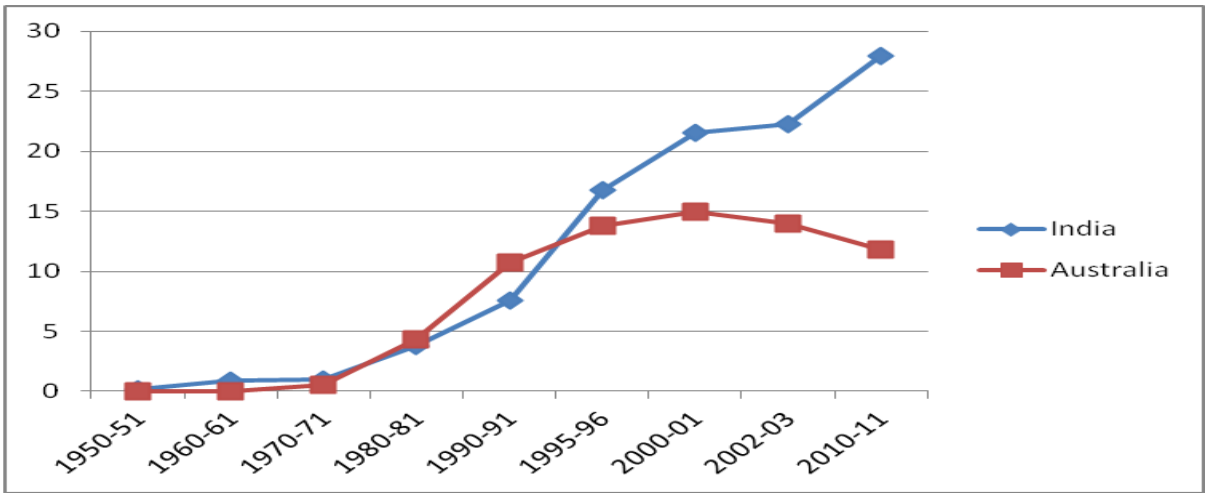
Table 1: Development Indicators in India and Australia

Sl.no.	Indicators	Year, unit	India	Australia
1.	Gross national income per capita	2010 in $	1,270	46,200
2.	Female Population	2010 as %	48.3	50.2
3.	Ratio of girls to boys enrolments in primary and secondary education (%)	2010	92	98
		1991	73	100
4.	Maternal mortality ratio per 1,00,000 live births	2008	230	8
5.	Women as % age of total labour force	2000	27.8	43.8
		2010	25.3	45.3
6.	Female part-time employment (% of total)	2005–10	------	70

Source: Table1.1, Table1-2, Table 1.3 , Table 2.2, Table 1.5, [10]

increased to 92 % in 2010. Thanks to Sarva Shikhsha Abhiyan, a compulsory primary education programme of the central government of India. Maternal mortality rate is 30 times more for 1,00,000 live birth in India than Australia. In short, Australian women have better socio-economic life than their Indian counterparts. However when it comes to comparing their participation in engineering education, the percentage of Australian women is lower than their Indian counterpart.

IJOART



Graph 1: Women engineers in India and Australia

The trend regarding participation of women in engineering has clearly emerged in the Table 2. and Fig-1 [3, 5 and 11]. In the beginning, participation of women in both countries was lowest in engineering in comparison of other stream of education. Over the years, it has increased but remained lowest. When compared these two countries,

Copyright © 2014 SciResPub.

ISSN 2278-7763

participation was almost same till 1990-91 but beyond it, growth of engineering in India is quite amazing. During the first decade of globalisation (1991-92 – 2000-01), it has grown almost three times and increased to 21.5 per cent in 2000-01 which further rose to 27.9 per cent in 2010-11 while, it has decreased in Australia during 2000 and 2010. Along with other reasons, a main factor for the decrease is decline in the number of girls studying science and mathematics in schools during this period. 'The research by John Mack and Barry Walsh reveals a growing gender disparity over the last 10 years, with just 1.5% of girls studying advanced mathematics alongside physics and chemistry. There was a disparity in educational choice as said by Dr. Wilson which was a major contributor to the decline in engineering participation, with 13.5% of girls choosing to study family and community studies in 2011, a subject that was not on

Table 2: **Percentage of Women Students in respective Disciplines in Both Countries**

SN	Years	India				Australia			
		Eng/Tech	Science	Medical	Arts	Engi/Tech	Science	Medical	Arts
1	1950-51	0.2	7.1	16.3	16.1	0	18	17.5	33
2	1960-61	0.9	10..5	21.9	24.6	0	17.7	15	44.6
3	1970-71	1.0	17.8	22.8	31.7	0.5	12	N/A	60
4	1980-81	3.8	28.8	24.4	37.7	4.3	33.6	38	62
5	1990-91	7.6	32.9	33.2	41.8	10.7	39.7	41	68
6	1995-96	16.8	37.0	39.8	40.6	13.8	42.2	45	68.7
6	2000-01	21.5	39.4	44.0	44.2	15	41.7	54	66
7	2002-03	22.3	40.2	44.7	45.4	14	34	55	68
8	2010-11	27.9	43.1	50.6	47	11.8	40	54	68

IJOART

Source: 1. data up to 2002-03 for India [5], For data 2010-11 –UGC, Higher Education in India at a Glance; Data for 2010-11- UGC

2. data on Australia up to 1970-71 [1]

For all other data: [3]

offer in 2001 [1,2 and 4]. In Australia, there is concern that the competition to obtain a higher tertiary entrance result score have seen high school students choosing easier subjects such as

Copyright © 2014 SciResPub.

ISSN 2278-7763

humanities compared to the more difficult subjects such mathematics and science. These subjects are also perceived as competitive and boring subjects which are unpopular choices for many girls which may have led to the under representation of girls and women in technology and engineering tertiary studies. Therefore, engineering is a male dominated profession. The culture of these male dominated careers, in turn, affected the girls' choice of tertiary studies. There is also a shortage of mathematics teachers as the supply of graduates in this area have gone to do medical, finance or commerce career [3 and 4].

3. CASE STUDIES ON WOMEN ENGINEERS IN AUSTRALIAN AND INDIAN LABOUR MARKET

All together 24 case studies[1] have been taken here. Out of which first half are from Australia and rest are from India. These case studies have been discussed with the belief that they may be able to decipher some of the reasons for the low participation. They are as follows:

E1 (49 years) is a high achiever from a selective school for girls. She obtained high marks in English, Mathematics and Chemistry in the early 1980s. She chose to study engineering and science as she is interested in both the applied and theoretical disciplines. She was always given the task of writing down data during all the practical work at the university.

IJOART

Upon graduation with good marks, she applied for many jobs but she was unsuccessful. Eventually she worked as a management trainee and never worked as an engineer. However, she was successful in the corporate world as she could implement logical thinking process to her varied projects. Her workplace was inflexible and working hours were long. She only took a few months maternity leave, less than the entitlement of 12 months, after the birth of her two children. She left the corporate world exhausted as combining motherhood with long hours was unsustainable. The stress of a marriage breakdown and being a single mother of two young children, now teenagers means having to work harder and long hours. She set up her own consultancy 4 years ago, training in occupational health and safety and first aid. In hindsight, she said she would have chosen to study a more female orientated profession as she felt she was never given a chance to work as a professional engineer.

E2 (31years) wanted to be an engineer as it is an applied subject. After finishing high school, she was highly stressed and decided to take some time away from studies. It was useful as she said it was a time for personal growth. A year later, she enrolled to study engineering at the university. She started as a civil design engineer and then briefly in construction. She was

Copyright © 2014 SciResPub.

ISSN 2278-7763

discouraged to continue onsite and transferred to the design office. She soon resigned and now works long hours as a construction engineer in another company. She enjoys the outdoor work but she now finds herself exhausted when she comes home. The older male engineers treated her like an assistant administration officer. She gets on well with contractors as she is physically strong and tolerant. She is not sure if she could combine family and work in the future, as the four women engineers she works with, three have no children or one with grown up adult children.

E3 (52 years) is hard working and a determined person. She got along well with the male blue collar workers and other male engineers of her age. Her male supervisor was sexist and discriminated against her. As an example, she would not be invited after work to join the other workers for a social in a small town where she worked. She soon left the company and moved with her husband to Melbourne. She applied for many jobs and she never received any interview as she felt she has a female name on the resume. Eventually she joined a research body where new legislation was introduced to recognise equal opportunity in the workplace. She has three children and it became harder to juggle a family while working fulltime, she subsequently resigned when she was in her mid thirties. She volunteered in her children's schools, played golf and joined a choir.

IJOART

E4 (53 years) is good in numeracy and she was encouraged by her mother to do engineering. Her college had programs to support girls in engineering. She worked in administration part time before she completed her engineering course and then changed to an engineering position upon graduating. She was not happy at work as her supervisor was unsupportive. It came as no surprise that she resigned from her job with the government department to have her first baby. She now regretted the decision as she found that it was very difficult to return to engineering after having three children. Her children are now adults. She helped in the kindergarten, school and sporting activities. She now works part time in a theatre serving food.

E5 (56 years) was studying for her engineering doctorate when her husband had a car accident. She did not complete her degree and cared for the family. She taught computer programming. She faced discrimination based on her accent. She left her teaching role after few years and now works in administration. She has an adult daughter who is now an engineer.

Copyright © 2014 SciResPub.

ISSN 2278-7763

E6 (31 years) is good in both Mathematics and Environmental Science. Her parents love nature and her father is a draftsman. She enjoyed university life but a lecturer once told her in front of the class of 40 that "...girls should not have done engineering" in response to a question she asked. She worked in design office and managed projects. Unfortunately, she felt she had not been briefed or supported which was disappointing. She has to struggle through many tasks and eventually resigned. Interestingly, both supervisors were female engineers. She then studied horticulture and now, happily supervising environmental community projects

E7 (33 years) achieved excellent results in her Higher School Certificate. She studied a combined degree in Engineering and Arts because she wanted to do practical work and also learn a new language. She also had a scholarship throughout her university course as well as work experience. She fitted in the engineering course very well and upon graduation, she applied to many engineering jobs but received very few interviews. She finally got a job as a process supervisor in a brewery. She was chosen because the company wanted someone to help to change their internal culture. It was not an engineering position. She was given overnight shift work. She faced verbal abuse and she was very unhappy. Her supervisor was unethical and sexist. He was also a bully. She soon applied successfully for an engineering position with a global company and she moved to New Zealand with her engineer husband. He landed in an engineering position easily and this has greatly developed his skills. In New Zealand, she was in charge of a gas plant and when she was seven months pregnant, her workload in an isolated plant did not change. She had to climb up many stairs to shutoff a control which was one of her many responsibilities and she feared for her safety and health. The workplace was 70 km away from home. She was discrimination as she was not given lighter duties and eventually, she resigned. Now, she has two young children. For career, she wants to be involved with local government and the community. She retrained to be a teacher as the job is flexible and is a family friendly career. She aspire to be a writer.

E8 (54 years) graduated in engineering over an extended time. She worked hard and she supported her husband while he was studying for his PhD. She reflected fondly about the projects she worked in Malaysia and the respect she received. When she returned to Australia, she worked for a consultant. She went on site to discuss a major project and the client asked if she could be replaced, as he preferred to deal with a male engineer on the project. She took a career break when her son was born. She had a stressful time combining full time work and

IJOART

Copyright © 2014 SciResPub.

ISSN 2278-7763

looking after her family. She has no support because her husband, an engineer was transferred interstate. She also had no support network that she could call on to assist in the new place.

E9 (22 years) is a high achiever and she was one of the top students in the state. Her parents were not happy when she announced to study engineering rather than medicine. Three years into her study of the combined degree of Engineering and Commerce, she told me that the course is too theoretical and she was pleased for doing Commerce too which will balance the engineering experience. She went to England for six months on an exchange program.

E10 (50 years) is strong in numeracy compared to literacy. She went to college 30 years ago and was very well supported as by policy, they were encouraging girls to study engineering. She then worked in a consultancy firm where she was highly regarded. She loves working as an engineer and continued to work very hard until her second child was born. She asked her director if she could bring the baby into work which was refused. She felt compromised and resigned soon after that. She taught at her old engineering college for few years and later, set up her own engineering consultancy business from home. She is very busy bringing up teenagers while working fulltime and helping her aged parents.

IJOART

Twenty five years ago, E11 (50 years), as a researcher, she received verbal and physical abuse from a male colleague who tried to undermine her. She was promoted to a senior research position for which he was unsuccessful. Being very upset, he sabotaged her research. She complained to the management but she received no support. A common bullying tactic is exclusion which she received. She also has a family. She felt that she should have had a mentor like the other men scientists. She volunteers in environmental educational program.

E12 (55 years) was good in Mathematics, Science and languages in high school. She has great communication skills and in 2012 organised the 30th reunion of her engineering university class. She has good engineering career specialising in designing water supply systems and project management. She was well regarded by her peers and chose to leave full time engineering to raise her family. She trained as a teacher and taught at the vocational level. She also volunteered in her children's school. She also consults in her husband's engineering company and continues volunteering in the community.

Copyright © 2014 SciResPub.

ISSN 2278-7763

Being a good student, E13 (47 years) wanted to be a civil engineer like her father but the idea was vehemently opposed by her guardian because a civil engineer has to go for field work frequently which is not an ideal situation for a woman. They wanted her to pursue medicine. The negotiating point for them was pursuing electrical engineering. She graduated in electrical engineering in 1988 from Maulana Azad Regional Engineering College (Now, NIT, Bhopal). She joined ITI (a public sector undertaking) at Allahabad, UP. When she got married, she could not manage and left job to join her husband. Later on, as her in-laws were at Delhi, she joined a reputed engineering college as guest faculty in 1992-93 later on as a permanent faculty. She did her ME and Ph.D. from the same college. As her husband is also an engineer, she has got the support as her husband. Her only son is also pursuing engineering.

E14 (52 years) is a Civil Engineer and works in a consultancy firm. When she expressed her preference for engineering profession it was opposed by the family members as no one in her paternal family was engineer. However, a maternal uncle, who was himself an engineer, supported her. She graduated in Civil Engineering from in 1982. She was selected through campus placement by big construction company but was fired when the company came to know that she is preparing for a job. After working for other organisations, she left to take care of her two kids. In 1995, she started her own consultancy firm but could not handle and now, working as a senior executive with a consultancy firm in New Delhi. Apart from her consultancy firm, she is quite busy with growth of women in the profession. She frequently participate in International conferences and seminars on engineering education and is founder President of Women in Science & Engineering (WISE) India. She has two grown up kids. Her son is studying civil engineering in UK.

IJOART

E15 (27 years) works as Contract faculty in computer engineering with a reputed engineering institution at Delhi for which she has migrated from her home town. Though she studied Biology at high school, she was more interested to join engineering like her father. She is eldest of five. All her three sisters are pursuing professional education and the brother studies in school. Her mother is a Post-graduate Degree holder in Zoology and was teaching in schools but as the daughters grew up, she preferred to stay at home to look after her daughters. She is Muslim by religion.

E16 (37 years) had Mathematics and Biology at plus two level[2]. But she could clear engineering entrance test only and graduated in computer engineering in 2002 at an

Copyright © 2014 SciResPub.

ISSN 2278-7763

government engineering college in Assam. Her father is a teacher who gave importance to education. Thus, all three sisters are well educated and are employed, but she is the only one who is an engineer. After graduation she started teaching in an engineering college as guest Faculty but migrated to Delhi to accompany her husband. At Delhi, she joined as contract faculty and pursuing Master's programme from the same technological university.

E17 (50 years) is daughter of a businessman in the capital. Family belonged to upper middle class. As she was good in mathematics and at that time, there was no entrance test. She joined engineering in a government engineering college. Just after passing final examination she got teaching job and later on, married her classmate. Her husband started his own business. She continued teaching till the time she completed 20 years of service. After that, she took voluntary retirement and joined her husband in his business. Her two children are now grown up but during their childhood, her mother looked after them, whenever required.

E18 (52 years) gives credit to her science teacher for joining engineering. The teacher use to give his students enough time to experience science in their day to day life contrary to today's children who are in the rat race of getting high marks. The teacher always helped her in exploring science. After plus two, engineering was an obvious choice. She has always tried to explore new and emerging fields. She gives credit to her husband and mother for her achievement as at the workplace, she has to fight for her rights. Now, she is senior scientist in one of the government's R&D lab.

IJOART

E19 (25 years) is daughter of an Indian Administrative Officer. She was born with proverbial silver spoon. As technical lines are more rewarding than traditional lines and now with so many private engineering college, getting admission is not difficult, she opted for engineering. Though she could not get campus placement but now, she works with an IT firm on a recommendation of one of her relative who is a very high post in the same organisation. For parents, engineering background was a good option for getting a better groom for their daughter but now, she is enjoying her independence and does not want to get married so early in her life. She is bargaining with parents for further study abroad.

E20 (30 years) is daughter of a college Professor. Everybody in her neighbourhood was trying for engineering, so, it was an automatic choice for her and her elder brother who is one year older. Both of them could not clear entrance test of government engineering college and the

Copyright © 2014 SciResPub.

ISSN 2278-7763

private engineering college was the only option for them for which they have paid high fees. Financially it was a tough decision and all four years were quite difficult for them but ultimately, it has paid off. Both of the siblings cleared their engineering and ultimately joined industry. Though timing was quite erratic but she was enjoying the independence. However, parents persuaded her for marriage. Though getting good match is difficult but as she was an engineer, it was not difficult for her. Ultimately, she has been married to an engineer who is working at Ireland, UK. She left job to join her husband and will work, if she gets there.

E21 (29 years), a civil engineer from not so good engineering college, is a daughter of civil engineer who is running a construction firm very successfully. Though she is sure that she can get a job but she is working in her father's firm. She is not in hurry to get married and concentrating on her work.

E22 (23 years) is one of the two daughters of a police officer. She wanted to pursue English literature but parents forced her to opt for engineering for early settlement and respect associated with engineering. She graduated B. Tech. in Information Technology. Being topper of her batch, she got selected through campus in an MNC but hectic time schedule and uncertainty she did not join. She is now preparing for the Indian Administrative Services[3].

IJOART

E23 (45 years) was good students in mathematics and opted for engineering. Her father was a government servant in Andhra Pradesh. After doing graduation in electrical engineering she joined State government. After marriage, she migrated to Delhi and could never join the work again. Her husband is a chartered accountant. Her only son is pursuing engineering.

Formerly a Class I Engineer of Government of India**,** E 24 (59 years) is a Mumbai based Project Administration Consultant in field in the construction sector. Basically, she has a rural background. Fondly, she remembers that once an engineer came to his village whom they all use to respect a lot. Being girl of one of the richest family of the village, she got the opportunity to talk to him and it was very inspiring moment for her. But ultimately, it was her brother-in-law[4] who found that she was very quick in solving mathematics and advised her to take up engineering. She did her B.Tech. in civil engineering from a government college. There was not a ladies toilet in the college and she has to share the ladies staff toilet with the clerk- the only ladies staff in the college. She has always to fight for her right. She feels that women engineers need some adjustment according to their domestic responsibilities and they

Copyright © 2014 SciResPub.

ISSN 2278-7763

will be far superior employees. She has had brilliant academic career and has received many national and international awards.

3 Interpretation of Case Studies

3.1 Opportunities for Engineering Education

Engineering seems to be a challenging profession for brilliant and high scoring students but it needs lots of concentration and hard work. At the same time, there are wider choices of tertiary studies available for girls [7] which are similarly stimulating but requires less time and concentration. That is one of the reasons for fewer women pursuing engineering in Australia. In case of India, getting admission was very difficult before opening of many private colleges if parents are ready to pay very high college fees. Globalisation, opening up of the economy and advent of information technology has expanded demand for engineering manpower. Early settlement, social recognition, higher chances of getting better groom are some of the reasons due to which parents are ready to pay higher tuition fees. Young women engineers are also enjoying their enhanced self esteem and economic independence.

3.2 Profession Selection

IJOART

From the case studies, it is clear that most of the adult children of women engineers in Australia has not opted for engineering at university except for one who has Sri Lankan heritage[5]. So, there is a freedom of letting young people choose to study in the areas they are interested in. However, this is not the case for new migrant families, as there are still strong expectations from parents. However, the case is not same for India. Most of the women engineers have either father or uncle, an engineer, and their off springs have opted for engineering. Could this be a cultural expectation in India to continue to study in areas to meet with the expectations of the parents?

3.3 Life-Work Balance

Though, women bear the larger proportion of housework and child care but housework is normally done by the husband and wife in Australia.. Currently there are insufficient childcare places for preschool aged children in Australia which makes it very difficult to combine work and motherhood. Many are also having the responsibility of looking after their aged parents. They are exhausted from working fulltime at the workplace and continuing to work more at home. However, in case of their Indian counterparts, earlier standard family size was quite large. So, either the old age parents prefer to stay with the son whose wife stays at home or their engineer daughter-in-law will hire a full-time help at reasonable price. So in case of

Copyright © 2014 SciResPub.

ISSN 2278-7763

senior engineers, their inability to get a job with their husband was the reason for unemployment and not the work pressure. In recent times, many women engineers are joining labour market but their parents are not so aged who requires care. In fact, they may take care of their grandchildren. However, with the school aged children, women engineers themselves do not want to travel or work for longer period outside home. Unless there is flexibility in their engineering profession, more women engineers will be leaving the profession during this stage of their lives.

3.4 Family Size

Many woman engineers in Australia have three children but their counterpart in India in the study, has one or two only. It needs to be further investigated that whether one or two children norm is common among Indian women and three among Australian or specific to engineers only. In case of three children, one can understand volume of house hold work which is required to put in on the regular basis. Theoretically, it is perceived as women participation in the labour market increases, number of children per women decreases which has culminated in a slogan, 'Development is the best contraceptive'.

IJOART

3.5 Less Flexibility in the Indian labour Market then Australian

As the number of women doing engineering is plateauing in Australia. Measures are being taken for retention of experienced people in the workforce, Flexible working legislation, Fair Work Act 2009 has been introduced. As a result, there have been women design engineers working part time when they become mothers. Time will tell if this legislation will help to encourage more girls to choose engineering as a career. For now, majority of female engineering students have chosen environmental engineering as this suggests they prefer caring, nurturing of natural life. Women engineers who are working full time either do not have children or have adult children, otherwise they leave. Indian labour market is not as flexible and with the school aged children, women engineers themselves do not want to travel or work for longer period. So, unless there is flexibility in engineering profession, more women engineers will be leaving the profession during this stage of their lives.

3.6 Self Perception for Unpaid Care Work

The capability of doing paid work has been given a lot of focus in Amartaya Sen's framework of development as freedom. His contention is that paid jobs help women become financially independent from their husbands and fathers and to make their own choices in the consumer and financial markets. He also adds that the freedom that goes with the paid labour brings

Copyright © 2014 SciResPub.

ISSN 2278-7763

important values for women such as self-esteem, dignity and autonomy [6]. A question often arise in this context that if all women would engage in paid work than who would do the unpaid caring? In all likelihood, either woman would be overburdened with a double workday or many caring needs would be unattended. Case studies done in Australia reveal that woman engineers have to do very hard work both at home and the workplace. So, many of them have left the mainstream engineering profession and have decided for both paid and unpaid care work in the education and community sector.

3.7 Cultural and Social Aspect Influences the Decision

The case studies have been able to show that not only economic aspect but the cultural and social aspect influences the decision. Engineering is still perceived as a competitive male profession. Girls and women prefer to engage in career which is socially acceptable and meaningful to them. So the social and cultural influences cannot be overlooked in conducting further studies.

4. EFFORTS TO ENHANCE PARTICIPATION OF WOMEN AT ENGINEERING IN AUSTRALIA AND INDIA

IJOART

There have been concerted efforts for over 30 years to encourage more women to study engineering and science [3 and 4]. Both in India and Australia, there have been many efforts to encourage students to continue studying mathematics and applied sciences in high school by offering scholarships and encouraging teachers to opt for better teaching methodologies to make these subjects more interesting and practical. The challenge is to increase number of female students to study mathematics and applied sciences and to encourage them to choose engineering as a career. At college level, there are reservations of seats for female students. Some companies provide female students with a supportive environment where they can gain insights into engineering from a female perspective with mentoring from successful female engineers. But if the participation is still very low, evaluation needs to be conducted as to whether these measures are effective. Role of association and societies like WISE and INWES in mentoring young women engineers in their professional career is very important. The advantage of having more women in these fields are well known as diversity will add to the richness of ideas, planning, problem solving, operation and construction of projects. Women engineers would bring a different perspective of thinking, planning and implementing projects which may be complementary to male engineers or scientists [8].

5. Conclusion

Copyright © 2014 SciResPub.

ISSN 2278-7763

Though India and Australia are quite different from each other on so many economic indicators but women participation is low at both places. However, it is important to note that till 1991 it was more or less same but Indian percentage participation has overtaken Australian. Second important aspect is large attrition during child bearing years. Unless steps are taken to prevent the attrition, there will be a continued loss economically to the country. Women engineers are an asset as they are good collaborators and communicators. It has been inferred that greater responsibility of care work, lake of support system for domestic work within and outside family, male chauvinism among some of the male bosses and opportunity of working part time are some of the reasons for low participation in Australia. While in India, availability of support system, expansion of engineering education system and financial independence at early age are some of the factors which are attracting young girls towards engineering education. As most of the mothers are house wife and at some point of time, they may have wished financial independence, are extending full support to their daughter and there are greater chances of getting better groom for their daughter also. However, they lack mentoring and there is need that associations of women engineers to extend their helping hands towards women engineers.

IJOART

Notes:

1. Half of the case studies (13 to 24) from India [9]
2. In India, school education is of 7+3+2 years. Plus two means last two years
3. Indian Administrative Services (IAS) in India is highest level of administrative services.
4. Husband of elder sister. When number of children of a couple is six or more. There is quite large difference between the age of younger and eldest sibling.
5. Cultural expectations of first generation migrant families.

Reference:

[1] Australian Bureau of Statistics (2013), *Education and Work*, National Client Services, n.d. Web. 10 Apr. 2013.

[2] John Mack and Walsh Barry, (2013*)*, "Study Finds More Girls Opting out of Maths and Science," Interview by Charis Palmer. *The Conversation*. N.p., 14 Feb.

[3] Kaspura, Andre (2013), "The Engineers Australia Survey of Working Environment and Engineering Careers, Rep. Australia: Policy and Public Relations, *Engineers Australia*. Web. 30 Apr.

[4]Fenton Susan Lee (2012), " The experience of Women Engineers in a male Dominated Profession and Their Life values – An Australian Perspective" paper presented at Regional Conference of INWES at Delhi, October 12-13.

Copyright © 2014 SciResPub.

ISSN 2278-7763

[5] Prabhuswamy, H. B. M. and Gudanty Raghvendra, (2011), Women in and Technical Education: A Statistical Analysis, Golden Research Thought, 01(06), 1-4.

[6] Sen, Amartya (1999), Development as Freedom, Anchor Books, A Division of Random House Inc, New York, 104- 107.

[7] Singh Seema (2012), "Are Women Engineers Discriminated" paper presented at the Regional Conference of INWES at Delhi, October 12-13.

[8] ---------- (2013), "Women in Engineering Education in India" (2013), Ravi Prakash Yadav (ed) Women Worker in Informal Sector, Aavishkar Publishers & Distributers, Jaipur, 115- 125.

[9] ---------- (2014), Self-restrain or Discrimination: Participation of Women Engineers in India", proceeding of 4th International Conference on Industrial Engineering and Operation Management which is scheduled between January 7 to 9' 2014 at Bali, Indonesia.

[10] World Bank (2012) World Development Indicators, World Bank, 2012. Web. 10 June 2012.

[11] UGC (2012), Higher Education in India at a Glance, University *Grants Commission* Publication, New Delhi, *UGC*. Web. 30 Apr. 2012.

IJOART

Copyright © 2014 SciResPub.